The structure and evolution of the northern Australian margin: Insights from the Papuan Fold and Thrust Belt, Papua New Guinea

Luke G. Mahoney

ORCID: 0000-0001-8515-4313

Submitted in total fulfilment of the requirements
of the degree of Doctor of Philosophy

April 2021

School of Earth Sciences,
The University of Melbourne

This thesis is dedicated to Papua New Guinea and its welcoming people.
Thank you for sharing your unique and beautiful part of the world with me.

(Photo: Lavani Valley, Hela Province)

Abstract

The Papuan Fold and Thrust Belt (PFTB) in Papua New Guinea (PNG), located on the leading edge of the northern Australian continental margin, has been subject to complex tectonism as a result of its location throughout much of the Cenozoic between the obliquely converging Australian and Pacific plates. The remoteness and inhospitable terrain characterising the PFTB make it one of the least well-known fold and thrust belts on Earth.

The architecture of the northern Australian continental margin has been affected by both extensional and compressional tectonic forces, which first formed, and subsequently deformed, the Papuan Basin in the period from the early Mesozoic through to the present-day. Defining the geology, structure and evolution of the PFTB and Papuan Basin is central to our understanding of the geological and tectonic evolution of the northern Australian margin.

In this thesis, a multidisciplinary approach is used to investigate the evolution of the PFTB, Papuan Basin and northern Australian continental margin. Field mapping and structural analysis within the remote Western Fold and Thrust Belt (WFTB) provide significantly improved constraints on the geology, structure and evolution of the fold belt. New geological constraints acquired over > 100 km of traverses suggest that the exposed Cenozoic Darai Limestone has very low shortening between ~ 12-22% yet structures in the Muller Range are elevated up to 7 km above regional. Structural work utilising regional-scale geological observations suggest that the inversion of pre-existing rift architecture on the northern Australian continental margin is the primary influence on the evolution of the area. The huge structural relief is produced by both tectonic inversion on deep-rooted normal faults and their linkage to the surface via triangle zones that form within the incompetent Mesozoic passive margin sedimentary sequence. Local- and regional-scale heterogeneities within the northern Australian continental margin, such as accommodation-zones and transfer structures are now expressed in the fold belt structure as discontinuities and cross-cutting structural features that are recognised throughout the PFTB.

The 2018 M_w 7.5 PNG Highlands earthquake and aftershock sequence has provided an unprecedented opportunity to observe and analyse the crustal processes that have ultimately controlled the evolution of the PFTB. Seismological, GPS and remote sensing data offer constraint on the complex nature and spatiotemporal distribution of crustal deformation during the event, revealing that the PFTB experienced up to 1.2 m of uplift and ground deformation over 7,500 km^2. Remarkable spatial and morphological similarities exist between the distribution of coseismic ground deformation associated with the event, and the less-inverted and uninverted extensional architecture that is well-constrained in the foreland across the Stable Platform. This suggests that the 2018 Highlands earthquake sequence was

related to tectonic inversion along a previously unidentified extensional fault system beneath the PFTB, indicating the northern Australian passive margin has had a primary control on the evolution of structural styles observed throughout the PFTB.

New low-temperature thermochronology data from extensive field surveys in the Muller Range were combined with legacy data in modern thermal history modelling tools to investigate the thermotectonic evolution of the WFTB and Papuan Basin. In particular, the Late Cretaceous to Oligocene history of the region is largely unknown due to the absence of a continuous stratigraphic record. Thermal history models based on these data suggest two major Cenozoic cooling episodes. The youngest, and best constrained, is clearly recorded in the stratigraphic record and relates to Neogene collision at the northern margin of the Australian continent. An older episode of comparable or greater magnitude occurred in the Eocene to Oligocene and may relate to the removal of 1,500-3,000 m of Late Cretaceous to Eocene stratigraphic section across the Muller Range prior to the widespread deposition of the shelfal Darai Limestone. It is suggested that extension along major faults beneath the Muller Range accommodated sedimentation from the Late Cretaceous to the Eocene, consistent with long-lived extensional structures observed in the foreland across the Stable Platform. The selective removal of this sequence across the Muller Range suggests it was uplifted in the Eocene to Oligocene, possibly in part facilitated by the inversion of extensional faults in the Muller Range area. This inversion is interpreted to have resulted from the Eocene to Oligocene collision of the expansive Sepik Terrane to the northwest of the PNG margin, an interpretation that has significant implications for the tectonic evolution of PNG and Southeast Asia.

The studies presented in this thesis provide several key insights that significant advance our understanding of the geological, structural and tectonic evolution of the PFTB, Papuan Basin and northern Australian margin. An ongoing theme relates to the complex interplay between spatial variations in the architecture of the margin and spatial and temporal variations in the compressional stress field associated with an evolving tectonic setting between the Australian and Pacific plates.

Table of Contents

Abstract ii
List of Figures vii
List of Tables ix
List of Acronyms and Abbreviations x
Declaration xii
Preface xiii
Acknowledgements xiv
Publications and conference abstracts xvii
Thesis outline xix

Chapter 1 Introduction 1

1.1. Thesis aims 4
References 5

Chapter 2 Complex fold and thrust belt structural styles: Examples from the Greater Juha area of the Papuan Fold and Thrust Belt, Papua New Guinea 7

Abstract 7
2.1. Introduction 8
2.2. Geological setting 10
2.2.1. Tectonic and stratigraphic framework 12
2.2.2. Structural styles 15
2.2.2.1. The Greater Juha area 17
2.2.2.2. Frontal structures 18
2.2.2.3. Eastern Muller Range 19
2.3. Methods 20
2.4. Geological and structural observations 23
2.4.1. Observed fault and fracture trends 26
2.4.2. Juha Anticline 27
2.4.3. Karius Ridge 27
2.4.4. Karius Plateau 29
2.4.5. Lavani Ridge 32
2.4.6. Lavani Valley 34
2.4.6.1. Emama Fault 34
2.4.6.2. Emama Backthrust 39
2.4.6.3. Lavani Backthrust 39
2.4.6.4. Arc-normal structures 40
2.4.6.5. Summary 42
2.4.7. Shortening analysis 43
2.5. Structural evolution of the Greater Juha area 44
2.5.1. 3D structural evolution of the Eastern Muller Range 48
2.5.1.1. Early Mesozoic extension 48
2.5.1.2. Cenozoic compression 50
2.6. Discussion 53
2.6.1. Controls on structural style 53
2.6.2. Arc-normal lineaments and structures 55
References 58
Supplementary material A2: Representative structural, strontium isotope and palynological data 65

Chapter 3 The 2018 M_w 7.5 Highlands earthquake in Papua New Guinea: Implications for structural style in an active fold and thrust belt 67

Abstract 67
3.1. Introduction 68
3.2. Tectonic and geological background 69
3.3. 2018 PNG Highlands earthquake sequence 75
3.3.1. Earthquake locations *78*
3.3.2. Crustal deformation *80*
3.3.2.1. Hides-Mananda zone *84*
3.3.2.2. Kutubu zone *86*
3.3.2.3. Lavani zone *88*
3.3.2.4. Moran zone *88*
3.3.2.5. Cecilia zone *89*
3.4. Discussion 91
3.4.1. Implications of seismicity and ground deformation for PFTB structural style *91*
3.4.2. Influence of crustal structure on earthquake-related stress release *98*
3.5. Conclusion 100
References 102
Supplementary material A3: GSI interferograms 109
Supplementary material B3: Figure 3.7. perspective view zoomed in version 113

Chapter 4 Late Cretaceous to Oligocene burial and collision in western Papua New Guinea: Indications from low-temperature thermochronology and thermal modelling 118

Abstract 118
4.1. Introduction 119
4.2. Geology 123
4.2.1. Early-middle Mesozoic *124*
4.2.2. Late Cretaceous to early Oligocene *125*
4.2.3. Middle Oligocene to early Miocene *128*
4.2.4. Middle-late Miocene to recent *128*
4.3. Sample acquisition and methodology 130
4.3.1. Low-temperature thermochronology *130*
4.4. Results 132
4.4.1. Apatite fission track results *133*
4.4.2. Apatite (U-Th-Sm)/He results *134*
4.4.3. Zircon (U-Th)/He results *136*
4.5. Thermal history reconstruction 137
4.5.1. Selection of samples for thermal modelling *140*
4.5.1.1. Sediment provenance *141*
4.5.2. Forward thermal history modelling approach *144*
4.5.3. Forward thermal history modelling results *145*
4.5.4. Inverse thermal history modelling approach *147*
4.5.4.1. Additional model constraints *149*
4.5.5. Inverse thermal history modelling results *150*
4.5.5.1. Western Muller Range *151*
4.5.5.2. South Strickland Gorge *152*
4.5.5.3. North Strickland Gorge *154*
4.5.5.4. Lavani Valley *155*
4.5.6. Summary: Muller Range T-t history *158*
4.6. Discussion 160
4.6.1. Regional thermal data *160*
4.6.2. Late Cretaceous to early Eocene heating *163*
4.6.3. Early Eocene to Oligocene cooling *167*
4.6.4. Late Miocene to recent *169*
4.7. Conclusion 171

References 173
Supplementary material A4: Methodology 183
Supplementary material B4: Existing AFT dataset 185
Supplementary material C4: AHe and ZHe age vs eU and Rs 185
Supplementary material D4: AFT data vs Dpar 187
Supplementary material E4: 50:50 split forward models 187
Supplementary material F4: Individual sample thermal history models 189

Chapter 5 Geological history of the northern Australian margin in the context of a regional cross-section through the Western Fold and Thrust Belt, Papua New Guinea 195

5.1. Late Palaeozoic to middle Miocene 197
5.1.1. Late Palaeozoic: New England Orogeny 198
5.1.2. Middle Triassic to Early Jurassic: Papuan Basin formation 200
5.1.3. Middle to Late Jurassic: Opening of the Sepik ocean basin 201
5.1.4. Late Jurassic to middle Cretaceous: Post-rift subsidence 202
5.1.5. Middle Cretaceous: Dynamic uplift 203
5.1.6. Late Cretaceous to Eocene: Coral Sea rifting and subsidence 207
5.1.7. Eocene to early Oligocene: Sepik Terrane collision 208
5.1.8. Oligocene to middle Miocene: Dynamic subsidence and impending Halmahera-Caroline Arc collision 212
5.2. Miocene to present 215
5.2.1. Middle to late Miocene: Halmahera-Caroline Arc collision (western collisions) 216
5.2.2. Early Pliocene to present: Halmahera-Caroline Arc collision (eastern collisions) 220
References 228
Supplementary material A5: Geological and tectonic evolution schematics 237

Chapter 6 Concluding remarks 243

6.1. Relationships between PFTB structural styles and the northern Australian continental margin . 243
6.1.1. Crustal and basement composition and fabric 243
6.1.2 Northern Australian margin/Papuan Basin structural architecture 245
6.1.3. Papuan Basin sediment thickness 246
6.2. Long-lived extension on the northern Australian continental margin 248
6.3. Multiple contractional episodes on the northern Australian margin 249
6.3.1. Sepik Terrane collision 249
6.3.2. Microplate kinematics and evolving compressional stresses 250
6.4. Future work 252
References 254

Appendix A 258

List of Figures

2.1. Tectonic components of New Guinea and the New Guinea Fold Belt 11
2.2. Schematic stratigraphy of the Papuan Fold and Thrust Belt 14
2.3. Location of key localities and data sources within the Greater Juha area 22
2.4. Geological map of the Greater Juha area 24-25
2.5. Photos showing the major structural components of the Greater Juha area 31
2.6. DEM and geological map of Lavani Valley and environs 33
2.7. Faulting within the Cretaceous Ieru Formation in Lavani Valley 37
2.8. Field photos and Schmidt stereonets showing lateral geological variation within Lavani Valley 38
2.9. Examples of outcrop-scale arc-normal structures in Lavani Valley 41
2.10. Proposed schematic structural evolution of the Greater Juha area 47
2.11. Model of the 3D evolution of the Eastern Muller Range 52
A2.1. Representative strike and dip data for the Greater Juha area 65
A2.2. Strontium isotope and palynological age constraints for the Greater Juha area 66
3.1. Tectonic, geological and structural setting of the 2018 PNG Highlands earthquake sequence 74
3.2. Photos showing the aftermath of the 2018 PNG Highlands earthquake sequence 78
3.3. GPS surface displacements, relocated earthquakes and surface rupturing interpreted from InSAR 83
3.4. Interpreted ascending interferograms with relocated earthquakes 83
3.5. Interpreted descending interferogram with relocated earthqaukes 86
3.6. Geological map vs interpreted composite ascending interferogram 91
3.7. Schematic perspective view of the Papuan Fold and Thrust Belt and Stable Platform, showing geological and geophysical observations pertinent to the 2018 PNG Highlands earthquake sequence 97
A3.1. Ascending interferogram with second observation + 21 hrs after mainshock 109
A3.2. Descending interferogram with second observation + 80 hrs after mainshock 110
A3.3. Composite ascending interferogram with second observations at + 14 days (east) and + 84 days (west) after mainshock 111
A3.4. SRTM-derived hillshade with relocated earthquakes and InSAR surface rupture interpretation 112
4.1. Tectonic-scale components of PNG 122
4.2. Sample localities and AFT data from the Muller Range, Western Fold and Thrust Belt 139
4.3. ZHe age vs eU plot showing increase in negative correlation with stratigraphic age 143
4.4. Forward models comprising two pre-depositional T-t paths – 80:20 rapid- vs slow-cooled grains 147
4.5. Thermal history modelling results for a pseudo-vertical profile in the Western Muller Range 152
4.6. Thermal history modelling results for a pseudo-vertical profile in the south Strickland Gorge 153
4.7. Thermal history modelling results for a pseudo-vertical profile in the north Strickland Gorge 155
4.8. Thermal history modelling results for a pseudo-vertical profile in the Lavani Valley 157
4.9. Combined thermal histories of 14 samples from the Muller Range 160
4.10. AFT age and mean track length for Ieru Formation samples across the Muller Range and Fly Platform 163
4.11. Proposed schematic evolution of the Eastern Muller Range 167
4.12. Drainage system and syn-orogenic depocentre distribution across the Fly Platform and frontal PFTB 171
C4.1. AHe age vs effective uranium concentration 185
C4.2. AHe age vs equivalent spherical radius 186
C4.3. ZHe age vs effective uranium concentration 186
C4.4. Uncorrected ZHe age vs equivalent spherical radius 187
D4.1. AFT single grain age and length vs Dpar for samples PY113-1929.5 and PY110-2171 187
E4.1. Forward models comprising two pre-depositional T-t paths – 50:50 rapid- vs slow-cooled grains 188
F4.1. Inverse thermal history modelling results for AFT data from eight Ieru Formation samples across the Muller Range 193
5.1. Tectonic and geological components of New Guinea and the New Guinea Fold Belt 196
5.2. Regional kinematic forward modelled cross-section A-A′ showing the geological evolution of the northern Australian margin from the late Palaeozoic to Miocene 204-205

5.2. Regional kinematic forward modelled cross-section A-A′ showing the geological evolution of the northern Australian margin from the late Palaeozoic to Miocene *204-205*
5.3. Schematic regional cross-section across the WFTB area of the northern Australian margin in the late Eocene, showing the nature of the Ieru Formation and possible extent of Late Cretaceous to Eocene strata *206*
5.4. Key features of the northern Australian margin during the Eocene to early Oligocene *211*
5.5. Key features of the northern Australian margin during the Oligocene to early Miocene *214*
5.6. Key features of the northern Australian margin during the early to middle Miocene *214*
5.7. Key features of the northern Australian margin during the middle Miocene *219*
5.8. Key features of the northern Australian margin during the middle to late Miocene *219*
5.9. Key features of the northern Australian margin during the Pliocene to present *222*
5.10. Regional kinematic forward modelled cross-section A-A′ showing the geological evolution of the northern Australian margin from the Miocene to Present *225-226*

List of Tables

Table 4.1. Rock sample location and descriptions *133*
Table 4.2. Muller Range apatite fission track (ICP-MS) data summary *134*
Table 4.3. Muller Range apatite (U-Th-Sm)/He data summary *135*
Table 4.4. Muller Range zircon (U-Th)/He data summary *138*
Table B4.1. Existing Muller Range apatite fission track dataset *185*

List of Acronyms and Abbreviations

General

AFT	Apatite fission track
AHe	Apatite (U-Th-Sm)/He thermochronology
AMSL	Above mean sea level
Ar-Ar	Argon-argon geochronology
DEM	Digital elevation model
eU	Effective uranium
GPS	Global positioning system
GSN	Global Seismograph Network
GSI	Geospatial Information Authority of Japan
InSAR	Interferometric synthetic aperture radar
ITRF	International Terrestrial Reference Frame
K-Ar	Potassium-argon geochronology
LOS	Line of sight
MaxT	Maximum post-depositional temperature
MCMC	Markov Chain Monte Carlo
MTL	Mean track length
M_w	Moment magnitude
NEIC	National Earthquake Information Centre
PAZ	Partial annealing zone
PRZ	Partial retention zone
SAR	Synthetic aperture radar
SRTM	Shuttle Radar Topography Mission
TLD	Track length distribution
TST	True stratigraphic thickness
U-Pb	Uranium-lead geochronology
USGS	United States Geological Survey
UTC	Coordinated universal time
VR	Vitrinite reflection
ZHe	Zircon (U-Th)/He thermochronology

List of Acronyms and Abbreviations (cont.)

Geographic

PNG	Papua New Guinea
- NGFB	New Guinea Fold Belt
- WPFTB	West Papuan Fold and Thrust Belt
- PFTB	Papuan Fold and Thrust Belt
- CFTB/KFTB	Central Fold and Thrust Belt/Kutubu Fold and Thrust Belt
- EFTB/AFTB	Eastern Fold and Thrust Belt/Aure Fold and Thrust Belt
- WFTB	Western Fold and Thrust Belt
- EMR	Eastern Muller Range
- WMR	Western Muller Range

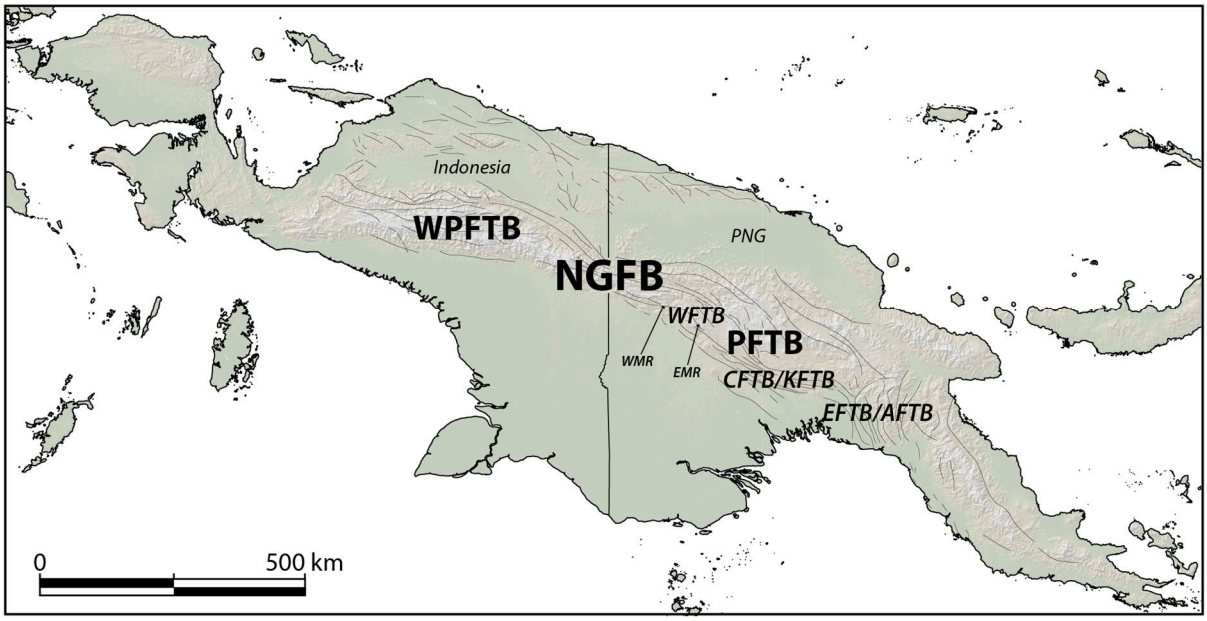

Declaration

This is to certify that:

i. The thesis comprises only my original work towards the PhD except where indicated in the Preface;
ii. due acknowledgement has been made in the text to all material used;
iii. the thesis is less than 100,000 words in length, excluding tables, maps, bibliographies and appendices.

Luke G. Mahoney

Preface

This thesis contains material that is published:

Mahoney, L., Stanaway, R., McLaren, S., Hill, K., Bergman, E., 2021. The 2018 M_w 7.5 Highlands earthquake in Papua New Guinea: Implications for structural style in an active fold and thrust belt. *Tectonics*, 40, pp.20. https://doi.org/10.1029/2020TC006667

Mahoney, L., McLaren, S., Hill, K., Kohn, B., Gallagher, K. and Norvick, M., 2019. Late Cretaceous to Oligocene burial and collision in western Papua New Guinea: Indications from low-temperature thermochronology and thermal modelling. *Tectonophysics*, 752, pp.81-112. https://doi.org/10.1016/j.tecto.2018.12.017

Mahoney, L., Hill, K., McLaren, S. and Hanani, A., 2017. Complex fold and thrust belt structural styles: Examples from the Greater Juha area of the Papuan Fold and Thrust Belt, Papua New Guinea. *Journal of Structural Geology*, 100, pp.98-119. https://doi.org/10.1016/j.jsg.2017.05.010

The published research papers are included within Appendix A of this thesis. The co-authors of these publications include the academic supervisors of this PhD from The University of Melbourne, Assoc. Prof. Sandra McLaren and Adj. Assoc. Prof. Kevin Hill, whose contributions were similar to those normally provided by advisors to a PhD Candidate including assistance with research direction and planning, logistical and financial support and feedback on written work. Dr. Richard Stanaway provided the GPS data presented in Chapter 3. Dr. Eric Bergman carried out the earthquake event relocation within Chapter 3. Prof. Barry Kohn, Dr. Ling Chung and Prof. Kerry Gallagher assisted with the data acquisition and thermal modelling in Chapter 4. The project execution, collection and interpretation of data and writing of the manuscripts was my own work.

Acknowledgements

First and foremost, I would like to thank the abundance of passionate and collaborative geoscientists with whom I have crossed paths over the years. While I cannot thank you all individually here, rest assured that your contributions to this thesis, and to my personal and professional development, are very much appreciated.

I would like to acknowledge my supervisors, Sandra McLaren and Kevin Hill, for their unwavering support and contributions to this thesis. I truly couldn't have asked for a better supervisory combo. Sandra, you have been a mentor and friend now for over a decade and I thank you a million times for the years of support, advice and knowledge sharing. I am continually inspired by your dedication to teaching and commitment to always put your students first. I immensely appreciate your support and encouragement to follow my interests and to pursue opportunities both within and outside of the academic community. Kevin, your enthusiasm and passion for geology is infectious and I thank you for making rocks—especially the folded and faulted variety—so damn interesting! I can't thank you enough for the knowledge that you have imparted to me and the opportunities that you have facilitated. To both Sandra and Kevin, I'm looking forward to continuing to collaborate with you into the future and I know that we will be good friends well beyond this thesis.

Thank you to the School of Earth Sciences at The University of Melbourne, particularly the Melbourne Thermochronology Lab and the Noble Gas Geochronology Research Group for supporting my research. Special thanks to Barry Kohn and Erin Matchan for patiently mentoring me within your respective fields of expertise. Thank you to Martin Norvick for showing an interest in my research and for sharing your extensive experience working within PNG. Thanks also to my office mates, coffee crew and the entire graduate cohort for the good times and

comradeship. A special thanks to Jackson McCaffrey for the friendship and for imparting some of his silky-smooth illustration/graphic design skills on me.

A collection of scientific colleagues outside of The University of Melbourne have also provided me with academic and professional support during my PhD candidature. I am grateful to the Basin GENESIS Hub community, particularly Luke Mondy, Sabin Zahirovic and Patrice Rey at EarthByte, for the countless hours of invaluable discussion and for mentoring me on geodynamic processes and modelling. You were all so welcoming during my visits to Sydney University and were never too busy to offer me a hand. I truly hope we can continue to collaborate into the future. To Kerry Gallagher at Géosciences Rennes, thank you for being so approachable and responsive while sharing your knowledge on thermochronology and thermal modelling. To Richard Stanaway, thank you for the invaluable insights into geodetics and for preparing me for remote PNG Fold Belt field work—I may not have made it back without you! To Hugh Davies, I am an admirer of your work and your commitment to PNG and its people. It is always a pleasure to speak with you and thank you for the assistance and feedback that you have provided me with over the years.

I am indebted to the PNG resources industry and its people for the support, encouragement and kindness that they have provided me over the years. First and foremost, this research would not have been possible without the sponsorship and support of Papuan Oil Search and I cannot overstate the opportunity that the organisation and its employees have provided me. I'm especially thankful for the mentorship and guidance that the PNG Exploration Team, both past and present, have given me over the years. To Nigel Wilson, Jeremy Iwanec, Keith Bradey, John Noonan, Steve Winn, Louise Sullivan, Pedro Restrepo, Marcus Parish, Patrick Haltmeier, Sam Algar, Mitch Furnass, Amanda Hanani, Brad Bailey, Scott Keenan, Scott Dyksterhuis and Julianne Lamb, thank you for all your support, discussion and encouragement. Melissia Craig, thanks for being my fellow suffering thesis-writing-

while-managing-full-time-work buddy. I'd also like to acknowledge the willingness to collaborate and friendly support offered to me by Oil Search's partner exploration teams at ExxonMobil and Santos. It is a pleasure to be surrounded by such bright and enthusiastic people. A big thank you to the team at Harmony Gold, particularly Dylan Jeffriess and Ben Rich, for facilitating my field visit to Kili Teke. Thanks also to Midland Valley (now PETEX) for providing me with access to the *Move* Suite software under the academic software licence initiative.

Last, but certainly not least, to Mum, Dad and Siobhan. Thank you for your unconditional support, encouragement, love and understanding. Mum and Dad, your work ethics, persistence, wisdom and positive attitudes are a constant source of inspiration and I thank you for imparting these traits to me. They have guided me through this thesis and will indeed accompany me through life. To my beautiful partner and best friend Siobhan, thank you for the unrelenting support, patience and understanding, particularly over the past few years while I've been finishing this thesis while working full-time. It's finally time to recapture our weekends.

Publications and conference abstracts

Mahoney, L., Stanaway, R., McLaren, S., Hill, K., Bergman, E., 2021. The 2018 M_w 7.5 Highlands earthquake in Papua New Guinea: Implications for structural style in an active fold and thrust belt. *In review: Tectonics.*

Mahoney, L., McLaren, S., Hill, K., Kohn, B., Gallagher, K. and Norvick, M., 2019. Late Cretaceous to Oligocene burial and collision in western Papua New Guinea: Indications from low-temperature thermochronology and thermal modelling. *Tectonophysics*, 752, pp.81-112.

Mahoney, L., Hill, K., McLaren, S. and Hanani, A., 2017. Complex fold and thrust belt structural styles: Examples from the Greater Juha area of the Papuan Fold and Thrust Belt, Papua New Guinea. *Journal of Structural Geology*, 100, pp.98-119.

Mahoney, L., Wilson, N., Restrepo, P., 2019. Papua New Guinea Exploration Workflows. *Proceedings of the 2019 South East Asia Petroleum Exploration Society (SEAPEX) Conference*, Singapore.

Mahoney, L., Hill, K., McLaren, S., 2017. Evolution of the North West Fold and Thrust Belt, Papua New Guinea: constraints from new data and multi-method structural modelling. *Geological Society of London, Fold and Thrust Belts: Structural Style, Evolution and Exploration Conference*, London, England.

Mahoney, L., Hill, K., McLaren, S., Hanani, A., 2017. Influence of Basin Architecture and Mechanical Stratigraphy on Structural Styles Within the Greater Juha Area of the Papuan Fold and Thrust Belt, Papua New Guinea. *AAPG/SEG International Conference and Exhibition 2017*, London, England.

Mahoney, L., Mclaren, S., Hill, K., 2015. Regional scale structural modelling along a geological transect: insights from the NW Fold and Thrust Belt, PNG. *Structural Geology and Tectonics Specialist Group (SGTSG) Conference 2015*, Caloundra, Australia.

Mahoney, L., Mclaren, S., Hill, K., 2015. Regional scale structural modelling along a geological transect across the NW Fold and Thrust Belt, PNG. *AAPG/SEG International Conference and Exhibition 2015*, Melbourne, Australia.

Co-authored

Hill, K., Mahoney, L., McLaren, S., 2020. Compressional Evolution of the PNG Margin; A Tale of Two Collisions. *The 1st AAPG/EAGE PNG Geosciences Conference, PNG's Oil and Gas Industry: Maturing Through Exploration and Production*, Port Moresby, Papua New Guinea.

Holm, R., Gold, D., White, L., Webb, M., Mahoney, L., McLaren, S., Heilbronn, K., Oesterle, J., Mizera, M., Saroa, D., Lunge, M., Webber, S., 2020. Provenance and Tectonics of the Allochthonous New Guinea Terranes: Implications for the Formation and Evolution of Regional Basins. *The 1st AAPG/EAGE PNG Geosciences Conference, PNG's Oil and Gas Industry: Maturing Through Exploration and Production*, Port Moresby, Papua New Guinea.

Ibrahim, Y., Rey, P., Mahoney, L., 2020. The Influence of Mechanical Stratigraphy on the Evolution of the Papua New Guinea Fold and Thrust Belt. *The 1st AAPG/EAGE PNG Geosciences Conference, PNG's Oil and Gas Industry: Maturing Through Exploration and Production*, Port Moresby, Papua New Guinea.

Kidu, J., Kendino, M., Restrepo-Pace, P., Mahoney, L., 2020. It all begins in the field and ends in the field: how we leverage our 90-year legacy to successfully explore in PNG. *The 1st AAPG/EAGE PNG Geosciences Conference, PNG's Oil and Gas Industry: Maturing Through Exploration and Production*, Port Moresby, Papua New Guinea.

Stanaway, R., Mahoney, L., Noonan, J., McLaren, S., 2020. Neotectonics of the Papuan Fold and Thrust Belt – insights from space geodetic analysis. *The 1st AAPG/EAGE PNG Geosciences Conference, PNG's Oil and Gas Industry: Maturing Through Exploration and Production*, Port Moresby, Papua New Guinea.

Szczepaniak, M., Bradey, K., Holland, D., Mahoney, L., 2020. Integrated PSDM Transect Modelling and Imaging across PNG. *The 1st AAPG/EAGE PNG Geosciences Conference, PNG's Oil and Gas Industry: Maturing Through Exploration and Production*, Port Moresby, Papua New Guinea.

Hill, K. and Mahoney, L., 2018. Compressional evolution of the PNG margin from an orogenic transect from Juha to the Sepik. *ASEG Extended Abstracts*, 2018(1), pp.1-3.

Thesis outline

This thesis contains an introductory chapter outlining key aspects of the literature relevant to the study, four main research chapters of which three have been published in international journals, and a concluding remarks chapter. The published chapters comprise an abstract, introduction, geological setting, methodology, results, discussion and conclusion and so there may be some minor repetition particularly within the introductory material. References and supplementary material are presented at the end of each chapter. The published versions of Chapters 2, 3 and 4 are included in Appendix A.

Chapter 1 provides a concise summary of our current state of knowledge of the tectonic and geological evolution of continental margins, fold and thrust belts and Papua New Guinea (PNG). This overview supplements much more comprehensive literature reviews provided within each of the three published chapters. This chapter also outlines the research questions and aims of this thesis.

Chapter 2 provides a detailed description and interpretation of the geological and structural evolution of the Greater Juha area in the Western Fold and Thrust Belt (WFTB) in PNG. This paper was based on observations made during more than three months of geological field work and mapping within areas of the WFTB that are so remote and inhospitable that there is very little previously published work. The new geological constraints were combined with legacy geological and geophysical data to characterise the 2D and 3D structural style and evolution of the area. This paper was published in the *Journal of Structural Geology* in July 2017.

Chapter 3 is a detailed geological, geophysical and geodetic study of the 2018 M_w 7.5 PNG Highlands earthquake in the Papuan Fold and Thrust Belt (PFTB) that occurred during my PhD candidature. This event provided an exceedingly rare opportunity to understand the processes impacting fold and thrust belt evolution and associated structural styles. This work uniquely links observations and interpretations made from the geological record with ongoing fold belt evolution.

Seismological, GPS and remote sensing data were interpreted and integrated in this chapter to examine the nature and spatiotemporal distribution of crustal deformation during the earthquake sequence. The insights were combined with existing geological knowledge of the region (Chapter 2) to define the factors impacting structural style and evolution of the PFTB. This study was published in *Tectonics* in April 2021.

Chapter 4 addresses significant gaps within the preserved stratigraphic record to investigate the poorly resolved Late Cretaceous to recent geological and tectonic evolution of the Papuan Basin and PFTB. In this paper, new rock samples collected during geological field work in the WFTB (Chapter 2) were analysed using low-temperature thermochronological techniques including apatite fission track, apatite (U-Th-Sm)/He and zircon (U-Th)/He. The new data were combined with existing data in modern thermal history modelling software to produce detailed thermal histories that have significant implications for the thermotectonic evolution of the northern Australian margin. This paper was published in *Tectonophysics* in February 2019.

Chapter 5 investigates the evolution of the WFTB and northern Australian margin using forward kinematic modelling along a regional cross-section which incorporates key geometric and temporal constraints from Chapters 2, 3 and 4. This chapter includes new work in the form of structural modelling but also provides a discussion of the geological and tectonic implications of the preceding chapters of the thesis. This chapter has been prepared as a standard thesis chapter.

In Chapter 6, I provide concluding remarks and discussion, integrating the different aspects of the research detailed in Chapters 2 to 5. Implications of this study are summarised together with a discussion of the remaining uncertainties and thoughts for future work.

Chapter 1
Introduction

The evolution of continental margins is generally complex, particularly within tectonic settings where the stress field can vary markedly both spatially and temporally. Preserved continental margins and present-day analogues reveal the complexities of continental rifting processes, with margin formation dependent on a range of factors including geodynamic context (e.g., Storey, 1995; Smallwood and White, 2002), tectonic and kinematic setting (e.g., Clifton *et al*., 2000; Wallace *et al*., 2005), crustal architecture and composition (e.g., Vauchez *et al*., 1997; Chorowicz, 2005). Deciphering margin geometry and evolution can be particularly challenging in complex tectonic regions (e.g., Southeast Asia) where continental margins have often experienced numerous tectonic events.

The stratigraphy and structure of sedimentary basins formed above tectonically (syn-rift) and thermally (post-rift) subsided rift margins commonly provide a valuable, but incomplete, record of margin evolution. Continental extension is often evidenced by changes in lithostratigraphy, reactivation of pre-existing rift architecture and/or deformation of overlying basin sediments. Continental compression commonly deforms the margin to produce a fold and thrust belt or can be more subtly indicated by unconformities in the stratigraphic section. Significant effort has been dedicated to understanding the styles of deformation (structural styles) within fold and thrust belts globally (e.g., Nemcok *et al*., 2005; Poblet and Lisle, 2011; Lacombe and Bellahsen, 2016). In the broadest sense, fold and thrust structures can be restricted to the typically weaker basin sediments (e.g., thin-skinned deformation), or may penetrate crystalline basement (thick-skinned deformation) as reactivated extensional structures (e.g., basin inversion), or as new thrust structures. Thus, fold and thrust belt structural styles result from a combination of the pre-compression margin architecture and an evolving

compressional stress field, and therefore provide a valuable record of continental margin evolution.

A particular focus of fold and thrust belt research relates to better understanding the distribution and occurrence of both natural hazards and resources (e.g., Groves *et al.*, 1998; Cooper, 2007; Stern *et al.*, 2016). The most frequent and damaging natural hazards within active contractional tectonic margins are volcanism and the occurrence of earthquakes; both have associated hazards including floods, tsunamis and landslides. In terms of resources, fold and thrust belts often host significant mineral and hydrocarbon wealth, but discovering these accumulations is challenging and often requires detailed understanding of the evolution and interplay of crustal geometry, pressure-temperature regimes and fluid migration.

The island of New Guinea, at the northern margin of the Australian continent, has arguably one of the most complex geological and tectonic histories in the world—largely the result of its long-term residence in the Australian and Pacific plate boundary zone. The Cenozoic assembly of New Guinea is particularly complex due to the involvement of several kinematically distinct microplates between the rapid obliquely converging Australian and Pacific plates (e.g., Tregoning *et al.*, 1998; Wallace *et al.*, 2004; Koulali *et al.*, 2015). Consequently, the present-day setting of New Guinea includes the full range of end-member tectonic processes from sea floor spreading to continent-continent collision (e.g., Baldwin *et al.*, 2012; Davies, 2012). The evolution of the northern margin of the Australian continent prior to and during the Cenozoic assembly of New Guinea has long been poorly understood with margin geometry and the timing of key events both associated with significant uncertainty (e.g., Hill and Hall, 2003; van Ufford and Cloos, 2005). Despite these unknowns, the geological history of this region is a key variable for understanding the tectonics of Southeast Asia and linking the Pacific and Tethyan tectonic domains.

Papua New Guinea (PNG) includes the eastern portion of the island of New Guinea together with a number of islands offshore to the east and north. The southern half of PNG comprises the northern Australian continental margin which experienced rifting in the early Mesozoic and was subsequently covered with sediments forming the Papuan Basin (e.g., Dow, 1977; Pigram and Panggabean, 1984; Home *et al*., 1990). The northern half of the island comprises a complex belt of rifted continental fragments and arc-derived terranes that have accreted to the margin throughout the Cenozoic (e.g., Pigram and Davies, 1987; Hill and Hall, 2003; Davies, 2012). These collisions have subsequently deformed the northern Australian margin, including sediments of the Papuan Basin, to create structurally complex fold and thrust belts that strike east-west to southeast-northwest across the centre of the island. These belts, collectively referred to as the Papuan Fold and Thrust Belt (PFTB), substantially mask the record of margin evolution and form rugged, inhospitable terrain that hinders the collection of geological, geophysical and geochronological data. This general paucity of data has meant that reconstruction of the complex geological and tectonic history of PNG and the northern Australian margin has been a significant challenge historically.

Yet such a significant fold and thrust belt as the PFTB has the potential to provide key new information for our understanding of fold and thrust belts globally. As such, the acquisition and interpretation of new data have immense value. The focus of this thesis has been on the acquisition and interpretation of new and existing data to better understand the geological and tectonic history of the PFTB and the northern Australian margin. The inhospitable terrain and inaccessibility of the PFTB makes access prohibitively expensive for stand-alone academic studies, and thus data acquisition during this thesis has been constrained by resource exploration operations in the region—which has required a high degree of flexibility and adaptability. As a result, I have taken an integrated, multidisciplinary approach to the range of research problems which this thesis addresses. In particular, I have

combined field geology and mapping, geological and geophysical interpretation, structural geology and modelling, remote sensing, seismology, geodetics, thermochronology and thermal modelling.

1.1. Thesis aims

The main aim of this thesis is to investigate the structure and evolution of the Papuan Fold and Thrust Belt (PFTB) and northern Australian margin by (1) defining the geology, structure and spatiotemporal development of the PFTB, with a particular focus on the remote and poorly understood Western Fold and Thrust Belt (WFTB), and (2) investigating significant unconformities within the stratigraphy of the Papuan Basin.

More specifically, the new data and associated studies presented within this thesis are aimed at addressing the following research questions:

- What structural styles exist within the WFTB, how did they evolve and how do they compare to better-constrained examples from neighbouring regions?
- What are the primary controls on spatial variations in structural style within the PFTB? What are the relative roles of thin-skinned and thick-skinned tectonics? How do these controls interact in space and time?
- How are significant variations in structural style accommodated laterally along the length of the PFTB?
- What was the geological and tectonic setting of the northern Australian margin over periods that are poorly recorded within the Papuan Basin stratigraphy?
- How many contractional events did the northern Australian margin experience throughout the Cenozoic? Did any earlier events have commonalities with, or an influence on, the subsequent evolution of the PFTB?

References

Baldwin, S.L., Fitzgerald, P.G., Webb, L.E., 2012. Tectonics of the New Guinea region. *Annual Review of Earth and Planetary Sciences*, 40, pp.495-520.

Chorowicz, J., 2005. The east African rift system. *Journal of African Earth Sciences*, 43(1-3), pp.379-410.

Clifton, A.E., Schlische, R.W., Withjack, M.O., Ackermann, R.V., 2000. Influence of rift obliquity on fault-population systematics: results of experimental clay models. *Journal of Structural Geology*, 22(10), pp.1491-1509.

Cooper, M., 2007. Structural style and hydrocarbon prospectivity in fold and thrust belts. In: Ries, A.C., Butler, R.W., Graham, R.H. (Eds.), *Deformation of the Continental Crust: The Legacy of Mike Coward*, Geological Society, London, Special Publications, 272, p.447-472.

Davies, H.L., 2012. The geology of New Guinea—the cordilleran margin of the Australian continent. *Episodes*, 35(1), pp.87-102.

Dow, D.B. 1977. A geological synthesis of Papua New Guinea. *Bureau of Mineral Resources Bulletin*, 201, 58 pp.

Groves, D.I., Goldfarb, R.J., Gebre-Mariam, M., Hagemann, S.G., Robert, F., 1998. Orogenic gold deposits: a proposed classification in the context of their crustal distribution and relationship to other gold deposit types. *Ore geology reviews*, 13(1-5), pp.7-27.

Hill, K.C., Hall, R., 2003. Mesozoic-Cenozoic evolution of Australia's New Guinea margin in a west Pacific context. *Geological Society of America*, Special Papers, 372, pp.265-290.

Home, P., Dalton, D., Brannan, J., 1990. Geological evolution of the Western Papuan Basin. In: Carman, G., Carman, Z. (Eds.), *Petroleum exploration, development, and production in Papua New Guinea: proceedings of the first PNG Petroleum Convention*, Papua New Guinea Chamber of Mines and Petroleum, Port Moresby, pp.107-118.

Koulali, A., Tregoning, P., McClusky, S., Stanaway, R., Wallace, L., Lister, G., 2015. New Insights into the present-day kinematics of the central and western Papua New Guinea from GPS. *Geophysical Journal International*, 202(2), pp.993-1004.

Lacombe, O., Bellahsen, N., 2016. Thick-skinned tectonics and basement-involved fold–thrust belts: insights from selected Cenozoic orogens. *Geological Magazine*, 153(5-6), pp.763-810.

Nemcok, M., Schamel, R., Gayer, R., 2005. Thrustbelts: Structural architecture, thermal regimes and petroleum systems. Cambridge University Press, 541 pp.

Pigram, C., Panggabean, H., 1984. Rifting of the northern margin of the Australian continent and the origin of some microcontinents in eastern Indonesia. *Tectonophysics*, 107, pp.331-353.

Pigram, C.J., Davies, H.L., 1987. Terranes and the accretion history of the New Guinea orogen. *BMR Journal of Australian Geology and Geophysics*, 10, pp.193-211.

Poblet, J., Lisle, R.J., 2011. Kinematic evolution and structural styles of fold-and-thrust belts. *Geological Society, London, Special Publications*, 349(1), pp.1-24.

Smallwood, J.R., White, R.S., 2002. Ridge-plume interaction in the North Atlantic and its influence on continental breakup and seafloor spreading. *Geological Society, London, Special Publications*, 197(1), pp.15-37.

Stern, R.J., Scholl, D.W. and Fryer, G., 2016. An introduction to convergent margins and their natural hazards. In: Duarte, J.C., Schellart, W.P. (Eds.), *Plate Boundaries and Natural Hazards*, pp.77-98.

Storey, B.C., 1995. The role of mantle plumes in continental breakup: case histories from Gondwanaland. *Nature*, 377, pp.301-308.

Tregoning, P., Lambeck, K., Stolz, A., Morgan, P., McClusky, S.C., van der Beek, P., McQueen, H., Jackson, R.J., Little, R.P., Laing, A., Murphy, B., 1998. Estimation of current plate motions in Papua New Guinea from Global Positioning System observations. *Journal of Geophysical Research: Solid Earth*, 103(B6), pp.12181-12203.

van Ufford, A.Q., Cloos, M., 2005. Cenozoic tectonics of New Guinea. *The American Association of Petroleum Geologists Bulletin*, 89(1), pp.119-140.

Vauchez, A., Barruol, G., Tommasi, A., 1997. Why do continents break-up parallel to ancient orogenic belts?. *Terra Nova*, 9(2), pp.62-66.

Wallace, L.M., Stevens, C., Silver, E., McCaffrey, R., Loratung, W., Hasiata, S., Stanaway, R., Curley, R., Rosa, R., Taugaloidi, J., 2004. GPS and seismological constraints on active tectonics and arc-continent collision in Papua New Guinea: Implications for mechanics of microplate rotations in a plate boundary zone. *Journal of Geophysical Research: Solid Earth*, 109, B05404.

Wallace, L.M., McCaffrey, R., Beavan, J., Ellis, S., 2005. Rapid microplate rotations and backarc rifting at the transition between collision and subduction. *Geology*, 33(11), pp.857-860.

Chapter 2

Complex fold and thrust belt structural styles: Examples from the Greater Juha area of the Papuan Fold and Thrust Belt, Papua New Guinea

Abstract

The remote and inhospitable Papuan Fold and Thrust Belt in Papua New Guinea is one of the youngest yet least well-documented fold and thrust belts on Earth. Within the frontal Greater Juha area we have carried out > 100 km of geological traverses and associated analyses that have added significantly to the contemporary geological and geophysical dataset. Our structural analysis provides evidence of major inversion, detachment and triangle zone faults within the uplifted Eastern Muller Range. We have used the dataset to develop a quasi-3D model for the Greater Juha area, with associated cross-sections revealing that the exposed Cenozoic Darai Limestone is well-constrained with very low shortening of 12.6-21.4% yet structures are elevated up to 7 km above regional. We suggest the inversion of pre-existing rift architecture is the primary influence on the evolution of the area and that structures link to the surface via triangle zones and detachment faults within the incompetent Mesozoic passive margin sedimentary sequence underlying competent Darai Limestone. Arc-normal oriented structures, dominantly oblique dextral, up-to-the-southeast, are pervasive across a range of scales and are here interpreted to relate at depth to weakened pre-existing basement cross-structures. It is proposed that Palaeozoic basement fabric controlled the structural framework of the basin during early Mesozoic rifting forming regional-scale accommodation zones and related local-scale transfer structures that are now expressed as regional-scale arc-normal lineaments and local-scale arc-normal structures, respectively. Transfer structures, including complexly breached relay ramps, utilise northeast-southwest striking weaknesses associated with the basement fabric, as a mechanism for accommodating displacement along major northwest-southeast striking normal faults. These structures have subsequently been inverted to form arc-normal oriented zones of tear faulting that accommodate laterally variable displacement along inversion faults and connected thrust structures.

2.1. Introduction

Globally, there has been significant effort to document structural styles within fold and thrust belts, revealing often complex relationships between basin evolution and the subsequent style of deformation during compression. Early basin extensional architecture and mechanical stratigraphy appear to be key controls on the subsequent evolution of both thick- and thin-skinned compressional deformation. But modern rift and rifted-margin structural analogues show that extensional architecture is often remarkably complex (e.g., East African Rift: Morley *et al.*, 1990; Chorowicz, 2005; North West Shelf, Australia: Longley *et al.*, 2002; Frankowicz and Clay, 2010) and a wide range of factors impact inversion geometry and style (e.g., Buchanan and Buchanan, 1995; Bonini *et al.*, 2012). Additionally, compression may occur in the presence of an evolving stress field associated with far- and near-field tectonism (e.g., Saintot and Angelier, 2002) or syn-orogenic sedimentation (e.g., Storti and McClay, 1995). For these reasons the relative influence of extension-related architecture and compression-related influences can be difficult to demonstrate, particularly where robust constraints on subsurface geometry are absent.

The Papuan Fold and Thrust Belt (PFTB) of Papua New Guinea (PNG) is located on the northern margin of the Australian plate (Fig. 2.1a) and has significant demonstrated mineral and hydrocarbon wealth. Yet the PFTB remains poorly understood geologically, due largely to its isolation and its complex tectonic history. As such, it has the potential to provide significant new insights into our understanding of fold belts globally.

Over the past few decades, the accessibility and affordability of aviation-based exploration as well as new specialized methods of data acquisition (e.g., Hornafius and Denison, 1993; Hill *et al.*, 1996) have significantly improved our understanding of the local-scale structure of the PFTB. Indeed the PFTB is currently

being actively explored for hydrocarbons and minerals involving drilling and the acquisition of widely-spaced 2D seismic data which substantially constrain geological models. Moreover, recent and ongoing tectonism in the PFTB means that present-day convergence vectors (e.g., Wallace *et al.,* 2004; Koulali *et al*., 2015; Stanaway and Noonan, 2015), earthquake solutions (e.g., Abers and McCaffrey, 1988; Ekström *et al.,* 2012) and contemporary landforms can aid structural and tectonic models.

Significant variations in structural style have been recognised across the PFTB, often related to pre-compression margin architecture (e.g., Hill, 1991; Buchanan and Warburton, 1996; Hill *et al.*, 2010). However the majority of studies are based on cross-sections and do not explain how along strike structural variations are accommodated. In particular, our understanding of the structure of the PFTB decreases significantly to the west of the extensively explored hydrocarbon-bearing frontal structures in the Kutubu Fold and Thrust Belt (KFTB) (Fig. 2.1b). The remote neighbouring Western Fold and Thrust Belt (WFTB) is characterised by a contrasting set of structural styles to that of the KFTB. Most obviously, it is characterised by comparatively higher surface elevations and broader structural wavelengths (Fig. 2.1b). Within the WFTB region, the Greater Juha area (Fig. 2.1c) is contiguous with the PFTB frontal hydrocarbon trend and is thus a highly prospective area undergoing active exploration. Indeed, the Juha Anticline and the Hides Anticline, 30 km further east, both contain large gas fields (Fig. 2.1c).

Here, new geological field observations together with legacy data have been used to construct cross-sections and a detailed geological map to document and understand structural styles within the Greater Juha area of the WFTB. Our contemporary dataset reveals a complex interplay of pre-compression rift architecture, mechanical stratigraphy and compressive stresses on the spatiotemporal evolution of the Greater Juha area.

2.2. Geological setting

The geological evolution of New Guinea is complex and much debated, with a number of key tectonic events having had significant influence on the rock record. At present, the island of New Guinea comprises three major tectonic provinces (after Hill and Hall, 2003): (1) the Stable Platform to the south, (2) the Mobile Belt to the north, and (3) the central New Guinea Fold Belt (NGFB) (Fig. 2.1a). The Stable Platform is the northern edge of the relatively undeformed Australian continent while the Mobile Belt comprises island arcs and microcontinents accreted to the leading edge of the Australian plate during the Cenozoic (e.g., Hill and Raza, 1999). The NGFB separates the Stable Platform and Mobile Belt and formed predominantly within sediments of the Australian continental margin during the late Miocene to Pliocene (Hill and Gleadow, 1989).

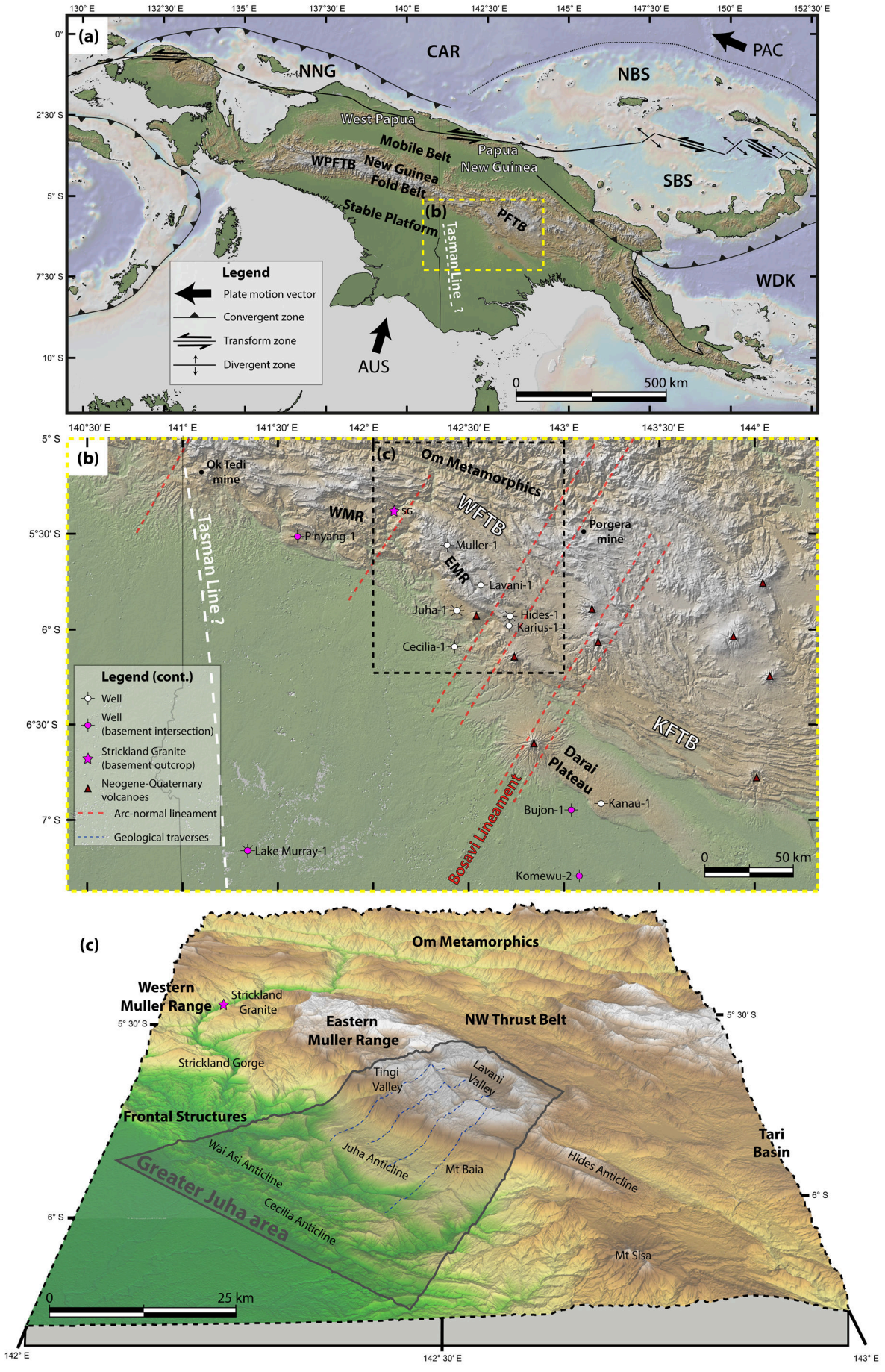
(a)
CAR
PAC
NNG
NBS
West Papua
Mobile Belt
Papua New Guinea
WPFTB
New Guinea Fold Belt
SBS
Stable Platform
(b)
PFTB
Tasman Line ?
WDK
AUS
Legend
Plate motion vector
Convergent zone
Transform zone
Divergent zone
0
500 km
(b)
(c)
Om Metamorphics
Ok Tedi mine
WMR
SG
WFTB
P'nyang-1
Muller-1
Porgera mine
EMR
Lavani-1
Juha-1
Hides-1
Karius-1
Cecilia-1
KFTB
Darai Plateau
Bujon-1
Kanau-1
Bosavi Lineament
Lake Murray-1
Komewu-2
Legend (cont.)
Well
Well (basement intersection)
Strickland Granite (basement outcrop)
Neogene-Quaternary volcanoes
Arc-normal lineament
Geological traverses
0
50 km
(c)
Om Metamorphics
Western Muller Range
Strickland Granite
Eastern Muller Range
NW Thrust Belt
Strickland Gorge
Tingi Valley
Lavani Valley
Frontal Structures
Tari Basin
Wai Asi Anticline
Juha Anticline
Mt Baia
Hides Anticline
Greater Juha area
Cecilia Anticline
Mt Sisa
0
25 km

Figure 2.1. *(previous page) (a) Tectonic components of New Guinea and the New Guinea Fold Belt. Tectonic elements modified from Hill and Hall (2003) and Baldwin et al. (2012). Trajectory of Tasman Line based on extent of Palaeozoic basement in outcrop and wells (see Figure 2.1b). AUS, Australian plate; CAR, Caroline microplate; NBS, North Bismarck plate; NNG; Northern New Guinea block; PAC, Pacific plate; PFTB, Papuan Fold and Thrust Belt; SBS, South Bismarck plate; WDK, Woodlark microplate; WPFTB, West Papuan Fold and Thrust Belt. Yellow box indicates the location of Figure 2.1b. (b) Structural elements of the PFTB including arc-normal lineaments and locations of late Palaeozoic-early Mesozoic basement within the Strickland Gorge and wells across the foreland and PFTB. Arc-normal lineaments based on Hill (1991) and Hill et al. (2000, 2002). EMR, Eastern Muller Range; KFTB, Kutubu Fold and Thrust Belt; WFTB, Western Fold and Thrust Belt; SG, Strickland Granite; WMR, Western Muller Range. Black dashed box indicates location of Figure 2.1c. (c) Structural elements of the WFTB, including the boundaries of the Greater Juha area which is the focus of this study. SRTM digital elevation model retrieved from USGS (2015).*

2.2.1. Tectonic and stratigraphic framework

The rock record of New Guinea (Fig. 2.2) reveals a complex geological evolution for the northern margin of the Australian continent, which is summarised briefly here. Further details and tectonic history reconstructions for New Guinea are given in Pigram and Symonds (1991), Hill and Raza (1999), Hill and Hall (2003) and Baldwin *et al.* (2012) and for Southeast Asia by Hall (1996, 1997, 2002, 2012), Metcalfe (2002) and Zahirovic *et al.* (2014, 2016).

Limited basement outcrop and well intersections suggest late Permian and Early Triassic metasediments and volcanics, and Middle to Late Triassic granites underlie most of the PFTB and the Stable Platform within PNG (Fig. 2.1b). The overlying Mesozoic stratigraphic sequence was subsequently attributed to the tectonic stages of rift-drift sequences and facilitated early ideas for early Mesozoic rifting on the New Guinea margin (e.g., Pigram and Panggabean, 1984). Northwest-southeast and WNW-ESE oriented grabens filled with early Mesozoic syn-rift sediments (Fig. 2.2) and associated normal faults have been suspected to underlie the PFTB (e.g., Hill, 1991) and have been identified across adjacent foreland regions (e.g., Home *et al.*, 1990; Kawagle and Meyers, 1996; Schofield, 2000). The cessation of

rifting in the Middle Jurassic was recorded throughout the Papuan Basin as a thick, widespread post-rift sequence dominated by fine-grained clastic sediments including the Jurassic Imburu mudstone and Cretaceous Ieru Formation (Fig. 2.2). During the early post-rift phase a number of prograding sandstone sequences were deposited, including the Early Cretaceous Toro Sandstone and Middle to Late Jurassic Koi Iange Sandstone (Fig. 2.2). Several of these sandstones host the main hydrocarbon accumulations in the PFTB. The Late Cretaceous to Palaeogene history of the Papuan Basin is largely unknown with a prominent top Ieru Formation unconformity located across most of southern PNG (Fig. 2.2). Subsequent subsidence during the late Oligocene to early Miocene accommodated the deposition of 1-2 km of Darai Limestone (Fig. 2.2) in southern New Guinea, building the Cenozoic platform.

Compression within the Mobile Belt began during the middle to late Miocene (14-12 Ma) and within the NGFB in the late Miocene to Pliocene (5-4 Ma) (Hill and Gleadow, 1989; Hill and Raza, 1999). The dominant orientation for compression-related structures throughout the PFTB reflects northeast-southwest compression, with an increasingly large sinistral strike-slip component recognised northwards in the Mobile Belt (e.g., Pigott *et al.*, 1985; Crowhurst *et al.*, 1997), related to east-west compressive stresses from the ongoing collision with the Finisterre Arc terrane (Hill and Raza, 1999). Contemporary seismicity suggests the PFTB is still undergoing compressive deformation with focal mechanisms suggesting northeast-southwest directed convergence (Ekström *et al.*, 2012). In fact, GPS plate velocities suggest that the PFTB may be accommodating up to 15 mm of convergence between the New Guinea Highlands (Mobile Belt) and Australian plate (Stable Platform) annually (Wallace *et al.*, 2004; Koulali *et al.*, 2015; Stanaway and Noonan, 2015).

In the late Miocene, crustal flexure associated with plate collision and Mobile Belt uplift resulted in the formation of foreland basins to the south and southwest of the Papuan Highlands (e.g., Davies, 1983). This prompted the deposition of variably

thick late Miocene to present, shallow marine to non-marine syn-orogenic sediments. The onset of late Miocene uplift is recorded by the deposition of calcareous clastics and reworked limestone fragments in the Orubadi Formation (Fig. 2.2) (Home *et al.*, 1990). In the Pliocene, the progression of uplift and erosion in the highlands, along with contemporary volcanism, contributed to the deposition of the thick non-marine Era and Strickland formations in the southwest of the PFTB (Fig. 2.2) (Davies, 1983; Home *et al.*, 1990).

Prominent stratovolcanoes and associated intrusions throughout PNG are, in general, poorly understood. Potassium-argon (K-Ar) data suggests that volcanism in the Papuan Highlands had begun by at least the middle Miocene (Page, 1976). However, the majority of the prominent stratovolcanoes and associated intrusions within the PFTB and on the Stable Platform formed during the Pliocene to Pleistocene (Webb, 1973; Loffler *et al.*, 1979).

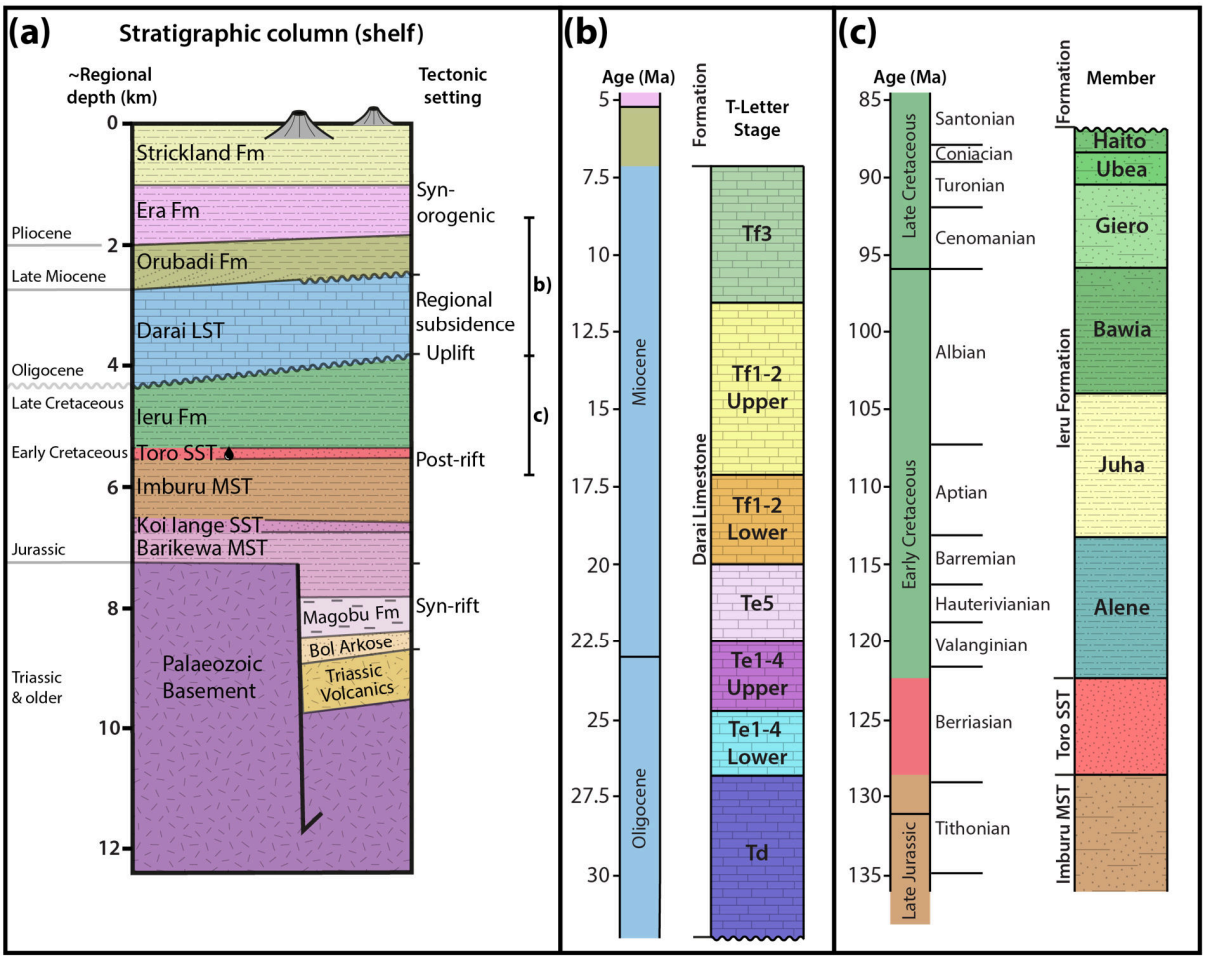

***Figure* 2.2.** *(previous page) Schematic stratigraphy of the Papuan Basin and Papuan Fold and Thrust Belt (a) true stratigraphic thicknesses (TSTs) estimated from seismic and well data across the foreland of the Greater Juha area; (b) subdivision of the Darai Limestone into T-Letter stages (following Lunt and Allen, 2004) as used here; (c) subdivision of the Ieru Formation (following Bradley, 2014) as used here. Note the thickness of syn-orogenic sediments is based on foreland thicknesses and compaction modelling from the Juha Anticline (Hanani et al., 2016); thickness and extent across the EMR is unknown due to Pliocene to Pleistocene uplift and erosion.*

2.2.2. Structural styles

The NGFB is characterised by variations in structural style along its length from the wide Kutubu Fold and Thrust Belt (KFTB) to the comparatively narrow, highly elevated West Papuan Fold and Thrust Belt (WPFTB) (Fig. 2.1a). Structural variations on the scale of the entire NGFB are most commonly attributed to the transition from hot, weak late Palaeozoic lithosphere in the east, to cold, strong Proterozoic lithosphere in the west, apparently coincident with the Tasman Line (Hill and Hall, 2003).

Diverse structural styles within the PFTB have previously been attributed to the relative role of thin- and thick-skinned tectonics (e.g., Hill *et al.,* 2000; Hill *et al.*, 2010). Structures observed at the surface within Darai Limestone are commonly detached within thick, incompetent underlying sediments. For instance, Hill *et al.* (2010) recognised multiple major detachment levels across the KFTB including within the Ieru Formation and Imburu/Barikewa Mudstones. Basement-involved faulting within the PFTB has often been related to the inversion of early Mesozoic extensional architecture such as grabens and half-grabens (e.g., Hill, 1991; Buchanan and Warburton, 1996). Well control to the north and south of the 40 km wide, 100 km long Darai Plateau to the southwest of the KFTB (Fig. 2.1b), make it the best documented inversion structure. An abrupt northward increase in sedimentary thickness from 2.2 km to 4.8 km across the frontal Darai Fault led Hill *et al.* (2010) to suggest it was originally a major, long-lived basin-bounding fault. Similar, largely

uninverted examples of basement extension structures have also been recognised in reflection seismic to the foreland of the KFTB (Schofield, 2000; McConachie *et al*., 2000) and across the foreland region directly to the southwest of the WFTB (Kawagle and Meyers, 1996; Bennett *et al*., 2000).

Regional northeast-southwest (arc-normal) lineaments cross-cutting the PFTB have long been recognised in both geological and geophysical datasets, commonly from distinct lateral changes in structural style and/or sublinear arrangements of volcanoes. The most prominent example is the approximately northeast-southwest trending Bosavi Lineament (Fig. 2.1b; e.g., Hill, 1989; Smith, 1990; Hill *et al*., 2008). The Bosavi Lineament marks the transition from the KFTB oil province to the WFTB gas province (e.g., Hill *et al*., 2008) and is characterised by a zone of structural disruption and an abundance of Pliocene to Pleistocene volcanoes. The structure appears to offset the KFTB and WFTB dextrally (Fig. 2.1b; Osborne, 1990), consistent with 3D numerical models that suggest arc-normal oriented weaknesses would be prone to oblique dextral, up-to-the-southeast offset during northeast-southwest compression (Gow *et al*., 2002).

Over the last few decades, other regional-scale northeast-southwest trending lineaments have been recognised in the NGFB, often related to the emplacement of New Guinea's mineralised intrusive bodies (e.g., Davies, 1991; Corbett, 1994; Mason, 1994; Hill *et al*., 2002; White *et al*., 2014). Lineaments recognised in West Papua have been linked to a similar northeast-southwest fabric within Proterozoic and Palaeozoic basement in northern Australia (Hill *et al.,* 1996). Recent work by White *et al.* (2014) using a range of geophysical data showed that the lineaments were most prominent in lower resolution data that imaged deeper in the crust (e.g., gravity and tomography), but were much less prevalent and much more complex than previously mapped. Arc-normal lineaments are most commonly related to the compressional reactivation of regional-scale lateral ramps, with local zones of dilatation linked to the intrusion of magmatic fluids (e.g., Hill, 1991; Hill *et al.,* 2002).

In addition to regional-scale lineaments, local-scale arc-normal structures have also been identified throughout the PFTB. In contrast to past studies, and to avoid ambiguity, we have chosen to differentiate arc-normal lineaments observed in regional-scale datasets from arc-normal structures observed in local-scale datasets, noting that the relationship between regional arc-normal lineaments and arc-normal structures is largely unknown. Geological and geophysical data suggest steeply-dipping arc-normal structures are abundant across the PFTB, most commonly recognised in basement structure and as tear faults within the sedimentary sequence (e.g., Hill, 1989; Hill *et al.,* 2008; Craig and Warvakai, 2009).

2.2.2.1. The Greater Juha area

The structurally complex Greater Juha area is located in the frontal trend of the WFTB where the dominant structural trend is northwest-southeast, connecting the WNW-ESE trends of the neighbouring KFTB and westernmost WFTB (Fig. 2.1b). The overall deformational style of the Greater Juha area appears transitional between the low-relief, dominantly thin-skinned style of the KFTB (e.g., Hill *et al.,* 2010) and the higher-relief, dominantly thick-skinned style of the westernmost WFTB (e.g., Eisenberg, 1996). The Greater Juha area is dominated by the Eastern Muller Range (EMR), which combined with the Western Muller Range (WMR) defines a large ~ 25 km wide uplifted region extending westward > 150 km to near the West Papua border (Fig. 2.1b). The rest of the Greater Juha area, as defined here, lies to the southwest of the EMR and comprises the ~ 15 km wide and ~ 25 km long Juha Anticline and much smaller < 5 km wavelength structures including the Wai Asi and Cecilia Anticlines (Fig. 2.1c). The Pliocene to Pleistocene syn-orogenic sediments are well-preserved across this frontal region where they are clearly co-planar with the underlying Darai Limestone. The extent and thickness of syn-orogenic sediments across the EMR prior to uplift and erosion is largely unconstrained.

2.2.2.2. Frontal structures

Despite considerable resource exploration throughout the frontal structures of the Greater Juha area, published geological and geophysical data are limited (e.g., Davies and Norvick, 1974; Craig and Warvakai, 2009; Hanani *et al*., 2016). The Cecilia Anticline demonstrates the forelandward extent of Cenozoic compression-related structures within the WFTB. It has been tested by a single well, Cecilia-1 (Fig. 2.3), which intersected the Cecilia Thrust and an associated Darai Limestone repeat, subsequently failing to reach the Early Cretaceous Toro Sandstone reservoir target (Texaco, 1971). In contrast, the nearby Juha Anticline has a long history of exploration following the discovery of a significant gas column in the Juha-1 well (Fig. 2.3) (Niugini Gulf Oil, 1983). Good geological and geophysical data coverage reveals the doubly plunging nature and lobate morphology of the wide Juha Anticline (Fig. 2.1c), but the subsurface geometry of the structure remains poorly constrained. Both thin-skinned (e.g., Hobson, 1986; Hill, 1989) and thick-skinned (e.g., Hanani *et al*., 2016) structural models have been proposed.

Regional seismic data have significantly improved our understanding of frontal structures across the Greater Juha area (Fig. 2.3). Initial seismic interpretations by Craig and Warvakai (2009) identified a common sub-Darai Limestone detachment for the Cecilia, Wai Asi and Strickland Anticlines (see Fig. 2.4a for structure locations), but made no attempt to interpret the deep structure. Subsequent geophysical interpretation and kinematic modelling of the frontal structure by Hanani *et al*. (2016) suggests an inverted graben-bounding basement fault beneath the wide Juha Anticline that shallows into a detachment horizon within the Jurassic sedimentary sequence, before eventually connecting to the Cecilia and Wai Asi Anticlines through triangle zones within the Ieru Formation.

2.2.2.3. Eastern Muller Range

In the Greater Juha area, the EMR is dominated by the Lavani Anticline and its eroded core, the Lavani Valley (Fig. 2.1c). The Lavani Valley is unique, characterised by Late Jurassic to Late Cretaceous sediments cropping out > 2.5 km above mean sea level (AMSL), suggesting uplift of > 7 km relative to regional depth in the foreland. Several seismic lines and gravity data were acquired during the Lavani Valley Seismic Survey in 1974, prior to drilling of the dry Lavani-1 well (Amoco, 1982). The generally poor-quality seismic and gravity data revealed (1) a large down-to-the-east basement-involved fault beneath the northwest end of Lavani Valley (LAV-74-06; Fig. 2.3), (2) a corresponding eastward decrease in gravity, and (3) a positive gravity anomaly directly to the southwest of Lavani Valley (Bidstone *et al.*, 1974). The Lavani-1 well spudded within Toro Sandstone near the centre of the Lavani Valley (Fig. 2.3) and initial interpretations of the well included a major northeast-dipping reverse or thrust fault at ~ 500 m repeating the Toro Sandstone section (Amoco, 1982). However, improved palynological dating and stratigraphic understanding has since revealed a Koi-Iange repeat overlying a ~ 1.8 km thick sequence of syn-rift sediments of the Magobu Formation (Denison, 1990). Although thrust repeats may have contributed to the thickening of the Magobu Formation within the Lavani-1 well, they are unlikely to be solely responsible for the observed thickness. The dry Muller-1 well (Mobil, 1991), located to the northwest of the Greater Juha area (Fig. 2.1b) on the northwest plunging nose of the Lavani Anticline, is the only other well in the EMR. It spudded in basal Darai Limestone and drilled a conformable sequence intersecting the Toro Sandstone reservoir at 1.8 km downhole depth (Mobil, 1991).

The evolution of the EMR is poorly understood, with previous workers proposing a range of models to explain uplift, including (1) basement-involved thrusting and inversion (e.g., Jenkins, 1974; Davies, 1983), (2) thin-skinned deformation (Hobson, 1986), (3) blind thrusting/passive-backthrusting (Buchanan and Warburton, 1996), (4) a basement-cored triangle zone (Hill, 1989), and (5)

igneous underplating (Buchanan and Warburton, 1996). Basement-involved thrusting is generally favoured due to the large positive gravity anomaly associated with the EMR (Bidstone *et al.*, 1974) and the discovery of Triassic (222 ± 4 Ma from K-Ar; Page, 1976) granite basement in the Strickland Gorge in the core of the Muller Range (Fig. 2.1c) (Jenkins and White, 1970; White and Marfleet, 1973). Interestingly, in contrast to the ~ 1.8 km of syn-rift sediment intersected in the Lavani-1 well, syn-rift sediments are absent in the Strickland Gorge with the Strickland Granite directly overlain by ~ 1.2 km of Jurassic post-rift sediments (Niugini Gulf Oil, 1983).

2.3. Methods

We present new data and models for the structure of the Greater Juha area based on new field observations and reinterpretations of the legacy dataset. Field access to the remote Greater Juha area was facilitated through a program of data acquisition carried out along > 100 km of traverses (Fig. 2.3) by Papuan Oil Search and ExxonMobil from 2013 to 2015. Very high rainfall upwards of 5,000 mm per annum is common across the frontal mountain range of the PFTB and has created a heavily karstified landform. Furthermore, steep terrain is prone to slumping and landslides that complicate the surface geology. Outcrop is limited (e.g., Fig. 2.5) due to thick vegetation, so geological data collection is challenging and the quality of field data can be variable.

Field work included the description of lithologies, macrofossil assemblages and sedimentary structures (way-up) along with the measurement of ~ 1,300 bedding, fault and fracture orientations (Fig. 2.3, inset). In addition, 157 Darai Limestone samples were collected for petrographic, biostratigraphic and $^{87}Sr/^{86}Sr$ analysis. Strontium isotope ratios were related to larger benthic foraminiferal T-Letter stages widely used in the Indo-Pacific (e.g., Lunt and Allen, 2004) and calibrated to the geological timescale by strontium isotope stratigraphy through the Papuan Basin in ongoing CSIRO research (Fig. 2.2b) (e.g., Allan *et al.*, 2000). An

additional 19 Mesozoic clastic samples were dated palynologically. Data obtained during this study were added to legacy data to form a contemporary database across the Greater Juha area comprising ~ 4,800 outcrops with both lithological descriptions and structural measurements. Of these ~ 1,300 outcrop samples were successfully dated using strontium isotope or palynological analyses (Fig. 2.3, inset). Legacy datasets are available in reports to the Papua New Guinea Government.

We also make extensive use of NASA Shuttle Radar Topography Mission (SRTM) data, sampled at 1 arc-second, or ~ 30 m resolution (USGS, 2015). Midland Valley's Move software suite was used for cross-section and map construction. Cross-sections were constructed perpendicular to strike and spaced in order to best represent lateral structural variations and to optimally utilise the available data. Seismic data within the PFTB are generally of poor to moderate quality, and thus the constraint on structure at depth is limited. In particular, data constraints drop off significantly below the top of the Ieru Formation and no attempt has been made to interpret structure at depths below the Ieru, except where well and seismic data exists such as across the frontal structures and within Lavani Valley (Fig. 2.3). Seismic lines recently acquired across the EMR (e.g., along Traverse 102, 103, 104, 108; Fig. 2.3) were not available at the time of this study, except for the shallow portion of Line 102.

The true stratigraphic thickness (TST) of Darai Limestone T-letter stages was estimated from traverse data and downhole strontium isotope ratio measurements in the Juha-1 well. TSTs were then combined with structural measurements to predict depth to the base of the Darai Limestone, following Hornafius and Denison (1993). TSTs for the Mesozoic sequence were estimated from a combination of traverse, well and seismic data, extrapolated from better constrained areas where necessary. For instance, substantial deformation and lack of outcrop within the Lavani Valley means that good quality data are limited and therefore TSTs are less

constrained. In this case, TSTs from wells across the neighbouring Hides, Juha and Muller structures (Fig. 2.1b and 2.3) provided a valuable guide.

The process of integrating the geological map and cross-sections produced a quasi-3D model of much higher quality than a simple 2D geological map. The cross-sections ensure the map is geologically plausible in the third-dimension and enable subsurface data such as reflection seismic and well-derived TSTs to be fully integrated.

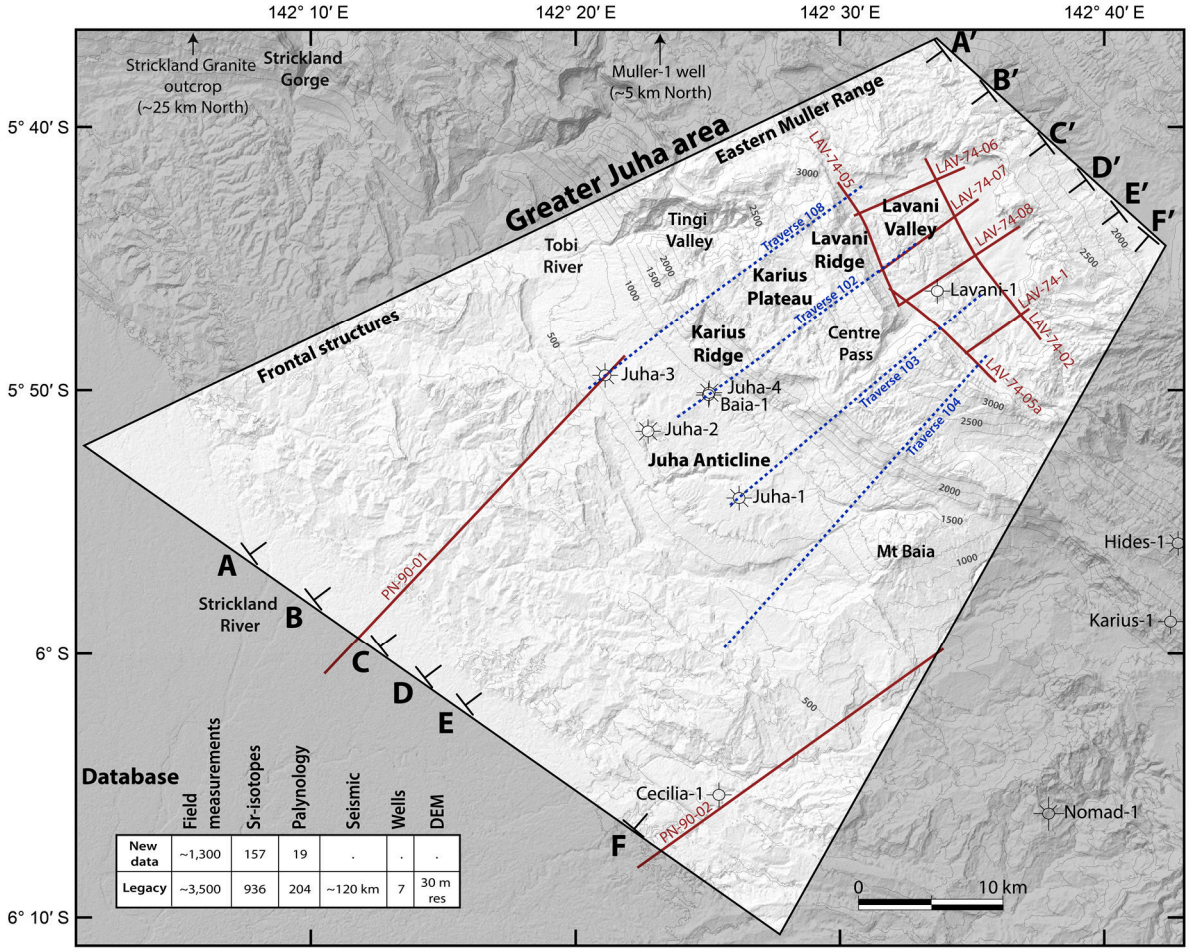

Figure 2.3. *Location of key localities and data sources within the Greater Juha area, including geological traverses (blue dash), available seismic lines (red), wells and cross-sections. Regional seismic lines PN-90-01 and PN-90-02, obtained in 1990 and reprocessed by Papuan Oil Search Ltd in 1996, have significantly improved our understanding of frontal structures. Lavani Valley seismic is of mostly poor quality and provides limited constraint. Geological traverses 102, 103, 104 and 108 have significantly increased the geological dataset across the Greater Juha area. SRTM digital elevation model retrieved from USGS (2015).*

2.4. Geological and structural observations

The Greater Juha area can be subdivided into five structural domains: the Juha Anticline, Karius Ridge, Karius Plateau, Lavani Ridge and Lavani Valley (Fig. 2.3). The structure of each domain is illustrated on the geological map and associated cross-sections in Figure 2.4. Strontium isotope, palynological and representative structural data used to constrain the geological map and cross-sections are presented in Figure A2.1 and Figure A2.2 in the supplementary material.

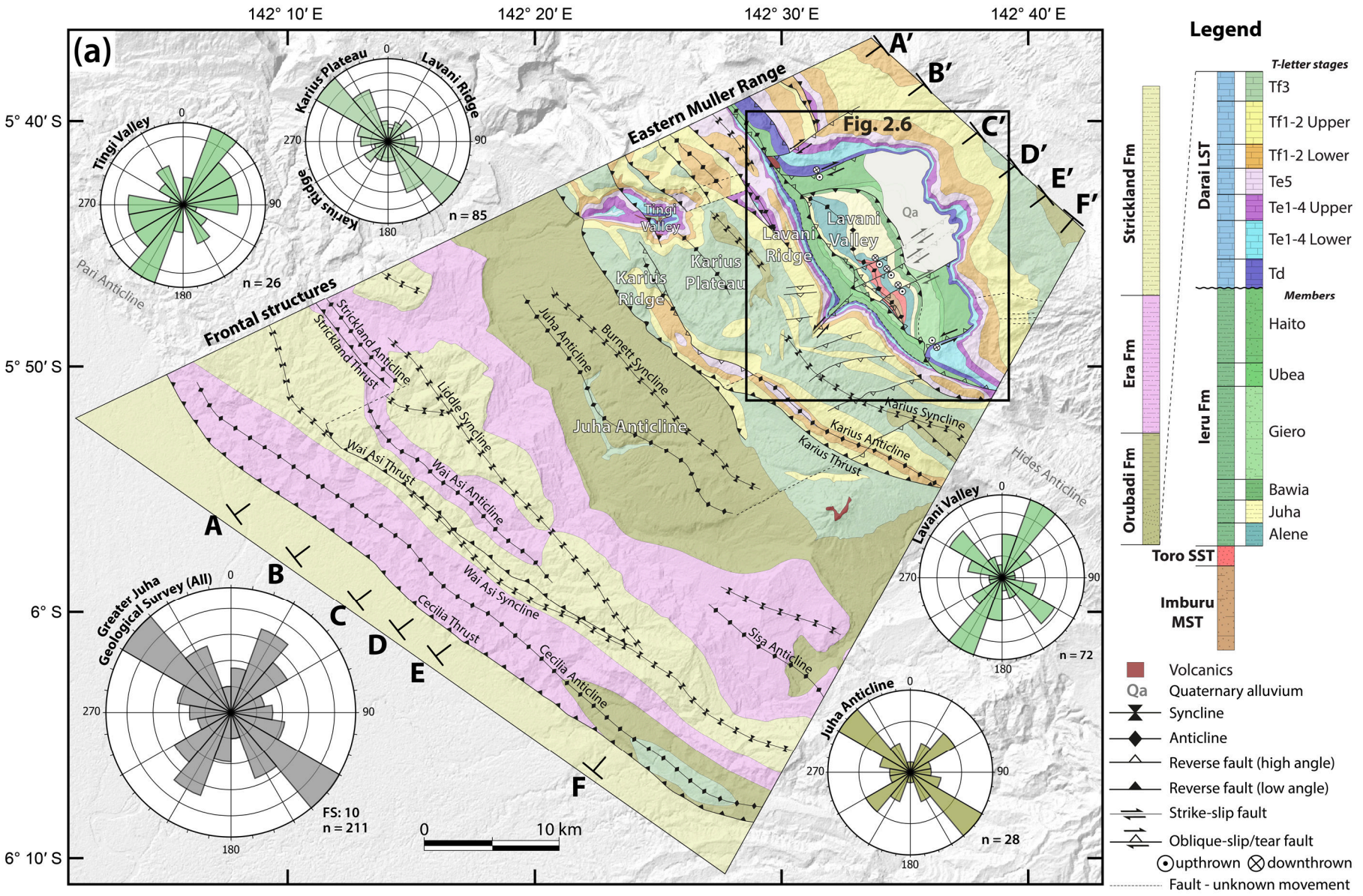
(a)
142° 10′ E
142° 20′ E
142° 30′ E
142° 40′ E
5° 40′ S
5° 50′ S
6° S
6° 10′ S
Eastern Muller Range
Fig. 2.6
A′
B′
C′
D′
E′
F′
Frontal structures
Pari Anticline
Tingi Valley
Karius Plateau
Lavani Ridge
Karius Ridge
Lavani Valley
Qa
Strickland Anticline
Strickland Thrust
Liddle Syncline
Juha Anticline
Burnett Syncline
Wai Asi Thrust
Wai Asi Anticline
Wai Asi Syncline
Cecilia Thrust
Cecilia Anticline
Sisa Anticline
Karius Syncline
Karius Anticline
Karius Thrust
Hides Anticline
A
B
C
D
E
F
n = 26
n = 85
n = 72
n = 28
FS: 10
n = 211
Greater Juha Geological Survey (All)
0
10 km
Legend
T-letter stages
Tf3
Tf1-2 Upper
Tf1-2 Lower
Te5
Te1-4 Upper
Te1-4 Lower
Td
Members
Haito
Ubea
Giero
Bawia
Juha
Alene
Strickland Fm
Era Fm
Orubadi Fm
Darai LST
Ieru Fm
Toro SST
Imburu MST
Volcanics
Quaternary alluvium
Syncline
Anticline
Reverse fault (high angle)
Reverse fault (low angle)
Strike-slip fault
Oblique-slip/tear fault
upthrown
downthrown
Fault - unknown movement

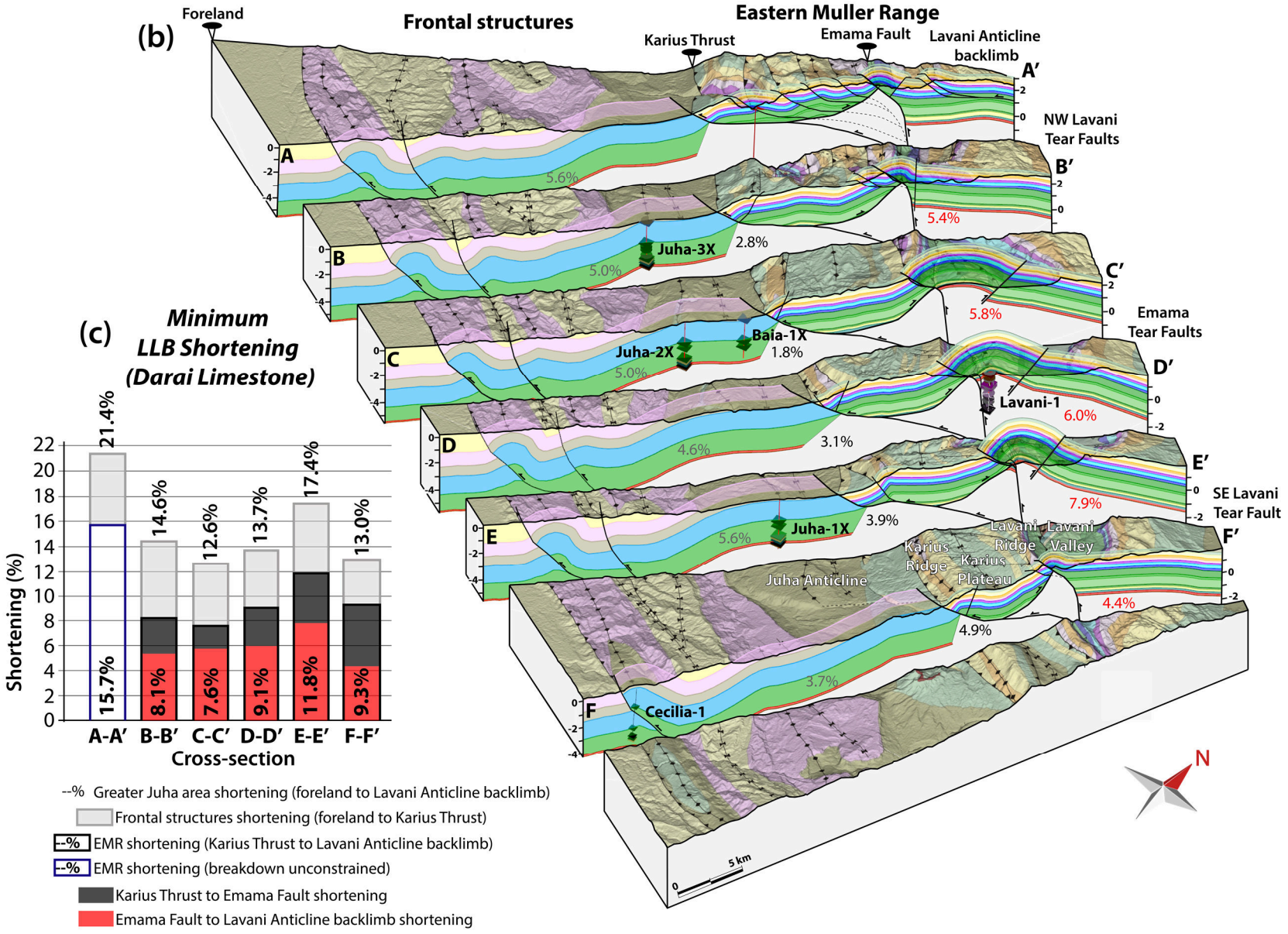
(b)
Foreland
Frontal structures
Eastern Muller Range
Karius Thrust
Emama Fault
Lavani Anticline backlimb
NW Lavani Tear Faults
Emama Tear Faults
SE Lavani Tear Fault
A
A′
B
B′
C
C′
D
D′
E
E′
F
F′
5.6%
5.4%
2.8%
Juha-3X
5.0%
5.8%
Baia-1X
1.8%
Juha-2X
5.0%
Lavani-1
6.0%
4.6%
3.1%
7.9%
3.9%
Juha-1X
5.6%
Karius Ridge
Lavani Ridge
Lavani Valley
Karius Plateau
Juha Anticline
4.4%
4.9%
3.7%
Cecilia-1
N
5 km
(c)
Minimum LLB Shortening (Darai Limestone)
Shortening (%)
21.4%
14.6%
12.6%
13.7%
17.4%
13.0%
15.7%
8.1%
7.6%
9.1%
11.8%
9.3%
A-A′
B-B′
C-C′
D-D′
E-E′
F-F′
Cross-section
--% Greater Juha area shortening (foreland to Lavani Anticline backlimb)
Frontal structures shortening (foreland to Karius Thrust)
--% EMR shortening (Karius Thrust to Lavani Anticline backlimb)
--% EMR shortening (breakdown unconstrained)
Karius Thrust to Emama Fault shortening
Emama Fault to Lavani Anticline backlimb shortening

Figure 2.4. *(previous pages) (a) Geological map of the Greater Juha area including rose plots for fault and fracture strike across each subarea (see Fig. 2.3 for key localities and constraining data). The number of structural measurements (n) varies while the frequency scale (FS) is 5, except where otherwise stated. Representative strike and dip data, along with strontium isotope and palynological age constraints are included in the supplementary material. (b) Block diagram of quasi-3D model including the Greater Juha geological map and the six cross-sections constraining it. The Darai Limestone and Ieru Formation are sub-divided into T-letter stages and members (e.g., Fig. 2.2), respectively, in the cross-sections only where data permits. The vertical axis is in kilometres relative to mean sea level and is exaggerated by 1.5 times. (c) Segmented and total line length balance (LLB) shortening of the Darai Limestone horizon across the Greater Juha area. Shortening per segment is also included in (b). SRTM digital elevation model retrieved from USGS (2015).*

2.4.1. Observed fault and fracture trends

Outcrop within the Greater Juha area is commonly faulted and fractured. More than 200 fault and fracture measurements reveal the overall dominance of northwest-southeast striking structures (Fig. 2.4a), consistent with the trend of the PFTB in this region (Fig. 2.1b). The majority of these arc-parallel faults and fractures are bedding sub-parallel and most plausibly relate to flexural slip and glide mechanisms. There is also a strong northeast-southwest striking structural trend which is pervasive across the Greater Juha area, particularly in the Lavani and Tingi valleys where the Ieru Formation dominates surface outcrop (Fig. 2.4a). This arc-normal trend is also evident in the Orubadi Formation across the Juha Anticline, but is less prominent in the Darai Limestone across Karius Ridge, Karius Plateau and Lavani Ridge (Fig. 2.4a). The reduced prominence in Darai Limestone may relate to its greater competence compared with mudstones and siltstones of the Ieru Formation. An alternate explanation is that arc-normal structures are more concealed within Darai Limestone outcrop due to denser vegetation and intense karstification.

The arc-normal structural trend can also be inferred on the SRTM digital elevation model (DEM) and identified in geological mapping (Fig. 2.4a), where it is expressed as (1) discrete faults, such as observed in abundance across the

southeastern end of Karius Plateau, (2) through-going zones characterised by the termination or disruption of structures, such as at the northwest and southeast ends of the Juha and Lavani anticlines, and/or (3) geomorphic features, such as Centre Pass (Fig. 2.3). The prevalence of this arc-normal structural trend across multiple scales suggests it has played an important role in the structural evolution of the area.

2.4.2. Juha Anticline

The Juha Anticline mainly exposes Orubadi Formation (Fig. 2.4) the basal unit of which is an often cross-bedded, medium- to coarse-grained calcarenite, which appears to control the surface expression of the anticline such that the bedding orientation approximates the slope (Fig. 2.4b). Field and seismic data suggest that the Orubadi Formation calcarenite lies conformably on the uppermost Darai Limestone across the entire Juha Anticline. Faulting and fracturing along two dominant structural trends (Fig. 2.4a) forms a tessellated landform consisting of cliff-faces up to several metres high and crevices up to several metres deep. Fault movement sense could be determined for several faults, with reverse, strike-slip and oblique-slip faults identified, leading us to the inference that this characteristic landform could relate to local transpressional and transtensional interactions between discrete blocks. The calcarenite comprises highly competent beds so is a good analogue for structures in the underlying, very competent Darai Limestone where heavy karstification may mask structural trends.

2.4.3. Karius Ridge

Karius Ridge is entirely composed of Darai Limestone and exhibits ~ 1 km of topographic relief from its base on the northeast-limb of the Juha Anticline to its crest on Karius Plateau (Fig. 2.3). The dominant bedding dip appears to be sub-parallel to the southwest-facing slope, although common boulders and slumping across steep terrain in this area (Fig. 2.5a) make it difficult to obtain high-confidence data.

The most prominent structures along the length of Karius Ridge are the Karius Thrust and associated Karius Anticline (Figs. 2.4 and 2.5a). Strontium isotope analyses show the Karius Thrust juxtaposes Tf3- to Te5-aged Darai Limestone in its hanging wall with younger Tf3-aged Darai Limestone and Orubadi Formation in its footwall, with the oldest hanging wall rocks cropping out in the hinge of the Karius Anticline (Fig. 2.4). Darai Limestone along Karius Ridge is anomalously deformed compared to the surrounding areas, with an increased abundance of arc-parallel faults and fractures and a stronger developed bedding-parallel stylolitic fabric. Over 30 southwest-facing cliffs, each up to several metres high, are particularly prominent on the southwest side of the ridge crest, inferred to relate to steeply northeast-dipping reverse faults (Fig. 2.5a). A stepped series of 10-20 northeast-facing cliffs, each up to 5 m high, dominate for ~ 1 km northeast from the crest of Karius Ridge, inferred to relate to steeply southwest-dipping backthrusts. These structures are here interpreted to be conjugate backthrusts in the hanging wall of the southwest-vergent Karius Thrust and appear to have contributed to the uplift and subsequent erosion of the Karius Anticline towards the northwest (Fig. 2.4). While a distinct fault was not observed in outcrop at the base of Karius Ridge, seismic data show the truncation of bedding at the base of the thrust sheet (Fig. 2.5e). The Karius Anticline appears to be tighter towards the southeast (Fig. 2.4b), which is consistent with observations of overturned bedding in the Karius-1 well and outcrop immediately to the southeast of the Greater Juha area (Fig. 2.3) (Johnstone and Emmett, 2000).

Darai Limestone cropping out on the southwest-facing slope of Karius Ridge is significantly older than on Karius Plateau (Fig. 2.4). This is a consistent geomorphic characteristic of frontal structures in the PFTB (e.g., KFTB: Hill *et al*., 2008; Mananda Anticline: Keenan and Hill, 2015) that is in part related to increased rainfall and weathering along southwest-facing slopes.

2.4.4. Karius Plateau

Elevation along Karius Plateau ranges from ~ 2-2.5 km AMSL along the crest of Karius Ridge to ~ 3.2-3.6 km AMSL at the crest of Lavani Ridge (Fig. 2.3). The plateau broadens from ~ 4 km wide in the southeast to ~ 11 km wide in the northwest (c.f. cross-sections F-F′ and B-B′ in Fig. 2.4b). Outcrop across the plateau is dominated by shallowly-dipping Darai Limestone that has suffered moderate to intense karstification, with abundant rillenkarren and sinkholes up to hundreds of metres across. While karstification makes it difficult to identify discrete structures, the landform is clearly intersected by sub-linear trending zones of cliffs up to 10 m high. These zones are interpreted to represent intersecting arc-parallel and arc-normal oriented structures that can also be readily observed cross-cutting Karius Plateau at the scale of the SRTM DEM (e.g., Fig. 2.6a).

Strontium isotope data show that Tf3- and TF1-2 (Upper)-aged Darai Limestone crops out across most of Karius Plateau except where the Orubadi Formation was observed on Traverse 108 and to the southeast of Traverse 104 (Figs. 2.3 and 2.4). Interestingly, the basal Orubadi Formation calcarenite conformably overlying Darai Limestone across the Juha Anticline is absent across Karius Plateau on Traverse 108, suggesting that the Orubadi Formation may unconformably overlie the Darai Limestone. This is consistent with observations of a similar unconformity around the Muller-1 well to the northwest of the Greater Juha Area (Fig. 2.3; e.g., Hornafius, 1993), suggesting an unconformity may extend across large portions of the EMR. Alternatively, these observations could be explained by the strongly diachronous nature of the Orubadi Formation in this region (e.g., Thornton *et al*., 1996).

The shallow structure of Karius Plateau is dominated by the Karius Syncline in the southeast passing into a series of southwest-verging thrusts in the northwest. The syncline tightens significantly towards the southeast in a similar style to the Karius Anticline (Fig. 2.4b). To the northwest of cross-section D-D′, the Karius

Syncline is replaced by an almost continuous southwest bedding dip in cross-section C-C′ and by gentle folding in cross-section B-B′. Further northwest on cross-section A-A′, smaller wavelength folds and small to moderate offset thrusts are inferred and strontium isotope ages show older Darai outcrops. This change in structural style is interpreted to be accommodated along an arc-normal oriented zone of tear faulting that extends from the northeast of Tingi Valley to Lavani Ridge (Fig. 2.4a).

The Tobi River has eroded up to 1 km into Karius Plateau to the northwest of the Greater Juha area, forming the steep-sided Tingi Valley (Fig. 2.3). In places, the Tobi River has eroded the entire Darai Limestone sequence (Fig. 2.4). A northeast-dipping thrust has tentatively been interpreted to cross-cut the Tingi Valley (Fig. 2.4), based on strontium isotope ratios and field observations. Intermediate volcanics of the Tingi Valley Igneous Complex, including both diorites and andesites, are abundant throughout the Tingi Valley with scattered hornblende-phyric andesitic boulders present as far away as Traverse 108 on Karius Plateau. Field observations suggest that the volcanics have spread out at the Darai Limestone/Ieru Formation contact, possibly facilitated by cave systems observed near the base of the Darai Limestone within Tingi Valley.

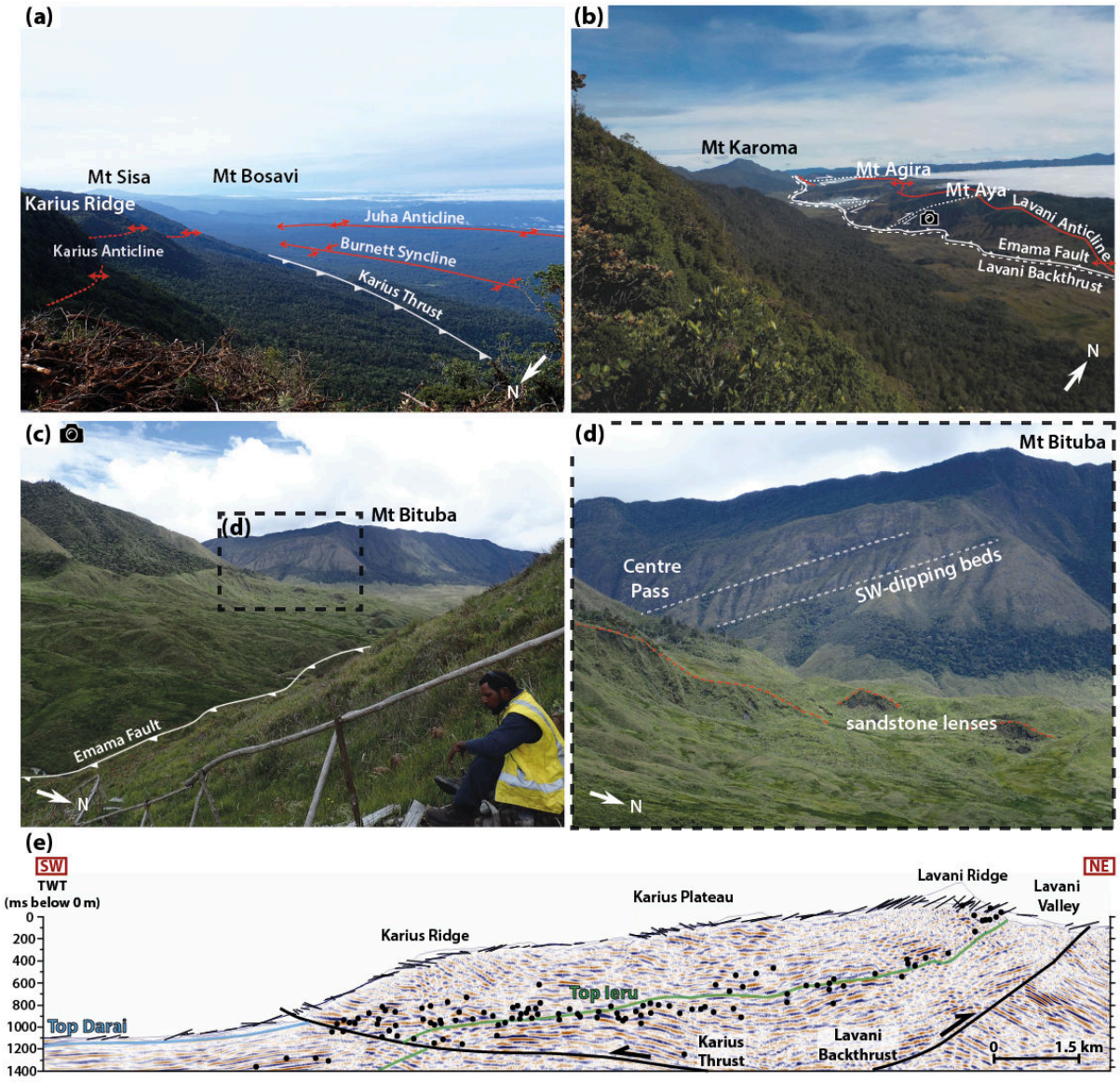

***Figure* 2.5.** *(a) Foreland structures and the steep southwest-facing slope of Karius Ridge, looking southeast; (b) The major structural components and landform of the Lavani Valley from Lavani Ridge (Mt Uraka), looking northwest; (c) Centre Pass looking west from Mt Aya, with photo location marked in (b); (d) Centre Pass showing distinct southwest-dipping beds and northwest-southeast striking sandstone lenses within Ieru Formation at the base of Lavani Ridge, looking west; (e) Reflection seismic data across the EMR show the shallowly northeast-dipping Karius Thrust and southwest-dipping Lavani Backthrust. Lines at surface are representative dip data and dots represent predicted Top-Ieru Formation depth estimates based on strontium isotope ratios.*

2.4.5. Lavani Ridge

The regionally prominent Lavani Ridge is bound to the northeast and southwest by steep slopes and is characterised by a variable crest elevation of ~ 3.2 km AMSL on Traverse 103 at Mt Uraka, to ~ 3.6 km AMSL on Traverse 108 at Mt Karoma (Fig. 2.6a). Structural measurements and strontium isotope data across Lavani Ridge reveals a persistent shallow southwest bedding dip, as do observations from the cross-cutting Centre Pass (Fig. 2.5c and d).

The southwest-facing slope of Lavani Ridge mostly comprises Tf3- and Tf1-2 (Upper)-aged Darai Limestone (Figs. 2.4 and 2.6b). Older areas of Tf1-2 (Lower)- and Te5-aged Darai Limestone on the crest and southwest side of Lavani Ridge around cross-sections A-A', B-B' and F-F' are interpreted to result from uplift in the hanging wall of southwest-verging thrust faults (Figs. 2.4 and 2.6b). This is consistent with field observations from these areas including an order of magnitude increase in the intensity of faulting and fracturing when compared to Karius Plateau, and an increased abundance of southwest-facing cliffs up to 10 m high.

The northeast-facing slope of Lavani Ridge (Fig. 2.5c) comprises a ~ 1 km, mostly conformable sequence from Tf1-2 (Upper)-aged Darai Limestone to Ieru Formation (Figs. 2.4 and 2.6b). Palynological data indicate that sandstones, siltstones and mudstones cropping out near the base of Lavani Ridge, in Lavani Valley, belong to the Haito and Ubea members of the Ieru Formation (Fig. 2.6b). Comparatively erosion-resistant, southwest-dipping sandstone beds form northwest-southeast striking ridges (Fig. 2.5d) that can be recognised in the high-resolution SRTM DEM and which demonstrate structural continuity (e.g., Fig. 2.6a).

Centre Pass is a prominent valley cross-cutting Lavani Ridge (Fig. 2.6a). The Emama River (Fig. 2.6a) appears to have once drained to the southwest through Centre Pass, but subsequent drainage reorganisation to the northeast and southeast of Lavani Valley has left Centre Pass virtually dry. The Tingi Valley has a similar geomorphic expression (Fig. 2.3) suggesting it is a potential modern analogue for

fluvial incision of Centre Pass into Lavani Ridge. Interestingly, the strike of Centre Pass is similar to the prominent arc-normal structural trend recognised throughout the Greater Juha area (Fig. 2.4a). Sinistral offset of Lavani Ridge across Centre Pass is here interpreted to be related to tear faulting (Fig. 2.4).

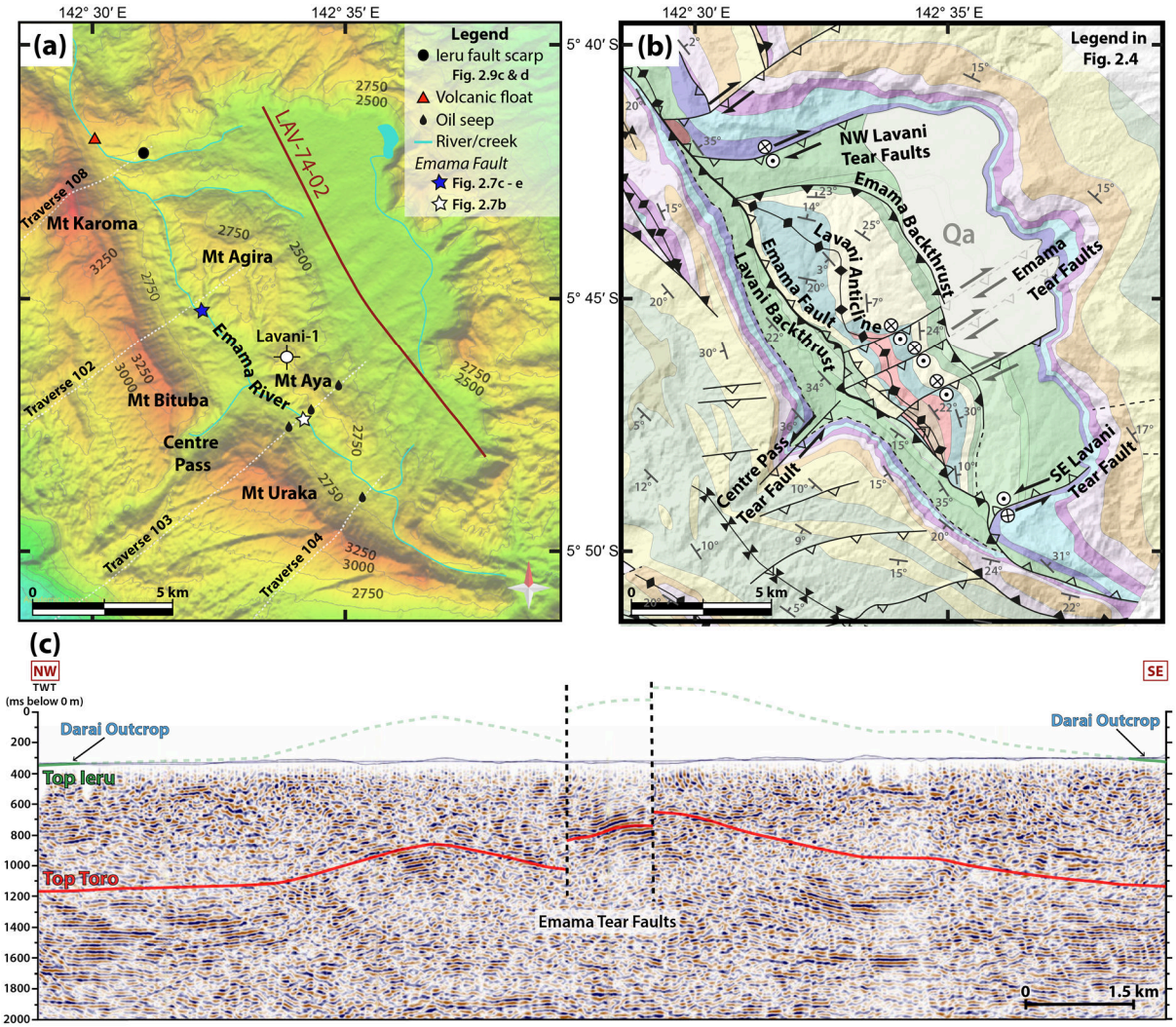

Figure 2.6. *(a) DEM of Lavani Valley and environs from SRTM dataset (USGS, 2015). Key geographic features and the location of geological traverses are indicated; (b) Detailed geological map of the Lavani Valley. Legend in Figure 2.4. Note the dominant up-to-the-southeast offset on the NW Lavani Tear Faults, Emama Tear Faults and the series of faults cross-cutting the southwestern end of Karius Plateau. Variable topography combined with the vertical component of motion on the oblique-slip Emama Tear Faults masks the dextral sense of shear in map view. (c) LAV-74-02 reflection seismic data along the length of Lavani Valley (location in (a) above) demonstrates up-to-the-southeast offset across the Emama Tear Faults, consistent with surface geological data (e.g., (b) above).*

2.4.6. Lavani Valley

The ~ 10 km wide and ~ 15 km long Lavani Valley is located along the hinge of the regionally prominent Lavani Anticline (Figs. 2.5b and 2.6). The surface geology is dominated by mudstones, siltstones and minor sandstones of the Ieru Formation, contributing significantly to its distinct, comparatively gentle sloping and open landform (Fig. 2.5b and 2.6a). The valley is almost completely surrounded by steep slopes of mostly conformable Darai Limestone that dip away to the southwest and northeast on either side (Fig. 2.4b). The geology of the Lavani Valley offers significant insight into the structure of the regionally-significant Lavani Anticline as a whole and indeed the entire EMR.

Dense grassland vegetation means that outcrop within the Lavani Valley is largely limited to the Emama River (Fig. 2.6a), and consequently observations are available mostly along strike, with few cross-cutting traverses. Our work provides new observations of the dip structure across this area. Importantly, observations suggest that while faulting and fracturing is pervasive throughout the Lavani Valley, deformation is clearly more severe within major fault zones such as around the regionally significant Emama Fault (Figs. 2.4b, 2.6b and c.f. Fig. 2.7a and b).

2.4.6.1. Emama Fault

The Emama River is a consistent feature at the base of the southwest side of Mt Agira and Mt Aya (Fig. 2.6a). Major fault zones were observed at two localities around 6 km apart within the Emama River (Fig. 2.6a), suggesting the river approximately follows the trace of a major fault.

Morphologically, the fault appears sub-vertical on Traverse 102, where it is expressed as a > 10 m wide zone of steep, contorted bedding with localised fault gouge and brecciation (Fig. 2.7c-e). Around Traverse 103 the fault dips towards the northeast with fault rounded and striated fine-grained sandstone fragments within highly sheared mudstones (Fig. 2.7b) suggesting that the amount of movement

accommodated within this zone is significant. Further, there is no evidence of a major fault along strike in reinterpretations of the Lavani-1 well, suggesting the fault must become very steep down-dip (Fig. 2.4b, cross-section D-D'). This fault is here referred to as the Emama Fault (Fig. 2.6b), a steeply northeast-dipping reverse fault that uplifts Mt Agira and Mt Aya in its hanging wall and which may be largely responsible for the formation of the Lavani Anticline.

In the uplifted northeast side of the Emama Fault, the geological complexity appears to increase from Mt Agira in the northwest to Mt Aya in the southeast (Fig. 2.6). The surface geology of Mt Agira comprises a ~ 5 km wavelength anticline, with the Alene and Juha members of the lowermost Ieru Formation cropping out at its peak at ~ 2.8 km AMSL (Fig. 2.8a). Its forelimb is characterised by predominantly southwest-dipping beds (Fig. 2.8b and c) consistent with the adjacent Lavani Ridge (Fig. 2.5d).

In contrast, Mt Aya has an apparent wavelength of ~ 2.5 km, is noticeably more asymmetric (Fig. 2.6a) and Toro Sandstone crops out at its crest at ~ 2.8 km AMSL (Fig. 2.8d). Traverse 103 demonstrates persistent shallow to moderate northeast dip along the southwest-facing slope of Mt Aya (Fig. 2.8e and f), suggesting the forelimb of the Lavani Anticline is mostly absent (Fig. 2.4b, cross-section E-E'). There is an accompanying increase in deformation intensity in this area, including widespread bedding sub-parallel shear strain, particularly evident in fine-grained lithologies (e.g., Fig. 2.7b). Traverse 103 also revealed a ~ 120 m thick sequence of fine- to coarse-grained sandstones located directly above intensely deformed Alene Member in the hanging wall of the Emama Fault. Earliest Cretaceous (Berriasian) palynological ages indicate that this sequence is the Toro Sandstone. Interestingly, previously unidentified sheared mudstone and siltstone directly overlying the sand-dominated sequence are of Late Jurassic (Tithonian) age, suggesting Imburu Mudstone directly overlies Toro Sandstone in this area. If correct, these are the oldest outcropping rocks in the Greater Juha area (Fig. 2.6b). Northeast-

dipping Toro Sandstone crops out again at the crest of Mt Aya (Fig. 2.8d) as originally reported by Bidstone *et al.* (1974). Several low to moderate confidence way-up indicators (e.g., graded-bedding, cross-bedding) along the length of Traverse 103 suggest that the sedimentary sequence is the right way up, however we are hesitant to completely rule out the possibility of an overturned forelimb.

Thus, the geometrically complex Emama Fault is a regionally significant structure that appears to be largely responsible for uplifting the Lavani Anticline in its hanging wall. Further, the intersection of thick syn-rift sediments nearly 2 km AMSL in the Lavani-1 well suggests the Emama Fault is connected to an inversion structure at depth; a decrease in Bouguer gravity from Lavani Ridge into Lavani Valley (Bidstone *et al.*, 1974) suggests that, despite inversion, basement remains deeper in the hanging wall of the Emama Fault.

In summary, geological field data from within Lavani Valley reveal the structural complexity of the Emama Fault and Lavani Anticline. Outcropping rocks become older towards the southeast of Lavani Valley (Fig. 2.6b), suggesting increased displacement and hanging wall uplift along the Emama Fault towards the southeast. The southwest-facing slope of Mt Aya provides important insight into the subsurface structure of the Lavani Valley. Here, thrusted repeats of Ieru Formation, Toro Sandstone and Imburu Mudstone are interpreted as stacked horses with the bounding faults merging into a foreland-vergent roof thrust within the incompetent Ieru Formation (Fig. 2.4b, cross-section E-E'). This roof thrust and the overlying hanging wall rocks have since eroded away adjacent to Mt Aya. It is unclear whether this structural style extends along strike to beneath Ieru Formation cropping out over Mt Agira (Fig. 2.6b), but if so, the roof thrust must lie just beneath the surface in the Alene Member, suggesting this is a prominent detachment layer. Alternatively, the structural style may change at a tear fault.

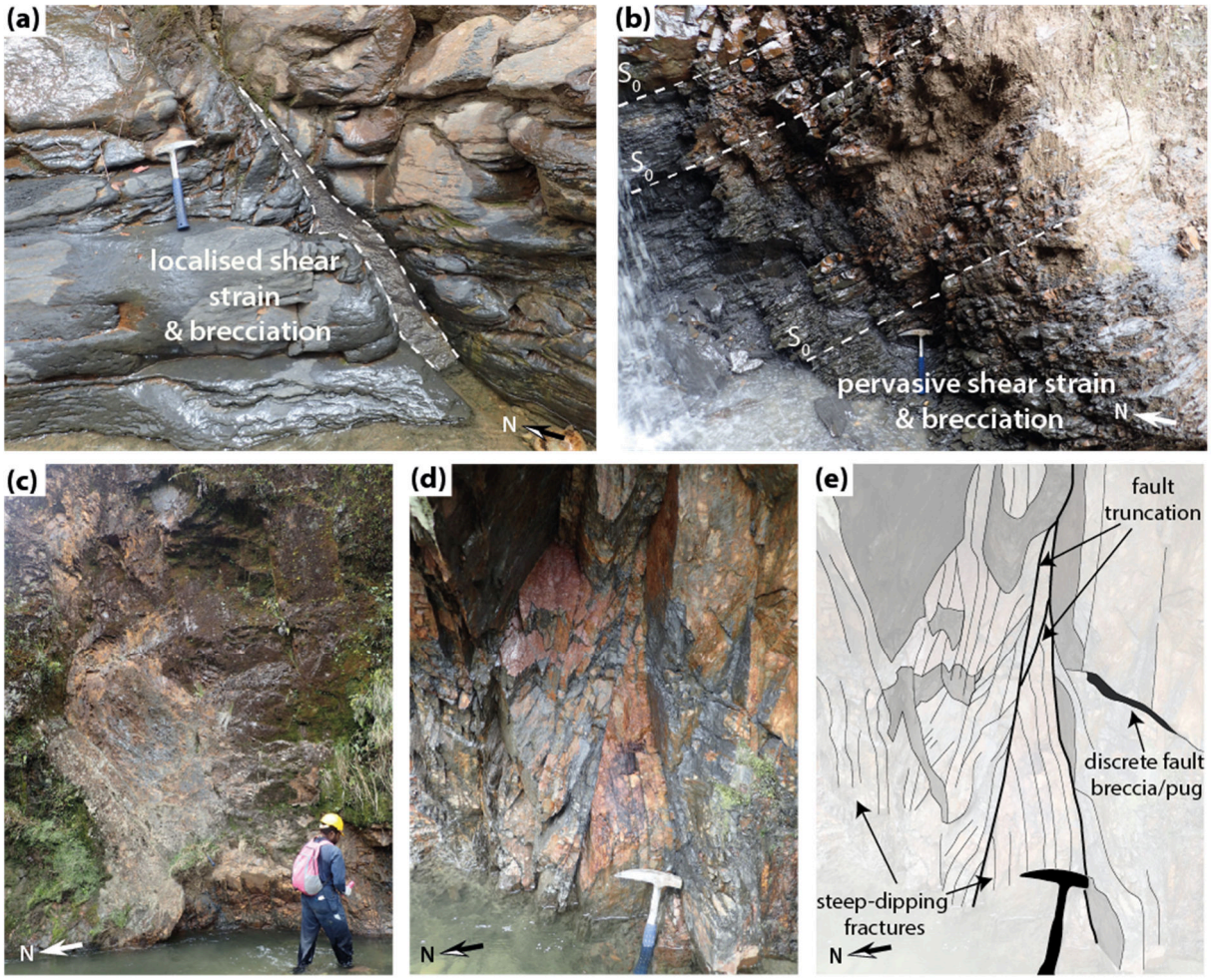

Figure 2.7. *Faulting within the Cretaceous Ieru Formation in Lavani Valley. (a) Abundant, widely distributed narrow/discrete (< 1 m) faults and (b-e) wide fault zones (> 10 m) with distributed shear strain. (b) shows the Emama Fault on Traverse 103; (c), (d) and (e) show the Emama Fault on Traverse 102. Location of Emama Fault photos marked in Figure 2.6a.*

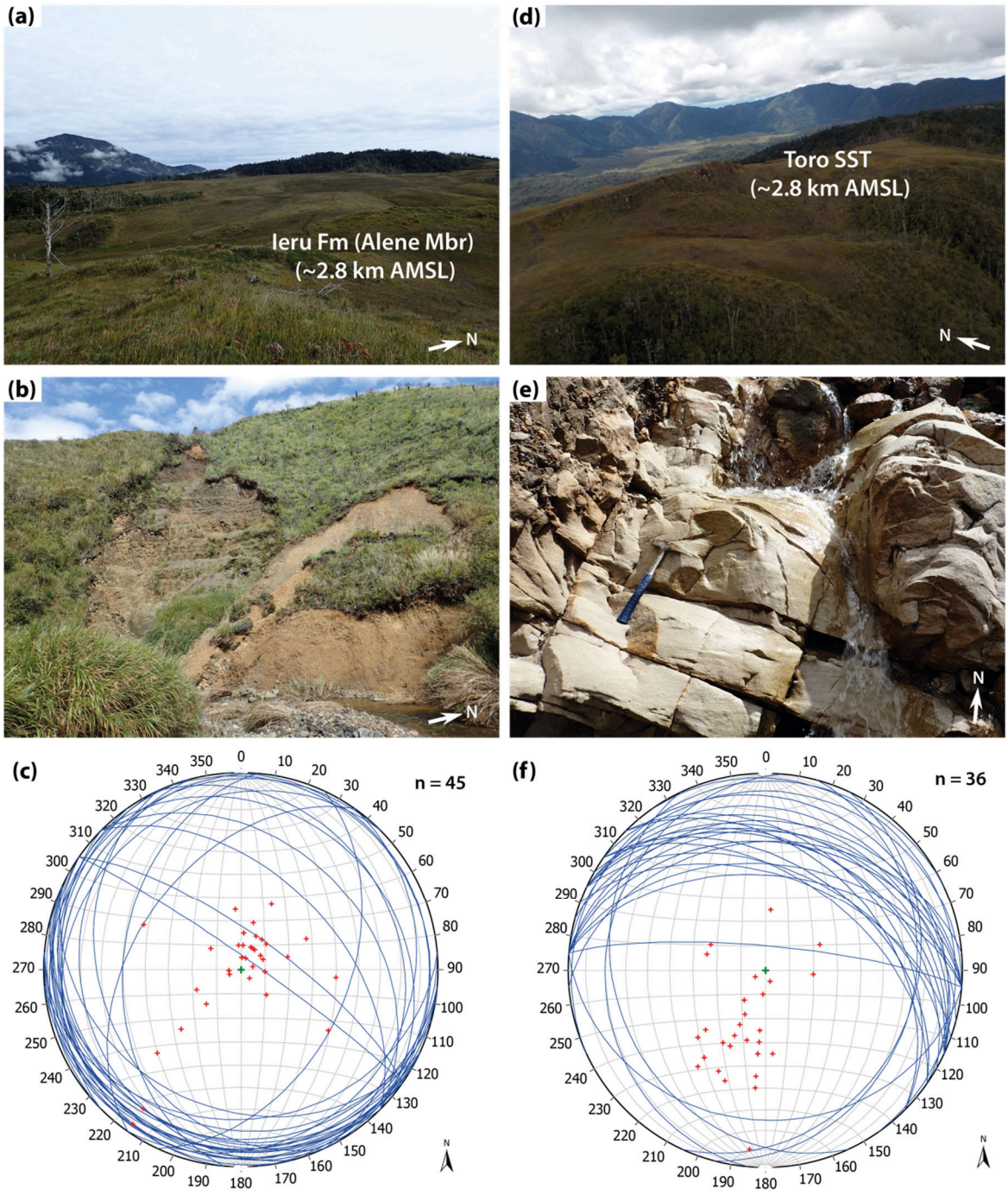

Figure 2.8. *Field photos and Schmidt stereonets (n = number of measurements) showing lateral geological variation within Lavani Valley. Mt Agira (Traverse 102) is associated with; (a) a relatively subdued landform; (b) Ieru Formation outcrop and a southwest bedding dip (b and c). In contrast, Mt Aya (Traverse 103) is associated with (d) a steeper landform; (e) older outcrop, including Toro Sandstone and (e) and (f) a northeast bedding dip.*

2.4.6.2. Emama Backthrust

Field data constraints across Mt Agira combined with the LAV-74-02 seismic line to the northeast (Fig. 2.6a and c) define an abrupt transition from lower to upper Ieru Formation members around the northern flank of Mt Agira (Fig. 2.6b). In the absence of steep bedding dips, the Emama Backthrust has been interpreted to explain this transition. Where it wraps around the northwestern flank of Mt Agira, the Emama Backthrust juxtaposes Bawia Member of the lowermost Ieru Formation with Haito Member of the uppermost Ieru Formation (Fig. 2.6b). The significance of the Emama Backthrust decreases towards the southeast where seismic line LAV-74-02 suggests older Ieru Formation crops out in its footwall (Fig. 2.6c). Moreover, it is plausible that uplift in the hanging wall of the Emama Backthrust has had a geomorphic control on the extent of Quaternary alluvium in the north of Lavani Valley (Fig. 2.6b).

2.4.6.3. Lavani Backthrust

Lavani Ridge appears to be located within the footwall of the Emama Fault, but is nevertheless associated with elevations > 3.2 km AMSL along its length, making it the highest topographic feature in the Greater Juha area. Furthermore the steep northeast-facing slope appears to be unique regionally within the WFTB, where the vast majority of steep slopes are southwest-facing (Fig. 2.1c). We interpret these characteristics to result from uplift along a significant backthrust within the Ieru Formation that originates from beneath Karius Ridge (Fig. 2.4b). This backthrust is imaged on seismic data where it truncates bedding beneath Lavani Ridge (Fig. 2.5e). Exactly where the backthrust intersects the surface within Lavani Valley is less clear, but strontium and palynological data from the northeast-facing slope of Lavani Ridge suggest a largely conformable sequence, such that the Lavani Backthrust may intersect the surface at approximately the same location as the Emama Fault (Figs. 2.4b, 2.5b and 2.6b). This makes it difficult to constrain the relative influence of the Emama Fault and Lavani Backthrust. Thickness variations within the lower Td Darai

Limestone, particularly to the southeast of Lavani Valley, suggest the Lavani Backthrust could plausibly have a splay near the Darai Limestone/Ieru Formation contact (Fig. 2.6b).

2.4.6.4. Arc-normal structures

Throughout Lavani Valley, arc-normal faults and fractures are pervasive (e.g., Fig. 2.9a and b) and may even be more abundant than arc-parallel structures (Fig. 2.4a). Interestingly, arc-parallel structures, typically bedding (S_0) parallel, show evidence of both brittle and semi-ductile (e.g., Fig. 2.9b) deformation. In contrast, cross-cutting arc-normal structures appear to have formed exclusively from brittle processes (Fig. 2.9a and b) and often displace arc-parallel structures.

Additionally, a small southeast-facing fault scarp (Fig. 2.9c and d) was observed within the Ieru Formation near the end of Traverse 108 (Fig. 2.6a). Such an observation is abnormal within the usually very fast weathering mudstones and siltstones of the Ieru Formation, suggesting that arc-normal faulting may still be active, at least within the Lavani Valley. Slickenfibres and striations confirm a northeast-southwest striking fault plane with at least a component of strike-slip movement (Fig. 2.9c and d). Thus, the scarp is likely to relate to a restraining bend/transpressional zone along a strike-slip or tear fault. Given its proximity to the abrupt northwest termination of the Lavani Valley, it seems plausible that this scarp is related to a larger zone of significant northeast-southwest striking faults, here collectively defined as the NW Lavani Tear Faults (Fig. 2.6b).

Other prominent northeast-southwest striking structures can be identified at the scale of Lavani Valley. The most significant of these appear to be located at the southeast termination of Lavani Valley (SE Lavani Tear Fault) and in a zone through the centre of Lavani Valley (Emama Tear Faults) (Fig. 2.6b). The tear faults bounding either end of the Lavani Valley are recognised by the vertical juxtaposition of older than expected Ieru Formation members with the Darai Limestone (Fig. 2.6b). The

Emama Tear Faults cutting through the centre of the valley are defined by lateral changes in landform, along with surface and subsurface geology (Fig. 2.6). Reflection seismic line LAV-74-02 demonstrates a component of up-to-the-southeast offset across the Emama Tear Faults (Fig. 2.6c), consistent with surface geological observations (e.g., Fig. 2.6b). Interestingly, the horizontal component of displacement along the Emama Tear Faults appears to be dextral between Mt Agira and Mt Aya and sinistral through the Lavani Ridge (Fig. 2.6b). The Emama Fault and Lavani Backthrust are located between this apparent change in movement sense, suggesting they may be related.

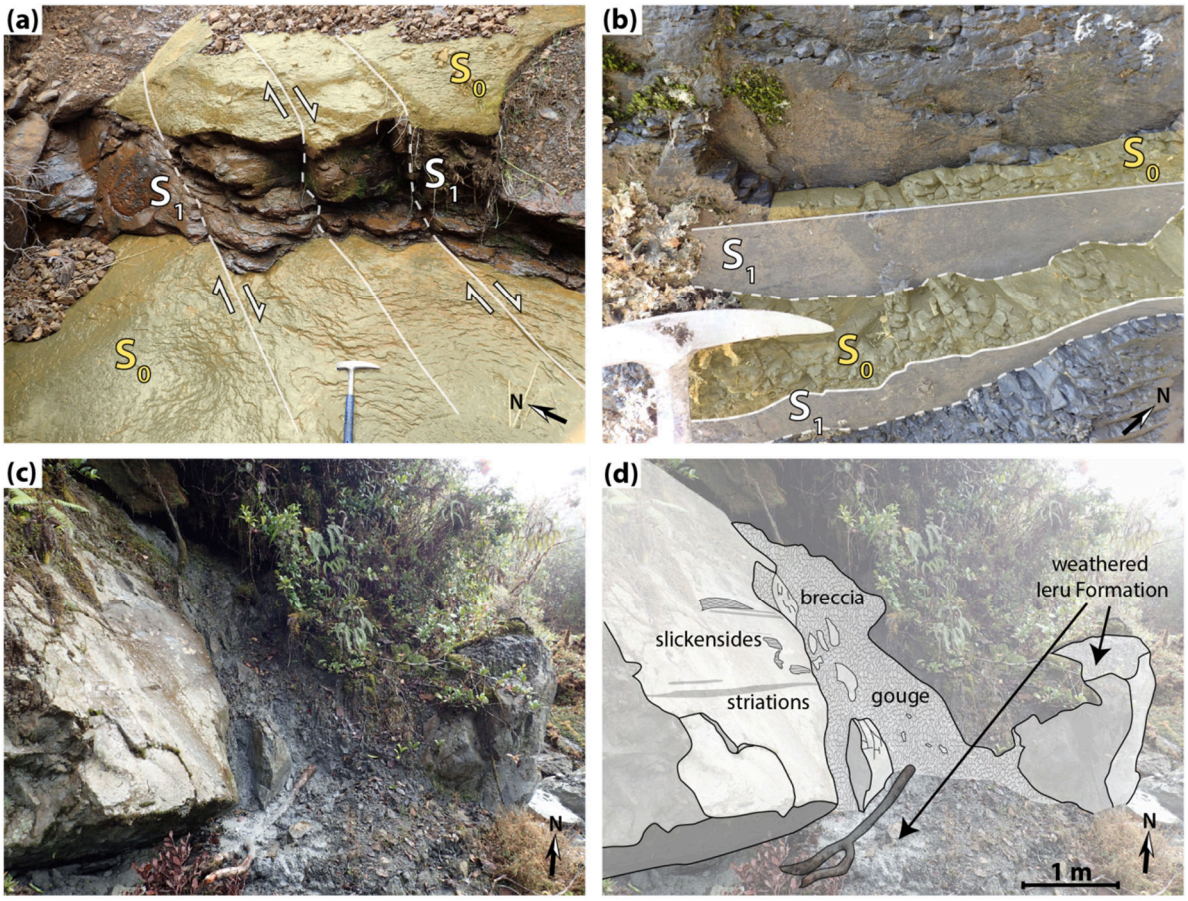

Figure 2.9. *Examples of outcrop-scale arc-normal structures (S_1) in Lavani Valley including (a) northeast-southwest striking faults, predominantly associated with a component of dextral offset; (b) abundant northeast-southwest striking fractures across which offset is indeterminate or absent. Note the apparent change from wavy, semi-ductile, bedding parallel deformation (S_0) to the much more*

sharply defined brittle deformation (S_1). (c and d) a fault scarp within fast weathering Ieru Formation suggesting very recent to active strike-slip faulting (see Figure 2.6a for location).

2.4.6.5. Summary

New observations presented here significantly improve our understanding of the structure of Lavani Valley. First, the Emama Fault is a geometrically complex, regionally significant structure that is largely responsible for uplifting the Lavani Anticline. Thick syn-rift sediments in the hanging wall suggest the Emama Fault is connected to an inversion structure at depth; a decrease in Bouguer gravity from Lavani Ridge into Lavani Valley (Bidstone *et al.*, 1974) suggests that, despite inversion, basement remains deeper in the hanging wall of the Emama Fault. The amplitude and wavelength of the Lavani Anticline decreases outwards from the northwest and southeast ends of Lavani Valley (Fig. 2.4b, cross-section A-A' and F-F'); suggesting that the Emama Fault may be associated with less displacement in these areas (at least at depth). Interestingly, outcropping rocks become older from the northwest to southeast of Lavani Valley (Fig. 2.6b) implying increased displacement and hanging wall uplift along the Emama Fault towards the southeast (Fig. 2.4b, c.f. cross-sections B-B' and E-E').

Forty kilometres along strike to the northwest, basement crops out at ~ 500 m AMSL in the Strickland Gorge yet it was not encountered in the Lavani-1 well that extends ~ 200 m below mean sea level, implying basement deepens towards the southeast. This is consistent with eastward decreasing Bouguer gravity and a large down-to-the-east basement fault recognised in seismic data within Lavani Valley (Bidstone *et al.*, 1974).

Together these observations show that areas with the deepest basement and thickest syn-rift sediments have undergone the most significant uplift during basin inversion. Thus, the pre-compression margin architecture was complex and appears to have had a significant influence on evolution. Moreover, arc-normal structures

appear to be closely associated with lateral changes in geology along the Lavani Valley and therefore may represent zones of tear faulting—some of which remain active.

2.4.7. Shortening analysis

Shortening calculations are a powerful method of quantitatively assessing lateral geological variation and can thus assist in identifying accommodating structures such as tear faults. Here, a line length balancing (LLB) technique was used to estimate shortening of the well-constrained Darai Limestone horizon in each of the cross-sections.

Minimum estimates for Darai Limestone shortening across the entire Greater Juha area vary from 12.6 to 21.4% (Fig. 2.4c), with the greatest shortening correlating with increased structural complexity along cross-section A-A′ (Fig. 2.4a and b). Here, shortening analyses are broken down into subareas (Fig. 2.4c) to investigate potential relationships between lateral shortening variations and arc-normal structures observed across the Greater Juha area (e.g., Section 2.4.6.4). It is important to note that the complexity of the Darai Limestone in the Lavani Anticline in cross-section A-A′ highlights the potential for complex structure within the hinge of the Lavani Anticline where the Darai Limestone has been eroded in Lavani Valley. Here, we present the simplest structural interpretation for eroded portions of the crest of the Lavani Anticline (e.g., Fig. 2.4b, C-C′ to E-E′) so that shortening estimates are likely to be minima.

Along the EMR (excluding cross-section A-A′), minimum shortening of the Darai Limestone from the Karius Thrust to the backlimb of the Lavani Anticline varies from 7.6 to 11.8% (Fig. 2.4c). Cross-section E-E′ was associated with the greatest shortening (11.8%), with shortening generally decreasing in sections to both the northwest and southeast. Cross-section A-A′ has anomalously high shortening (15.7%) but with additional surface geological constraints meaning that this

represents a maximum rather than minimum shortening estimate. However, comparably high shortening may at least partially be attributed to an interpreted increase in structural complexity (Fig. 2.4a and b).

Shortening estimates from the Emama Fault to the backlimb of the Lavani Anticline show a similar trend to the Greater Juha area and EMR shortening estimates (Fig. 2.4c). Importantly, cross-section E-E′ has minimal shortening in Darai Limestone interpreted above the eroded Lavani Anticline, yet has still undergone at least 700 m more shortening than cross-section F-F′, which has an almost complete Darai limestone section. Furthermore, E-E′ has ~ 450 m more shortening than cross-section C-C′. We suggest that lateral shortening variations of this magnitude may be at least partially accommodated along the SE Lavani Tear Fault and Emama Tear Faults respectively (Figs. 2.4b and 2.6b). Shortening variation is much less significant between cross-sections C-C′ and B-B′ (< 100 m) and thus does not offer convincing support for the presence of the NW Lavani Tear Faults, interpreted based on field observations and geological constraints (Fig. 2.4a).

Shortening of the Darai Limestone from the Karius Thrust to the Emama Fault appears much lower, varying from 1.8 to 4.9%. With the exception of cross-section A-A′, there is a general increased shortening trend from northwest to southeast, consistent with increased tightening of the Karius Syncline (Fig. 2.4a and b). Interestingly, the presence of the Centre Pass Tear Fault is supported by a difference in shortening between cross-sections C-C′ (1.8%) and E-E′ (3.9%) that equates to at least 300 m of lateral shortening variation accommodated along this structure.

2.5. Structural evolution of the Greater Juha area

There is significant evidence for extension and rifting along the New Guinea margin in the early Mesozoic, including in the foreland directly adjacent to the Greater Juha area. Observations outlined here suggest this variable pre-existing rift architecture almost certainly underlies the Greater Juha area and has had significant influence on

the evolution of structural styles during Cenozoic compression of the New Guinea margin.

There is substantial geological and geophysical evidence suggesting that the Juha and Lavani anticlines formed above partially inverted grabens. Firstly, these structures can be linked through substantial similarities in orientation and morphology (Fig. 2.1c), with their large wavelengths, asymmetric limbs and lobate morphologies characteristic of inversion structures (e.g., McClay, 1995; Bonini *et al.,* 2012). Geophysical data across the Lavani Valley (Bidstone *et al.,* 1974) and the thick Triassic syn-rift sequence intersected at ~ 1.9 km AMSL in the Lavani-1 well (> 7 km above its foreland regional) presents a strong argument for the partial inversion of a graben beneath Lavani Valley. In fact, in order to sufficiently uplift the Lavani Anticline while still honouring geophysical observations of only partial inversion (i.e. basement hanging wall remains lower than basement footwall), the Lavani half-graben is likely originally to have been very deep, containing more than 7 km of syn-rift sediments (e.g., c.f. Fig. 2.10a and e).

Evidence from the Juha Anticline is less convincing but limited seismic and gravity data suggest it is also underlain by a deep graben (e.g., Hanani *et al*., 2016). Therefore the pre-compression architecture of the Greater Juha area may have included a set of listric northeast-dipping basement extensional faults and rotated basement hanging wall blocks responsible for the formation of the Juha and Lavani half-grabens (Fig. 2.10a).

Compression associated with continental collision along the New Guinea margin was originally accommodated within the Greater Juha area by the inversion of the normal-faults bounding the Lavani half-graben. The resulting steep Lavani inversion fault intersected the surface as the Emama Fault and the less significant Emama Backthrust, uplifting the Lavani Anticline (Fig. 2.10b). This occurred out-of-sequence early in the evolution of the WFTB, as indicated by the relatively undeformed backlimb of the Lavani Anticline (Figs. 2.1 and 2.4a and b).

We suggest that during the evolution of the Lavani Anticline, the Lavani inversion fault shallowed into the incompetent Mesozoic sedimentary sequence beneath Lavani Ridge and, to a lesser extent, Karius Plateau. A single triangle zone—or more plausibly multiple triangle zones—formed within the Mesozoic sequence over this time, connected to a passive roof thrust, the Lavani Backthrust, within the Ieru Formation (Fig. 2.10c). This style of deformation relates to competence variations within the stratigraphic column, with the competent Darai Limestone much more resistant to shortening than the less competent underlying Mesozoic sequence. The forelandward propagating triangle zone(s) uplifted the Lavani Ridge, at least temporarily forming a frontal monocline (Fig. 2.10c) – a common characteristic of triangle zone-related deformation (e.g., Cooper, 1996 and examples within).

The Karius Thrust and associated Karius Anticline are here attributed to the most recent pulse of movement along the Lavani inversion fault (Fig. 2.10d). The now dry Centre Pass valley (see Section 2.4.5) provides considerable insight into the relative temporal evolution of this area of the EMR, with incision of the valley into the Lavani Ridge pre-dating uplift along Karius Ridge. Note the similarities between the structure of the Lavani Anticline in Figure 2.10d compared to the present structure of the Juha Anticline on Figure 2.10e (Hanani *et al*., 2016). This is consistent with the southwest propagation of the same structural style.

Despite their morphological similarities, the Juha Anticline has experienced significantly less uplift than the Lavani Anticline (Fig. 2.10e). One obvious difference between the two structures is the absence of an emergent frontal fault on the Juha Anticline (Fig. 2.4a and b). This characteristic suggests the Juha inversion fault shallows into the Mesozoic sedimentary sequence before connecting with forelandward structures (Fig. 2.10e), as suggested by Hanani *et al*. (2016). Important implications of this relationship are that displacement along the Juha inversion fault

is restricted by the limited amount of displacement observed along structures towards the foreland (Fig. 2.4b).

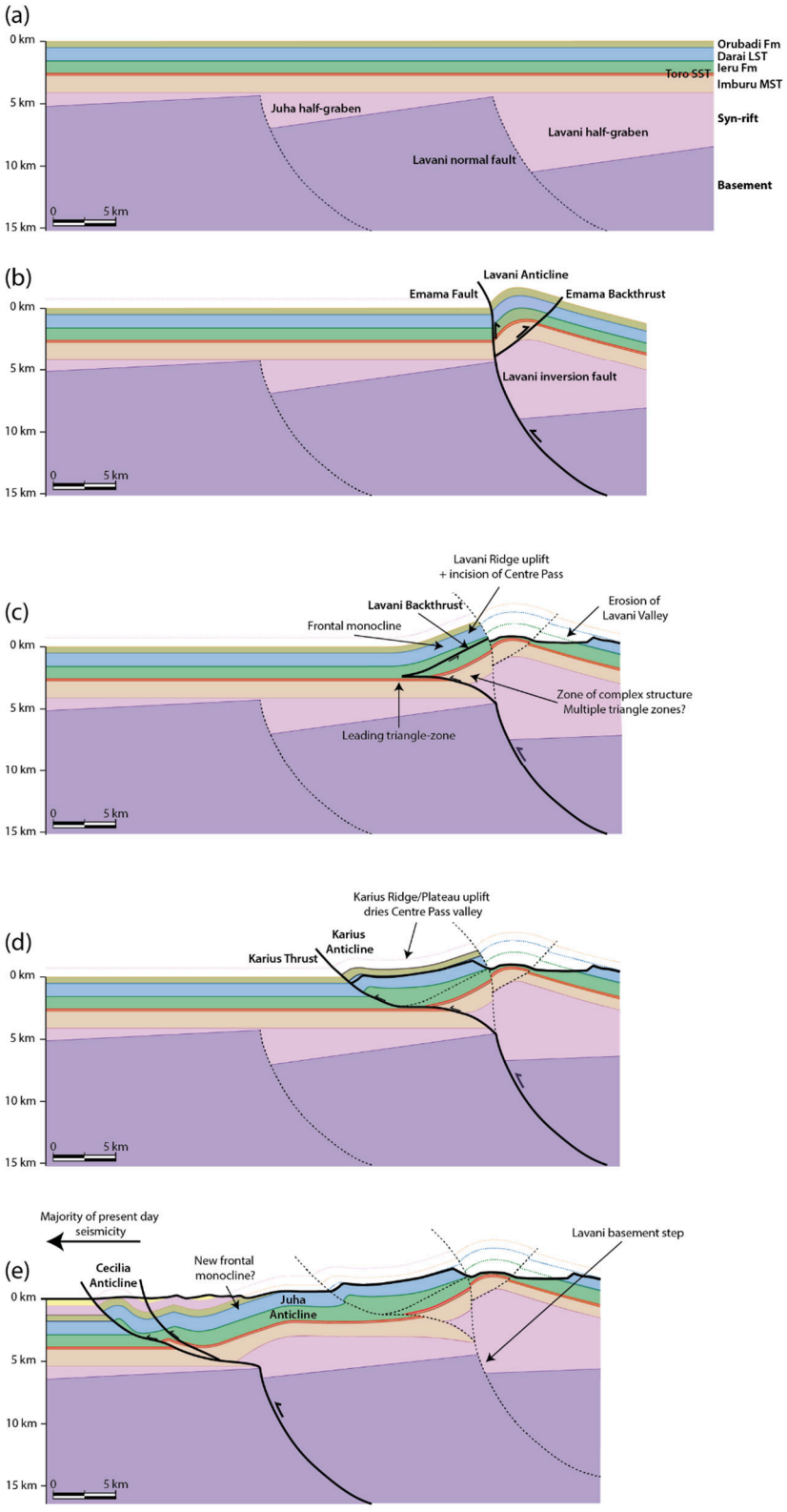

Figure 2.10. *(previous page) Proposed schematic structural evolution of the Greater Juha area: (a) prior to compression; (b) during initial inversion and reverse displacement along the Lavani inversion fault, Emama Fault and Emama Backthrust; (c) during displacement along the Lavani Backthrust; (d) during displacement along the Karius Thrust and (e) during displacement along the Juha inversion.*

2.5.1. 3D structural evolution of the Eastern Muller Range

Observations from geological and geophysical data across Mt Aya in the Lavani Valley form a crucial foundation for our understanding of the 3D structural evolution of the EMR. In particular, the intersection of thick syn-rift sediments in the Lavani-1 well suggests the area was a regionally significant depocentre during early Mesozoic rifting. But at the same time these sediments have been uplifted such that Jurassic strata crop out at the crest of Mt Aya indicating it has experienced the greatest uplift in the EMR and possibly in the entire PFTB. Thus, there is a strong correlation between the magnitude of extension along the half-graben bounding Lavani normal fault and subsequent inversion along the Lavani inversion fault, a relationship also recently recognised within the Taranaki Basin in New Zealand (Reilly *et al*., 2016). The following model for the evolution of the EMR fits well with this type of inversion fault behaviour.

2.5.1.1. Early Mesozoic extension

Northeast-southwest to NNE-SSW extension of the Papua New Guinea margin in the early Mesozoic (e.g., Home *et al.,* 1990) was associated with the formation of the regionally extensive northwest-southeast striking Lavani normal fault beneath the present-day EMR (Fig. 2.11a). Over the course of the extensional evolution, a regional-scale, southeast-dipping relay ramp formed from at least as far northeast as the Muller-1 well (Fig. 2.1b) to the southeast-end of the present-day Lavani Valley. This ramp may have formed to transfer extension between the Lavani normal fault beneath the EMR and another major basin-bounding normal fault to the north which

continues into the WMR or Om Beds/Om Metamorphics (Figs. 2.1b and 2.11a). Syn-rift sediments accumulated on this regional relay ramp during its evolution, leading to thicker sediments towards the base of the ramp around the present-day Lavani Valley.

Displacement along the Lavani normal fault was greatest towards its centre beneath the present-day Lavani Valley, and decreased towards the southeast and northeast ends, thus approximating a commonly observed normal fault displacement-distance relationship (e.g., Muraoka and Kamata, 1983; Peacock and Sanderson, 1991; Gupta and Scholz, 2000; Frankowicz and McClay, 2010), but with an apparent level of asymmetry resulting from displacement decreasing more abruptly towards the southeast than the northwest (Fig. 2.11b). Here, this asymmetry is interpreted to have been accommodated along a number of cross-cutting, oblique-slip normal faults that breached the footwall block including the southeast-dipping relay ramp (Fig. 2.11b). Alternatively, the development of secondary oblique to cross-cutting structures could plausibly relate to an evolving extension direction on the New Guinea margin, in a style analogous to the nearby Bonaparte Basin in North West Australia (Frankowicz and McClay, 2010). A smaller relay ramp may have also formed at the southeast end of the present-day Lavani Valley, but if so, was abruptly breached to accommodate a more rapid transition to higher displacement along the Lavani normal fault to the northwest (Fig. 2.11a and b). This scenario would have left a transfer fault that during subsequent extension may have connected the Lavani normal fault to another normal fault towards the east (Fig. 2.11a).

Relay ramps form as a means of transferring extension between overlapping normal faults and breaching is common (e.g., Hus *et al.*, 2005; Fossen and Rotevatn, 2016). The example presented here differs in that multiple normal faults cross-cut the southeast-dipping relay ramp, representing a distributed zone of breaching rather than a single breach (Fig. 2.11a and b). Outcrop-scale evidence from better

constrained extensional systems suggest that breached ramps are commonly complex, often involving multiple cross-cutting faults (Soliva and Benedicto, 2004). Pre-existing weaknesses are a likely influence on the evolution of multiple cross-cutting faults, as observed in Canyonlands National Park, Utah, where cross-cutting normal faults have formed along relay ramp-intersecting joint sets (Trudgill and Cartwright, 1994; Fossen and Rotevatn, 2016).

2.5.1.2. Cenozoic compression

Northeast-southwest compression associated with the formation of the PFTB reached the Muller Range around the late Miocene (Hill and Gleadow, 1989). The regional extent and large displacement of the Lavani normal fault made it particularly preconditioned for subsequent inversion (as per Eisenstadt and Withjack, 1995; Kelly *et al.*, 1999; Panien *et al.*, 2005; Reilly *et al.*, 2016). However, despite significant inversion and hanging wall uplift along the Lavani inversion fault, the hanging wall remains lower than the footwall located beneath Lavani Ridge and Karius Plateau in the present-day (Figs. 2.10e and 2.11d) (e.g., Bidstone *et al.*, 1974).

Reverse displacement along the Lavani inversion fault was heterogeneously distributed with a strong correlation with its original extensional displacement (c.f. Fig. 2.11b and d). Similar to the rifting phase, inversion-related displacement differences were accommodated along the length of the relay ramp by inversion of oblique-slip cross-structures that subsequently dispersed into the sedimentary sequence forming the distributed regions of tear faulting observed in Lavani Valley (Fig. 2.11d). These zones are therefore characterised by the opposite movement sense to the original extension-related basement cross-structures (c.f. Fig. 2.11b and c). The greatest reverse displacement along the Lavani inversion fault and associated Emama Fault occurred around Mt Aya, where the sedimentary sequence was uplifted more than 7 km above regional. The great depth of basement beneath Mt

Aya prior to compression (Fig. 2.11a and b) was crucially important in allowing such significant uplift without an associated present-day gravity high.

During the evolution of the EMR, the Lavani inversion fault shallowed to form triangle zones beneath Lavani Ridge and Karius Plateau, with shortening of the Mesozoic sedimentary sequence accommodated along the Lavani Backthrust (Figs. 2.10c and 2.11d). Continued heterogeneous displacement along the Lavani inversion fault was then transferred to the surface largely along the Lavani Backthrust, causing increased northeast-directed thrusting of the Lavani Ridge into the southeast-end of Lavani Valley, driving sinistral offset at the Centre Pass Tear Fault (Fig. 2.11d). This model for the evolution of Centre Pass also accounts for opposing movement senses observed along the seemingly continuous Emama Tear Faults and Centre Pass Tear Fault; that is, each formed from a consistent shortening regime, but relate to structures with opposing vergence. During the final stages in the evolution of the EMR, the Karius Thrust uplifted Karius Ridge creating the Karius Anticline and Karius Syncline across Karius Plateau (Figs. 2.10d and 2.11d).

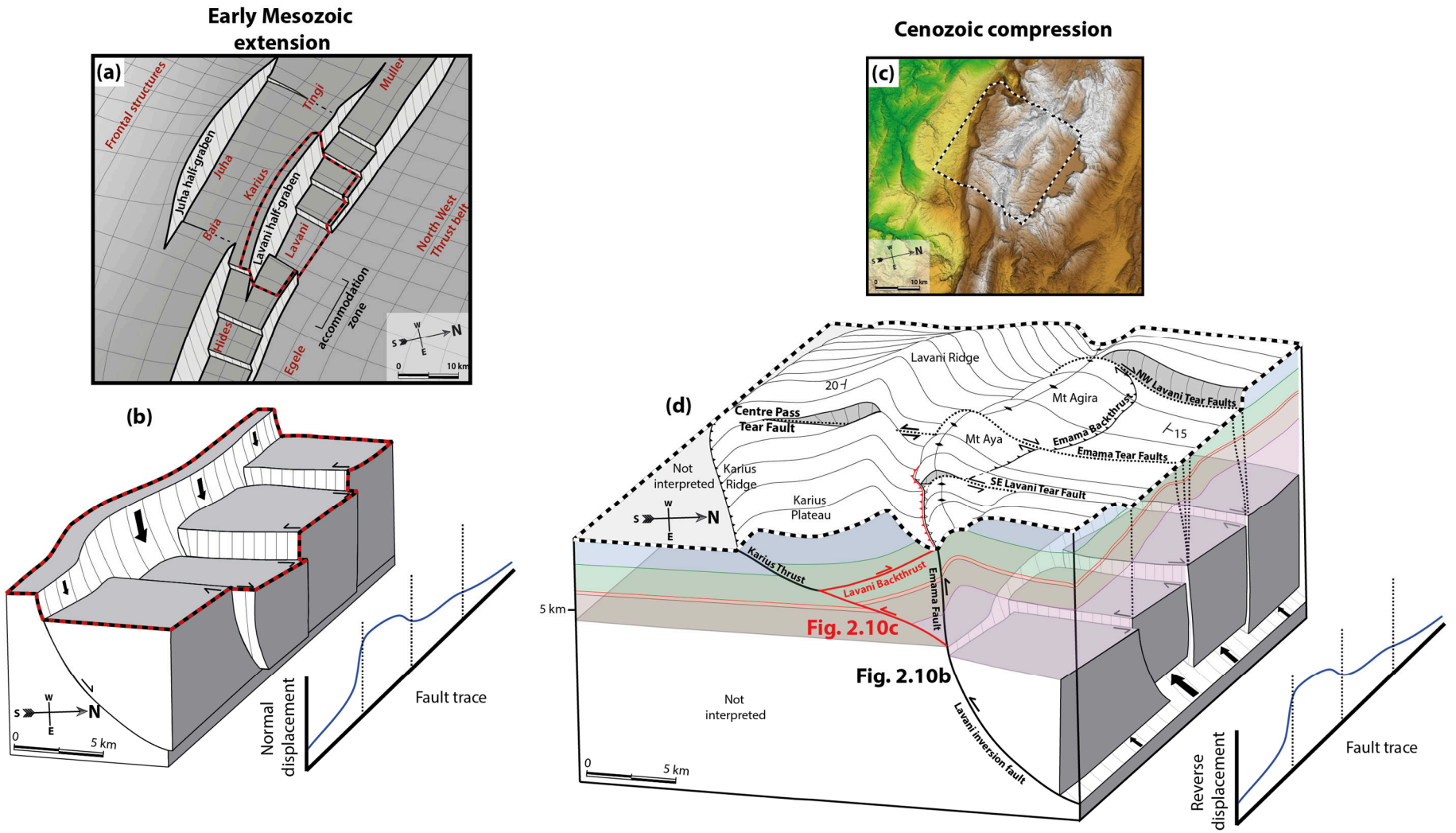
Early Mesozoic extension
(a)
Frontal structures
Juha half-graben
Juha
Karius
Tingi
Mullet
Lavani half-graben
Lavani
Baia
North West Thrust belt
accommodation zone
Hides
Egele
W
S
N
E
0
10 km
(b)
W
S
N
E
0
5 km
Normal displacement
Fault trace
Cenozoic compression
(c)
W
S
N
E
0
10 km
(d)
Lavani Ridge
20
Mt Agira
NW Lavani Tear Faults
Centre Pass Tear Fault
Mt Aya
Emama Backthrust
15
Emama Tear Faults
Not interpreted
Karius Ridge
SE Lavani Tear Fault
Karius Plateau
W
S
N
E
Karius Thrust
Lavani Backthrust
Emama Fault
5 km
Fig. 2.10c
Fig. 2.10b
Not interpreted
Lavani inversion fault
0
5 km
Reverse displacement
Fault trace

Figure 2.11. *(previous page) Model of the 3D evolution of the Eastern Muller Range, (a) Schematic early Mesozoic rift architecture beneath the Greater Juha area with red labels marking the location of present-day structural features; (b) Schematic early Mesozoic rift architecture beneath the Lavani Valley showing the Lavani normal fault, southeast-dipping relay ramp and cross-cutting normal structures. Location marked by dashed red box in (a); (c) SRTM DEM across the Eastern Muller Range (USGS, 2015); (d) Cenozoic inversion to form the Eastern Muller Range, including basement-connected tear faults with opposing movement sense to original cross-cutting normal structures. Note: Mt Aya is simplified by showing its pre-erosion geometry – i.e. shown prior to the erosion of the forelimb of the Lavani Anticline and associated surface exposure of Toro Sandstone and Imburu Mudstone. Location marked by dashed box in (c).*

2.6. Discussion

2.6.1. Controls on structural style

The well-constrained Darai Limestone shows very low shortening of 12.6 – 21.4% across the Greater Juha area (see Section 2.4.7), which is unusual given the high magnitude of uplift across the EMR. In comparison, the much less elevated KFTB (Fig. 2.1b) is characterised by > 40% shortening (Hill, 1991). Triangle zone-related deformation is often invoked to explain large, internally complex mountain front structures characterised by only minor near-surface shortening (e.g., Suppe, 1980; Jones, 1982) and this model is consistent with structures observed within the leading-edge of the PFTB including (from southeast to northwest) the Puri Anticline (Medd, 1996), Cecilia Anticline (Hanani *et al.*, 2016) and P'nyang Anticline (Eisenberg, 1996). In the elevated EMR, the regionally-prominent Lavani Backthrust provides a mechanism to transfer shortening within the incompetent early Mesozoic sequence through the competent Darai Limestone. Through time, as the Lavani Anticline was initially uplifted and eroded to form the Lavani Valley, this discontinuity within the Darai Limestone provided an easy pathway for shortening to reach the surface without having to be accommodated within thick competent Darai Limestone towards the foreland. Geological and geomorphic evidence suggests that the significance of the Lavani Backthrust decreases towards the

northwest of the EMR, limiting the amount of shortening it can accommodate. In this area there is a recognisable change in structural style including increased structural complexity, more distributed and greater overall shortening within the Darai Limestone (e.g., cross-section, A-A') meaning there are more structures likely to account for uplift of the EMR.

We suggest the inversion of pre-existing rift architecture is the primary influence on the evolution of the Greater Juha area. A number of prominent detachment-levels have been recognised within the Mesozoic sedimentary sequence in the KFTB (e.g., Hill *et al*., 2008, 2010), but their relationship with basement-inversion structures has often been unclear. In the Greater Juha area, thrust structures detach from similar horizons (e.g., Cecilia Anticline, Karius Thrust, both detached in the Ieru Formation) but with better-constrained connections to nearby inversion structures. For instance, the extensive and relatively undeformed backlimb of the Lavani Anticline suggests that thrust structures (including triangle zones) across the EMR (e.g., Karius Thrust, Lavani Backthrust) are proximally linked to the steep Lavani inversion fault, rather than distally to structures within the neighbouring North West Thrust Belt (Fig. 2.1c). Basement-connected triangle zones have been identified in other fold and thrust belts (e.g., Zapata and Allmendinger, 1996; Sterne, 2006), but in general appear less abundant than triangle zones with prominent sedimentary detachments (e.g., floor thrusts). The evolution of triangle zones within the Greater Juha area is likely to be controlled by competence contrasts within the stratigraphic column, in particular between (1) competent crystalline basement, (2) largely incompetent early Mesozoic sediments, and (3) competent Darai Limestone. Perhaps the best documented analogue for this structure style is the Ellesmerian mountain front in North Greenland. There, balanced cross-sections reveal steeply-dipping, basement-connected inversion structures that connect to a major roof backthrust at the base of a thick carbonate shelf sequence, thus similarly forming triangle zones within the enclosed incompetent basinal sediments, and an

elevated mountain front monocline (Soper and Higgins, 1990). Given access and logistical challenges in the PFTB, identifying analogues from better understood fold and thrust belts worldwide is likely to be crucial to improve our understanding of subsurface structure.

Also, robust geochronological data are required to constrain the temporal evolution of the Greater Juha area and to help develop kinematic and mechanical structural models. Furthermore, additional modelling is required to understand (1) why the generally similar Lavani and Juha anticlines differ in having an emergent frontal fault (Emama Fault) and blind frontal fault (Juha inversion fault), respectively, and (2) the geometric evolution of the Lavani inversion fault from the steep-dipping Emama Fault to shallowly-dipping detachments and thrust structures within the sedimentary sequence.

2.6.2. Arc-normal lineaments and structures

Arc-normal oriented structures are pervasive across a range of scales within the Greater Juha area of the PFTB. We suggest this observed trend relates directly to zones of tear faulting that connect at depth to weakened pre-existing basement cross-structures that have inverted during compression to accommodate lateral displacement variations (Fig. 2.11d). The dominant movement sense along arc-normal structures is oblique dextral, up-to-the-southeast, consistent with structures also observed within the KFTB (Hill *et al.,* 2008, 2010), the Hides Anticline (Johnston and Emmett, 2000), between the Cecilia, Wai Asi and Strickland Anticlines (Craig and Warvakai, 2009), in the EMR (e.g., Legari Tear; Hornafius, 1993), WMR (Eisenberg, 1996) and in the WPFTB (White *et al.,* 2014). Regional-scale arc-normal lineaments are also commonly associated with dextral offset, including the Bosavi Lineament (e.g., Osborne, 1990) and a lineament interpreted to run through the Strickland Gorge (Hill, 1989) (Fig. 2.1b).

Observations from geological data across the Greater Juha area highlight the secondary presence of arc-normal structures with oblique sinistral, up-to-the-northwest movement sense (e.g., Figs. 2.4a and 2.11d). We found no convincing evidence of regionally-continuous arc-normal lineaments intersecting the Greater Juha area. This suggests that regional-scale lineaments observed across the PFTB may consist of less continuous, smaller-scale arc-normal structures and thus may not necessarily relate to regional-scale rift architecture (i.e. transfer faults). For instance, arc-normal structures across Lavani Valley appear to be basement-connected, but discontinuous, as they do not appear to disturb the backlimb of the Lavani Anticline and Lavani Ridge. Even the apparently continuous Emama Tear Faults and Centre Pass Tear Fault appear to have differing movement senses (Fig. 2.6b). We suggest the Emama Tear Faults relate to foreland-vergent inversion along the underlying Lavani normal fault, while the Centre Pass Tear Fault relates to hinterland-vergent thrusting along the Lavani Backthrust, and thus the latter is not directly related to an underlying basement structure (Fig. 2.11d). This highlights the importance of understanding the relationship between arc-parallel structural style and arc-normal structures, something that is often overlooked during cross-section based studies.

The controls on, and relationships between, local-scale arc-normal structures and regional-scale arc-normal lineaments within the PFTB are largely unclear, but are likely to be complex. Early Mesozoic rift architecture is clearly influencing lateral variations in structural style across the PFTB (e.g., Hill, 1991; Hill *et al.,* 2010) however arc-normal structures and lineaments that appear to accommodate this variation may ultimately relate to a complex basement fabric beneath the PFTB with an overall northeast to southwest orientation (e.g., White *et al.*, 2014).

The influence of basement fabrics on rift architecture (e.g., Smith and Mosley, 1993; Ring, 1994; Corti *et al.,* 2007) and subsequent inversion (e.g., Piquer *et al*., 2016) is well-established elsewhere. Thus, it is plausible that Palaeozoic basement fabric controlled the structural framework of the Papuan Basin during rifting in the early

Mesozoic, forming regional-scale accommodation zones and related local-scale transfer structures that are now expressed as regional-scale arc-normal lineaments and local-scale arc-normal structures, respectively. Transfer structures, including complexly breached relay ramps, utilise northeast-southwest striking weaknesses associated with the basement fabric, as a mechanism for accommodating displacement along major northwest-southeast striking normal faults (e.g., Fig 2.11a). These structures have subsequently been inverted to form arc-normal oriented zones of tear faulting that accommodate laterally variable displacement along inversion faults and connected thrust structures. Additional work should focus on developing a more robust understanding of the relationship between basement fabric, early Mesozoic rift architecture and subsequent Cenozoic inversion, and the 3D spatiotemporal evolution of the PFTB.

References

Abers, G., McCaffrey, R., 1988. Active deformation in the New Guinea fold-and-thrust belt: Seismological evidence for strike-slip faulting and basement-involved thrusting. *Journal of Geophysical Research: Solid Earth,* 93, pp.13332-13354.

Allen, T.L., Trotter, J.A., Whitford, D.J., Korsch, M.J., 2000. Strontium isotope stratigraphy and the Oligocene-Miocene T-Letter "Stages" in Papua New Guinea. In: Buchanan, P., Grainge, A., Thornton, R. (Eds.), *Petroleum exploration, development, and production in Papua New Guinea: proceedings of the fourth PNG Petroleum Convention*, Papua New Guinea Chamber of Mines and Petroleum, Port Moresby, pp.155-168.

Amoco PNG Exploration Company, 1982. Lavani 1 well completion report, 137 pp.

Baldwin, S., Fitzgerald, P., Webb, L., 2012. Tectonics of the New Guinea Region. *Annual Review of Earth and Planetary Sciences*, 40, pp.495-520.

Bennett, D.J., Brand, R.P., Mills, C.R., Morris, B.D., 2000. Exploration potential of the West Bosavi area, Papuan foreland basin, Papua New Guinea. In: Buchanan, P., Grainge, A., Thornton, R. (Eds.), *Petroleum exploration, development, and production in Papua New Guinea: proceedings of the fourth PNG Petroleum Convention*, Papua New Guinea Chamber of Mines and Petroleum, Port Moresby, pp.139-154.

Bidstone, B.J., St. John, V.P., Thomas, E.G., 1974. Report on the Lavani Valley seismic and gravity survey, Geological Survey of Papua New Guinea archive file F1/S/74-21 (unpubl.)

Bonini, M., Sani, F., Antonielli, B., 2012. Basin inversion and contractional reactivation of inherited normal faults: A review based on previous and new experimental models. *Tectonophysics*, 522, pp.55-88.

Bradley, G., 2014. Western Papuan Basin to Western Aure: Generalised Cenozoic - Jurassic Chronostratigraphy (unpubl.), 1 pp.

Buchanan, J.G., Buchanan, P.G. (Eds.), 1995. *Basin inversion*, Geological Society, London, Special Publications, 88.

Buchanan, P., Warburton, J., 1996. The influence of pre-existing basin architecture in the development of the Papuan fold and thrust belt: implications for petroleum prospectivity. In: Buchanan, P. (Ed.), *Petroleum exploration, development, and production in Papua New Guinea: proceedings of the third PNG Petroleum Convention*, Papua New Guinea Chamber of Mines and Petroleum, Port Moresby, pp.89-109.

Chorowicz, J., 2005. The East African Rift. *Journal of African Earth Sciences*, 43, pp.379-410.

Cooper, M., 1996. Passive-roof duplexes and pseudo-passive-roof duplexes at mountain fronts: A review. *Bulletin of Canadian Petroleum Geology*, 44, pp.410-421.

Corbett, G., 1994. Regional structural control of selected Cu/Au occurrences in Papua New Guinea. In Rogerson, R (Ed.), *Proceedings of the PNG Geology, Exploration and Mining Conference 1994*, Australasian Institute of Mining and Metallurgy, pp.57-70.

Corti, G., van Wijk, J., Cloetingh, S., Morley, C.K., 2007. Tectonic inheritance and continental rift architecture: Numerical and analogue models of the East African Rift system. *Tectonics*, 26, TC6006.

Craig, M., Warvakai, K., 2009. Structure of an active foreland fold and thrust belt, Papua New Guinea. *Australian Journal of Earth Sciences,* 56, pp.719-738.

Crowhurst, P., Hill, K., Foster, D., 1997. The structural and tectonic development of the Frieda River Mineral district, NW Papua New Guinea. In Hancock, G. (Ed.), *Proceedings of the PNG Geology, Exploration and Mining Conference 1997*, Australasian Institute of Mining and Metallurgy, pp.51-60.

Davies, H., 1983. Wabag 1:250 000 geological series explanatory notes Sheet SB/54-8, Geological Survey of Papua New Guinea, PNG Department of Minerals and Energy, Port Moresby.

Davies, H., 1991. Regional geologic setting of some mineral deposits of the New Guinea region. In: Rogerson, R. (Ed), *Proceedings of the Papua New Guinea Geology, Exploration and Mining Conference 1991*, Australasian Institute of Mining and Metallurgy, pp.49–57.

Davies, H., Norvick, M., 1974. Blucher Range 1:250 000 geological series explanatory notes Sheet SB/54-07, Geological Survey of Papua New Guinea, PNG Department of Minerals and Energy, Port Moresby.

Denison, C. N., 1990. Palynostratigraphic revision of Amoco Lavani-1 well, Papua New Guinea (unpubl.), 6 pp.

Eisenberg, L.I., 1996. Strontium isotope analysis and structural interpretation of P'nyang Anticline, Papuan Fold Belt, Western Highlands Province, Papua New Guinea. In: Buchanan, P. (Ed.), *Petroleum exploration, development, and production in Papua New Guinea: proceedings of the third PNG Petroleum Convention*, Papua New Guinea Chamber of Mines and Petroleum, Port Moresby, pp.231-244.

Eisenstadt, G., Withjack, M.O., 1995. Estimating inversion: results from clay models. *Geological Society, London, Special Publications,* 88, pp.119-136.

Ekström, G., Nettles, M., Dziewonski, A., 2012. The global CMT project 2004-2010: Centroid-moment tensors for 13,017 earthquakes. *Physics of the Earth and Planetary Interiors*, 200, pp.1-9.

Fossen, H., Rotevatn, A., 2016. Fault linkage and relay structures in extensional settings—A review. *Earth Science Reviews*, 154, pp.14-28.

Frankowicz, E., McClay, K.R., 2010. Extensional fault segmentation and linkages, Bonaparte Basin, outer North West Shelf, Australia. *The American Association of Petroleum Geologists Bulletin*, 94, pp.977-1010.

Gow, P.A., Upton, P., Zhao, C., Hill, K.C., 2002. Copper–gold mineralisation in New Guinea: numerical modelling of collision, fluid flow and intrusion-related hydrothermal systems. *Australian Journal of Earth Sciences*, 49, pp.753-771.

Gupta, A., Scholz, C.H., 2000. A model of normal fault interaction based on observations and theory. *Journal of Structural Geology*, 22, pp.865-879.

Hall, R., 1996. Reconstructing Cainozoic SE Asia. In: Hall, R., Blundell, D. (Eds.), *Tectonic Evolution of SE Asia*, Geological Society of London Special Publication, 106, pp.153-184.

Hall, R., 1997. Cainozoic tectonics of SE Asia and Australasia. In: Howes, J., Noble, R. (Eds.), *Proceedings of the International Conference on Petroleum Systems of SE Asia and Australia*, Indonesian Petroleum Association, Jakarta, pp.47-62.

Hall, R., 2002. Cenozoic geological and plate tectonic evolution of SE Asia and the SW Pacific: computer-based reconstructions, model and animations. *Journal of Asian Earth Sciences*, 20, pp.353-434.

Hall, R., 2012. Late Jurassic–Cenozoic reconstructions of the Indonesian region and the Indian Ocean. *Tectonophysics*, 570, pp.1-41.

Hanani, A., Lennox, P., Hill, K.C., 2016. The Geology and Structural Style of the Juha Gas Field, Papua New Guinea. *ASEG Extended Abstracts 2016*, pp.1-7.

Hill, K.C., 1989. The Muller Anticline, Papua New Guinea; basement cored, inverted extensional fault structures with opposite vergence. *Tectonophysics*, 158, pp.227-245.

Hill, K.C., 1991. Structure of the Papuan Fold Belt, Papua New Guinea. *The American Association of Petroleum Geologists Bulletin*, 75, pp.857-872.

Hill, K.C., Bradey, K., Iwanec, J., Wilson, N., Lucas, K., 2008. Structural exploration in the Papua New Guinea Fold Belt. In: Blevin, J.E., Bradshaw, B.E., Uruski, C. (Eds.), *Eastern Australian Basins Symposium III*, Petroleum Exploration Society of Australia, Special Publication, 225238.

Hill, K.C., Gleadow, A., 1989. Uplift and thermal history of the Papuan Fold Belt, Papua New Guinea: Apatite Fission track analysis. *Australian Journal of Earth Sciences*, 36, pp.515-539.

Hill, K.C., Hall, R., 2003. Mesozoic-Cenozoic evolution of Australia's New Guinea margin in a west Pacific context. *Geological Society of America Special Papers*, 372, pp.265-290.

Hill, K.C., Kendrick, R., Crowhurst, P., Gow, P., 2002. Copper–gold mineralisation in New Guinea: tectonics, lineaments, thermochronology and structure. *Australian Journal of Earth Sciences*, 49, pp.737-752.

Hill, K.C., Lucas, K., Bradey, K., 2010. Structural styles in the Papuan Fold Belt, Papua New Guinea: constraints from analogue modelling. In: Goffey, G. (Ed.), *Hydrocarbons in Contractional Belts*, Geological Society, London, Special Publications, 348, pp.33-56.

Hill, K.C., Norvick, M., Keetley, J., Adams, A., 2000. Structural and stratigraphic shelf-edge hydrocarbon plays in the Papuan Fold Belt. In: Buchanan, P., Grainge, A., Thornton, R. (Eds.), *Petroleum exploration, development, and production in Papua New Guinea: proceedings of the fourth PNG Petroleum Convention*, Papua New Guinea Chamber of Mines and Petroleum, Port Moresby, pp.67-85.

Hill, G.S., Price, S.J. Foster, M.S., Stephenson, R.W., Ellis, D., Lyslo, J.A., 1996. Seismic acquisition in the Papuan Fold Belt – a new approach. In: Buchanan, P. (Ed.), *Petroleum exploration, development, and production in Papua New Guinea: proceedings of the third PNG Petroleum Convention*, Papua New Guinea Chamber of Mines and Petroleum, Port Moresby, pp.445-458.

Hill, K.C, Raza, A., 1999. Arc-continent collision in Papua Guinea: constraints from fission track thermochronology. *Tectonics,* 18, pp.950-966.

Hill, K.C, Simpson, R., Kendrick, R., Crowhurst, P., O'Sullivan, P., Saefudin, I., 1996, Hydrocarbons in New Guinea, controlled by basement fabric, Mesozoic extension and Tertiary Convergent margin tectonics. In: Buchanan, P. (Ed.), *Petroleum exploration, development, and production in Papua New Guinea: proceedings of the third PNG Petroleum Convention*, Papua New Guinea Chamber of Mines and Petroleum, Port Moresby, pp.63-76.

Hobson, D.M., 1986. A thin-skinned model for the Papuan thrust belt and some implications for hydrocarbon exploration. *Australian Petroleum Exploration Association Journal*, 26, pp.214-224.

Home, P., Dalton, D., Brannan, J., 1990. Geological evolution of the Western Papuan Basin. In: Carman, G., Carman, Z. (Eds.), *Petroleum exploration, development, and production in Papua New Guinea: proceedings of the first PNG Petroleum Convention*, Papua New Guinea Chamber of Mines and Petroleum, Port Moresby, pp.107-118.

Hornafius, J.S., 1993. The 1990-1991 Muller Range Geological Survey – PPL 93. Mobil Exploration Niugini (unpubl.)

Hornafius, J.S., Denison, R.E., 1993. Structural interpretations based on strontium isotope dating of the Darai Limestone, Papuan Fold Belt, New Guinea. In: Carman, G., Carman, Z. (Eds.), *Petroleum exploration, development, and production in Papua New Guinea: proceedings of the second PNG Petroleum Convention*, Papua New Guinea Chamber of Mines and Petroleum, Port Moresby, pp.313-324.

Hus, R., Acocella, V., Funiciello, R., De Batist, M., 2005. Sandbox models of relay ramp structure and evolution. *Journal of Structural Geology*, 27, pp.459-473.

Jenkins, D., 1974. Detachment tectonics in western Papua New Guinea. *Geological Society of America Bulletin*, 85, pp.533-548.

Jenkins, D., White, M.F., 1970. Report on the Stricklnad River survey, Permit 46, Papua New Guinea. BP Petroleum Development Australian Pty Ltd, Geological survey of Papua New Guinea archive file 4 BS (unpubl.)

Johnstone, D., Emmett, J., 2000. Petroleum geology of the Hides Gas Field, Southern Highlands, Papua New Guinea. In: Buchanan, P., Grainge, A., Thornton, R. (Eds.), *Petroleum exploration, development, and production in Papua New Guinea: proceedings of the fourth PNG Petroleum Convention*, Papua New Guinea Chamber of Mines and Petroleum, Port Moresby, pp.319-335.

Jones, P.B., 1996. Triangle zone geometry, terminology and kinematics. *Bulletin of Canadian Petroleum Geology*, 44, pp.139-152.

Kawagle, S.A., Meyers, J.B., 1996. Structural and sequence geometry of the Kiunga area, Papuan foreland basin, Papua New Guinea. In: Buchanan, P. (Ed.), *Petroleum exploration, development, and production in Papua New Guinea: proceedings of the third PNG Petroleum Convention*, Papua New Guinea Chamber of Mines and Petroleum, Port Moresby, pp.175-193.

Keenan, S.E., Hill, K.C., 2015. The Mananda Anticline, Papua New Guinea: A third Oil Discovery, Appraisal Programme and Deep Potential. In: AAPG/SEG International Conference and Exhibition 2015.

Kelly, P.G., Peacock, D.C.P., Sanderson, D.J., McGurk, A.C., 1999. Selective reverse-reactivation of normal faults, and deformation around reverse-reactivated faults in the Mesozoic of the Somerset coast. *Journal of Structural Geology*, 21, pp.493-509.

Koulali, A., Tregoning, P., McClusky, S., Stanaway, R., Wallace, L., Lister, G., 2015. New Insights into the present-day kinematics of the central and western Papua New Guinea from GPS. *Geophysical Journal International*, 202, pp.993-1004.

Löffler, E., MacKenzie, D., Webb, A., 1980. Potassium-argon ages from some of the Papua New Guinea Highlands volcanoes, and their relevance to Pleistocene geomorphic history. *Journal of the Geological Society of Australia*, 26, pp.387-397.

Longley, I.M., Buessenschuett, C., Clydsdale, L., Cubitt, C.J., Davis, R.C., Johnson, M.K., Marshall, N.M., Murray, A.P., Somerville, R., Spry, T.B., Thompson, N.B., 2002. The North West Shelf of Australia–a Woodside perspective. *The sedimentary basins of Western Australia*, 3, pp.27-88.

Lunt, P., Allan, T., 2004. Larger foraminifera in Indonesian biostratigraphy, calibrated to isotopic dating. In: GRDC Museum Workshop on Micropalaeontology, Bandung, pp.1-109.

McClay, K.R., 1995. The geometries and kinematics of inverted fault systems: a review of analogue model studies. *Geological Society, London, Special Publications*, 88, pp.97-118.

McConachie, B., Lanzilli, E., Kendrick, D., Burge, C., 2000. Extensions of the Papuan Basin Foreland Geology into Eastern Irian Jaya (West Papua) and the New Guinea Fold Belt in Papua New Guinea. In: Buchanan, P., Grainge, A., Thornton, R. (Eds.), *Petroleum exploration, development, and production in Papua New Guinea: proceedings of the fourth PNG Petroleum Convention*, Papua New Guinea Chamber of Mines and Petroleum, Port Moresby, pp.219-238.

Medd, D.M., 1996. Triangle zone deformation at the leading edge of the Papuan Fold Belt. In: Buchanan, P. (Ed.), *Petroleum exploration, development, and production in Papua New Guinea: proceedings of the third PNG Petroleum Convention*, Papua New Guinea Chamber of Mines and Petroleum, Port Moresby, pp.217-229.

Metcalfe, I., 2002. Permian tectonic framework and palaeogeography of SE Asia. *Journal of Asian Earth Sciences,* 20, pp.551-566.

Mobil Exploration Niugini, 1991. Muller 1X well completion report, 58 pp.

Morley, C.K., Nelson, R.A., Patton, T.L., Munn, S.G., 1990. Transfer Zones in the East African Rift System and Their Relevance to Hydrocarbon Exploration in Rifts. *The American Association of Petroleum Geologists Bulletin*, 74, pp.1234-1253.

Muraoka, H., Kamata, H., 1983. Displacement distribution along minor fault traces. *Journal of Structural Geology*, 5, pp.483-495.

Niugini Gulf Oil Pty Ltd, 1983. Juha 1 well completion report, 77 pp.

Osborne, D.G., 1990. The hydrocarbon potential of the western Papuan Basin foreland—with reference to worldwide analogues. In: Carman, G., Carman, Z. (Eds.), *Petroleum exploration,*

development, and production in Papua New Guinea: proceedings of the first PNG Petroleum Convention, Papua New Guinea Chamber of Mines and Petroleum, Port Moresby, pp.197-213.

Page, R., 1976. Geochronology of igneous and metamorphic rocks in the New Guinea Highlands. *Bureau of Mineral Resources Australia Bulletin*, 162, 117 pp.

Panien, M., Schreurs, G., Pfiffner, A., 2005. Sandbox experiments on basin inversion: testing the influence of basin orientation and basin fill. *Journal of Structural Geology*, 27, pp.433-445.

Peacock, D.C.P., Sanderson, D.J., 1991. Displacements, segment linkage and relay ramps in normal fault zones. *Journal of Structural Geology*, 13, pp.721-733.

Pigott, J.D., Trumbly, N.I., O'Neal, M.V., 1985. Northern New Guinea wrench fault system: a manifestation of Late Cenozoic interactions between Australian and Pacific plates. *Tectonics*, 4, pp.613-620.

Pigram, C., Panggabean, H., 1984. Rifting of the northern margin of the Australian continent and the origin of some microcontinents in eastern Indonesia. *Tectonophysics,* 107, pp.331-353.

Pigram, C., Symonds, P.A., 1991. A review of the timing of the major tectonic events in the New Guinea Orogen. *Journal of Southeast Asian Earth Sciences*, 6, pp.307-318.

Piquer, J., Berry, R.F., Scott, R.J., Cooke, D.R., 2016. Cenozoic structural evolution of the Main Cordillera of Central Chile. *Journal of Structural Geology*, 89, pp.101-117.

Reilly, C., Nicol, A., Walsh, J., 2016. Importance of pre-existing fault size for the evolution of an inverted fault system. *Geological Society, London, Special Publications,* 439, SP439-2.

Ring, U., 1994. The influence of preexisting structure on the evolution of the Cenozoic Malawi rift (East African rift system). *Tectonics*, 13, pp.313-326.

Saintot, A., Angelier, J., 2002. Tectonic paleostress fields and structural evolution of the NW-Caucasus fold-and-thrust belt from Late Cretaceous to Quaternary. *Tectonophysics*, 357, pp.1-31.

Schofield, S., 2000. The Bosavi Arch and the Komewu Fault Zone: Their control on basin architecture and the prospectivity of the Papuan foreland. In: Buchanan, P., Grainge, A., Thornton, R. (Eds.), *Petroleum exploration, development, and production in Papua New Guinea: proceedings of the fourth PNG Petroleum Convention*, Papua New Guinea Chamber of Mines and Petroleum, Port Moresby, pp.101-122.

Smith, R.I., 1990. Tertiary plate tectonic setting and evolution of Papua New Guinea. In: Carman, G., Carman, Z. (Eds.), *Petroleum exploration, development, and production in Papua New Guinea: proceedings of the first PNG Petroleum Convention*, Papua New Guinea Chamber of Mines and Petroleum, Port Moresby, pp.229-244.

Smith, M., Mosley, P., 1993. Crustal heterogeneity and basement influence on the development of the Kenya Rift, East Africa. *Tectonics,* 12, pp.591-606.

Soliva, R., Benedicto, A., 2004. A linkage criterion for segmented normal faults. *Journal of Structural Geology*, 26, pp.2251-2267.

Soper, N.J., Higgins, A.K., 1990. Models for the Ellesmerian mountain front in North Greenland: a basin margin inverted by basement uplift. *Journal of Structural Geology*, 12, pp.83-97.

Stanaway, R., Noonan, J., 2015. Geodetic Measurement of Deformation within the Papuan Fold and Thrust Belt. American Association of Petroleum Geologists International Conference and Exhibition, 13th-16th September 2015, Melbourne, Australia.

Sterne, E.J.N., 2006. Stacked,"evolved" triangle zones along the southeastern flank of the Colorado Front Range. *The Mountain Geologist*, 43, pp.65-92.

Storti, F., McClay, K., 1995. Influence of syntectonic sedimentation on thrust wedges in analogue models. *Geology*, 23, pp.999-1002.

Suppe, J., 1980. Imbricated structure of western foothills belt, southcentral Taiwan. *Petroleum Geology of Taiwan*, 17, pp.1-16.

Texaco Overseas Petroleum Company, 1971. Cecilia 1 well completion report, 130 pp.

Thornton, R., Emmett, J., Laslo, J., Gottschalk, R., 1996. Integrated structural and stratigraphic analysis in PPL 175, Papuan Fold Belt, Papua New Guinea. In: Buchanan, P. (Ed.), *Petroleum exploration, development, and production in Papua New Guinea: proceedings of the third PNG Petroleum Convention*, Papua New Guinea Chamber of Mines and Petroleum, Port Moresby, pp.195-215.

Trudgill, B., Cartwright, J., 1994. Relay-ramp forms and normal-fault linkages, Canyonlands National Park, Utah. *Geological Society of America Bulletin*, 106, pp.1143-1157.

USGS, 2015. Shuttle Radar Topography Mission, 1-arc second, Global Land Cover Facility, University of Maryland, College Park, Maryland. Accessed through USGS EarthExplorer.

Wallace, L., Stevens, C., Silver, E., McCaffrey, R., Loratung, W., Hasiata, S., Stanaway, R., Curley, R., Rosa, R., Taugaloidi, J., 2004. GPS and seismological constraints on active tectonics and arc-continent collision in Papua New Guinea: Implications for mechanics of microplate rotations in a plate boundary zone. *Journal of Geophysical Research*, 109(B5).

Webb, A., 1973. Geochronology report on samples submitted by BMR West Sepik party. Australian Mineral Development Laboratories Report AN3049/73 (unpubl.)

White, M.F., Marfleet, M.J., 1973. Laigap geological survey, Permit 46, Papua New Guinea. BP Petroleum Development Australian Pty Ltd, Geological survey of Papua New Guinea archive file 13 BL (unpubl.)

White, L.T., Morse, M.P., Lister, G.S., 2014. Lithospheric-scale structures in New Guinea and their control on the location of gold and copper deposits. *Solid Earth*, 5, pp.163-179.

Zahirovic, S., Seton, M., Müller, R. D., 2014. The Cretaceous and Cenozoic tectonic evolution of Southeast Asia, *Solid Earth*, 5, pp.227-273.

Zahirovic, S., Matthews, K. J., Flament, N., Müller, R. D., Hill, K. C., Seton, M., Gurnis, M., 2016. Tectonic evolution and deep mantle structure of the eastern Tethys since the latest Jurassic. *Earth Science Reviews*, 162, pp.293-337.

Zapata, T.R., Allmendinger, R.W., 1996. Thrust-front zone of the Precordillera, Argentina: a thick-skinned triangle zone. *The American Association of Petroleum Geologists Bulletin*, 80, pp.359-381.

Supplementary material A2: Representative structural, strontium isotope and palynological data

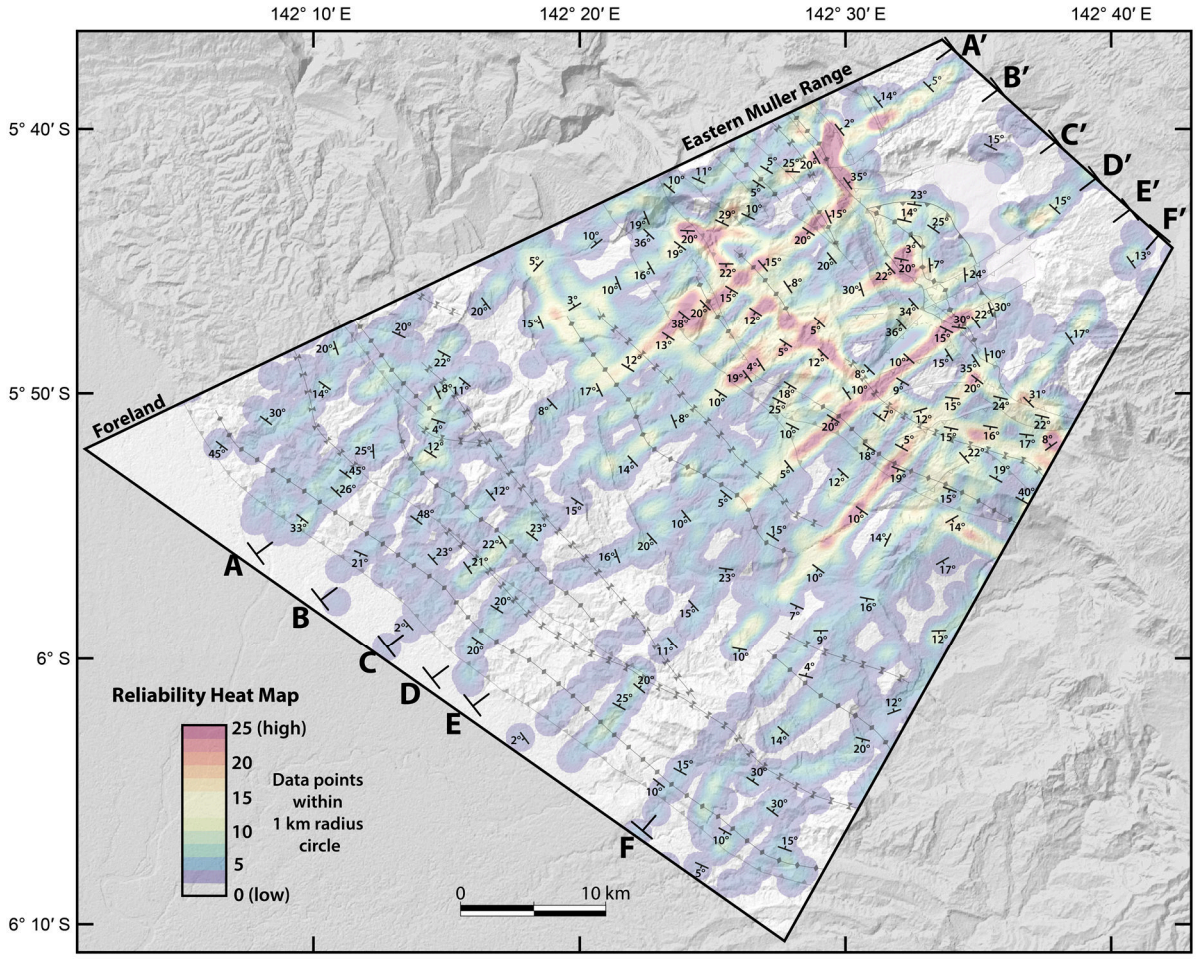

Figure A2.1. *Representative strike and dip data for the Greater Juha area, including new data collected in this study along with heritage data obtained from reports to the Papua New Guinea Government. Reliability heat map based on data density with high reliability corresponding to > 25 data points within a 1 km radius circle.*

Figure A2.2. *(next page) Strontium isotope (Orubadi Formation, Darai Limestone) and palynological (Ieru Formation, Toro Sandstone, Imburu Formation) age constraints on the Greater Juha area geological map and cross-sections. The colour coded circles correspond to Darai Limestone T-letter stages and Ieru Formation member colours within the legend. The scattered strontium ages within the Orubdai Formation relate to reworked Darai Limestone bioclasts.*

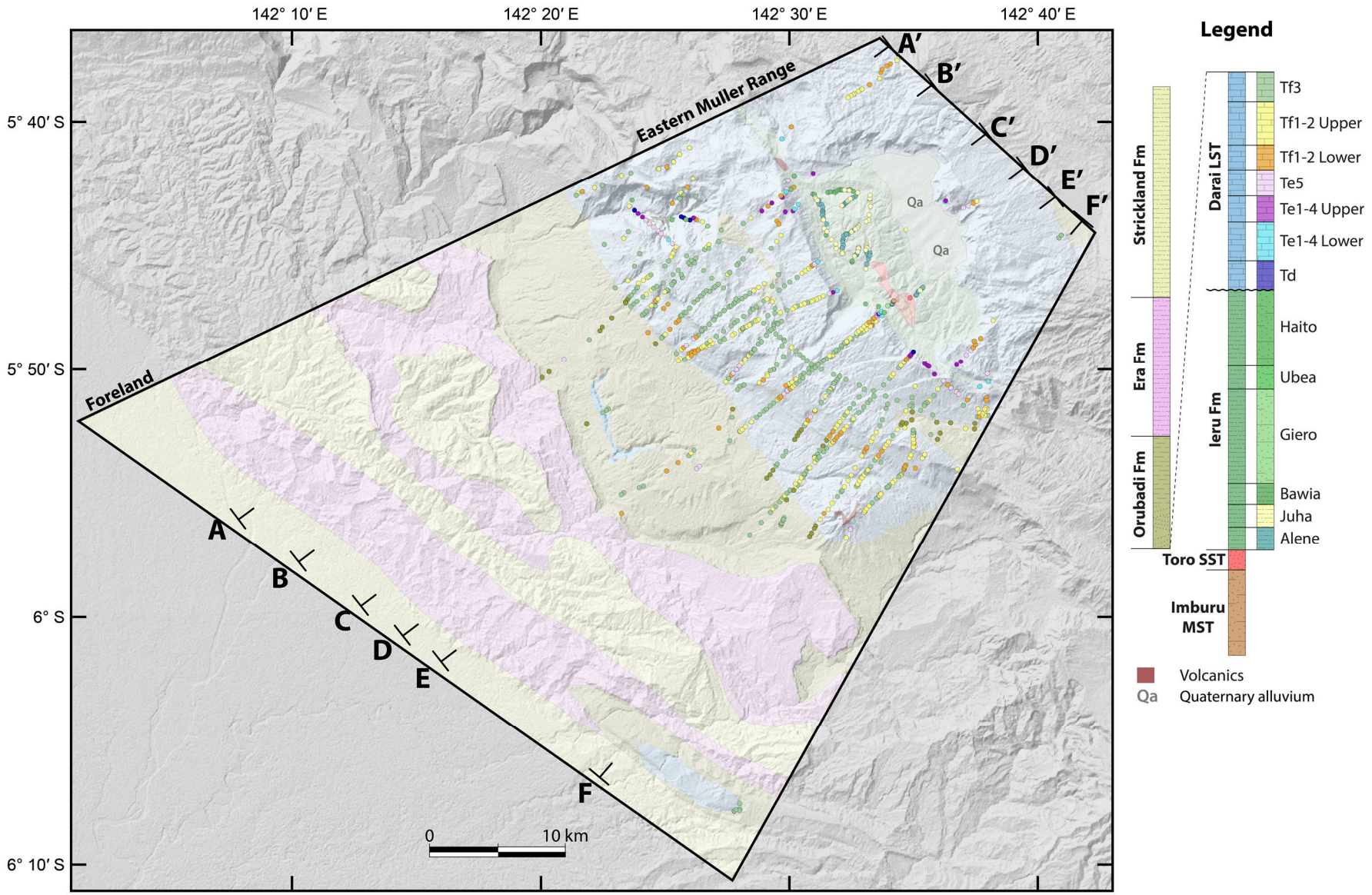
142° 10′ E
142° 20′ E
142° 30′ E
142° 40′ E
5° 40′ S
5° 50′ S
6° S
6° 10′ S
Eastern Muller Range
Foreland
A′
B′
C′
D′
E′
F′
A
B
C
D
E
F
Qa
Qa
0
10 km
Legend
Strickland Fm
Era Fm
Orubadi Fm
Darai LST
Tf3
Tf1-2 Upper
Tf1-2 Lower
Te5
Te1-4 Upper
Te1-4 Lower
Td
Ieru Fm
Haito
Ubea
Giero
Bawia
Juha
Alene
Toro SST
Imburu MST
Volcanics
Qa
Quaternary alluvium

Chapter 3

The 2018 M_w 7.5 Highlands earthquake in Papua New Guinea: Implications for structural style in an active fold and thrust belt

Abstract

The Papuan Fold and Thrust Belt (PFTB) in Papua New Guinea is actively forming within a complex tectonic setting at the boundary of the obliquely converging Australian and Pacific plates. The tectonic setting and inaccessibility of the PFTB make it one of the least well-understood fold and thrust belts on Earth. On 25th February 2018, a M_w 7.5 earthquake occurred within the PFTB, triggering an aftershock sequence which included five events ≥ M_w 6. In this study, we combine seismological, GPS and remote sensing observations to investigate the spatiotemporal distribution of crustal deformation during these events. All earthquakes ≥ M_w 6 were related to reverse offset on northeast-dipping fault planes and five out of the six, including the mainshock, were associated with mid-crustal focal depths (~ 15-30 km). During the sequence, the PFTB underwent up to 1.2 m of uplift and ground deformation occurred over 7,500 km^2. Combining these observations with our geological knowledge of this convergent margin highlights the primary control of the northern Australian passive margin on PFTB structural style. We propose that the earthquake sequence was related to tectonic inversion on a hidden extensional fault system beneath the PFTB and lateral variations along this fault zone had significant influence on the complex distribution of ground deformation. It follows that this fault system has had an important control on the evolution of variable structural styles within the PFTB. This study highlights the complexity that can characterise the evolution and structural style of fold and thrust belts.

3.1. Introduction

The processes by which continental crust accommodates shortening at convergent tectonic margins is a topic of broad interest as these processes control the distribution of natural hazards and resources (e.g., Groves *et al.*, 1998; Cooper, 2007; Stern *et al.*, 2016). Fold and thrust belts form in response to crustal shortening at such margins and often contain myriad deformational styles—also termed structural styles—which commonly differ between deformed belts or even within individual belts. Many tectonic and geological factors are recognised to influence fold and thrust belt structural styles, most of which relate in some way to (1) the tectonic setting, (2) the crustal composition and architecture of the deforming margin, and/or (3) the dynamic interaction between fold and thrust belt evolution and surface processes. Comprehensive reviews of the factors influencing fold and thrust belt evolution and structural style are provided in Nemcok *et al.* (2005), Poblet and Lisle (2011) and Lacombe and Bellahsen (2016).

One of the most discussed characteristics of fold and thrust belt structural style relates to the degree to which crystalline basement rocks are involved in contractional deformation. Where only the sedimentary cover is involved, it is known as thin-skinned deformation; where basement rocks are involved, it is known as thick-skinned deformation. However, it is often difficult to identify the relative influences of thin- and thick-skinned processes from the many other factors that influence fold and thrust belt evolution, and due to the time frame over which they act. Furthermore, fold and thrust belt interpretation is inherently biased towards overemphasising thin-skinned deformation, as thick-skinned processes are often more difficult to identify, both geologically and geophysically, due to the depth at which they commonly occur.

In actively deforming fold and thrust belts, such as the Papuan Fold and Thrust Belt (PFTB) in Papua New Guinea (PNG), the nature and distribution of contemporaneous seismicity and the associated crustal deformation provide valuable insight into evolutionary processes and geological structure at both the surface and in the subsurface. On the 25th February 2018 UTC (26th February PNG local time), a M_w 7.5 earthquake occurred within a remote area of the PFTB (also known as the PNG Highlands). It was the largest seismic event ever recorded in the region with modern seismic instruments. The ensuing aftershock sequence, as recorded on global seismic monitoring networks, was spread across > 7500 km^2 of the PFTB. The earthquake shaking and associated extensive slope failure in steep mountainous terrain collectively devastated the local inhabitants and resulted in a widespread humanitarian crisis (e.g., WHO, 2018).

In this paper, we use seismological, GPS and remote sensing observations to investigate the nature and spatiotemporal distribution of crustal deformation during the 2018 PNG Highlands earthquake sequence. We combine the new insights with our geological knowledge of this convergent margin to define the factors impacting the structural style and evolution of the PFTB.

3.2. Tectonic and geological background

Papua New Guinea (PNG) is the eastern half of the island of New Guinea, with the western half being part of Indonesia. The island has undergone a complex tectonic and geological history, particularly throughout the Cenozoic, associated with its location between the obliquely converging Australian and Pacific plates (Fig. 3.1, inset map). Detailed reviews of the tectonic history of PNG can be found in Pigram and Symonds (1991), Hill and Hall (2003) and van Ufford and Cloos (2005). The present-day setting of PNG is one of the most

tectonically complex regions in the world, comprising an assortment of tectonic features including rotating microplates, subduction zones, orogenic belts, rifts and transform boundaries (e.g., Baldwin *et al.*, 2012, Koulali *et al.*, 2015). These microplate interactions combine to accommodate ~ 110 mm yr^{-1} of convergence between the Pacific and Australian plates (DeMets *et al.*, 1994; Tregoning *et al.*, 1998).

Onshore PNG can be split into three major tectonic components following Hill and Hall (2003). In the south, the Stable Platform (SP; Fig. 3.1, inset map) represents the northern Australian continental margin which has been shaped by Mesozoic and Cenozoic extension but remains largely unaffected by Cenozoic deformation along the northern margin. The Stable Platform preserves the passive margin architecture that formed the Papuan Basin which continues to the north into what is now the Papuan Fold and Thrust Belt (PFTB). Along the northern margin of PNG, the intensely deformed Mobile Belt (MB; Fig. 3.1, inset map) comprises an assortment of island arcs and continental terranes that have been accreted to the leading edge of the northern Australian continental margin during collisional events throughout the Cenozoic. The PFTB separates the Stable Platform and Mobile Belt and comprises laterally discontinuous folded and thrusted structures that collectively form a ~ 550 km long northwest to southeast trending belt across PNG (Fig. 3.1). The PFTB formed in response to shortening within the Australian continental passive margin including within the Papuan Basin sediments during convergent movements throughout the Cenozoic, most significantly from the late Miocene to present (Hill and Raza, 1999; van Ufford and Cloos, 2005; Mahoney *et al.*, 2019).

Active deformation is presently occurring within onshore PNG, evidenced by widespread seismicity (e.g., Fig. 3.1, inset map). Earthquake locations show that deformation is concentrated around major convergent

(Ramu-Markham; RMFZ) and strike-slip (Bewani-Torricelli; BTFZ) fault zones to the north and, to a lesser extent, within the PFTB (e.g., Fig. 3.1) which may accommodate up to 20% of Australian and Pacific plate convergence (e.g., Abers and McCaffrey, 1988, 1994; Wallace *et al.*, 2004). Recent modelling of GPS velocities suggests that the PFTB is rotating in a clockwise manner relative to the Australian plate, with the rate of convergence varying from 6.8 mm yr^{-1} in the west to 12 mm yr^{-1} in the east (Koulali *et al.*, 2015). Although it is largely unclear how the associated lateral variations in crustal shortening are accommodated within the northern Australian passive margin and PFTB, abundant arc-normal oriented structures and lineaments are observed throughout the PFTB (e.g., Hill *et al.*, 1996; 2008; White *et al.*, 2014; Mahoney *et al.*, 2017) and may provide a suitable mechanism.

The geological complexity, isolation and challenging terrain of the PFTB makes it one of the least well-understood fold belts in the world. Data acquisition is expensive and geological studies are largely limited to resource exploration activities aimed at exploiting a range of richly endowed natural resources. The PFTB contains an abundance of late Miocene to Pliocene intrusions, some of which host world-class copper-gold deposits (e.g., Porgera, Ok Tedi mines) and a prolific petroleum system including some large hydrocarbon accumulations (e.g., Hides Gas Field, Kutubu Oil Field). Crustal structure is perceived as the primary control on both mineral and hydrocarbon systems and thus most studies have focussed on understanding the structure and evolution of the margin and PFTB (e.g., Findlay, 1974; Jenkins, 1974; Hobson, 1986; Hill, 1991; Buchanan and Warburton, 1996; Mason, 1996; Medd, 1996; Thornton *et al.*, 1996; Hill *et al.*, 2000; 2002; 2008; 2010; Keetley *et al.*, 2001; Hanani *et al.*, 2016; Hill and Mahoney, 2018; Mahoney *et al.*, 2017; Darnault and Hill, 2020; Giddings *et al.*, 2020).

While it is beyond the scope of this study to provide a comprehensive review of PFTB structural styles, we include an overview of the key structural elements. Various structural styles have been proposed for the PFTB, with an overall progression evident from models primarily comprising thin-skinned deformation (e.g., Findlay, 1974; Jenkins, 1974; Hobson, 1986) to models with variable combinations of both thin- and thick-skinned deformation (e.g., Mahoney *et al.*, 2017; Darnault and Hill, 2020; Giddings *et al.*, 2020). This transition has been driven by multiple factors including (1) the recognition of pre-existing basement heterogeneities, including both uninverted and inverted Mesozoic extensional structures (e.g., Fig. 3.1) within the northern Australian passive margin in seismic reflection data, mostly across the Stable Platform where seismic imaging is of the highest quality (e.g., Kawagle and Meyers, 1996; Bennett *et al.*, 2000; McConachie *et al.*, 2000; Schofield, 2000), (2) the identification of uplifted syn-rift sediments and basement in outcrop and in wells drilled within the PFTB (e.g., Davies and Norvick, 1974; Bain *et al.*, 1975; Amoco, 1982; Eisenberg, 1996), and (3) the increasing recognition, on a global scale, of the important control of passive margin architecture on fold and thrust belt geometry and evolution (e.g., Buchanan and Buchanan, 1995; Bonini *et al.*, 2012; Hinsch *et al.*, 2019).

Almost all contemporary structural cross-sections across the PFTB incorporate thick-skinned deformation, most commonly in the form of inverted normal faults. The associated shortening links through the overlying Papuan Basin sediments as a spatially variable assortment of thin-skinned deformational styles, often including multiple detachment levels, thrusts, backthrusts and associated fault-related folding (e.g., Fig. 3.1, cross-sections). Indeed, many workers propose spatial variations within the passive margin architecture as the primary influence on significant lateral changes in structural style observed throughout the PFTB (Hill, 1991; Buchanan and Warburton,

1996; Hill *et al.*, 2000; Mahoney *et al.*, 2017). However, as seismic imaging across the fold belt is generally of poor quality (e.g., Hill *et al.*, 2008; 2010), the nature and extent of the extensional architecture deep beneath the PFTB is poorly understood and the degree to which it is involved has been difficult to demonstrate.

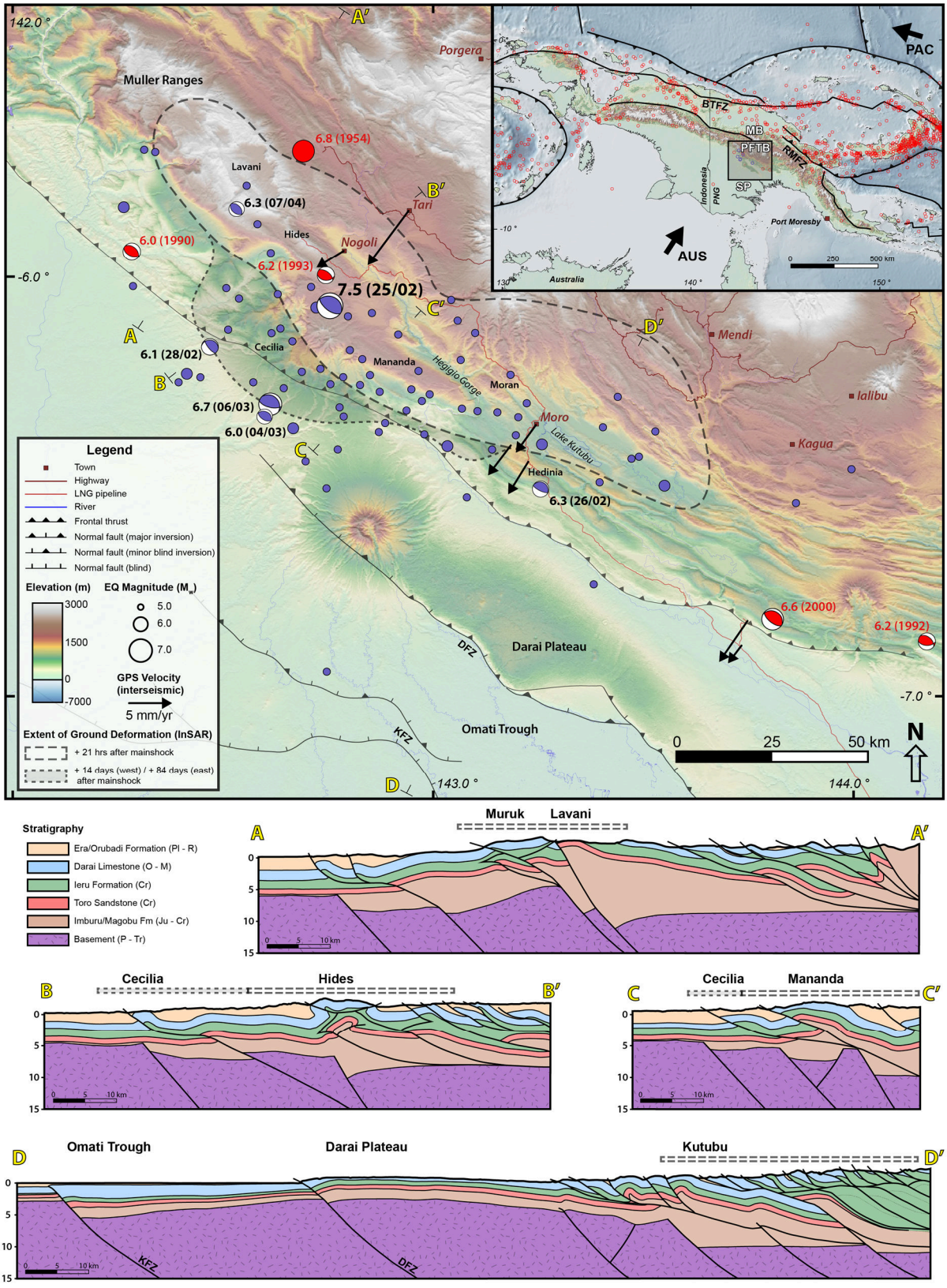

Figure 3.1. *Tectonic, geological and structural setting of the 2018 PNG Highlands earthquake sequence. Main map: Earthquake locations, extent of earthquake-related ground deformation and major geological elements of the PFTB. Blue circles are seismic events > M_w 5 related to the 2018 PNG Highlands earthquake sequence (UTC occurrence day/month in brackets; events plotted up to*

May 2019) and red circles are historical events > M_w 6 (year in brackets). GPS velocities (Stanaway and Noonan, 2015; Stanaway et al., 2020) plotted with respect to the Australian plate using ITRF2014 plate motion model (Altamimi et al., 2017). Subsurface faults on the Stable Platform after Schofield (2000). Inset map: Tectonic setting of New Guinea including PNG Highlands earthquake-related (blue) and historical (red) seismic events > M_w 6. Black lines represent tectonic boundaries modified from Hill and Hall (2003) and Baldwin et al. (2012). All earthquake data were accessed via the USGS Earthquake Portal (USGS, 2020). SRTM digital elevation model retrieved from USGS (2015). Cross-sections: structural cross-sections along the length of the PFTB illustrating our contemporary understanding of structural styles. Note the along strike structural variability and the complex interactions between thick- and thin-skinned deformation. Cross-sections are constrained by surface (i.e. field geological) and subsurface (i.e. well, seismic reflection) data and have been calibrated with the Bouguer gravity dataset shown in Figure 3.7. AUS, Australian plate; PAC, Pacific plate; SP, Stable Platform; PFTB, Papuan Fold and Thrust Belt; MB, Mobile Belt; BTFZ, Bewani-Torricelli Fault Zone; RMFZ, Ramu-Markham Fault Zone; DFZ, Darai Fault Zone; KFZ, Komewu Fault Zone.

3.3. 2018 PNG Highlands earthquake sequence

The 2018 M_w 7.5 PNG Highlands earthquake occurred on the 25th February 2018 at 17:45 UTC (03:45 on 26th February PNG local time), with an epicentre located ~ 96 km west of Mendi (Fig. 3.1) and hypocentral depth in the range variable 15-30 km, depending on the agency determining the location. The moment tensor solution provided by the US Geological Survey (USGS) indicates that the mainshock was associated with reverse movement along an approximately northwest to southeast striking fault, with a dip of ~ 30° towards the northeast; consistent with the convergent tectonic setting and the structural orientation of the PFTB at the epicentral location (Fig. 3.1). The USGS finite-fault model comprises a single fault plane, but they note that the complex source time function and variable rake is suggestive of a multi-fault rupture (USGS, 2018). Other published finite-fault inversion studies utilising seismic data and coseismic observations from spaceborne synthetic aperture radar (SAR) data have yielded highly variable predictions of the number and orientation of fault/s activated during the event. After testing both

single- and multiple-fault models, Wang *et al.* (2020) conclude that a four-fault model best fits the data, whereas Zhang *et al.* (2020) argue for a single-fault model. Chong and Huang (2020) present a model containing three-faults (including a detachment). The preferred fault plane orientation in all the aforementioned finite-fault studies strikes northwest to southeast and dips towards the northeast, however the fault dips vary significantly from 6° to 55° (33°, USGS, 2018; 6-26°, Chong and Huang, 2020; 32-55°, Wang *et al.*, 2020; 30°, Zhang *et al.*, 2020).

The 2018 PNG Highlands earthquake was the largest ever recorded in the region with modern seismic instruments, with a return period estimated at ~ 150 years (McCue *et al.*, 2018). The mainshock was followed by an aftershock sequence which included five events ≥ M_w 6, spread across ~ 100 km of the frontal portion of the PFTB (Fig. 3.1). By comparison, the USGS earthquake catalogue containing events from 1904 to present includes only five historical (e.g., prior to 2018) earthquakes ≥ M_w 6 in the frontal area of the PFTB (Fig. 3.1). The largest aftershock (M_w 6.7) in the earthquake sequence was the third largest event ever recorded—the second largest event was a M_w 6.8 earthquake in 1954, with an epicentral location ~ 40 km to the north-northwest of the 2018 PNG Highlands earthquake (Fig. 3.1). The final aftershock ≥ M_w 6 and equal third largest earthquake in the sequence was a M_w 6.3 event which occurred 41 days following the main rupture. Five out of the six earthquakes ≥ M_w 6, including the mainshock, were associated with focal depths within the upper- to mid-crust (~ 15-30 km). Preferred moment tensor solutions for all five aftershocks ≥ M_w 6 are consistent with the mainshock, indicative of reverse movement along northeast-dipping faults with only minor variations in orientation and degree of obliquity (Fig. 3.1).

Shaking associated with the earthquake sequence caused widespread slope failure in the steep topography of the PFTB, particularly within gorges and the unstable flanks of the large Pliocene to Pleistocene stratovolcanoes in the area (e.g., Fig. 3.2a). Landslides were particularly catastrophic along the southern wall of the

Hegigio Gorge (Fig. 3.1), where giant slabs of the Miocene Darai Limestone broke free from the steep backlimb of the Mananda Anticline, sliding along bedding-parallel failure planes into the gorge below (Fig. 3.2b). Although surface ruptures were not directly observed following the earthquake sequence, this is most likely because of the remote and densely vegetated nature of the area. Indeed, published analyses of remotely sensed data suggest that significant surface rupturing did likely occur (e.g., Chong and Huang, 2020; Wang *et al.*, 2020). At Lake Kutubu (Fig. 3.1), uplift in the northwest manifested as an increase in the lake bank height relative to the water level (~ 1 m; e.g., Fig. 3.2c), while subsidence in the south led to flooding. The "severe to violent" earthquake shaking (USGS, 2018; based on scale from Worden *et al.*, 2012) and associated extensive land slips and rock falls devastated local communities with at least 125 fatalities and widespread building and infrastructure damage (WHO, 2018). Operations at the nearby Porgera and Ok Tedi mines were suspended temporarily and oil and gas operations and associated facilities were closed for months.

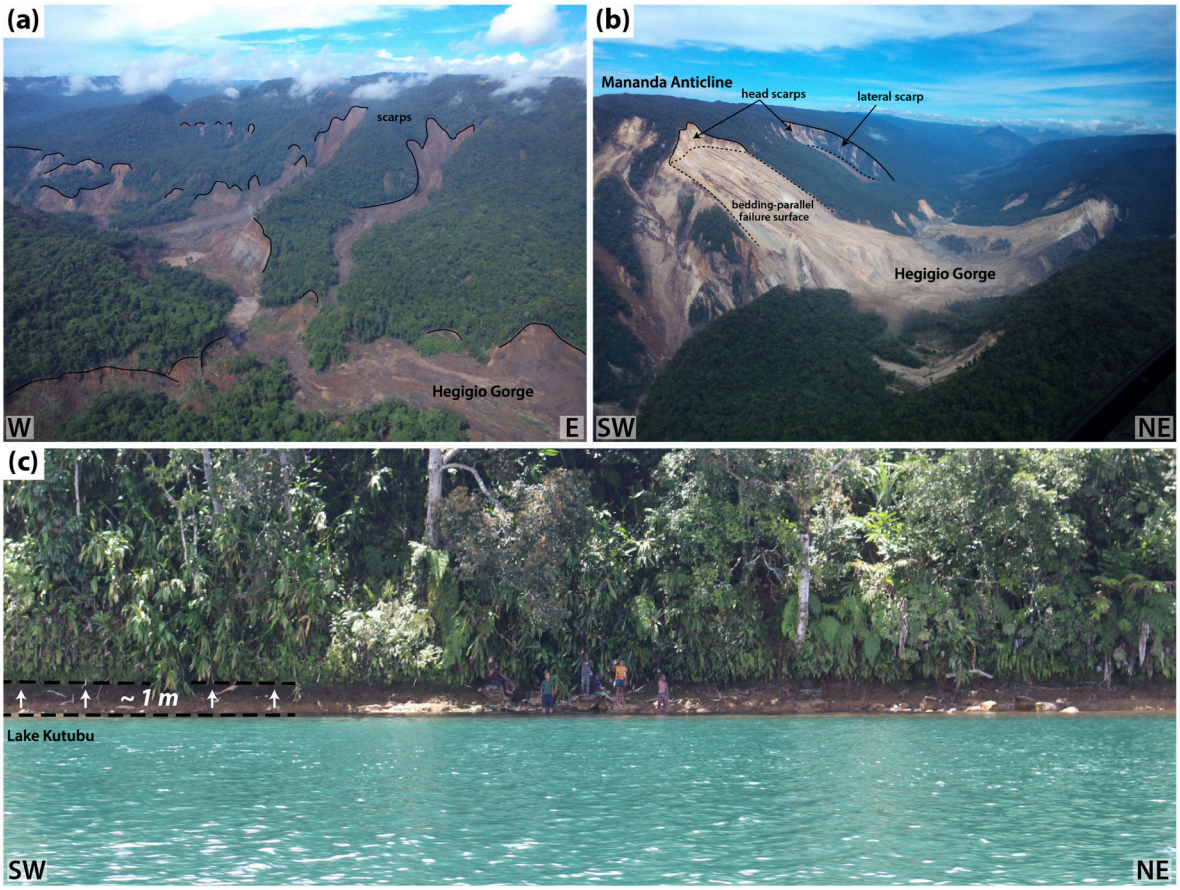

Figure 3.2. *Photos showing the aftermath of the 2018 PNG Highlands earthquake sequence: (a) northern wall of the Hegigio Gorge showing landslides within unconsolidated reddy-brown volcanic rocks in the flanks of the Mt Kerewa stratovolcano; (b) southern wall of the Hegigio Gorge showing bedding-parallel sliding of large slabs of Darai Limestone from the backlimb of the Mananda Anticline; (c) northwest bank of Lake Kutubu showing an increase in the lake bank height relative to the water level. Photo credits: (a) and (b) Papuan Oil Search, (c) Nick Hannaford. Photo locations are shown in Figure 3.6.*

3.3.1. Earthquake locations

The earthquake locations shown in Figure 3.1 were resolved by the USGS National Earthquake Information Centre (NEIC) based on recordings from the Global Seismographic Network (GSN) and the global 1-D travel time model AK135 (Kennett *et al.*, 1995). The GSN includes a single station within PNG, located in the nation's capital of Port Moresby > 600 km from the 2018 PNG Highlands earthquake mainshock location. This is the only GSN station within

1,500 km of the event. The next closest seismographs are scattered throughout Northern Australia, Southeast Asia and the Pacific Islands (e.g., Gee and Leith, 2011). Because of the remoteness of the PNG Highlands earthquake sequence relative to the GSN, significant earthquake location uncertainties exist which could be in the order of 10-30 km, depending on the magnitude of velocity variations within the surrounding regions (USGS, 2018). Local seismograph recordings are central to identifying velocity variations and thus, where present, provide a valuable means of refining earthquake locations. Although the Port Moresby Geophysical Observatory (PMGO) operates a limited local seismograph network across PNG (e.g., Ghasemi *et al.*, 2018), its condition is unknown and no data were available to this study.

In lieu of arrival time data from local seismic stations, we attempted to reduce the locational uncertainty of the earthquake cluster using the multiple event earthquake relocation software mloc, which incorporates the hypocentroidal decomposition method of Jordan and Sverdrup (1981). A detailed description of mloc can be found on the program website (https://seismo.com/mloc/). To minimise the biasing effect of unknown velocity structure, the available NEIC dataset was restricted to teleseismic P arrivals—the most stable and accurate branch of the global travel time model—between 30-90° and ~ 24,000 readings were used to estimate the absolute locations of the earthquake cluster. The relative locations of events within the cluster (e.g., cluster vectors) were recalculated using a larger dataset including all available arrival time data.

The relocated earthquakes are plotted in Figures 3.3 and 3.4. The M_w 7.5 mainshock shifted ~ 10 km towards the east, but the most prominent overall trend was for events to shift between 5-15 km towards the northeast. We believe the relocated events are a significant improvement on the USGS locations because (1) numerous events that were previously located

forelandward of the frontal thrust shifted to within the PFTB, and (2) the relocated events provide an improved fit with the distribution of ground deformation observed during the earthquake sequence (e.g., Fig. 3.4). Although the relocated events are improved, we suspect based on the data and analyses presented within this study that many are still located 5-10 km forelandward (i.e. towards the southwest) of their true locations. This is, however, difficult to demonstrate in the absence of local velocity calibration and earthquake locations remain poorly constrained.

3.3.2. Crustal deformation

In this section we combine GPS measurements with remote sensing observations to analyse the spatiotemporal distribution of crustal deformation associated with the 2018 PNG Highlands earthquake and aftershock sequence. To support oil and gas exploration and development within the remote frontal PFTB, a geodetic network has been established and maintained since 2005 across much of the area affected by the PNG Highlands earthquake sequence. GPS measurements for many of the stations in the PFTB network have < 20 mm accuracy (95% CI) and so provide a high fidelity means of monitoring both interseismic and coseismic displacement and for ground truthing remotely sensed geodetic observations such as interferometric synthetic aperture radar (InSAR). InSAR is a powerful technique for measuring widespread ground deformation (e.g., Gabriel *et al.*, 1989; Rosen *et al.*, 2000) and thus is an effective tool for understanding the spatial and temporal distribution of displacement related to earthquake sequences. Following the PNG Highlands earthquake, the Geospatial Information Authority of Japan (GSI) published a series of InSAR displacement maps produced from Advanced Land Observing Satellite 2 (ALOS-2) data (GSI, 2018). In this section, we use GPS- and InSAR-derived

displacements to analyse the magnitude and distribution of coseismic deformation associated with the PNG Highlands earthquake sequence.

Approximately 700 GPS stations within the PFTB have been surveyed since 2005, however the remoteness of most of the sites means that only a small proportion have been re-observed regularly. For these sites, each set of observed positions can be stacked to form a time series of station movement within the ITRF2014, allowing for the estimation of interseismic site velocities (e.g., velocities largely due to secular plate motion). The ITRF2014 trajectories have been transformed to an Australian plate frame using ITRF2014 plate motion model of the Australian plate (Altamimi *et al.*, 2017). Observations made after the 2018 PNG Highlands earthquake can therefore be isolated from the time series analysis in order to estimate coseismic displacement arising from the event.

Following the 2018 PNG Highlands earthquake, a GPS resurvey of 71 sites was conducted between the 15th March and 5th October 2018, across ~ 200 km of the strike-length of the frontal PFTB. Every effort was made to avoid survey stations that had been disturbed during the earthquake sequence by localised ground instability. Observations were taken at variable time following the mainshock and consequently include some postseismic deformation and additional coseismic deformation from the aftershock sequence. In some cases, there is also a significant time lag between previous observations (pre-earthquake) and the occurrence of the event, so it is noted that additional movements (e.g., unrelated to the PNG Highlands earthquake sequence) during this time could be incorrectly attributed to the PNG Highlands earthquake sequence.

GPS measurements reveal the spatial distribution of ground deformation during the earthquake sequence in remarkable detail (Fig. 3.3). Significant variations in vertical and horizontal displacement were detected, suggestive of

a complex pattern of deformation, potentially associated with movement along multiple faults. The most dominant surface displacement was up and to the southwest, recorded at Muruk, Hides, Nogoli and Moran (Fig. 3.3). From northwest to southeast across these areas, an overall trend towards increased vertical and decreased horizontal displacement was detected. Angore, Agogo and Moro were also uplifted, but with dominantly south to southeast horizontal movement (Fig. 3.3). Areas of subsidence and east to northeast horizontal displacements were observed at Hedinia, Iagifu and Usano, to the south of the uplifted zone (Fig. 3.3).

A composite ascending interferogram is shown with GPS measurement locations in Figure 3.4 and shows the lateral extent of ground deformation within the PFTB, extending ~ 170 km in a northwest-southeast direction and ~ 50 km in a northeast-southwest direction. The InSAR-derived displacement appears broadly consistent with GPS control points (c.f. Figs. 3.3 and 3.4) but would not be expected to be in perfect agreement due to the InSAR being a one-dimensional measurement along the line of sight (LOS) of the satellite. One of the advantages of the InSAR technique is that it provides a widespread and mostly continuous map of ground deformation. The distribution of earthquakes relative to LOS displacement (i.e. earthquakes mostly located to the south-southwest) suggest that ground deformation was related to hanging wall uplift (e.g., fault-related folding) along northeast-dipping fault planes—which is consistent with moment tensor and finite-fault model solutions (USGS, 2018; Wang *et al.*, 2020; Zhang *et al.*, 2020). We interpret at least five distinct zones of ground deformation based on GPS measurements and the ascending and descending interferograms published on the GSI website (GSI, 2018), along with an abundance of small-scale features that may represent surface ruptures such as fissures or scarps.

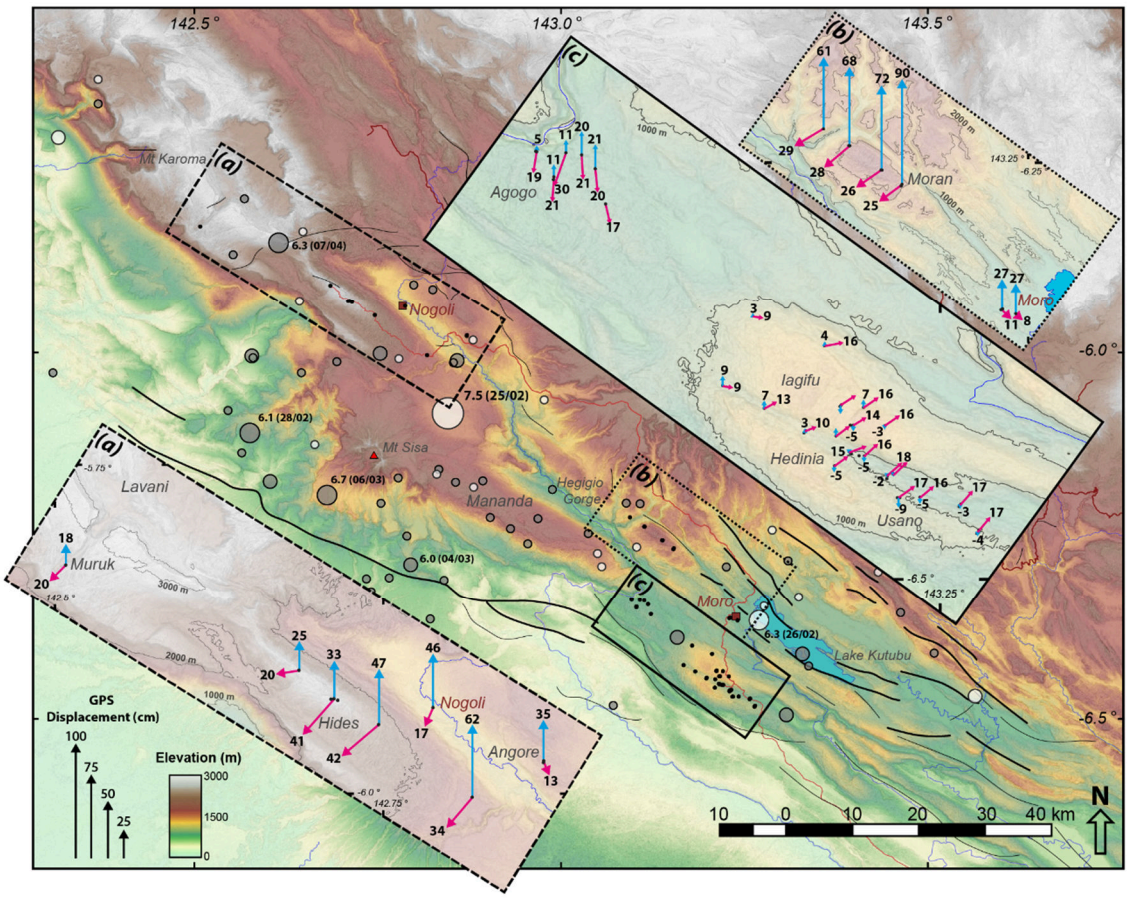
142.5 °
143.0 °
143.5 °
-6.0 °
-6.5 °
Mt Karoma
(a)
(b)
(c)
6.3 (07/04)
Nogoli
7.5 (25/02)
6.1 (28/02)
Mt Sisa
6.7 (06/03)
Lavani
Mananda
Hegigio Gorge
6.0 (04/03)
Muruk
Agogo
Moran
Iagifu
Hedinia
Usano
Moro
6.3 (26/02)
Lake Kutubu
Hides
Angore
GPS Displacement (cm)
Elevation (m)
10 0 10 20 30 40 km
N

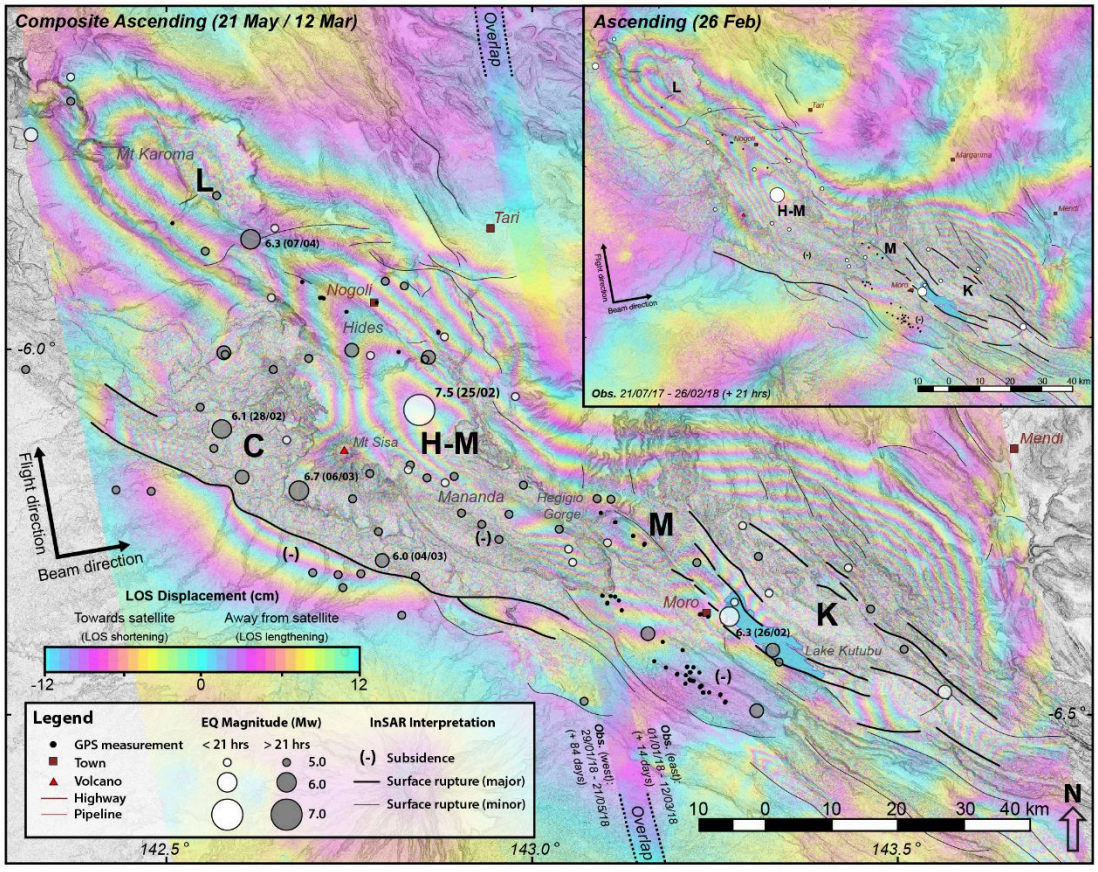
Composite Ascending (21 May / 12 Mar)
Overlap
Ascending (26 Feb)
Mt Karoma
L
Tari
6.3 (07/04)
Nogoli
Hides
7.5 (25/02)
6.1 (28/02)
C
Mt Sisa
H-M
6.7 (06/03)
Mananda
Hegigio Gorge
M
(-)
6.0 (04/03)
Mendi
Moro
K
6.3 (26/02)
Lake Kutubu
Flight direction
Beam direction
LOS Displacement (cm)
Towards satellite (LOS shortening)
Away from satellite (LOS lengthening)
-12 0 12
Obs. 21/07/17 - 26/02/18 (+ 21 hrs)
Obs. (west): 29/01/18 - 21/05/18 (+ 84 days)
Obs. (east): 01/01/18 - 12/03/18 (+ 14 days)
Legend
GPS measurement
Town
Volcano
Highway
Pipeline
EQ Magnitude (Mw)
< 21 hrs
> 21 hrs
5.0
6.0
7.0
InSAR Interpretation
(-) Subsidence
Surface rupture (major)
Surface rupture (minor)
10 0 10 20 30 40 km
N

Figure 3.3. *(previous page, top) GPS surface displacements, relocated earthquakes > M_w 5 and surface rupturing interpreted from InSAR (e.g., Figs. 3.4 and 3.5). Legend shown in Figure 3.4. Vectors show coseismic displacements observed by static GPS and are in terms of ITRF2014. Events > M_w 6 are labelled with magnitude and UTC occurrence time (day/month). Magenta arrows show horizontal displacement and blue arrows show vertical displacement. For display purposes—(a) and (b) insets are spatially exaggerated x 1.75; (c) inset is spatially exaggerated x 3.5. GPS displacement arrows are displayed at a consistent scale in all insets.*

Figure 3.4. *(previous page, bottom) Ascending interferograms (GSI, 2018) collectively showing the evolution of LOS displacement, relocated earthquakes > M_w 5 and interpretation of coseismic surface rupturing related to the 2018 PNG Highlands earthquake sequence. Earthquake data are split at the time of the second ascending observation in the inset (14:46, 26th February 2018 (UTC) or + 21 hrs after mainshock): white circles represent earthquakes before the satellite pass and grey circles represent earthquakes after the satellite pass. Events > M_w 6 are labelled with magnitude and occurrence time (day/month). Main: Interpreted composite ascending interferogram showing surface deformation associated with the mainshock and aftershock sequence, up to the second observation dates of 12th March 2018 (+ 14 days after mainshock) in the east and 21st May 2018 (+ 84 days after mainshock) in the west. Inset: Interpreted ascending interferogram showing the distribution of earthquakes and extent of surface deformation up to the 26th Feb 2018 (+ 21 hrs after mainshock). H-M, Hides-Mananda zone; K, Kutubu zone; L, Lavani zone; M, Moran zone; C, Cecilia zone. InSAR analysis was carried out by the Geospatial Information Authority of Japan (GSI) using ALOS-2 data of the Japan Aerospace Exploration Agency (JAXA). The interferograms are published on the GSI website (GSI, 2018).*

3.3.2.1. Hides-Mananda zone

The elongate, oval-shaped Hides-Mananda ground deformation zone is spatially the most significant, with a northeast to southwest extent of ~ 25-30 km and strike length of ~ 80 km from the northwestern end of the Hides Anticline to the southeastern end of the Mananda Anticline (Fig. 3.4). GPS measurements along the length of the Hides Anticline indicate increasing uplift from 25 cm in the northwest to 62 cm in the southeast (Fig. 3.3a). LOS shortening (displacement towards the satellite) on the composite ascending interferogram reaches a maximum of ~ 70 cm immediately to the north of the

Mananda Anticline in the Hegigio Gorge—the focus of landslide activity during the earthquake sequence (e.g., Fig. 3.2a and b). Ground movement decreased rapidly towards the southeast of the Hegigio Gorge, with GPS measurements at Agogo recording up to 21 cm of uplift and up to 30 cm of approximately south-directed movement (Fig. 3.3c).

The M_w 7.5 mainshock occurred within the northwest of the Hides-Mananda zone and, as the only earthquake > M_w 6 within the zone, it was probably the source of most of the observed ground deformation. There is no field or remotely sensed evidence for surface rupturing around the Hides Anticline, suggesting that most of the displacement was related to fault slip at depth—an observation that is supported by finite-fault slip inversions (e.g., S1-S2 in Wang *et al.*, 2020; Asperity A in Zhang *et al.*, 2020). However, to the southwest of the Mananda Anticline, within the frontal-most structures of the fold belt, an area of strong interferometric decorrelation on the interferograms relates to an abundance of near-surface movements which are probably mostly landslides, but could also be surface rupturing associated with the Hides-Mananda uplift zone (e.g., Fig. 3.4). Indeed, Chong and Huang (2020) detect surface rupturing on the Mananda Fault along with several major landslides throughout the area using SAR sub-pixel offsets. An oval-shaped area of LOS lengthening (displacement away from the satellite) is evident on the descending interferogram (Fig. 3.5) centred on the Mananda Anticline, immediately to the north of the suspected surface rupture zone. It is, however, unclear whether this occurrence is related to local slope failure or ground subsidence related to the overthrusting of the Hides-Mananda zone to the north.

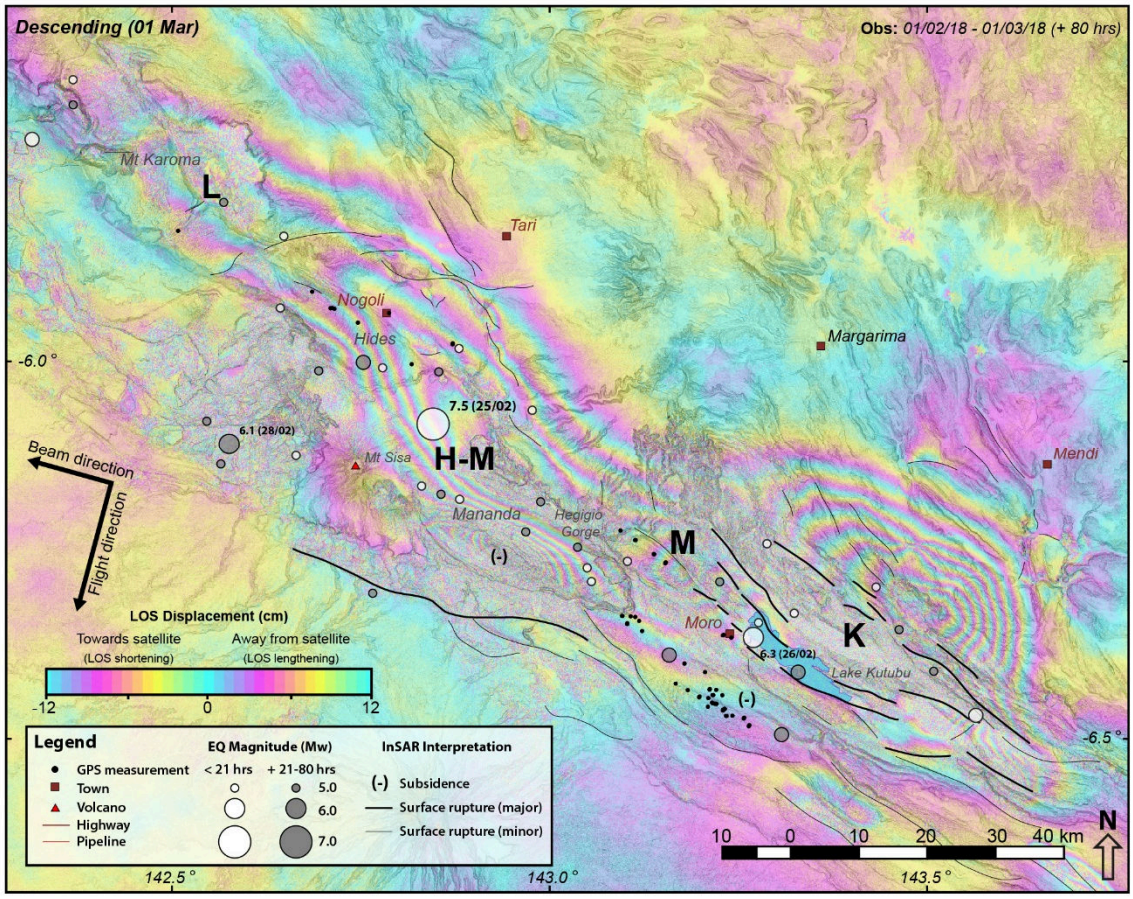

Figure 3.5. *Interpreted descending interferogram (GSI, 2018) with second observation at 02:05, 1st March 2018 (UTC), + 80 hrs after mainshock. Relocated earthquakes > M_w 5 occurring prior to the time of second observation plotted (e.g., events occurring within 80 hrs of the 2018 PNG Highlands mainshock), along with an interpretation of possible surface rupturing. Note the oval-shaped area of LOS lengthening centred on the Mananda Anticline and the circular area of LOS shortening centred on the Moran Anticline—features that are less evident on the ascending interferograms (e.g., Fig. 3.4). Descending LOS displacements differ from ascending LOS displacements due to differences in satellite sensor viewing geometry (e.g., western ground motion may contribute to cancelling out uplift in the descending geometry).*

3.3.2.2. Kutubu zone

The Kutubu zone is located to the east of the Hides-Mananda zone and signifies a hinterland-directed shift in the overall ground deformation trend relative to the fold belt (Fig. 3.4). LOS shortening in the Kutubu zone strikes northwest to southeast and is parabolic in shape: convex to the northeast and sub-linear to

the southwest. The zone has similar spatial dimensions to the Hides-Mananda zone—a southwest to northeast extent of ~ 30 km and strike length of ~ 70 km—which gives the two zones an en echelon appearance (Fig. 3.4). GPS observations within the Kutubu zone were limited to its southern margin at Moro where 27 cm of uplift and 8-11 cm of southeast displacement was recorded (Fig. 3.3b). Immediately to the south of the Kutubu zone, GPS measurements from the Hedinia, Iagifu and Usano anticlines indicated a decrease in the magnitude of vertical displacement and change to northeast horizontal movement, which ranged from 9 cm in the northwest to 17 cm in the southeast (Fig. 3.3c). Vertical ground movements at Hedinia and Iagifu were variable with a general northwest to southeast trend from uplift (up to 9 cm) to subsidence (up to 5 cm). Further to the southeast, Usano also underwent subsidence of between 2-9 cm (Fig. 3.3c). Subsidence and northeast movement throughout this area of the frontal fold belt most likely resulted from footwall subsidence in response to the overthrusting of the Kutubu zone to the north.

Based on the interferograms, the Kutubu zone underwent the greatest magnitude of ground displacement during the earthquake and aftershock sequence, reaching > 120 cm of LOS shortening to the northeast of Lake Kutubu (Fig. 3.4). The largest aftershock in the area was a M_w 6.3 event with an epicentral location to the southwest of the zone. Most of the seismicity and associated ground deformation in the Kutubu zone occurred within 21 hours of the mainshock (Fig. 3.4, c.f. inset and main). A prominent zone of interferometric decorrelation in the area of greatest LOS shortening to the north and northeast of Lake Kutubu suggests significant near-surface deformation may have occurred, attributable in part to landslides, but also potentially indicative of surface rupturing—as predicted within this area based on SAR analyses and finite-fault modelling (e.g., USGS, 2018; Mubi Fault in Chong and Huang, 2020; S4 in Wang *et al.*, 2020).

3.3.2.3. Lavani zone

The Lavani zone is centred on the Lavani Valley to the northwest of the Hides Anticline in the Eastern Muller Range. The ascending interferograms suggest that ground deformation within this zone extended ~ 30 km southwest to northeast and ~ 40 km from northwest to southeast (Fig. 3.4). The only GPS locality within the Lavani zone was at Muruk, which underwent 18 cm of uplift and 20 cm of southwest displacement (Fig. 3.3a). On the ascending interferograms, the greatest magnitude of LOS shortening in the Lavani zone was ~ 40 cm around Mt Karoma (Fig. 3.4)—which is the highest mountain in this region of the fold belt reaching ~ 3,600 m above mean sea level. The Lavani zone appears semicontinuous to the Hides-Mananda zone, with a slightly en echelon appearance. The two zones are differentiated based on (1) a "saddle" evident within interferometric displacement between the northwestern end of the Hides Anticline and southeastern end of Lavani Valley, and (2) significant rake angle differences in finite-fault models (e.g., USGS, 2018; S2 and S3 in Wang *et al.*, 2020). The largest seismic event within the zone was a M_w 6.3 aftershock which occurred at a mid-crustal depth (~ 18 km) over 40 days after the mainshock. However, a comparison of ascending interferograms from prior to, and following this aftershock (Fig. 3.4, c.f. inset and main) suggests that the event was not associated with significant ground deformation and that most of the ground deformation in the Lavani zone occurred within 21 hours of the mainshock. There is a paucity of evidence for near-surface deformation within the Lavani zone, except for some minor approximately west to east striking discontinuities within the interferograms (e.g., Figs. 3.4 and 3.5).

3.3.2.4. Moran zone

The Moran zone is most identifiable within the descending interferogram (Fig. 3.5), located between the more extensive Hides-Mananda and Kutubu zones. The zone is characterised by a circular area of LOS shortening with a diameter

of ~ 20 km, centered on the Moran Anticline. Despite being located over 30 km from the mainshock epicentre, the Moran zone was associated with the greatest magnitude of ground deformation of all the areas surveyed by GPS. Uplift reached 90 cm near the crest of the Moran Anticline (Fig. 3.3b). Measurements along the length of the anticline revealed a trend of increasing uplift to the southeast, from 61 cm to 90 cm, with an accompanying decrease in horizontal southwest movement from 29 cm to 25 cm (Fig. 3.3b).

The Moran zone is recognisable on both the ascending and descending interferograms (Figs. 3.4 and 3.5) but is located within an area of significant interferometric decorrelation. This makes it difficult to determine the precise magnitude of LOS shortening, which appears to be ~ 60-90 cm (Figs. 3.4 and 3.5), an amount that is broadly consistent with GPS measurements. Uplift in the Moran zone occurred within 21 hours of the mainshock, coeval with uplift in the neighbouring Hides-Mananda and Kutubu zones (Fig. 3.4, inset). The complex pattern of ground deformation evident on the interferograms plausibly relates to increased structural complexity within the area. The abundance and severity of interferometric decorrelation in this zone results from widespread slope failure—also recognised in SAR sub-pixel offsets (Chong and Huang, 2020)—within the unconsolidated volcanic and volcanoclastic rocks surrounding the Moran Anticline, which is located between the towering Mt Kerewa stratovolcano to the north and the steep-sided Hegigio Gorge to the south (e.g., Figs. 3.2a and 3.6).

3.3.2.5. Cecilia zone

The Cecilia zone is located to the west and southwest of the Hides-Mananda zone and represents the most forelandward extent of ground deformation resulting from the 2018 PNG Highlands earthquake sequence (Fig. 3.4, main). No GPS measurements were acquired within this zone due to its remoteness and the absence of infrastructure such as buildings and roads. The Cecilia zone

is characterised by a greater severity of interferometric decorrelation than the other zones—a result of the steep terrain and geology of the area, which is dominated by unconsolidated syn-orogenic sediments and volcanic and volcanoclastic rocks surrounding the Mt Sisa stratovolcano (Fig. 3.6). The decorrelation challenges any detailed interpretation of ground deformation.

But it is clear from the interferograms that, unlike the other zones, most of the ground deformation within this area occurred > 21 hours after the mainshock (Fig. 3.4, c.f. main and inset). Deformation most likely resulted from a series of aftershocks that occurred within the Cecilia zone following the mainshock, including: a M_w 6.1 event ~ 2.5 days later; a M_w 6 event ~ 7 days later and a M_w 6.7 event ~ 9 days later (e.g., Fig. 3.6). The southwesterly edge of interferometric decorrelation forms a linear trend that parallels the strike of the frontal thrust of the PFTB, a structure that has historically been associated with some of the largest seismic events in the PFTB (Fig. 3.1). In the Cecilia zone, the frontal thrust and associated hanging wall anticline—the Cecilia Anticline—clearly deform the southern flank of Mt Sisa, a Pliocene to Pleistocene stratovolcano, signifying neotectonic activity on the thrust (e.g., Fig. 3.6). We interpret the sublinear trend in the interferogram at leading edge of the Cecilia Anticline as a potential surface rupture (Figs. 3.4 and 3.6). The ascending interferogram indicates a parabolic convex to the southwest zone of LOS lengthening up to ~ 36 cm directly to the southwest of the Cecilia Thrust (Figs. 3.4 and 3.6), potentially indicative of footwall subsidence, possibly in response to overthrusting of the Cecilia Anticline. Chong and Huang (2020) and Wang *et al.* (2020) do not recognise ground deformation, surface rupturing and/or faulting within this area, but it is noted that their second SAR observations of this area (28/02/2018 and 01/03/2018, respectively) pre-date the occurrence of the M_w 6 and M_w 6.7 aftershocks.

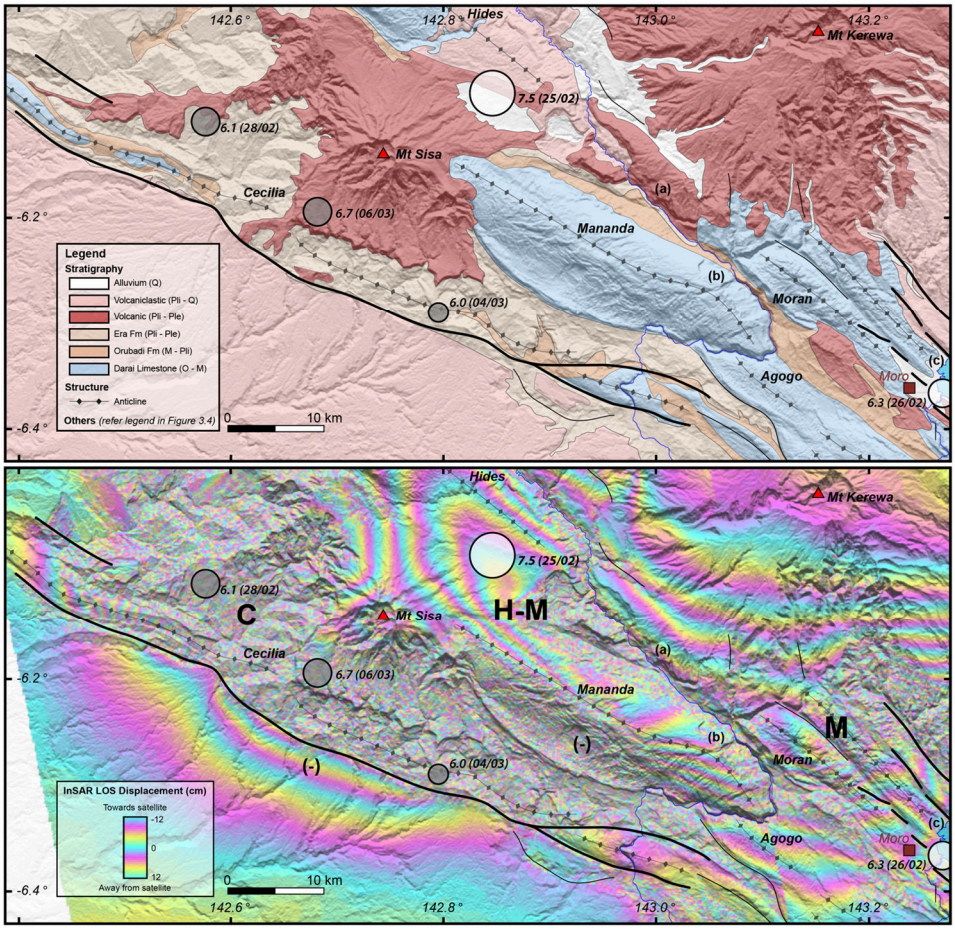

Figure 3.6. *Geological map (top) and interpreted composite ascending interferogram (bottom) for part of the area affected by the 2018 PNG Highlands earthquake. Maps are plotted at the same scale and include both relocated earthquakes > M_w 6 and interpreted coseismic surface rupturing. Note (1) the folded southern flank of Mt Sisa—a Pliocene to Pleistocene stratovolcano—suggestive of recent activity on the frontal thrust and associated Cecilia Anticline, and (2) the sublinear trend along the frontal thrust within the interferogram, interpreted here as a major surface rupture. Geological map modified from Brown and Robinson (1982). Labels (a), (b) and (c) represent the locations of photos shown in Figure 3.2. Composite ascending interferogram retrieved from GSI (2018), observation dates are detailed within Figure 3.4 (main). SRTM digital elevation model retrieved from USGS (2015).*

3.4. Discussion

3.4.1. Implications of seismicity and ground deformation for PFTB structural style

The distribution of seismicity and ground deformation associated with the 2018 PNG Highlands earthquake sequence has provided significant new insight into

the controls on structural style within the PFTB. The broad spatial distribution of seismicity and ground deformation, along with the mid-crustal hypocentral depths of many of the largest seismic events, implies a deep crustal influence on the earthquake sequence. Indeed, there is a clear disparity between the dimensions of fold and thrust structures within the PFTB (typically 10s to 100s of square kilometres) and the spatial extent of ground deformation associated with the PNG Highlands earthquake sequence (> 7,500 km^2; e.g., Figs. 3.1 and 3.7). In contrast, there are remarkable spatial and morphological similarities between the ground deformation and the Darai Plateau located ~ 50 km to the south on the Stable Platform (Figs. 3.1 and 3.7). The Darai Plateau is bound to the southwest by an inverted listric extensional fault, the Darai Fault, across which to the northeast the thickness of Papuan Basin sediments more than doubles (Fig. 3.1, D-D', DFZ; Hill *et al.*, 2010). Approximately 50 km south of the Darai Plateau, the Omati Trough has a similar spatial extent and is bound to the southwest by the Komewu Fault—a similar listric extensional fault that had undergone only very minor inversion (Fig. 3.1, D-D', KFZ). The Komewu Fault also accommodates significant sediment thickening towards the northeast into the Omati Trough (Fig. 3.1, D-D'; Schofield, 2000). As such, the Komewu and Darai faults formed as a pair of major northeast-dipping listric extensional faults on the northern Australian passive margin that have likely had a principal control on the formation of the Papuan Basin. The comparable scale and form of ground deformation observed during the PNG Highlands earthquake sequence, along with its location along the same approximately north-south trend defined by the Omati Trough and Darai Plateau (e.g., Fig. 3.1), is compelling evidence that the earthquake sequence initiated along an analogous listric normal fault located deep beneath the PFTB (e.g., Fig. 3.7e). While several authors have hypothesised that major extensional structures exist beneath the PFTB (e.g., Hill, 1991; Buchanan and Warburton, 1996; Hill *et al.*, 2008), their existence has not been convincingly demonstrated due to the poor

quality of seismic imaging and a lack of deep well penetrations. We believe that our analysis of the PNG Highlands earthquake sequence and associated ground deformation provides important new support for the presence of a major actively-inverting extensional structure beneath the PFTB.

Airborne and land-based gravity datasets are used to delineate density distributions within the earth and one of their common applications has been to investigate the basement architecture beneath fold and thrust belts (e.g., Snyder and Barazangi, 1986; Ayarza *et al.*, 2005; Ali *et al.*, 2009; Vera *et al.*, 2010). A merged dataset comprising the highest resolution Bouguer corrected gravity data available across this area of PNG is shown in Figure 3.7c. The Bouguer gravity anomaly decreases into the Omati Trough and increases over the inverted Darai Plateau, as expected for deeper and shallower high-density basement respectively (e.g., Fig. 3.1, D-D'). Excluding these areas, there is an overall regionally decreasing trend in the Bouguer gravity anomaly towards the northeast, which is consistent with sedimentary thickening and deepening basement into the Papuan Basin. Interestingly, there is an abrupt decrease in the Bouguer gravity anomaly of > 50 mGal evident near the leading edge of the fold belt in the east which wraps around towards the hinterland in the west (Fig. 3.7c). The abrupt nature of this decrease suggests a step-like decrease in density towards the northeast, as would be expected across a significant (> 3 km offset) normal fault. This provides further evidence for the presence of a major extensional structure beneath the PFTB, across which the Papuan Basin sediment fill is likely to thicken significantly towards the northeast. Additionally, the lateral distribution of this step-like decrease in Bouguer gravity anomaly correlates well with the distribution of seismicity and ground deformation associated with the PNG Highlands earthquake sequence (e.g., Fig. 3.7). We interpret this relationship as additional evidence that the 2018

PNG Highlands earthquake was related to inversion on a significant but previously unidentified listric extensional fault beneath the PFTB.

Prior to discussing the nature of this concealed structure in more detail, it is important to note that while we refer to the Komewu and Darai faults as single faults above for simplicity, they are more likely complex extensional "zones" comprising multiple listric normal faults that interact as single extensional structures at a regional scale. Such structures are detected across the Stable Platform in seismic images (e.g., Kawagle and Meyers, 1996; McConachie *et al.*, 2000; Schofield, 2000). The detailed architecture of the Komewu Fault Zone is particularly well-resolved by a dense network of 2D seismic lines of good quality (enabled by flat topography), which facilitates imaging of multiple overlapping listric normal faults connected by soft- and hard-linked transfer zones (e.g., Schofield, 2000). No seismic data exists across the Darai Fault Zone, but transfer zones are clearly evident within the leading edge of the Darai Plateau (e.g., Figs. 3.1 and 3.7d). The transfers within the inverted fault system are likely to reflect underlying complexities within the extensional fault zone that are analogous to those imaged within less-inverted structures in the adjacent Komewu Fault Zone (e.g., Fig. 3.7e). This kind of extensional architecture has been suspected beneath parts of the fold belt (e.g., Hill *et al.*, 2010; Mahoney *et al.*, 2017), but has been difficult to demonstrate.

It follows that the major extensional structure beneath the PFTB that has been reactivated during the 2018 PNG Highlands earthquake sequence comprises a similarly complex zone of listric normal faults, which we refer to collectively as the Lavani-Kutubu Fault Zone. Indeed, the compressional reactivation (i.e. inversion) of multiple normal faults during the earthquake sequence provides a possible explanation for the distinct zones of ground deformation (e.g., Section 3.3.2) and is consistent with the preferred finite-fault model of Wang *et al.* (2020) which includes four faults that extend to mid-

crustal depths. For example, the observed en echelon appearance of the Hides-Mananda and Kutubu ground deformation zones (e.g., Figs. 3.4 and 3.7) may reflect the reactivation of two (or more) listric normal faults separated by basement transfer zones (e.g., Fig. 3.7e). While it is not uncommon for multiple faults to fail during large earthquake sequences within convergent settings (e.g., Kao and Chen, 2000; Xu *et al.*, 2009, Jiang *et al.*, 2018; amongst many others), there are very few documented examples of multiple pre-existing extensional structures actively inverting during a single seismic event (e.g., Hirata *et al.*, 2005; Kato *et al.*, 2006; 2008; Camanni *et al.*, 2013; 2016).

An unexplained element of the ground deformation during the 2018 PNG Highlands earthquake sequence remains the complex distribution of interpreted surface rupturing (e.g., Figs. 3.4 and 3.5). In contrast to the broad overall wavelength of ground deformation, the distribution of surface rupturing appears to conform well with the topographic expression of fold and thrust structures—many of which exhibit evidence for neotectonics (e.g., Fig. 3.6). There appear to be lateral variations in how crustal shortening associated with the deep seismic event has been accommodated throughout the sedimentary section. For instance, across the Kutubu and Cecilia ground deformation zones, surface rupturing appears to have been concentrated to the southwest (e.g., Fig. 3.4), as would be expected for reverse offset on a foreland vergent fault system. Towards the northwest, surface rupturing is interpreted to the northeast of the Hides-Mananda ground deformation zone, particularly around the Hides Anticline, potentially reflecting an increased prevalence of hinterland vergent faults within the sedimentary section. Interestingly, these observations are generally consistent with our understanding of structural style along the length of the PFTB, which transitions from abundant, small-wavelength and low-relief foreland vergent structures in the southeast to larger-wavelength, high-relief structures comprising abundant backthrusting

and triangle zone faulting in the northwest (Fig. 3.1, c.f. A-A′/B-B′ and C-C′/D-D′).

However, in apparent disagreement with the interpreted surface rupturing to the north of Hides, GPS measurements indicate that the Hides Anticline was shifted up to 42 cm towards the southwest during the 2018 PNG Highlands earthquake sequence (Fig. 3.3a), highlighting the primary influence on ground deformation to have been inversion on the underlying northeast-dipping Lavani-Kutubu Fault Zone. The surface rupturing in this area may relate to shallower, smaller-scale structures, such as antithetic faults, that have formed as a means of accommodating deep crustal shortening through the complex mechanical stratigraphy of the Papuan Basin. The complex distribution of ground deformation and surface rupturing during the PNG Highlands earthquake sequence aptly demonstrates the enormous complexity and laterally-variable interaction between inverting passive margin architecture and shallow fold and thrust structures. As such, it is unsurprising that structural style is a topic of ongoing debate in the PFTB, and indeed, in fold and thrust belts worldwide.

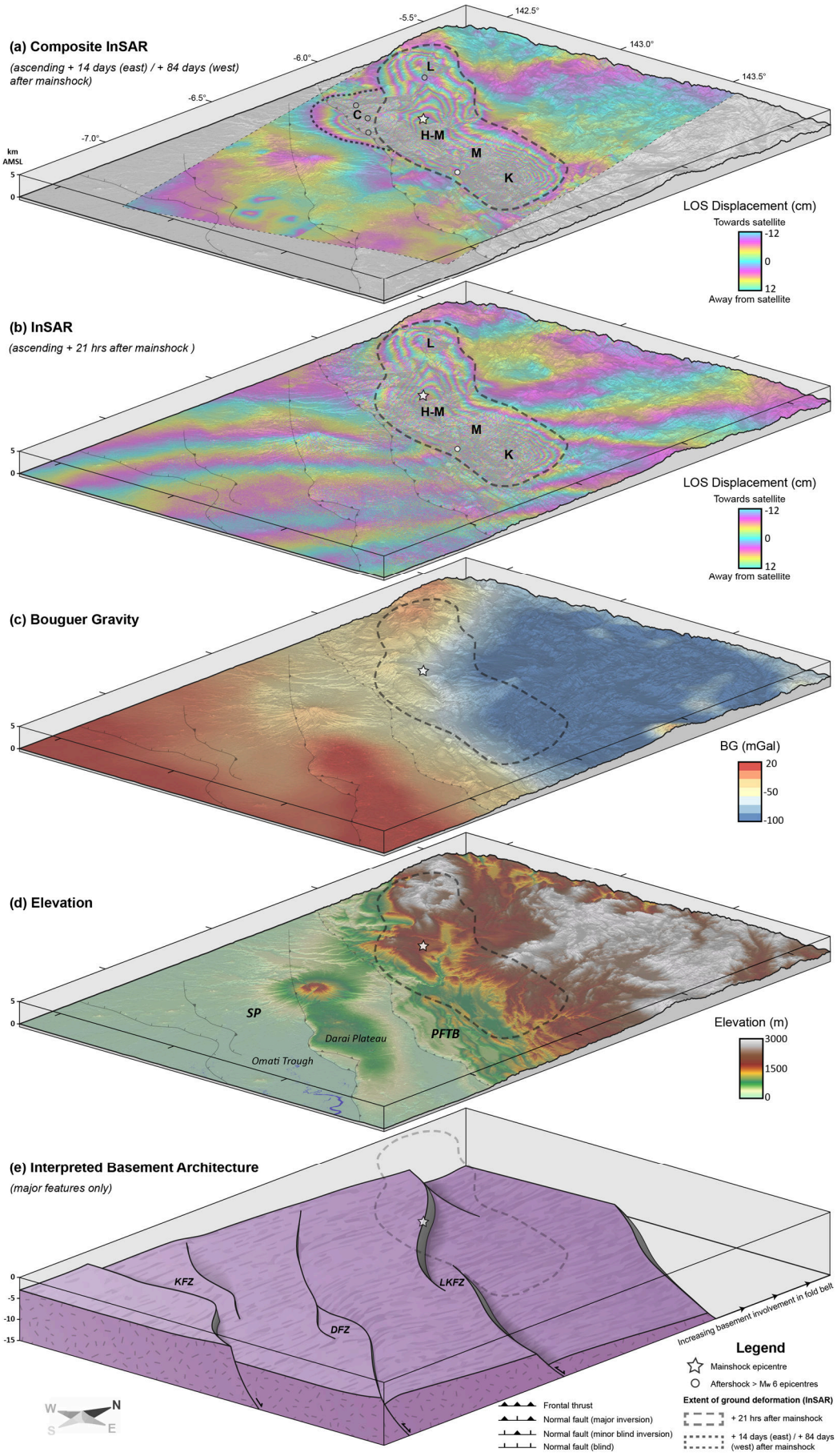
(a) Composite InSAR
(ascending + 14 days (east) / + 84 days (west) after mainshock)
142.5°
143.0°
143.5°
-5.5°
-6.0°
-6.5°
-7.0°
km AMSL
5
0
L
C
H-M
M
K
LOS Displacement (cm)
Towards satellite
-12
0
12
Away from satellite
(b) InSAR
(ascending + 21 hrs after mainshock)
L
H-M
M
K
LOS Displacement (cm)
Towards satellite
-12
0
12
Away from satellite
(c) Bouguer Gravity
BG (mGal)
20
-50
-100
(d) Elevation
SP
Darai Plateau
Omati Trough
PFTB
Elevation (m)
3000
1500
0
(e) Interpreted Basement Architecture
(major features only)
0
-5
-10
-15
KFZ
DFZ
LKFZ
Increasing basement involvement in fold belt
W
N
S
E
Legend
Mainshock epicentre
Aftershock > Mw 6 epicentres
Extent of ground deformation (InSAR)
+ 21 hrs after mainshock
+ 14 days (east) / + 84 days (west) after mainshock
Frontal thrust
Normal fault (major inversion)
Normal fault (minor blind inversion)
Normal fault (blind)

Figure 3.7. *(previous page) Schematic perspective view of the Papuan Fold and Thrust Belt and Stable Platform, showing geological and geophysical observations pertinent to the 2018 PNG Highlands earthquake sequence. (a) Composite ascending interferogram (GSI, 2018) with second observation dates of 12th March 2018 (+ 14 days after mainshock) in the east and 21st May 2018 (+ 84 days after mainshock) in the west (Fig. 3.4, main). (b) Ascending interferogram (GSI, 2018) with second observation date of 26th Feb 2018 (+ 21 hrs after mainshock) (Fig. 3.4, inset). Ground deformation zones (refer Section 3.3.2): L, Lavani; H-M, Hides-Mananda; M, Moran; K, Kutubu; C, Cecilia. (c) Regional Bouguer corrected gravity dataset comprising high-resolution airborne data merged with open-file land-based data. Airborne gravity data provided by Sander Geophysics, Ottawa, Canada. (d) 30 m SRTM digital elevation model (USGS, 2015). Note the spatial and morphological similarities between the topographic expression of the Darai Plateau and extent of ground deformation during the earthquake sequence. SP, Stable Platform; PFTB, Papuan Fold and Thrust Belt. (e) Schematic block model showing the basement architecture of the northern Australian passive margin. Major fault zones include the Komewu Fault Zone (KFZ), the Darai Fault Zone (DFZ) and the Lavani-Kutubu Fault Zone (LKFZ). Earthquake epicentre colours are consistent with Figure 3.4. See Supplementary Material B3 for zoomed versions of this figure.*

3.4.2. Influence of crustal structure on earthquake-related stress release

Another interesting aspect of the 2018 PNG Highlands earthquake sequence relates to the spatial and temporal release of stress during the seismic event and the implications this has for understanding the influences on the evolution of the PFTB. In the ~ 21 hrs following the M_w 7.5 mainshock, the aftershock sequence and associated ground deformation formed a northwest to southeast trend that tracked the deep extensional fault system that we have interpreted beneath the PFTB (e.g., the Lavani-Kutubu Fault Zone; Fig. 3.7, c.f. b and e). Seismicity over this period likely represented the propagation of slip into regions that experienced relatively small slip during the mainshock. Interestingly, within the initial 21 hrs of the earthquake sequence, the general abundance and magnitude of aftershocks and the lateral extent of ground deformation away from the epicentral location was greater to the southeast than northwest (e.g., Fig. 3.4, inset). We believe this relates to lateral variations in the underlying margin architecture. Indeed, the lower Bouguer gravity

anomaly in the east versus the west (Fig. 3.7c) implies that high-density crystalline basement is likely deeper—indicating that the Papuan Basin sediments are thicker and therefore the underlying crust may be more attenuated and weaker than it is in the northwest. As a result, it more readily underwent shortening and uplift to accumulate strain, and large seismic events were limited to approximately the first 21 hrs or so of the earthquake sequence in these areas. In the northwest, the sequence impinged on less attenuated and thus stronger crust, which was much more resistant to strain. Following the mainshock, stress accumulated on the basement footwall high in this area, to eventually be released more slowly as a series of large aftershocks to the south and west of the mainshock (e.g., within the Cecilia and Lavani zones), including four > M_w 6 aftershocks between ~ 2.5-41 days after the mainshock. The mid-crustal focal depths and moment tensors of these events are similar to the mainshock (Fig. 3.1), leading to our hypothesis that they were either related to (1) inversion on subsidiary listric extensional faults located inboard (to the southwest) of the main extensional fault trend activated during the mainshock (e.g., Fig. 3.1, A-A'), and/or (2) reverse movement on a deep-rooted shortcut thrust within the footwall block of the main extensional fault trend (e.g., Fig. 3.1, B-B'). Interestingly, the hypothesised transition from stronger crust in the west to weaker crust in the east also provides a fitting explanation for the clockwise rotation of the PFTB recognised from modelling of GPS velocities (e.g., Koulali *et al.*, 2015).

Where complex patterns of stress release have been observed within contractional settings, crustal heterogeneities such as changes in composition or structure are most often invoked as the primary controlling factors (e.g., Kato *et al.*, 2006; Mercier *et al.*, 2011). The most significant change in crustal composition on the northern Australian passive margin is the Tasman Line—a transition from stronger Proterozoic lithosphere in the west to weaker late Palaeozoic crust in the east (e.g., Hill and Hall, 2003). Wang *et al.* (2020) propose this transition was the principle control on strain partitioning observed during the 2018 PNG Highlands earthquake.

But observations from outcrop and well intersections throughout the Stable Platform and PFTB in PNG suggest that Palaeozoic and younger basement rocks extend to at least near the PNG-Indonesia border (e.g., Figure 2.1 in Chapter 2), thus the crustal transition begins over 100 km from the westernmost extent of ground deformation associated with the PNG Highlands earthquake. This leads us to believe that crustal structure, rather than composition, was the primary control on the pattern of stress release and strain partitioning during the PNG Highlands earthquake and we can therefore infer that basement structure has also had a principal role in the evolution of variable structural styles observed throughout the PFTB. Although crustal composition may not have been the primary control on PNG Highland earthquake-related deformation, it likely had an important indirect influence having impacted the form and distribution of basement structure (e.g., the Komewu, Darai and Lavani-Kutubu fault zones) during the evolution of the margin—an association that is well-documented in extensional settings worldwide (e.g., Smith and Mosley, 1993; Brune *et al.*, 2017; Kharazizadeh *et al.*, 2017).

3.5. Conclusion

Our study of the 2018 M_w 7.5 PNG Highlands earthquake and aftershock sequence has yielded significant insight into the structure and evolution of the Papuan Fold and Thrust Belt. We have identified and delineated an actively inverting, basin-bounding extensional fault system beneath the PFTB, indicating that the architecture of the northern Australian passive margin has a primary control on structural style. The observed distribution of seismicity and ground deformation is indicative of a thick-skinned system that is both spatially and temporally linked to complex thin-skinned structural styles observed within the thick and mechanically variable sediments of the Papuan Basin. Given the estimated return period for a seismic event of this magnitude is ~ 150 years (McCue *et al.*, 2018), it is possible that the PFTB has experienced over 30,000 comparably sized events—each associated with similarly

complex crustal and ground deformation—during its evolution from the late Miocene to present. This highlights the true complexity that characterises the evolution and resulting structural styles of the PFTB. An improved understanding of the PFTB requires that we (1) accept and embrace the spatiotemporal complexity that has been so well-demonstrated during the 2018 PNG Highlands earthquake sequence, (2) acknowledge the limitations of, and challenge the capability of, traditional and generic fold and thrust belt models to account for such complexity, and (3) seek more bespoke solutions—ideally tools and techniques that can incorporate pre-existing anisotropies within the deforming margin, the mechanical stratigraphy of the cover sequence and the evolving stress conditions under which the fold and thrust belt formed.

References

Abers, G., McCaffrey, R., 1988. Active deformation in the New Guinea fold-and-thrust belt: Seismological evidence for strike-slip faulting and basement-involved thrusting. *Journal of Geophysical Research: Solid Earth*, 93(B11), pp.13332-13354.

Abers, G.A., McCaffrey, R., 1994. Active arc-continent collision: Earthquakes, gravity anomalies, and fault kinematics in the Huon-Finisterre collision zone, Papua New Guinea. *Tectonics*, 13(2), pp.227-245.

Ali, M.Y., Sirat, M., Small, J., 2009. Integrated gravity and seismic investigation over the Jabal Hafit structure: Implications for basement configuration of the frontal fold-and-thrust belt of the northern Oman Mountains. *Journal of Petroleum Geology*, 32(1), pp.21-37.

Altamimi, Z., Métivier, L., Rebischung, P., Rouby, H., Collilieux, X., 2017. ITRF2014 plate motion model. *Geophysical Journal International*, 209(3), pp.1906-1912.

Amoco, 1982. Lavani 1 Well Completion Report, 137 pp.

Ayarza, P., Alvarez-Lobato, F., Teixell, A., Arboleya, M.L., Teson, E., Julivert, M., Charroud, M., 2005. Crustal structure under the central High Atlas Mountains (Morocco) from geological and gravity data. *Tectonophysics*, 400(1-4), pp.67-84.

Bain, J.H.C., Mackenzie, D.E., Ryburn, R.J., 1975. Geology of the Kubor Anticline, Central Highlands of Papua New Guinea. Bureau of Mineral Resources, Geology and Geophysics Bulletin 155, Australian Government Publishing Service, 116 pp.

Baldwin, S.L., Fitzgerald, P.G., Webb, L.E., 2012. Tectonics of the New Guinea region. *Annual Review of Earth and Planetary Sciences*, 40, pp.495-520.

Bennett, D.J., Brand, R.P., Mills, C.R., Morris, B.D., 2000. Exploration potential of the West Bosavi area, Papuan foreland basin, Papua New Guinea. In: Buchanan, P., Grainge, A., Thornton, R. (Eds.), *Petroleum Exploration, Development, and Production in Papua New Guinea: Proceedings of the Fourth PNG Petroleum Convention.* Papua New Guinea Chamber of Mines and Petroleum, Port Moresby, pp.139–154.

Bonini, M., Sani, F., Antonielli, B., 2012. Basin inversion and contractional reactivation of inherited normal faults: A review based on previous and new experimental models. *Tectonophysics*, *522*, pp.55-88.

Brown, C.M., Robinson, G.P., 1982. Kutubu 1:250 000 Geological Series Explanatory Notes Sheet SB/54-12, Geological Survey of Papua New Guinea. PNG Department of Minerals and Energy, Port Moresby.

Brune, S., Heine, C., Clift, P.D., Pérez-Gussinyé, M., 2017. Rifted margin architecture and crustal rheology: reviewing Iberia-Newfoundland, central South Atlantic, and South China Sea. *Marine and Petroleum Geology*, 79, pp.257-281.

Buchanan, J.G., Buchanan, P.G. (eds), 1995. *Basin inversion.* Geological Society, London, Special Publications, 88, 596 pp.

Buchanan, P., Warburton, J., 1996. The influence of pre-existing basin architecture in the development of the Papuan fold and thrust belt: implications for petroleum prospectivity. In: Buchanan, P. (Ed.), *Petroleum Exploration, Development, and Production in Papua New Guinea: Proceedings of the Third PNG Petroleum Convention*. Papua New Guinea Chamber of Mines and Petroleum, Port Moresby, pp. 89-109.

Camanni, G., Brown, D., Alvarez-Marron, J., Wu, Y.M., Chen, H.A., 2013. The Shuilikeng fault in the central Taiwan mountain belt. *Journal of the Geological Society*, 171(1), pp.117-130.

Camanni, G., Alvarez-Marron, J., Brown, D., Ayala, C., Wu, Y.M., Hsieh, H.H., 2016. The deep structure of south-central Taiwan illuminated by seismic tomography and earthquake hypocenter data. *Tectonophysics*, 679, pp.235-245.

Chong, J.H., Huang, M.H., 2020. Refining the 2018 Mw 7.5 Papua New Guinea Earthquake Fault-Slip Model Using Subpixel Offset. *Bulletin of the Seismological Society of America*.

Cooper, M., 2007. Structural style and hydrocarbon prospectivity in fold and thrust belts: a global review. *Special Publication-Geological Society of London*, 272, pp.447-472.

Davies, H., Norvick, M., 1974. Blucher Range 1:250 000 Geological Series Explanatory Notes Sheet SB/54-07. Geological Survey of Papua New Guinea, PNG Department of Minerals and Energy, Port Moresby.

DeMets, C., Gordon, R.G., Argus, D.F., Stein, S., 1994. Effect of recent revisions to the geomagnetic reversal time scale on estimates of current plate motions. *Geophysical research letters*, 21(20), pp.2191-2194.

Darnault, R., Hill, K.C., 2020. Four-dimensional analog and geometrical modeling of the Hides anticline, Papua New Guinea: Structure of a giant gas field. *AAPG Bulletin*, 104(4), pp.961-985.

Eisenberg, L.I., 1996. Strontium isotope analysis and structural interpretation of P'nyang Anticline, Papuan Fold belt, Western Highlands Province, Papua New Guinea. In: Buchanan, P. (Ed.), *Petroleum Exploration, Development, and Production in Papua New Guinea: Proceedings of the Third PNG Petroleum Convention.* Papua New Guinea Chamber of Mines and Petroleum, Port Moresby, pp.231-244.

Findlay, A.L., 1974. The structure of foothills south of the Kubor Range, Papua New Guinea. *The APPEA Journal*, 14(1), pp.14-20.

Gabriel, A.K., Goldstein, R.M., Zebker, H.A., 1989. Mapping small elevation changes over large areas: Differential radar interferometry. *Journal of Geophysical Research: Solid Earth*, 94(B7), pp.9183-9191.

Gee, L.S., Leith, W.S., 2011. The Global Seismographic Network: U.S. Geological Survey Fact Sheet 2011-3021, 2 p.

Ghasemi, H., Itikarai, I., Hazelwood., M, Mckee, C., Allen, T., 2018. A low-cost seismic network for Papua New Guinea. *Australian Earthquake Engineering Society 2018 Conference Extended Abstract,* Perth, Australia, 10 pp.

Giddings, J.A., Aden, L.J., Darby, B.J., Leech, D.L., Lyons, D.Y., Djakic, A.L., Barwick, D., Iwanec, J.B., Parish, M., The Muruk Gas Field: Insights into Structural Style in The Western Foldbelt of Papua

New Guinea. *2020 AAPG/EAGE 1st Petroleum Geoscience Conference and Exhibition, PNG's Oil and Gas Industry Maturing through Exploration, Development and Production*, Port Moresby, 4 pp.

Groves, D.I., Goldfarb, R.J., Gebre-Mariam, M., Hagemann, S.G., Robert, F., 1998. Orogenic gold deposits: a proposed classification in the context of their crustal distribution and relationship to other gold deposit types. *Ore geology reviews*, 13(1-5), pp.7-27.

GSI, 2018. The 2018 Papua New Guinea Earthquake: Crustal deformation detected by ALOS-2 data, Geospatial Information Authority of Japan, data accessed 16 October 2020, <https://www.gsi.go.jp/cais/topic180301-index-e.html>

Hanani, A., Lennox, P., Hill, K.C., 2016. The geology and structural style of the Juha Gas Field, Papua New Guinea. ASEG Extended Abstract 2016, pp.1-7.

Hill, K.C., 1991. Structure of the Papuan Fold belt, Papua New Guinea. *American Association of Petroleum Geology Bulletin*, 75, 857-872.

Hill, K.C., Bradey, K., Iwanec, J., Wilson, N., Lucas, K., 2008. Structural exploration in the Papua New Guinea Fold Belt. In: Blevin, J.E., Bradshaw, B.E., Uruski, C. (Eds.), *Eastern Australian Basins Symposium III, Petroleum Exploration Society of Australia, Special Publication,* pp.225-238.

Hill, K.C., Hall, R., 2003. Mesozoic-Cenozoic evolution of Australia's New Guinea margin in a west Pacific context. *Geological Society of America, Special Papers*, pp.265-290.

Hill, K.C., Kendrick, R.D., Crowhurst, P.V., Gow, P.A., 2002. Copper-gold mineralisation in New Guinea: Tectonics, lineaments, thermochronology and structure. *Australian Journal of Earth Sciences*, 49(4), pp.737-752.

Hill, K.C., Lucas, K., Bradey, K., 2010. Structural styles in the Papuan Fold Belt, Papua New Guinea: constraints from analogue modelling. In: Goffey, G. (Ed.), *Hydrocarbons in Contractional Belts.* Geological Society, London, Special Publications 348, pp.33-56.

Hill, K., Mahoney, L., 2018. Compressional evolution of the PNG margin from an orogenic transect from Juha to the Sepik. *ASEG Extended Abstracts*, 2018(1), pp.1-3.

Hill, K.C., Norvick, M., Keetley, J., Adams, A., 2000. Structural and stratigraphic shelf-edge hydrocarbon plays in the Papuan Fold Belt. In: Buchanan, P., Grainge, A., Thornton, R. (Eds.), *Petroleum Exploration, Development, and Production in Papua New Guinea: Proceedings of the Fourth PNG Petroleum Convention.* Papua New Guinea Chamber of Mines and Petroleum, Port Moresby, pp. 67-85.

Hill, K.C., Raza, A., 1999. Arc-continent collision in Papua Guinea: Constraints from fission track thermochronology. *Tectonics*, 18(6), pp.950-966.

Hill, K.C., Simpson, R., Kendrick, R., Crowhurst, P., O'Sullivan, P., Saefudin, I., 1996. Hydrocarbons in New Guinea, controlled by basement fabric, Mesozoic extension and Tertiary Convergent margin tectonics. In: Buchanan, P. (Ed.), *Petroleum Exploration, Development, and Production in Papua New Guinea: Proceedings of the Third PNG Petroleum Convention.* Papua New Guinea Chamber of Mines and Petroleum, Port Moresby, pp.63-76.

Hinsch, R., Asmar, C., Nasim, M, Abbas, M.A., Sultan, S., 2019. Linked thick-to thin-skinned inversion in the central Kirthar Fold Belt of Pakistan. *Solid Earth*, 10(2), pp.425-446.

Hirata, N., Sato, H., Sakai, S.I., Kato, A., Kurashimo, E., 2005. Fault system of the 2004 Mid Niigata Prefecture Earthquake and its aftershocks. *Landslides*, 2(2), pp.153-157.

Hobson, D.M., 1986. A thin skinned model for the Papuan thrust belt and some implications for hydrocarbon exploration. *The APPEA Journal*, 26(1), pp.214-225.

Jenkins, D.A., 1974. Detachment tectonics in western Papua New Guinea. *Geological Society of America Bulletin*, 85(4), pp.533-548.

Jiang, Z., Huang, D., Yuan, L., Hassan, A., Zhang, L., Yang, Z., 2018. Coseismic and postseismic deformation associated with the 2016 Mw 7.8 Kaikoura earthquake, New Zealand: fault movement investigation and seismic hazard analysis. *Earth, Planets and Space*, 70(1), p.62.

Jordan, T.H., Sverdrup, K.A., 1981. Teleseismic location techniques and their application to earthquake clusters in the south-central Pacific. *Bulletin of the Seismological Society of America*, 71(4), pp.1105-1130.

Kao, H., Chen, W.P., 2000. The Chi-Chi earthquake sequence: Active, out-of-sequence thrust faulting in Taiwan. *Science*, 288(5475), pp.2346-2349.

Kato, A., Sakai, S.I., Hirata, N., Kurashimo, E., Iidaka, T., Iwasaki, T., Kanazawa, T., 2006. Imaging the seismic structure and stress field in the source region of the 2004 mid-Niigata prefecture earthquake: Structural zones of weakness and seismogenic stress concentration by ductile flow. *Journal of Geophysical Research: Solid Earth*, 111(B8), 18 pp.

Kato, A., Sakai, S., Kurashimo, E., Igarashi, T., Iidaka, T., Hirata, N., Iwasaki, T., Kanazawa, T., 2008. Imaging heterogeneous velocity structures and complex aftershock distributions in the source region of the 2007 Niigataken Chuetsu-oki Earthquake by a dense seismic observation. *Earth, planets and space*, 60(11), pp.1111-1116.

Kawagle, S.A., Meyers, J.B., 1996. Structural and sequence geometry of the Kiunga area, Papuan foreland basin, Papua New Guinea. In: Buchanan, P. (Ed.), *Petroleum Exploration, Development, and Production in Papua New Guinea: Proceedings of the Third PNG Petroleum Convention.* Papua New Guinea Chamber of Mines and Petroleum, Port Moresby, pp.175-193.

Keetley, J.T., Hill, K.C., Nguyen, C., 2001. Mesoscopic Fold and Thrust Structures at Cape Liptrap, Victoria, Australia—A PNG Analogue? *PESA Eastern Australasian Basins Symposium, Melbourne, Petroleum Exploration Society of Australia Special Publication*, pp.179-186.

Kennett, B.L., Engdahl, E.R., Buland, R., 1995. Constraints on seismic velocities in the Earth from traveltimes. *Geophysical Journal International*, 122(1), pp.108-124.

Kharazizadeh, N., Schellart, W.P., Duarte, J.C., Hall, M., 2017. Influence of lithosphere and basement properties on the stretching factor and development of extensional faults across the Otway Basin, southeast Australia. *Marine and Petroleum Geology*, 88, pp.1059-1077.

Koulali, A., Tregoning, P., McClusky, S., Stanaway, R., Wallace, L., Lister, G., 2015. New Insights into the present-day kinematics of the central and western Papua New Guinea from GPS. *Geophysical Journal International*, 202(2), pp.993-1004.

Lacombe, O., Bellahsen, N., 2016. Thick-skinned tectonics and basement-involved fold–thrust belts: insights from selected Cenozoic orogens. *Geological Magazine*, 153(5-6), pp.763-810.

Mahoney, L., Hill, K., McLaren, S., Hanani, A., 2017. Complex fold and thrust belt structural styles: Examples from the Greater Juha area of the Papuan Fold and Thrust Belt, Papua New Guinea. *Journal of Structural Geology*, 100, pp.98-119.

Mahoney, L., Mclaren, S., Hill, K., Kohn, B., Gallagher, K., Norvick, M., 2019. Late Cretaceous to Oligocene burial and collision in western Papua New Guinea: Indications from low-temperature thermochronology and thermal modelling. *Tectonophysics*, 752, pp.81-112.

Mason, R.A., 1996. Structure of the Western Papuan Fold Belt. In: Buchanan, P. (Ed.), *Petroleum Exploration, Development, and Production in Papua New Guinea: Proceedings of the Third PNG Petroleum Convention.* Papua New Guinea Chamber of Mines and Petroleum, Port Moresby, pp. 161-173.

McConachie, B., Lanzilli, E., Kendrick, D., Burge, C., 2000. Extensions of the Papuan Basin Foreland geology into Eastern Irian Jaya (West Papua) and the new Guinea Fold Belt in Papua New Guinea. In: Buchanan, P., Grainge, A., Thornton, R. (Eds.), *Petroleum Exploration, Development, and Production in Papua New Guinea: Proceedings of the Fourth PNG Petroleum Convention.* Papua New Guinea Chamber of Mines and Petroleum, Port Moresby, pp.219-238.

McCue, K., Gibson, G., Love, D., 2018. The Mainshock of 25 February 2018 and Aftershocks in the Central Highlands of Papua New Guinea. *Australian Earthquake Engineering Society 2018 Conference Extended Abstract,* Perth, Australia, 23 pp.

Medd, D.M., 1996. Triangle zone deformation at the leading edge of the Papuan fold belt. In: Buchanan, P. (Ed.), *Petroleum Exploration, Development, and Production in Papua New Guinea: Proceedings of the Third PNG Petroleum Convention.* Papua New Guinea Chamber of Mines and Petroleum, Port Moresby, pp.217-229.

Mercier de Lépinay, B., Deschamps, A., Klingelhoefer, F., Mazabraud, Y., Delouis, B., Clouard, V., Hello, Y., Crozon, J., Marcaillou, B., Graindorge, D., Vallée, M., 2011. The 2010 Haiti earthquake: A complex fault pattern constrained by seismologic and tectonic observations. *Geophysical Research Letters*, 38(22), 7 pp.

Nemcok, M., Schamel, R., Gayer, R., 2005. Thrustbelts: Structural architecture, thermal regimes and petroleum systems. Cambridge University Press, 541 pp.

Pigram, C.J., Symonds, P.A., 1991. A review of the timing of the major tectonic events in the New Guinea Orogen. *Journal of Southeast Asian Earth Sciences*, 6(3-4), pp.307-318.

Poblet, J., Lisle, R.J., 2011. Kinematic evolution and structural styles of fold-and-thrust belts. *Geological Society, London, Special Publications*, 349(1), pp.1-24.

Rosen, P.A., Hensley, S., Joughin, I.R., Li, F.K., Madsen, S.N., Rodriguez, E., Goldstein, R.M., 2000. Synthetic aperture radar interferometry. *Proceedings of the IEEE*, 88(3), pp.333-382.

Schofield, S., 2000. The Bosavi Arch and Komewu Fault Zone: their control on basin architecture and the prospectivity of the Papuan Foreland. In: Buchanan, P., Grainge, A., Thornton, R. (Eds.), *Petroleum Exploration, Development, and Production in Papua New Guinea: Proceedings of the Fourth PNG Petroleum Convention.* Papua New Guinea Chamber of Mines and Petroleum, Port Moresby, pp.101-122.

Smith, M., Mosley, P., 1993. Crustal heterogeneity and basement influence on the development of the Kenya Rift, East Africa. *Tectonics*, 12(2), pp.591-606.

Snyder, D.B., Barazangi, M., 1986. Deep crustal structure and flexure of the Arabian plate beneath the Zagros collisional mountain belt as inferred from gravity observations. *Tectonics*, 5(3), pp.361-373.

Stanaway, R., Mahoney, L., Noonan, J., McLaren, S., 2020. Neotectonics of the Papuan Fold and Thrust Belt - Insights from Space Geodetic Analysis. *2020 AAPG/EAGE 1st Petroleum Geoscience Conference and Exhibition, PNG's Oil and Gas Industry Maturing through Exploration, Development and Production*, Port Moresby, 8 pp.

Stanaway, R., Noonan, J.W., 2015. Geodetic Measurement of Deformation Within the Papuan Fold and Thrust Belt. *2015 International Conference and Exhibition, Society of Exploration Geophysicists and American Association of Petroleum Geologists,* Melbourne, Australia, pp. 114-114.

Stern, R.J., Scholl, D.W., Fryer, G., 2016. An introduction to convergent margins and their natural hazards. *Plate Boundaries and Natural Hazards*, pp.77-98.

Thornton, R.C.N., Emmett, J.K., Lyslo, J.A., Gottschalk, R.R., 1996. Integrated structural and stratigraphic analysis in PPL 175, Papuan Fold Belt, Papua New Guinea. In: Buchanan, P. (Ed.), *Petroleum Exploration, Development, and Production in Papua New Guinea: Proceedings of the Third PNG Petroleum Convention.* Papua New Guinea Chamber of Mines and Petroleum, Port Moresby, pp.195-215.

Tregoning, P., Lambeck, K., Stolz, A., Morgan, P., McClusky, S.C., van der Beek, P., McQueen, H., Jackson, R.J., Little, R.P., Laing, A., Murphy, B., 1998. Estimation of current plate motions in Papua New Guinea from Global Positioning System observations. *Journal of Geophysical Research: Solid Earth*, 103(B6), pp.12181-12203.

USGS, 2015. Shuttle Radar Topography Mission, 1-Arc Second, Global Land Cover Facility. University of Maryland, College Park, Maryland. Data accessed 16 October 2020 through USGS EarthExplorer, <https://earthexplorer.usgs.gov/>

USGS, 2018. United States Geological Survey Events Page: M 7.5 – 83km SW of Porgera, Papua New Guinea, Earthquake Hazards Program, viewed 16 October 2020, <https://earthquake.usgs.gov/earthquakes/eventpage/us2000d7q6>

USGS, 2020. United States Geological Survey Earthquake portal, Earthquake Hazards Program, data accessed 16 October 2020, <https://www.usgs.gov/natural-hazards/earthquake-hazards/earthquakes>

van Ufford, A.Q., Cloos, M., 2005. Cenozoic tectonics of New Guinea. *AAPG Bulletin*, 89(1), pp.119-140.

Vera, E.A.R., Folguera, A., Valcarce, G.Z., Giménez, M., Ruiz, F., Martínez, P., Bottesi, G.,Ramos, V.A., 2010. Neogene to Quaternary extensional reactivation of a fold and thrust belt: the Agrio belt in the Southern Central Andes and its relation to the Loncopué trough (38–39 S). *Tectonophysics*, 492(1-4), pp.279-294.

Wallace, L.M., Stevens, C., Silver, E., McCaffrey, R., Loratung, W., Hasiata, S., Stanaway, R., Curley, R., Rosa, R., Taugaloidi, J., 2004. GPS and seismological constraints on active tectonics and arc-continent collision in Papua New Guinea: Implications for mechanics of microplate rotations in a plate boundary zone. *Journal of Geophysical Research: Solid Earth*, 109, B05404.

Wang, S., Xu, C., Li, Z., Wen, Y., Song, C., 2020. The 2018 Mw 7.5 Papua New Guinea Earthquake: A Possible Complex Multiple Faults Failure Event With Deep-Seated Reverse Faulting. *Earth and Space Science*, *7*(3), p.e2019EA000966.

White, L.T., Morse, M.P., Lister, G.S., 2014. Lithospheric-scale structures in New Guinea and their control on the location of gold and copper deposits. *Solid Earth,* 5(1), pp.163-179.

Worden, C.B., Gerstenberger, M.C., Rhoades, D.A., Wald, D.J., 2012. Probabilistic relationships between ground-motion parameters and modified Mercalli intensity in California. *Bulletin of the Seismological Society of America*, 102(1), pp.204-221.

WHO, 2018. Papua New Guinea earthquake, World Health Organisation, viewed 16 October 2020, <https://www.who.int/westernpacific/emergencies/papua-new-guinea-earthquake>

Xu, X., Wen, X., Yu, G., Chen, G., Klinger, Y., Hubbard, J., Shaw, J., 2009. Coseismic reverse-and oblique-slip surface faulting generated by the 2008 Mw 7.9 Wenchuan earthquake, China. *Geology*, 37(6), pp.515-518.

Zhang, X., Feng, W., Du, H., Li, L., Wang, S., Yi, L., Wang, Y., 2020. The 2018 Mw 7.5 Papua New Guinea earthquake: A dissipative and cascading rupture process. *Geophysical Research Letters*, *47*(17), 10 pp.

Supplementary material A3: GSI interferograms

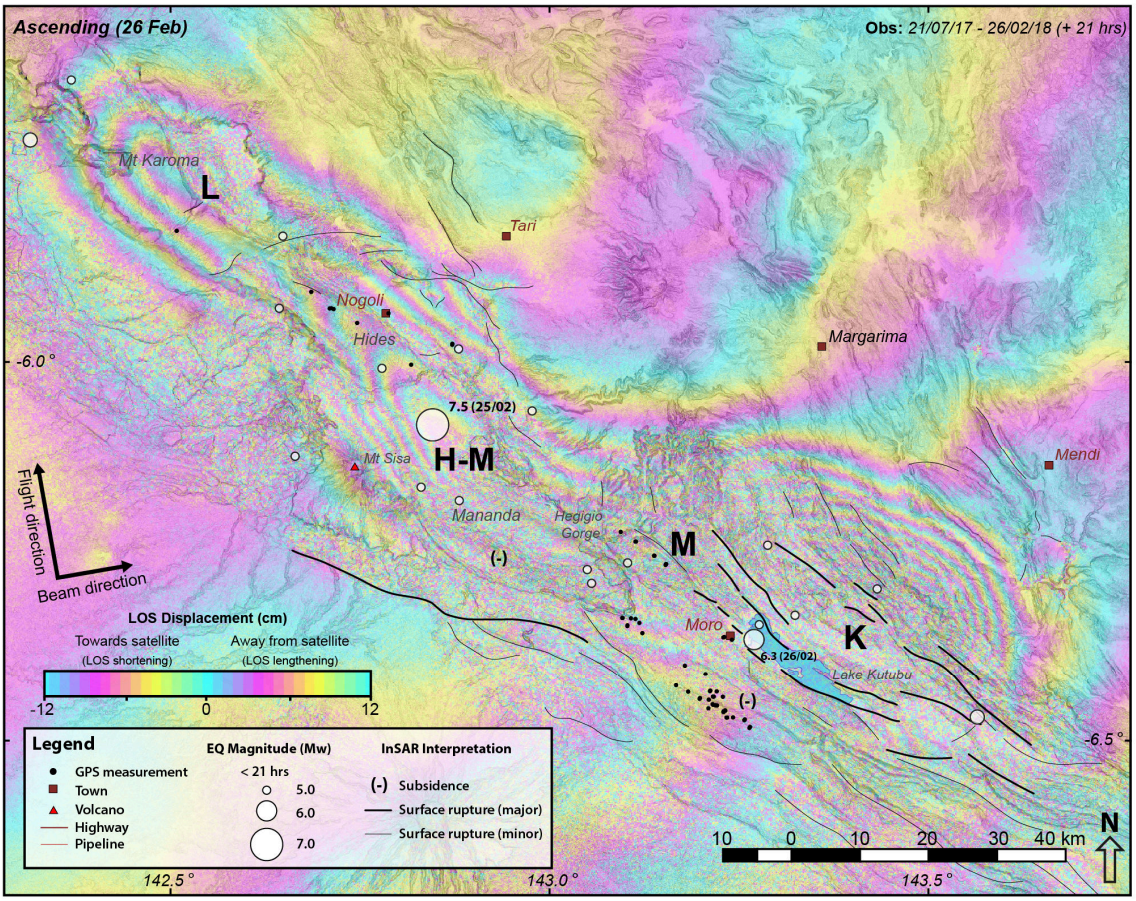

Figure A3.1. *Ascending interferogram (GSI, 2018) with second observation at 14:46, 26th February 2018 (UTC), + 21 hrs after mainshock. Relocated earthquakes > M_w 5 occurring prior to the time of second observation plotted (e.g., events occurring within 21 hrs of the PNG Highlands mainshock), along with an interpretation of possible surface rupturing.*

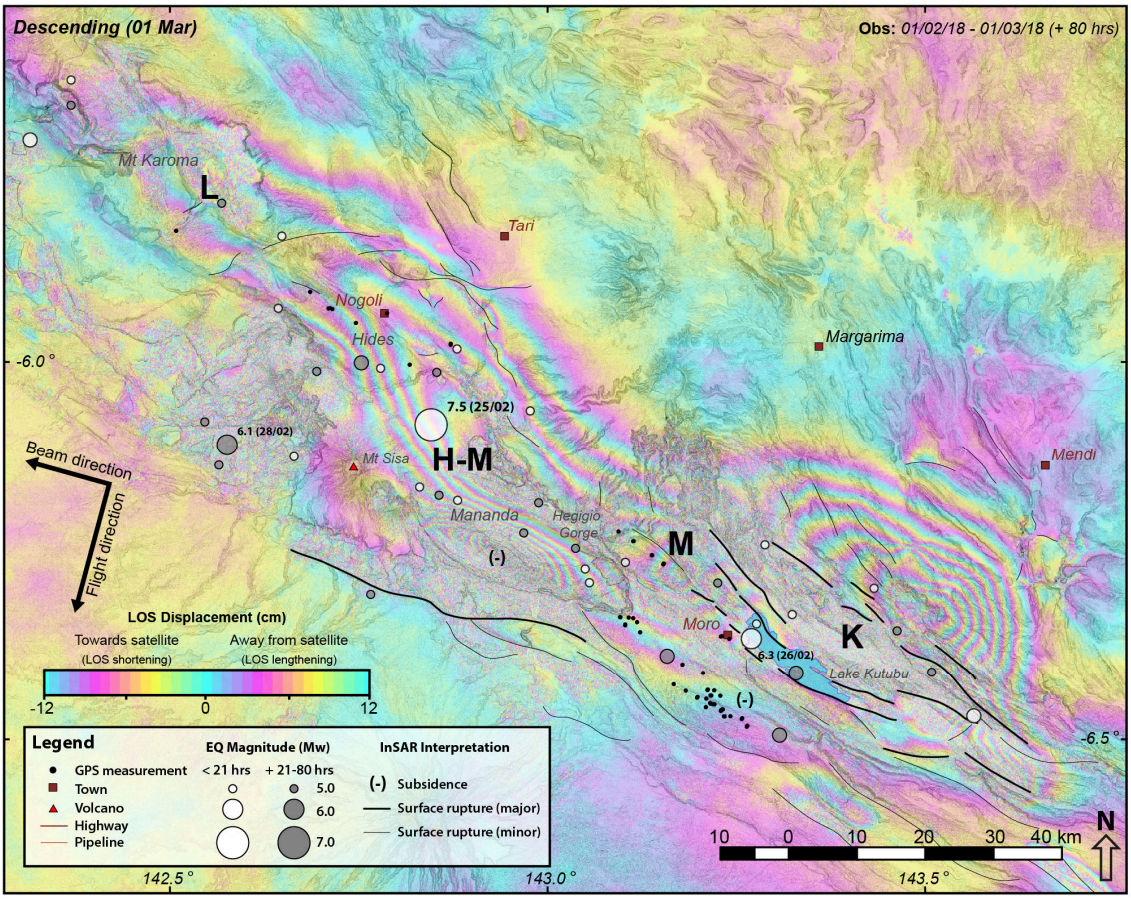

Figure A3.2. *Descending interferogram (GSI, 2018) with second observation at 02:05, 1st March 2018 (UTC), + 80 hrs after mainshock. Relocated earthquakes > M_w 5 occurring prior to the time of second observation plotted (e.g., events occurring within 80 hrs of the PNG Highlands mainshock), along with an interpretation of possible surface rupturing. Note the oval-shaped area of LOS lengthening centred on the Mananda Anticline—a feature that is much less evident on ascending interferograms (e.g., Fig. A3.1 and A3.3).*

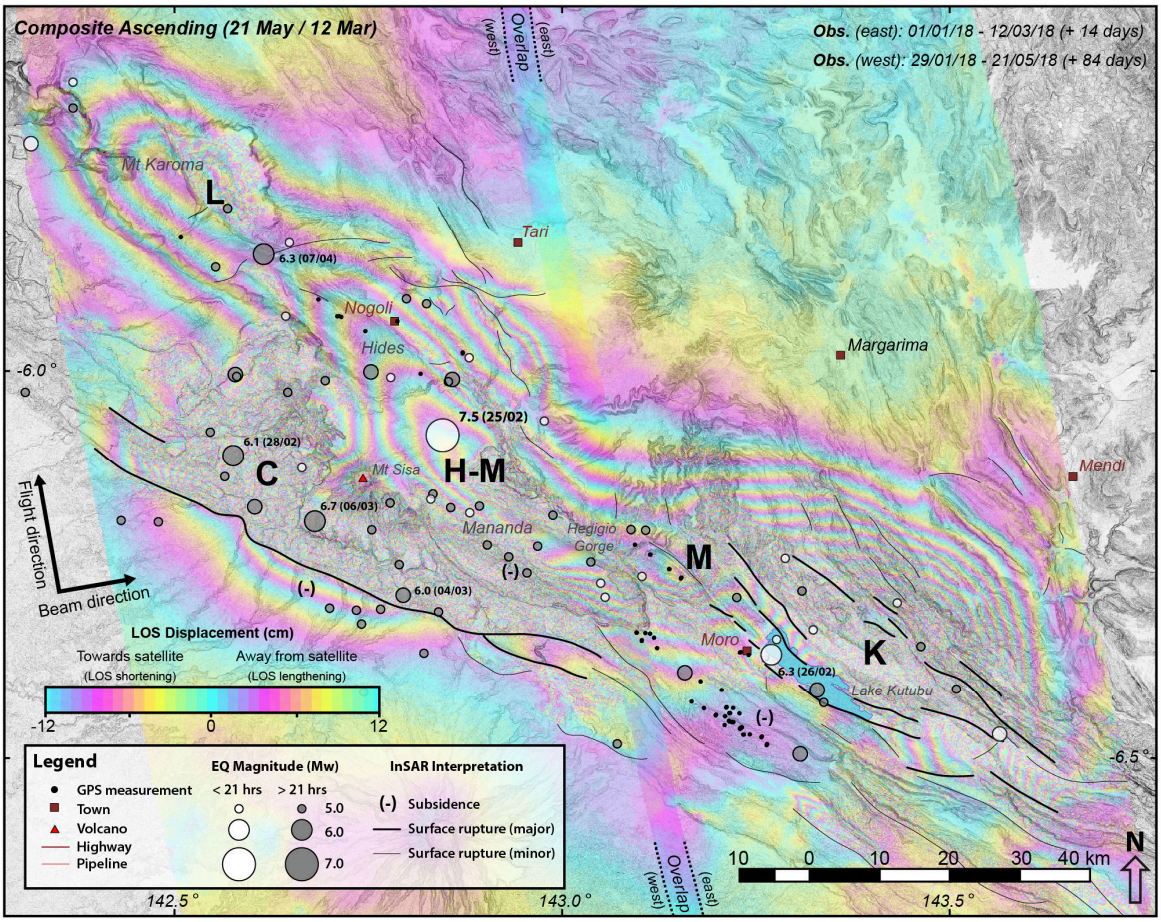

Figure A3.3. *Composite ascending interferogram (GSI, 2018) with second observations at: (East) 14:46, 12th March 2018 (UTC), + 14 day after mainshock and (west) 14:46, 21st May 2018, + 84 days after mainshock. Includes relocated earthquakes > M_w 5 occurring prior to July 2018, and an interpretation of possible surface rupturing.*

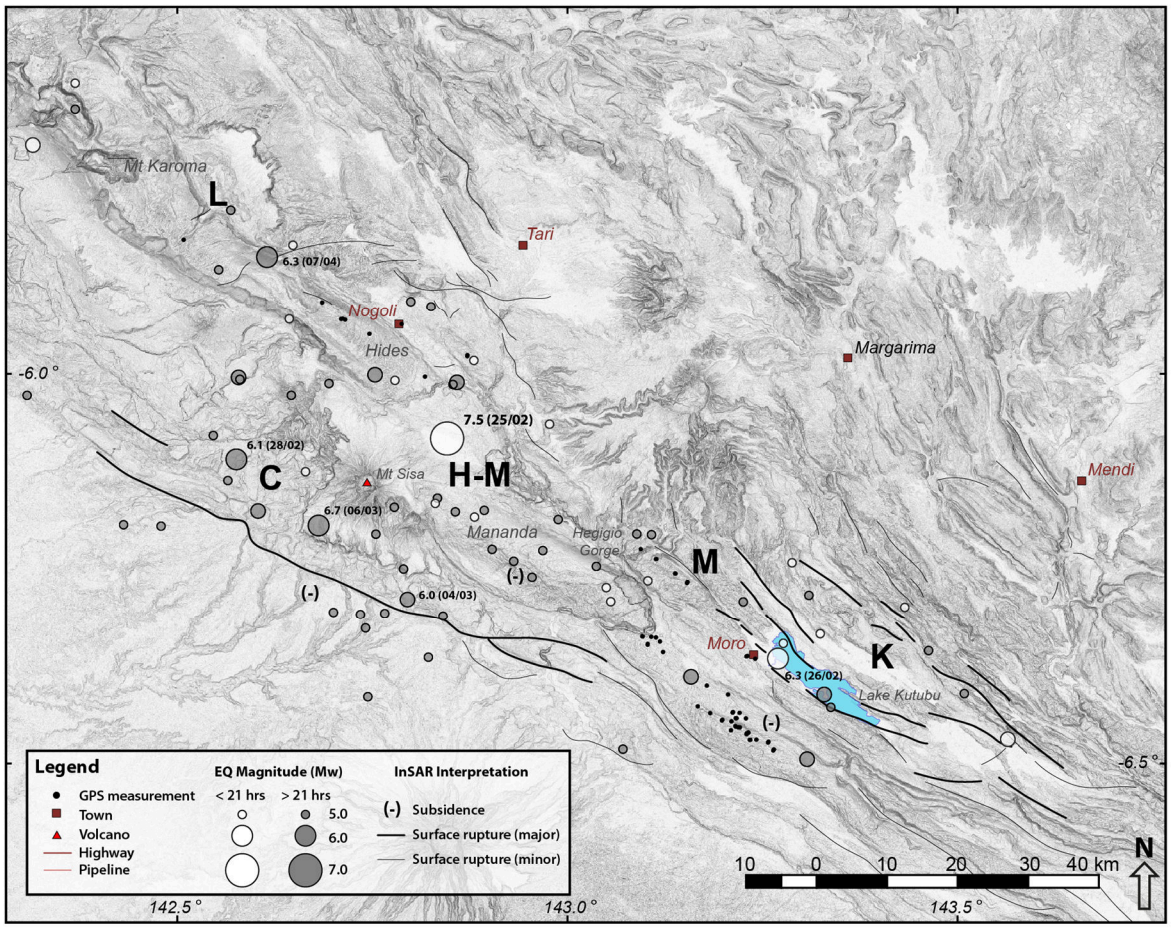

Figure A3.4. *Relocated earthquakes > M_w 5 occurring prior to July 2018 and InSAR surface rupture interpretation (e.g., Fig. A3.3) shown over 30 m SRTM-derived hillshade. Note the concordance of the interpreted surface ruptures with topographic features such as prominent faults and folds. Spatial scale is consistent with figures A3.1-A3.3.*

Supplementary material B3: Figure 3.7. perspective view zoomed in version

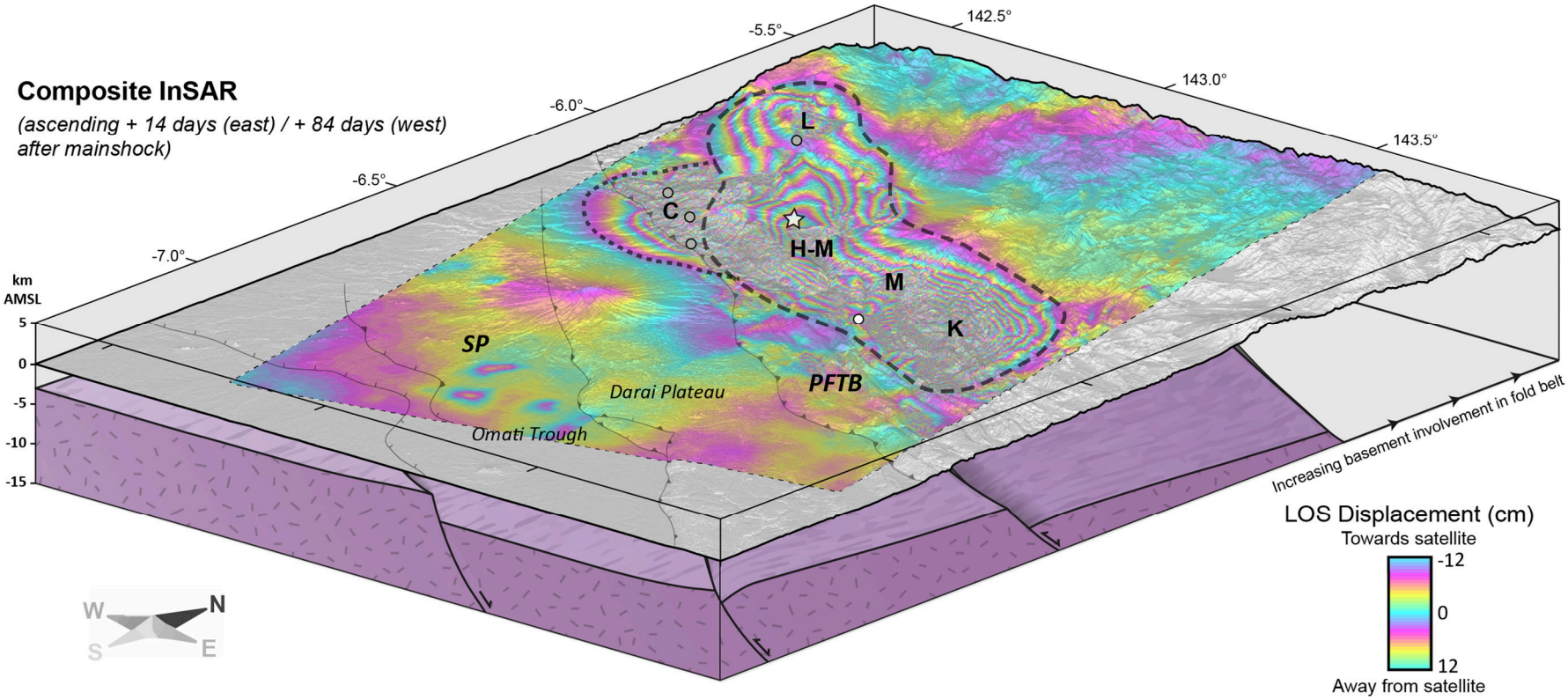

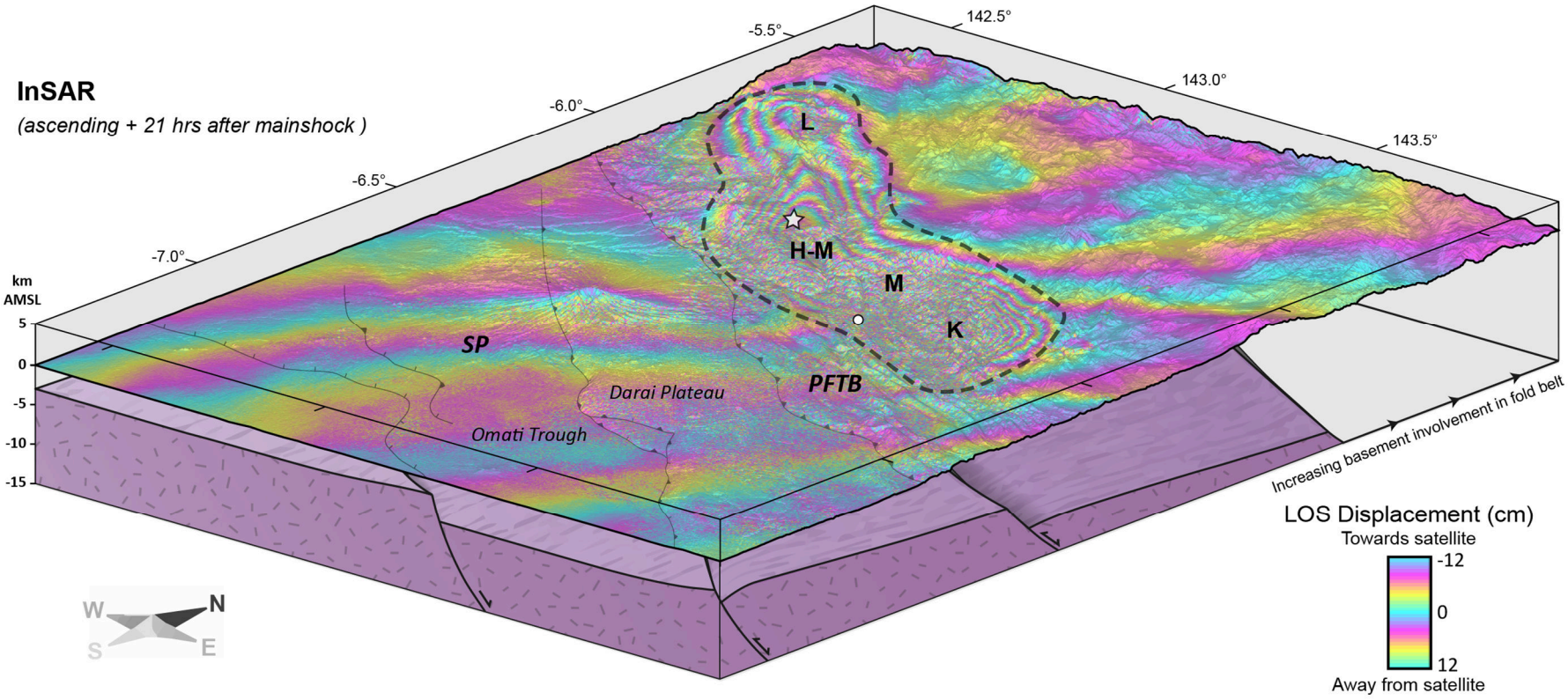
InSAR
(ascending + 21 hrs after mainshock)
-5.5°
142.5°
-6.0°
143.0°
-6.5°
143.5°
-7.0°
km
AMSL
5
0
-5
-10
-15
L
H-M
M
K
SP
PFTB
Darai Plateau
Omati Trough
Increasing basement involvement in fold belt
W
N
S
E
LOS Displacement (cm)
Towards satellite
-12
0
12
Away from satellite

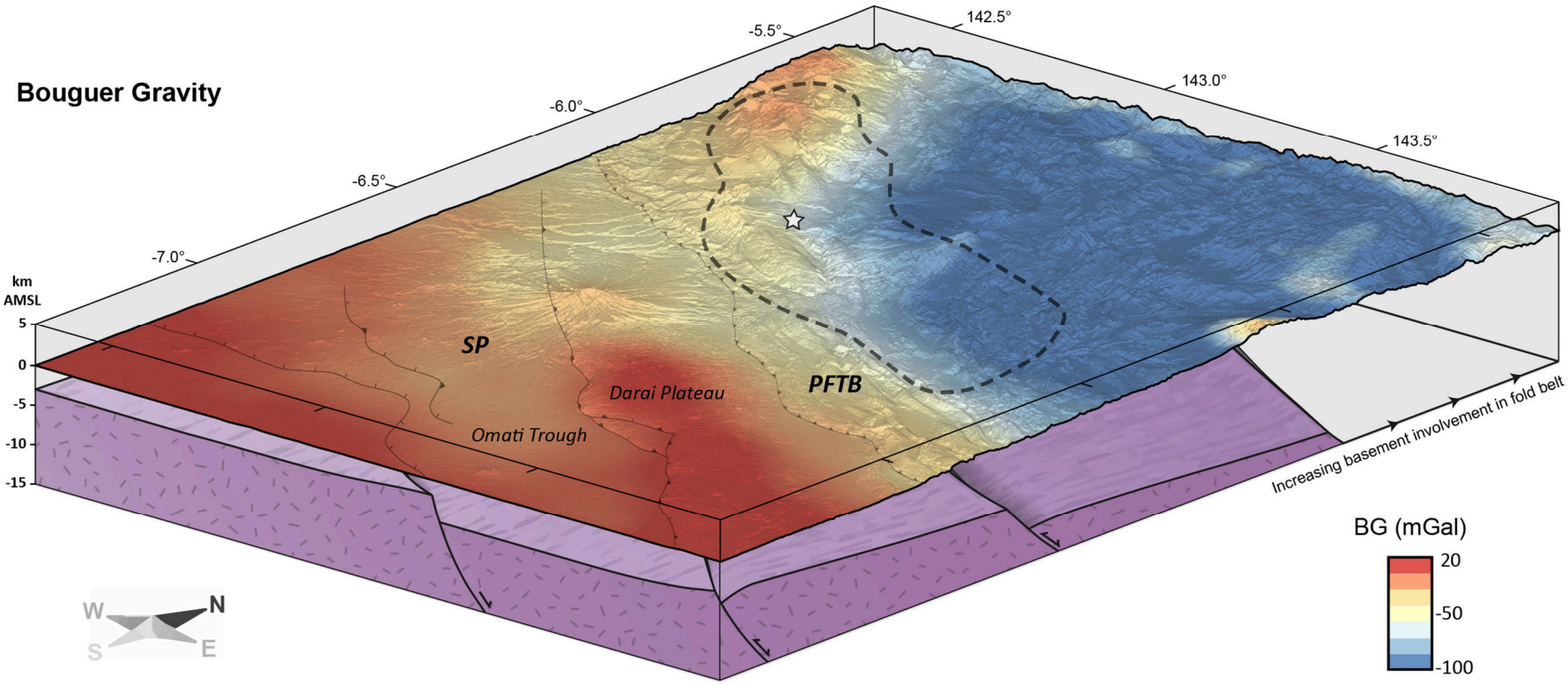
Bouguer Gravity
-5.5°
142.5°
-6.0°
143.0°
-6.5°
143.5°
-7.0°
km
AMSL
5
0
-5
-10
-15
SP
Darai Plateau
PFTB
Omati Trough
Increasing basement involvement in fold belt
W
N
S
E
BG (mGal)
20
-50
-100

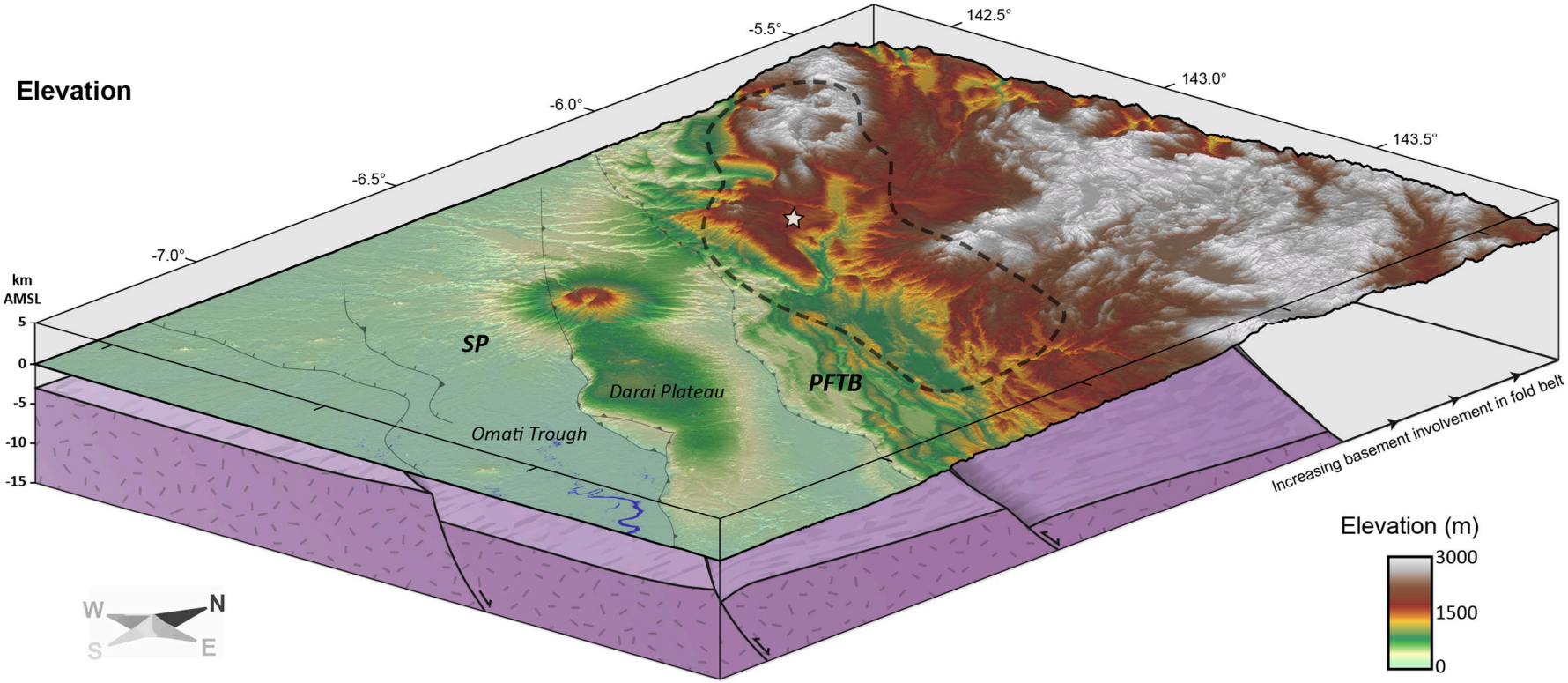
Elevation
-5.5°
142.5°
-6.0°
143.0°
-6.5°
143.5°
-7.0°
km
AMSL
5
0
-5
-10
-15
SP
Darai Plateau
PFTB
Omati Trough
Increasing basement involvement in fold belt
W
N
S
E
Elevation (m)
3000
1500
0

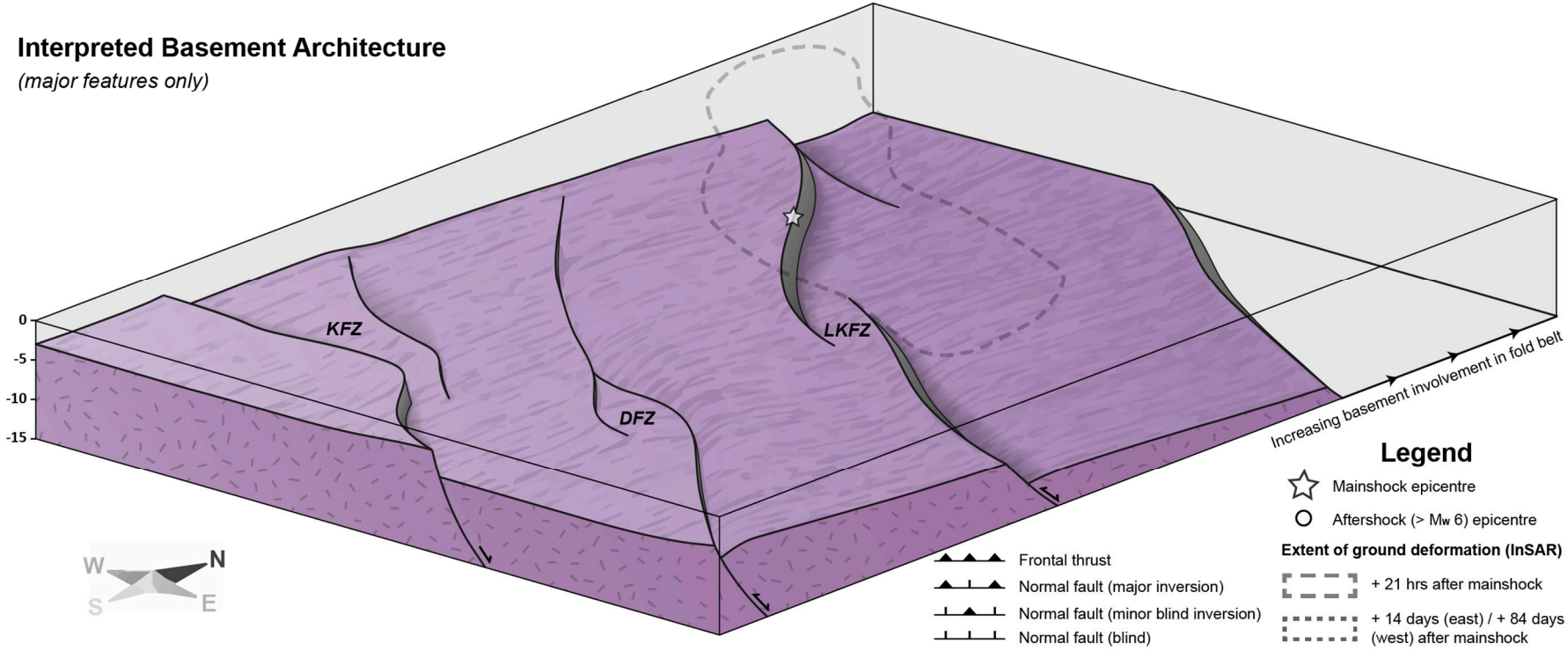
Interpreted Basement Architecture
(major features only)
0
-5
-10
-15
KFZ
DFZ
LKFZ
Increasing basement involvement in fold belt
W
N
S
E
Legend
Mainshock epicentre
Aftershock (> Mw 6) epicentre
Extent of ground deformation (InSAR)
+ 21 hrs after mainshock
+ 14 days (east) / + 84 days (west) after mainshock
Frontal thrust
Normal fault (major inversion)
Normal fault (minor blind inversion)
Normal fault (blind)

Chapter 4

Late Cretaceous to Oligocene burial and collision in western Papua New Guinea: Indications from low-temperature thermochronology and thermal modelling

Abstract

Recent field and analytical work have considerably improved our understanding of the structure of the Muller Range along the frontal trend of the Papuan Fold and Thrust Belt (PFTB) in western Papua New Guinea (PNG). However numerous questions remain unresolved concerning the geological evolution of the region. In particular, the Late Cretaceous to Oligocene history of the region is largely unknown due to the absence of a continuous stratigraphic record. Here, we use both new and existing low-temperature thermochronology data to investigate the geological history of the Muller Range. Thermal history models based on these data suggest two major Cenozoic cooling episodes. The youngest, and best constrained, is clearly recorded in the stratigraphic record and relates to Neogene collision at the northern margin of the Australian continent. An older episode of comparable or greater magnitude occurred in the Eocene to Oligocene and may relate to the removal of 1,500-3,000 m of Late Cretaceous to Eocene section across the Muller Range prior to the widespread deposition of the shelfal Darai Limestone. We suggest that extension along major faults beneath the Muller Range accommodated sedimentation from the Late Cretaceous to the Eocene, consistent with long-lived extensional structures observed in neighbouring regions. In contrast to the Muller Range area, an almost continuous Late Cretaceous to Eocene stratigraphic sequence is preserved in the hinterland < 50 km to the northeast. The selective removal of this sequence across the Muller Range suggests it was uplifted in the Eocene to Oligocene, possibly in part facilitated by the inversion of extensional faults in the Muller Range area. We suggest that this inversion was related to the Eocene to Oligocene collision of the expansive Sepik Terrane to the northwest of the PNG margin. The new data and interpretations presented here have significant implications for the evolution of the PFTB and for tectonic reconstructions of PNG.

4.1. Introduction

Tectonic reconstruction techniques have advanced significantly during the past decade to incorporate global kinematic and geodynamic controls, often validated using detailed seismic tomography (e.g., Zahirovic *et al*., 2014; 2016). This provides an excellent plate-scale framework for Papua New Guinea (PNG; Fig. 4.1), but investigating the detailed tectonic history remains particularly challenging due to complex Cenozoic tectonism, a lack of preserved oceanic crust and a general paucity of data from the isolated and inhospitable highlands.

The Papuan Basin, located on the leading edge of the northern Australian continental margin, has been subject to complex Cenozoic tectonism responsible for the formation of the Papuan Fold and Thrust Belt (PFTB). Current understanding of the geological history of the Papuan Basin is based on the Mesozoic to recent stratigraphic record, which chronicles early Mesozoic rifting, protracted passive margin development and subsequent Cenozoic orogenesis (e.g., Home *et al*., 1990). A long standing question for the Papuan Basin is the origin of a prominent, regional Late Cretaceous to Oligocene unconformity that extends across most of the southern Papuan Basin (e.g., Jenkins, 1974; Brown *et al*., 1980; Home *et al*., 1990). Reconstructing what occurred on the margin over this time is vital for improving our understanding of the geological history and economic potential of the Papuan Basin.

Surrounding regions, such as the complexly deformed Mobile Belt to the north and Coral Sea to the southeast (Fig. 4.1a), offer some insight into the context of the southern Papuan Basin during the key period from the Late Cretaceous to Oligocene. For example, to the southeast, Late Cretaceous to Eocene oceanic crust flooring the Coral Sea Basin suggests regional extensional tectonism (Weissel and Watts, 1979; Pigram and Symonds, 1991), which may have eventually led to rifting along the eastern and northern margins of PNG (Francis, 1990; Pigram and Symonds, 1991; 1993; Davies *et al*., 1997). Late Cretaceous to Palaeogene uplift and erosion in the southwest across the Fly Platform (Fig. 4.1a; e.g., Schofield, 2000), in

part inferred from thermochronology and palaeotemperature data (e.g., Hill, 1989a; 1990; Cooper *et al*., 2012), has been linked by some authors to thermally-driven uplift associated with Coral Sea rifting (e.g., Brown *et al*., 1980; Home *et al*., 1990). More recently, coupled plate tectonic and mantle convection modelling has shown that middle Cretaceous to recent uplift of the eastern Australian margin may relate to continuous dynamic uplift (e.g., Muller *et al*., 2016). While the latter study did not consider the PNG margin, a northward extension of this model may provide a plausible alternate explanation for regional Late Cretaceous to Palaeogene uplift and erosion.

To the north of the Papuan Basin, the complexly deformed Mobile Belt (Fig. 4.1a) records Palaeogene collision on the northern PNG margin (e.g., Dow *et al*., 1972; Dow, 1977), however the number and timing of accretion events are widely debated (e.g., Pigram and Davies, 1987; Hill and Hall, 2003; van Ufford and Cloos, 2005; Davies, 2012). While the details vary, many tectonic reconstructions include an initial Palaeogene collisional event, interpreted to relate to the docking of an expansive terrane at the northern PNG margin, referred to here as the Sepik Terrane (e.g., Pigram and Davies, 1987; Crowhurst *et al*., 1996; Davies *et al*., 1996; Hill and Hall, 2003; Hall, 2012; Schellart and Sparkman, 2015). This event resulted in a highly deformed assemblage of continental and intra-oceanic arc fragments that are collectively referred to as the Sepik Complex (e.g., Rogerson *et al*., 1987; Davies, 1990). The Sepik Complex makes up most of the area known as the Mobile Belt, with the suture between the Mobile Belt and fold belt delineated by a disjointed ophiolite belt that extends along the length of the New Guinea Fold Belt (NGFB) and Papuan Peninsula (Fig. 4.1a). In the Western Fold and Thrust Belt (WFTB) in PNG, the ophiolite belt is presently located < 100 km from the frontal fold belt (Fig. 4.1a), but the associated Palaeogene compressional event has gone largely unrecognised in the stratigraphy and structure of the fold belt.

Low-temperature thermochronology methods such as fission-track (e.g., Gleadow *et al*., 2002) and (U-Th)/He (e.g., Farley, 2002; Guenthner *et al*., 2013) can provide useful constraints on the thermal history of rocks across a range of geological processes (e.g., burial and exhumation) and have proven to be particularly suitable for investigating large gaps in the geological record (e.g., Japsen *et al*., 2011; Green and Duddy, 2016). In PNG, the absence of Late Cretaceous to Oligocene stratigraphy throughout much of the frontal PFTB and Fly Platform means that low-temperature thermochronology data from samples underlying the unconformity can be particularly valuable to identify and calibrate thermal events that can offer insight into the geological history of the margin. The isolated and inhospitable nature of the fold belt and Fly Platform means that previous thermochronological studies are limited, with the bulk of current apatite fission track (AFT) data based on studies by Hill and Gleadow (1989; 1990). Although hampered by poor apatite yields, Hill and Gleadow (1989; 1990) revealed that the Muller Range in the WFTB experienced greater temperatures than the Fly Platform, subsequently relating increased temperatures to deeper late Miocene to Pliocene burial by syn-orogenic sediments.

The recent Greater Juha and Pynang-Blucher geological surveys in the inhospitable Muller Range (e.g., Mahoney *et al*., 2017) provided a rare new opportunity to collect additional samples for thermochronological work. Indeed, the Muller Range provides one of few locations across the frontal PFTB where coarse-grained clastic rocks suitable for thermochronological analysis crop out. In addition, proximity to the April Ultramafics (Fig. 4.1a) makes the Muller Range an important area for investigating the evolution of the PNG margin. Here, we utilise the thermal modelling program QTQt (Gallagher, 2012) to model new AFT and (U-Th)/He data together with the existing AFT dataset to produce detailed thermal histories. In particular, the incorporation of modern annealing and diffusion models (e.g., Ketcham *et al*. 2007; Gautheron *et al*. 2009; Guenthner *et al*. 2013) permits further

investigation of the enigmatic Late Cretaceous to Oligocene thermotectonic history of the PNG margin.

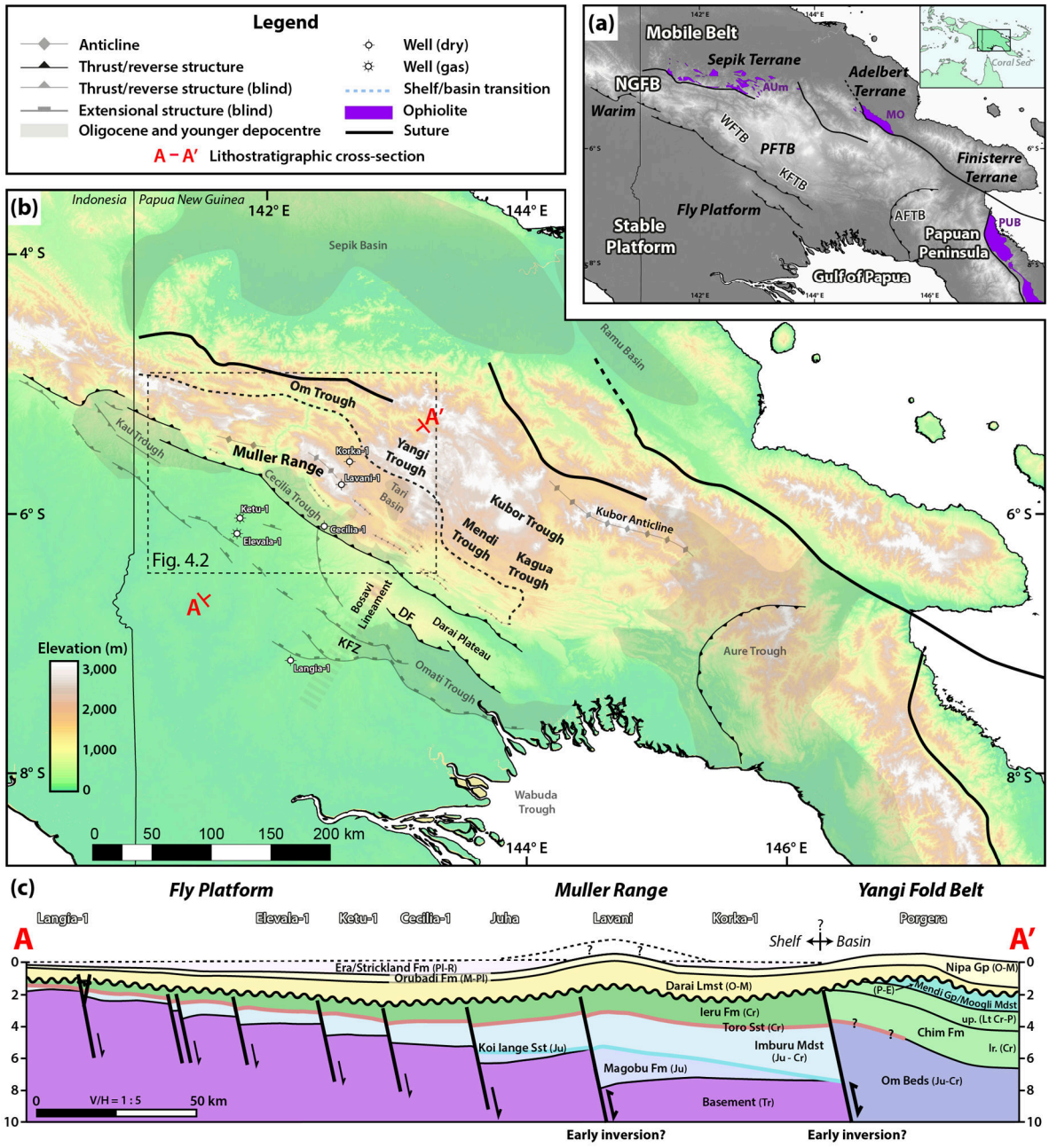

Figure 4.1. *(a) Tectonic-scale components of PNG. Frontal thrusts define the southerly extent of the PFTB while ophiolites delineate the suture zone between the PFTB and Mobile Belt. Tectonic features from Bain et al. (1975). AFTB, Aure Fold and Thrust Belt; KFTB, Kutubu Fold and Thrust Belt; NGFB, New Guinea Fold Belt; PFTB, Papuan Fold and Thrust Belt; WFTB, Western Fold and Thrust Belt; AUm, April Ultramafics; MO, Marum Ophiolite; PUB, Papuan Ultramafic Belt. (b) Major geological components of PNG. Geological features, including shelf/basin transition (as reflected in the stratigraphic record) from Bain et al. (1975). Only the largest anticlines that delineate*

the frontal trend of the PFTB are marked. Subsurface faults on the Stable Platform after McConachie and Lanzilli (2000). KFZ, Komewu Fault Zone; DF, Darai Fault. SRTM digital elevation model retrieved from USGS (2015). (c) Simplified early-thrust (Pliocene) lithostratigraphy of the Papuan Basin in western PNG, showing the relationship between long-lived extensional faults and basinward sedimentary thickening. Note the thick Late Cretaceous to Eocene sequence beneath the Yangi Fold Belt is absent across the frontal fold belt and Fly Platform. The extent to which thick Pliocene to recent molasse sedimentation covered the Muller Range and Yangi Fold Belt is unknown and depends on the interpreted timing of inversion. Refer to Figure 4.2 for detailed stratigraphic legend. Modified from Bennett et al. (2000), Hill et al. (2000) and Mahoney et al. (2017).

4.2. Geology

The island of New Guinea comprises a number of key tectonic components (after Hill and Hall, 2003): (1) the Stable Platform, (2) the Mobile Belt, and (3) the New Guinea Fold Belt (NGFB) (Fig. 4.1a). The Stable Platform is the northern edge of the relatively undeformed Australian continent while the Mobile Belt comprises island arcs and microcontinents accreted to the leading edge of the Australian plate during the Cenozoic (e.g., Hill and Raza, 1999). The NGFB separates the Stable Platform and Mobile Belt and formed predominantly within sediments of the Australian continental margin during the late Miocene to Pliocene (Hill and Gleadow, 1989). In PNG, the Stable Platform and NGFB are commonly referred to as the Fly Platform and PFTB, respectively (Fig. 4.1a).

The Fly Platform and PFTB are primarily underlain by Palaeozoic to early Mesozoic crystalline basement continuous with the Palaeozoic Tasman Orogen of eastern Australia (e.g., Hill and Hall, 2003; Crowhurst *et al*., 2004). In contrast, western New Guinea is largely underlain by late Proterozoic basement (e.g., Parris, 1994). Limited outcrop and well intersections throughout the NGFB and Stable Platform suggest this transition occurs somewhere near the modern international border between PNG and Indonesia (e.g., Figure 2.1 in Chapter 2; Hill and Hall, 2003). The extent to which the formation of the Papuan Basin was controlled by crustal heterogeneity has been discussed in detail (e.g., Hill, 1991, Mahoney *et al*.,

2017) but is largely unproven due to the general absence of basement outcrop and the poor quality of most geophysical imaging.

The stratigraphic and tectonic history of PNG is discussed briefly here, with a focus on those details relevant to our study of the Late Cretaceous to recent evolution of the margin. Detailed reviews of the stratigraphy of PNG and the Papuan Basin are provided by Dow (1977) and Home *et al*. (1990), respectively. Comprehensive tectonic history reconstructions can be found in Pigram and Symonds (1991), Hill and Raza (1999), Hill and Hall (2003), van Ufford and Cloos (2005); Baldwin *et al*. (2012) and Zahirovic *et al.* (2014, 2016).

4.2.1. Early-middle Mesozoic

The non-marine to marine syn-rift sediment sequence overlying basement across much of the margin led to early ideas of early Mesozoic rifting (e.g., Pigram and Panggabean, 1984). Subsequently, abundant typically northwest-southeast and WNW-ESE oriented basement extension structures have been recognised in reflection seismic across the Stable Platform with hanging wall thickening suggesting that extension was long-lived from the early Mesozoic to Neogene (Fig. 4.1; Fischer and Warburton, 1996; Kawagle and Meyers, 1996; Bennett *et al*., 2000; Schofield, 2000; McConachie and Lanzilli, 2000; McConachie *et al*., 2000; Hill *et al*., 2010). Significant early Mesozoic extensional structures are also suspected beneath parts of the PFTB, including from west to east, beneath the westernmost PFTB (Mason, 1996), Muller Range (Mahoney *et al*., 2017), Juha Anticline (Hanani *et al*., 2016), Mananda Anticline (Keenan and Hill, 2015) and Kutubu Fold and Thrust Belt (KFTB) (e.g., Buchanan and Warburton, 1996; Hill *et al*., 2010; 2015). These authors suggest that the basement features exerted a primary control on the subsequent evolution of fold and thrust structures. The largest and best-known inverted extensional structure in the PFTB is in the Eastern Muller Range, evidenced most convincingly by the thick syn-rift sediment sequence (e.g., Magobu Formation; Fig. 4.1c) intersected in the Lavani-1 well (Amoco, 1982; Mahoney *et al*., 2017). Other

significant extensional structures are commonly interpreted at significant shelf/basin facies transitions observed throughout the present-day fold belt, for instance along the Om-Yangi-Mendi-Kagua trend (Fig. 4.1b, Hill *et al*., 2000).

The cessation of an initial phase of Middle Jurassic rifting is recorded throughout the Papuan Basin as a thick, widespread post-rift sequence mostly dominated by fine-grained clastic sediments including the Jurassic to Cretaceous-aged Imburu Mudstone and Cretaceous-aged Ieru Formation (Fig. 4.1c). A number of prograding sandstone sequences were deposited during the early post-rift phase, the most prominent of which are the Jurassic Koi Iange and Early Cretaceous Toro sandstones (Fig. 4.1c). These sands are thickest along the front of the present PFTB suggesting that this area was a near shelf-edge depocentre in the Late Jurassic to earliest Cretaceous (e.g., Home *et al*., 1990; Hill *et al*., 2000).

The middle Cretaceous (ca. Cenomanian) marks the onset of an influx of coarse-grained clastic sediments across the northern Australian continental shelf (e.g., Giero, Ubea, Haito members of the upper Ieru Formation; Sari *et al*., 1996; Bradley, 2014) with a westward migration of the basin axis reflected in the stratigraphy (Jenkins, 1974; Schofield, 2000). The preserved sequence is characterised by significant spatial variations in thickness (e.g., Sari *et al*, 1996), potentially highlighting complex margin architecture at this time. This coarse-grained clastic influx and sedimentation rate increase is inferred to be related to the onset of rifting in the Coral Sea (e.g., Home *et al*., 1990), however it also correlates remarkably well with widespread uplift along the entire eastern Gondwanan margin (Muller *et al*., 2000; 2016).

4.2.2. Late Cretaceous to early Oligocene

The Late Cretaceous to Oligocene histories of the frontal PFTB and Fly Platform regions are largely unknown due to the general absence of a preserved stratigraphic record from this time. Angular unconformities have been recognised in reflection

seismic across the Fly Platform (e.g., McConachie *et al*., 2000; Schofield, 2000), frontal PFTB (Hanani, 2012) and in the Gulf of Papua (Botsford *et al*., 2012; Cooper *et al*., 2012), suggesting at least some uplift occurred over this time.

In contrast, more complete sequences of Late Cretaceous and Palaeogene sediments are preserved in other areas of the New Guinea margin, including from west to east, the western NGFB (e.g., van Ufford and Cloos, 2005), the Yangi and Mendi troughs (e.g., Hill *et al*., 2000), the Gulf of Papua (e.g., Botsford *et al*., 2012) and the Aure Trough (Home *et al*., 1990; Carman, 1993). The Yangi and Mendi troughs provide the best insight into the adjacent frontal PFTB and Fly Platform (Fig. 4.1). In these areas, Late Cretaceous mudstones of the Chim Formation are recorded with estimated thicknesses of 1,500-3,000 m (e.g., Davies and Norvick, 1974; Davies, 1983; Hill *et al*., 1990). The Palaeocene Moogli Mudstone and Eocene Mendi Group, the latter comprising mostly carbonates with variable clastic content, have a similar distribution with combined thicknesses of > 1,000 m preserved throughout the Yangi and Mendi troughs (e.g., Davies, 1983; Brown and Robinson, 1982; Gunson *et al*., 1997; 2000). Mendi Group sediments have also been intersected in wells towards the Gulf of Papua including in the Omati and Wabuda troughs (Fig. 4.1b) and in the Morehead Graben to the far southwest of the Fly Platform (e.g., Tcherepanov *et al*., 2008; Cooper *et al*., 2012). Reflection seismic and well data show that Eocene strata in the Warim and Gulf of Papua regions (Fig. 4.1) lap out onto an apparently emergent Mesozoic high centred on the Fly Platform (e.g., McConachie *et al*., 2000), suggesting that there were limited Eocene strata deposited across the area.

While details regarding the nature and specific timing of Sepik Terrane collision remain controversial (e.g., Pigram and Davies, 1987, Davies *et al*., 1997; van Ufford and Cloos, 2005), there is general agreement that it accreted to the PNG margin during the Palaeogene. An Eocene or Oligocene collision is most commonly suggested from geological evidence and from studies utilising kinematic plate tectonic models and/or seismic tomography (e.g., Schellart and Sparkman, 2015;

Zahirovic *et al*., 2016; Tobin *et al*., 2018). Geological evidence providing the most compelling evidence for an Eocene or Oligocene collision includes:

(1) Late Cretaceous to Eocene recrystallised limestones making up basement in the Sepik Basin (e.g., Fig. 4.1) are unconformably overlain by late Oligocene to middle Miocene conglomerates (Amogu Conglomerate) and limestones (Puwani Limestone) (Norvick and Hutchison, 1980; Hutchinson and Norvick, 1980; Wilson *et al*., 1993).

(2) Map relationships around the Sepik Terrane suture zone suggest that deformed and metamorphosed Late Cretaceous to Eocene rocks (Salumei Formation) are overlain by significantly less deformed late Oligocene fine-grained micritic limestones (Kera Formation; Davies, 1983).

(3) Oligocene K-Ar and Rb-Sr ages of metamorphic minerals in the Ambunti Metamorphics just north of the April Ultramafics (Page, 1976).

(4) A major phase of Oligocene sinistral strike-slip faulting and fault reactivation limited to the northwest of the Bosavi Lineament on the Fly Platform (e.g., Kawagle and Meyers, 1996; McConachie and Lanzilli, 2000; McConachie *et al*., 2000).

(5) The short-lived deposition of coarse-grained clastics across the Stable Platform in the Oligocene, including the Stanley Sandstone on the western Fly Platform and Sirga Formation in western New Guinea (e.g., McConachie and Lanzilli, 2000; McConachie *et al*., 2000).

Interestingly, there is very little evidence of Eocene to Oligocene collision in the fold belt, even directly adjacent to the suspected Sepik Terrane suture zone delineated by the April Ultramafics (Fig. 4.1a).

The unconformity observed across the frontal PFTB and Fly Platform becomes much more widespread in the Oligocene, coincident with one of the largest eustatic sea level falls in the Cenozoic (e.g., Haq *et al*., 1987; 2014). At this time, the unconformity extended into basinward areas (e.g., Hill *et al*., 2000) and across most

of western and central New Guinea (as discussed in detail by van Ufford and Cloos, 2005).

4.2.3. Middle Oligocene to early Miocene

The Aure Trough (Fig. 4.1b) contains the oldest syn-orogenic sediments on the margin (ca. 32 Ma; Edwards, 1950; Brown *et al*., 1975), interpreted to relate to the collision of the Papuan Peninsula (e.g., Davies *et al*., 1997). Many authors suggest an earlier or synchronous collision of the Sepik Terrane (Fig. 4.1a) along the northern margin (e.g., Pigram and Davies, 1987; Hall, 2012; Schellart and Sparkman, 2015; amongst others), however this collision is less clearly recorded in the stratigraphic record and remains controversial.

Nevertheless, subsequent middle Oligocene to early Miocene subsidence of the PNG margin accommodated the deposition of up to 2,000 m of the widespread Darai Limestone in shelfal areas and basinal equivalents of the Nipa Group to the north (Fig. 4.1c; e.g., Pigram and Symonds, 1991). Many structures across the Stable Platform from the Indonesian border to the Gulf of Papua (Fig. 4.1) were either reactivated or initiated in the middle to late Oligocene, with reverse and normal offset observed in reflection seismic data leading to interpretations of a largely sinistral strike-slip structural setting (e.g., Kawagle and Meyers, 1996; McConachie and Lanzilli, 2000; McConachie *et al*., 2000). Significant Darai Limestone growth observed across structures on the Fly Platform (e.g., Schofield, 2000; Hill *et al*., 2010) has led to suggestions that northwest-southeast oriented faulting acted as a regional hinge producing a middle to late Oligocene graben to the north (McConachie and Lanzilli, 2000).

4.2.4. Middle-late Miocene to recent

The New Guinea margin experienced a significant phase of arc-continent collision and mountain building from the middle-late Miocene to recent. Middle to late Miocene (ca. 12 Ma) compressional deformation is interpreted from

thermochronology data across the Mobile Belt (e.g., Hill and Raza, 1999), coincident with the initial influx of syn-orogenic flysch into the fold belt (e.g., Thornton *et al*., 1996). The PFTB may have been undergoing compressional deformation by 5-4 Ma (Hill and Gleadow, 1989), approximately synchronous with a transition to thick molasse syn-orogenic sedimentation in a number of foreland depocentres (Fig. 4.1). The nature and extent of syn-orogenic sediments is complex (e.g., Jones, 1991; Thornton *et al*., 1996) and particularly poorly known across uplifted and eroded areas of the PFTB, such as in the Muller Range (Fig. 4.1b and c).

The dominant orientation for compression-related structures throughout the PFTB reflects northeast-southwest compression, with an increasingly large sinistral strike-slip component recognised northwards in the Mobile Belt (e.g., Pigott *et al*., 1985; Crowhurst *et al*., 1997), related to east-west compressive stresses from the ongoing collision with the Finisterre Terrane (Fig. 4.1a; Hill and Raza, 1999). On the Stable Platform, Pliocene to Pleistocene inversion is observed along structures to the east of the Bosavi Lineament, but not from the Bosavi Lineament to the Indonesian border (McConachie and Lanzilli, 2000).

Prominent stratovolcanoes and associated intrusions throughout PNG are, in general, poorly understood. Potassium argon (K-Ar) data suggests that volcanism in the Mobile Belt had begun by at least the middle Miocene (Page, 1976). However, the majority of the prominent stratovolcanoes and associated intrusions within the PFTB and on the Fly Platform formed during the Pliocene to Pleistocene with an overall younging trend towards the south (Webb, 1973; Loffler *et al*., 1979). Significant stratovolcanoes between the KFTB and WFTB, and associated flows up to 2,000 m thick within the Tari Basin, appear to have amassed along the regionally significant northeast-trending Bosavi Lineament (Fig. 4.1b). To the west, the Muller Range and adjacent areas commonly contain Pliocene to Pleistocene intrusions (e.g., Davies and Norvick, 1974).

4.3. Sample acquisition and methodology

Approximately 20 sedimentary samples were collected for low-temperature thermochronology analyses from the Muller Range during the Greater Juha and Pynang-Blucher geological surveys (2014-2016) (e.g., Mahoney *et al*, 2017). Apatite and zircon mineral separation was performed using conventional rock crushing, sieving and heavy mineral concentration techniques (shaking table, magnetic, heavy liquid, and methylene iodide centrifuge). Papuan Basin sediments have notoriously low yields (e.g., Hill and Gleadow, 1989; 1990), yet sufficiently large samples are difficult to obtain from remote areas of the PFTB. A single basement sample, originally collected by Davies and Norvick (1974) in the Strickland Gorge, was also obtained from the Mineral Resources Authority (MRA) in Port Moresby. This is the only known basement outcrop in the region. Apatite and/or zircon concentrates from four samples, originally used for AFT analysis (Hill and Gleadow, 1990), were also recovered from The University of Melbourne archives.

Although sampling along a vertical profile is optimal for thermochronological studies, such transects were not possible within the Greater Juha area due to a lack of outcrop, inhospitable terrain, intense karstification and thick vegetation. To enhance the resolution of our thermal models, we combine our new AFT, apatite (U-Th-Sm)/He and zircon (U-Th)/He data with existing AFT data published in Hill and Gleadow (1989; 1990). Thermal modelling approaches have advanced significantly since these data were obtained and much more information can now be extracted.

4.3.1. Low-temperature thermochronology

Here, we summarise the low-temperature thermochronology methods utilised in this study, including the apatite fission track (AFT) and (U-Th)/He techniques. Additional methodological details can be found in Supplementary Material A4. All analyses were performed at The University of Melbourne following the method of Gleadow *et al*. (2015).

AFT thermochronology relies on the production and retention of thermally sensitive linear damage traces, or fission tracks, from the spontaneous fission of ^{238}U (e.g., Gleadow *et al*., 2002). Over geological timescales fission tracks are generally considered to be stable at temperatures below ~ 50-60°C, to undergo rapid complete annealing above ~ 110-120°C and to progressively shorten at temperatures in-between, within what is known as the partial annealing zone (PAZ) (Gleadow and Duddy, 1981). The annealing characteristics of fission tracks are known to be a function of both time and temperature (e.g., Laslett *et al*., 1987; Ketcham *et al*., 2007) and thus combining track lengths and AFT age permits thermal history reconstruction of a sample within the PAZ (e.g., Gallagher, 1995; Ketcham, 2005). Where possible, apatite compositional variations such as chlorine content, or a compositional proxy such as Dpar, should be measured, as the annealing behaviour of fission tracks varies significantly depending on composition (e.g., Green *et al*., 1986; Barbarand *et al*., 2003). Reviews of the AFT technique are provided by Gleadow *et al*. (2002) and Donelick *et al*., (2005).

(U-Th-Sm)/He thermochronology relies on the production and thermally sensitive retention of ^{4}He during the radiogenic decay of ^{238}U, ^{235}U, ^{232}Th and ^{147}Sm (e.g., Farley, 2002). Comprehensive reviews of apatite and zircon (U-Th-Sm)/He methodologies can be found in Farley (2002), Farley and Stockli (2002) and Reiners *et al*., (2005).

^{4}He diffusivity is a function of time, temperature, crystal size and accumulated radiation damage (e.g., Farley, 2000; Reiners and Farley, 2001, Shuster *et al*., 2006). Over geological timescales, ^{4}He is partially retained at temperatures between ~ 40°C and ~ 80°C in apatite, and between ~ 130-210°C in zircon, with the upper threshold of this partial retention zone (PRZ) representing the temperature above which ^{4}He is nearly instantaneously lost (e.g., Farley, 2002; Wolfe and Stockli, 2010). However, our understanding of the complex interplay of factors influencing helium retentivity is still developing, with grain size, grain breakage, parent isotope

zonation, U- and/or Th-rich inclusions and α-radiation damage likely to represent some of the primary influences on natural age dispersion (standard deviation of age/mean age), which can exceed 200% (e.g., Wildman *et al*., 2016). As a result, data interpretation and thermal history modelling of He data relies on close consideration of these influences, while the sample-averaged (U-Th-Sm)/He age is often difficult to interpret. Grain geometries are directly measured in our analyses, while models for the influence of α-radiation damage on the effective diffusivity of He are parameterised using the proxy effective uranium concentration (eU = U + 0.235*Th ppm). Additional information regarding the factors that cause age dispersion in apatite (U-Th-Sm)/He (AHe) datasets (also relevant to Zircon (U-Th)/He (ZHe) data) can be found in Fitzgerald *et al*., (2006), Wildman *et al*., (2016) and Danišík *et al*., (2017).

4.4. Results

Only nine of the sedimentary samples collected yielded sufficient apatite and/or zircon grains for analysis. Apatite and zircon were particularly sparse in sedimentary samples, with fine- to medium-grained argillaceous sandstones generally providing the best yields. The single basement sample from the Strickland Gorge and all four Lavani-1 well samples recovered from The University of Melbourne archives had sufficient apatite or zircon for analysis. The location and lithological description of samples that provided datable yields is provided in Table 4.1.

Three samples were newly analysed using the AFT technique, seven samples using the apatite (U-Th-Sm)/He technique, and 12 samples using the zircon (U-Th)/He technique (Table 4.1). The new AFT, AHe and ZHe analytical data are listed in Tables 4.2-4.4 and summarised below.

Table 4.1. *Sample descriptions (circle = existing data - see Supplementary Material B4; tick = new data/modelling).*

Region / Sample No.	Longitude	Latitude	Sample type	Metres below base Darai	Elevation Metres AMSL	Formation (member)	Lithology	Geological survey	Analysis AHe	AFT	ZrHe	QTQt
WMR												
R34832	141.920	-5.330	Surface	120	1,345	Ieru Fm (Haito Mbr)	Fine-grained argillaceous sst	Fly-Palmer (White *et al.* 1973)		o		✓
R34831	141.914	-5.353	Surface	718	1,000	Ieru Fm (Giero Mbr)	Fine-grained sst	Fly-Palmer (White *et al.* 1973)		o		✓
PY110-2171	141.726	-5.497	Surface	1,064	802	Ieru Fm	Fine- to medium-grained sst	P'nyang-Blucher 2016	✓	✓	✓	✓
Strick North												
R34809	142.147	-5.364	Surface	131	530	Ieru Fm	Sst (90% quartz)	Strickland River (Jenkins and White, 1970)		o		✓
R34810	142.146	-5.370	Surface	424	520	Ieru Fm	Fine-grained sst	Strickland River (Jenkins and White, 1970)		o		✓
R34811	142.138	-5.416	Surface	1,079	900	Toro SST	Fine-grained sst	Strickland River (Jenkins and White, 1970)		o		✓
R34808	142.095	-5.392	Surface	2,300	300	Basement	Quartz orthoclase biotite granite	Blucher Range (Davies and Norvick, 1974)	✓	o	✓	✓
Strick South												
R34835	141.985	-5.578	Surface	690	290	Ieru Fm (Giero Mbr)	Fine-grained argillaceous sst	Fly-Palmer (White *et al.* 1973)		o		✓
PY113-1863	141.946	-5.561	Surface	650	435	Ieru Fm	Fine-grained argillaceous sst	P'nyang-Blucher 2016	✓			
PY113-1893	141.966	-5.565	Surface	906	327	Ieru Fm	Fine-grained siltst	P'nyang-Blucher 2016	✓		✓	
PY113-1929.5	141.967	-5.560	Surface	1,028	324	Ieru Fm	Fine-grained sst	P'nyang-Blucher 2016	✓	✓	✓	✓
PY113-1977.5	141.970	-5.554	Surface	1,080	535	Ieru Fm	Fine-grained argillaceous sst	P'nyang-Blucher 2016	✓		✓	
PY113-1998.5	141.971	-5.552	Surface	1,308	624	Toro SST	Fine- to medium-grained sst	P'nyang-Blucher 2016			✓	
R34833	142.004	-5.548	Surface	1,830	800	Koi Iange	Fine-grained sst	Fly-Palmer (White *et al.* 1973)		o		✓
Lavani												
R34854	142.522	-5.767	Surface	120	2,880	Ieru Fm (Haito Mbr)	Fine-grained argillaceous sst	Lavani Anticline (Findlay and Leckie, 1973)		o		✓
GJLAV-1	142.566	-5.791	Surface	500	2,582	Ieru Fm (Giero Mbr)	Medium-grained argillaceous sst	Greater Juha (Mahoney *et al* . 2017)			✓	✓
GJLAV-4	142.570	-5.789	Surface	1,414	2,673	Toro SST	Medium-grained sst	Greater Juha (Mahoney *et al* . 2017)	✓		✓	✓
GJLAV-7	142.570	-5.789	Surface	1,423	2,682	Toro SST	Medium-grained sst	Greater Juha (Mahoney *et al* . 2017)			✓	✓
R34899	142.568	-5.775	Cuttings	2,377	1,728	Koi Iange/Magobu	Fine- to medium-grained sst	Lavani-1 well			✓	✓
R34900	142.568	-5.775	Cuttings	3,055	1,050	Koi Iange/Magobu	Fine- to medium-grained sst	Lavani-1 well			✓	✓
R34901	142.564	-5.769	Cuttings	3,686	431	Magobu	Fine-grained sst	Lavani-1 well		✓		✓
R34902	142.568	-5.775	Cuttings	4,386	-299	Magobu Fm	Medium- to coarse-grained sst	Lavani-1 well		o	✓	✓

4.4.1. Apatite fission track (AFT) results

Ieru Formation samples PY110-2171 and PY113-1929.5 are laterally ~ 25 km apart, share a similar structural context on the southern limb of the Muller Anticline and are sampled from similar stratigraphic levels approximately 1,000 m below the base of the Darai Limestone (e.g., Fig. 4.2). Central AFT ages of 76.5 ± 4.1 Ma and 83.1 ± 5.7 Ma from PY110-2171 and PY113-1929.5 are within analytical error (Table 4.2). The confined mean track lengths (MTLs) are 11.4 ± 0.2 μm and 11.0 ± 0.2 μm, respectively. The standard deviation ranges from 1.8 μm to 2.0 μm and Dpars of ~ 1.78-1.85 μm are within analytical error. Both samples fail the chi-squared test for age homogeneity, thus necessitating further investigation prior to thermal modelling (discussed in Section 4.5.1).

Hill and Gleadow (1989; 1990) collected AFT data from six Ieru Formation samples throughout the Muller Range, with central ages ranging from 45.6 Ma to

79.8 Ma, MTLs ranging from 10.3 μm to 12.1 μm and standard deviations from 1.8 μm to 2.6 μm (Fig. 4.2, Supplementary Material B4). AFT ages for new and existing data from the Muller Range fall between 45.6 Ma and 83.1 Ma and are characterised by short to moderate MTLs (< 12.1 μm), low to moderate standard deviations (< 2.6 μm) and generally negatively skewed length distributions.

Reanalysis of Magobu Formation sample R34901 returned a central age of 10.7 ± 3.1 Ma, which is within analytical error of a central age of 9.9 ± 4.4 Ma calculated from Hill and Gleadow's (1990) original data following the updated formulae given in Galbraith (2005). The sparsity of track lengths in both analyses precludes the calculation of a statistically significant MTL and standard deviation. Hill and Gleadow (1990) collected AFT data from several sub-Ieru Formation stratigraphic samples, all returning middle-late Miocene to Pliocene central ages (3.8-12.4 Ma) with significant variations in mean track lengths ranging from 9.5-14.2 μm (Supplementary Material B4).

Table 4.2. *Muller Range apatite fission track (ICP-MS) data summary*

Region	Formation	No. of grains	N_S	ρ_s	^{238}U	Dpar	Dispersion	Chi-squared probability	Pooled age	[a]Central age	N_L	MTL	SD
Sample No.				x10^{6}cm^{-2}	(ppm)	(μm)	(%)	(%)	(Ma ± 1σ)	(Ma ± 1σ)		(μm ± SE)	(μm)
WMR													
PY110-2171	Ieru Fm	55	1000	0.359	9.47	1.85	27	<1	76.0 ± 4.2	76.5 ± 4.1	108	11.4 ± 0.2	1.8
Strick South													
PY113-1929.5	Ieru Fm	31	472	0.373	8.03	1.78	23	<1	85.8 ± 5.8	83.1 ± 5.7	99	11.0 ± 0.2	2.0
Lavani													
R34901	Magobu Fm	40	55	0.059	21.81	1.31	100	<1	5.4 ± 6.7	10.7 ± 3.1	-	-	-

[a] Central ages calculated following Galbraith (2005)

4.4.2. Apatite (U-Th-Sm)/He (AHe) results

AHe data for 45 grains across seven samples are detailed in Table 4.3. Single grain ages for sedimentary samples (n=33) range from ~ 1 Ma to 68 Ma, with ~ 70% of ages < 10 Ma. Intrasample age dispersion is large. The Strickland Gorge basement sample R34808 yielded AHe ages (n=11) with significantly less dispersion ranging from ~ 1 to 4 Ma, with only one pre-Pleistocene (> 2.5 Ma) age. eU concentrations range from

3 to 86 ppm for sedimentary samples and 12 to 49 ppm for the basement sample. Neither eU concentration nor grain size show a significant correlation with AHe age (Supplementary Material C4, Figs. C4.1 and C4.2).

Table 4.3. *Muller Range apatite (U-Th-Sm)/He data summary*

Region	Formation	Lab. No.	^{4}He	Mass	[a]Mean FT	U	Th	Sm	Th/U ratio	[b][eU]	Uncorrected Age	Age	Grain length	Grain half-width	[c]Rs	[d]MWAR	[e]SD	[f]Grain morphology
Sample No.			(ncc)	(mg)		(ppm)	(ppm)	(ppm)		(ppm)	(Ma ±1σ)	(Ma ±1σ)	(μm)	(μm)	(μm)			
WMR																		
PY110-2171		13803	0.035	0.0225	0.83	1.9	10.5	96.3	5.54	4.4	2.8 ± 0.2	**3.4 ± 0.2**	307.7	93.8	107.9	-	-	2T
PY110-2171		13805	0.185	0.0091	0.77	0.9	9.5	68.8	11.09	3.1	52.3 ± 3.1	***68.3 ± 4.2**	247.6	66.6	78.7	-	-	2T
PY110-2171		13960	0.165	0.0257	0.81	4.2	24.1	127.1	5.78	9.9	5.3 ± 0.3	**6.5 ± 0.4**	203.5	-	-	79.1	2.7	0T, 0T
PY110-2171		13961	0.065	0.0211	0.78	3.1	18.1	85.7	5.80	7.4	3.4 ± 0.2	**4.3 ± 0.3**	270.5	-	-	62.3	3.0	0T, 0T
PY110-2171	Ieru Fm	13962	0.070	0.0151	0.78	5.3	19.7	189.1	3.73	9.9	3.8 ± 0.2	**4.8 ± 0.3**	276.7	-	-	62.0	1.4	1T, 1T
PY110-2171		14058	0.044	0.0159	0.79	6.3	25.3	140.4	4.03	12.2	1.8 ± 0.1	**2.3 ± 0.1**	215.0	-	-	67.4	5.0	1T, 0T
PY110-2171		14059	0.045	0.0096	0.74	15.9	54.2	212.1	3.42	28.6	1.3 ± 0.1	**1.8 ± 0.1**	188.3	-	-	59.1	5.3	2T, 1T
PY110-2171		14281	0.062	0.0149	0.75	1.6	11.3	81.8	7.25	4.3	7.9 ± 0.5	***10.5 ± 0.7**	313.5	-	-	57.0	1.5	1T, 1T
PY110-2171		14282	0.053	0.0161	0.78	5.8	28.4	145.2	4.87	12.5	2.1 ± 0.1	**2.8 ± 0.2**	217.7	-	-	70.1	1.6	1T, 2T
PY110-2171		14283	0.086	0.0138	0.77	4.3	18.7	165.2	4.40	8.7	5.7 ± 0.3	**7.5 ± 0.5**	225.2	-	-	65.0	9.3	1T, 2T
Strick North																		
R34808		11612	0.054	0.0071	0.74	13.5	30.3	57.3	2.23	20.6	3.0 ± 0.2	**4.1 ± 0.3**	376.4	49.9	66.1	-	-	1T
R34808		11613	0.032	0.0051	0.72	25.6	33.7	113.0	1.32	33.5	1.5 ± 0.1	**2.1 ± 0.1**	227.0	52.2	63.7	-	-	2T
R34808		11614	0.039	0.0048	0.69	25.3	60.7	93.9	2.39	39.6	1.7 ± 0.1	**2.4 ± 0.1**	276.7	45.9	59.0	-	-	2T
R34808		11615	0.044	0.0068	0.75	22.9	52.0	101.1	2.28	35.1	1.5 ± 0.1	**2.0 ± 0.1**	245.5	57.9	70.3	-	-	2T
R34808		11616	0.025	0.0035	0.72	33.2	69.1	122.6	2.08	49.4	1.2 ± 0.1	**1.7 ± 0.1**	201.5	49.9	60.0	-	-	1T
R34808	Basement	11686	0.046	0.0116	0.82	22.7	26.0	75.1	1.15	28.8	1.1 ± 0.1	**1.4 ± 0.1**	300.9	74.5	89.6	-	-	1T
R34808		11687	0.028	0.0078	0.79	20.2	24.8	72.8	1.23	26.0	1.1 ± 0.1	**1.4 ± 0.1**	154.0	70.9	72.8	-	-	0T
R34808		11688	0.031	0.0053	0.76	24.2	61.0	118.7	2.52	38.5	1.3 ± 0.1	**1.6 ± 0.1**	208.8	61.5	71.3	-	-	1T
R34808		11689	0.040	0.0201	0.84	11.9	36.6	100.2	3.08	20.5	0.8 ± 0.0	**0.9 ± 0.1**	347.6	91.8	109.0	-	-	1T
R34808		11690	0.026	0.0075	0.79	22.1	42.2	108.9	1.91	32.0	0.9 ± 0.1	**1.1 ± 0.1**	250.7	66.2	78.6	-	-	1T
R34808		11691	0.021	0.0108	0.79	7.7	18.4	81.6	2.38	12.0	1.3 ± 0.1	**1.7 ± 0.1**	289.1	60.9	75.5	-	-	0T
Strick South																		
PY 113-1863.0		13793	0.069	0.0033	0.68	5.8	19.5	170.8	3.35	10.4	15.9 ± **1.0**	**23.3 ± 1.4**	169.1	48.8	56.8	-	-	2T
PY 113-1863.0		13795	0.104	0.0024	0.72	49.0	37.1	382.9	0.76	57.7	6.0 ± **0.4**	**8.4 ± 0.5**	144.6	51.7	57.1	-	-	1T
PY 113-1863.0	Ieru Fm	13796	0.032	0.0018	0.67	42.4	72.6	378.5	1.71	59.5	2.4 ± **0.1**	**3.5 ± 0.2**	137.4	45.5	51.2	-	-	1T
PY 113-1863.0		13958	0.113	0.0034	0.72	66.1	82.7	157.3	1.25	85.5	3.2 ± **0.2**	**4.5 ± 0.3**	90.8	60.7	54.6	-	-	0T
PY 113-1863.0		13959	0.024	0.0057	0.75	6.9	6.8	27.4	0.99	8.5	4.1 ± **0.3**	**5.5 ± 0.3**	204.5	52.6	62.7	-	-	0T
PY 113-1863.0		14060	0.155	0.0079	0.72	8.6	23.8	94.6	2.76	14.2	11.2 ± **0.7**	**15.6 ± 1.0**	188.9	-	-	50.9	10.0	1T, 0T
PY 113-1893.0		13808	0.378	0.0161	0.83	20.6	20.3	112.3	0.98	25.4	7.6 ± 0.5	**9.1 ± 0.6**	203.0	88.8	92.7	-	-	0T
PY 113-1893.0		13963	0.043	0.0032	0.70	26.6	100.0	353.9	3.76	50.1	2.2 ± 0.1	**3.1 ± 0.2**	212.7	-	-	46.1	0.5	2T, 2T
PY 113-1893.0	Ieru Fm	13964	0.069	0.0076	0.73	3.6	19.7	238.1	5.49	8.2	8.7 ± 0.5	**12.0 ± 0.7**	152.7	-	-	52.7	13.6	1T, 0T
PY 113-1893.0		13965	0.242	0.0086	0.78	2.8	12.6	102.7	4.44	5.8	38.9 ± 2.4	**49.6 ± 3.1**	173.7	70.2	75.0	-	-	0T
PY 113-1893.0		14061	0.032	0.0120	0.76	2.8	17.2	108.6	6.22	6.8	3.1 ± 0.2	**4.1 ± 0.3**	165.2	-	-	60.2	5.8	0T, 1T
PY113-1929.5		13837	0.117	0.0058	0.73	2.3	10.4	84.7	4.62	4.7	34.2 ± 2.0	**46.9 ± 2.9**	263.7	46.9	59.7	-	-	0T
PY113-1929.5		13838	0.028	0.0042	0.71	2.2	10.3	121.2	4.63	4.6	11.4 ± 0.7	**16.0 ± 1.0**	147.1	58.7	62.9	-	-	2T
PY113-1929.5		13840	0.079	0.0048	0.73	4.8	18.9	228.3	3.98	9.2	14.1 ± 0.8	**19.4 ± 1.2**	162.8	59.8	65.6	-	-	2T
PY113-1929.5		13841	0.044	0.0021	0.61	4.3	16.2	138.3	3.74	8.1	20.5 ± 1.2	**33.5 ± 2.1**	175.9	38.1	47.0	-	-	2T
PY113-1929.5	Ieru Fm	13966	0.031	0.0156	0.78	1.5	6.6	80.3	4.35	3.1	5.3 ± 0.3	**6.8 ± 0.4**	199.2	-	-	62.6	2.0	0T, OT
PY113-1929.5		14063	0.088	0.0098	0.76	7.3	25.9	335.4	3.56	13.4	5.3 ± 0.3	**7.0 ± 0.4**	200.9	-	-	59.7	10.3	1T, 1T
PY113-1929.5		14062	0.058	0.0152	0.76	2.4	10.0	126.5	4.18	4.8	6.3 ± 0.4	**8.3 ± 0.5**	236.5	-	-	60.1	1.8	0T, 2T
PY113-1929.5		14285	0.359	0.0124	0.78	36.0	3.7	135.1	0.10	36.9	6.4 ± 0.4	**8.3 ± 0.5**	195.8	-	-	56.2	1.5	0T, 0T
PY113-1929.5		14286	0.017	0.0080	0.73	1.6	6.8	115.5	4.20	3.2	5.2 ± 0.3	**7.2 ± 0.4**	153.3	-	-	56.9	2.2	0T, 1T
PY 113-1977.5	Ieru Fm	14456	0.094	0.0204	0.85	10.7	9.5	26.5	0.89	12.9	2.9 ± 0.2	**3.5 ± 0.2**	253.6	178.9	157.3	89.4	-	0T
Lavani																		
GJLAV-4		12243	0.026	0.0075	0.77	2.0	9.9	211.3	4.90	4.3	6.1 ± 0.4	**7.9 ± 0.5**	174.7	65.4	71.4	-	-	0T
GJLAV-4	Toro SST	12244	0.039	0.0045	0.74	6.5	36.6	230.5	5.65	15.1	4.6 ± 0.3	**6.2 ± 0.4**	208.1	56.6	66.7	-	-	1T
GJLAV-4		12246	0.032	0.0020	0.65	13.8	49.5	242.0	3.59	25.4	5.2 ± 0.3	**8.0 ± 0.5**	175.0	40.3	49.2	-	-	1T
Durango		13772	6.959	-	1.00	-	-	-	20.43	-	- - -	**31.0 ± 1.9**	-	-	-	-	-	-
Durango		14108	3.665	-	1.00	-	-	-	21.89	-	- - -	**31.2 ± 1.9**	-	-	-	-	-	-
Durango		14466	6.379	-	1.00	-	-	-	22.86	-	- - -	**31.7 ± 2.0**	-	-	-	-	-	-

[a] F_T is the α-ejection correction after Farley et al. (1996) calculated using mass-weighted radius.
[b] Effective uranium content [U ppm + 0.235*Th ppm].
[c] Rs = (3*(grain length)*(grain half-width)/(2*(grain length + grain half-width))
[d] MWAR is the mass-weighted average radius of apatite crystals analysed.
[e] Standard deviation of the MWAR is used as a guide for the 'tightness' of the range of single crystal radii picked within a sample.
[f] Grain morphology - 0T = no crystal terminations, 1T = one crystal termination and 2T = 2 crystal terminations.
*Analysis is problematic.

4.4.3. Zircon (U-Th)/He (ZHe) results

ZHe data for 65 grains across 12 samples are detailed in Table 4.4. These analyses provide good coverage of the stratigraphic column: five samples from the Ieru Formation, three from the Toro Sandstone, three from the Koi Iange/Magobu formations and a single basement sample. Across all samples ~ 97% of single grain ages fall between 1-250 Ma. Negative ZHe vs eU correlations generally increase with stratigraphic age, from absent in the Ieru Formation samples to strong in the basement sample (Fig. 4.3 and Supplementary Material C4, Fig. C4.3), suggesting α-radiation damage is a major control on the age dispersion observed within the Koi Iange/Magobu formations and basement samples. Samples show variably weak to strong relationships between grain size and ZHe age (Supplementary Material C4, Fig. C4.4).

Ieru Formation sample PY113-1977.5 was an outlier returning mostly anomalously young single grain ages (n=5), potentially related to a local influence such as volcanic activity, warm fluid circulation or another unknown factor leading to enhanced He loss. Consequently, this sample is excluded from further examination. Other single grain analyses on Ieru Formation samples PY110-2171, PY113-1893, PY113-1929.5 and GJLAV-1 (combined n=20) from the middle to lower Ieru Formation yielded ages of 66-422 Ma, with 80% of ages between ~ 66-122 Ma and 20% of ages > 169 Ma (Fig. 4.3a). eU contents vary significantly from 96-614 ppm, but show no clear correlation with age (Fig. 4.3a).

Toro Sandstone samples GJLAV-4, GJLAV-7 and PY113-1998.5 (combined n=14) yielded significantly older ZHe ages of 129-291 Ma, with > 50% of ages between 200-250 Ma (Fig. 4.3b). eU contents vary significantly from 213-751 ppm, but again show no significant correlation with age (Fig. 4.3b).

Koi Iange and Magobu formation samples R34899, R34900 and R34901 (combined n=18) from the Lavani-1 well showed significant variation in single grain ages from 1-246 Ma and eU contents from 76-2959 ppm. There is a strong negative correlation between eU concentration and age (Fig. 4.3c), with the oldest age (~ 246 Ma) showing the least accumulated radiation damage (eU=76 ppm) and the youngest age (~ 1 Ma) showing the most (eU=2959 ppm) with almost complete loss of helium retentivity.

Single grain ages from Strickland Gorge basement sample R34808 (n=8) show high dispersion from 32-187 Ma. However, eU content is also highly variable, ranging from 268-929 ppm, with a very strong negative ZHe vs eU correlation (Fig. 4.3d).

4.5. Thermal history reconstruction

The software QTQt (Gallagher, 2012) was used to perform both forward and inversion modelling to reconstruct thermal histories from new and existing low-temperature thermochronology data. Initially, the AFT dataset was explored using forward modelling, with a focus on investigating the importance of pre-depositional thermal histories of apatite grains within the Ieru Formation. The thermal history of the Muller Range was then further evaluated through inversion of AFT data and the joint-inversion of AFT, AHe and ZHe data in a series of vertical profiles.

Table 4.4. *Muller Range zircon (U-Th)/He data summary*

Region / Sample No.	Formation	Lab. No.	^{4}He (ncc)	Mass (mg)	[a]Mean FT	U (ppm)	Th (ppm)	Th/U ratio	[b][eU] (ppm)	Uncorrected Age (Ma ±1σ)	Age (Ma ±1σ)	Grain length (μm)	Grain half-width (μm)	[c]Rs (μm)	[d]Grain morphology
WMR															
PY110-2171		13798	21.420	0.0066	0.78	237.8	77.4	0.33	256.0	80.7 ± 5.0	**103.4 ± 6.4**	240.8	45.0	56.8	2T
PY110-2171		13799	10.342	0.0071	0.77	100.0	108.0	1.08	125.3	73.2 ± 4.5	**95.0 ± 5.9**	251.0	45.4	57.7	2T
PY110-2171	Ieru Fm	13800	5.367	0.0033	0.74	123.9	92.8	0.75	145.7	67.2 ± 4.2	**90.8 ± 5.6**	162.4	41.9	49.9	2T
PY110-2171		13801	23.992	0.0062	0.77	114.7	43.5	0.38	124.9	191.9 ± 11.9	**249.2 ± 15.4**	236.2	44.0	55.6	2T
PY110-2171		13802	13.269	0.0050	0.75	191.3	95.6	0.50	213.7	76.1 ± 4.7	**101.4 ± 6.3**	221.8	40.6	51.5	2T
Strick North															
R34808		11372	36.385	0.0066	0.78	365.7	221.4	0.61	417.7	83.3 ± 5.2	**107.5 ± 6.7**	240.0	22.6	30.9	2T
R34808		11373	27.998	0.0077	0.76	715.2	907.4	1.27	928.5	24.4 ± 1.5	**32.1 ± 2.0**	312.8	20.2	28.4	2T
R34808		11374	41.884	0.0068	0.76	524.7	628.0	1.20	672.3	56.6 ± 3.5	**74.7 ± 4.6**	283.5	20.2	28.3	2T
R34808	Basement	11375	46.980	0.0078	0.79	515.8	187.3	0.36	559.8	68.9 ± 4.3	**87.4 ± 5.4**	257.9	23.6	32.4	2T
R34808		11376	40.949	0.0067	0.77	236.4	157.6	0.67	273.4	140.5 ± 8.7	**182.0 ± 11.3**	248.1	22.1	30.4	2T
R34808		11575	26.463	0.0043	0.74	227.7	171.7	0.75	268.1	139.6 ± 8.6	**187.4 ± 11.6**	199.2	20.2	27.5	2T
R34808		11576	25.713	0.0039	0.75	298.2	199.8	0.67	345.1	115.8 ± 7.2	**154.3 ± 9.6**	169.7	22.5	29.8	2T
R34808		11577	29.564	0.0060	0.77	316.2	348.6	1.10	398.1	78.5 ± 4.9	**101.3 ± 6.3**	205.7	24.4	32.7	2T
Strick South															
PY 113-1893.0		13813	21.028	0.0092	0.77	140.1	51.6	0.37	152.2	94.4 ± 5.8	**122.3 ± 7.6**	363.9	80.4	98.8	2T
PY 113-1893.0		13814	9.220	0.0050	0.76	156.5	107.4	0.69	181.8	62.7 ± 3.9	**82.6 ± 5.1**	206.7	86.7	91.6	2T
PY 113-1893.0	Ieru Fm	13815	23.595	0.0036	0.72	94.9	116.4	1.23	122.3	304.0 ± 18.8	**422.0 ± 26.2**	201.9	72.2	79.8	2T
PY 113-1893.0		13816	21.105	0.0079	0.77	308.7	88.3	0.29	329.4	50.7 ± 3.1	**65.9 ± 4.1**	325.0	80.0	96.3	2T
PY 113-1893.0		13817	18.891	0.0046	0.75	303.6	200.5	0.66	350.8	71.9 ± 4.5	**95.9 ± 5.9**	207.2	81.6	87.8	2T
PY113-1929.5		13832	7.337	0.0073	0.79	81.9	60.3	0.74	96.1	67.4 ± 4.2	**85.9 ± 5.3**	234.7	48.8	60.6	2T
PY113-1929.5		13833	54.535	0.0081	0.80	483.1	556.6	1.15	613.9	71.3 ± 4.4	**89.5 ± 5.5**	222.3	55.4	66.6	2T
PY113-1929.5	Ieru Fm	13834	6.076	0.0045	0.76	116.8	83.0	0.71	136.3	61.8 ± 3.8	**81.7 ± 5.1**	185.3	44.6	53.9	2T
PY113-1929.5		13835	66.479	0.0064	0.77	307.6	154.4	0.50	343.9	187.8 ± 11.6	**243.4 ± 15.1**	243.7	43.6	55.5	2T
PY113-1929.5		13836	62.436	0.0104	0.80	389.0	113.3	0.29	415.6	94.8 ± 5.9	**117.7 ± 7.3**	292.6	50.5	64.6	2T
PY113-1977.5		13921	0.399	0.0050	0.76	103.6	80.7	0.78	122.6	4.0 ± 0.3	***5.4 ± 0.3**	215.5	83.3	90.1	2T
PY113-1977.5		13922	1.505	0.0044	0.74	548.1	276.4	0.50	613.0	3.4 ± 0.2	***4.6 ± 0.3**	216.6	76.4	84.8	2T
PY113-1977.5	Ieru Fm	13925	1.214	0.0030	0.73	694.5	131.9	0.19	725.5	3.3 ± 0.2	***4.6 ± 0.3**	150.7	85.6	81.9	2T
PY113-1977.5		14454	1.827	0.0109	0.78	535.2	168.4	0.31	574.8	1.9 ± 0.1	***2.4 ± 0.1**	398.0	83.2	103.2	2T
PY113-1977.5		14455	23.994	0.0053	0.74	405.4	183.1	0.45	448.4	61.7 ± 3.8	***83.1 ± 5.2**	231.7	80.9	89.9	2T
PY 113-1998.5		13818	50.236	0.0042	0.74	372.4	130.5	0.35	403.1	177.7 ± 11.0	**239.0 ± 14.8**	208.9	76.8	84.2	2T
PY 113-1998.5		13819	41.868	0.0076	0.79	317.3	114.4	0.36	344.2	102.6 ± 6.3	**129.4 ± 8.0**	239.2	99.2	105.2	2T
PY 113-1998.5	Toro SST	13820	53.064	0.0038	0.75	469.7	166.1	0.35	508.7	166.6 ± 10.3	**221.1 ± 13.7**	166.5	89.9	87.6	2T
PY 113-1998.5		13821	92.713	0.0054	0.77	389.8	338.9	0.87	469.4	224.2 ± 13.9	**291.3 ± 18.1**	198.4	95.1	96.4	2T
PY 113-1998.5		13822	72.889	0.0069	0.79	535.4	68.4	0.13	551.5	122.6 ± 7.6	**155.8 ± 9.7**	238.7	93.0	100.4	2T
Lavani															
GJLAV-1		12271	44.649	0.0091	0.80	218.9	65.8	0.30	234.3	135.2 ± 8.4	**169.5 ± 10.5**	276.0	24.4	33.7	2T
GJLAV-1		12272	17.397	0.0037	0.74	401.5	174.4	0.43	442.4	64.3 ± 4.0	**86.3 ± 5.4**	177.6	20.6	27.7	2T
GJLAV-1	Ieru Fm	12273	17.301	0.0042	0.75	389.6	380.3	0.98	479.0	53.0 ± 3.3	**71.0 ± 4.4**	185.6	21.2	28.6	2T
GJLAV-1		12274	37.205	0.0060	0.77	423.1	237.9	0.56	479.0	81.5 ± 5.0	**106.3 ± 6.6**	235.3	21.5	29.6	2T
GJLAV-1		12275	9.703	0.0043	0.75	196.5	120.6	0.61	224.8	61.7 ± 3.8	**82.4 ± 5.1**	194.6	20.7	28.0	2T
GJLAV-4		12248	78.120	0.0082	0.79	286.7	108.4	0.38	312.2	193.9 ± 12.0	**244.0 ± 15.1**	253.5	24.7	33.8	2T
GJLAV-4		12249	42.142	0.0046	0.75	280.8	118.0	0.42	308.5	178.5 ± 11.1	**238.8 ± 14.8**	219.2	19.5	26.9	2T
GJLAV-4	Toro SST	12250	57.667	0.0081	0.78	229.1	72.6	0.32	246.1	181.9 ± 11.3	**232.6 ± 14.4**	289.1	22.0	30.7	2T
GJLAV-4		12251	37.711	0.0063	0.76	237.6	130.0	0.55	268.1	137.3 ± 8.5	**180.7 ± 11.2**	269.1	20.0	28.0	2T
GJLAV-4		12252	101.335	0.0087	0.79	387.4	118.4	0.31	415.2	179.6 ± 11.1	**226.0 ± 14.0**	272.0	24.1	33.1	2T
GJLAV-7		12266	74.998	0.0093	0.80	236.2	154.6	0.65	272.5	190.8 ± 11.8	**238.0 ± 14.8**	256.4	26.4	35.9	2T
GJLAV-7	Toro SST	12267	177.538	0.0137	0.83	718.5	137.1	0.19	750.7	116.4 ± 7.2	**140.3 ± 8.7**	292.2	29.9	40.7	2T
GJLAV-7		12269	63.134	0.0105	0.81	182.3	131.8	0.72	213.2	185.5 ± 11.5	**228.1 ± 14.1**	248.8	29.3	39.4	2T
GJLAV-7		12475	66.918	0.0060	0.76	351.0	143.5	0.41	384.7	176.7 ± 10.9	**232.4 ± 14.4**	259.4	20.1	27.9	2T
R34899		13853	21.195	0.0034	0.73	211.3	152.9	0.72	247.3	150.6 ± 9.3	**204.5 ± 12.7**	172.5	39.9	48.6	2T
R34899		13854	13.786	0.0027	0.71	164.7	114.5	0.70	191.6	151.3 ± 9.4	**211.4 ± 13.1**	166.9	35.9	44.3	2T
R34899	Koi lange/Magobu Fm	13855	24.169	0.0040	0.75	409.8	283.4	0.69	476.4	77.8 ± 4.8	**104.1 ± 6.5**	183.1	41.8	51.0	2T
R34899		14073	1.029	0.0027	0.74	2865.0	397.8	0.14	2958.5	0.8 ± 0.0	**1.1 ± 0.1**	130.8	49.7	54.0	2T
R34899		14074	22.149	0.0039	0.76	330.2	32.7	0.10	337.9	102.9 ± 6.4	**135.7 ± 8.4**	181.2	41.9	51.0	2T
R34899		14075	6.753	0.0027	0.70	448.7	163.6	0.36	487.2	29.8 ± 1.8	**42.4 ± 2.6**	164.0	35.9	44.2	2T
R34900		13847	35.601	0.0065	0.78	192.0	167.6	0.87	231.4	148.8 ± 9.2	**191.5 ± 11.9**	224.6	47.4	58.7	2T
R34900	Koi lange/Magobu Fm	13848	38.540	0.0044	0.75	373.8	172.1	0.46	414.3	127.2 ± 7.9	**169.6 ± 10.5**	206.0	40.2	50.5	2T
R34900		13849	20.401	0.0077	0.80	109.7	23.3	0.21	115.2	148.1 ± 9.2	**185.8 ± 11.5**	235.5	50.6	62.5	2T
R34900		13850	25.188	0.0036	0.74	252.4	183.4	0.73	295.5	141.0 ± 8.7	**189.3 ± 11.7**	164.3	44.3	52.3	2T
R34900		13851	12.828	0.0014	0.66	374.8	289.2	0.77	442.7	110.7 ± 6.9	**166.8 ± 10.3**	109.9	36.5	41.1	2T
R34902		13842	15.685	0.0063	0.78	284.4	172.6	0.61	324.9	49.4 ± 3.1	**62.9 ± 3.9**	200.1	52.1	62.0	2T
R34902		13843	8.647	0.0039	0.75	419.5	333.9	0.80	498.0	27.3 ± 1.7	**36.5 ± 2.3**	168.6	45.2	53.4	2T
R34902		13845	11.585	0.0044	0.75	157.7	172.5	1.09	198.3	81.1 ± 5.0	**107.6 ± 6.7**	182.1	45.2	54.3	2T
R34902	Magobu Fm	13846	7.083	0.0033	0.74	224.4	168.5	0.75	264.0	49.6 ± 3.1	**67.4 ± 4.2**	158.0	42.7	50.4	2T
R34902		14070	9.739	0.0031	0.72	261.7	195.7	0.75	307.7	59.6 ± 3.7	**83.1 ± 5.1**	156.9	41.7	49.4	2T
R34902		14071	43.711	0.0082	0.82	420.9	19.7	0.05	425.5	83.9 ± 5.2	**102.7 ± 6.4**	215.7	57.7	68.2	2T
R34902		14072	9.642	0.0042	0.75	69.1	27.3	0.40	75.5	183.7 ± 11.4	**245.8 ± 15.2**	189.2	41.8	51.4	2T
Fish Canyon Tuff		13829	9.658	0.0077	0.79	317.2	165.2	0.52	356.0	22.8 ± 1.4	**29.0 ± 1.8**	249.7	95.8	103.8	2T
Fish Canyon Tuff		13830	9.499	0.0074	0.79	339.8	196.9	0.58	386.1	21.7 ± 1.3	**27.4 ± 1.7**	223.6	103.2	105.9	2T
Fish Canyon Tuff		14410	9.250	0.0074	0.78	324.4	173.0	0.53	365.0	22.1 ± 1.4	**28.2 ± 1.7**	248.3	93.9	102.2	2T
Fish Canyon Tuff		14412	5.908	0.0045	0.74	333.7	197.8	0.59	380.2	21.2 ± 1.3	**28.6 ± 1.8**	188.2	87.7	89.8	2T
Fish Canyon Tuff		14579	9.653	0.0064	0.78	391.1	185.9	0.48	434.8	22.0 ± 1.4	**28.4 ± 1.8**	233.2	90.9	98.1	2T

[a]F_T is the α-ejection correction after Farley et al. (1996).

[b]Effective uranium concentration (U ppm + 0.235 Th ppm).

[c]Rs = (3*(grain length)*(grain half-width)/(2*(grain length + grain half-width))

[d]Grain morphology - 0T = no terminations, 1T = one termination, 2T = 2 terminations.

*Analysis is problematic.

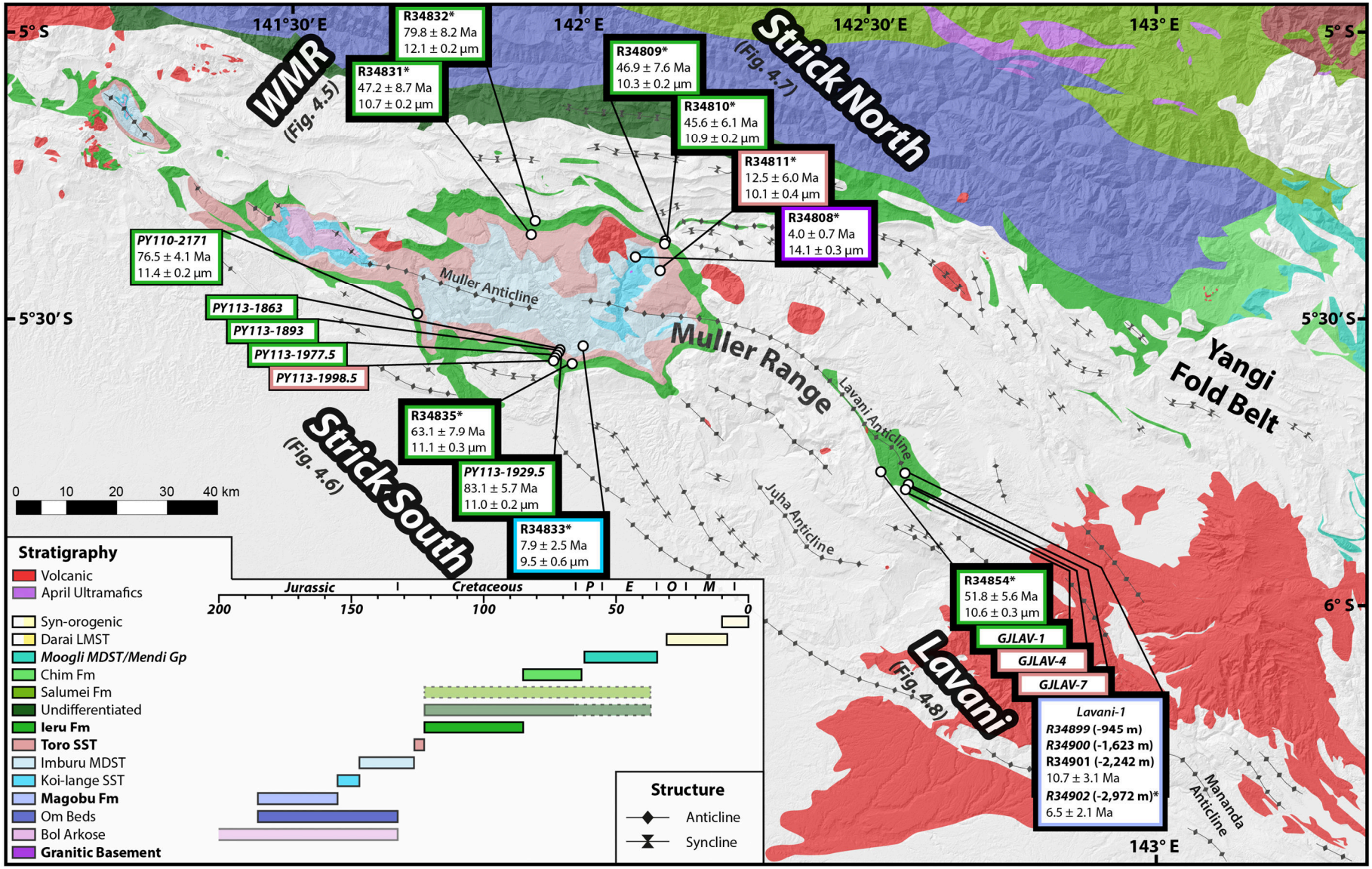
5° S
141°30′ E
142° E
142°30′ E
143° E
5°30′ S
6° S
WMR
(Fig. 4.5)
Strick North
(Fig. 4.7)
Strick South
(Fig. 4.6)
Lavani
(Fig. 4.8)
Muller Range
Yangi Fold Belt
Muller Anticline
Lavani Anticline
Juha Anticline
Mananda Anticline
R34832* 79.8 ± 8.2 Ma 12.1 ± 0.2 µm
R34831* 47.2 ± 8.7 Ma 10.7 ± 0.2 µm
R34809* 46.9 ± 7.6 Ma 10.3 ± 0.2 µm
R34810* 45.6 ± 6.1 Ma 10.9 ± 0.2 µm
R34811* 12.5 ± 6.0 Ma 10.1 ± 0.4 µm
R34808* 4.0 ± 0.7 Ma 14.1 ± 0.3 µm
PY110-2171 76.5 ± 4.1 Ma 11.4 ± 0.2 µm
PY113-1863
PY113-1893
PY113-1977.5
PY113-1998.5
R34835* 63.1 ± 7.9 Ma 11.1 ± 0.3 µm
PY113-1929.5 83.1 ± 5.7 Ma 11.0 ± 0.2 µm
R34833* 7.9 ± 2.5 Ma 9.5 ± 0.6 µm
R34854* 51.8 ± 5.6 Ma 10.6 ± 0.3 µm
GJLAV-1
GJLAV-4
GJLAV-7
Lavani-1
R34899 (-945 m)
R34900 (-1,623 m)
R34901 (-2,242 m)
10.7 ± 3.1 Ma
R34902 (-2,972 m)*
6.5 ± 2.1 Ma
0 10 20 30 40 km
Stratigraphy
Volcanic
April Ultramafics
Syn-orogenic
Darai LMST
Moogli MDST/Mendi Gp
Chim Fm
Salumei Fm
Undifferentiated
Ieru Fm
Toro SST
Imburu MDST
Koi-lange SST
Magobu Fm
Om Beds
Bol Arkose
Granitic Basement
Jurassic
Cretaceous
P
E
O
M
200
150
100
50
0
Structure
Anticline
Syncline

Figure 4.2. *(previous page) Sample localities and AFT data from the Muller Range, Western Fold and Thrust Belt. Asterisked samples represent AFT ages and mean track lengths from Hill and Gleadow (1989; 1990). Samples are grouped in four vertical profiles for QTQt modelling: WMR: Western Muller Range, Strick North: north Strickland Gorge, Strick South: south Strickland Gorge, Lavani: Lavani Valley. Geological information from Davies and Norvick, 1974; Davies, 1983; Brown and Robinson, 1982. SRTM digital elevation model retrieved from USGS (2015). Location marked on Figure 4.1.*

4.5.1. Selection of samples for thermal modelling

Thermal history modelling of AFT data can reliably be carried out when measured single grain ages are statistically consistent with a single population (e.g., Carter and Gallagher, 2004). The standard approaches to assessing population homogeneity include the chi-squared (χ^2) and dispersion tests, with $P(\chi^2)$ values of < 0.05 or dispersion values of $> 20\%$ most commonly relating to multiple apatite populations and/or differential annealing kinetics between grains of differing composition within a single population (e.g., Galbraith and Laslett, 1993).

The bulk of AFT data available to this study was obtained from the Ieru Formation (Table 4.1), with all samples failing the chi-squared test and being associated with moderate to high dispersion (Table 4.2 and Supplementary Material B4). Conventionally, these data would be separated into independent populations for thermal history modelling, ideally based on some compositional criterion (i.e. Cl wt%, Dpar kinetic indicator). This provides a test of the potential influence of differing annealing kinetics on single grain age dispersion and a means for allowing for overdispersion in the apatite age distribution. However a large proportion of AFT data from the Papuan Basin dataset are old and thus chemical composition data are limited. Dpar measurements were obtained from samples PY113-1929.5 and PY110-2171, but the Dpar-AFT age and Dpar-track length trends (Supplementary Material D4) did not imply any obvious statistically meaningful apatite populations.

Given this, we believe that multiple sources of apatite are the best explanation for the observed heterogeneity in single grain ages.

A concern with inverting data as a single population from a sample with multiple apatite populations is that we will not account for multiple independent pre-depositional thermal histories. In particular, inherited tracks (i.e. those formed prior to deposition) may significantly influence the model-predicted palaeotemperatures, including the timing and magnitude of maximum temperatures (e.g., Carter and Gallagher, 2004). In the following section, we discuss our current understanding of Papuan Basin sediment provenance and use forward thermal modelling to explore the potential influence that multiple apatite populations (and inherited tracks) could have on thermal history reconstructions.

4.5.1.1. Sediment provenance

The pioneering regional PNG AFT studies of Hill and Gleadow (1989; 1990) revealed at least two sources of apatite in the Ieru Formation: (1) a large Albian to Cenomanian contemporaneous volcanic component (AFT age ≈ stratigraphic age), and (2) a considerably smaller basement component (AFT age > stratigraphic age). This is consistent with ZHe ages from the Ieru Formation (e.g., Fig. 4.3a) which indicate that ~ 80% of zircon grains relate to a contemporaneous source and ~ 20% relate to an older pre-depositional source. In contrast, the pre-Ieru Formation strata, including the directly underlying Toro Sandstone, primarily comprise ZHe age (and age vs eU trends) that are suggestive of a source that underwent significant cooling in the Triassic (ca. 250-200 Ma; Fig. 4.3b-d).

This transition in sediment provenance is consistent with our understanding of the palaeogeographic evolution of the Papuan Basin (e.g., Home *et al*., 1990; *Hill et al*., 2000; Norvick, 2003) in particular that (1) during the Triassic to earliest Cretaceous (top basement to Toro Sandstone) the shoreline was close to the southern edge of the present-day fold belt and sands were likely sourced from exposed

basement to the south, and (2) in the Early Cretaceous, flooding of the margin moved the shoreline thousands of kilometres inland to mainland Australia, flooding basement sources of sand and thus reflecting a transition to primarily locally-sourced apatite and zircon from nearby contemporaneous volcanics such as the Kondaku Tuff on the flanks of the Kubor Anticline (Fig. 4.1b; Bain *et al*., 1975). This understanding of sediment provenance is used to guide forward thermal modelling aimed at exploring the potential influences of the contemporaneous volcanic and basement apatite populations on thermal history modelling.

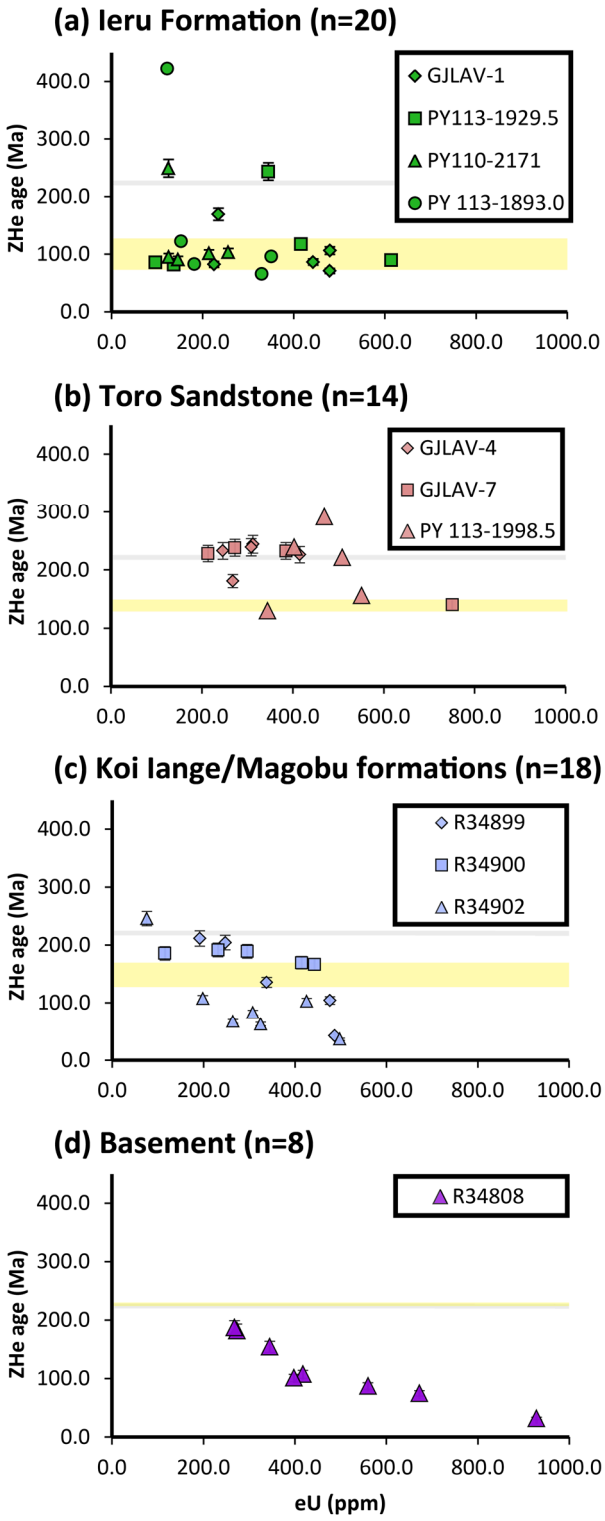

Figure 4.3. *ZHe age vs eU plot showing increase in negative correlation with stratigraphic age from Ieru Formation (a) to crystalline basement (d). Corrected ZHe ages plotted with 6.2% analytical uncertainty (1σ) bars. Yellow squares/bars represent the stratigraphic age of each formation. Grey line is the minimum known age of crystalline basement beneath the Papuan Basin (222 ± 4 Ma; Page, 1976). n = number of single grain ages in plot.*

4.5.2. Forward thermal history modelling approach

Here, we use forward modelling of AFT data to assess the viability of a range of thermal history scenarios. The assessment of forward model results involves comparing predicted and observed data, or more specifically, the ability of a given thermal history to reproduce the observed AFT age, MTL and track length distribution (TLD). The forward models presented here were qualitatively assessed against observed AFT data from the three uppermost Ieru Formation samples, R34809, R34832 and R34854. All three samples were located < 131 m below the base of the Darai Limestone (Table 4.1), enabling us to robustly constrain the Oligocene to late Miocene thermal history and thus focus on exploring plausible time-temperature paths in less well-constrained areas (e.g., Fig. 4.4). The AFT ages for these samples range from 46.9 ± 7.6 Ma to 79.8 ± 8.2 Ma, with mean track lengths ranging from 10.3 ± 0.2 to 12.1 ± 0.2 μm (Supplementary Material B4). The samples share considerable similarity in TLD, including a major peak at ~ 10-12 μm and a negative skew due to a tail of short track lengths (Supplementary Material F4, Fig. F4.1).

To account for multiple sources of apatite within the Ieru Formation, each forward model comprised two independent pre-depositional time-temperature paths, including (1) a slowly-cooled path from temperatures below the PAZ in the Early Triassic to surface temperatures in the Albian to Cenomanian, and (2) a rapidly-cooled path from temperatures below the PAZ to surface temperatures in the Albian to Cenomanian (Fig. 4.4). Therefore, apatite grains that experienced the slow-cooling path spent considerably longer (> 50 Ma) in the PAZ prior to deposition (Fig. 4.4). Multiple pre-depositional history models were tested with three post-depositional thermal histories: (a) a Pliocene to recent thermal peak only, (b) a Late

Cretaceous to Oligocene thermal peak only[1] and (c) both Late Cretaceous to Oligocene and Pliocene to recent thermal peaks (Fig. 4.4). Each of the post-depositional thermal histories (a-c) were tested with maximum temperatures of 60°C, 80°C, 90°C, 100°C and 110°C (Fig. 4.4). Forward modelling utilised the annealing model of Ketcham *et al*. (2007) with apatite chlorine content fixed at 0.40 wt%, which equates to Dpar values between 1.5-2.5 μm based on Cl-Dpar comparisons in Donelick *et al* (2005).

The predicted AFT age and MTL from each of the pre-depositional time-temperature paths was used to calculate weighted averages for each sample, with the weighting based on the assumed relative abundance of rapidly-cooled and slowly-cooled grains (e.g., 80:20 in Fig. 4.4). This enabled the resulting AFT age and MTL predictions to be directly compared to the observed data, with predicted data outside of the range ± the error of the observed AFT age (e.g., 39.3-88 Ma) and MTL (e.g., 10.1-12.3 μm) discarded. The final predicted track length distribution histograms were subsequently constructed by combining the results for accepted models. These were compared directly to a composite TLD histogram comprising the three upper Ieru Formation samples (normalised to 100 tracks).

4.5.3. Forward thermal history modelling results

A total of 52 individual forward models were run to explore the potential influences of mixed apatite provenance on observed Ieru Formation AFT data. This included 26 forward models for the scenario considered most representative (e.g., Section 4.5.1.1) comprising 80% rapidly-cooled apatite and 20% slowly-cooled apatite (Fig. 4.4). The additional 26 forward models comprising 50% rapidly-cooled and 50% slowly-cooled apatite are included and discussed in Supplementary Material E4.

[1] All three post-depositional thermal histories include Oligocene to late Miocene heating associated with the deposition of 1,000-1,500 m of Darai Limestone, but the maximum temperature associated with this burial remains at a palaeotemperature lower than the uppermost boundary of the PAZ.

The 80:20 modelling included 26 independent time-temperature paths yielding 13 central AFT age, MTL and length distribution predictions. Of these, only four were consistent with the observed values from the three uppermost Ieru Formation samples. Despite significantly different post-depositional thermal histories, all four accepted models were characterised by maximum temperatures of 90 or 100°C (Fig. 4.4). Model (a), comprising only a Pliocene to recent thermal peak produced the worse TLD fit, failing to reproduce the short track length component and asymmetric distribution recorded within the observed data (Fig. 4.4a). The best-fit TLD was produced by Model (b), comprising a Late Cretaceous to Oligocene thermal peak only and a maximum temperature of 90°C (Fig. 4.4b).

Thus, forward modelling of multiple apatite populations (Fig. 4.4 and Supplementary Material E4) suggests that (1) a Late Cretaceous to Oligocene thermal peak and maximum temperatures of around 90-100°C are required to best reproduce the observed data, and (2) thermal histories involving only a Pliocene to recent thermal peak do not satisfactorily reproduce the observed data. These forward modelling results provide a baseline for comparison to subsequent inversion modelling in which a single population is assumed, given we cannot separate the data without knowing the pre-depositional histories of different populations.

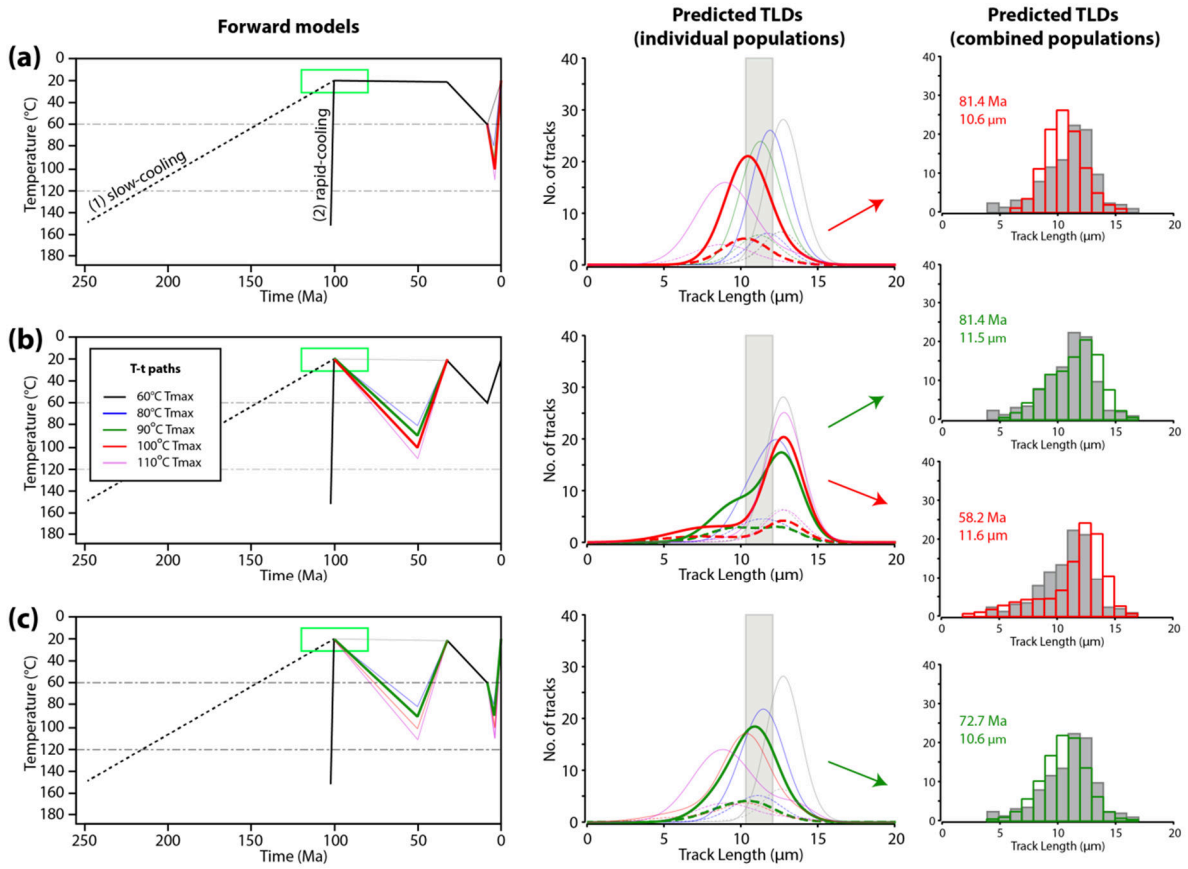

Figure 4.4. *Left: Forward models comprising two pre-depositional T-t paths (1-2), tested across a range of different post-depositional thermal histories (a-c). The green box represents a reasonable stratigraphic age range for the upper Ieru Formation samples. Middle: Predicted TLD curves for rapidly-cooled (solid line) and slowly-cooled (dashed line) apatite populations, weighted based on a relative abundance of 4:1 (80:20%). Thicker red and green lines represent TLD curves from accepted models (i.e. models from which the weighted average of the predicted data fits within the observed data range). Light grey shade represents the MTL range from the observed data (e.g., 10.3 ± 0.2 to 12.1 ± 0.2 um). Right: TLD histograms (normalised to 100 tracks) comprising the combined rapidly-cooled and slow-cooled TLD curves for the four accepted models compared with a composite TLD histogram (dark grey) comprising observed data from three upper Ieru Formation samples.*

4.5.4. Inverse thermal history modelling approach

Thermal histories were subsequently inferred from the new and existing AHe, AFT and ZHe data using a Bayesian transdimensional Markov Chain Monte Carlo (MCMC) inversion approach implemented within the software QTQt (Gallagher, 2012). QTQt allows the user to select from a range of annealing (AFT) and diffusion

(U-Th/He) models. For AFT data, we used the multi-kinetic annealing model of Ketcham *et al*. (2007), utilising the sample-average Dpar kinetic value for new data and an average of 0.40 Cl wt% for heritage data without composition/kinetic parameter measurements. ZHe and AHe data from euhedral (2T) grains were jointly inverted taking into account radiation damage accumulation and annealing models of Guenthner *et al*. (2013) and Gautheron *et al*. (2009), respectively. Fragmented apatites with a single intact crystal termination (1T) were modelled using the fragmentation model of Brown *et al*. (2013). AHe data from composite grain aliquots were not used in thermal modelling. Where available, published vitrinite reflectance (VR) data were also inverted, using the EasyRo% model of Sweeney and Burnham (1990).

QTQt utilises a Bayesian framework (Gallagher, 2012), with the prior incorporating a range of information, including a user-defined time-temperature domain and multiple thermal history constraints (e.g., present-day temperature), discussed in more detail in Section 4.5.4.1 below. Using the MCMC approach, the user-defined modelling space is sampled by iteratively applying random perturbations to the thermal history or parameters. If the perturbation produces a thermal history with an improved posterior probability, it will tend to be accepted and that thermal history contributes to the final posterior probability distribution. A major advantage of the thermal modelling approach employed by QTQt is that the data determines the complexity of the thermal history, with the Bayesian approach favouring simpler solutions with adequate data fit over more complex ones, thus minimising the possibility of over interpreting thermal histories (Gallagher *et al*., 2009). Further, QTQt allows multiple samples to be modelled jointly as a vertical profile. An additional model parameter in vertical profile modelling is the temperature offset between the top and bottom samples, which can be fixed or allowed to vary through time. Gallagher *et al.* (2005) and Gallagher (2012) show that modelling multiple samples in a vertical profile is generally preferable to modelling

single samples as the latter can produce overly complex thermal histories as a result of overfitting or effectively fitting the noise in the data.

In all of the single sample and vertical profile thermal history models presented in Section 4.5.5, the MCMC sampler was initially allowed to explore the model space producing 50,000 t-T paths that were subsequently discarded (burn-in) prior to 250,000 t-T paths that were used to approximate the posterior distribution (post burn-in). QTQt offers a range of individual outputs that should all be considered following any given model run. Basic descriptions of the individual outputs can be found in Section 4.5.5, with additional details provided in Gallagher (2012).

4.5.4.1. Additional model constraints

We define the basic prior for MCMC sampling in terms of a time range of the oldest age in the profile ± oldest age in the profile and a temperature range of 70° ± 70° for individual samples, and 100° ± 100°C or 150° ± 150°C for vertical profiles. The offset temperature parameter prior (e.g., the temperature difference between the top and bottom sample) was estimated based on a geothermal gradient of 27.5°C/km and this offset temperature gradient was allowed to vary between 25°C/km and 30°C/km during the inversion. The model was allowed to explore pre-depositional thermal histories for all the samples. All models included some additional prior geological constraints (e.g., time-temperature regions through which all proposed thermal history models must pass) including at least (1) the stratigraphic age and assumed depositional palaeotemperature of the sample, and (2) the present-day temperature of the sample. The stratigraphic age was determined from palaeontological age-dates on or near the sample, with an appropriate range (often 10-20 Ma) reflecting confidence in the age dating. The present-day temperature for surface samples was 20 ° ± 10°C or 10° ± 10°C, depending on the elevation from which the samples were collected.

Initial modelling involved minimal constraints to explore the thermal history information retrievable from the data alone. Subsequent modelling involved at least two additional geological constraint domains, related to the well-constrained chronostratigraphy of the Oligocene to late Miocene Darai Limestone. Sr-isotope and palaeontological dating enable estimates for the timing of initiation and cessation of Darai Limestone deposition (e.g., Eisenberg *et al*., 1996), while knowledge of Darai Limestone thickness from nearby geological traverses, reflection seismic and/or well data were used to estimate the burial and potential temperature range of the sample based on geothermal gradients of 25°C/km and 30°C/km. Where time-temperature models deviated significantly from known Darai Limestone chronostratigraphic reference curves (Eisenberg *et al*., 1996), additional constraints were implemented between the initiation and cessation of deposition, thus redirecting the model to explore less-constrained components of the thermal history.

4.5.5. Inverse thermal history modelling results

Here we present thermal histories from four areas within the Muller Range (Fig. 4.2). We initially extracted thermal history information from individual Ieru Formation samples based on the inversion of AFT data alone (presented in Supplementary Material F4), followed by the joint-inversion of multiple samples along pseudo-vertical profiles combining AFT, He and VR data (where available). The pseudo-vertical profile modelling output includes the expected thermal history model (which is the weighted mean of the posterior distribution) presented with the 95% confidence intervals shown for the upper and lower samples (e.g., Fig. 4.5). The maximum posterior model (the best Bayesian model in that it tries to balance model simplicity with data fit) is also shown alongside the observed versus predicted data (e.g., Fig. 4.5). Unless otherwise stated, the temperatures reported are from the expected model and are from the uppermost sample for pseudo-vertical sections. However, the expected model is not a model sampled during the inversion. While it captures the general form of the thermal histories, it does not always represent the

magnitudes of individual temperature changes that lead to better data fits. This is due to the smoothing over time and temperature when calculating the average of many thermal histories composed of linear heating and cooling segments. We observed that the expected model generally underestimates thermal maxima, by up to 20°C versus the maximum posterior model that tends to fit the observed data better. Thus, the expected model should be considered alongside the maximum posterior model and the maximum temperatures reported below are considered to be conservative (low) estimates.

Post-deposition refers to the period following the deposition of the uppermost (i.e. youngest) stratigraphic sample, which is Ieru Formation in all cases below. Thermal peaks correspond to individual heating/cooling events; and multiple thermal peaks may characterise an individual samples thermal history. MaxT refers to the maximum post-depositional temperature and is therefore reached only once for a given thermal history.

4.5.5.1. Western Muller Range (WMR)

Ieru Formation samples R34831 and R34832 are located on the northern limb of the Muller Anticline with ~ 600 m of vertical stratigraphic separation (Fig. 4.2). Both samples were deposited in the middle to late Cretaceous (ca. 125-85 Ma; e.g., White *et al*. 1973). Pseudo-vertical profile thermal history modelling (Fig. 4.5) indicates these samples experienced rapid cooling from a maximum temperature of ~ 100°C in the Eocene (ca. 55-50 Ma) to the initiation of Darai Limestone deposition (ca. 30 Ma). The 95% credibility intervals suggest that Eocene to Oligocene cooling is well-recorded within the data, which implies comparably poorly resolved Late Cretaceous to Eocene heating in the order of ~ 40°C (Fig. 4.5). The profile result suggests that a second thermal peak was reached at 8 Ma as the thermal history does not subsequently reach significantly higher temperatures. This timing is concurrent with the cessation of Darai Limestone deposition and is followed by the onset of rapid cooling to present-day surface temperatures. Any post-Darai Limestone

heating is poorly resolved but is likely to be insignificant. Importantly, the modelled thermal history suggests that maxT was reached during the Eocene, with temperatures ~ 15-20°C greater than at the late Miocene (post-Darai) thermal peak.

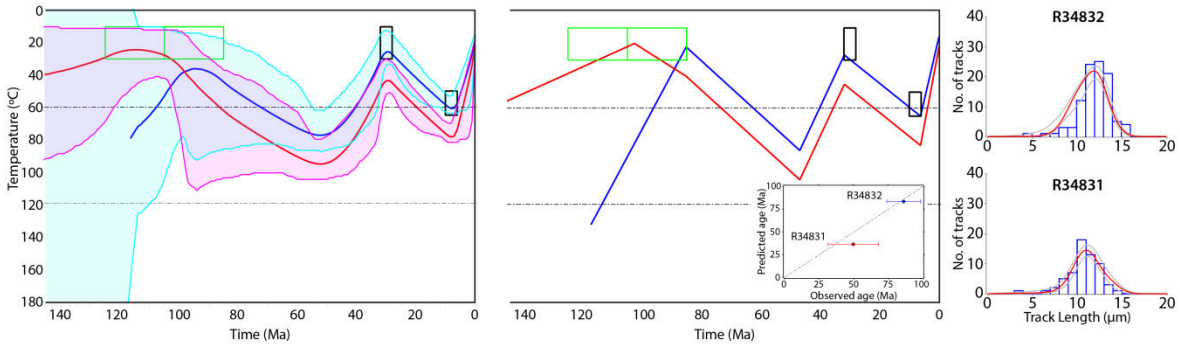

Figure 4.5. *Thermal history modelling results for a pseudo-vertical profile in the Western Muller Range (WMR). The time-temperature domain on the left includes the expected model (weighted mean of the posterior distribution) with 95% confidence intervals for the uppermost (blue) and lowermost (pink) samples. The time-temperature domain in the centre includes the max posterior model (a relatively simple thermal history that fits the observed data adequately). Dot-and-dash lines represent the AFT PAZ. The green boxes represent the stratigraphic age/temperature constraint while the black boxes represent additional thermal history constraints discussed in Section 4.5.4.1. Observed (blue histograms) versus predicted (red curves) track length distributions and 95% confidence intervals (grey curves) are included on the right. The inset shows the observed AFT ages (and errors) plotted against the predicted ages. Track length distribution and age predictions were obtained from the max posterior model.*

4.5.5.2. South Strickland Gorge (Strick South)

A pseudo-vertical profile thermal history model was produced for the southern Strickland Gorge using data from three AFT and five ZHe single grain analyses, with sample separation deduced from the measured section of White *et al*. (1973). The profile includes Ieru Formation samples R34835 and PY113-1929.5, together with Koi Iange sample R34833 (Figs. 4.2 and 4.6). Palaeontological evidence suggests that the Ieru Formation samples were depositied in the Cretaceous (ca. 130-80 Ma) and the Koi Iange sample was deposited in the latest Jurassic (ca. 150-145 Ma; White *et al*.,

1973). The uppermost (R34835) and lowermost (R34833) samples are characterised by 1,140 m stratigraphic separation.

The resulting thermal history predictions are in reasonable agreement with the observed data (Fig. 4.6), with the thermal history model suggesting a significant phase of cooling from a thermal peak in the Campanian (ca. 75 Ma) until Darai Limestone deposition (ca. 30 Ma), necessitating rapid post-depositional heating of ~ 60°C from the middle Cretaceous (ca. 100 Ma) to the Campanian (ca. 75 Ma). Post-Darai Limestone heating is negligible prior to cooling to present-day surface temperatures. The thermal model suggests maxT was reached during the Campanian (ca. 75 Ma) with temperatures ~ 15-20°C greater than the late Miocene (post-Darai) thermal peak.

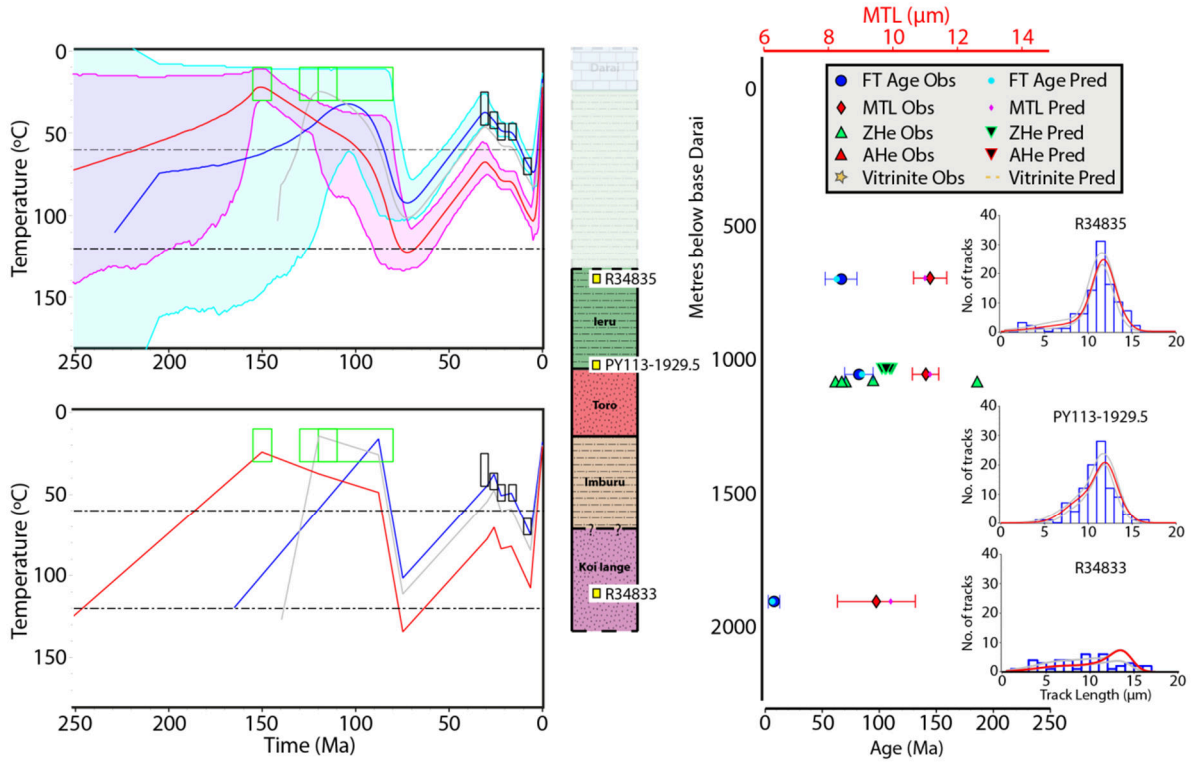

Figure 4.6. *Thermal history modelling results for a pseudo-vertical profile in the southern Strickland Gorge (Strick South). The upper time-temperature domain (left) includes the expected model (weighted mean of the posterior distribution) with 95% confidence intervals for the uppermost (blue) and lowermost (pink) samples. The lower time-temperature domain (left) includes the max posterior model (a relatively simple thermal history that fits the observed data adequately). Dot-and-dash lines represent the AFT PAZ. The green boxes represent the stratigraphic age/temperature constraint while*

the black boxes represent additional thermal history constraints discussed in Section 4.5.4.1. The vertical profile (centre) is based on the measured sections of White et al. (1973). Observed versus predicted data (right) includes ages, mean track lengths (MTL), track length distributions, vitrinite reflectance (where available) and associated errors. Model predictions were obtained from the max posterior model. Legend for observed versus predicted data (top right) relevant to all subsequent thermal model figures.

4.5.5.3. North Strickland Gorge (Strick North)

A pseudo-vertical profile was produced for the northern Strickland Gorge based on the measured section of Jenkins and White (1970). Thermal modelling incorporated four AFT analyses from Ieru Formation samples R34809 and R34810, Toro Sandstone sample R34811 and basement sample R34808 (Figs. 4.2 and 4.7). These data were inverted alongside nine AHe and eight ZHe single grain ages from sample R34808, with an additional time-temperature constraint placed on this basement sample to reproduce its high-temperature K-Ar biotite emplacement age of 222 ± 4 Ma (Page, 1976). Limited palaeontological data in the vicinity of this profile necessitates wide stratigraphic age estimates of middle to late Cretaceous (ca. 120-80 Ma) for the Ieru Formation samples and Early Cretaceous (ca. 132-122 Ma) for the Toro Sandstone sample. The uppermost (R34809) and lowermost (R34808) samples are characterised by ~ 2,170 m stratigraphic separation (Fig. 4.7).

The resulting thermal history predictions provide an acceptable fit to the observed data (Fig. 4.7), except for the predicted ZHe single grain ages which fail to reproduce the dispersion in ages related to the very strong eU vs age trend observed within sample R34808 (cf. Figs. 4.3 and 4.7). This may be a limitation of the Guenthner *et al*., (2013) radiation damage-diffusion model, as suggested by Johnson *et al*., (2017) and Mackintosh *et al*., (2017).

The thermal history model (Fig. 4.7) suggests that these data record two periods of post-depositional cooling, consistent with the single sample models (R34809 and R34810; Supplementary Material F4). The earlier cooling to the initiation

of Darai Limestone deposition (ca. 30 Ma) began from a thermal maximum during the earliest Eocene (ca. 55 Ma), necessitating prior heating of ~ 50°C from the Late Cretaceous (ca. 90 Ma). A second rapid cooling to present-day surface temperatures initiated at ca. 7-6 Ma, necessitating ~ 20°C of heating in the 1-2 Ma following the cessation of Darai Limestone deposition (ca. 8 Ma). Thermal modelling suggests that considering the uncertainties, the earliest Eocene and late Miocene thermal maxima were of approximately similar magnitude.

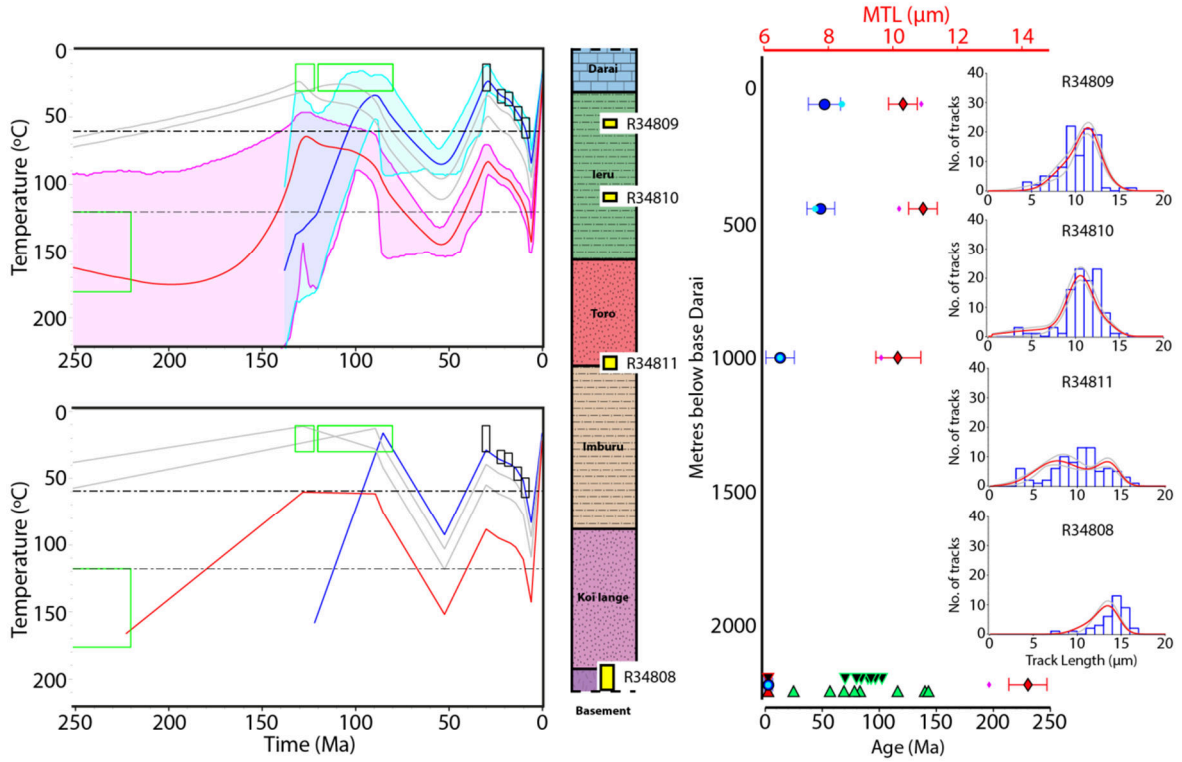

Figure 4.7. *Thermal history modelling results for a pseudo-vertical profile in the northern Strickland Gorge (Strick North). Refer to Figure 4.6 caption for model details and legend. The vertical profile (centre) is based on the measured sections of Jenkins and White (1970).*

4.5.5.4. Lavani Valley (Lavani)

A pseudo-vertical profile was produced for Lavani Valley in the Eastern Muller Range (Fig. 4.8) using constraints from field data (Mahoney *et al.*, 2017) and the Lavani-1 well (Amoco, 1982; Denison, 1990). Thermochronology data was available for five samples, including Ieru Formation sample R34854, Toro Sandstone sample

LAV#4 and Magobu and/or Koi Iange Formation samples R348900, R348901 and R348902.

Upper Ieru Formation sample R34854 has a particularly well-constrained stratigraphic context (120 m below Base Darai Limestone) and age (ca. 88-84 Ma) from recent field work and associated palynological age determinations (Mahoney *et al*., 2017). Sample LAV#4, identified as Toro Sandstone based on lithology and stratigraphic context, was collected from a structurally very complex area and thus required a wide stratigraphic age constraint of 145-125 Ma. Stratigraphic ages for samples R348900, R348901 and R348902 are also poorly constrained due to indeterminate palynology and a generally poor understanding of the stratigraphy at the base of the Lavani-1 well (e.g., Amoco, 1982; Denison, 1990). Here, these samples are interpreted to belong to the Magobu and/or Koi Iange formations, with stratigraphic constraints placed between 165-135 Ma. Wider depositional constraints are favoured where the stratigraphy is poorly known, as they allow for the data to control the thermal history if there is appropriate information. The pseudo-vertical transect required the projection of surface samples R34854 and LAV#4 to the (now eroded) core of the Lavani Anticline above the Lavani-1 well. Prior to late Miocene to Pleistocene erosion, the uppermost (R34854) and lowermost (R348902) samples were separated by ~ 4,250 m of stratigraphic section (Fig. 4.8).

Thermal modelling utilised AFT age and track length data from Ieru Formation sample R34854, along with AFT ages from Magobu Formation samples R34901 and R34902. These data were inverted together with two AHe and five ZHe single grain ages from lower Toro sample LAV#4, along with 12 ZHe single grain ages from Magobu Formation samples R34900 and R34902. Although not used here for specific thermal history calibration, VR data from the Lavani-1 well (Amoco, 1982) provides additional validation of maxT predictions.

In general, the thermal model predictions reproduce the observed data well (Fig. 4.8). The predicted ZHe single grain ages again fail to reproduce the very strong

age dispersion (eU vs age trend) observed within sample R34902 (cf. Fig. 4.3 and 4.8). The predicted VR reproduces the general observed trend reasonably well, although the observations are somewhat underpredicted and overpredicted at the top and bottom of the well respectively. This suggests that at the time of maxT the geothermal gradient was slightly lower than the ~ 25°C/km gradient predicted by the model.

The resulting thermal history (Fig. 4.8) suggests these data record two periods of post-depositional cooling. The first period of cooling, from a thermal peak in the early Eocene (ca. 50-45 Ma) to the initiation of Darai Limestone deposition (ca. 30 Ma), requires prior heating of ~ 60°C from the Late Cretaceous (ca. 85 Ma). The second period of cooling to present-day temperatures commenced at ca. 5 Ma and requires post-Darai Limestone heating of ~ 15-20°C. The magnitude of the early Eocene and late Miocene-Pliocene thermal maxima are very similar.

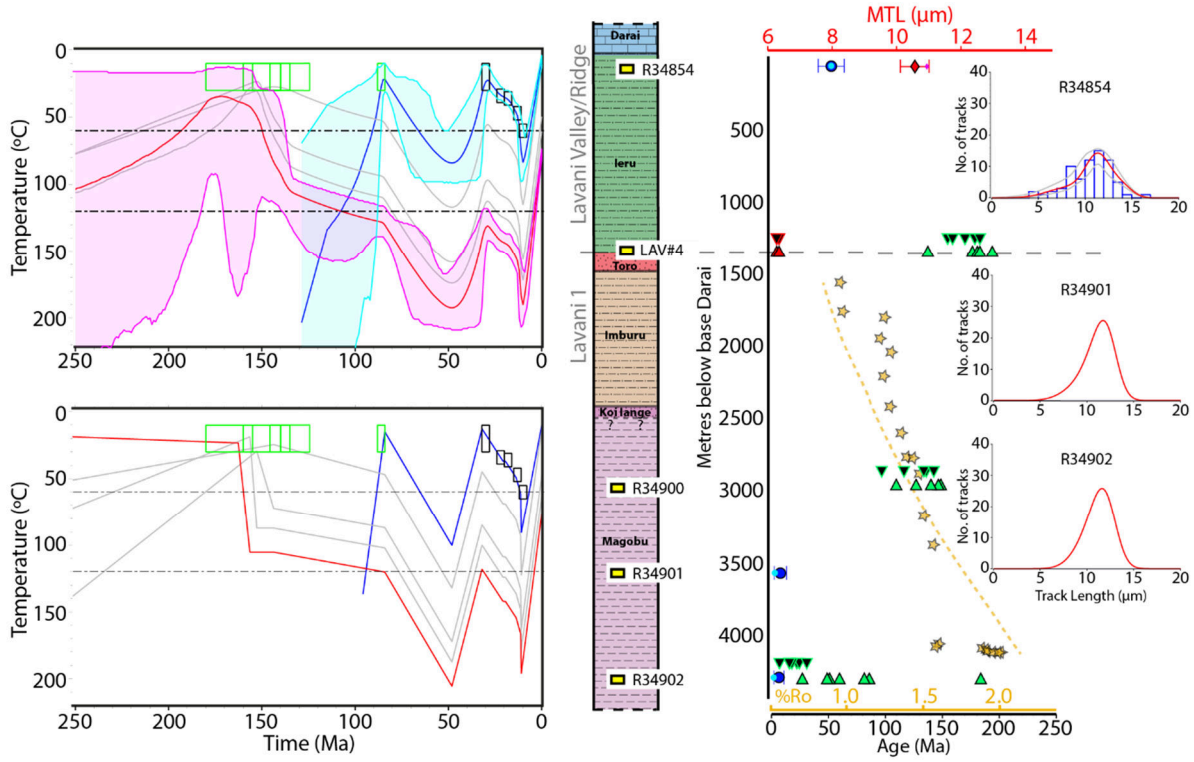

Figure 4.8. *Thermal history modelling results for a pseudo-vertical profile in the Lavani Valley (Lavani). Refer to Figure 4.6 caption for model details and legend. Only predicted track length distributions are shown for samples R34901 and R34902, as no track lengths were measured. The*

vertical profile (centre) is based on recent field work (Mahoney et al., 2017) and the Lavani-1 well (Amoco, 1982; Denison, 1990).

4.5.6. Summary: Muller Range T-t history

Both forward and inversion thermal history models for the Muller Range indicate two significant thermal peaks during the Late Cretaceous to Eocene and from the late Miocene to recent (Figs. 4.4 and 4.9; Supplementary Material F4, Fig. F4.1). The consistency between forward and inversion models is reassuring, particularly given that only the former accounts for the possible influence of mixed apatite provenance through the inclusion of multiple independent pre-depositional thermal histories. Therefore, while AFT single grain ages are dispersed and not apparently related to the influence of any kinetic annealing factors, inherited tracks appear to have only a minor influence on the post-depositional thermal history.

The origin of early Eocene to Oligocene cooling indicated by thermal history modelling is unknown, but if erosional, the event is represented stratigraphically as a regionally expansive Late Cretaceous to early Oligocene unconformity (refer Section 4.2.2). In contrast, the late Miocene to recent cooling is better known and likely related to the onset of uplift and erosion associated with the formation of the PFTB (e.g., Hill and Gleadow, 1989). Considering the uncertainties, thermal history models suggest that the Late Cretaceous to earliest Eocene (ca. 75-55 Ma) and late Miocene to Early Pliocene (ca. 5-3 Ma) thermal maxima were of a similar magnitude (Fig. 4.9).

The seven Ieru Formation samples included in thermal modelling profiles experienced a maxT of ~ 75-100°C, implying ~ 55-80°C post-depositional heating and subsequent cooling prior to Darai Limestone deposition (Fig. 4.9). ZHe data from four Ieru Formation samples (Fig. 4.3a) suggests that either (1) maxT was not high enough for significant helium loss from variably radiation damaged grains, or (2) the radiation damage largely accumulated post-maxT. ZHe single grain ages are mostly

similar to Ieru Formation stratigraphic ages (120-80 Ma), suggesting that the zircon grains underwent rapid cooling prior to deposition, consistent with indications of rapid pre-depositional cooling in the majority of thermal models (Fig. 4.9). Thus it seems highly likely that the majority of zircon grains in the Ieru Formation were sourced from contemporaneous volcanics, as suggested by Hill (1989).

Modelling suggests that the two Toro Sandstone samples underwent ~ 90-100°C of post-depositional heating to an early Eocene maxT of ~ 110-120°C (Fig. 4.9). As for the Ieru Formation samples, ZHe data from the Toro Sandstone suggests that either (1) maxT was not high enough for significant helium loss from variably radiation damaged grains, or (2) the radiation damage largely accumulated post-maxT. ZHe single grain ages cluster around the Triassic (ca. 250-200 Ma; Fig. 4.3b), consistent with the range of granitic basement ages reported from PNG (e.g., Page, 1976; Davies, 1990) and eastern Australia (e.g., Murray, 2003; Glen, 2005). Thermal history modelling indicates protracted pre-depositional cooling (Fig. 4.9) suggesting that zircon grains in the Toro Sandstone may be sourced from slowly exhumed crystalline basement.

The five Koi Iange/Magobu Formation samples included in thermal modelling profiles attained a maxT of ~ 120-190°C, requiring ~ 100-170°C post-depositional heating (Fig. 4.9). ZHe single grain ages show a weak negative correlation with eU (Fig. 4.3c), suggesting that the maximum temperatures experienced by the samples were sufficient to initiate preferential helium loss from the radiation damaged zircon grains. The grain with the lowest eU yielded a Triassic age (Fig. 4.3c). Thermal modelling of Koi Iange/Magobu zircon suggests protracted cooling prior to deposition (Fig. 4.9), as also observed in the overlying Toro Sandstone zircon grains. Thus zircon grains within the Koi Iange/Magobu may have also been sourced from slowly exhumed crystalline basement.

The Strickland Gorge basement sample reached a maxT of ~ 145°C, significantly lower than Koi Iange and Magobu samples from Lavani Valley and

consistent with much less burial as also indicated from measured stratigraphic sections (cf. Figs. 4.7 and 4.8).

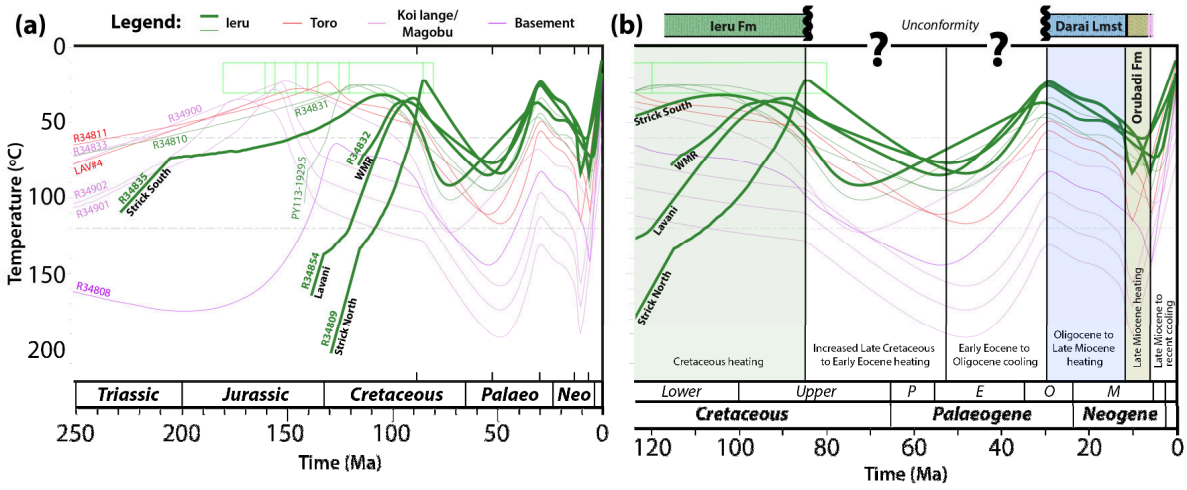

Figure 4.9. *Combined thermal histories of 14 samples from the Muller Range from (a) the Triassic to recent and (b) the middle Cretaceous to recent. Time-temperature paths from pseudo-vertical profile expected models with the uppermost (Ieru Formation) sample for each profile included as a solid line. Grey dot-and-dash lines represent the AFT PAZ. The green boxes represent the stratigraphic age range for each sample.*

4.6. Discussion

In this section, we compare low-temperature thermochronology data from the Muller Range with the regional Papuan Basin dataset, before proposing potential mechanisms to explain the two major thermal peaks clearly recorded in data across the Muller Range. We subsequently discuss the wider implications of the Muller Range thermal history modelling for the evolution of the PFTB, the tectonic evolution of the PNG margin.

4.6.1. Regional thermal data

Our contemporary understanding of the thermal history of the Papuan Basin varies significantly both spatially and temporally. In contrast with observations from the Muller Range, thermochronology data from foreland areas provide significantly less

evidence for a Late Cretaceous to Eocene thermal peak. Moreover, maxT is likely to have occurred in the late Miocene to recent in parts of the Fly Platform including the Cecilia Graben, Morehead Graben and Omati Trough (e.g., Lund *et al*., 1998; Cooper *et al*., 2012). Hill and Gleadow (1990) found that fission track age distributions and lengths for upper Ieru Formation samples from wells throughout much of the Fly Platform and frontal structures of the KFTB (e.g., Iehi and Barikewa anticlines) were mostly similar, characterised predominantly by contemporaneous Albian to Cenomanian AFT ages and long track lengths (12.9-14.5 μm) (Fig. 4.10). These data are thus suggestive of minimal post-depositional annealing and maximum temperatures ≤ 60°C. In contrast, upper Ieru Formation samples from the Muller Range are characterised by significantly younger Late Cretaceous to early Eocene AFT ages and comparably much shorter track lengths (10.3-12.1 μm) (Fig. 4.10), with thermal history models necessitating a Late Cretaceous to early Eocene thermal maximum in the order of ~ 75-100°C (Fig. 4.9).

AFT from older, deeper samples in a number wells across the Fly Platform (e.g., Aramia-1, Komewu-1 and -2, Kanau-1 and Iamara-1) and frontal KFTB (e.g., Iehi 1) do however record some minor evidence for higher palaeotemperatures (Hill, 1989a). Detrital apatite in younger Eocene and early Miocene samples from the Fly Platform have very long track lengths (e.g., Hill, 1989a) similar to those of the upper Ieru Formation, again suggesting that maxT is likely to have been ≤ 60°C post deposition. Thus Late Cretaceous to Eocene heating within the foreland region cannot be ruled out, but its magnitude must have been significantly less (~ 15-40°C) than in the Muller Range (~ 55-80°C).

In apparent contrast, Cooper *et al*. (2012) discuss a number of wells in the central foreland area (e.g., Koko-1, Langia-1 and Panakawa-1) where VR records an abrupt increase in maximum palaeotemperature below the Late Cretaceous to Eocene unconformity. Notably, this observed trend relies heavily on very limited VR data from above the Ieru Formation (e.g., in the Langia-1 well). The significant

increase in maturity within the Ieru Formation is traditionally interpreted as being related to increased heat flow associated with Late Cretaceous to Palaeocene Coral Sea rifting, with accompanying uplift and erosion of up to ~ 3,300 m of overlying sediments (Cooper *et al*., 2012). Similarly, Hill *et al*. (2010) used combined AFT and VR data from the Kanau-1 well on the Darai Plateau (Fig. 4.10) to suggest Late Cretaceous to Palaeogene heating, uplift and erosion of > 2,000 m of sediments above the Ieru Formation prior to Darai Limestone deposition. The deposition and subsequent removal of this thickness of sediment would demand a thermal perturbation comparable to or in excess of that proposed here for the Muller Range. However recent work on the Kanau-1 and Bosavi-1 wells, including analyses of porosity profiles, pressures, AFT and VR data, led Callot *et al*. (2017) to conclude that < 600m of Late Cretaceous to Palaeogene sediments were eroded from the Darai Plateau prior to deposition of the Darai Limestone. Cooper *et al*., (2012) propose that elevated palaeotemperature data may relate to the selective advection of hot fluids from early Miocene to Pliocene volcanism through sandier units within the basal stratigraphy. Interestingly, the inclusion of heat advection into their burial history modelling reduces the earlier Late Cretaceous to Eocene burial related heating to magnitudes more consistent with those predicted from AFT data across the foreland and much less than those recorded within the Muller Range.

Duddy *et al*. (1994) also recognised high maximum palaeotemperatures in the Ieru Formation and overlying syn-orogenic sequence in an unidentified well from the foreland region. They suggested that these observations related to post-Miocene advection of hot fluids from the thrust front, through confined aquifers near the Darai Limestone and syn-orogenic sequence contact, and potentially in the Toro Formation. It seems equally likely that hot fluids could have related to Pliocene to Pleistocene volcanism. Nevertheless, the inconsistencies between AFT and VR data, and spatially between wells, highlights that the spatiotemporal thermal history of the foreland region neighbouring the Muller Range is likely to be complex.

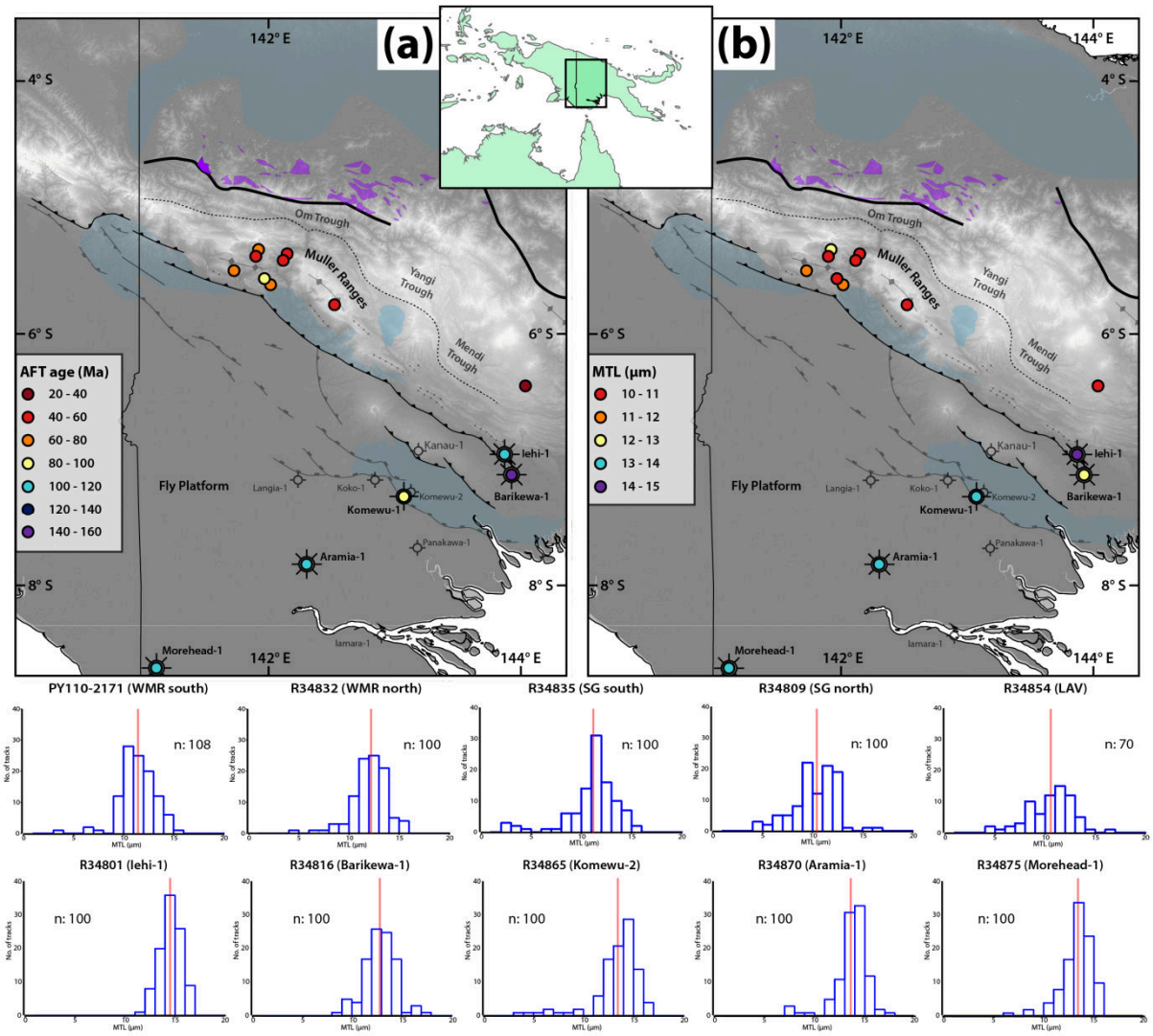

Figure 4.10. *(a) AFT age and (b) mean track length (MTL) for Ieru Formation samples across the Muller Range and Fly Platform. Refer to Figure 4.1 for detailed legend. Track length distributions for five representative Ieru Formation samples from the Muller Range (upper bottom) and Fly Platform (lower bottom). Red line represents MTL and n is the number of track lengths measured in AFT analysis.*

4.6.2. Late Cretaceous to early Eocene heating

Thermal models clearly indicate a significant Eocene cooling event occurred across the Muller Range, thus requiring significant earlier heating. Late Cretaceous to Palaeocene Coral Sea rifting is the most common explanation for (1) pre-Darai Limestone heating recorded in thermochronology and palaeotemperature data (e.g.,

Hill and Gleadow, 1990), and (2) uplift and erosion interpreted from the stratigraphic record (Brown *et al*., 1980; Home *et al*., 1990) and regional seismic reflection data (Schofield, 2000). However, as discussed above, the Papuan Basin dataset clearly records significant spatiotemporal variation and this needs to be taken into consideration in any regional explanation.

Any reasonable hypothesis for Late Cretaceous to Eocene heating (e.g., 55-80°C) in the Muller Range must account for the absence of such a robust thermal perturbation across the foreland and frontal KFTB regions. We suggest that margin architecture and continental collision in northern PNG are central to understanding the thermal history of the margin. We do not wish to completely disregard the influence of regional explanations such as increased basal heat flow in the Late Cretaceous to Palaeocene associated with Coral Sea rifting (Home *et al*., 1990), or mantle upwelling (Muller *et al*., 2016), but rather to focus on accounting for the local variations recorded in the thermochronology dataset.

We suggest that long-lived crustal extension and associated burial may provide a geologically plausible explanation for Late Cretaceous to Eocene heating in the Muller Range. Indeed, major extensional structures are suspected beneath and adjacent to the Muller Range (e.g., Hill, 1989b; Buchanan and Warburton, 1996; Mahoney *et al*., 2017), but are poorly understood primarily due to poor subsurface constraints typical of the fold belt. On the Fly Platform, extensional structures have undergone significantly less or no tectonic inversion and are consequently better constrained by geological and geophysical data, providing valuable analogues for understanding the extensional architecture of the Papuan Basin. These faults show compelling evidence of being long-lived from early Mesozoic to Neogene (e.g., Fischer and Warburton, 1996; Kawagle and Meyers, 1996; Bennett *et al*., 2000; Schofield, 2000; McConachie and Lanzilli, 2000; McConachie *et al*., 2000; Hill *et al*., 2010). Furthermore, they noticeably control Cretaceous Ieru Formation depocentres across the Fly Platform (e.g., McConachie and Lanzilli, 2000; Schofield, 2000) and in

the frontal KFTB (e.g., Sari *et al*., 1996). In fact, continued extension along major structures during the westward migration of the basin axis in the middle Cretaceous (Jenkins, 1974; Sari *et al*., 1996) may have been crucial to the preservation of significantly thicker sequences in hanging wall blocks versus often uplifted and eroded footwall blocks (e.g., Schofield , 2000).

The youngest preserved Ieru Formation in the Muller Range is late Turonian/early Coniacian (ca. 88 Ma, Mahoney *et al*., 2017), while the oldest overlying Darai Limestone is late Oligocene (ca. 32 Ma, Eisenberg *et al*., 1996), as a result much of the Late Cretaceous to Oligocene history is unknown. This prominent unconformity is commonly interpreted as representing the cessation of deposition across the area prior to commencement of Darai Limestone deposition in the Oligocene (e.g., Home *et al*., 1990; Hill *et al*., 2000; Norvick, 2003). But the results of the Muller Range thermal modelling presented here necessitate 55-80°C of heating of the upper Ieru Formation over this time, which is unlikely to be explained without invoking burial. Further, any proposed mechanism should explain significantly less heating across the adjacent foreland. Volcanism may provide an alternate mechanism but can be discounted given the absence of Late Cretaceous to Eocene volcanics recorded in the region.

We suggest that major basin-bounding faults beneath the Muller Range were actively accommodating sediments throughout the Late Cretaceous to Eocene, providing a plausible mechanism for heating the underlying Ieru Formation sediments. In fact, given observations of significantly thicker hanging wall sequences across structures on the Fly Platform, it would be somewhat anomalous if basinward faults beneath the Muller Range did not also accommodate significantly thicker hanging wall sequences. In the Turonian (ca. 90-88.5 Ma; upper Giero/lower Ubea) burial rates significantly increased towards the Muller Range in the northwest, with the uppermost Ieru Formation characterised by very significant spatial variations in thickness, highlighting complex margin architecture at this time, including an

embayment in the present-day Muller Range area (Sari *et al*., 1996). It therefore seems plausible that extension along major pre-existing faults beneath the present-day Muller Range resulted in the formation of an active depocentre from the Late Cretaceous to Eocene.

Therefore, as the Papuan Basin retreated towards the northwest during the Late Cretaceous, and while active extensional structures on the largely emergent Fly Platform were sheltering Ieru Formation from regional uplift, similar structures in more basinward areas (including the present-day Muller Range) were potentially actively accommodating rapid sedimentation (Fig. 4.11a). Extension and associated subsidence may have accommodated sedimentation into the Palaeocene and Eocene, as recorded in the Yangi Fold Belt < 50 km to the northeast (Fig. 4.2) where an almost complete Late Cretaceous (Chim Formation) to Eocene (Mendi Group) sequence up to an estimated 4,000 m thick is preserved (e.g., Davies, 1983; Gunson *et al*., 1997; 2000). High global eustatic sea level over this time (e.g., Haq *et al*., 1987; 2014) may have maximised the available accommodation space and thus continued extension may not have even been necessary. Assuming that Late Cretaceous to Eocene heating was primarily related to burial, sediment thickness beneath the Muller Range may have been up to 2,200-3,200 m at a palaeogeothermal gradient of 25°C or up to 1,800-2,600 m at a paleogeothermal gradient of 30°C. This magnitude of burial seems reasonable compared to the preserved sequence in the Yangi Fold Belt. However it is largely unclear whether this Late Cretaceous to Eocene sequence was regionally continuous (e.g., Fig. 4.11a) or restricted to local depocentres. Further low-temperature thermochronology data from the WFTB could contribute to resolving this question.

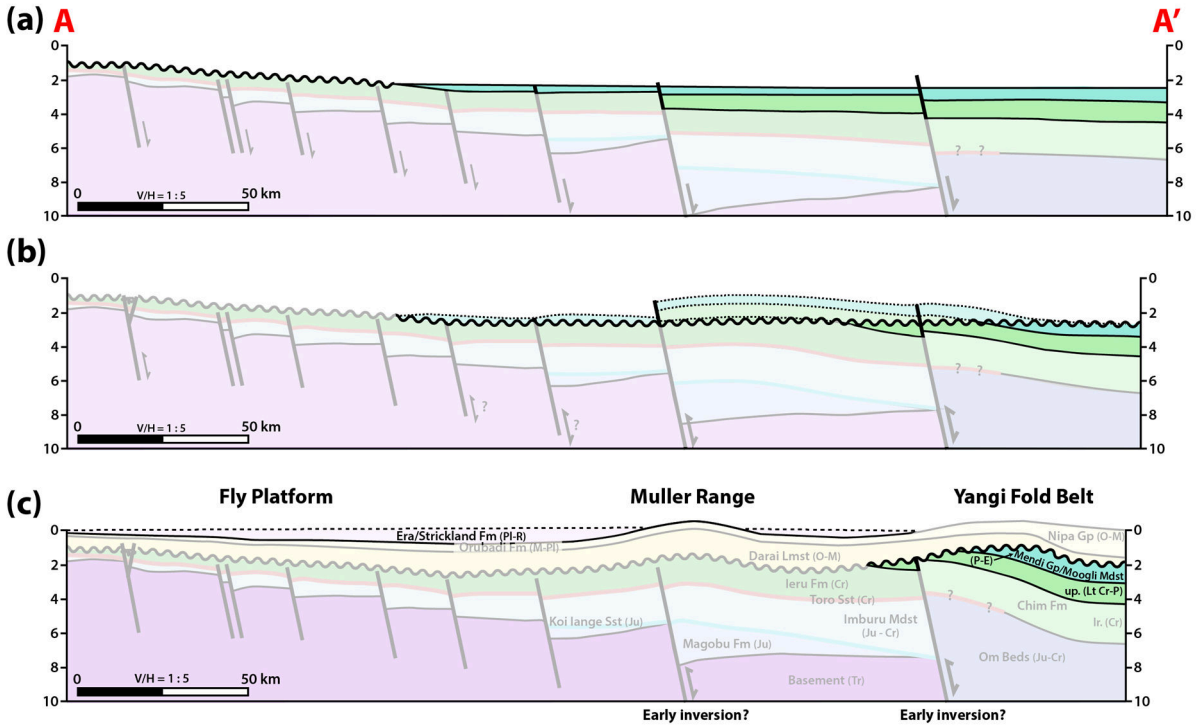

Figure 4.11. *Proposed schematic evolution of the Eastern Muller Range based on low-temperature thermochronology data and thermal modelling: (a) Early Eocene distribution of Late Cretaceous to Eocene sediments (opaque colours); (b) Eocene to Oligocene uplift and erosion associated with collision of the Sepik Terrane (Fig. 4.1a) in western PNG; (c) Late Miocene to Pliocene uplift associated with the initiation of the PFTB. Note syn-orogenic sediments (e.g., Era/Strickland formations) were deposited to the northeast and southwest of the Muller Range from the late Miocene to recent.*

4.6.3. Early Eocene to Oligocene cooling

Thermochronology data across the Muller Range also clearly record an Eocene to Oligocene cooling event of ~ 55-80°C (e.g., Fig. 4.9). As discussed in Section 4.6.1, AFT data across the Fly Platform records significantly less heating and cooling despite proximity to rifting in the Coral Sea. A rift-related heating mechanism is therefore unlikely to explain the magnitude of the thermal peak observed in the distal Muller Range located > 100 km further to the northwest. Thus, we suggest that Cenozoic collision and continental accretion at the northern PNG margin provides a possible mechanism to explain Eocene cooling in the Muller Range. We suggest the

collision of the Sepik Terrane (Fig. 4.1a) provides an appropriate process for significant uplift and erosion, particularly given the Muller Range is underlain by significant extensional structures and located < 50 km south of the suture zone delineated by the April Ultramafics (Fig. 4.1).

The geology and extent of the Sepik Complex is particularly poorly known due to the overlying Sepik and Ramu basins, nevertheless it is generally considered to make up a large proportion of the Mobile Belt (e.g., Zahirovic *et al*., 2016). Further ambiguity exists due to the late Miocene collision of the Finisterre and Adelbert terranes, which produced significant structural complexity and are the primary events recorded in isotopic data across the Mobile Belt (e.g., Crowhurst *et al*., 1996; Hill and Raza, 1999). Further plate realignment in the Pliocene led to intense sinistral strike-slip deformation that has also significantly disarticulated the northern PNG margin (Pigott *et al*., 1985; Crowhurst *et al*., 1997).

If the Sepik Terrane collided with northern PNG in the Palaeogene, it seems unlikely that the fold belt was undisturbed, particularly given its location directly adjacent to the suspected suture delineated by the April Ultramafics (Fig. 4.1a). As a comparison, the seismically active thrust front associated with the recent collision of the much smaller Finisterre and Adelbert terranes is > 250 km from the suspected suture (Marum Ophiolite) (Fig. 4.1a). Our new low-temperature thermochronology data and thermal models show a significant period of Eocene to Oligocene cooling across the Muller Range and provide, for the first time, potential evidence from the fold belt of the initiation of collision at the PNG margin.

We suggest that the Eocene to Oligocene collision of the Sepik Terrane in western PNG reactivated extensional structures across the WFTB and Fly Platform, including major faults around the present-day Om Beds and Muller Range (Fig. 4.11b). This activity uplifted Late Cretaceous to Eocene strata that subsequently underwent extensive erosion prior to the initiation of Darai Limestone deposition in the Oligocene. The > 40 km wide Darai Plateau on the Fly Platform (Fig. 4.1b and

4.12) may provide a contemporary analogue for this style of large-wavelength inversion. The uplift and erosion were restricted to an area directly to the south and southwest of the colliding terrane, with Late Cretaceous to Eocene sediments preserved in the adjacent Yangi Fold Belt (e.g., Fig. 4.2). These sediments led Hill *et al*. (2000) and Norvick (2003) to suggest that the coastline was located in the Yangi area over this time. However, missing section indicated from this study suggests that the Late Cretaceous to Eocene coastline may have been located further south, at least to the south of major extensional structures within and adjacent to the Muller Range.

Given this model invokes Eocene to Oligocene uplift and erosion, we may expect to see an angular unconformity at the Ieru Formation/Darai Limestone contact throughout the Muller Range. However, only limited evidence exists for this angular unconformity in either geological or geophysical data. There are several reasons why this postulated angular unconformity is not prominently evident in the Muller Range, including (1) Ieru Formation outcrop weathers quickly and is thus extremely limited, (2) 2D seismic reflection data is generally of insufficient quality to identify subtle dip variations, (3) the uppermost Ieru Formation is usually drilled with air-foam with no rock returns, and (4) the Ieru Formation is commonly highly deformed at the contact with the mechanically strong Darai Limestone, particularly near major inversion faults (e.g., Mahoney *et al.*, 2017) making it impossible to discriminate between pre- and post-Darai Limestone structuring. Thus we do not think it is reasonable to reject this model based on a lack of local evidence to support an angular unconformity.

4.6.4. Late Miocene to recent

Thermal history models also provide significant insight into the late Miocene to recent evolution of the Muller Range. High palaeotemperatures suggested from AFT and VR data from Lavani Valley and Strickland Gorge have previously been attributed to thick syn-orogenic sediment depocentres (e.g., Cecilia Trough, Tari Basin) extending across the Muller Range prior to late Miocene to recent uplift and

erosion (Amoco, 1982; Hill, 1989a). However, low-temperature thermochronology data consistently record only minor post-Darai Limestone heating (< 20°C), suggesting (1) < 1,000 m of syn-orogenic burial prior to uplift of the Muller Range, and (2) the absence of a significant regional heating event associated with late Miocene to Pliocene volcanics and intrusives identified throughout the Muller Range (e.g., Fig. 4.2). Thermal history models suggest that cooling, interpreted here to relate to uplift and erosion, began in the late Miocene (ca. 10-5 Ma) in the Strickland Gorge, consistent with the cooling of Strickland Basement (R34808) below the AFT closure temperature at ca. 4 Ma (Hill and Gleadow, 1990).

Therefore, the thick late Miocene to recent syn-orogenic sediments characterising neighbouring depocentres are likely to have thinned significantly, or have been completely absent, across the Muller Range. Although facies changes (Mahoney *et al*., 2017) and angular unconformities (e.g., Hornafius, 1993) have been observed towards the centre of the Muller Range, evidence of onlap has yet to be recognised on either flank. The present-day Darai Plateau may represent a useful analogue for the Muller Range at ca. 5 Ma. Active seismicity indicates the Darai Plateau is currently undergoing uplift and erosion, while Quaternary sediments are being deposited to the northeast and southwest by the Kikori and Turama river systems, respectively (Fig. 4.12). In the late Miocene, the Muller Range was undergoing uplift and erosion perhaps representing the most easterly extent of thick-skinned deformation documented in the NGFB in Indonesia (Weiland and Cloos, 1996; Cloos *et al*., 2005). Over this time, sediments were being deposited to the northeast (Tari Basin) and southwest (Cecilia Trough) by the proto-Tagari and Strickland river systems, respectively (Fig. 4.12). This suggests that the Muller Range formed early in the evolution of the WFTB and coeval to the formation of thick syn-orogenic depocentres to the northeast and southwest.

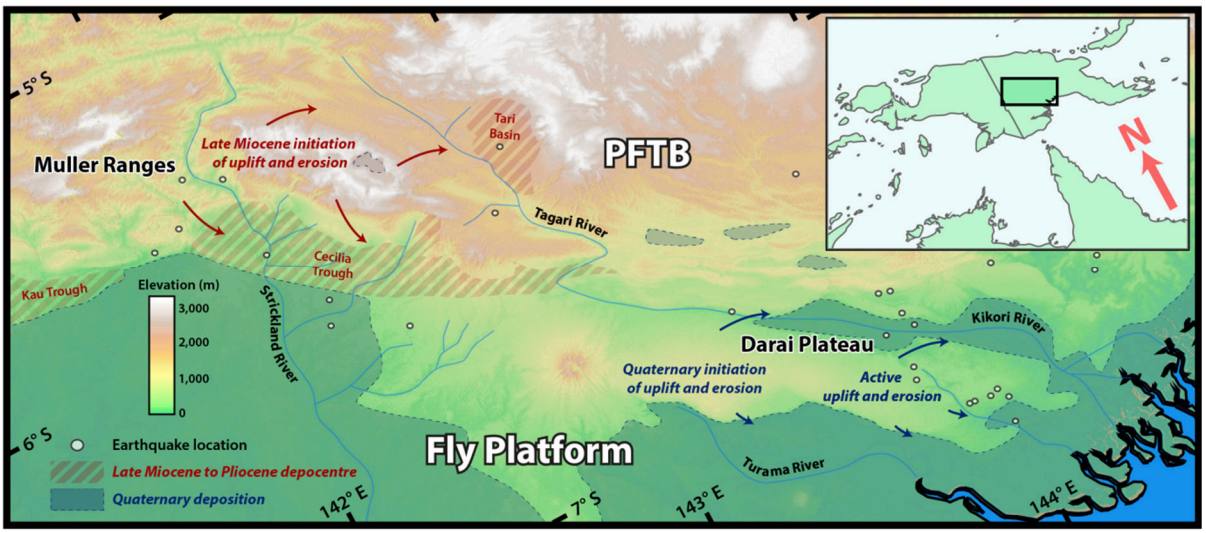

Figure 4.12. *Drainage system and syn-orogenic depocentre distribution across the Fly Platform and frontal PFTB. Arrows show the dominant direction of sediment transport away from uplifted areas. Earthquake locations sourced from Ekström et al. (2012).*

4.7. Conclusion

We have combined new and existing low-temperature thermochronology data with modern thermal history modelling techniques to provide insight into the thermotectonic history of the Muller Range in western PNG. Our models suggest two major episodes of cooling during the Cenozoic. The oldest cooling episode occurred during the Eocene to Oligocene and plausibly relates to the removal of 1,500-3,000 m of Late Cretaceous to Eocene section from the Muller Range area. The general absence of a thermal event at this time on the Fly Platform suggests that uplift and erosion in the Muller Range resulted from a local influence such as the collision of the Sepik Terrane with the northwest PNG margin. The youngest cooling episode during the late Miocene to recent resulted from the west-to-east propagation of uplift and erosion associated with the formation of the Papuan Fold and Thrust Belt. The Muller Range underwent initial uplift in the late Miocene, early in the evolution of the WFTB and coeval to the formation of thick syn-orogenic depocentres to the northeast and southwest. The new data and interpretations

presented here provide new constraints on the evolution of the Papuan Fold and Thrust Belt and have significant implications for tectonic reconstructions of PNG.

References

Amoco PNG Exploration Company, 1982. Lavani 1 well completion report, 137 pp.

Bain, J.H.C., Davies, H.L., Hohnen, P.D., Ryburn, R.J., Smith, I.E., Grainger, R., Tingey, R.J., Moffat, M.R., 1973. Geological Map of Papua New Guinea 1:1,000,000 scale. Bureau of Mineral Resources, Australia.

Bain, J.H.C., Mackenzie, D.E., Ryburn, R.J., 1975. Geology of the Kubor anticline, central highlands of Papua New Guinea. *Bureau of Mineral Resources, Geology and Geophysics Bulletin*, 155, Australian Government Publishing Service, 116 pp.

Baldwin, S.L., Fitzgerald, P.G., Webb, L.E., 2012. Tectonics of the New Guinea region. *Annual Review of Earth and Planetary Sciences*, 40, pp.495-520.

Barbarand, J., Carter, A., Wood, I., Hurford, T., 2003. Compositional and structural control of fission-track annealing in apatite. *Chemical Geology*, 198, pp.107-137.

Bennett, D.J., Brand, R.P., Mills, C.R., Morris, B.D., 2000. Exploration potential of the West Bosavi area, Papuan foreland basin, Papua New Guinea. In: Buchanan, P., Grainge, A., Thornton, R. (Eds.), *Petroleum exploration, development, and production in Papua New Guinea: proceedings of the fourth PNG Petroleum Convention*, Papua New Guinea Chamber of Mines and Petroleum, Port Moresby, pp.139-154.

Botsford, A., Endebrock, L., Harrington, A., 2012. Structural and stratigraphic evolution of the Gulf of Papua, Papua New Guinea: New insights from a modern 3D seismic survey. In: *AAPG International Conference and Exhibition 2012*, Search and Discovery Article #10456, 12 pp.

Bradley, G., 2014. Western Papuan Basin to Western Aure: Generalised Cenozoic - Jurassic Chronostratigraphy (unpubl.), 1 pp.

Brown, R.W., Beucher, R., Roper, S., Persano, C., Stuart, F., Fitzgerald, P., 2013. Natural age dispersion arising from the analysis of broken crystals. Part I: Theoretical basis and implications for the apatite (U–Th)/He thermochronometer. *Geochimica Cosmochimica Acta*, 122, pp.478-497.

Brown, C. M., Pieters, P.E., Robinson, G.P., 1975. Stratigraphic and structural development of the Aure trough and adjacent shelf and slope areas. *The Australian Petroleum Exploration Association Journal*, 15, pp.61-71.

Brown, C.M., Pigram, C.J., Swarko, S.K., 1980. Mesozoic stratigraphy and geological history of Papua New Guinea. *Palaeogeography, Palaeoclimatology, Palaeoecology*, 29, pp.301-322.

Brown, C.M., Robinson, G.P., 1982. Kutubu 1:250 000 geological series explanatory notes Sheet SB/54-12, Geological Survey of Papua New Guinea, PNG Department of Minerals and Energy, Port Moresby.

Buchanan, P., Warburton, J., 1996. The influence of pre-existing basin architecture in the development of the Papuan fold and thrust belt: implications for petroleum prospectivity. In: Buchanan, P. (Ed.), *Petroleum exploration, development, and production in Papua New Guinea: proceedings of the third PNG Petroleum Convention*, Papua New Guinea Chamber of Mines and Petroleum, Port Moresby, pp.89-109.

Callot, J.P., Sassi, W., Roure, F., Hill, K., Wilson, N., Divies, R., 2017. Pressure and Basin Modeling in Foothill Belts: A study of the Kutubu area, Papua New Guinea Fold and Thrust Belt. In: AbuAli, M., Moretti, I., Nordgard Bolas, H. (Eds), *Petroleum systems analysis — case studies*, AAPG Memoir, 114, pp.165-190.

Carman, G., 1993. Palaeogeography of the Coral Sea, Darai and Foreland Megasequences in the eastern Papuan Basin. In: Carman, G., Carman, Z. (Eds.), *Petroleum exploration, development, and production in Papua New Guinea: proceedings of the second PNG Petroleum Convention*, Papua New Guinea Chamber of Mines and Petroleum, Port Moresby, pp.291-309.

Carter, A., Gallagher, K., 2004. Characterizing the significance of provenance on the inference of thermal history models from apatite fission-track data—a synthetic data study. In: Bernet, M., Spiegel, C. (Eds.), *Detrital thermochronology — provenance analysis, exhumation, and landscape evolution of mountain belts*, Colorado, Geological Society of America Special Paper, 378, pp.7-23.

Cloos, M., Sapiie, B., Quarles van Ufford, A., Weiland, R.J., Warren, P.Q., McMahon, T.P., 2005. Collisional delamination in New Guinea: The geotectonics of subducting slab breakoff. *Geological Society of America Special Paper*, 400, 51 pp.

Cooper, G., Kendrick, D., Waina, F., Hamilton, C., Nongkas, M., 2012. New insights in to the structural and thermal development of the Papuan Foreland: Implications for hydrocarbon charge and prospectivity. In: *Eastern Australasian Basins Symposium IV*, Brisbane, 14 pp.

Crowhurst, P.V., Hill, K.C., Foster, D.A., Bennett, A.P., 1996. Thermochronological and geochemical constraints on the tectonic evolution of northern Papua New Guinea. *Geological Society, London, Special Publications*, 106(1), pp.525-537.

Crowhurst, P., Hill, K., Foster, D., 1997. The structural and tectonic development of the Frieda River Mineral district, NW Papua New Guinea. In Hancock, G. (Ed.), *Proceedings of the PNG Geology, Exploration and Mining Conference 1997*, Australasian Institute of Mining and Metallurgy, pp.51-60.

Crowhurst, P., Maas, R., Hill, K.C., Foster, D.A., Fanning, C.M., 2004. Isotopic constraints on crustal architecture and Permo-Triassic tectonics in New Guinea: Possible links with eastern Australia. *Australian Journal of Earth Sciences*, 51, pp.107-122.

Danišík, M., McInnes, B.I., Kirkland, C.L., McDonald, B.J., Evans, N.J., Becker, T., 2017. Seeing is believing: Visualization of He distribution in zircon and implications for thermal history reconstruction on single crystals. *Science Advances*, 3(2), e1601121.

Davies, H., Norvick, M., 1974. Blucher Range 1:250 000 geological series explanatory notes Sheet SB/54-07, Geological Survey of Papua New Guinea, PNG Department of Minerals and Energy, Port Moresby.

Davies, H., 1983. Wabag 1:250 000 geological series explanatory notes Sheet SB/54-8, Geological Survey of Papua New Guinea, PNG Department of Minerals and Energy, Port Moresby.

Davies, H.L., 1990. Structure and evolution of the Border Region of New Guinea. In: Carman, G., Carman, Z. (Eds.), *Petroleum exploration, development, and production in Papua New Guinea:*

proceedings of the first PNG Petroleum Convention, Papua New Guinea Chamber of Mines and Petroleum, Port Moresby, pp.245-269.

Davies, H.L., Winn, R.D. KenGemar, P., 1996. Evolution of the Papuan Basin: A view from the orogeny. In: Carman, G., Carman, Z. (Eds.), *Petroleum exploration, development, and production in Papua New Guinea: proceedings of the second PNG Petroleum Convention*, Papua New Guinea Chamber of Mines and Petroleum, Port Moresby, pp.53-62.

Davies, H.L., Perembo, R.C.B., Winn, R.D., Kengemar, P., 1997. Terranes of the New Guinea Orogen. In: Hancock, G. (Ed.), *Proceedings of the PNG Geology, Exploration and Mining Conference*, Madang, Australian Institute of Mining and Metallurgy, pp.61-66.

Davies, H.L., 2012. The geology of New Guinea—the cordilleran margin of the Australian continent. *Episodes*, 35(1), pp.87-102.

Denison, C. N., 1990. Palynostratigraphic revision of Amoco Lavani-1 well, Papua New Guinea (unpubl.), 6 pp.

Donelick, R.A., 1993. Method of fission track analysis utilizing bulk chemical etching of apatite. U.S. Patent 5,267,274.

Donelick, R.A., O'Sullivan, P.B., Ketcham, R.A., 2005. Apatite fission-frack analysis. *Reviews in Mineralogy and Geochemistry*, 58, pp.49-94.

Dow, D.B., Smit, J.A., Bain, J.H.C., Ryburn, R.J., 1972. Geology of the Sepik region, New Guinea. *Bureau of Mineral Resources Bulletin*, 133, 88 pp.

Dow, D.B. 1977. A geological synthesis of Papua New Guinea. *Bureau of Mineral Resources Bulletin*, 201, 58 pp.

Duddy, I.R., Green, P.F., Bray, R.J., Hegarty, K.A., 1994. Recognition of the thermal effects of fluid flow in sedimentary basins. *Geological Society, London, Special Publications*, 78 (1), pp.325-345.

Edwards, A. B., 1950. The petrology of the Miocene sediments of Aure trough, Papua. *Proceedings of the Royal Society of Victoria*, 60, pp.123-148.

Eisenberg, L.I., 1996. Strontium isotope analysis and structural interpretation of P'nyang Anticline, Papuan Fold Belt, Western Highlands Province, Papua New Guinea. In: Buchanan, P. (Ed.), *Petroleum exploration, development, and production in Papua New Guinea: proceedings of the third PNG Petroleum Convention*, Papua New Guinea Chamber of Mines and Petroleum, Port Moresby, pp.231-244.

Ekström, G., Nettles, M., Dziewonski, A., 2012. The global CMT project 2004-2010: Centroid-moment tensors for 13,017 earthquakes. *Physics of the Earth and Planetary Interiors*, 200, pp.1-9.

Farley, K.A. 1996. The effects of long alpha-stopping distances on (U-Th)/He ages. *Geochimica Cosmochimica Acta*, 60, pp.4223-4229.

Farley, K.A., 2000. Helium diffusion from apatite: General behavior as illustrated by Durango fluorapatite. *Solid Earth*, 105, pp.2903-2914.

Farley, K.A., 2002. (U-Th)/He dating: techniques, calibrations, and applications. *Reviews in Minerology and Geochemistry*, 47, pp.819-844.

Farley, K.A., Stockli, D.F., 2002. (U-Th)/He Dating of Phosphates: Apatite, Monazite, and Xenotime. *Reviews in Minerology and Geochemistry*, 48, pp.559-577.

Findlay, A.L., Leckie, G.G., 1973. Report on the Lavani anticline geological survey, Permit 46, Papua New Guinea. BP Petroleum Development Australia Pty Ltd Report 26 (unpubl.). Geological Survey of Papua New Guinea Data File 12 BS.

Fischer, M.W., Warburton., 1996. The importance of pre-Tertiary basin architecture for hydrocarbon accumulation in the Papuan Fold and Thrust Belt: models, analogues and implications. In: Buchanan, P. (Ed.), *Petroleum exploration, development, and production in Papua New Guinea: proceedings of the third PNG Petroleum Convention*, Papua New Guinea Chamber of Mines and Petroleum, Port Moresby, pp.111-131.

Fitzgerald, P.G., Baldwin, S.L., Webb, L.E., O'Sullivan, P.B., 2006. Interpretation of (U–Th)/He single grain ages from slowly cooled crustal terranes: A case study from the Transantarctic Mountains of southern Victoria Land. *Chemical Geology*, 225, pp.91-120.

Francis, G., 1990. The North New Guinea Basin, and associated intra-basins. In: Carman, G., Carman, Z. (Eds.), *Petroleum exploration, development, and production in Papua New Guinea: proceedings of the first PNG Petroleum Convention*, Papua New Guinea Chamber of Mines and Petroleum, Port Moresby, pp.445-460.

Galbraith, R.F., Laslett, G.M., 1993. Statistical models for mixed fission track ages. *Nuclear Tracks and Radiation Measurements*, 21(4), pp.459-470.

Galbraith, R.F., 2005. *Statistics for fission track analysis*. Chapman and Hall/CRC Press, 219 pp.

Gallagher, K., 1995. Evolving temperature histories from apatite fission-track data. *Earth and Planetary Science Letters*, 136(3-4), pp.421-435.

Gallagher, K., Stephenson, J., Brown, R., Holmes, C., Fitzgerald, P., 2005. Low temperature thermochronology and modeling strategies for multiple samples 1: Vertical profiles. *Earth and Planetary Science Letters*, *237*(1-2), pp.193-208.

Gallagher, K., Charvin, K., Nielsen, S., Sambridge, M., Stephenson, J., 2009. Markov chain Monte Carlo (MCMC) sampling methods to determine optimal models, model resolution and model choice for Earth Science problems. *Marine and Petroleum Geology*, 26(4), pp.525-535.

Gallagher, K., 2012. Transdimensional inverse thermal history modeling for quantitative thermochronology. *Journal of Geophysical Research*, 117, pp.1-16.

Gautheron, C., Tassan-Got, L., Barbarand, J., Pagel, M., 2009. Effect of alpha-damage annealing on apatite (U–Th)/He thermochronology. *Chemical Geology*, 266, pp.157-170.

Gleadow, A.J.W., Duddy, I.R., 1981. A natural long-term track annealing experiment for apatite. *Nuclear Tracks*, 5, pp.169-174.

Gleadow, A.J., Belton, D., Kohn, B., Brown, R.W., 2002. Fission track dating of phosphate minerals and the thermochronology of apatite. *Reviews in Mineralogy and Geochemistry*, 48(1), pp.579-630.

Gleadow, A.J.W., Gleadow, S.J., Belton, D.X., Kohn, B.P., Krochmal, M.S., Brown, R.W., 2009. Coincidence mapping - a key strategy for the automatic counting of fission tracks in natural minerals. In: Lisker, F., Ventura, B., Glasmacher, U.A. (Eds.), *Thermochronological methods: from*

palaeotemperature constraints to landscape evolution models. Geological Society, London, Special Publications, 324, pp.25-36.

Gleadow, A., Harrison, M., Kohn, B., Lugo-Zazueta, R., Phillips, D., 2015. Fish Canyon Tuff apatite: a new look at an old low-temperature thermochronology standard. *Earth and Planetary Science Letters*, 424, pp.95-108.

Glen, R.A., 2005. The Tasmanides of eastern Australia. *Geological Society, London, Special Publication*, 246, pp.23-96.

Green, P.F., Duddy, I.R., Gleadow, A.J.W., Tingate, P.R., Laslett, G.M., 1986. Thermal annealing of fission tracks in apatite 1. A qualitative description. *Chemical Geology:Isotope Geoscience section*, 59, pp.237-253.

Green, P.F., Duddy, I., 2016. Episodic regional burial and subsequent exhumation exert a major influence on hydrocarbon prospectivity. In: *AAPG/SEG International Conference and Exhibition 2015*, Search and Discovery Article #30449, 26 pp.

Guenthner, W.R., Reiners, P.W., Ketcham, R.A., Nasdala, L., Giester, G., 2013. Helium diffusion in natural zircon: radiation damage, anisotropy, and the interpretation of zircon (U-Th)/He thermochronology. *American Journal of Science*, 313, pp.145–198.

Gunson, M., Haig, D.W., Kruman, B., Mason, R.A., Perembo, R.C.B., Stewart, R., 1997. Stratigraphic reconstruction of the Porgera region, Papua New Guinea. In: Hancock, G. (Ed.), *Proceedings of the PNG Geology, Exploration and Mining Conference*, Madang, Australian Institute of Mining and Metallurgy, pp.99-108.

Gunson, M., Hall, G., Johnston, M 2000. Foraminiferal coloration index as a guide to hydrothermal gradients around the Porgera Intrusive Complex, Papua New Guinea. *Economic Geology*, 95, pp.271-282.

Hall, R., 2012. Late Jurassic–Cenozoic reconstructions of the Indonesian region and the Indian Ocean. *Tectonophysics*, 570-571, pp.1-41.

Hanani, A., 2012. The Geology and Structural Style of the Juha Gas Field, Papua New Guinea. Honours Thesis (unpubl.), The University of New South Wales, Sydney, 214 pp.

Hanani, A., Lennox, P., Hill, K.C., 2016. The Geology and Structural Style of the Juha Gas Field, Papua New Guinea. *ASEG Extended Abstracts 2016*, pp.1-7.

Haq, B.U., Hardenbol, J., Vail, P.R., 1987. Chronology of fluctuating sea levels since the Triassic. *Science*, 235, pp.1156-1167.

Haq, B.U., 2014. Cretaceous eustasy revisited. *Global and Planetary Change*, 113, pp.44-58.

Hasebe, N., Barbarand, J., Jarvis, K., Carter, A., Hurford, A.J., 2004. Apatite fission-track chronometry using laser ablation ICP-MS. *Chemical Geology*, 207(3-4), pp.135-145.

Hill, K.C., 1989a. The structure, timing and thermal history of the Papuan Fold Belt, Papua New Guinea. PhD Thesis (unpubl.). The University of Melbourne, Melbourne.

Hill, K.C., 1989b. The Muller Anticline, Papua New Guinea; basement cored, inverted extensional fault structures with opposite vergence. *Tectonophysics*, 158, pp.227-245.

Hill, K.C., Gleadow, A., 1989. Uplift and thermal history of the Papuan Fold Belt, Papua New Guinea: Apatite Fission track analysis. *Australian Journal of Earth Sciences*, 36, pp.515-539.

Hill, K.C., Gleadow, A., 1990. Apatite fission track analysis of the Papuan Basin. In: Carman, G., Carman, Z. (Eds.), *Petroleum exploration, development, and production in Papua New Guinea: proceedings of the first PNG Petroleum Convention*, Papua New Guinea Chamber of Mines and Petroleum, Port Moresby, pp.119-136.

Hill, K.C., Medd, D., Darvall, P., 1990. Structure, stratigraphy, geochemistry and hydrocarbons in the Kagua-Kubor area, Papua New Guinea. In: Carman, G., Carman, Z. (Eds.), *Petroleum exploration, development, and production in Papua New Guinea: proceedings of the first PNG Petroleum Convention*, Papua New Guinea Chamber of Mines and Petroleum, Port Moresby, pp.351-366.

Hill, K.C., 1991. Structure of the Papuan Fold Belt, Papua New Guinea. *The American Association of Petroleum Geologists Bulletin*, 75, pp.857-872.

Hill, K.C., Raza, A., 1999. Arc-continent collision in Papua Guinea: Constraints from fission track thermochronology. *Tectonics*, 18(6), pp.950-966.

Hill, K.C., Norvick, M., Keetley, J., Adams, A., 2000. Structural and stratigraphic shelf-edge hydrocarbon plays in the Papuan Fold Belt. In: Buchanan, P., Grainge, A., Thornton, R. (Eds.), *Petroleum exploration, development, and production in Papua New Guinea: proceedings of the fourth PNG Petroleum Convention*, Papua New Guinea Chamber of Mines and Petroleum, Port Moresby, pp.67-85.

Hill, K.C., Hall, R., 2003. Mesozoic-Cenozoic evolution of Australia's New Guinea margin in a west Pacific context. *Geological Society of America Special Papers*, 372, pp.265-290.

Hill, K.C., Lucas, K., Bradey, K., 2010. Structural styles in the Papuan Fold Belt, Papua New Guinea: constraints from analogue modelling. In: Goffey, G. (Ed.), *Hydrocarbons in Contractional Belts*, Geological Society, London, Special Publications, 348, pp.33-56.

Hill, K.C, Wightman, R., Munro, L., 2015. Structural Style in the Eastern Papuan Fold Belt, From Wells, Seismic, Maps and Modelling. In: *AAPG/SEG International Conference and Exhibition 2015*.

Home, P., Dalton, D., Brannan, J., 1990. Geological evolution of the Western Papuan Basin. In: Carman, G., Carman, Z. (Eds.), *Petroleum exploration, development, and production in Papua New Guinea: proceedings of the first PNG Petroleum Convention*, Papua New Guinea Chamber of Mines and Petroleum, Port Moresby, pp.107-118.

Hornafius, J.S., 1993. The 1990-1991 Muller Range Geological Survey – PPL 93. Mobil Exploration Niugini (unpubl.).

House, M.A., Farley, K.A., Stockli, D., 2000. Helium chronometry of apatite and titanite using Nd-YAG laser heating. *Earth and Planetary Science Letters*, 183(3-4), pp.365-368.

Hutchison, D.S., Norvick, M.S., 1978. Wewak 1:250,000 geological series explanatory notes Sheet SA/54-16, Geological Survey of Papua New Guinea, PNG Department of Minerals and Energy, Port Moresby.

Japsen, P., Chalmers, J.A., Green, P.F., Bonow, J.M., 2012. Elevated, passive continental margins: Not rift shoulders, but expressions of episodic, post-rift burial and exhumation. *Global and Planetary Change*, 90, pp.73-86.

Jenkins, D., 1974. Detachment tectonics in western Papua New Guinea. *Geological Society of America Bulletin*, 85, pp.533-548.

Jenkins, D., White, M.F., 1970. Report on the Strickland River survey, Permit 46, Papua. BP Petroleum Development Report 89 (unpubl.). Geological Survey of Papua New Guinea Data File 4 BS.

Johnson, J. E., Flowers, R. M., Baird, G. B., Mahan, K. H. 2017. "Inverted" zircon and apatite (U–Th)/He dates from the Front Range, Colorado: High-damage zircon as a low-temperature (<50 °C) thermochronometer. *Earth and Planetary Science Letters*, 466, pp.80-90.

Jones, R.W., 1991. Cenozoic stratigraphy of the Papuan Basin, Papua New Guinea (unpubl.). GSPNG Open File No. F/R/91-215.

Kawagle, S.A., Meyers, J.B., 1996. Structural and sequence geometry of the Kiunga Area, Papuan Foreland Basin, Papua New Guinea. In: Buchanan, P. (Ed.), *Petroleum exploration, development, and production in Papua New Guinea: proceedings of the third PNG Petroleum Convention*, Papua New Guinea Chamber of Mines and Petroleum, Port Moresby, pp.175-193.

Keenan, S.E., Hill, K.C., 2015. The Mananda Anticline, Papua New Guinea: A third Oil Discovery, Appraisal Programme and Deep Potential. In: *AAPG/SEG International Conference and Exhibition 2015*.

Ketcham, R.A., 2005. Forward and inverse modeling of low-temperature thermochronology data. *Reviews in Mineralogy and Geochemistry*, 58, pp.275-314.

Ketcham, R.A., Carter, A., Donelick, R.A., Barbarand, J., Hurford, A.J., 2007. Improved modeling of fission-track annealing in apatite. *American Mineralogist*, 92, pp.799-810.

Laslett, G.M., Green, P..F., Duddy, I.R., Gleadow, A.J.W., 1987. Thermal annealing of fission tracks in apatite 2. A quantitative analysis. *Chemical Geology: Isotope Geoscience section*, 65, pp.1-13.

Löffler, E., MacKenzie, D., Webb, A., 1980. Potassium-argon ages from some of the Papua New Guinea Highlands volcanoes, and their relevance to Pleistocene geomorphic history. *Journal of the Geological Society of Australia*, 26, pp.387-397.

Ludwig, K.R., 2003. User's manual for Isoplot 3.00, a geochronlogical toolkit for microsoft excel. *Berkeley Geochronology Center Special Publication*, 4, pp.25-32.

Lund, D., Waples, D., Robinson, P. 1998. The thermal history and hydrocarbon maturation, generation and migration in the Foreland Region of the Papuan Basin. Report for the PPL179, PPL188 and PPL193 Joint Ventures (unpubl.), Oil Search Ltd.

Mackintosh, V., Kohn, B., Gleadow, A., Tian, Y., 2017. Phanerozoic morphotectonic evolution of the Zimbabwe Craton: Unexpected outcomes from a multiple low-temperature thermochronology study. *Tectonics*, 36(10), pp.2044-2067.

Mahoney, L., Hill, K., McLaren, S., Hanani, A., 2017. Complex fold and thrust belt structural styles: Examples from the Greater Juha area of the Papuan Fold and Thrust Belt, Papua New Guinea. *Journal of Structural Geology*, 100, pp.98-119.

McConachie, B., Lanzilli, E., 2000. Stanley gas condensate field discovery and the oil potential of the Western Papuan Basin. In: Buchanan, P., Grainge, A., Thornton, R. (Eds.), *Petroleum exploration, development, and production in Papua New Guinea: proceedings of the fourth PNG Petroleum Convention*, Papua New Guinea Chamber of Mines and Petroleum, Port Moresby, pp.427-442.

McConachie, B., Lanzilli, E., Kendrick, D., Burge, C., 2000. Extensions of the Papuan Basin foreland geology into Eastern Irian Jaya (West Papua) and the New Guinea Fold Belt in Papua New Guinea. In: Buchanan, P., Grainge, A., Thornton, R. (Eds.), *Petroleum exploration, development, and production in Papua New Guinea: proceedings of the fourth PNG Petroleum Convention*, Papua New Guinea Chamber of Mines and Petroleum, Port Moresby, pp.219-237.

Muller, R.D., Gaina, C., Tikku, A., Mihut, D., Cande, S.C., Stock, J.M., 2000. Mesozoic/Cenozoic tectonic events around Australia. In: Richards, M.A., Gordon, R.G. van der Hilst, R.D. (Eds.), *The History and Dynamics of Global Plate Motions*, American Geophysical Union Geophysical Monograph, 121, pp.161-188.

Muller, R.D., Flament, N, Matthews, K.J., Williams, S.E., 2016. Formation of Australian continental margin highlands driven by plate-mantle interaction. *Earth and Planetary Science Letters*, 441, pp.60-70.

Murray, C.G., 2003. Granites of the northern New England Orogen. In: *The Ishihara Symposium: Granites and associated metallogenesis*, Geoscience Australia, pp.101-108.

Norvick, M.S., 2003. New palaeogeographic maps of the northern margins of the Australian plate: updated report (unpubl.). Report for Geoscience Australia, September 2003.

Norvick, M.S., Hutchison, D.S., 1980. Aitape-Vanimo 1:250,000 geological series explanatory notes Sheet SA/54-15, Geological Survey of Papua New Guinea, PNG Department of Minerals and Energy, Port Moresby.

Page, R., 1976. Geochronology of igneous and metamorphic rocks in the New Guinea Highlands. *Bureau of Mineral Resources Australia Bulletin*, 162, 117 pp.

Parris K.R., 1994. Basement structures and implications for control of igneous activity, Central Ranges, Irian Jaya, Indonesia. PT Freeport Indonesia Report (unpubl.).

Pigott, J.D., Trumbly, N.I., O'Neal, M.V., 1985. Northern New Guinea wrench fault system: a manifestation of Late Cenozoic interactions between Australian and Pacific plates. *Tectonics*, 4, pp.613-620.

Pigram, C., Panggabean, H., 1984. Rifting of the northern margin of the Australian continent and the origin of some microcontinents in eastern Indonesia. *Tectonophysics*, 107, pp.331-353.

Pigram, C., Davies, H.L. 1987. Terranes and accretion history of the New Guinea Orogen. *Bureau of Mineral Resources Journal of Australian Geology and Geophysics*, 10, pp.193-212.

Pigram, C., Symonds, P.A., 1991. A review of the timing of the major tectonic events in the New Guinea Orogen. *Journal of Southeast Asian Earth Sciences*, 6, pp.307-318.

Pigram, C., Symonds, P.A., 1993. Eastern Papuan Basin—A new model for the tectonic development and implications for petroleum prospectivity. In: Carman, G., Carman, Z. (Eds.), *Petroleum exploration, development, and production in Papua New Guinea: proceedings of the second PNG*

Petroleum Convention, Papua New Guinea Chamber of Mines and Petroleum, Port Moresby, pp.213-231.

Reiners, P.W., Farley, K.A., 2001. Influence of crystal size on apatite (U-Th)/He thermochronology: an example from the Bighorn Mountains, Wyoming. *Earth and Planetary Science Letters*, 188, pp.413-420.

Reiners, P.W., Ehlers, T.A., Zeitler, P.K., 2005. Past, present and future of thermochronology. In: Reiners, P.W., Ehlers, T.A. (Eds.), *Low-temperature thermochronology: techniques, interpretations, and applications*, pp.1-18.

Rogerson, R.J., Hilyard, D., Finlayson, E.J., Holland, D.S., Nion, S.T.S., Sumaiang, R.S., Duguman, J., Loxton, C.D.C., 1987. The geology and mineral reserves of the Sepik headwaters region, Papua New Guinea. *Geological Survey of Papua New Guinea Memoir*, 12, 130 pp.

Sari, J., Failing, R., Wulff, K., 1996. The Giero Sandstone: A potentially new play in the Papuan Basin. In: Buchanan, P. (Ed.), *Petroleum exploration, development, and production in Papua New Guinea: proceedings of the third PNG Petroleum Convention*, Papua New Guinea Chamber of Mines and Petroleum, Port Moresby, pp.301-312.

Schellart, W.P., Spakman, W., 2015. Australian plate motion and topography linked to fossil New Guinea slab below Lake Eyre. *Earth and Planetary Science Letters*, 421, pp.107-116.

Schofield, S., 2000. The Bosavi Arch and Komewu Fault Zone: Their control on basin architecture and the prospectivity of the Papuan Foreland. In: Buchanan, P., Grainge, A., Thornton, R. (Eds.), *Petroleum exploration, development, and production in Papua New Guinea: proceedings of the fourth PNG Petroleum Convention*, Papua New Guinea Chamber of Mines and Petroleum, Port Moresby, pp.101-122.

Shuster, D.L., Flowers, R.M., Farley, K.A., 2006. The influence of natural radiation damage on helium diffusion kinetics in apatite. *Earth and Planetary Science Letters*, 249, pp.148-161.

Sweeney, J.J., Burnham, A.K., 1990. Evaluation of a simple model of vitrinite reflectance based on chemical kinetics. *AAPG Bulletin*, 74, pp.1559-70.

Tcherepanov, E.N., Droxler, A.W., Lapointe, P., Dickens, G.R., Bentley, S.J., Beaufort, L., Peterson, L.C., Daniell, J., Opdyke, B.N., 2008. Neogene evolution of the mixed carbonate-siliciclastic system in the Gulf of Papua, Papua New Guinea. *Journal of Geophysical Research: Earth Surface*, 113, 15 pp.

Thornton, R., Emmett, J., Laslo, J., Gottschalk, R., 1996. Integrated structural and stratigraphic analysis in PPL 175, Papuan Fold Belt, Papua New Guinea. In: Buchanan, P. (Ed.), *Petroleum exploration, development, and production in Papua New Guinea: proceedings of the third PNG Petroleum Convention*, Papua New Guinea Chamber of Mines and Petroleum, Port Moresby, pp.195-215.

Tobin, J., Zahirovic, S., Hassan, R., Rey, P., 2018. Tectonic and Geodynamic Evolution of the Northern Australian Margin and New Guinea. *ASEG Extended Abstracts 2018*, 7 pp.

USGS, 2015. Shuttle Radar Topography Mission, 1-arc second, Global Land Cover Facility, University of Maryland, College Park, Maryland. Accessed through USGS EarthExplorer.

van Ufford, A.Q., Cloos, M., 2005. Cenozoic tectonics of New Guinea. *The American Association of Petroleum Geologists Bulletin*, 89(1), pp.119-140.

Vermeesch, P., 2008. Three new ways to calculate average (U–Th)/He ages. *Chemical Geology*, 249(3-4), pp.339-347.

Webb, A., 1973. Geochronology report on samples submitted by BMR West Sepik party. Australian Mineral Development Laboratories Report AN3049/73 (unpubl.)

Weiland, R.J., Cloos, M., 1996. Pliocene-Pleistocene asymmetric unroofing of the Irian fold belt, Irian Jaya, Indonesia: Apatite fission-track thermochronology. *Geological Society of America Bulletin*, 108(11), pp.1438-1449.

Weissel, J.K., Watts, A.B., 1979. Tectonic evolution of the Coral Sea Basin. *Journal of Geophysical Research*, 84, pp.4572-4582.

White, M.F., Boxall, A.M., Findlay, A.L., Sweetman, I.A.D., Visser, B., 1973. Report on the Fly-Palmer geological survey. BP Petroleum Development Report (unpubl.). Geological Survey of Papua New Guinea data file 4 BQ.

Wildman, M., Brown, R., Beucher, R., Persano, C., Stuart, F., Gallagher, K., Schwanethal, J., Carter, A., 2016. The chronology and tectonic style of landscape evolution along the elevated Atlantic continental margin of South Africa resolved by joint apatite fission track and (U-Th-Sm)/He thermochronology. *Tectonics*, 35, pp.511-545.

Wilson, C., Barrett, R., Howe, R., Leu, L.K., 1993. Occurrence and character of outcropping limestones in the Sepik Basin: Implications for hydrocarbon exploration. In: Buchanan, P. (Ed.), *Petroleum exploration, development, and production in Papua New Guinea: proceedings of the third PNG Petroleum Convention*, Papua New Guinea Chamber of Mines and Petroleum, Port Moresby, pp.111-124.

Wolfe, M.R., Stockli, D.F., 2010. Zircon (U-Th)/He thermochronometry in the KTB drill hole, Germany, and its implications for bulk He diffusion kinetics in zircon. *Earth and Planetary Science Letters*, 295, pp.69-82.

Zahirovic, S., Seton, M., Müller, R. D., 2014. The Cretaceous and Cenozoic tectonic evolution of Southeast Asia. *Solid Earth*, 5, pp.227-273.

Zahirovic, S., Matthews, K. J., Flament, N., Müller, R. D., Hill, K. C., Seton, M., Gurnis, M., 2016. Tectonic evolution and deep mantle structure of the eastern Tethys since the latest Jurassic. *Earth Science Reviews*, 162, pp.293-337.

Supplementary material A4: Methodology

A4.1. Apatite fission track method

Apatite grains were mounted in epoxy resin (250 μm thick), ground and polished to an optical finish (1 μm) and etched in 5N HNO_3 at 20°C for 20 seconds to reveal the spontaneous fission tracks. Reflected light images of etched mounts were considerably improved through the application of a gold coating (5-7 nm thick) using a vacuum unit. Apatite grains favoured for analysis were characterised by (1) polished surfaces parallel to the crystallographic c-axis, (2) homogeneous track distributions, and (3) minimal dislocations and imperfections.

AFT analysis was carried out using an autonomous digital microscope operating under *Autoscan TrackWorks* control software (Gleadow *et al*., 2009). Spontaneous tracks were counted automatically on digital image sets using *FastTracks* image analysis software and manually corrected where necessary (Gleadow *et al*., 2009). *FastTracks* was also used to manually measure 3D confined track lengths and automatically determine their orientations in regards to the crystallographic c-axis direction; allowing anisotropic annealing and etching to be addressed in subsequent thermal modelling. Dpar (the long axis of a track etch pit parallel to the crystallographic c-axis) was used as a proxy for chemical composition (Donelick, 1993).

^{238}U concentrations were measured directly using laser-ablation ICP-MS (inductively coupled mass spectrometry) with uranium concentrations calibrated against NIST 612 standard glass with Mud Tank and Durango apatite as secondary reference standards. Fission Track ages were calculated from the spontaneous track densities and single grain ^{238}U concentrations following Hasebe *et al*. (2004) using an aggregate constant of 2.001×10^{-3}.

A4.2. (U-Th-Sm)/He method

(U-Th-Sm)/He analysis followed the protocol of House *et al*. (2000) for laser He extraction from both apatite and zircon grains. Clear, non-fractured grains were generally favoured for analysis, but given low apatite yields were not always available. Grain geometries were microscopically imaged and measured for applying α-ejection correction (Farley *et al*., 1996), prior to being loaded into platinum capsules. Although single grain analyses were preferred, in some cases ^{4}He yields were too low and multiple grain capsules were required.

Apatite grains were outgassed using laser under vacuum at 900°C for 5 minutes, while zircon grains were outgassed at 1200°C for 20 minutes. ^{4}He content was determined using a Balzers quadrupole mass spectrometer with a hot blank run after each extraction to verify complete outgassing. Outgassed grains were then dissolved and analysed for parent isotopes using solution ICP-MS. Analytical uncertainties for The University of Melbourne helium facility are conservatively assessed to be ~6.2%, including the α-ejection correction, an estimated 5 μm uncertainty in grain dimensions, gas analysis (estimated as < 1%) and ICP-MS analytical uncertainties. This does not account for possible heterogeneity in parent isotope distributions.

Supplementary material B4: Existing AFT dataset

Table B4.1. *Existing Muller Range apatite fission track dataset obtained by Hill and Gleadow (1989; 1990) using the external detector method*

Region / Sample No.	Formation	No. of grains	ρ_D (N_D) x10^{6}cm^{-2}	ρ_s (N_s) x10^{6}cm^{-2}	ρ_i (N_i) x10^{6}cm^{-2}	Correlation Coefficient	[b]Dispersion (%)	Chi-squared probability (%)	Pooled age (Ma ± 1σ)	[a]Central age (Ma ± 1σ)	Uranium (ppm)	N_L	MTL (µm ± SE)	SD (µm)
WMR														
R34832	Ieru Fm	20	1.240 (5282)	0.737 (777)	1.869 (1971)	0.929	21	<1	85.6 ± 4.0	79.8 ± 8.2	19.6	100	12.1 ± 0.2	1.77
R34831	Ieru Fm	20	1.240 (5282)	0.169 (189)	1.165 (1300)	0.824	65	<1	31.7 ± 2.5	47.2 ± 8.7	12.2	61	10.7 ± 0.2	1.85
Strick North														
R34809	Ieru Fm	20	1.197 (5140)	0.734 (330)	2.610 (1173)	0.938	45	<1	58.7 ± 3.8	46.9 ± 7.6	28.6	100	10.3 ± 0.2	2.23
R34810	Ieru Fm	21	1.197 (5140)	0.346 (299)	1.406 (1214)	0.792	43	<1	51.4 ± 3.5	45.6 ± 6.1	15.4	100	10.9 ± 0.2	2.16
R34811	Toro SST	21	1.197 (5140)	0.054 (44)	1.188 (967)	-0.102	205	<1	9.5 ± 1.5	12.5 ± 6.0	13	81	10.1 ± 0.4	3.15
R34808	Basement	31	1.197 (5140)	0.066 (44)	3.632 (2409)	0.229	50	8.5	3.8 ± 0.6	4.0 ± 0.7	39.7	37	14.1 ± 0.3	1.8
Strick South														
R34835	Ieru Fm	20	1.24 (5282)	0.594 (510)	1.990 (1708)	0.976	33	<1	65.0 ± 3.5	63.1 ± 7.9	20.9	100	11.1 ± 0.3	2.58
R34833	Koi Iange	30	1.24 (5282)	0.031 (30)	1.249 (1228)	0.109	140	<1	5.3 ± 1.0	7.9 ± 2.5	13.1	43	9.5 ± 0.6	3.96
Lavani														
R34854	Ieru Fm	20	1.237 (5142)	0.671 (467)	2.892 (2012)	0.963	34	<1	50.0 ± 2.8	51.8 ± 5.6	30.7	70	10.6 ± 0.3	2.27
R34901	Magobu Fm	40	1.224 (4245)	0.145 (112)	2.495 (1931)	0.092	92	<1	12.4 ± 1.2	9.9 ± 4.4	26.7	10	13.2 ± 1.0	-
R34902	Magobu Fm	30	1.224 (4245)	0.031 (19)	1.490 (910)	0.249	117	<1	4.5 ± 1.0	6.5 ± 2.1	16	1	14.2	-

[a] Central ages calculated following Galbraith (2005)
[b] Dispersion calculated in RadialPlotter (Vermeesch, 2009)
All other data directly from Hill and Gleadow (1989; 1990)

Supplementary material C4: AHe and ZHe age vs eU and Rs

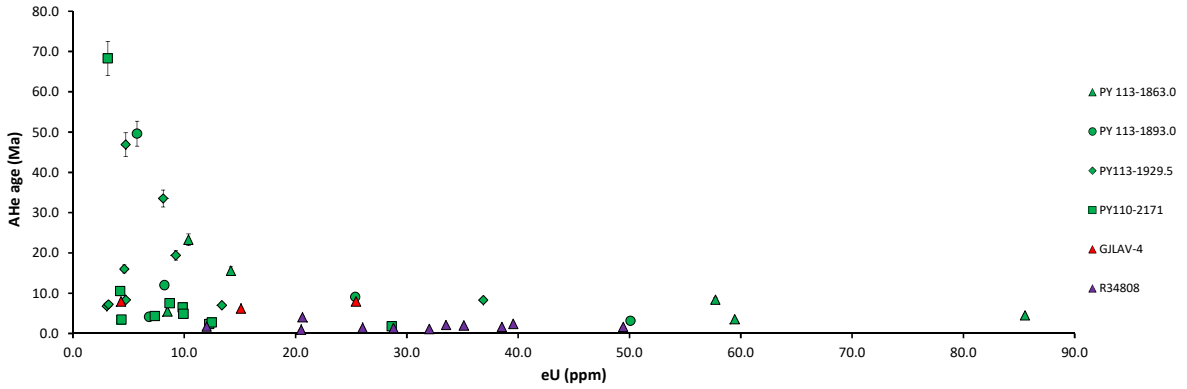

Figure C4.1. *AHe age vs effective uranium concentration (eU)*

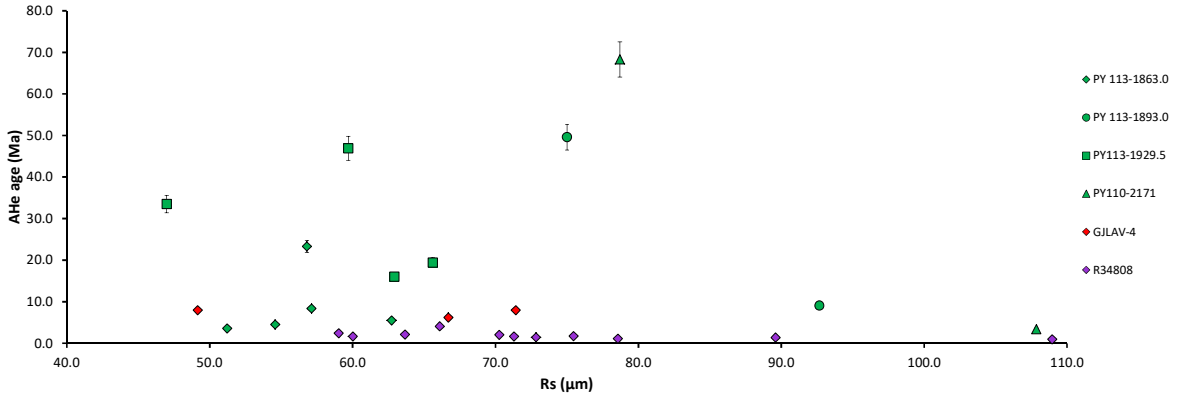

Figure C4.2. *AHe age vs equivalent spherical radius (Rs).*

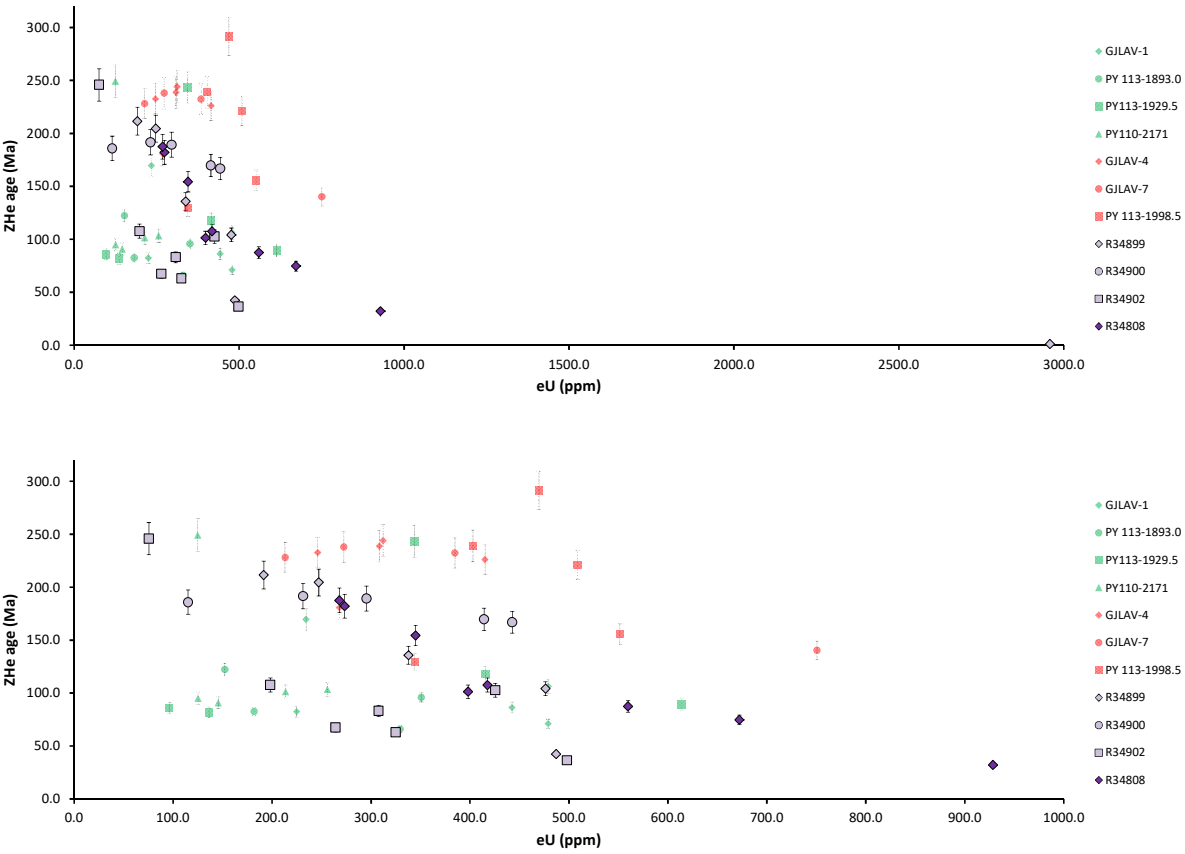

Figure C4.3. *ZHe age vs effective uranium concentration (eU). Bottom graph excludes the anomalously high eU grain in R34899.*

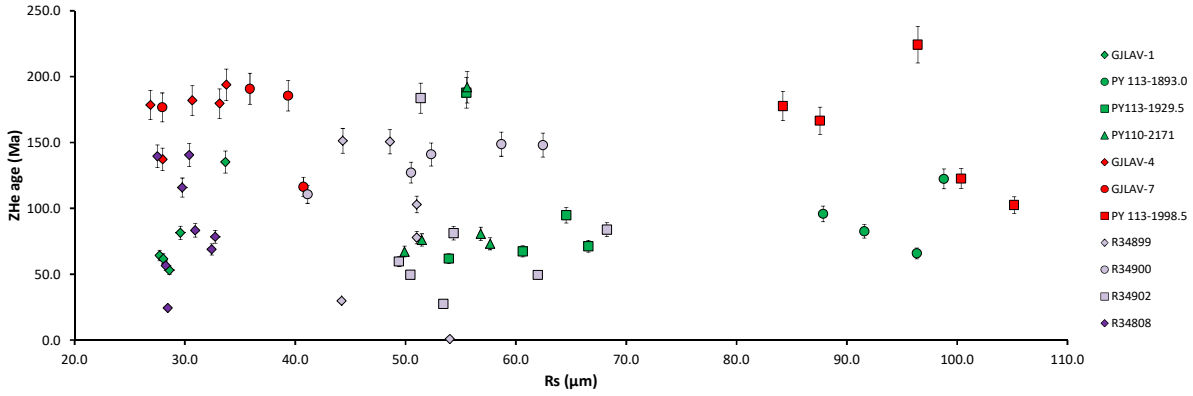

Figure C4.4. *Uncorrected ZHe age vs equivalent spherical radius (Rs).*

Supplementary material D4: AFT data vs Dpar

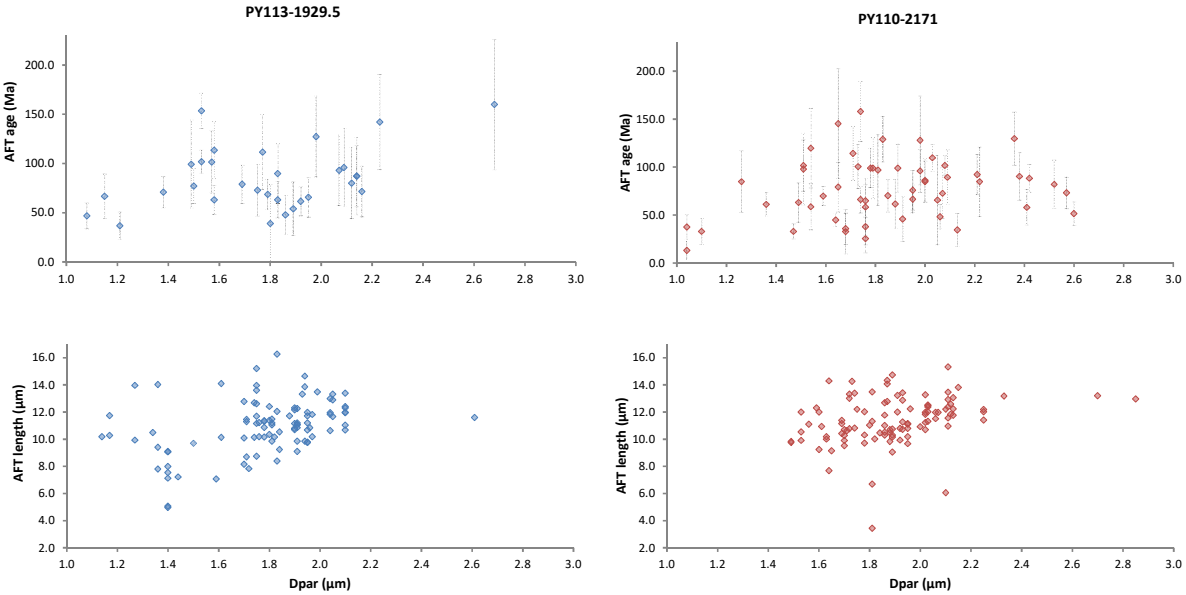

Figure D4.1. *AFT single grain age (top) and length (bottom) vs Dpar for samples PY113-1929.5 (left) and PY110-2171 (right).*

Supplementary material E4: 50:50 split forward models

Additional (50:50 split) forward models

Evidence is presented within Section 4.5.1.1 to support an 80:20 split of rapidly-cooled and slowly-cooled apatite within the Ieru Formation. To explore the influence that a greater proportion of slowly-cooled apatite may have on the resulting thermal

history, we also carried out forward modelling with a 50:50 split, following the same approach described in Section 4.5.2.

The 50:50 modelling included 26 independent time-temperature paths yielding 13 central AFT age and MTL predictions. Of these, only two fell within error of the observed data range (see Section 4.5.2) from the three uppermost Ieru Formation samples; two less than with the 80:20 modelling (Section 4.5.3). The accepted models resulted from thermal histories that including a Late Cretaceous to Oligocene thermal peak, both with (Fig. E4.1c) and without (Fig. E4.1b) the Pliocene to recent thermal peak. No models involving only a Pliocene to recent thermal peak were accepted. Both accepted models reasonably reproduced the composite TLD and were characterised by maxT of 90 or 100°C (Fig. E4.1). This magnitude of maxT is also consistent with all four accepted 80:20 models (Fig. 4.4).

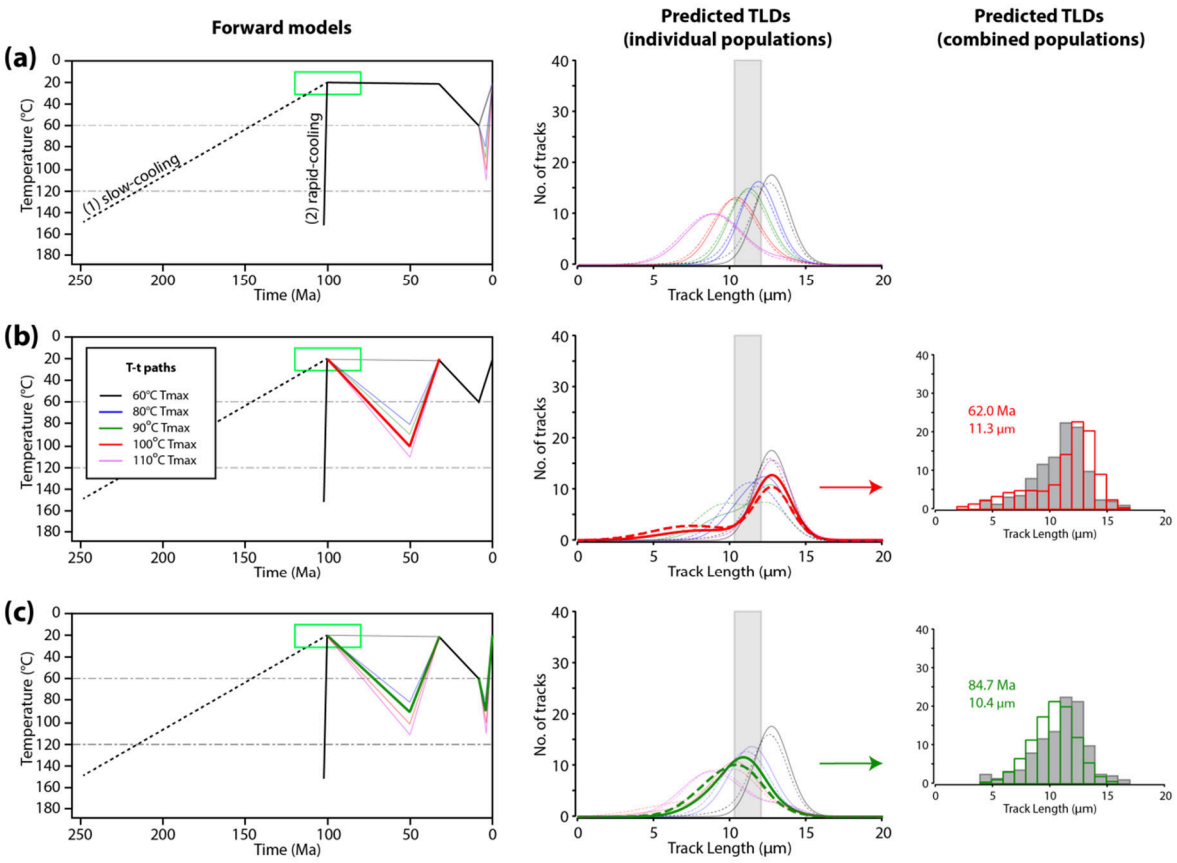

Figure E4.1. *(previous page) Left: Forward models comprising two pre-depositional T-t paths (1-2), tested across a range of different post-depositional thermal histories (a-c). The green box represents a reasonable stratigraphic age range for the upper Ieru Formation samples. Middle: Predicted TLD curves for rapidly-cooled (solid line) and slow-cooled (dashed line) apatite populations, weighted based on a relative abundance of 1:1 (50:50%). Thicker red and green lines represent TLD curves from accepted models (i.e. models from which the weighted average of the predicted data fits within the observed data range). Light grey shade represents the MTL range from the observed data (e.g., 10.3 ± 0.2 to 12.1 ± 0.2 um). Right: TLD histograms (normalised to 100 tracks) comprising the combined rapidly-cooled and slow-cooled TLD curves for the two accepted models compared with a composite TLD histogram (grey) comprising observed data from three upper Ieru Formation samples. Approach described in Section 4.5.2.*

Supplementary material F4: Individual sample thermal history models

Thermal history modelling of AFT data from individual Ieru Formation samples

In this section, we present and discuss the results of initial thermal history modelling of AFT data from individual Ieru Formation samples collected throughout the Muller Range. The results of single-sample thermal history models are grouped into four areas within the Muller Range, similar to multi-sample profile modelling. In the most part, the single sample thermal histories are remarkably consistent with pseudo-vertical profile models (cf. Supplementary Material F4 and Section 4.5.5).

The individual Ieru Formation sample model output is represented as a colour map of the marginal posterior probability distribution of time-temperature histories (Fig. F4.1). The expected model (which is the weighted mean of the posterior distribution) and the maximum posterior model (the best Bayesian model in that it tries to balance model simplicity with data fit) are also shown. The observed AFT age and TLD histogram are presented alongside those predicted by the maximum posterior model, thus providing a visual assessment of model performance (e.g., Fig. F4.1). As with the pseudo-vertical profile modelling results (Section 4.5.5), thermal peaks correspond to individual heating/cooling events; and multiple thermal peaks may characterise an individual samples thermal history.

MaxT refers to the maximum post-depositional temperature experienced and is thus only experienced once for a given thermal history.

Western Muller Range (WMR)

Despite being located on the north and south limbs of the Muller Anticline (Fig. 4.2) and separated by 900 m stratigraphically, Ieru Formation samples R34832 and PY110-2171 appear to have experienced remarkably similar post-depositional thermal histories (Fig. F4.1), including two significant periods of cooling following deposition in the middle to late Cretaceous (ca. 120-85 Ma). Initial cooling occurred from a maximum temperature of ~ 100-80°C in the Aptian to Albian (ca. 120-100 Ma) until the initiation of Darai Limestone deposition (ca. 30 Ma). The cessation of Darai Limestone deposition at ca. 8 Ma gave way to a second post-depositional cooling to present-day surface temperatures, with neither model showing evidence of significant post-Darai Limestone heating.

Ieru Formation sample R34831 is adjacent to and ~ 600 m stratigraphically below R34832 on the northern limb of the Muller Anticline (Fig. 4.2). Fewer track lengths were available for thermal modelling of R34831 (n=61) versus R34832 (n=100) and PY110-2171 (n=108). The thermal history of R34831, also deposited in the middle to late Cretaceous (ca. 125-85 Ma), is characterised by a comparably more rapid cooling from a maximum temperature of ~ 100°C in the Eocene (ca. 55-50 Ma) to the initiation of Darai Limestone deposition (ca. 30 Ma). The data imply a secondary thermal peak of ~ 80°C at ca. 5 Ma necessitating relatively insignificant post-Darai Limestone heating of ~ 10-20°C prior to rapid cooling to present-day surface temperatures.

Data from the WMR record a significant cooling event between the Late Cretaceous to Eocene, but cannot resolve the timing particularly well (Fig. F4.1). This

low resolution then leads us to jointly-invert these data as a pseudo-vertical profile to see if the resolution improves (Section 4.5.5.1).

South Strickland Gorge (Strick South)

Samples R34835 and PY113-1929.5 were collected from the middle and lower Ieru Formation, respectively, at the southern end of the Strickland Gorge (Fig. 4.2), where they are vertically separated by ~ 330 m of stratigraphic section. Both samples were deposited in the Cretaceous (ca. 130-80 Ma) and appear to have experienced similar post-depositional thermal histories (Fig. F4.1) including prolonged cooling from Late Cretaceous (ca. 90-75 Ma) maximum temperatures of ~ 85-90°C until the initiation of Darai Limestone deposition (ca. 30 Ma). Following the cessation of Darai Limestone deposition at ca. 8 Ma, the data are consistent with a second phase of cooling from ~ 70-80°C to present-day surface temperatures, with neither model showing evidence of post-Darai Limestone heating.

North Strickland Gorge (Strick North)

Samples R34809 and R34810 were collected from the upper to middle Ieru Formation in the northern Strickland Gorge ~ 25 km to the northwest of the southern Strickland Gorge profile (Fig. 4.2). Nearby palaeontological dating is limited, thus necessitating a wide stratigraphic age estimate of middle to Late Cretaceous (ca. 120-80 Ma). Individual thermal history models (Fig. F4.1) reveal a consistent post-depositional phase of cooling from maximum temperatures of ~ 80-95°C in the earliest Palaeocene (ca. 65 Ma) until the initiation of Darai Limestone deposition (ca. 30 Ma). Following the cessation of Darai Limestone deposition (ca. 8 Ma), sample R34810 appears to have immediately experienced a second cooling event to present-day surface temperatures—albeit the data imply significant uncertainty. In contrast, sample R34809 records more rapid cooling to surface temperatures beginning at ca. 5-4 Ma,

from greater temperatures (~ 80°C), that are comparable to the early Palaeocene thermal peak. Vertical profile modelling is clearly necessary to resolve the variation recorded within these data.

Lavani Valley (Lavani)

Sample R34854 was collected from the upper Ieru Formation within Lavani Valley in the Eastern Muller Range (Fig. 4.2). Its stratigraphic context (120 m below Base Darai Limestone) and age (ca. 88-84 Ma) are particularly well-constrained by recent field work (Mahoney *et al*., 2017). The thermal history model for sample R34854 (Fig. F4.1) was the only single sample model that required additional constraints to obtain a geologically reasonable thermal history—based on knowledge of Darai Limestone deposition between its initiation at ca. 30 Ma and cessation at ca. 10 Ma (e.g., Eisenberg *et al*., 1996). Despite considerable uncertainty (Fig. F4.1), the resulting thermal history suggests that the sample experienced two periods of cooling following Late Cretaceous deposition. An initial cooling started in the early Eocene (ca. 50 Ma) with a transition from ~ 80°C to near-surface temperatures prior to the commencement of Darai Limestone deposition (ca. 30 Ma). A second cooling event from ~ 75-80°C at ca. 6 Ma to present-day surface temperatures implies post-Darai Limestone heating of ~ 10-15°C.

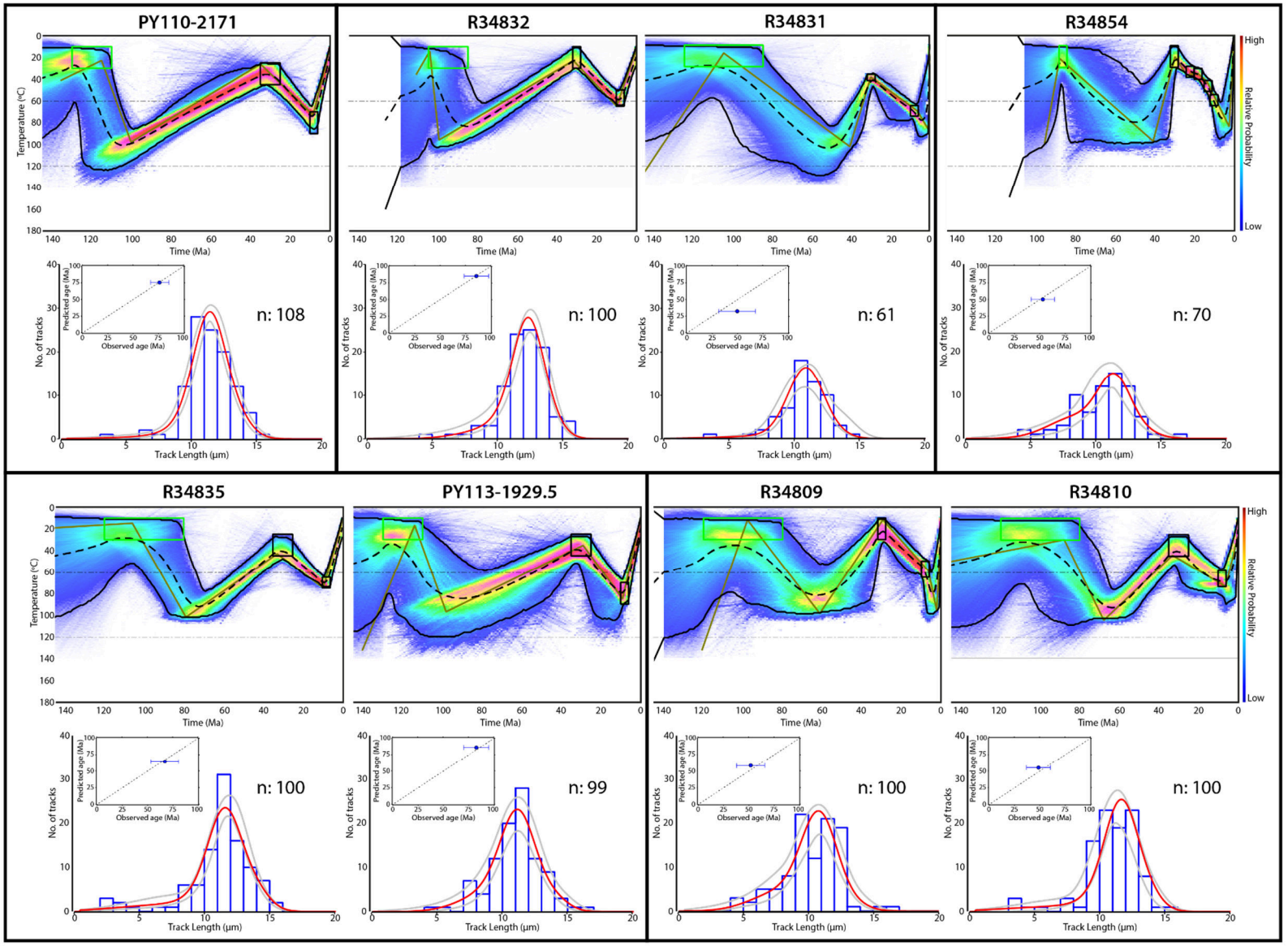
PY110-2171
R34832
R34831
R34854
R34835
PY113-1929.5
R34809
R34810
Temperature (°C)
Time (Ma)
Relative Probability
High
Low
No. of tracks
Predicted age (Ma)
Observed age (Ma)
Track Length (µm)
n: 108
n: 100
n: 61
n: 70
n: 100
n: 99
n: 100
n: 100

Figure F4.1. *(previous page) Inverse thermal history modelling results for AFT data from eight Ieru Formation samples across the Muller Range highlighting two significant thermal peaks during (1) the Cretaceous to Oligocene, and (2) the late Miocene to recent. The upper figure for each sample includes a colour map showing the marginal posterior probability distribution of time-temperature histories. The dashed line represents the expected model (weighted mean of the posterior distribution) and the solid brown line represents the max posterior model (the simplest, best fit time-temperature path). Dot-and-dash lines represent the AFT PAZ. The green box represents individual stratigraphic age/temperature constraints while the black boxes represent additional thermal history constraints discussed in Section 4.5.4.1. The lower figure for each sample shows the observed (blue histograms) versus predicted (red curves) track length distributions. The grey curves show the 95% confidence interval around the predicted track length distribution, n = the total number of measured track lengths. The insets show the observed AFT ages (and errors) plotted against the predicted ages. Track length distribution and age predictions were obtained from the max posterior model.*

Chapter 5

Geological history of the northern Australian margin in the context of a regional cross-section through the Western Fold and Thrust Belt, Papua New Guinea

The Western Fold and Thrust Belt (WFTB) in Papua New Guinea (PNG) represents a key transitional zone between narrow, high mountains in western New Guinea (e.g., the West Papuan Fold and Thrust Belt; WPFTB) and wide, low fold and thrust structures in the east (e.g., the Kutubu Fold and Thrust Belt; KFTB). Although the origin of this major transition in structural style is poorly understood, differences likely reflect lateral differences in the pre- and syn-collisional histories of the northern Australian margin. Given its location within this key transitional area, the WFTB has potential to provide important insights into the heterogeneity and evolution of the broader northern Australian margin.

In this chapter, the structure and evolution of the WFTB is explored in more detail using forward kinematic modelling along a section that extends 160 km from the Stable Platform to Mobile Belt in PNG (Fig. 5.1). The findings of the previous chapters in this thesis, and the references within, offer key geometric and temporal constraints on the section and more broadly on the tectonic evolution of the northern Australian and western Pacific regions.

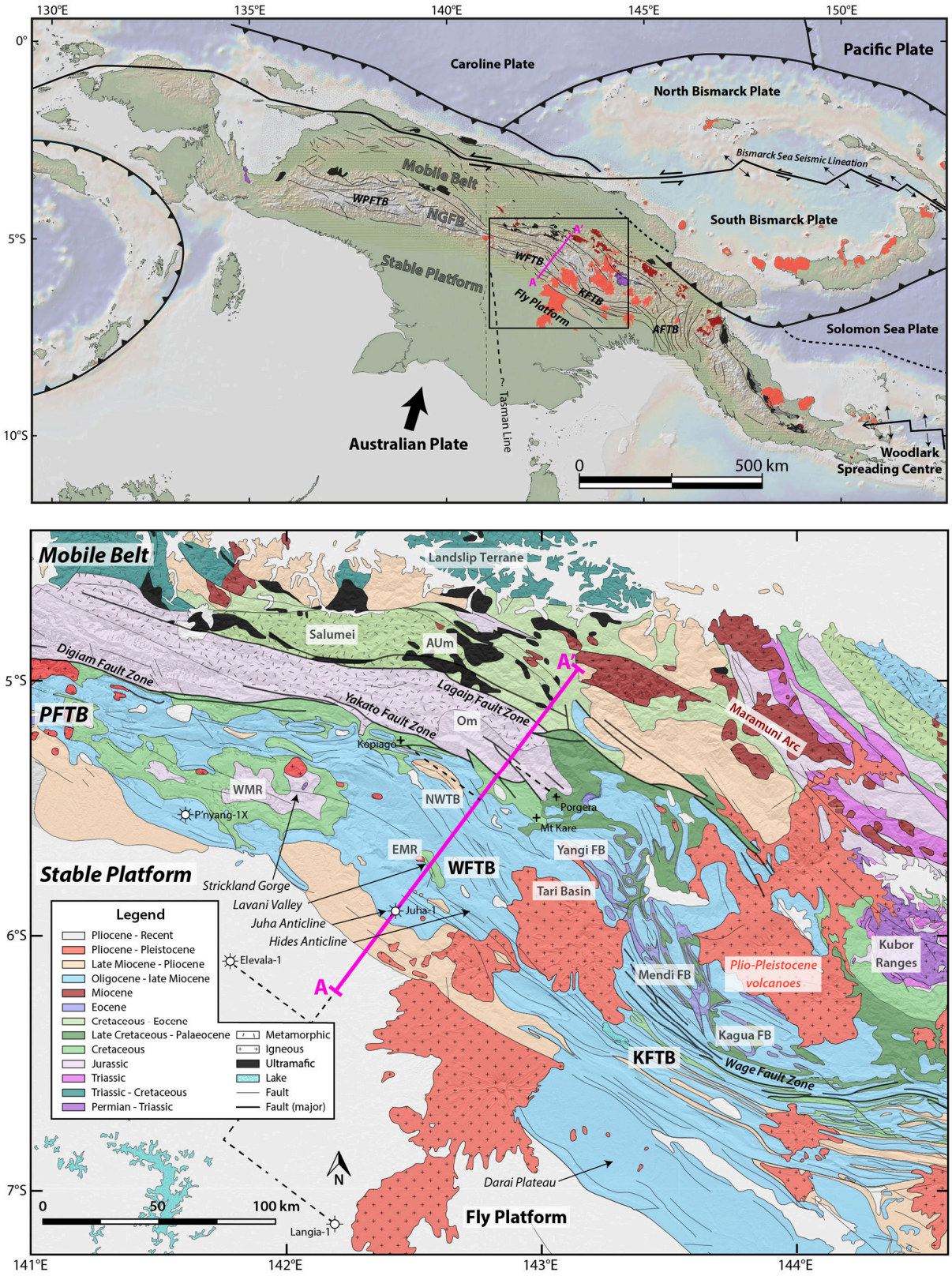

Figure 5.1. *(top) Tectonic and geological components of New Guinea and the New Guinea Fold Belt. (bottom) Geological map of the Papuan Fold and Thrust Belt including the key areas and geological features mentioned in the text. A-A′ marks the approximate (fully-shortened) extent of the regional cross-section in Figure 5.2. The dashed lines show the extent of Figure 5.3, including the key*

constraining wells and localities. Geological units and faults modified from the Coordinating Committee for Geoscience Programmes in East and Southeast Asia 1:2 million scale geological map. NGFB, New Guinea Fold Belt; PFTB, Papuan Fold and Thrust Belt; WPFTB, West Papuan Fold and Thrust Belt; WFTB, Western Fold and Thrust Belt; KFTB, Kutubu Fold and Thrust Belt; AFTB, Aure Fold and Thrust Belt; WMR, Western Muller Range; EMR, Eastern Muller Range; NWTB, Northwest Thrust Belt; AUm, April Ultramafics.

5.1. Late Palaeozoic to middle Miocene

During the Palaeozoic, the northern Australian continental margin was the northernmost extent of long-lived convergence between the proto-Pacific plate and the eastern Gondwanan margin (e.g., Hill and Hall, 2003). Numerous terranes accreted to the Proterozoic core of the Australian continent over this time, resulting in assembly of eastern Australia (e.g., Sheibner, 1974) and southern PNG (e.g., Thompson, 1967).

The Papuan Basin subsequently formed in the early Mesozoic, preserving components of the structural and stratigraphic record of the northern Australian margin. But the Papuan Basin record is incomplete, with no Late Cretaceous to early Oligocene sediments preserved in southern PNG (e.g., Jenkins, 1974; Home *et al*., 1990) such that the geological history of the northern Australian margin is poorly known in this period. Further challenges to understanding this interval are provided by the complex geology and evolution of the Mobile Belt in northern PNG (e.g., Rogerson and Hilyard, 1990; Davies, 2012). The complex tectonic setting of the northern Australian margin throughout the Neogene, together with orogenic overprinting by the Papuan Fold and Thrust Belt (PFTB), make understanding the history of the margin exceedingly challenging.

New insights into the spatiotemporal evolution of the PFTB, Papuan Basin and northern Australian margin (as presented in Chapters 2, 3 and 4), together with recent improvements in tectonic and geodynamic modelling (e.g., Schellart and Sparkman, 2015; Muller *et al*., 2016; Zahirovic *et al*., 2016; Tobin *et al*., 2018) have

facilitated improved understanding of the deep history of the margin. The following sections (5.1.1 – 5.1.8) provide a detailed review of the current state of knowledge of the late Palaeozoic to middle Miocene geological history of the northern Australian margin, with reference to the previous chapters in this thesis and the forward kinematic model presented in Figure 5.2.

5.1.1. Late Palaeozoic: New England Orogeny

The complex Palaeozoic to earliest Mesozoic history of the northeastern Australian margin is recorded in the crystalline basement rocks of southern PNG, most of which are buried beneath the thick and laterally extensive Mesozoic and Cenozoic sediments of the Papuan Basin. Thus, our understanding of the early history of PNG is limited and derived from only a small number of outcrops and well intersections across the Stable Platform and Fold Belt.

In the WFTB, granitic outcrop interpreted to be crystalline basement has been mapped within the deeply eroded Strickland Gorge (Fig. 5.1; Jenkins and White, 1970); biotite K-Ar age data suggest a minimum age of emplacement in the Triassic (222 ± 4 Ma; Page, 1976). Approximately 40 km to the west of the Strickland Gorge, in the frontal Western Muller Range, a Late Triassic granodiorite was intersected in the P'nyang-1X well (Fig. 5.1) and records a biotite K-Ar age of 205 ± 5 Ma (Valenti, 1993).

The only known non-igneous basement outcrop in the PFTB is located within the Kubor Ranges (Fig. 5.1), where deformed late Permian to Early Triassic low grade metamorphic rocks (Omung Metamorphics; Bain *et al*., 1975; van Wyck and Williams, 2002) are intruded by Middle to Late Triassic granites with muscovite K-Ar ages between 220-240 Ma (Page, 1976). Granitic basement has also been intersected in several wells across the Fly Platform, with K-Ar ages that range from middle Permian to Middle Triassic (e.g., Davies, 1990; Schofield, 2000). The Mabaduan granites on the southern coast of PNG and granites on the Torres Strait

islands have Carboniferous to early Permian K-Ar ages (Willmott *et al*., 1969; Richards and Willmott, 1970). The structure of basement in PNG is also poorly known, with geological and geophysical observations suggesting northeast-southwest to NNE-SSW oriented primary structural fabrics consistent with much of northern Australia (e.g., Australasian Petroleum Company, 1961; Hill, 1991; White *et al*., 2014). As outlined in Chapter 2 of this thesis, this basement fabric is likely to have had a significant role in the subsequent evolution of the northern Australian margin, including within the WFTB.

The eastern Gondwanan margin experienced successive arc and microcontinent accretion and associated contractional tectonism from the latest Proterozoic (ca. 600 Ma) through to the early Mesozoic (ca. 220 Ma). This deformed belt, known as the Tasman Fold Belt, comprises several broadly north-south oriented orogenic belts that extend along the entire eastern margin of the Australian continent (e.g., Crawford *et al*., 2003; Glen, 2005). Demonstrating the nature and continuity of these belts to the northeastern Australian margin (e.g., proto-PNG) is problematic due to the paucity of outcrop and the absence of high-resolution potential field datasets.

Available observations of basement in PNG suggest continuity with the most easterly component of the Tasman Fold Belt System, the New England Fold Belt, which is associated with (1) a late Permian (ca. 265) to Late Triassic (ca. 230 Ma) orogenic event (Hunter-Bowen Orogeny), (2) extensive Carboniferous to Permian magmatism (e.g., Connors-Auburn Arch), and (3) extensive late Permian to Late Triassic magmatism (e.g., Holcombe *et al*., 1997). These observations suggest a laterally extensive magmatic arc and associated orogenic event extending along the eastern and northeastern Gondwanan margin at this time (e.g., Hill and Hall, 2003; Crowhurst *et al*., 2004).

5.1.2. Middle Triassic to Early Jurassic: Papuan Basin formation

Evidence of Middle Triassic to Jurassic rifting is well-preserved within the basal stratigraphic sequence of the Papuan Basin (e.g., Pigram and Panggabean, 1984; Home *et al*., 1990), but the nature, origin and spatial extent of the event are poorly understood.

In the WFTB, early Mesozoic rift architecture significantly influenced the Cenozoic uplift of the regionally significant Muller Range (e.g., Chapter 2). Extensive exposures of Mesozoic stratigraphy within the Muller Range (e.g., Fig. 5.1) make it a valuable area to understand rift evolution. In the Western Muller Range, basin initiation is marked by the deposition of a granitic conglomerate, the Bol Arkose. This unit was probably locally sourced from the degradation of uplifted rift flanks (Fig. 5.2b) and its extent outside the Western Muller Range is largely unknown. In the Eastern Muller Range rifting is recorded by the thick Late Triassic to Early Jurassic terrestrial syn-rift Magobu Formation (Fig. 5.2b and c) that underlies the Lavani Valley (e.g., Chapter 2) and which is suspected to also underlie the adjacent Juha and Hides anticlines (e.g., Hanani *et al*., 2016; Darnault and Hill, 2020). Zircon (U-Th)/He (ZHe) data suggest that Palaeozoic-aged Australian continental basement is the likely source of sediments into the Magobu Formation (e.g., Chapter 4).

The early Mesozoic stratigraphy varies significantly throughout the WFTB, pointing to the complexity of the margin over this time. For instance, both the Bol Arkose and Magobu Formation are not found above basement in the Strickland Gorge, suggesting this area may have been an uplifted rift flank. Moreover, very thick Magobu Formation is known from beneath the Eastern Muller Range (Chapter 2), yet this unit is completely absent in the Western Muller Range (e.g., Jenkins and White, 1970). This observation is likely to reflect abrupt lateral changes in extensional architecture facilitated by accommodation structures that have preferentially formed along pre-weakened basement fabrics (e.g., Chapter 2). The strike of major inversion structures across the WFTB (e.g., the Lavani, Juha and

Hides anticlines) and the distribution of uplift associated with the 2018 PNG Highlands earthquake sequence (Chapter 3) suggests an underlying control from northwest-southeast oriented extensional faults.

Middle Triassic to Early Jurassic rifting has also been recognised in other areas of the northeastern Australian margin, including the (1) Gulf of Papua, (2) Fly Platform, and (3) Kubor Ranges (e.g., Home *et al*., 1990; Hill, 1991). The main rift axis is northwest-southeast or WNW-ESE across the fold belt, Stable Platform and westernmost Gulf of Papua (e.g., Home *et al*., 1990; McConachie *et al*., 2000; Schofield, 2000) and northeast-southwest to north-south throughout the remainder of the Gulf of Papua (Home *et al*., 1990; Bulois *et al*., 2018). In a tectonic context, it seems plausible that Triassic rifting may have been related to a late Permian to Middle Triassic orogenic event, as also observed within the northern New England Fold Belt in eastern Australia (e.g., Holcombe *et al*., 1997).

5.1.3. Middle to Late Jurassic: Opening of the Sepik ocean basin

Protracted rifting on the northeastern Australian margin led to marine incursion in the Middle to Late Jurassic and the deposition of the Om Beds in a restricted basin towards the north of the WFTB (Fig. 5.2d; e.g., Davies, 1983). To the south, the Om Beds are absent throughout the Muller Range where Late Jurassic shelf sands of the Koi Iange Sandstone are observed to directly overlie basement in parts of the Western Muller Range (e.g., Jenkins and White, 1970) and overlie Magobu Formation in the Eastern Muller Range (e.g., Chapter 2). Zircon (U-Th)/He analyses suggest a Palaeozoic-aged Australian basement provenance for the Koi Iange Sandstone (e.g., Chapter 4), potentially related to emergent and/or uplifted rift shoulders to the south. The transition from Koi Iange Sandstone to Om Beds suggests a change from shelfal to deeper marine depositional environment between the Muller Range and the Om Basin (e.g., Fig. 5.2d).

Marine incursion was driven by the formation of new oceanic crust to the north of the Om Basin (e.g., Pigram and Panggabean, 1984), associated with the opening of the Sepik ocean basin (e.g., Fig. 5.2d). Zahirovic *et al*. (2016) suggested the Late Jurassic for this continental breakup event based on several observations including (1) Jurassic granites in the Bena Bena metamorphics (Davies, 2012), (2) Late Jurassic ophiolites exposed in the Central Ophiolite Belt in West Papua (Permana, 1998; Pubellier *et al*., 2003), and (3) the onset of subduction-influenced Early Cretaceous volcanism in eastern New Guinea (the Kondaku Tuff; Rickwood, 1954; Dow, 1977). Constraints on which terranes, if any, rifted from the margin at this time are limited, largely due to the composite nature and regional present-day dispersal of northern Gondwanan continental terranes throughout Southeast Asia (e.g., Audley-Charles, 1988; Metcalfe, 1996) and the Mobile Belt in New Guinea (e.g., Hutchinson and Norvick, 1980; Crowhurst *et al*., 2004).

5.1.4. Late Jurassic to middle Cretaceous: Post-rift subsidence

During the Late Jurassic to middle Cretaceous, the combined effects of post-rift thermal subsidence and an overall rise in eustatic sea levels (e.g., Haq *et al*., 2014) caused a marine transgression across the northeastern Australia margin. Subsidence increased towards strongly attenuated crust (e.g., McKenzie, 1978) in the north and northeast, resulting in a northward increase in Late Jurassic to middle Cretaceous sediment thickness across the WFTB (e.g., Fig. 5.2e; White *et al*., 1973; Davies, 1983).

The Late Jurassic to Early Cretaceous Imburu Formation and Toro Sandstone represent a progradational stratigraphic sequence with a significant coarse-grained clastic component. Zircon (U-Th)/He and apatite fission track (AFT) data suggest a Palaeozoic-aged Australian basement provenance (e.g., Chapter 4; Hill and Gleadow, 1990), most likely the emergent platform in southern PNG (e.g., Norvick, 2003). While the basinward extent of the Toro Sandstone is poorly constrained in the WFTB, the significant Yakato Fault Zone may have been actively controlling the shelf edge over this time (Fig. 5.2e; e.g., Fischer and Warburton, 1996), analogous to

the Digiam Fault Zone in the west (e.g., Mason, 1996) and Wage Fault Zone in the east (Fig. 5.1; e.g., Hill *et al*., 2000).

During the Early Cretaceous, rising eustatic sea levels (e.g., Haq *et al*., 2014) and dynamic subsidence related to subduction beneath eastern Gondwana (e.g., Harrington *et al*., 2017), combined to drown the Papuan Basin. This terminated coarse-grained clastic sedimentation from the northern Australian continent and initiated the deposition of the condensed, fine-grained Alene, Juha and Bawia members of the Ieru Formation (e.g., Phelps and Denison, 1993). Zircon (U-Th)/He and AFT data from the Ieru Formation records transition to a primarily contemporaneous sediment source (e.g., Chapter 4; Hill and Gleadow, 1990), likely from widespread volcanic activity in PNG (e.g., Kondaku Tuff; Rickwood, 1954; Dow, 1977), eastern Australia (e.g., Whitsunday Volcanics; Bryan *et al*., 1997) and Antarctica (e.g., Norvick *et al*., 2003).

5.1.5. Middle Cretaceous: Dynamic uplift

In the middle Cretaceous (ca. Cenomanian), dynamic uplift of the eastern Australian margin (Muller *et al*., 2016) extended north to PNG (Harrington *et al*., 2017), resulting in uplift of the Fly Platform and the initiation of coarser-grained clastic sedimentation in more distal areas of the margin, including in the WFTB. The Giero and Ubea members of the Ieru Formation prograded from the platform to the north and northeast (Sari *et al*., 1996), with basinward thickening interpreted here to be at least partially controlled by reactivated Triassic extensional structures (e.g., Figs. 5.2f and 5.3; Fischer and Warburton, 1996). A northward-younging trend in Darai Limestone subcrop observed across the Fly Platform (e.g., Jenkins, 1974) is therefore partly depositional and partly erosional (e.g., Fig. 5.3), making it difficult to demonstrate the extent and magnitude of middle Cretaceous uplift and erosion. Spatially limited AFT data provide a maximum constraint on uplift and erosion across the Fly Platform of ~ 1.5 km (Hill and Gleadow, 1990 and Chapter 4).

(a) Late Palaeozoic

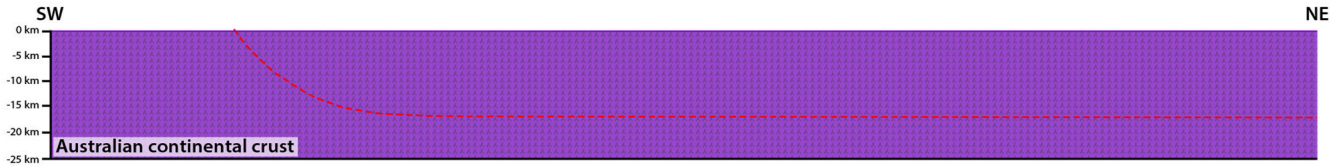

(b) Middle Triassic to Early Jurassic

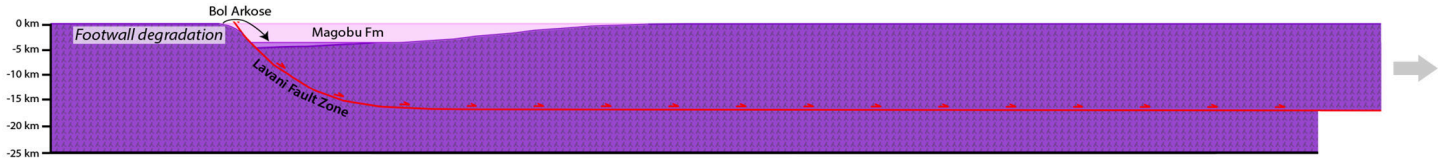

(c)

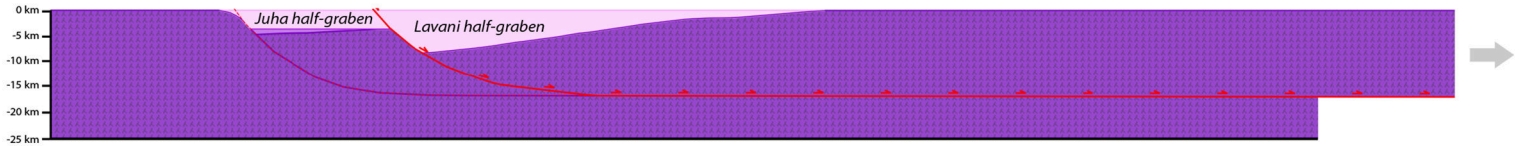

(d) Middle to Late Jurassic

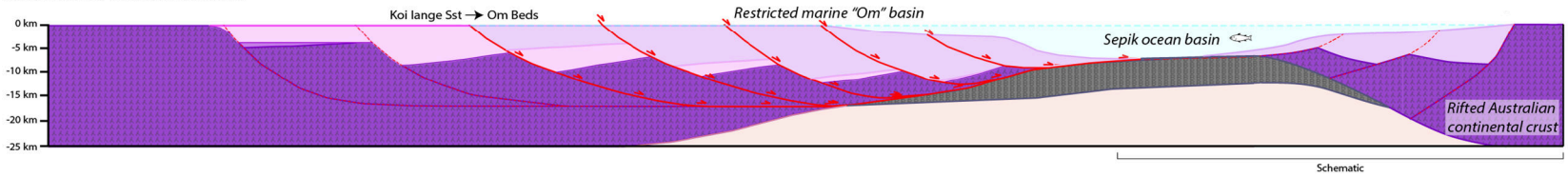

(e) Late Jurassic to middle Cretaceous

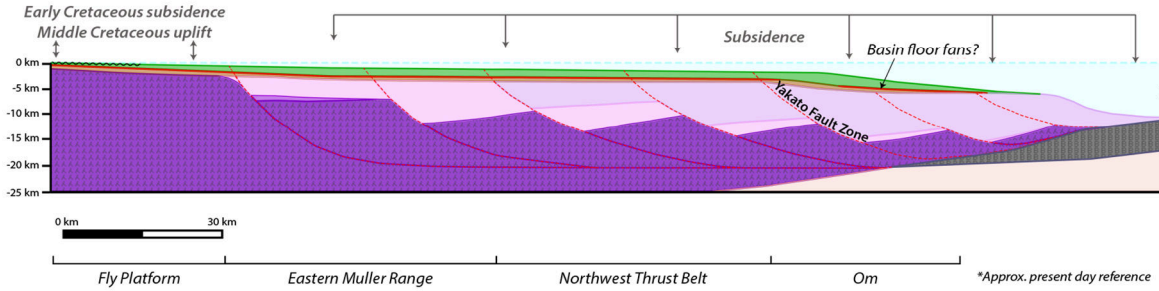

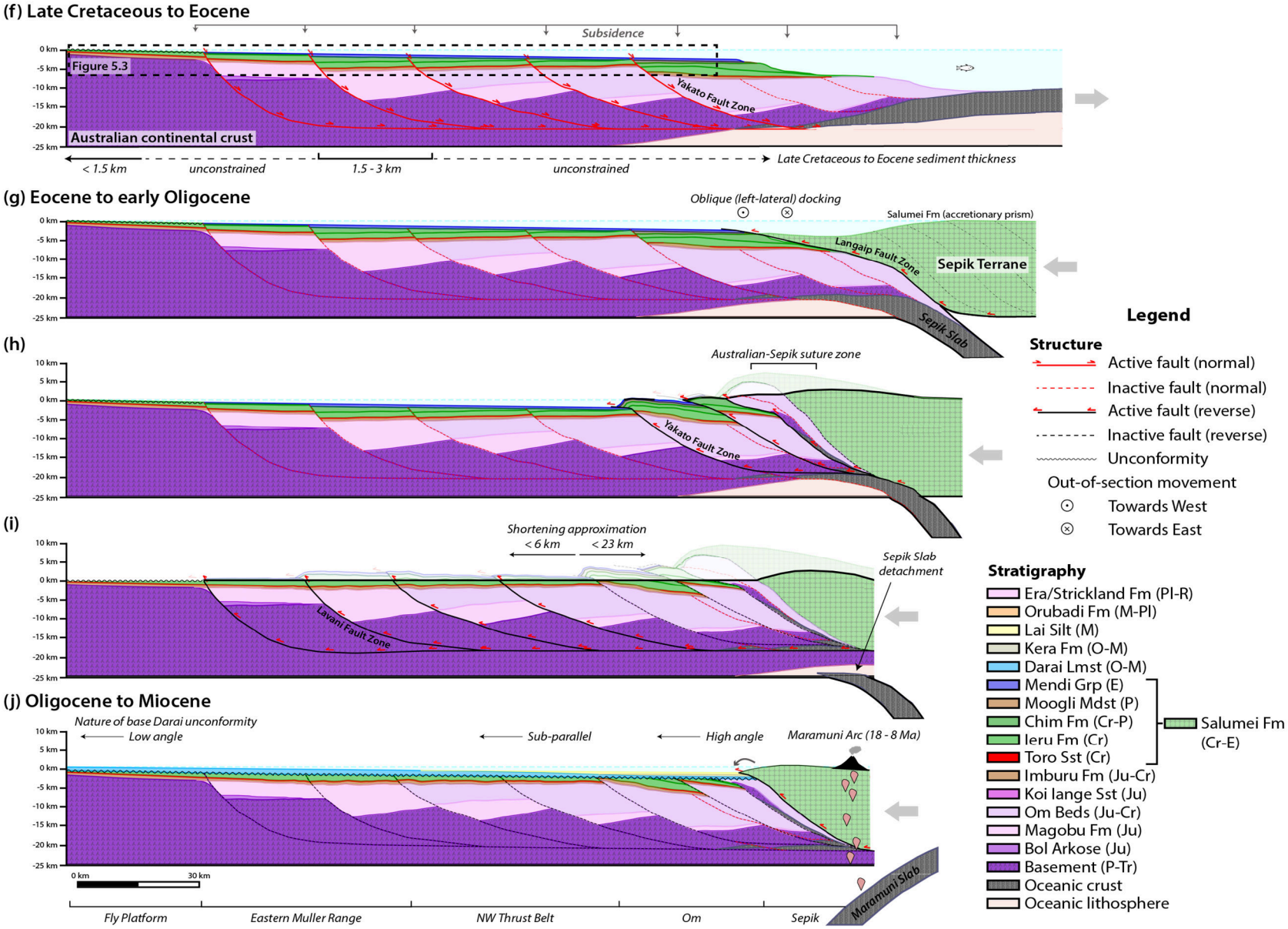
(f) Late Cretaceous to Eocene
Subsidence
Figure 5.3
Yakato Fault Zone
Australian continental crust
< 1.5 km
unconstrained
1.5 - 3 km
unconstrained
Late Cretaceous to Eocene sediment thickness
(g) Eocene to early Oligocene
Oblique (left-lateral) docking
Salumei Fm (accretionary prism)
Langaip Fault Zone
Sepik Terrane
Sepik Slab
(h)
Australian-Sepik suture zone
Yakato Fault Zone
(i)
Shortening approximation
< 6 km
< 23 km
Sepik Slab detachment
Lavani Fault Zone
(j) Oligocene to Miocene
Nature of base Darai unconformity
Low angle
Sub-parallel
High angle
Maramuni Arc (18 - 8 Ma)
0 km
30 km
Fly Platform
Eastern Muller Range
NW Thrust Belt
Om
Sepik
Maramuni Slab
Legend
Structure
Active fault (normal)
Inactive fault (normal)
Active fault (reverse)
Inactive fault (reverse)
Unconformity
Out-of-section movement
Towards West
Towards East
Stratigraphy
Era/Strickland Fm (Pl-R)
Orubadi Fm (M-Pl)
Lai Silt (M)
Kera Fm (O-M)
Darai Lmst (O-M)
Mendi Grp (E)
Moogli Mdst (P)
Chim Fm (Cr-P)
Ieru Fm (Cr)
Toro Sst (Cr)
Salumei Fm (Cr-E)
Imburu Fm (Ju-Cr)
Koi Iange Sst (Ju)
Om Beds (Ju-Cr)
Magobu Fm (Ju)
Bol Arkose (Ju)
Basement (P-Tr)
Oceanic crust
Oceanic lithosphere

Figure 5.2. *(previous pages) Regional kinematic forward modelled cross-section (A-A′ in Fig. 5.1) showing the geological evolution of the WFTB area of the northern Australian margin from the late Palaeozoic to Miocene. (a) Palaeozoic northern Australian continental margin (e.g., prior to Papuan Basin formation); (b-c) initial Middle Triassic to Early Jurassic rifting and localised syn-rift sediment deposition; (d) continued Jurassic rifting and Sepik ocean basin formation; (e) Late Jurassic to middle Cretaceous post-rift subsidence and widespread sediment deposition, followed by dynamic uplift across the Fly Platform; (f) Late Cretaceous to Eocene extension, post-rift subsidence and sediment deposition (Chapter 4); (g-i) Eocene to early Oligocene oblique docking of the Sepik Terrane with the northern Australia margin and associated tectonic inversion and erosion (Chapter 4); (j) Widespread Oligocene to Miocene carbonate deposition and relative quiescence on the northern Australia margin—impending Halmahera-Caroline Arc collision (e.g., Section 5.2).*

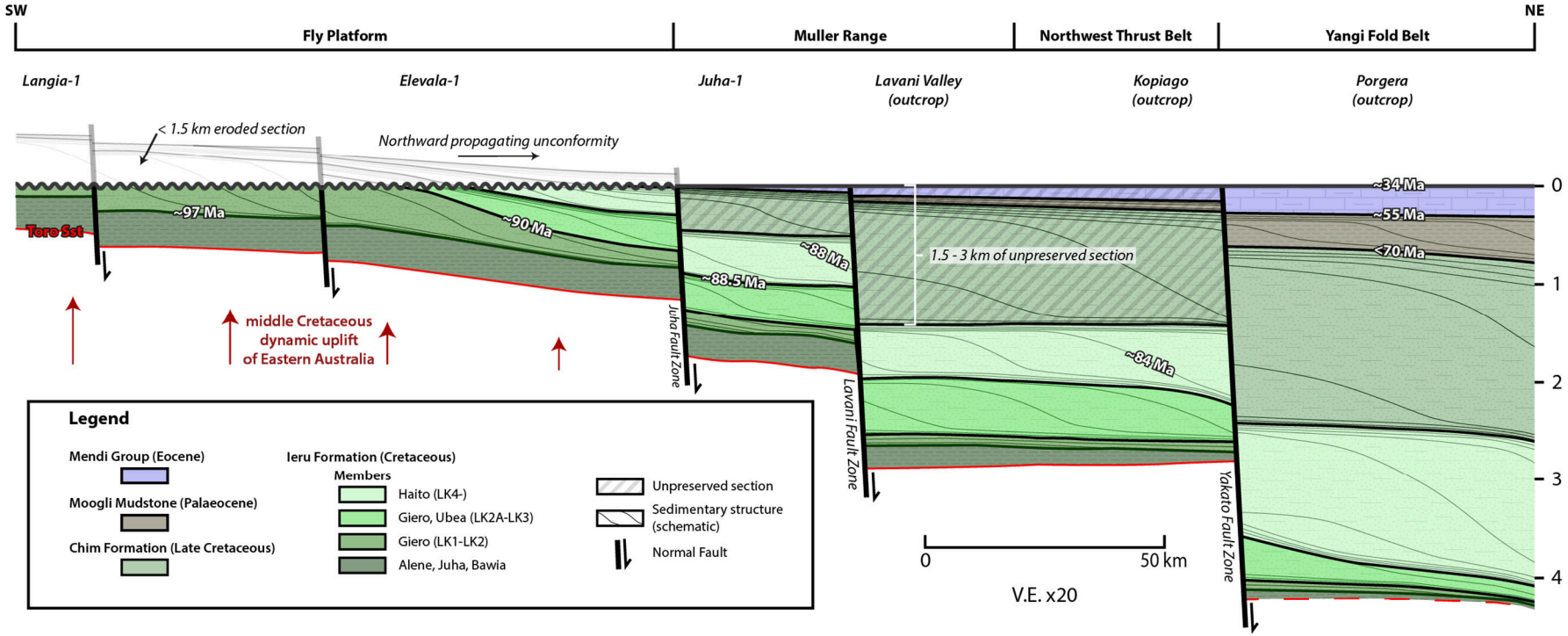

Figure 5.3. *Schematic regional cross-section across the WFTB area of the northern Australian margin (approximate location marked in Fig. 5.1) in the late Eocene, showing the nature of the Cretaceous Ieru Formation and possible extent of Late Cretaceous to Eocene strata.*

5.1.6. Late Cretaceous to Eocene: Coral Sea rifting and subsidence

The Late Cretaceous marked the onset of rifting along much of the northeastern Australian margin (e.g., Francis, 1990), including in the Coral Sea where oceanic spreading occurred from the Palaeocene to Eocene (Weissel and Watts, 1979). Although Late Cretaceous to Eocene-aged sediments are absent across the western and central Fly Platform and the frontal PFTB, thick and extensive sedimentary sequences are preserved in distal areas of the margin (e.g., Chapter 4; Hill *et al*., 2000). For example, in the WFTB, the Yangi Fold Belt (Fig. 5.1) preserves a 2.5-4.5 km thick, almost continuous sequence of Late Cretaceous to Eocene strata (Fig. 5.3; Chapter 4) that includes (1) 1.5-3 km of Late Cretaceous Chim Formation mudstones (e.g., Davies and Norvick, 1974; Davies, 1983; Hill *et al*., 1990), (2) ~ 0.5 km of Palaeocene Moogli Mudstone (e.g., Gunson *et al*., 1997; 2000), and (3) 0.5-1 km Eocene Mendi Group carbonates (e.g., Davies, 1983). The lack of preserved Late Cretaceous to Eocene strata in the frontal PFTB, and abrupt northeastward transition to thick Late Cretaceous to Eocene strata in the Yangi-Mendi-Kagua fold belts (Fig. 5.1), has led to the interpretation that active extension along major basin-bounding fault zones, such as the Yakato Fault Zone, restricted sedimentation to the most distal areas of the margin (e.g., Hill *et al*., 2000). However, thermochronology and thermal modelling presented in Chapter 4 of this thesis suggest that in the Eocene, 1.5-3 km of Late Cretaceous to Eocene sediments may have covered the Muller Range area (Fig. 5.3). It is noted that a general paucity of thermochronology data precludes our understanding of (1) the relative amount of Late Cretaceous, Palaeocene and Eocene sediment that covered the Muller Range, and (2) the extent and continuity of this missing section across other parts of the fold belt (i.e. in the Northwest Thrust belt (NWTB); Fig. 5.3).

The mechanism to account for the deposition of thick Late Cretaceous to Eocene sediments during an overall eustatic sea level fall (e.g., Haq *et al*., 2014) is problematic. Cretaceous to Eocene sediment thickening has been recorded across

extensional growth faults in the Fly Platform (e.g., Fischer and Warburton, 1996; McConachie *et al*., 2000; Schofield, 2000) and PFTB (e.g., Hill *et al*., 2010), suggesting the margin experienced multiple phases of extension over this time and supporting the inference that Coral Sea rifting propagated across the entire northeastern Australian margin (Francis, 1990; Pigram and Symonds, 1991; 1993; Davies *et al*., 1997). Similarly, the eastern Australian margin also experienced several episodes of extension during its evolution since the Mesozoic (e.g., Crawford *et al*., 2003; Higgins *et al*., 2015). Therefore, it is plausible that Late Cretaceous to Eocene sedimentation across the WFTB was facilitated by a combination of extension along new and/or pre-existing basement normal faults and subsequent post-rift thermal subsidence (e.g., Figs. 5.2f and 5.3). It is unclear whether rifting at the northeastern Australian margin progressed to breakup or whether it failed, perhaps contemporaneously with the Eocene cessation of sea floor spreading in the Coral Sea (e.g., Gaina *et al*., 1998; 1999).

5.1.7. Eocene to early Oligocene: Sepik Terrane collision

The Eocene was marked by a significant change in Pacific plate motion as demonstrated by the prominent bend in the Hawaiian-Emperor seamount chain at ca. 43 Ma (Clague and Dalrymple, 1989). This reorganization of plate motions is thought to have resulted from the initiation of the Izu-Bonin-Mariana subduction system in the Northwest Pacific (e.g., Faccenna *et al*., 2012). A coeval major change in subduction at the northern Australian margin marks the onset of rapid northward motion of the Australian plate and the convergence of the margin with a series of terranes that subsequently accreted forming the New Guinea Mobile Belt (e.g., van Ufford and Cloos, 2005).

Although the Eocene to early Oligocene evolution of the northeastern Australian margin is poorly recorded in the stratigraphy of the Papuan Basin, the adjacent Mobile Belt provides some insight. For example, the southern Sepik Complex directly north of the WFTB comprises highly deformed Late Cretaceous to

Eocene arc volcanics and volcanogenic sediments of the Salumei Formation, mixed with linear, highly sheared and thrust-bounded bodies of the April Ultramafics (Fig. 5.1; e.g., Davies, 1983; Davies, 2012). Further north, the Amanab-Idenburg-Landslip Terranes variably comprise low- to high-grade Mesozoic to early Cenozoic metamorphics, ultramafic ribbons and fragments of Palaeozoic-aged continental crust (e.g., Davies, 1990; Crowhurst, 1999; Davies, 2012). Collectively, the Salumei and Landslip areas (Fig. 5.1) are likely to represent an accretionary prism that formed during northward subduction at the leading edge of the continental nucleus of the Sepik Terrane (Fig. 5.2g; Hill and Mahoney, 2018). Although it is generally agreed that the Sepik Terrane collided with the northern Australian margin during the Eocene to Oligocene, the precise timing remains poorly known (as discussed in Chapter 4).

Despite being immediately adjacent to the Australian-Sepik suture zone, the WFTB contains limited evidence for Eocene to Oligocene Sepik Terrane collision. However, thermochronological data reported in Chapter 4 of this thesis has revealed a significant cooling event in the Muller Range at this time, interpreted to be related to the uplift and erosion of up to 3 km of Late Cretaceous to Eocene sediments and thus potentially highlighting the extent of Sepik-related deformation across the Papuan Basin (see discussion in Chapter 4). Here, the removal of these sediments is interpreted to relate to the broad inversion of long-lived extensional structures, particularly major extensional faults beneath the Muller Range, in response to collision of the Sepik Terrane ~ 50-80 km to the north (Figs. 5.2h-i and 5.4). According to the kinematic model presented in Figure 5.2, up to 29 km of crustal shortening may have been accommodated across the WFTB, most of which was partitioned to the Lagaip and Yakato fault zones immediately adjacent to the suture (Figs. 5.1 and 5.2g-h). Less than 6 km of shortening is required for the broad inversion and removal of Late Cretaceous to Eocene sediments across the Muller Range and Northwest Thrust Belt (Fig. 5.2i). This style of broad inversion may have

been analogous to the more recent inversion of the Darai Fault Zone to form the Darai Plateau (Fig. 5.1; e.g., Hill *et al*., 2010). But without the mechanically strong Darai Limestone 'carapace' that caps the Darai Plateau, the uplifted areas of the Muller Range and Northwest Thrust Belt would have been reduced to a planation surface much more rapidly. Alternatively, uplift and erosion in the Muller Range may relate to a flexural basement forebulge associated with tectonic loading at the Sepik Terrane deformation front (e.g., Pigram *et al*., 1989; 1990 and Pigram and Symonds, 1991). The extent of uplift and erosion into the Northwest Thrust Belt and Om areas is poorly constrained, due to a general absence of geological and thermochronological data.

One of the difficulties recognising such a significant tectonic event has been the widespread nature of an early Oligocene unconformity across the entire northern Australian margin from the Northwest Shelf (e.g., Apthorpe, 1988) to the Northeast Shelf (e.g., Davies *et al*., 1989). In the most part, this unconformity may relate to the largest eustatic sea level fall in the Cenozoic (e.g., Haq *et al*., 1987; 2014). In the Papuan Basin, the unconformity has increased temporal significance (e.g., van Ufford and Cloos, 2005) and shows significant spatial variation (e.g., Fig. 5.3; Jenkins, 1974), highlighting the possible influence of uplift related to the Sepik Terrane collisional event. In the Yangi Fold Belt (Fig. 5.1) to the southeast of the Australian-Sepik suture zone, the preserved Mendi Group comprises micritic limestones that record continuous deposition throughout the Eocene. These sediments record a general transition from basal argillaceous sediment to upper calcarenitic sediment reflecting progressive shallowing with partial emergence likely in the west (Davies, 1983). It is plausible that the actively subducting Sepik Slab caused initial subsidence of the margin (e.g., Gurnis *et al*., 1998), that accounted for the deposition of the lower Mendi Group immediately prior to and during the early stages of terrane accretion. This event was followed by late Eocene to early Oligocene continental collision, slab

detachment and associated uplift which provided the source of clastic detritus for the upper Mendi Group.

In a tectonic context, the Sepik Terrane may have been a part of an Eocene arc that extended along the entire northern and eastern Australian margins (e.g., Inner Melanesian Arc; van Ufford and Cloos, 2005), with early- to middle-Eocene docking of the Sepik Terrane along the northern Australian margin (e.g., Weiland, 1999; Schellart and Sparkman, 2015; Tobin *et al*., 2018) largely coeval with collisional orogenesis along the entire length of the subduction zone. The proto-Papuan Peninsula—likely a part of the same arc—docked with the northeastern Australian margin slightly later at ca. 35 Ma (e.g., Worthing and Crawford, 1996). The proto-Papuan Peninsula collision is well-recorded by thick syn-orogenic sediments in the Aure Trough, starting at ca. 32 Ma (Fig. 5.5; e.g., Edwards, 1950; Brown *et al*., 1975; Slater *et al*., 1988). The absence of syn-orogenic sediments associated with the Sepik Terrane collision in western New Guinea may relate to the orientation of the margin, with strongly oblique soft-docking in western New Guinea and more orthogonal hard-docking and associated orogenesis in eastern New Guinea.

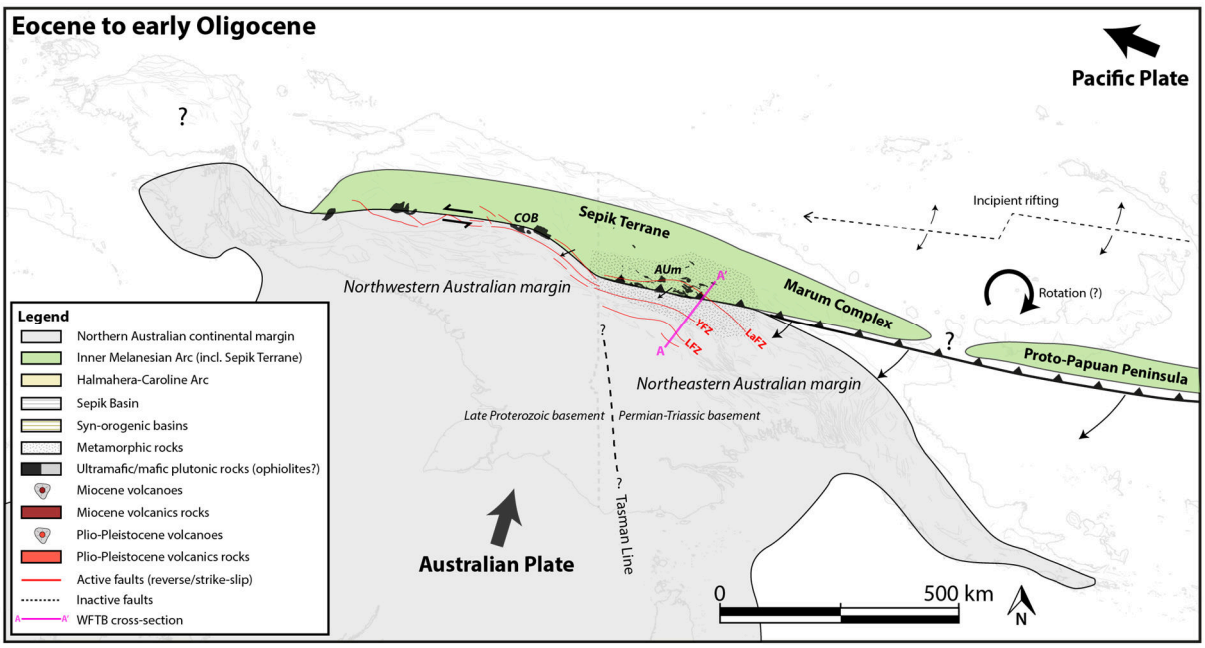

Figure 5.4. *Key geological and tectonic features of the northern Australian margin during the Eocene to early Oligocene. COB, Central Ophiolite Belt; Aum, April Ultramafics; LaFZ, Langaip Fault*

Zone; YFZ, Yakato Fault Zone; LFZ, Lavani Fault Zone. Note it is beyond the scope of this study to provide a detailed tectonic history of western New Guinea.

5.1.8. Oligocene to middle Miocene: Dynamic subsidence and impending Halmahera-Caroline Arc collision

The second period of terrane accretion at the northern Australian margin occurred from the middle Miocene to present (e.g., Hill and Raza, 1999), associated with the collision of the Palaeogene Halmahera Arc (e.g., Jaques, 1976) and its eastward extension, the Caroline Arc, collectively referred to here as the Halmahera-Caroline Arc, at the southern edge of the Caroline Plate (e.g., Zahirovic *et al*., 2016; Hill and Hall, 2003).

During the Neogene—prior to middle Miocene orogenesis—extensive carbonate sedimentation characterised the entire northern Australian margin (Norvick, 2003; van Ufford and Cloos, 2005). In the WFTB, the Oligocene to late Miocene Darai shelf limestones reached thicknesses of up to 1.6 km in the frontal PFTB but were significantly thinner to the south on the Fly Platform and to the north towards the Mobile Belt (e.g., Fig. 5.2j). In more distal areas of the margin, the Darai Limestone is absent and instead basinal equivalent sediments including the late Oligocene to early Miocene Kera Formation and middle Miocene Lai Siltstone (e.g., Davies, 1983) were deposited. Field observations suggest the Neogene and the underlying strata are paraconformable across the central WFTB (e.g., NWTB), but an angular unconformable exists across the northern WFTB (e.g., Yangi FB) (Davies, 1983) where Sepik-related deformation was most significant (e.g., Fig. 5.2j). The Lai Siltstone, preserved across the Northwest Thrust Belt and Yangi Fold Belt, contains volcanic clasts and Late Cretaceous to Palaeogene fauna suggesting a Salumei Formation source. Thus, at least parts of the Sepik Complex may have been emergent during the middle Miocene (e.g., Fig. 5.2j). It is unclear whether this relates

to (1) remnant topography from the Sepik Terrane collision, (2) the earliest stages of the Halmahera-Caroline Arc collision, or (3) a combination of these controls.

The Sepik Terrane—now sutured to the northern Australian continental margin—was associated with early Miocene extension, which formed the enigmatic Sepik Basin (Fig. 5.5) whose evolution is debated (e.g., Doust, 1990; Crowhurst, 1999; Hill *et al*., 1993). The margin was also characterised by significant Maramuni Arc volcanism throughout the Miocene (18-8 Ma; Page, 1976; Dow, 1977; Hill and Hall, 2003), interpreted to relate to southward subduction of the Maramuni Slab (e.g., Figs. 5.2j and 5.6). The westerly extent of Miocene volcanics into West Papua is largely unknown, in part due to a lack of geological data and in part due to the extensive coverage of the younger North Coast Basin (e.g., van Ufford and Cloos, 2005). The regional flooding of the northern Australian margin, despite long-term eustatic sea level fall, was driven by dynamic subsidence associated with the down going Maramuni Slab (e.g., Harrington *et al*., 2017) and Australia's northward movement over remnant slabs beneath Southeast Asia (e.g., Sandiford, 2007). Maramuni Slab subduction accommodated rapid convergence between the northern Australian margin and the Halmahera-Caroline Arc, with initial docking suspected between 14-12 Ma (Hill and Raza, 1999; Weiland and Cloos, 1996; Kendrick, 2000). The Neogene evolution of the WFTB and northern Australian margin is discussed in detail within the next section.

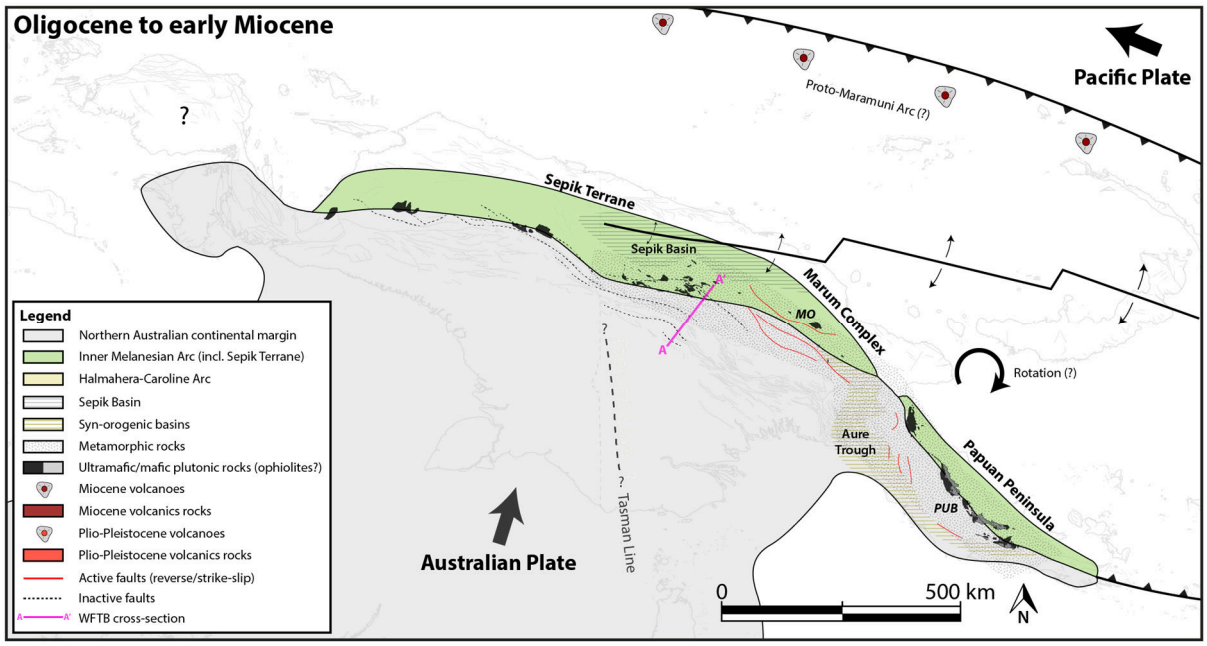

Figure 5.5. *Key geological and tectonic features of the northern Australian margin during the Oligocene to early Miocene. MO, Marum Ophiolites; PUB, Papuan Ultramafic Belt.*

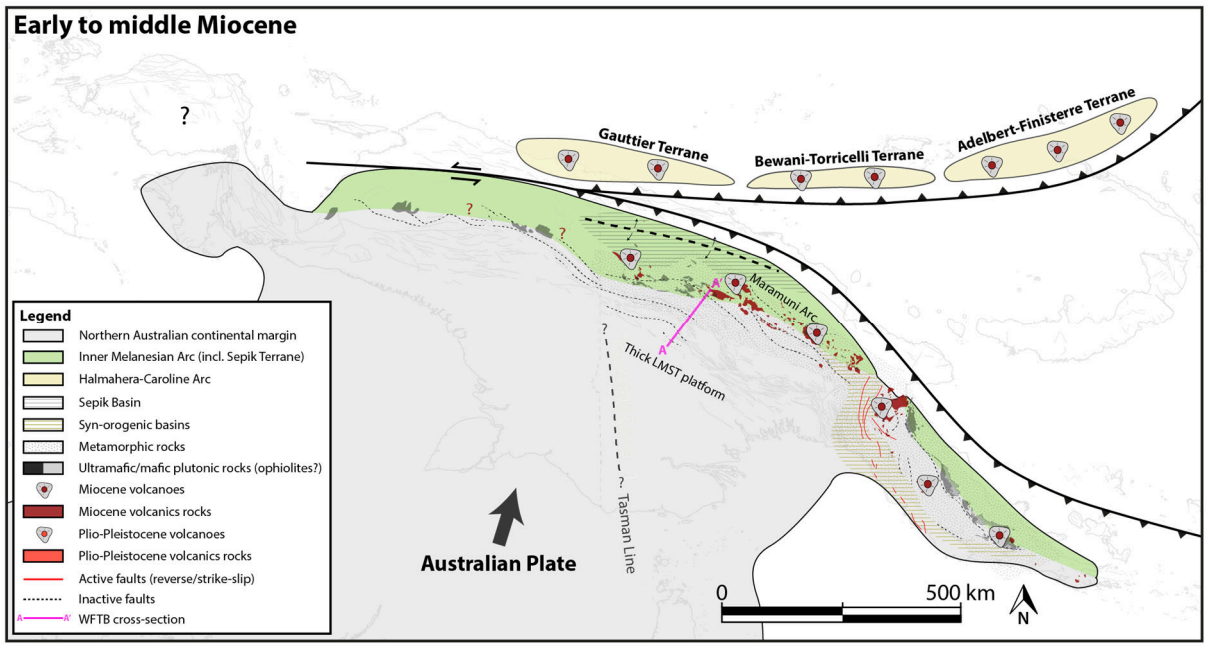

Figure 5.6. *Key geological and tectonic features of the northern Australian margin during the early to middle Miocene.*

5.2. Miocene to present

During the Miocene, oblique convergence between the Australian plate (moving to the north) and the Pacific plate (moving to the northwest) led to a series of arc accretion events at the northern Australian margin. The resultant complex geological and tectonic evolution included the development of the NGFB, including the PFTB. Significant ambiguity exists regarding the nature and timing of terrane accretion throughout the Neogene (e.g., van Ufford and Cloos, 2005 and references therein). Tectonic reconstructions are complicated by the partial decoupling of the margin geology from Pacific and Australian plate motions, due to the involvement of a number of microplates as demonstrated by present-day geodetic data (e.g., Wallace *et al*., 2004; 2005; Koulali *et al*., 2015). Published tectonic models for the northern Australian margin generally rely on limited geological and geochronological data, mostly from the Mobile Belt in PNG, and/or New Guinea's tectonic and geodynamic context within Southeast Asia or global plate models (e.g., Hill and Raza, 1999; Hill and Hall, 2003; Hall, 2012; Zahirovic *et al*., 2016). The structure and evolution of the NGFB is often overlooked, however significant spatiotemporal variations in structural style are present and have potential to provide key insight into the geological and tectonic history of the margin from the Miocene to present.

The following sections of this thesis provide a review of the Miocene to present geological history of the northern Australian margin, with a focus on recent advances in our understanding of the structure and evolution of the PFTB (as outlined in Chapters 2, 3 and 4 of this thesis). As with Section 5.1, the evolution of the margin is presented here alongside forward kinematic modelling of the same regional section across the WFTB in PNG (e.g., Fig. 5.1).

5.2.1. Middle to late Miocene: Halmahera-Caroline Arc collision (western collisions)

Throughout the Miocene, the rapid northward motion of the Australian plate was accommodated by subduction zones to the north of New Guinea (e.g., Hall, 2002; Hill and Hall, 2003) and the Halmahera-Caroline Arc converged rapidly with the northern Australian margin. The Halmahera-Caroline Arc comprised several distinct intra-oceanic terranes, including from west to east, the Gauttier, Bewani-Torricelli, Adelbert-Finisterre and New Britain terranes (Figs. 5.6 and 5.7, e.g., Pigram and Davies, 1987; Hill and Hall, 2003). Ongoing convergence between the Australian and Pacific plates ultimately resulted in the collision of much of the strike length of the Halmahera-Caroline Arc with the Australian plate in the middle Miocene (Fig. 5.7). This collision further deformed the Mobile Belt and formed the NGFB at the northern Australian margin (e.g., Hill and Gleadow, 1989; Hill and Raza, 1999; Hill and Hall, 2003). Given the wider tectonic context of the oblique convergence between the Pacific and Australian plates, it is likely that the middle to late Miocene phase of Halmahera-Caroline Arc collision occurred in an oblique style, with oblique docking of both the Gauttier and Bewani-Torricelli terranes by the late Miocene (Fig. 5.8) as suggested by Hall (2012) and consistent with the style of collision interpreted here for the Sepik Terrane (e.g., Section 5.1.7).

Preserved syn-orogenic sediments together with thermochronological data from the NGFB suggest the Halmahera-Caroline Arc accreted to the northern margin beginning in the northwest and propagating to the southeast (Figs. 5.7-5.9). In western New Guinea, influxes of siliciclastic material (Makats Formation) occurred as early as 16-14 Ma in the North Coast basin overlying the Mobile Belt (Fig. 5.7; Visser and Hermes, 1962). From ca. 14-12 Ma, the Akimeugah and Iwur basins formed over Australian continental basement in West Papua, where siliciclastic material (Akimeugah and Iwur formations) began to be the dominant sediment (Fig. 5.7; e.g., Dow, 1977; van Ufford and Cloos, 2005), representing a significant shift in facies and sediment source from the underlying thick shelfal limestones (New

Guinea Limestone). In eastern New Guinea, siliciclastic material had reached the hinterland region of the WFTB in PNG by ca. 11 Ma (Fig. 5.7; Lai Siltstone; Davies, 1980), with the presence of Late Cretaceous to Palaeogene fauna suggesting an emergent source region within the Sepik Complex, most likely the Salumei Formation (e.g., Fig. 5.2j). Siliciclastic material had replaced the deposition of thick shelfal limestones in the frontal fold belt region by ca. 7 Ma (Fig. 5.8; Orubadi Formation; e.g., Chapter 2). The exception to the northwest to southeast age progression of the margin is the Aure Trough, which records continuous syn-orogenic sediment accumulation from the Oligocene to present. Although spatially limited, existing thermochronology studies are consistent with a northwest to southeast progression of the Halmahera-Caroline Arc collision and thus orogenesis, suggesting that uplift of the NGFB commenced prior to ca. 7 Ma in the WPFTB in Indonesia (e.g., Weiland and Cloos, 1996; Cloos *et al*., 2005) and prior to ca. 4 Ma in the Mobile Belt and WFTB in PNG (e.g., Hill and Gleadow, 1990; Chapter 4).

In the WFTB, the middle to late Miocene component of Halmahera-Caroline Arc-related orogenesis likely initiated early inversion of the same long-lived, northwest-southeast trending structures that are interpreted to have been previously reactivated during the collision of the Sepik Terrane in the Eocene to Oligocene (e.g., Chapter 4 and Fig. 5.8, Langaip, Yakato and Lavani fault zones). But the complex contractional overprinting associated with later Pliocene to Pleistocene orogenesis makes it difficult to decipher the nature of the earlier late Miocene inversion. Several late Miocene to earliest Pliocene igneous centres, including the Porgera and Mt Kare mineral deposits (Fig. 5.1), appear to cluster around these deep-seated structures, suggesting that their reactivation may have produced crustal dilation and created important conduits for the migration of mineralised fluids (e.g., Hill *et al*., 2002). The Langaip Fault Zone—representing the approximate suture between the Australian continental margin and the Sepik Terrane—was likely reactivated, further exhuming the remnants of the earlier collisional zone, including the accretionary prism

(Salumei/Landslip areas) and obducted oceanic crust (April Ultramafics; e.g., Fig. 5.1 and Fig. 5.10). The reactivation of the Yakato Fault Zone marked the recommencement of uplift of the most distal sediments overlying the Australian continental margin (e.g., Om Beds). During its evolution, the Yakato Fault Zone likely shallowed into multiple detachments within the thick sedimentary pile marking the onset of deformation within the Northwest Thrust Belt (NWTB) (Fig. 5.10a and b). Late Miocene shortening of the NWTB was restricted to the area north of the Kendupwa Volcanics, which were emplaced conformably on the underlying sediments in the Pliocene (4.2-4 Ma (K-Ar); Webb, 1973), prior to being deformed in the Aiago Syncline (Davies, 1983).

As indicated by the thermochronology data presented in Chapter 4 of this thesis, the uplift of the Muller Range initiated prior to 4 Ma with thick syn-orogenic depocentres likely to have formed on its flanks. This indicates that initial inversion along the Lavani Fault Zone was at least partially coeval with the more hinterlandward Yakato and Langaip fault zones (Fig. 5.10a). Despite similarities in timing, the structural style of the Lavani Fault Zone differed significantly from the foreland-vergent Yakato and Langaip fault zones, potentially due to the mechanical influences of a thinning Papuan Basin sedimentary section toward the south. The Lavani Fault Zone and associated splays formed several forelandward propagating triangle zones within multiple detachment levels, which were responsible for uplifting the Muller Range area within the constraints of minimal shortening recorded within the Darai Limestone (e.g., Chapter 2; Fig. 5.10a-c). Perhaps the best analogue for understanding the initial phase of inversion along the Lavani Fault Zone is the Hides Anticline, located < 10 kms along strike to the southeast (Fig. 5.1). The structure of the Hides Anticline is much better known as a result of it hosting a giant gas field. Data interpretation and physical modelling demonstrate that the Hides Anticline is characterised by a similar structural style to that interpreted here for early inversion along the Lavani Fault Zone, that is, one dominated by triangle

zone style deformation within multiple sedimentary detachments (e.g., Darnault and Hill, 2020).

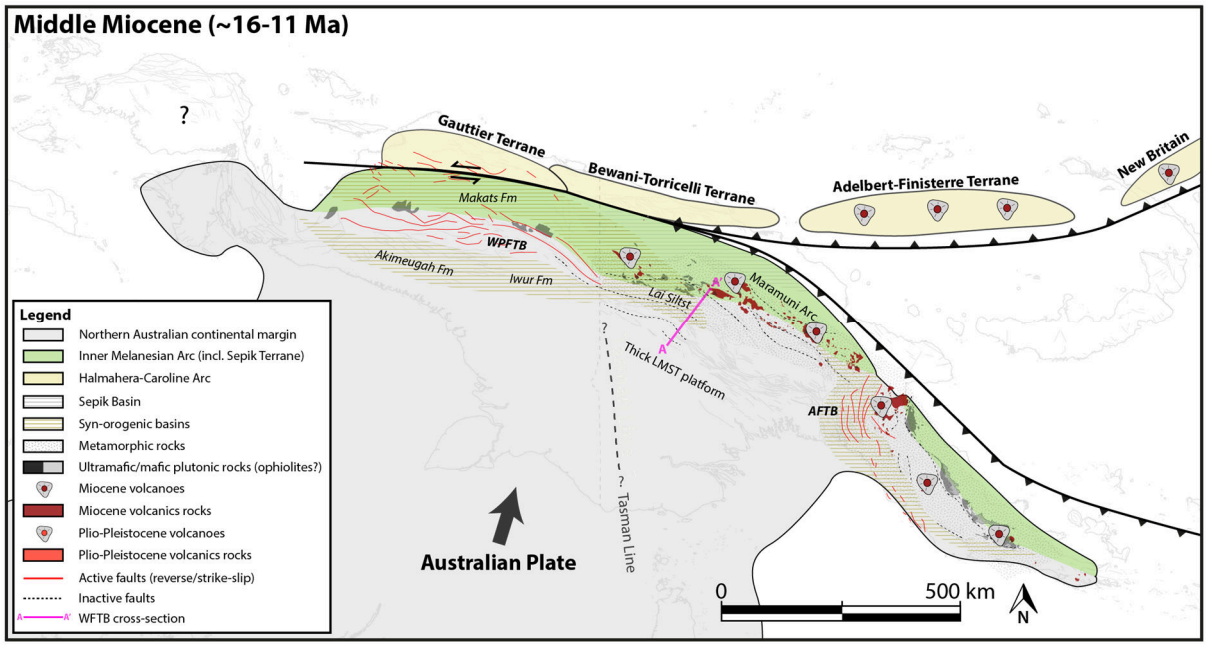

Figure 5.7. *Key geological and tectonic features of the northern Australian margin during the middle Miocene. WPFTB, West Papuan Fold and Thrust Belt; AFTB, Aure Fold and Thrust Belt.*

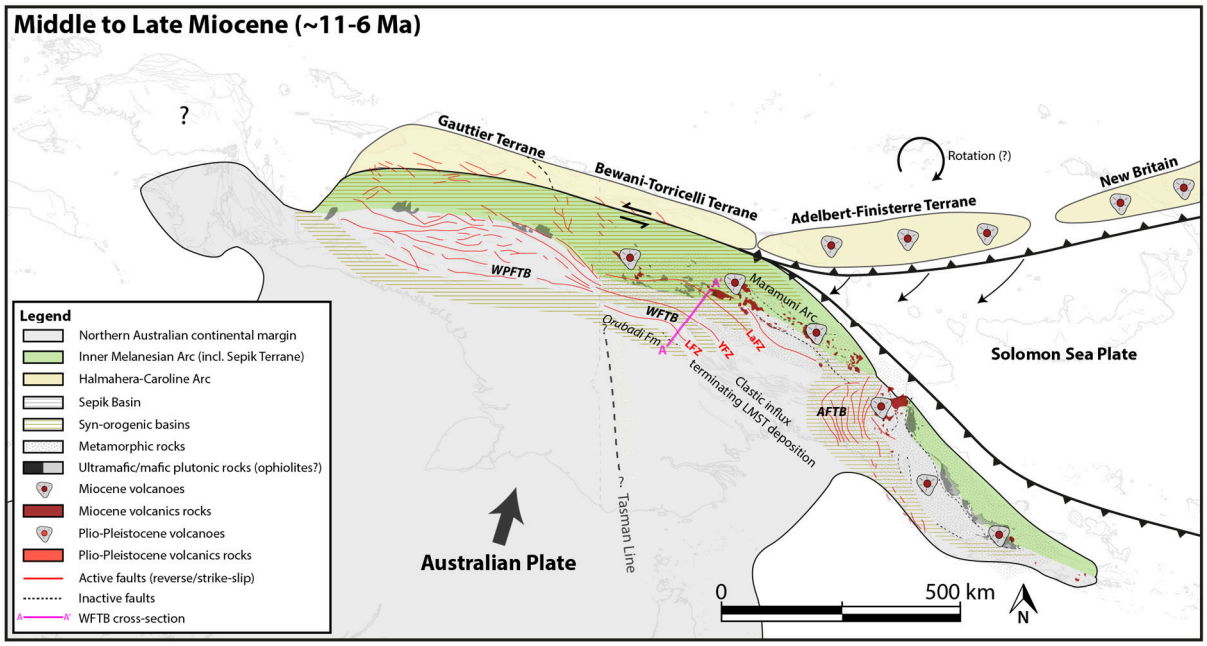

Figure 5.8. *Key geological and tectonic features of the northern Australian margin during the middle to late Miocene. WPFTB, West Papuan Fold and Thrust Belt; WFTB, Western Fold and Thrust Belt;*

AFTB, Aure Fold and Thrust Belt; LaFZ, Langaip Fault Zone; YFZ, Yakato Fault Zone; LFZ, Lavani Fault Zone.

5.2.2. Early Pliocene to present: Halmahera-Caroline Arc collision (eastern collisions)

By the earliest Pliocene, the northwest to southeast docking of the Halmahera-Caroline Arc was well underway, with the Gauttier and Bewani-Torricelli terranes largely sutured to the northern Australian margin. The Adelbert-Finisterre Terrane was rapidly converging with the northeastern margin of PNG, likely colliding with the margin at ca. 4-3.5 Ma, as clearly evidenced by a change in provenance from continental- to volcanic-rich materials in the Ramu basin overlying the Mobile Belt (Abbott *et al*., 1994a; Abbott *et al*., 1994b; Abbott, 1995). The initial docking of the Adelbert-Finisterre Terrane with the northwest to southeast trending continental margin in eastern New Guinea prompted a significant tectonic reorganisation to the north of PNG and marked the initiation of microtectonic complexity that characterises the region in the present-day (e.g., Wallace *et al*., 2004; 2005; Koulali *et al*., 2015). The rapidly-evolving compressional stress regime associated with the collision of the Adelbert-Finisterre Terrane contributed significantly to the evolution of structural complexities within the PFTB and is thus reviewed in detail in the following paragraphs.

As outlined above, docking of the Adelbert-Finisterre Terrane with the PNG margin first occurred in the northwest, pinning it to the margin while oceanic crust was still being subducted at the New Britain Trench to the east (cf. Figs. 5.8 and 5.9). This initiated rapid clockwise rotation of the remainder of the Adelbert-Finisterre Terrane (e.g., Taylor, 1979) and, further east, the New Britain Arc. This change in kinematics was accommodated by the splitting of the Bismarck microplates from the Caroline Plate at ca. 3.5 Ma, at which point the North Bismarck Plate started moving northwest with the Caroline Plate, prompting a change from oblique convergence to

largely strike-slip deformation in northern New Guinea that has been recognised within both the geological record (e.g., Bewani-Torricelli Fault Zone) and from earthquake focal mechanisms (e.g., Pigott *et al*., 1985; Cooper and Taylor, 1987; Crowhurst *et al*., 1996). The South Bismarck Plate, largely pinned at its northwestern end by the initial Adelbert-Finisterre Terrane collision, began rotating in a clockwise direction accommodated by the rapid subduction of oceanic crust at the New Britain Trench and by the initiation of rapid extension along parts of the Bismarck Sea Seismic Lineation (e.g., Wallace *et al*., 2004; Fig. 5.9). Pinning on the northwestern end of the Adelbert-Finisterre Terrane and the associated rotation was responsible for the formation of the West Bismarck Fault (Fig. 5.9), a large dextral strike-slip fault that eventually disarticulated the Adelbert and Finisterre blocks (e.g., Wallace *et al*., 2004; Holm and Richards, 2013).

The variable nature of the Halmahera-Caroline Arc collision, particularly from largely oblique collision in the west (e.g., Gauttier and Bewani-Torricelli terranes) to increasingly orthogonal collision in the east (e.g., Adelbert-Finisterre Terrane), prompted significant spatiotemporal changes in compressive stresses that have significantly contributed to the geological complexity of the NGFB. For instance, the increased width of the NGFB in PNG (max. 250 km) when compared with Indonesia (max. 150 km; Fig. 5.1) has previously been related to variations in crustal composition (e.g., Gow *et al*., 2002; Hill and Hall, 2003), but could equally be explained by variations in stress regime from arc-oblique collision in the west and arc-normal collision in the east. Western PNG (including the WFTB) is likely to have had a particularly complex history of compressive stresses, due to its proximity to both the Bewani-Torricelli Terrane and Adelbert-Finisterre Terrane collisions (e.g., the transitional zone between arc-oblique and arc-normal stresses). Indeed, significant structural complexities exist within the transitional area between the WFTB and KFTB (Fig. 5.1), most significantly (1) disparities in the trend of the fold belt, and (2) the presence of complex structural styles (e.g., Yangi Fold Belt; Hill *et al*.,

2000) with complex interference patterns that are suggestive of poly-deformation. Tectonic-scale variations in the compressional stress field may provide a suitable mechanism to account for the development of these complexities.

Other significant features throughout this transitional area are the large Pliocene to Pleistocene stratovolcanoes, the evolution of which is poorly understood. A combination of complex tectonics and evolving compressional stress field on the northern Australian margin may provide a plausible explanation. Magmatic fluids could have been sourced from the clockwise rotation and southwest-directed subduction of the proto-Solomon Sea Slab beneath central PNG, with emplacement of the volcanoes controlled by crustal-scale dilation resulting from abrupt lateral changes in compressive stresses at the leading edge of the Adelbert-Finisterre Terrane collision.

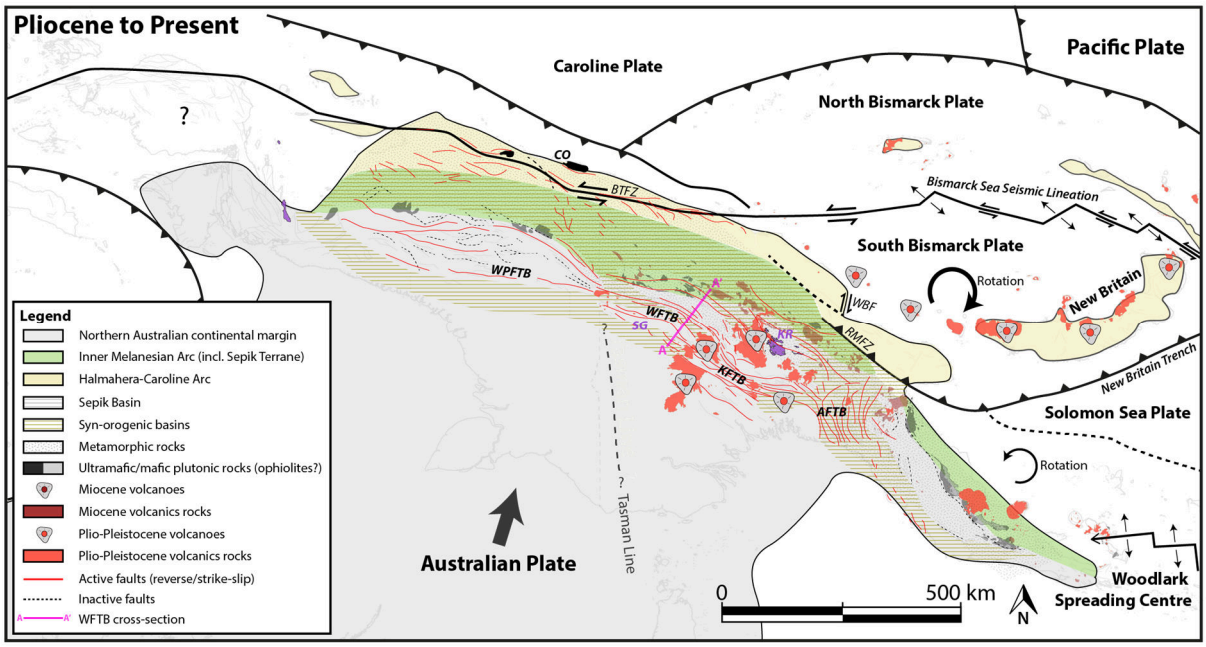

Figure 5.9. *Key geological and tectonic features of the northern Australian margin during the Pliocene to present. Purple indicates the location of basement outcrop, including in the Kubor Ranges (KR) and Strickland Gorge (SG). BTFZ, Bewani-Torricelli Fault Zone; RMFZ, Ramu-Markham fault zone; WBF, West Bismarck Fault; WPFTB, West Papuan Fold and Thrust Belt; WFTB, Western Fold and Thrust Belt; KFTB, Kutubu Fold and Thrust Belt; AFTB, Aure Fold and Thrust Belt; CO, Cyclops Ophiolite.*

In the WFTB, inversion along the Yakato and Lavani fault zones continued into the Pliocene, forming two coeval thrust fronts (Fig. 5.10b). The Yakato Fault Zone shallowed into a series of detachments within the thick sedimentary pile, reaching the surface as thrust faults responsible for forming the NWTB. The southwesterly extent of the NWTB is indicated by the stacking of thrust sheets on the backlimb of the Western Muller Range (Davies and Norvick, 1974), providing evidence for earlier, or coeval uplift of the Muller Range. A forelandward propagating monocline formed in the upper stratigraphy of the Eastern Muller Range area, in response to continued inversion along the Lavani Fault Zone and associated triangle zone style deformation within the underlying sedimentary section (e.g., Chapter 2; Fig. 5.10b). Crustal thickening in the Muller Range and adjacent syn-orogenic sediment loading in the foreland produced 1-1.5 km of subsidence, forming the Cecilia Trough.

From the earliest Pliocene to present, geomorphology becomes an important tool for unravelling the evolution of the WFTB. Erosion related to uplift above the Lavani Fault Zone formed the Lavani Valley at the crest of the Muller Range, most likely in the interval between 4 Ma and 2 Ma. The Lavani Valley drained to the southwest, incising Centre Pass into the frontal monocline (e.g., Lavani Ridge; Chapter 2) and forming a steep-sided river valley that extended into the foreland joining the Strickland River on the Fly Platform. Triangle zone style deformation continued to propagate towards the foreland throughout the Pleistocene, with a basement footwall shortcut fault required in the current model (Fig. 5.10c) to maximise uplift across the frontal Eastern Muller Range within low shortening constraints indicated by the near-surface Darai Limestone (e.g., Chapter 2). At least partially coeval inversion was likely occurring in the Juha graben, forming the Juha Anticline within the Cecilia depocentre. The reactivation of deep-rooted basement structures may have provided fluid conduits for igneous rocks, such as those found in the Tingi Valley, dated at ca. 1.9-1.8 Ma (ZHe; Mahoney, 2019 (unpub.)) and at Mt

Baia on the eastern end of the Juha Anticline, dated at ca. 1.7 Ma (U-Pb; Holm, 2013). Like the Lavani Fault Zone, the Juha Fault Zone shallowed into the sedimentary sequence forming a series of triangle zones and shallow-detached foreland-vergent structures including the Wai Asi and Cecilia Anticlines (e.g., Craig and Warvakai, 2009; Fig. 5.10d). In the current structural model, a second basement footwall shortcut fault evolves within the Juha Fault Zone, primarily to form a structural high identifiable on seismic images beneath the Cecilia Anticline (e.g., Hanani, 2012).

The propagation of uplift towards the southwest caused the Lavani Valley to tilt towards the northeast, prompting a drainage rearrangement which included the abandonment of drainage to the southwest through Centre Pass and across the Cecilia Trough and the onset of a more eastward and northward drainage system. This rearrangement also marked the onset of Quaternary sediment accumulation in the north of Lavani Valley (e.g., Chapter 2). The present-day analogue for the Lavani Valley-Centre Pass drainage system during the Pliocene (e.g., prior to northeast tilting) is the Tingi Valley-Tobi River drainage system located just 20 km to the northwest (e.g., Chapter 2), which presently drains to the southwest through the Cecilia depocentre where it merges with the Strickland River on the Fly Platform. The frontal fold belt structures, along with many hinterlandward structures, are still actively deforming as indicated in seismic records and as most recently demonstrated during the 2018 PNG Highlands earthquake sequence (e.g., Chapter 3).

(a) Middle to late Miocene (~11-4 Ma)

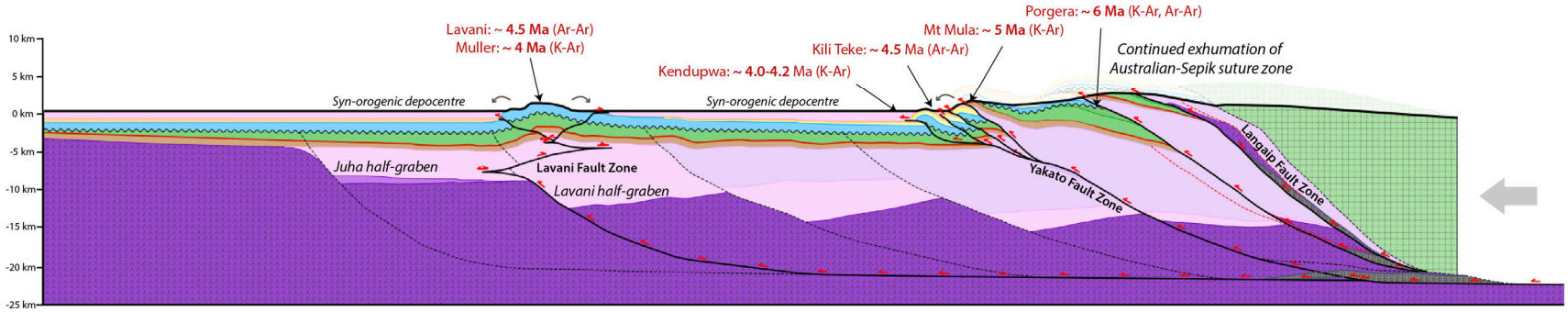

(b) Pliocene (~4-2 Ma)

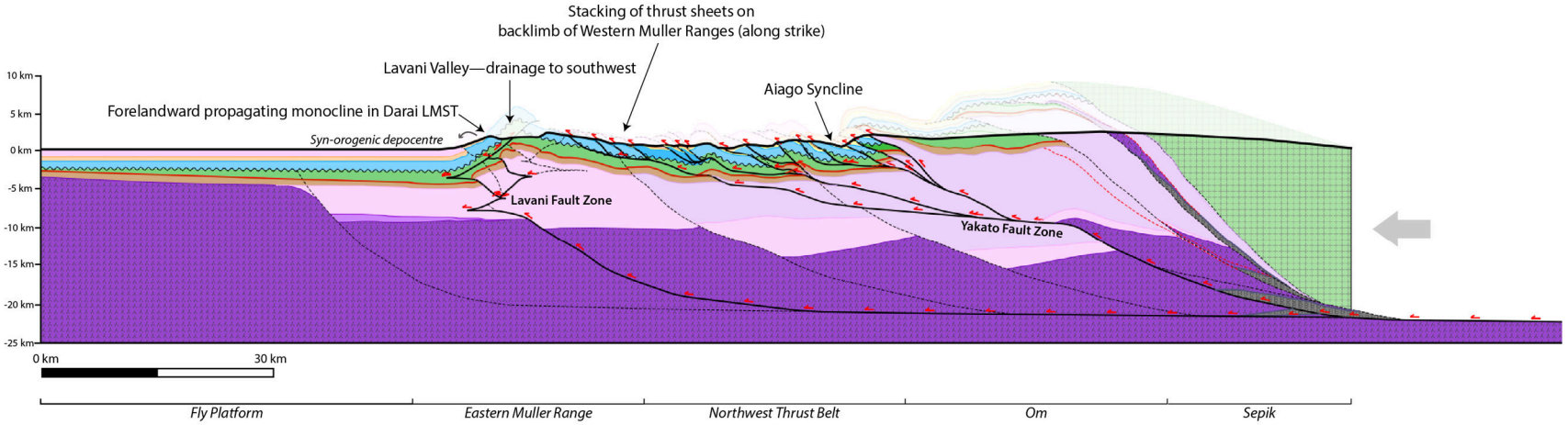

(c) Pleistocene (< 2 Ma)

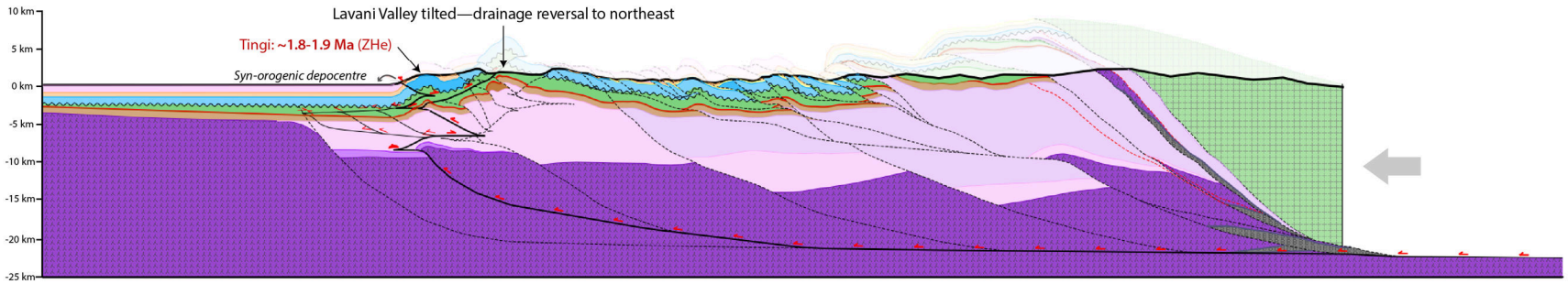

(d) Pleistocene to Present (< 2 Ma)

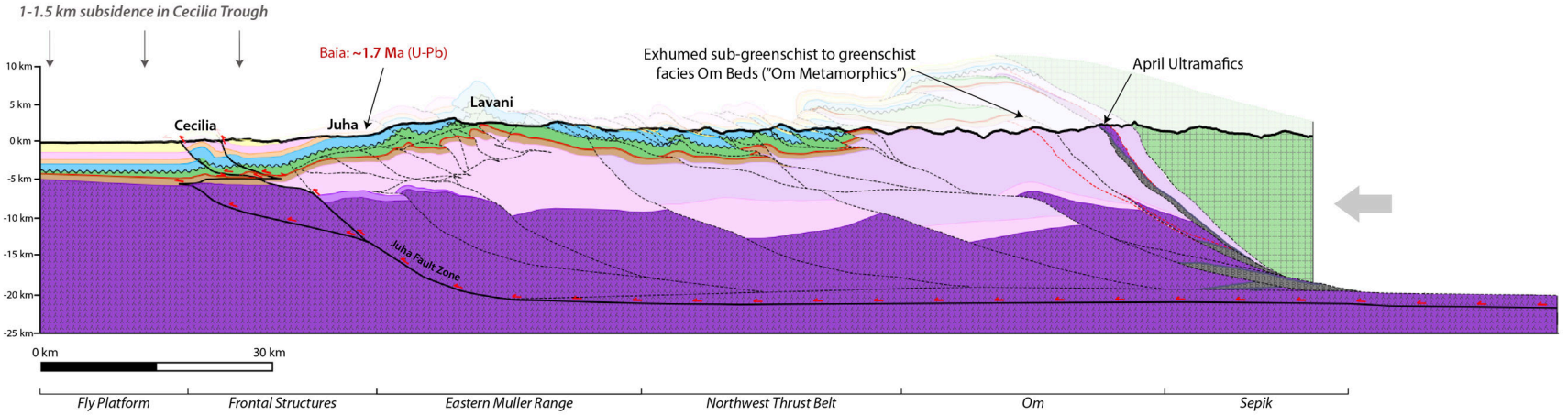

Figure 5.10. *(continuation of Fig. 5.2) Regional kinematic forward modelled cross-section (A-A' in Fig. 5.1) showing the geological evolution of the WFTB area of the northern Australian margin during Halmahera-Caroline Arc collision from the Miocene to present. (a) Middle Miocene to late Miocene reactivation of major fault zones previously active during Sepik Terrane collision (e.g., Fig. 5.2g-i); (b) Complex Pliocene folding and faulting on coeval deformation fronts in the Northwest Thrust Belt and Muller Range; (c) Pleistocene uplift of the frontal Eastern Muller Range; (d) Pleistocene to present evolution of frontal-most fold belt structures. Om Metamorphics facies from Mason (1996). Structural geometries within the Greater Juha area (e.g., Muller Range and Frontal Structures) based on constraints from Chapter 2. Geochronological age determinations of igneous rocks (red text): Porgera (Fleming et al., 1986; Richards and McDougall, 1990); Mt Mula (Kennecott, 1992); Kendupwa (Webb, 1973); Kili Teke, Lavani and Tingi (Mahoney, 2019 (unpub.)); Muller (Denison, 1990); Baia (Holm, 2013).*

References

Abbott, L.D., 1995. Neogene tectonic reconstruction of the Adelbert-Finisterre-New Britain collision, northern Papua New Guinea. *Journal of Southeast Asian Earth Sciences*, *11*(1), pp.33-51.

Abbott, L.D., Silver, E.A.,Galewsky, J., 1994b. Structural evolution of a modern arc-continent collision in Papua New Guinea. *Tectonics*, *13*(5), pp.1007-1034.

Abbott, L.D., Silver, E.A., Thompson, P.R., Filewicz, M.V., Schneider, C., 1994a. Stratigraphic constraints on the development and timing of arc-continent collision in northern Papua New Guinea. *Journal of Sedimentary Research*, *64*(2b), pp.169-183.

Apthorpe, M., 1988. Cainozoic depositional history of the North West Shelf. *The North West shelf, Australia, Symposium*, pp. 55-84.

Audley-Charles, M.G., 1988. Evolution of the southern margin of Tethys (North Australian region) from early Permian to late Cretaceous. *Geological Society of London, Special Publication*, 37(1), pp.79–100.

Australasian Petroleum Company, 1961. The Geological Results of Petroleum Exploration in Western Papua. *Journal of the Geological Society of Australia*, 8, 133 pp.

Bain, J.H.C., Mackenzie, D.E., Ryburn, R.J., 1975. Geology of the Kubor anticline, central highlands of Papua New Guinea. Bureau of Mineral Resources, *Geology and Geophysics Bulletin,* 155, Australian Government Publishing Service, 116 pp.

Brown, C. M., Pieters, P.E., Robinson, G.P., 1975. Stratigraphic and structural development of the Aure trough and adjacent shelf and slope areas. *The Australian Petroleum Exploration Association Journal*, 15, pp.61-71.

Bryan, S.E., Constantine, A.E., Stephens, C.J., Ewart, A., Schön, R.W., Parianos, J., 1997. Early Cretaceous volcano-sedimentary successions along the eastern Australian continental margin: Implications for the break-up of eastern Gondwana. *Earth and Planetary Science Letters*, 153(1-2), pp.85-102.

Bulois, C., Pubellier, M., Chamot-Rooke, N., Delescluse, M., 2018. Successive rifting events in marginal basins: The example of the Coral Sea region (Papua New Guinea). *Tectonics*, *37*(1), pp.3-29.

Clague, D.A., Dalrymple, G.B., 1989. Tectonics, geochronology, and origin of the Hawaiian-Emperor volcanic chain. *The Geology of North America*, pp.188-217.

Cloos, M., Sapiie, B., Quarles van Ufford, A., Weiland, R.J., Warren, P.Q., McMahon, T.P., 2005. Collisional delamination in New Guinea: The geotectonics of subducting slab breakoff. *Geological Society of America, Special Paper,* 400, 51 pp.

Cooper, P., Taylor, B., 1987. Seismotectonics of New Guinea: A model for arc reversal following arc-continent collision. *Tectonics*, *6*(1), pp.53-67.

Craig, M., Warvakai, K., 2009. Structure of an active foreland fold and thrust belt, Papua New Guinea. *Australian Journal of Earth Sciences,* 56, pp.719-738.

Crawford, A.J., Meffre, S., Symonds, P.A., 2003. 120 to 0 Ma tectonic evolution of the southwest Pacific and analogous geological evolution of the 600 to 220 Ma Tasman Fold Belt System. *Special Papers-Geological Society of America*, pp.383-404.

Crowhurst, P.V., 1999. *The tectonic history of northern Papua New Guinea.* PhD thesis, La Trobe University, Melbourne.

Crowhurst, P.V., Hill, K.C., Foster, D.A., Bennett, A.P., 1996. Thermochronological and geochemical constraints on the tectonic evolution of northern Papua New Guinea. *Geological Society, London, Special Publications*, 106(1), pp.525-537.

Crowhurst, P., Maas, R., Hill, K.C., Foster, D.A., Fanning, C.M., 2004. Isotopic constraints on crustal architecture and Permo-Triassic tectonics in New Guinea: Possible links with eastern Australia. *Australian Journal of Earth Sciences*, 51, pp.107-122.

Darnault, R., Hill, K.C., 2020. Four-dimensional analog and geometrical modelling of the Hides anticline, Papua New Guinea: Structure of a giant gas field. *AAPG Bulletin*, 104(4), pp.961-985.

Davies, H.L. 1980. Palaeontological data for the Wabag sheet area. Geological Survey of Papua New Guinea, Report 80/30.

Davies, H., 1983. Wabag 1:250 000 geological series explanatory notes Sheet SB/54-8, Geological Survey of Papua New Guinea, PNG Department of Minerals and Energy, Port Moresby.

Davies, H.L., 1990. Structure and evolution of the Border Region of New Guinea. In: Carman, G., Carman, Z. (Eds.), *Petroleum exploration, development, and production in Papua New Guinea: proceedings of the first PNG Petroleum Convention*, Papua New Guinea Chamber of Mines and Petroleum, Port Moresby, pp.245-269.

Davies, H.L., 2012. The geology of New Guinea—the cordilleran margin of the Australian continent. *Episodes,* 35 (1), pp.87-102.

Davies, H., Norvick, M., 1974. Blucher Range 1:250 000 geological series explanatory notes Sheet SB/54-07, Geological Survey of Papua New Guinea, PNG Department of Minerals and Energy, Port Moresby.

Davies, H.L., Perembo, R.C.B., Winn, R.D., Kengemar, P., 1997. Terranes of the New Guinea Orogen. In: Hancock, G. (Ed.), *Proceedings of the PNG Geology, Exploration and Mining Conference*, Madang, Australian Institute of Mining and Metallurgy, pp.61-66.

Davies, P.J., Symonds, P.A., Feary, D.A., Pigram, C.J., 1989. The evolution of the carbonate platforms of northeast Australia. In: Crevello, P.D., Wilson, J.L., Sarg, J.F., Read, J.F (Eds.), Controls on carbonate platform and basin development, *SEPM Special Publications*, 44.

Denison, R.E., 1990. K-Ar age dates. In: Hornafius, S.J., The 1990-1992 Muller Range Geological Survey, PPL 93, Papua New Guinea (unpubl.), 159 pp.

Doust, H., 1990. Geology of the Sepik Basin, Papua New Guinea. In: Carman, G., Carman, Z. (Eds.), *Petroleum exploration, development, and production in Papua New Guinea: proceedings of the first PNG Petroleum Convention*, Papua New Guinea Chamber of Mines and Petroleum, Port Moresby, pp.461-478.

Dow, D.B. 1977. A geological synthesis of Papua New Guinea. *Bureau of Mineral Resources Bulletin*, 201, 58 pp.

Edwards, A.B., 1950. The petrology of the Miocene sediments of Aure trough, Papua: *Proceedings of the Royal Society of Victoria*, 60, pp.123-148.

Faccenna, C., Becker, T.W., Lallemand, S., Steinberger, B., 2012. On the role of slab pull in the Cenozoic motion of the Pacific plate. *Geophysical Research Letters*, 39(3).

Fischer, M.W., Warburton., 1996. The importance of pre-Tertiary basin architecture for hydrocarbon accumulation in the Papuan Fold and Thrust Belt: models, analogues and implications. In: Buchanan, P. (Ed.), *Petroleum exploration, development, and production in Papua New Guinea: proceedings of the third PNG Petroleum Convention*, Papua New Guinea Chamber of Mines and Petroleum, Port Moresby, pp.111-131.

Fleming, A.W., Handley, G.A., Williams, K.L., Hills, A.L., Corbett, G.J., 1986. The Porgera gold deposit, Papua New Guinea. *Economic Geology*, 81(3), pp.660-680.

Francis, G., 1990. The North New Guinea Basin and associated infra-basins. In: Carman, G., Carman, Z. (Eds.), *Petroleum exploration, development, and production in Papua New Guinea: proceedings of the first PNG Petroleum Convention*, Papua New Guinea Chamber of Mines and Petroleum, Port Moresby, pp.445-460.

Gaina, C., Müller, D.R., Royer, J.Y., Stock, J., Hardebeck, J., Symonds, P., 1998. The tectonic history of the Tasman Sea: a puzzle with 13 pieces. *Journal of Geophysical Research: Solid Earth*, 103(B6), pp.12413-12433.

Gaina, C., Müller, R.D., Royer, J.Y., Symonds, P., 1999. Evolution of the Louisiade triple junction. *Journal of Geophysical Research: Solid Earth*, 104(B6), pp.12927-12939.

Glen, R.A., 2005. The Tasmanides of eastern Australia. In: Vaughan, A.P.M., Leat, P.T., Pankhurst, R.J. (Eds.), *Terrane Processes at the margins of Gondwana*. Geological Society, London, Special Publications, 246, pp.23-96.

Gow, P.A., Upton, P., Zhao, C., Hill, K.C., 2002. Copper-gold mineralisation in New Guinea: Numerical modelling of collision, fluid flow and intrusion-related hydrothermal systems. *Australian Journal of Earth Sciences*, 49(4), pp.753-771.

Gunson, M., Haig, D.W., Kruman, B., Mason, R.A., Perembo, R.C.B., Stewart, R., 1997. Stratigraphic reconstruction of the Porgera region, Papua New Guinea. In: Hancock, G. (Ed.), *Proceedings of the PNG Geology, Exploration and Mining Conference*, Madang, Australian Institute of Mining and Metallurgy, pp.99-108.

Gunson, M., Hall, G., Johnston, M 2000. Foraminiferal coloration index as a guide to hydrothermal gradients around the Porgera Intrusive Complex, Papua New Guinea. *Economic Geology*, 95, pp.271-282.

Gurnis, M., Müller, R.D., Moresi, L., 1998. Cretaceous vertical motion of Australia and the AustralianAntarctic discordance. *Science*, 279(5356), pp.1499-1504.

Hall, R., 2002. Cenozoic geological and plate tectonic evolution of SE Asia and the SW Pacific: computer-based reconstructions, model and animations. *Journal of Asian Earth Sciences*, 20(4), pp.353-431.

Hall, R., 2012. Late Jurassic–Cenozoic reconstructions of the Indonesian region and the Indian Ocean. *Tectonophysics*, 570, pp.1-41.

Hanani, A., 2012. The Geology and Structural Style of the Juha Gas Field, Papua New Guinea. Honours Thesis (unpubl.), The University of New South Wales, Sydney, 214 pp.

Hanani, A., Lennox, P., Hill, K.C., 2016. The geology and structural style of the Juha Gas Field, Papua New Guinea. *ASEG Extended Abstracts 2016*, pp.1-7.

Haq, B.U., Hardenbol, J., Vail, P.R., 1987. Chronology of fluctuating sea levels since the Triassic. *Science*, 235, pp.1156-1167.

Haq, B.U., 2014. Cretaceous eustasy revisited. *Global and Planetary Change*, 113, pp.44-58.

Harrington, L., Zahirovic, S., Flament, N., Müller, R.D., 2017. The role of deep Earth dynamics in driving the flooding and emergence of New Guinea since the Jurassic. *Earth and Planetary Science Letters*, 479, pp.273-283.

Higgins, K., Hashimoto, T., Rollet, N., Colwell, J., Hackney, R., Milligan, P., 2015. Structural analysis of extended Australian continental crust: Capel and Faust basins, Lord Howe Rise. *Geological Society, London, Special Publications*, 413(1), pp.9-33.

Hill, K.C., 1991. Structure of the Papuan Fold Belt, Papua New Guinea. *The American Association of Petroleum Geologists Bulletin*, 75, pp.857-872.

Hill, K.C., Gleadow, A., 1989. Uplift and thermal history of the Papuan Fold Belt, Papua New Guinea: Apatite Fission track analysis. *Australian Journal of Earth Sciences*, 36, pp.515-539.

Hill, K.C., Gleadow, A., 1990. Apatite fission track analysis of the Papuan Basin. In: Carman, G., Carman, Z. (Eds.), *Petroleum exploration, development, and production in Papua New Guinea: proceedings of the first PNG Petroleum Convention*, Papua New Guinea Chamber of Mines and Petroleum, Port Moresby, pp.119-136.

Hill, K.C., Grey, A., Foster, D., Barrett, R., 1993. An alternative model for the Oligo-Miocene evolution of northern PNG and the Sepik-Ramu basins. In: Carman, G., Carman, Z. (Eds.), *Petroleum exploration, development, and production in Papua New Guinea: proceedings of the second PNG Petroleum Convention*, Papua New Guinea Chamber of Mines and Petroleum, Port Moresby, pp.241-259.

Hill, K.C., Hall, R., 2003. Mesozoic-Cenozoic evolution of Australia's New Guinea margin in a west Pacific context. *Geological Society of America, Special Papers, 372*, pp.265-290.

Hill, K.C., Kendrick, R.D., Crowhurst, P.V., Gow, P.A., 2002. Copper-gold mineralisation in New Guinea: Tectonics, lineaments, thermochronology and structure. *Australian Journal of Earth Sciences*, *49*(4), pp.737-752.

Hill, K.C., Lucas, K., Bradey, K., 2010. Structural styles in the Papuan Fold Belt, Papua New Guinea: constraints from analogue modelling. In: Goffey, G. (Ed.), *Hydrocarbons in Contractional Belts*, Geological Society, London, Special Publications, 348, pp.33-56.

Hill, K., Mahoney, L., 2018. Compressional evolution of the PNG margin from an orogenic transect from Juha to the Sepik. *ASEG Extended Abstracts*, 2018(1), pp.1-3.

Hill, K.C., Medd, D., Darvall, P., 1990. Structure, stratigraphy, geochemistry and hydrocarbons in the Kagua-Kubor area, Papua New Guinea. In: Carman, G., Carman, Z. (Eds.), *Petroleum exploration, development, and production in Papua New Guinea: proceedings of the first PNG Petroleum Convention*, Papua New Guinea Chamber of Mines and Petroleum, Port Moresby, 351-366.

Hill, K.C., Norvick, M., Keetley, J., Adams, A., 2000. Structural and stratigraphic shelf-edge hydrocarbon plays in the Papuan Fold Belt. In: Buchanan, P., Grainge, A., Thornton, R. (Eds.), *Petroleum Exploration, Development, and Production in Papua New Guinea: Proceedings of the Fourth PNG Petroleum Convention.* Papua New Guinea Chamber of Mines and Petroleum, Port Moresby, pp.67-85.

Hill, K.C., Raza, A., 1999. Arc-continent collision in Papua Guinea: Constraints from fission track thermochronology. *Tectonics*, 18(6), pp.950-966.

Holcombe, R.J., Stephens, C.J., Fielding, C.R., Gust, D., Little, T.A., Sliwa, R., Kassan, J., McPhie, J., Ewart, A., 1997. Tectonic evolution of the northern New England Fold Belt: the Permian–Triassic Hunter–Bowen event. *Tectonics and metallogenesis of the New England Orogen*, 19, pp.52-65.

Holm, R.J., 2013. Magmatic arcs of Papua New Guinea: insights into the late Cenozoic tectonic evolution of the northern Australian plate boundary. PhD thesis, James Cook University, Queensland, Australia, 220 pp.

Holm, R.J., Richards, S.W., 2013. A re-evaluation of arc–continent collision and along-arc variation in the Bismarck Sea region, Papua New Guinea. *Australian Journal of Earth Sciences*, 60(5), pp.605-619.

Home, P., Dalton, D., Brannan, J., 1990. Geological evolution of the Western Papuan Basin. In: Carman, G., Carman, Z. (Eds.), *Petroleum exploration, development, and production in Papua New Guinea: proceedings of the first PNG Petroleum Convention*, Papua New Guinea Chamber of Mines and Petroleum, Port Moresby, pp.107-118.

Hutchison, D.S., Norvick, M.S., 1980. Geology of the North Sepik region, Papua New Guinea. Australian BMR Record 1980/24, 97 pp.

Jaques, A.L., 1976. High K_2O-island arc volcanics from the Finisterre and Adelbert Ranges, northern Papua New Guinea. *Geological Society of America Bulletin*, 87, pp.861-867.

Jenkins, D.A., 1974. Detachment tectonics in western Papua New Guinea. *Geological Society of America Bulletin*, 85(4), pp.533-548.

Jenkins, D., White, M.F., 1970. Report on the Strickland River survey, Permit 46, Papua. BP Petroleum Development Report 89 (unpubl.). Geological Survey of Papua New Guinea Data File 4 BS.

Kendrick, R.D., 2000. *Structure, tectonics and thermochronology of the Irian Jaya Fold Belt, Irian Jaya, Indonesia.* PhD thesis, La Trobe University, Melbourne.

Kennecott, 1992. Kennecott Explorations (Australia) Ltd, exploration licence 1011-Urei River, Papua New Guinea, Annual Report to February 26, 1993 (unpubl.).

Koulali, A., Tregoning, P., McClusky, S., Stanaway, R., Wallace, L., Lister, G., 2015. New Insights into the present-day kinematics of the central and western Papua New Guinea from GPS. *Geophysical Journal International*, 202(2), pp.993-1004.

Mason, R.A., 1996. Structure of the Western Papuan Fold Belt. In: Buchanan, P. (Ed.), *Petroleum Exploration, Development, and Production in Papua New Guinea: Proceedings of the Third PNG Petroleum Convention*. Papua New Guinea Chamber of Mines and Petroleum, Port Moresby, pp.161-173.

McConachie, B., Lanzilli, E., Kendrick, D., Burge, C., 2000. Extensions of the Papuan Basin foreland geology into Eastern Irian Jaya (West Papua) and the New Guinea Fold Belt in Papua New Guinea. In: Buchanan, P., Grainge, A., Thornton, R. (Eds.), *Petroleum exploration, development, and production in Papua New Guinea: proceedings of the fourth PNG Petroleum Convention*, Papua New Guinea Chamber of Mines and Petroleum, Port Moresby, pp.219-237.

McKenzie, D., 1978. Some remarks on the development of sedimentary basins. *Earth and Planetary science letters*, 40(1), pp.25-32.

Metcalfe, I., 1996. Gondwanaland dispersion, Asian accretion and evolution of eastern Tethys. *Australian Journal of Earth Sciences*, 43(6), pp.605-623.

Muller, R.D., Flament, N., Matthews, K.J., Williams, S.E., 2016. Formation of Australian continental margin highlands driven by plate-mantle interaction. *Earth and Planetary Science Letters*, 441, pp.60-70.

Norvick, M.S., 2003. New palaeogeographic maps of the northern margins of the Australian plate: updated report (unpubl.). Report for Geoscience Australia, September 2003.

Page, R., 1976. Geochronology of igneous and metamorphic rocks in the New Guinea Highlands. *Bureau of Mineral Resources Australia Bulletin*, 162, 117 pp.

Permana, H., 1998. Dynamique de la mise en place des ophiolites d'Irian Jaya (Indonesie). PhD thesis, Universite de Nantes, 314 pp.

Phelps, J.C., Denison, C.N., 1993. Stratigraphic thickness variations and depositional systems of the Ieru Formation, Southern Highlands and western Provinces, Papua New Guinea. In: Carman, G., Carman, Z. (Eds.), *Petroleum exploration, development, and production in Papua New Guinea: proceedings of the second PNG Petroleum Convention*, Papua New Guinea Chamber of Mines and Petroleum, Port Moresby, pp.169-190.

Pigott, J.D., Trumbly, N.I., O'Neal, M.V., 1985. Northern New Guinea wrench fault system: a manifestation of late Cenozoic interactions between Australian and Pacific plates. *Tectonics*, 4, pp.613-620.

Pigram, C.J., Davies, H.L., 1987. Terranes and the accretion history of the New Guinea orogen. *BMR Journal of Australian Geology and Geophysics*, 10, pp.193-211.

Pigram, C.J., Davies, P.J., Feary, D.A., Symonds, P.A., 1989. Tectonic controls on carbonate platform evolution in southern Papua New Guinea: Passive margin to foreland basin. *Geology*, 17(3), pp.199-202.

Pigram, C.J., Davies, P.J., Feary, D.A., Symonds, P.A., Chaproniere, G.C.H., 1990. Controls on Tertiary carbonate platform evolution in the Papuan Basin: new play concepts. In: Carman, G., Carman, Z. (Eds.), *Petroleum exploration, development, and production in Papua New Guinea: proceedings of the first PNG Petroleum Convention*, Papua New Guinea Chamber of Mines and Petroleum, Port Moresby, pp.185-195.

Pigram, C., Panggabean, H., 1984. Rifting of the northern margin of the Australian continent and the origin of some microcontinents in eastern Indonesia. *Tectonophysics,* 107, pp.331-353.

Pigram, C., Symonds, P.A., 1991. A review of the timing of the major tectonic events in the New Guinea Orogen. *Journal of Southeast Asian Earth Sciences*, 6, pp.307-318.

Pigram, C., Symonds, P.A., 1993. Eastern Papuan Basin—A new model for the tectonic development and implications for petroleum prospectivity. In: Carman, G., Carman, Z. (Eds.), *Petroleum exploration, development, and production in Papua New Guinea: proceedings of the second PNG Petroleum Convention*, Papua New Guinea Chamber of Mines and Petroleum, Port Moresby, pp.213-231.

Pubellier, M., Ali, J., Monnier, C., 2003. Cenozoic Plate interaction of the Australia and Philippine Sea Plates: "hit-and-run" tectonics. *Tectonophysics*, 363(3), pp. 181–199.

Richards, J.P., McDougall, I., 1990. Geochronology of the Porgera gold deposit, Papua New Guinea: Resolving the effects of excess argon on K-Ar and 40Ar39Ar age estimates for magmatism and mineralization. *Geochimica et Cosmochimica Acta*, 54(5), pp.1397-1415.

Richards, J.R., Willmott, W.F., 1970. K-Ar age of biotites from Torres Strait. Australian Journal of Science, 32(9), pp.369-370.

Rickwood, F.K., 1954. The geology of the western highlands of New Guinea. *Journal of the Geological Society of Australia,* 2(1), pp.63–82.

Rogerson, R.J., Hilyard, D.B., 1990. Scrapland: a suspect composite terrane in Papua New Guinea. In: Carman, G., Carman, Z. (Eds.), *Petroleum exploration, development, and production in Papua New Guinea: proceedings of the first PNG Petroleum Convention*, Papua New Guinea Chamber of Mines and Petroleum, Port Moresby, pp.271-282.

Sandiford, M., 2007. The tilting continent: a new constraint on the dynamic topographic field from Australia. *Earth and Planetary Science Letters*, 261(1-2), pp.152-163.

Sari, J., Failing, R., Wulff, K., 1996. The Giero Sandstone: A potentially new play in the Papuan Basin. In: Buchanan, P. (Ed.), *Petroleum exploration, development, and production in Papua New Guinea: proceedings of the third PNG Petroleum Convention*, Papua New Guinea Chamber of Mines and Petroleum, Port Moresby, pp.301-312.

Scheibner, E., 1974. Fossil fracture zones (transform faults), segmentation, and correlation problems in the Tasman Fold Belt System. In: Denmead A. K., Tweedale G. W., Wilson A. F. (Eds.), *The Tasman Geosyncline—a Symposium in Honour of Professor Dorothy Hill*, Geological Society of Australia, Queensland Division, Brisbane, pp.65–98.

Schellart, W.P., Spakman, W., 2015. Australian plate motion and topography linked to fossil New Guinea slab below Lake Eyre. *Earth and Planetary Science Letters,* 421, pp.107-116.

Schofield, S., 2000. The Bosavi Arch and Komewu Fault Zone: Their control on basin architecture and the prospectivity of the Papuan Foreland. In: Buchanan, P., Grainge, A., Thornton, R. (Eds.), *Petroleum exploration, development, and production in Papua New Guinea: proceedings of the fourth PNG Petroleum Convention*, Papua New Guinea Chamber of Mines and Petroleum, Port Moresby, 101-122.

Slater, A., Balkwill, H.R., Fong, G.U., 1988. Seismic evidence for structural style in the offshore Kerema area Papua New Guinea: Application to petroleum exploration. In: *Seventh offshore South East Asia Conference, Singapore*: South East Asia Exploration Society, pp. 141-149.

Taylor, B., 1979. Bismarck Sea: Evolution of a back-arc basin. *Geology*, 7(4), pp.171-174.

Thompson, J.E., 1967. A geological history of Eastern New Guinea. *The APPEA Journal*, 7(1), pp.83-93.

Tobin, J., Zahirovic, S., Hassan, R., Rey, P., 2018. Tectonic and Geodynamic Evolution of the Northern Australian Margin and New Guinea. *ASEG Extended Abstracts* 2018, 7 pp.

Valenti, G.L., 1993. P'nyang Field: discovery and geology of a gas giant in the western Papuan Fold Belt, Western Province, Papua New Guinea. In: Carman, G., Carman, Z. (Eds.), *Petroleum exploration, development, and production in Papua New Guinea: proceedings of the second PNG Petroleum Convention*, Papua New Guinea Chamber of Mines and Petroleum, Port Moresby, pp.413-430.

van Ufford, A.Q., Cloos, M., 2005. Cenozoic tectonics of New Guinea. *AAPG bulletin*, 89(1), pp.119-140.

van Wyck, N., Williams, I.S., 2002. Age and provenance of basement metasediments from the Kubor and Bena Bena Blocks, central Highlands, Papua New Guinea: Constraints on the tectonic evolution of the northern Australian cratonic margin. *Australian Journal of Earth Sciences*, 49(3), 565-577.

Visser, W.A., Hermes, J.J., 1962. Geological results of the exploration for oil in Netherlands New Guinea. *Verhandellngen Konlnklijk Nederlands Geologlsch en Mljnbouwkundig Genootschap, Geologische Serte* 20.

Wallace, L.M., Stevens, C., Silver, E., McCaffrey, R., Loratung, W., Hasiata, S., Stanaway, R., Curley, R., Rosa, R., Taugaloidi, J., 2004. GPS and seismological constraints on active tectonics and arc-continent collision in Papua New Guinea: Implications for mechanics of microplate rotations in a plate boundary zone. *Journal of Geophysical Research: Solid Earth*, 109, B05404.

Wallace, L.M., McCaffrey, R., Beavan, J., Ellis, S., 2005. Rapid microplate rotations and backarc rifting at the transition between collision and subduction. *Geology*, 33(11), pp.857-860.

Webb, A., 1973. Geochronology report on samples submitted by BMR West Sepik party. Australian Mineral Development Laboratories Report AN3049/73 (unpubl.)

Weiland, R.J., 2000. Emplacement of the Irian Ophiolite and unroofing of the Ruffaer Metamorphic Belt of Irian Jaya, Indonesia. PhD thesis. University of Texas, 526 pp.

Weiland, R.J., Cloos, M., 1996. Pliocene-Pleistocene asymmetric unroofing of the Irian fold belt, Irian Jaya, Indonesia: Apatite fission-track thermochronology. *Geological Society of America Bulletin*, 108(11), pp.1438-1449.

Weissel, J.K., Watts, A.B., 1979. Tectonic evolution of the Coral Sea Basin. *Journal of Geophysical Research*. 84, pp.4572-4582.

White, M.F., Boxall, A.M., Findlay, A.L., Sweetman, I.A.D., Visser, B., 1973. Report on the Fly-Palmer geological survey. BP Petroleum Development Report (unpubl.). Geological Survey of Papua New Guinea data file 4 BQ.

White, L.T., Morse, M.P., Lister, G.S., 2014. Lithospheric-scale structures in New Guinea and their control on the location of gold and copper deposits. *Solid Earth*, 5(1), pp.163-179.

Willmott, W.F., Palfreyman, W.D., Trail, D.S., Whitaker, W.G., 1969. The Igneous Rocks of Torres Strait, Queensland and Papua. *Bureau of Mineral Resources Australia*, 1969/119, 114 pp.

Worthing, M.A, Crawford, A,J., 1996. The igneous geochemistry and tectonic setting of metabasites from the Emo metamorphics, Papua New Guinea: a record of the evolution and destruction of a backarc basin. *Mineralogy and Petrology*, 58 (1-2), pp.79–100.

Zahirovic, S., Matthews, K. J., Flament, N., Müller, R. D., Hill, K. C., Seton, M., Gurnis, M., 2016. Tectonic evolution and deep mantle structure of the eastern Tethys since the latest Jurassic. *Earth Science Reviews*, 162, pp.293-337.

Supplementary material A5: Geological and tectonic evolution schematics

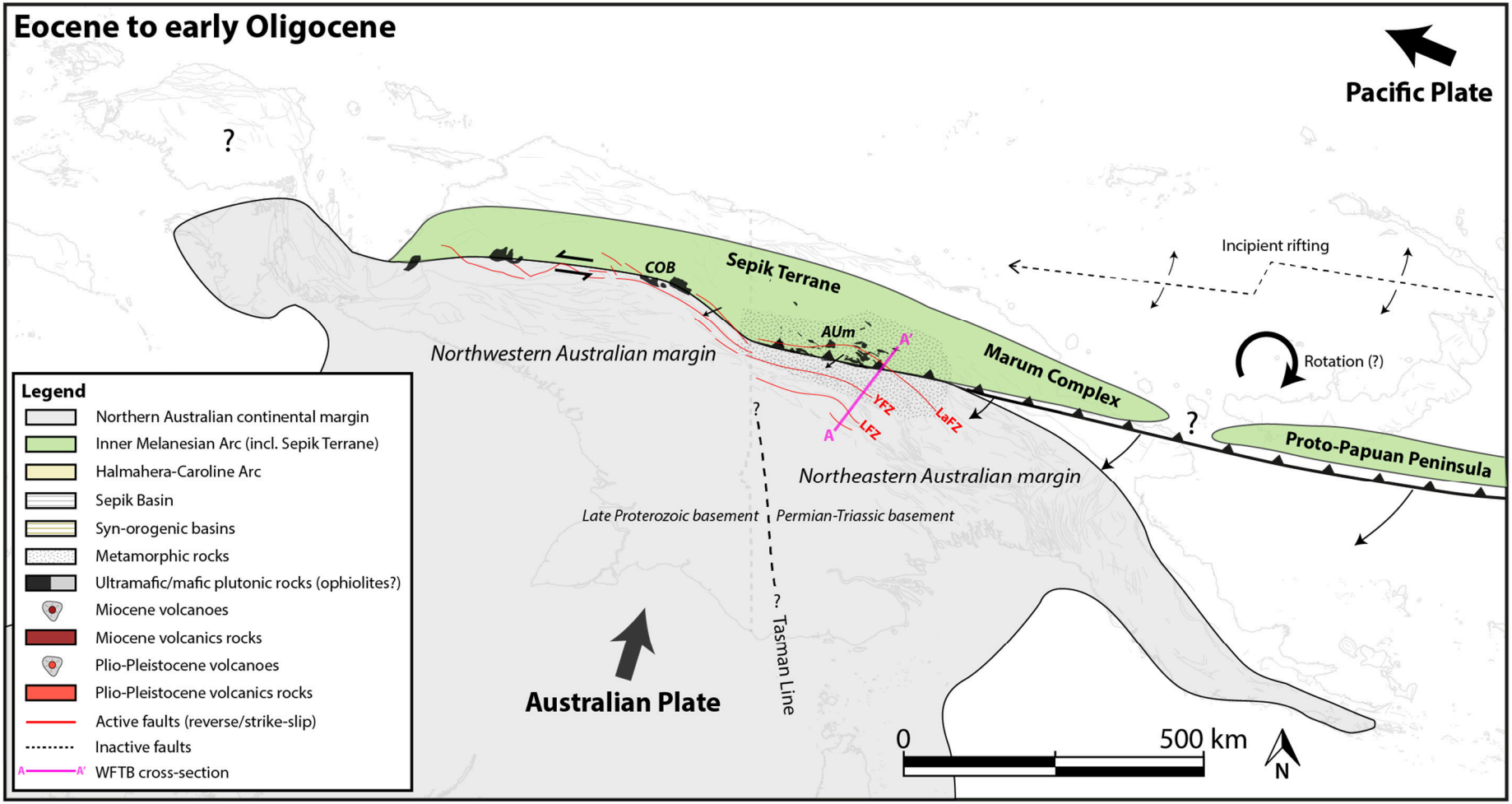

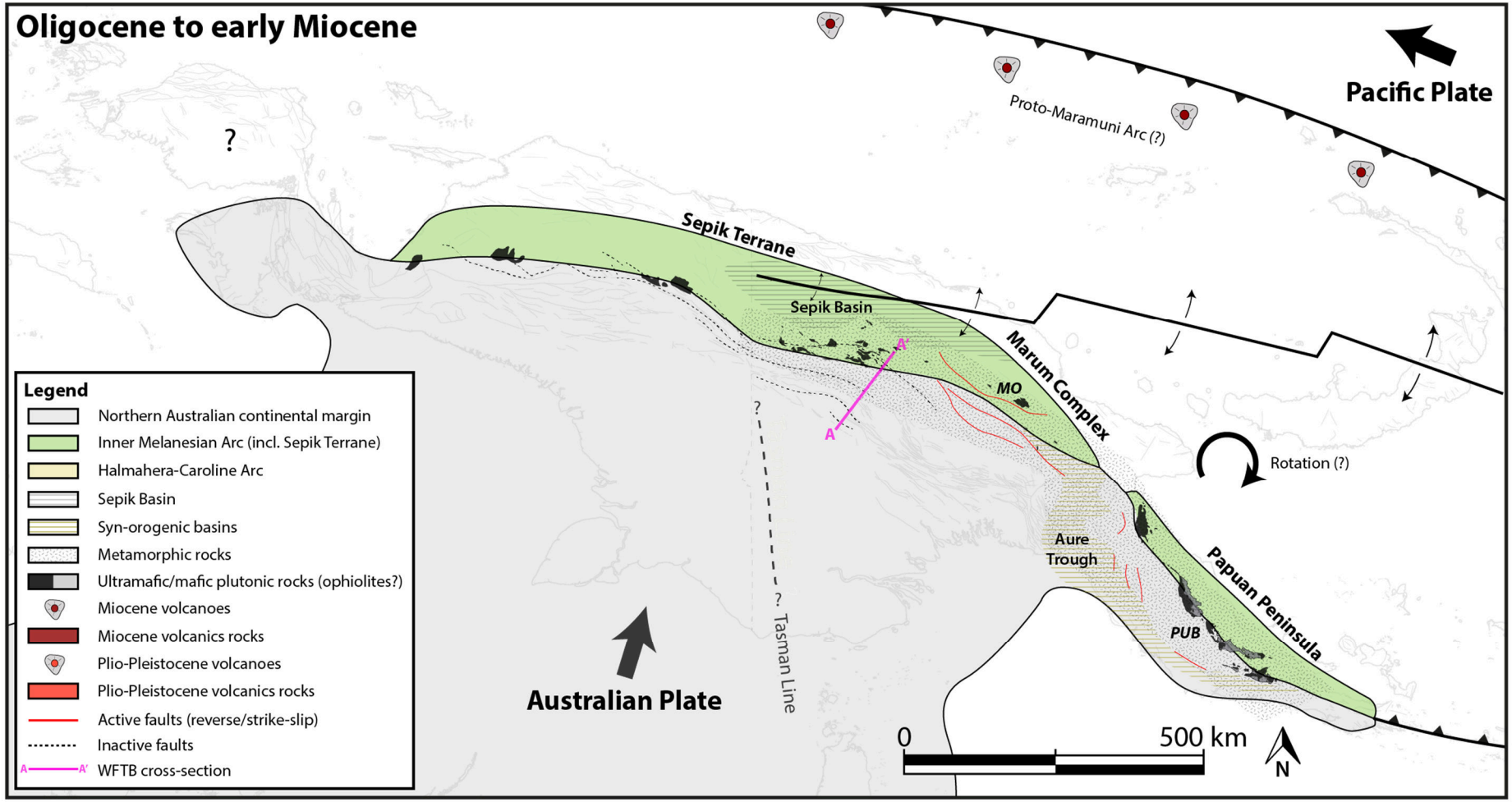
Oligocene to early Miocene
?
Proto-Maramuni Arc (?)
Pacific Plate
Sepik Terrane
Sepik Basin
A
A'
MO
Marum Complex
Rotation (?)
Aure
Trough
Papuan Peninsula
PUB
? Tasman Line
Australian Plate
0
500 km
N
Legend
Northern Australian continental margin
Inner Melanesian Arc (incl. Sepik Terrane)
Halmahera-Caroline Arc
Sepik Basin
Syn-orogenic basins
Metamorphic rocks
Ultramafic/mafic plutonic rocks (ophiolites?)
Miocene volcanoes
Miocene volcanics rocks
Plio-Pleistocene volcanoes
Plio-Pleistocene volcanics rocks
Active faults (reverse/strike-slip)
Inactive faults
WFTB cross-section

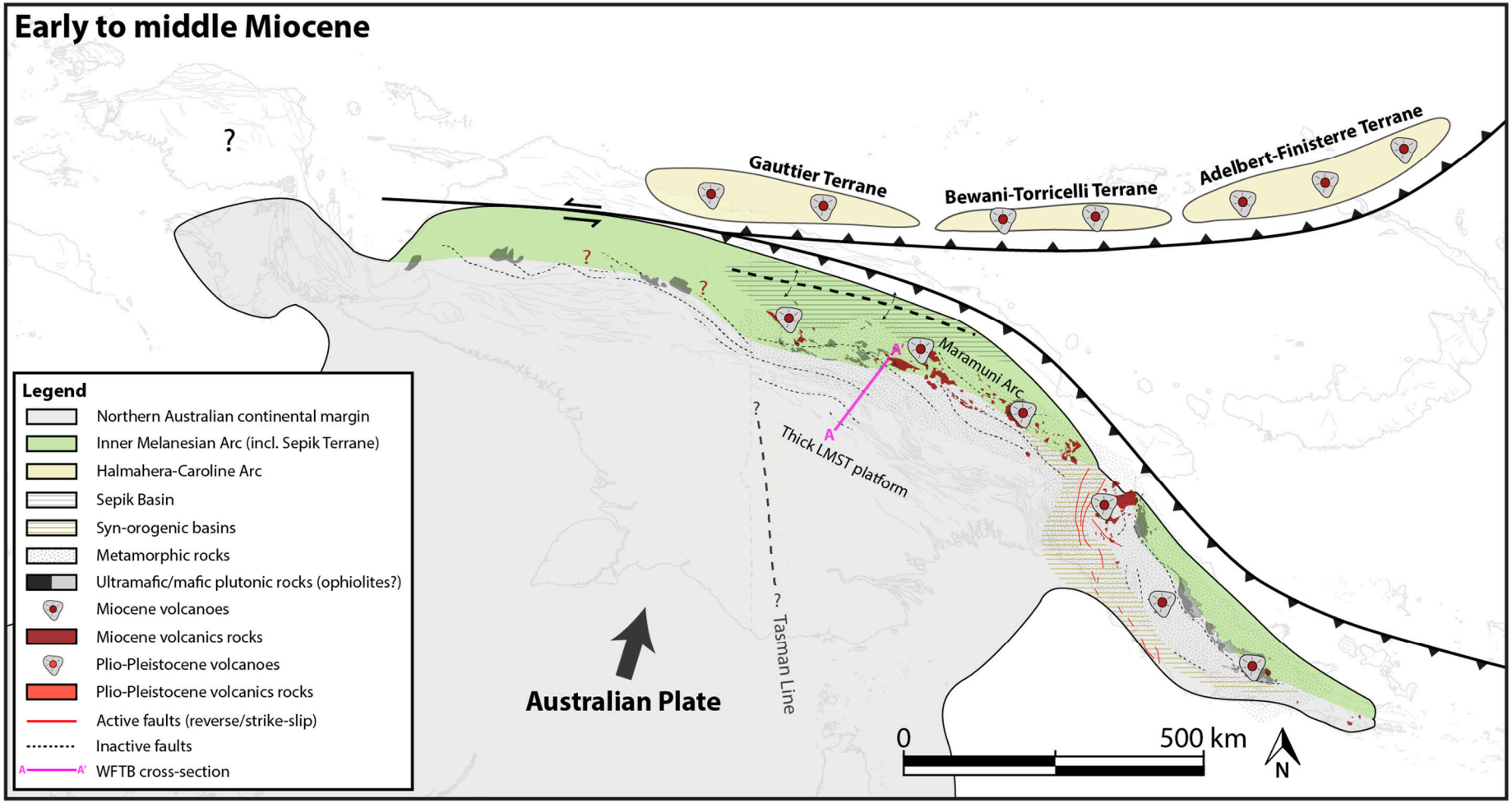
Early to middle Miocene
?
Gauttier Terrane
Bewani-Torricelli Terrane
Adelbert-Finisterre Terrane
Maramuni Arc
A
A'
Thick LMST platform
? Tasman Line
Australian Plate
0
500 km
N
Legend
Northern Australian continental margin
Inner Melanesian Arc (incl. Sepik Terrane)
Halmahera-Caroline Arc
Sepik Basin
Syn-orogenic basins
Metamorphic rocks
Ultramafic/mafic plutonic rocks (ophiolites?)
Miocene volcanoes
Miocene volcanics rocks
Plio-Pleistocene volcanoes
Plio-Pleistocene volcanics rocks
Active faults (reverse/strike-slip)
Inactive faults
WFTB cross-section

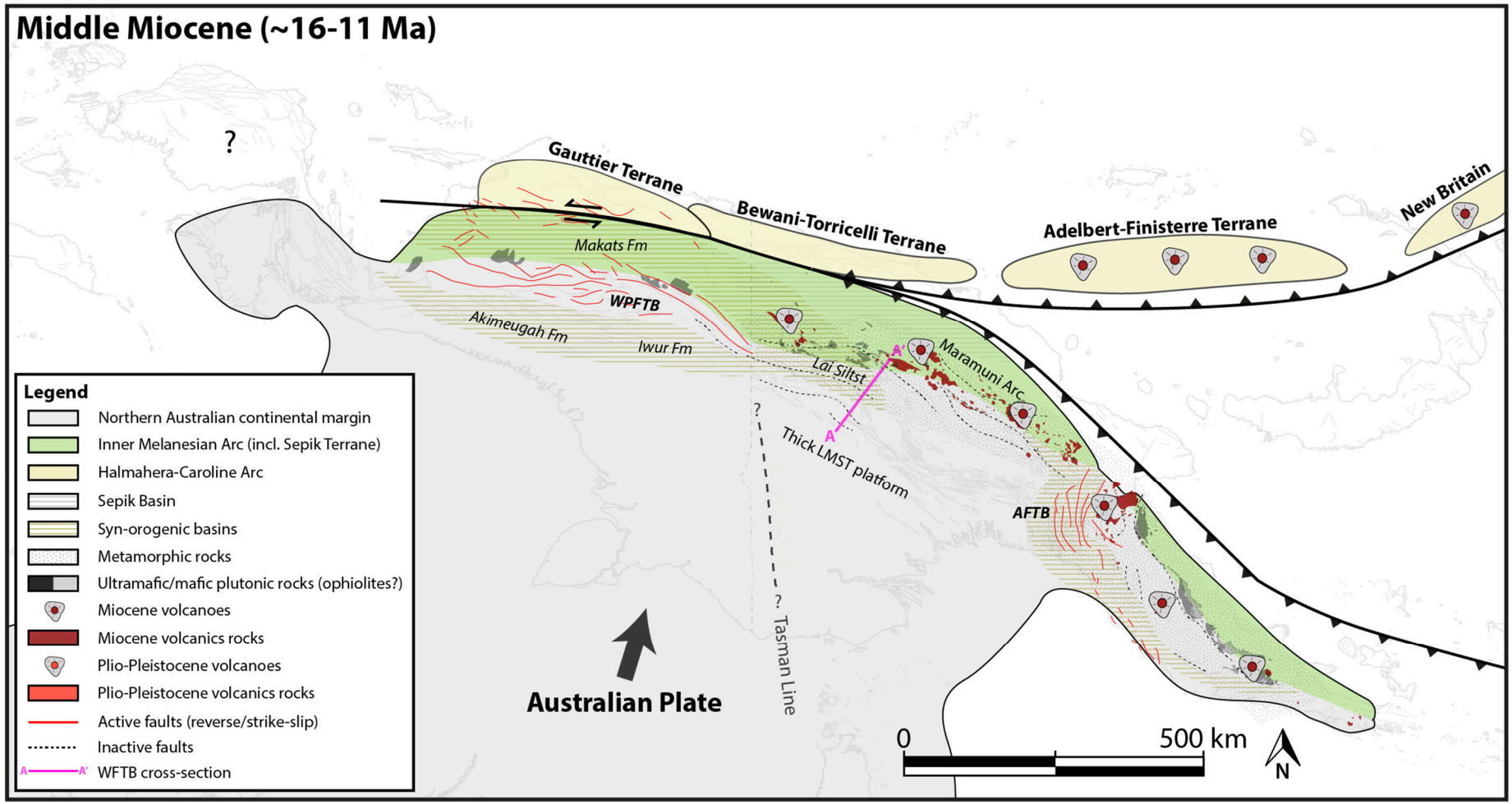
Middle Miocene (~16-11 Ma)
?
Gauttier Terrane
Bewani-Torricelli Terrane
Adelbert-Finisterre Terrane
New Britain
Makats Fm
WPFTB
Akimeugah Fm
Iwur Fm
Lai Siltst
Maramuni Arc
A
A'
Thick LMST platform
AFTB
? Tasman Line
Australian Plate
0
500 km
N
Legend
Northern Australian continental margin
Inner Melanesian Arc (incl. Sepik Terrane)
Halmahera-Caroline Arc
Sepik Basin
Syn-orogenic basins
Metamorphic rocks
Ultramafic/mafic plutonic rocks (ophiolites?)
Miocene volcanoes
Miocene volcanics rocks
Plio-Pleistocene volcanoes
Plio-Pleistocene volcanics rocks
Active faults (reverse/strike-slip)
Inactive faults
WFTB cross-section

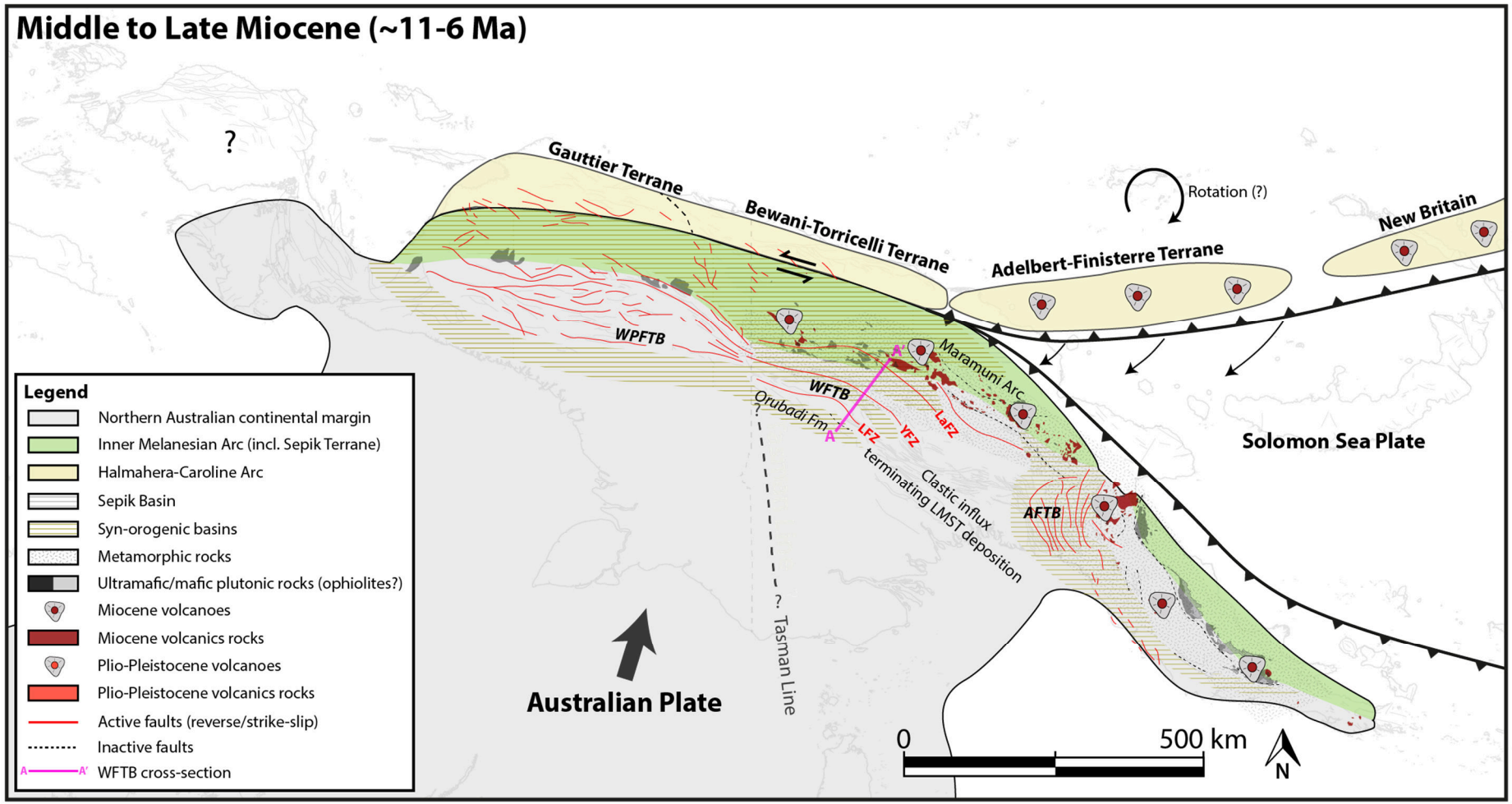
Middle to Late Miocene (~11-6 Ma)
?
Gauttier Terrane
Bewani-Torricelli Terrane
Rotation (?)
Adelbert-Finisterre Terrane
New Britain
WPFTB
WFTB
Maramuni Arc
A
A'
Orubadi Fm
LFZ
YFZ
LaFZ
Clastic influx
terminating LMST deposition
AFTB
Solomon Sea Plate
Australian Plate
? Tasman Line
0
500 km
N
Legend
Northern Australian continental margin
Inner Melanesian Arc (incl. Sepik Terrane)
Halmahera-Caroline Arc
Sepik Basin
Syn-orogenic basins
Metamorphic rocks
Ultramafic/mafic plutonic rocks (ophiolites?)
Miocene volcanoes
Miocene volcanics rocks
Plio-Pleistocene volcanoes
Plio-Pleistocene volcanics rocks
Active faults (reverse/strike-slip)
Inactive faults
WFTB cross-section

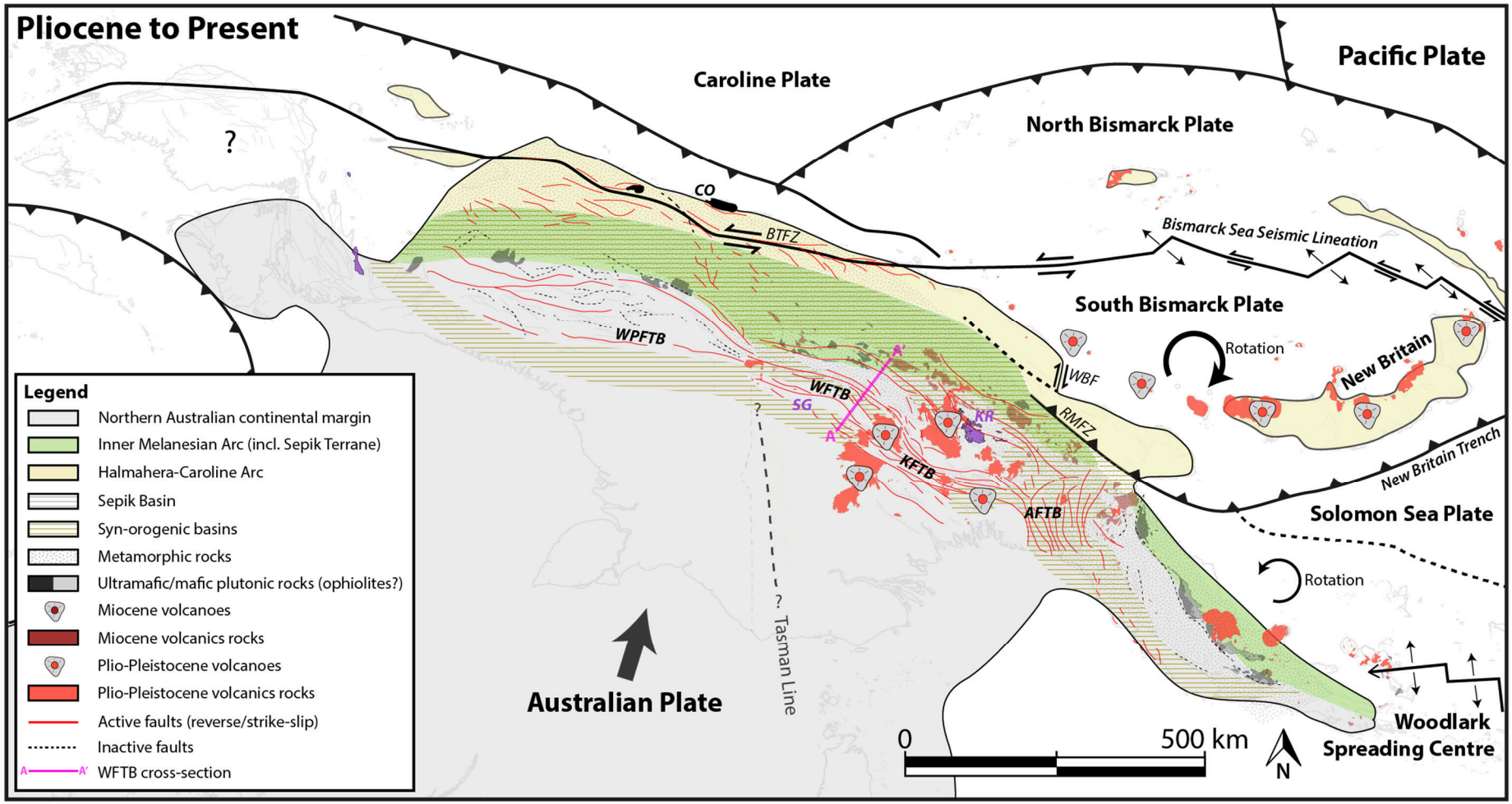
Pliocene to Present
Caroline Plate
Pacific Plate
North Bismarck Plate
South Bismarck Plate
Solomon Sea Plate
Australian Plate
CO
BTFZ
Bismarck Sea Seismic Lineation
WPFTB
WFTB
SG
KR
KFTB
AFTB
WBF
RMFZ
Rotation
New Britain
New Britain Trench
Tasman Line
Woodlark
Spreading Centre
0
500 km
N
Legend
Northern Australian continental margin
Inner Melanesian Arc (incl. Sepik Terrane)
Halmahera-Caroline Arc
Sepik Basin
Syn-orogenic basins
Metamorphic rocks
Ultramafic/mafic plutonic rocks (ophiolites?)
Miocene volcanoes
Miocene volcanics rocks
Plio-Pleistocene volcanoes
Plio-Pleistocene volcanics rocks
Active faults (reverse/strike-slip)
Inactive faults
WFTB cross-section

Chapter 6
Concluding remarks

Understanding the geology, structure and evolution of the Papuan Basin and Papuan Fold and Thrust Belt (PFTB) in Papua New Guinea (PNG) is central to our understanding of the geological and tectonic evolution of the northern Australian margin. Achieving the aims of this thesis has required an integrated multidisciplinary approach which has provided a number of key insights that significantly advance our understanding of the Papuan Basin, PFTB and fold and thrust belts globally. The studies presented in this thesis have revealed the complex geological history of the northern Australian margin, which has included multiple episodes of extension and contraction that have significantly impacted the subsequent evolution of the PFTB. This chapter includes some final remarks on the structure and evolution of the PFTB and northern Australian margin.

6.1. Relationships between PFTB structural styles and the northern Australian continental margin

6.1.1. Crustal and basement composition and fabric

There is significant uncertainty surrounding the crustal and basement architecture of the northern Australian continental margin, mostly due to its extensive burial beneath the Papuan Basin. Based on limited outcrop and well intersections throughout New Guinea, and from extrapolation from the Australian mainland, it is generally accepted that the most significant crustal-scale feature on the northern Australian margin is the Tasman Line—the transition from stronger Proterozoic lithosphere in the west to weaker late Palaeozoic lithosphere in the east (e.g., Hill and Hall, 2003). In addition to uncertainty regarding the nature and whereabouts of the Tasman Line in New Guinea, the composition and fabric of basement on either

side is poorly constrained. Observations from eastern Australia—where the Tasman Line is considerably better constrained by outcrop and high-resolution geophysical datasets—indicate that (1) the crustal transition is characterised by a zone, rather than a discrete feature (e.g., Direen and Crawford, 2003; Kennett *et al*., 2004), and (2) that the spatial distribution of basement compositions and fabrics is extremely complex (e.g., Crawford *et al*., 2003; Glen, 2005). It has been proposed that the lithospheric changes across the Tasman Line have had a primary control on the evolution of lateral variations in structural style that exist throughout the New Guinea Fold Belt (e.g., Hill and Hall, 2003; Cloos *et al*., 2005). However, it is exceedingly difficult to identify the relative impact of this lithospheric transition from other processes acting at a similar scale, in particular, the influence of spatial and temporal variations in compressive stresses that are associated with the complex tectonic setting within which the northern Australian margin and New Guinea orogen evolved (discussed further in Section 6.3.2).

At the scale of the PFTB, this thesis has demonstrated the importance of basement structural fabric in controlling the extensional evolution of the Papuan Basin (e.g., Chapters 2 and 3). The influence of basement fabric on the rift architecture of the Papuan Basin has previously been suggested (e.g., Hill *et al*., 1996) and indeed this relationship is well-known from basins worldwide (Smith and Mosley, 1993; Ring, 1994; O'Brien *et al*., 1996; Corti *et al*., 2007). The new results presented within this thesis suggest that rather than having a direct control on the contractional evolution on the northern Australian margin, the principal impact of basement fabrics has instead been on the extensional architecture of the margin, that is, for example, the location of major extensional faults, accommodation zones and transfers structures. The resulting rift architecture in turn has had the primary influence on the contractional evolution of the margin (discussed in the next section).

6.1.2 Northern Australian margin/Papuan Basin structural architecture

A second important result has been recognition of the role of the extensional architecture of the Papuan Basin in controlling the subsequent contraction evolution of the northern Australian margin and PFTB. It is argued that the presence of significant extensional structures beneath the PFTB should not be unexpected, particularly given that well-constrained analogues exist throughout the adjacent foreland area (e.g., Komewu Trough, Darai Plateau; Kawagle and Meyers, 1996; Bennett *et al*., 2000; McConachie *et al*., 2000; Schofield, 2000). The presence of extensional structures beneath the PFTB and their influence on subsequent contraction evolution has long been discussed (e.g., Hill, 1991; Buchanan and Warburton; 1996; Hill *et al*., 2000), but has proven difficult to convincingly demonstrate given that the deep structure of the fold belt cannot be imaged clearly.

The new detailed geological mapping, interpretation and associated structural analyses carried out in the Western Fold and Thrust Belt (WFTB; Chapter 2) have significantly improved our understanding of the important influence that pre-existing rift architecture has had, and continues to have, on subsequent PFTB evolution and structural style. For example, the large magnitude of uplift within the Muller Range area of the WFTB has resulted in the partial exhumation of the deep structure and stratigraphy of the Papuan Basin, making it an exceptional area for better understanding the influence of rift architecture on subsequent PFTB structural styles. Here, major basement-linked rift-related normal faults (i.e., pre-existing weaknesses) have undergone tectonic inversion and have exerted a primary influence on the contractional evolution and present-day structural style of the region (e.g., Chapter 2)

The seismological, GPS and remote sensing study of the 2018 PNG Highlands earthquake (Chapter 3) revealed an exceptional example of pre-existing extensional structures undergoing active tectonic inversion. For the first time, this work has defined the spatial extent of a major extensional fault zone located deep beneath the

PFTB, showing that it shares remarkable dimensional and morphological similarities to well-constrained extensional fault zones across the foreland area.

Additionally, heterogeneities within the Papuan Basin rift system (e.g., transfer zones), which are also recognised throughout the foreland area (e.g., Schofield, 2000), are shown to have had significant control on lateral variations in structural style observed throughout the PFTB. The important influence of transfer zones within rift basins on subsequent tectonic inversion processes is well-established within the literature globally (e.g., Flinch and Casas, 1996; Konstantinovskaya *et al*., 2007; Farrant *et al*., 2012). Within the structure of the PFTB, this influence is interpreted to be expressed variably as both hard-linked (i.e., arc-normal faults; Chapter 2) and more subtle soft-linked features (i.e., earthquake deformation zones; Chapter 3).

6.1.3. Papuan Basin sediment thickness

Another key outcome of this thesis has been recognition of the important role that Papuan Basin sediment thickness and mechanical stratigraphy have had on contractional evolution and the resulting structural styles observed throughout the PFTB. Not unexpectedly, based on contemporary understanding of rift basin evolution elsewhere, there is a relationship between sediment thickness within the Papuan Basin and the extensional architecture of the margin—most notably sediment thickness increases in the hanging wall of major extensional structures. This relationship is observable across seismically well-defined fault zones throughout the foreland (e.g., Komewu Fault Zone; Schofield, 2000) and is interpreted based on various lines of evidence within the PFTB (e.g., Lavani/Lavani-Kutubu Fault Zone; Chapters 2-4). But due to a lack of control on the deep structure of the PFTB, it is difficult to constrain the relative importance of (1) the pre-existing mechanical weaknesses within the margin (i.e., the extensional faults), and (2) the influence of sediment thickness variations, on fold belt structural evolution and style. It is likely that both are important, but additional data and more focussed

studies are required to investigate this further. Structural modelling tools capable of incorporating pre-existing anisotropies within the deforming margin and the thermomechanical properties of the cover sequence could provide valuable insights.

Here I propose that sediments of the Papuan Basin act as a mechanical buffer between actively inverting structures within crystalline basement and the near surface structuring evident throughout the PFTB. Where Papuan Basin sediments are thinner, the thick-skinned component of deformation is more strongly coupled to the near-surface structure and is therefore more recognisable at the surface (e.g., the Darai Fault Zone and Darai Plateau). Where Papuan Basin sediments are thicker, the thick-skinned component of deformation is less directly coupled to the surface structuring and is thus less recognisable at the surface; (e.g., the Lavani-Kutubu Fault Zone and earthquake-related uplift zone; Chapter 3). Indeed, sediment thickness may be an important, if not primary control on significant lateral changes in structural style observed between the Kutubu Fold and Thrust Belt (KFTB) and WFTB regions of the PFTB. When compared with the KFTB, the WFTB has undergone less near-surface structural shortening yet is more elevated and contains significantly fewer but much larger wavelength structures (Chapter 2). Moreover, the WFTB is also characterised by a greater Bouguer gravity anomaly, suggesting crystalline basement is potentially shallower and the crust less attenuated (Section 3.4.2). Towards the northwest of the WFTB region, Papuan Basin sedimentary thickness decreases significantly towards the Strickland Gorge where crystalline basement is exposed at the surface (Chapters 2 and 4). While some deep grabens do exist within the WFTB (e.g., the Juha and Lavani half-grabens; Chapter 2), in a regional context, the region appears to lie closer to the flank of the Papuan Basin—which is thickest towards the northeast and east (e.g., Jenkins, 1974, Home *et al*, 1990). Therefore, it is plausible that the reduced sediment thickness in the WFTB has resulted in increased coupling between thick-skinned (basement-linked) structures and the surface structure when compared to the KFTB (e.g., Chapter 3).

6.2. Long-lived extension on the northern Australian continental margin

It is generally accepted that thickness variations within the poorly resolved syn-rift and early post-rift stratigraphy of the Papuan Basin make the largest contribution to the total sediment thickness variations and most balanced and restorable cross-sections through the PFTB are drawn accordingly (e.g., Thornton *et al*., 1996; Hill *et al*., 2008; Macaulay *et al*., 2020). In these examples, what is overlooked—or perhaps omitted due to a paucity of constraining data—is that in the foreland syn-sedimentary growth is observed throughout the stratigraphy of the Papuan Basin (e.g., Osborne, 1990; Fischer and Warburton, 1996; McConachie *et al*., 2000; Schofield, 2000), which suggests that the northern Australia continental margin experienced multiple phases of extension from the Triassic to the Neogene. Significant sediment thickness variations have also been recognised within the Papuan Basin stratigraphy in the PFTB (e.g., Jenkins, 1974; Home *et al*., 1990; Hirst and Price, 1996; Sari *et al*., 1996; Hill *et al*., 2000), but identifying what has accommodated these variations is difficult due to (1) the general paucity of wells, (2) the poor quality of subsurface imaging, and (3) the complex contractional overprint. The only published and robustly-constrained example of such a long-lived extensional structure within the PFTB was defined by a number of wells and associated sidetracks within the crest of the Mananda Anticline (e.g., Fig. 3.1), which intersected a normal fault with significant sedimentary growth within the Cretaceous rocks within its hanging wall (Keenan and Hill, 2015). It seems probable that similar structures exist in abundance throughout the PFTB and that they likely contribute to accommodating the observed thickness changes, but locating them is likely to remain problematic, at least in the absence of significant improvements in subsurface imaging within this challenging terrain.

The thermochronological data and thermal models presented in Chapter 4 of this thesis have led to the interpretation that Late Cretaceous to Eocene extension

occurred on the major Lavani/Lavani-Kutubu Fault Zone beneath the Muller Range, significantly contributing to the accommodation of between 1.5-3 km of sediment that is absent within the present-day fold belt. The same extensional architecture is interpreted to control large lateral variations in Triassic syn-rift sediment thickness throughout the area (e.g., Chapter 2), suggesting the fault zone has a long-lived extensional history similar to that observed across structures within the foreland. Indeed, it is plausible that basinward extensional faults beneath the PFTB accommodated even greater hanging wall growth than equivalent structures within the foreland. Consistent with observations from the Muller Range, thickness discrepancies may not necessarily been preserved in the present-day fold belt.

6.3. Multiple contractional episodes on the northern Australian margin

6.3.1. Sepik Terrane collision

The number and timing of accretion events at the northern Australian margin during the Cenozoic is widely debated, with disagreement as to whether the margin has experienced a single collisional event (e.g., Hamilton, 1979; Cooper and Taylor, 1987) or multiple collisional events (e.g., Crowhurst *et al*., 1996; Davies *et al*., 1996; Hill and Hall, 2003; Hall, 2012; Zahirovic *et al*., 2016). In the most part, these different interpretations are based on the presence or absence of Sepik Terrane collision with the northern Australian margin prior to the undisputed Neogene collisions (see Chapter 4 for a detailed review).

Recently, new tectonic and geodynamic modelling studies have provided additional support for reconstructions comprising multiple Cenozoic collisions, with indications that the Sepik Terrane most likely collided with the northern Australian continental margin in the Eocene (Schellart and Spakman, 2015; Tobin *et al*., 2018). Interestingly, the thermochronology data and thermal modelling presented in Chapter 4 of this thesis reveal a significant Eocene to Oligocene cooling event in the

Muller Range area of the WFTB, located < 50 km south of the present-day location of the Sepik Terrane. This cooling event is interpreted to relate to removal of between 1.5-3 km of sediments across the area, which could plausibly be driven by the Eocene to Oligocene collision of the Sepik Terrane at the northern Australian continental margin—an interpretation that is independently-derived but supports recent tectonic and geodynamic modelling. Here I suggest that the Sepik Terrane collided with the northern Australian continental margin in a highly oblique style (i.e., a soft docking) so that tectonic shortening of the margin was relatively minor and was mostly accommodated by the broad inversion of pre-existing basement weaknesses (Section 5.1.7).

A significant remaining uncertainty relates to the spatial distribution of orogenesis/tectonic inversion related to the Sepik Terrane collision—was the uplift local (e.g., limited to the Muller Range) or more regionally extensive? A more expansive thermochronological dataset is required to address this question. An additional uncertainty relates to the processes responsible for accommodating the widespread deposition of thick Oligocene to Miocene shelfal Darai Limestone directly following the Sepik Terrane collision and orogenesis. Focussed studies on this key Eocene to Miocene period of the evolution of the northern Australian margin are required to address these uncertainties.

6.3.2. Microplate kinematics and evolving compressional stresses

Seminal GPS studies in the last two decades have significantly improved our understanding of the kinematics and present-day tectonic setting of PNG and the PFTB (e.g., Wallace *et al*., 2004; 2005; Koulali *et al*., 2015; Stanaway and Noonan, 2015; Stanaway *et al*., 2020). These studies have highlighted the complexity that characterises the boundary zone between the Australian and Pacific plates, comprising an intricately interlinked assortment of tectonic microplates and boundaries that collectively act to decouple the motion of the northern Australian margin on the Australian plate from the motion of the obliquely converging Pacific

plate. An important implication of this observed microtectonic complexity is that the recent Neogene contractional evolution of the margin (including the PFTB) has likely been significantly influenced by spatiotemporal variations in the compressional stress field.

Indeed, both the preserved syn-orogenic record and thermochronological database suggest that Neogene orogenesis progressed from northwest to southeast across New Guinea (except for the Aure Trough; see Chapter 5 for discussion). Following Hill and Hall (2003), Hall (2012) and many others, I interpret the Neogene collision of the Halmahera-Caroline Arc in northern New Guinea predominantly to have occurred obliquely, consistent with the style of collision interpreted for the older Sepik Terrane collision (e.g., Chapter 5) and consistent with the observation of significant strike-slip faulting throughout the Mobile Belt, both within the geological record and from earthquake focal mechanisms (e.g., Pigott *et al*., 1985; Cooper and Taylor, 1987; Crowhurst *et al*., 1996). The significant implication of this interpretation is that the New Guinea orogen has primarily evolved within a strike-slip and oblique-slip tectonic regime. This is challenging to recognise due to subsequent Pliocene to recent overprinting in the east (e.g., in the PFTB)—which is related to the more orthogonal/arc-normal compressive stresses resulting from the rapid-rotation and collision of the Adelbert-Finisterre Terrane. The PFTB is the most studied area within the New Guinea Fold Belt due to its abundant resource endowment and is also the area that is most directly affected by arc-normal compressive stresses related to the ongoing collision of the Adelbert-Finisterre Terrane to the northeast, therefore introducing a significant bias to the general understanding of the New Guinea orogen.

Here I suggest that the KFTB, and to a lesser extent the WFTB, represent fold and thrust belts that have formed predominantly from arc-normal stresses associated with the collision of the Adelbert-Finisterre Terrane, but that they lie within what is primarily an oblique- to strike-slip orogen. This interpretation has

additional implications for the formation of the regional-scale lineaments and associated stratovolcanoes (and mineral accumulations) identified throughout the PFTB (e.g., the Bosavi Lineament). Lithospheric-scale spatial and temporal changes in compressive stresses need to be accommodated within the crust beneath PNG and the resulting structures could provide opportunities for crustal dilation that in turn form important fluid migration pathways.

In summary, the data, analyses and interpretations presented in this thesis suggest that the primary controls on the evolution of the northern Australian margin are (1) spatial variations in the architecture of the margin, and (2) spatial and temporal variations in the compressional stress field, associated with a complexly evolving tectonic setting between the Australian and Pacific plates. Determining the relative influence of these factors requires improved constraints on the architecture and evolution of the margin and detailed reconstructions of the tectonic history of the region, particularly throughout the Cenozoic.

6.4. Future work

This thesis provides significant new insights into the evolution of the PFTB, Papuan Basin and northern Australian margin. But scope for further work exists. The PFTB remains one of the least well-documented fold and thrust belts on Earth. This is in part attributable to the challenges posed by the remoteness and inhospitable terrain, which make new geological studies prohibitively expensive except where pertinent to resource exploration efforts. I do note that the PFTB does have a very long history of mineral and hydrocarbon exploration and production (e.g., Buchanan *et al*., 2000; Williamson and Hancock, 2005; and references therein), such that data do exist but are largely unpublished and remain difficult for the international scientific community to access. Improving the ease-of-access to PNG geoscience data should be a priority as careful analysis of that data would undoubtedly improve the collective understanding of the geology and evolution of the northern Australian

margin and PFTB. Ideally, this would take the form of a publicly accessible online data repository—for example a smaller-scale version of online portals such as AUSGIN (Australia) and Earth Explorer (USGS). This type of initiative would be best implemented by PNG Government Agencies (such as the Department of Petroleum and Energy and the Mineral Resources Authority) with support from industry stakeholders interested in unlocking the full resource potential of PNG.

Additionally, this thesis has highlighted the following future work directions:

- The development and application of improved structural modelling tools able to reproduce the level of structural complexity observed within the PFTB. Such tools should be capable of producing evolving three-dimensional models incorporating (1) pre-existing anisotropies within the deforming margin, (2) the mechanical stratigraphy of the cover sequence, (3) rapidly evolving stress conditions, (4) tectonic and geodynamic context, and (5) surface processes.
- The implementation of more expansive GPS monitoring networks throughout the PNG landmass, including within the PFTB, to better understand the present-day kinematics of the margin.
- Improved earthquake awareness, including seismic hazard mapping and local seismic monitoring capabilities.
- Regional-scale studies utilising low-temperature thermochronology to investigate spatial variations in the evolution of the northern Australian margin including the Papuan Basin and PFTB.

References

Bennett, D.J., Brand, R.P., Mills, C.R., Morris, B.D., 2000. Exploration potential of the West Bosavi area, Papuan foreland basin, Papua New Guinea. In: Buchanan, P., Grainge, A., Thornton, R. (Eds.), *Petroleum exploration, development, and production in Papua New Guinea: proceedings of the fourth PNG Petroleum Convention*, Papua New Guinea Chamber of Mines and Petroleum, Port Moresby, pp.139-154.

Buchanan, P.H., Grainge, A.M., Thornton, R.C.N., 2000. *Petroleum exploration, development, and production in Papua New Guinea: proceedings of the fourth PNG Petroleum Convention*, Papua New Guinea Chamber of Mines and Petroleum, Port Moresby, 612 pp.

Buchanan, P., Warburton, J., 1996. The influence of pre-existing basin architecture in the development of the Papuan fold and thrust belt: implications for petroleum prospectivity. In: Buchanan, P. (Ed.), *Petroleum Exploration, Development, and Production in Papua New Guinea: Proceedings of the Third PNG Petroleum Convention*. Papua New Guinea Chamber of Mines and Petroleum, Port Moresby, pp.89-109.

Cloos, M., Sapiie, B., Quarles van Ufford, A., Weiland, R.J., Warren, P.Q., McMahon, T.P., 2005. Collisional delamination in New Guinea: The geotectonics of subducting slab breakoff. *Geological Society of America, Special Paper,* 400, 51 pp.

Cooper, P., Taylor, B., 1987. Seismotectonics of New Guinea: A model for arc reversal following arc-continent collision. *Tectonics*, *6*(1), pp.53-67.

Corti, G., van Wijk, J., Cloetingh, S., Morley, C.K., 2007. Tectonic inheritance and continental rift architecture: Numerical and analogue models of the East African Rift system. *Tectonics*, 26, TC6006.

Crawford, A.J., Meffre, S., Symonds, P.A., 2003. 120 to 0 Ma tectonic evolution of the southwest Pacific and analogous geological evolution of the 600 to 220 Ma Tasman Fold Belt System. *Special Papers-Geological Society of America*, pp.383-404.

Crowhurst, P.V., Hill, K.C., Foster, D.A., Bennett, A.P., 1996. Thermochronological and geochemical constraints on the tectonic evolution of northern Papua New Guinea. *Geological Society, London, Special Publications*, 106(1), pp.525-537.

Davies, H.L., Winn, R.D., KenGemar, P., 1996. Evolution of the Papuan Basin-a view from the orogen. In: Buchanan, P. (Ed.), *Petroleum exploration, development, and production in Papua New Guinea: proceedings of the third PNG Petroleum Convention*, Papua New Guinea Chamber of Mines and Petroleum, Port Moresby, pp.53-62.

Direen, N.G., Crawford, A.J., 2003. The Tasman Line: where is it, what is it, and is it Australia's Rodinian breakup boundary?. *Australian Journal of Earth Sciences*, 50(4), pp.491-502.

Farrant, A.R., Hopson, P.M., Woods, M.A., Booth, K.A., Evans, D.J., 2012. Comment on "Structural geology of the Upper Cretaceous Chalk Central Mass, Isle of Wight, UK" by Rory Mortimore. Proceedings of the Geologists' Association, 122(2), 2012, pp.298-331. *Proceedings of the Geologists' Association*, 123(3), pp.533-536.

Fischer, M.W., Warburton., 1996. The importance of pre-Tertiary basin architecture for hydrocarbon accumulation in the Papuan Fold and Thrust Belt: models, analogues and implications. In: Buchanan, P. (Ed.), *Petroleum exploration, development, and production in Papua New Guinea: proceedings of the third PNG Petroleum Convention*, Papua New Guinea Chamber of Mines and Petroleum, Port Moresby, pp.111-131.

Flinch, J.F., Casas, J.M., 1996. Inversion of a transfer system into lateral ramps: an example from the South-Central Pyrenees (Spain). *Geologische Rundschau*, 85(2), pp.372-379.

Glen, R.A., 2005. The Tasmanides of eastern Australia. In: Vaughan, A.P.M., Leat, P.T., Pankhurst, R.J. (Eds.), *Terrane Processes at the margins of Gondwana*. Geological Society, London, Special Publications, 246, pp.23-96.

Hall, R., 2012. Late Jurassic–Cenozoic reconstructions of the Indonesian region and the Indian Ocean. *Tectonophysics,* 570, pp.1-41.

Hamilton, W.B., 1979. *Tectonics of the Indonesian region* (Vol. 1078). US Government Printing Office, 308 pp.

Hill, K.C., 1991. Structure of the Papuan Fold Belt, Papua New Guinea. *The American Association of Petroleum Geologists Bulletin*, 75, pp.857-872.

Hill, K.C., Bradey, K., Iwanec, J., Wilson, N., Lucas, K., 2008. Structural exploration in the Papua New Guinea Fold Belt. In: Blevin, J.E., Bradshaw, B.E., Uruski, C. (Eds.), *Eastern Australian Basins Symposium III, Petroleum Exploration Society of Australia, Special Publication,* pp.225-238.

Hill, K.C., Hall, R., 2003. Mesozoic-Cenozoic evolution of Australia's New Guinea margin in a west Pacific context. *Geological Society of America, Special Papers, 372*, pp.265-290.

Hill, K.C., Norvick, M., Keetley, J., Adams, A., 2000. Structural and stratigraphic shelf-edge hydrocarbon plays in the Papuan Fold Belt. In: Buchanan, P., Grainge, A., Thornton, R. (Eds.), *Petroleum Exploration, Development, and Production in Papua New Guinea: Proceedings of the Fourth PNG Petroleum Convention.* Papua New Guinea Chamber of Mines and Petroleum, Port Moresby, pp.67-85.

Hill, K.C., Simpson, R., Kendrick, R., Crowhurst, P., O'Sullivan, P., Saefudin, I., 1996. Hydrocarbons in New Guinea, controlled by basement fabric, Mesozoic extension and Tertiary Convergent margin tectonics. In: Buchanan, P. (Ed.), *Petroleum Exploration, Development, and Production in Papua New Guinea: Proceedings of the Third PNG Petroleum Convention.* Papua New Guinea Chamber of Mines and Petroleum, Port Moresby, pp.63-76.

Hirst, J.P.P., Price, C.A., 1996. Sequence stratigraphy and sandstone geometry of the Toro and Imburu Formations, within the Papuan Fold Belt and Foreland. In: Buchanan, P. (Ed.), *Petroleum Exploration, Development, and Production in Papua New Guinea: Proceedings of the Third PNG Petroleum Convention.* Papua New Guinea Chamber of Mines and Petroleum, Port Moresby, pp.279-299.

Jenkins, D.A., 1974. Detachment tectonics in western Papua New Guinea. *Geological Society of America Bulletin*, 85(4), pp.533-548.

Kawagle, S.A., Meyers, J.B., 1996. Structural and sequence geometry of the Kiunga Area, Papuan Foreland Basin, Papua New Guinea. In: Buchanan, P. (Ed.), *Petroleum exploration, development, and production in Papua New Guinea: proceedings of the third PNG Petroleum Convention*, Papua New Guinea Chamber of Mines and Petroleum, Port Moresby, pp.175-193.

Keenan, S.E., Hill, K.C., 2015. The Mananda Anticline, Papua New Guinea: A third Oil Discovery, Appraisal Programme and Deep Potential. In: AAPG/SEG International Conference and Exhibition 2015, Melbourne.

Kennett, B.L., Fishwick, S., Reading, A.M., Rawlinson, N., 2004. Contrasts in mantle structure beneath Australia: relation to Tasman Lines?. *Australian Journal of Earth Sciences*, 51(4), pp.563-569.

Konstantinovskaya, E.A., Harris, L.B., Poulin, J., Ivanov, G.M., 2007. Transfer zones and fault reactivation in inverted rift basins: Insights from physical modelling. *Tectonophysics*, 441(1-4), pp.1-26.

Koulali, A., Tregoning, P., McClusky, S., Stanaway, R., Wallace, L., Lister, G., 2015. New Insights into the present-day kinematics of the central and western Papua New Guinea from GPS. *Geophysical Journal International*, 202(2), pp.993-1004.

Macaulay, E., Fowler, D., Wightman, R., Cebastiant, A., 2020. An overview of structural style, trap configuration and reservoir connectivity in the Western and Central Fold Belt, Papua New Guinea. *AAPG/EAGE 1st Petroleum Geoscience Conference and Exhibition, PNG's Oil and Gas Industry Maturing through Exploration, Development and Production*, Port Moresby.

McConachie, B., Lanzilli, E., Kendrick, D., Burge, C., 2000. Extensions of the Papuan Basin foreland geology into Eastern Irian Jaya (West Papua) and the New Guinea Fold Belt in Papua New Guinea. In: Buchanan, P., Grainge, A., Thornton, R. (Eds.), *Petroleum exploration, development, and production in Papua New Guinea: proceedings of the fourth PNG Petroleum Convention*, Papua New Guinea Chamber of Mines and Petroleum, Port Moresby, pp.219-237.

O'Brien, G.W., Higgins, R., Symonds, P., Quaife, P., Colwell, J., Blevin, J., 1996. Basement control on the development of extensional systems in Australia's Timor Sea: an example of hybrid hard linked/soft linked faulting?. *The APPEA Journal*, 36(1), pp.161-201.

Osborne, D.G., 1990. The hydrocarbon potential of the western Papuan Basin foreland—with reference to worldwide analogues. In: Carman, G., Carman, Z. (Eds.), *Petroleum exploration, development, and production in Papua New Guinea: proceedings of the first PNG Petroleum Convention,* Papua New Guinea Chamber of Mines and Petroleum, Port Moresby, pp.197-213.

Pigott, J.D., Trumbly, N.I., O'Neal, M.V., 1985. Northern New Guinea wrench fault system: a manifestation of late Cenozoic interactions between Australian and Pacific plates. *Tectonics*, 4, pp.613-620.

Ring, U., 1994. The influence of preexisting structure on the evolution of the Cenozoic Malawi rift (East African rift system). *Tectonics,* 13, pp.313-326.

Sari, J., Failing, R., Wulff, K., 1996. The Giero Sandstone: A potentially new play in the Papuan Basin. In: Buchanan, P. (Ed.), *Petroleum exploration, development, and production in Papua New Guinea:*

proceedings of the third PNG Petroleum Convention, Papua New Guinea Chamber of Mines and Petroleum, Port Moresby, pp.301-312.

Schellart, W.P., Spakman, W., 2015. Australian plate motion and topography linked to fossil New Guinea slab below Lake Eyre. *Earth and Planetary Science Letters*, 421, pp.107-116.

Schofield, S., 2000. The Bosavi Arch and Komewu Fault Zone: Their control on basin architecture and the prospectivity of the Papuan Foreland. In: Buchanan, P., Grainge, A., Thornton, R. (Eds.), *Petroleum exploration, development, and production in Papua New Guinea: proceedings of the fourth PNG Petroleum Convention*, Papua New Guinea Chamber of Mines and Petroleum, Port Moresby, pp.101-122.

Smith, M., Mosley, P., 1993. Crustal heterogeneity and basement influence on the development of the Kenya Rift, East Africa. *Tectonics,* 12, pp.591-606.

Stanaway, R., Mahoney, L., Noonan, J., McLaren, S., 2020. Neotectonics of the Papuan Fold and Thrust Belt - Insights from Space Geodetic Analysis. *2020 AAPG/EAGE 1st Petroleum Geoscience Conference and Exhibition, PNG's Oil and Gas Industry Maturing through Exploration, Development and Production*, Port Moresby, 8 pp.

Stanaway, R. and Noonan, J.W., 2015. Geodetic Measurement of Deformation Within the Papuan Fold and Thrust Belt. *2015 International Conference and Exhibition, Society of Exploration Geophysicists and American Association of Petroleum Geologists,* Melbourne, Australia, pp.114-114.

Thornton, R.C.N., Emmett, J.K., Lyslo, J.A. and Gottschalk, R.R., 1996. Integrated structural and stratigraphic analysis in PPL 175, Papuan Fold Belt, Papua New Guinea. In: Buchanan, P. (Ed.), *Petroleum Exploration, Development, and Production in Papua New Guinea: Proceedings of the Third PNG Petroleum Convention.* Papua New Guinea Chamber of Mines and Petroleum, Port Moresby, pp.195-215.

Tobin, J., Zahirovic, S., Hassan, R., Rey, P., 2018. Tectonic and Geodynamic Evolution of the Northern Australian Margin and New Guinea. *ASEG Extended Abstracts* 2018, 7 pp.

Wallace, L.M., Stevens, C., Silver, E., McCaffrey, R., Loratung, W., Hasiata, S., Stanaway, R., Curley, R., Rosa, R., Taugaloidi, J., 2004. GPS and seismological constraints on active tectonics and arc-continent collision in Papua New Guinea: Implications for mechanics of microplate rotations in a plate boundary zone. *Journal of Geophysical Research: Solid Earth*, 109, B05404.

Wallace, L.M., McCaffrey, R., Beavan, J., Ellis, S., 2005. Rapid microplate rotations and backarc rifting at the transition between collision and subduction. *Geology*, 33(11), pp.857-860.

Williamson, A., Hancock, G., 2005. *The geology and mineral potential of Papua New Guinea*. Papua New Guinea Department of Mining, *152* pp.

Zahirovic, S., Matthews, K. J., Flament, N., Müller, R. D., Hill, K. C., Seton, M., Gurnis, M., 2016. Tectonic evolution and deep mantle structure of the eastern Tethys since the latest Jurassic. *Earth Science Reviews*, 162, pp.293-337.

Appendix A

Journal of Structural Geology 100 (2017) 98–119

Contents lists available at ScienceDirect

Journal of Structural Geology

journal homepage: www.elsevier.com/locate/jsg

Complex fold and thrust belt structural styles: Examples from the Greater Juha area of the Papuan Fold and Thrust Belt, Papua New Guinea

Luke Mahoney [a, *], Kevin Hill [b], Sandra McLaren [a], Amanda Hanani [b]

[a] School of Earth Sciences, The University of Melbourne, VIC, 3010, Australia
[b] Papuan Oil Search Ltd, Sydney, NSW, 2000, Australia

ARTICLE INFO

Article history:
Received 9 February 2017
Received in revised form
5 May 2017
Accepted 23 May 2017
Available online 25 May 2017

Keywords:
Fold and thrust belt
Structural style
Basin inversion
Arc-normal structures
Papua New Guinea
Papuan basin

ABSTRACT

The remote and inhospitable Papuan Fold Belt in Papua New Guinea is one of the youngest yet least well-documented fold and thrust belts on Earth. Within the frontal Greater Juha area we have carried out >100 km of geological traverses and associated analyses that have added significantly to the contemporary geological and geophysical dataset. Our structural analysis provides evidence of major inversion, detachment and triangle zone faults within the uplifted Eastern Muller Ranges. We have used the dataset to develop a quasi-3D model for the Greater Juha area, with associated cross-sections revealing that the exposed Cenozoic Darai Limestone is well-constrained with very low shortening of 12.6–21.4% yet structures are elevated up to 7 km above regional. We suggest the inversion of pre-existing rift architecture is the primary influence on the evolution of the area and that structures link to the surface via triangle zones and detachment faults within the incompetent Mesozoic passive-margin sedimentary sequence underlying competent Darai Limestone. Arc-normal oriented structures, dominantly oblique dextral, up-to-the-southeast, are pervasive across a range of scales and are here interpreted to relate at depth to weakened pre-existing basement cross-structures. It is proposed that Palaeozoic basement fabric controlled the structural framework of the basin during Early Mesozoic rifting forming regional-scale accommodation zones and related local-scale transfer structures that are now expressed as regional-scale arc-normal lineaments and local-scale arc-normal structures, respectively. Transfer structures, including complexly breached relay ramps, utilise northeast-southwest striking weaknesses associated with the basement fabric, as a mechanism for accommodating displacement along major northwest-southeast striking normal faults. These structures have subsequently been inverted to form arc-normal oriented zones of tear faulting that accommodate laterally variable displacement along inversion faults and connected thrust structures.

1. Introduction

Globally, there has been significant effort to document structural styles within fold and thrust belts, revealing often complex relationships between basin evolution and the subsequent style of deformation during compression. Early basin extensional architecture and mechanical stratigraphy appear to be key controls on the subsequent evolution of both thick- and thin-skinned compressional deformation. But modern rift and rifted-margin structural analogues show that extensional architecture is often remarkably complex (e.g., East African Rift: Morley et al., 1990; Chorowicz, 2005; North West Shelf, Australia: Longley et al., 2002; Frankowicz and McClay, 2010) and a wide range of factors impact inversion geometry and style (e.g., Buchanan and Buchanan, 1995; Bonini et al., 2012). Additionally, compression may occur in the presence of an evolving stress field associated with far- and near-field tectonism (e.g., Saintot and Angelier, 2002) or syn-tectonic sedimentation (e.g., Storti and McClay, 1995). For these reasons the relative influence of extension-related architecture and compression-related influences can be difficult to demonstrate, particularly where robust constraints on subsurface geometry are absent.

The Papuan Fold Belt (PFB) of Papua New Guinea (PNG) is

* Corresponding author.
E-mail address: luke.g.mahoney@gmail.com (L. Mahoney).

http://dx.doi.org/10.1016/j.jsg.2017.05.010
0191-8141/

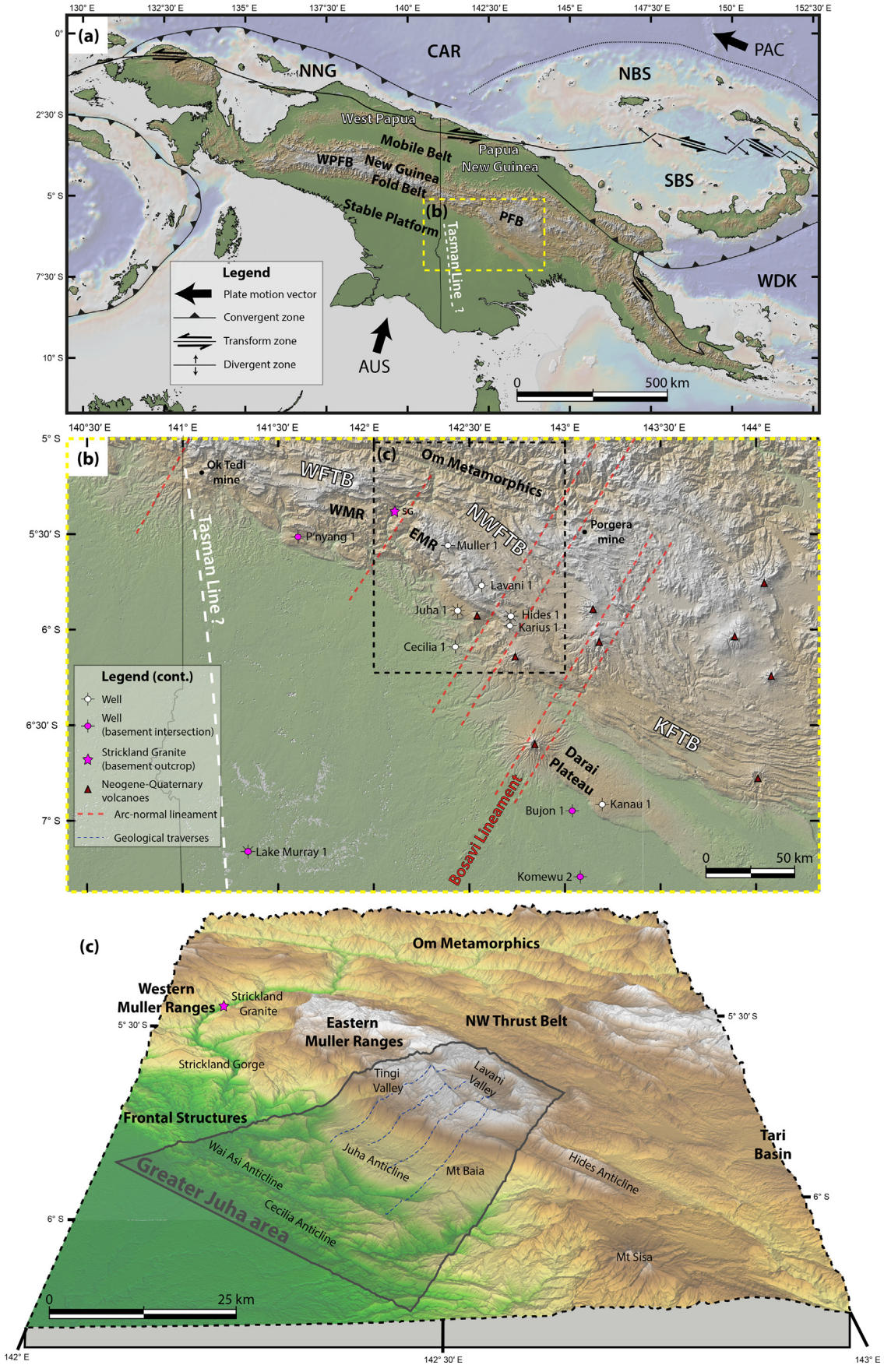
(a)
CAR
PAC
NNG
NBS
West Papua
Mobile Belt
WPFB
New Guinea
Fold Belt
Papua
New Guinea
SBS
Stable Platform
(b)
PFB
Tasman Line ?
WDK
AUS
Legend
Plate motion vector
Convergent zone
Transform zone
Divergent zone
0
500 km
(b)
Ok Tedi mine
WFTB
(c)
Om Metamorphics
WMR
SG
NWFTB
P'nyang 1
EMR
Muller 1
Porgera mine
Lavani 1
Juha 1
Hides 1
Karius 1
Cecilia 1
Legend (cont.)
Well
Well (basement intersection)
Strickland Granite (basement outcrop)
Neogene-Quaternary volcanoes
Arc-normal lineament
Geological traverses
KFTB
Darai Plateau
Bujon 1
Kanau 1
Bosavi Lineament
Lake Murray 1
Komewu 2
0
50 km
(c)
Om Metamorphics
Western Muller Ranges
Strickland Granite
Eastern Muller Ranges
NW Thrust Belt
Strickland Gorge
Tingi Valley
Lavani Valley
Frontal Structures
Tari Basin
Wai Asi Anticline
Juha Anticline
Mt Baia
Hides Anticline
Greater Juha area
Cecilia Anticline
Mt Sisa
0
25 km

located on the northern margin of the Australian plate (Fig. 1a) and has significant demonstrated mineral and hydrocarbon wealth. Yet the PFB remains poorly understood geologically, due largely to its isolation and its complex tectonic history. As such, it has the potential to provide significant new insights into our understanding of fold belts globally.

Over the past few decades, the accessibility and affordability of aviation-based exploration as well as new specialized methods of data acquisition (e.g., Hornafius and Denison, 1993; Hill et al., 1996a) have significantly improved our understanding of the local-scale structure of the PFB. Indeed the PFB is currently being actively explored for hydrocarbons and minerals involving drilling and the acquisition of widely-spaced 2D seismic data which substantially constrain geologic models. Moreover, recent and ongoing tectonism in the PFB means that present day convergence vectors (e.g., Wallace et al., 2004; Koulali et al., 2015; Stanaway and Noonan, 2015), earthquake solutions (e.g., Abers and McCaffrey, 1988; Ekström et al., 2012) and contemporary landforms can aid structural and tectonic models.

Significant variations in structural style have been recognised across the PFB, often related to pre-compression margin architecture (e.g., Hill, 1991; Buchanan and Warburton, 1996; Hill et al., 2010). However the majority of studies are based on cross-sections and do not explain how along-strike structural variations are accommodated. In particular, our understanding of the structure of the PFB decreases significantly to the west of the extensively explored hydrocarbon-bearing frontal structures in the Kutubu Fold and Thrust Belt (KFTB) (Fig. 1b). The remote neighbouring North West Fold and Thrust Belt (NWFTB) is characterised by a contrasting set of structural styles to that of the KFTB. Most obviously, it is characterised by comparatively higher surface elevations and broader structural wavelengths (Fig. 1b). Within the NWFTB region, the Greater Juha area (Fig. 1c) is contiguous with the PFB frontal hydrocarbon trend and is thus a highly prospective area undergoing active exploration. Indeed, the Juha Anticline and the Hides Anticline, 30 km further east, are both large gasfields (Fig. 1c).

Here, new geological field observations together with legacy data have been used to construct cross-sections and a detailed geological map to document and understand structural styles within the Greater Juha area of the NWFTB. Our contemporary dataset reveals a complex interplay of pre-compression rift architecture, mechanical stratigraphy and compressive stresses on the spatio-temporal evolution of the Greater Juha area.

2. Geological setting

The geological evolution of New Guinea is complex and much-debated, with a number of key tectonic events having had significant influence on the rock record. At present, the island of New Guinea comprises three major tectonic provinces (after Hill and Hall, 2003): (1) the Stable Platform to the south, (2) the Mobile Belt to the north and (3) the central New Guinea Fold Belt (NGFB) (Fig. 1a). The Stable Platform is the northern edge of the relatively undeformed Australian continent while the Mobile Belt comprises island arcs and microcontinents accreted to the leading edge of the Australian plate during the Cenozoic (e.g., Hill and Raza, 1999). The NGFB separates the Stable Platform and Mobile Belt and formed predominantly within sediments of the Australian continental margin during the Late Miocene to Pliocene (Hill and Gleadow, 1989).

2.1. Tectonic and stratigraphic framework

The rock record of New Guinea (Fig. 2) reveals a complex geological evolution for the northern margin of the Australian continent, which is summarised briefly here. Further details and tectonic history reconstructions for New Guinea are given in Pigram and Symonds (1991), Hill and Raza (1999), Hill and Hall (2003) and Baldwin et al. (2012) and for SE Asia by Hall (1996, 1997, 2002, 2012), Metcalfe (2002) and Zahirovic et al. (2014, 2016).

Limited basement outcrop and well intersections suggest Late Permian and Early Triassic metasediments and volcanics, and Middle to Late Triassic granites underlie most of the PFB and the Stable Platform within PNG (Fig. 1b). The overlying Mesozoic stratigraphic sequence was subsequently attributed to the tectonic stages of rift-drift sequences and facilitated early ideas for Early Mesozoic rifting on the New Guinea margin (e.g., Pigram and Panggabean, 1984). Northwest-southeast and WNW-ESE oriented grabens filled with Early Mesozoic syn-rift sediments (Fig. 2) and associated normal faults have been suspected to underlie the PFB (e.g., Hill, 1991) and have been identified across adjacent foreland regions (e.g., Home et al., 1990; Kawagle and Meyers, 1996; Schofield, 2000). The cessation of rifting in the Middle Jurassic was recorded throughout the Papuan Basin as a thick, widespread post-rift sequence dominated by fine-grained clastic sediments including the Jurassic-aged Imburu mudstone and Cretaceous-aged Ieru Formation (Fig. 2). During the early post-rift phase a number of prograding sandstone sequences were deposited, including the Early Cretaceous Toro Sandstone and Middle to Late Jurassic Koi Iange Sandstone (Fig. 2). Several of these sandstones host the main hydrocarbon reserves in the PFB. The Late Cretaceous to Palaeogene history of the Papuan Basin is largely unknown with a prominent top Ieru unconformity located across most of southern PNG (Fig. 2). Subsequent subsidence during the Late Oligocene to Early Miocene accommodated the deposition of 1–2 km of Darai Limestone (Fig. 2) in southern New Guinea, building the Cenozoic platform.

Compression within the Mobile Belt began during the Middle to Late Miocene (12–14 Ma) and within the NGFB in the Late Miocene to Pliocene (5-4 Ma) (Hill and Gleadow, 1989; Hill and Raza, 1999). The dominant orientation for compression-related structures throughout the PFB reflects northeast-southwest compression, with an increasingly large sinistral strike-slip component recognised northwards in the Mobile Belt (e.g., Pigott et al., 1985; Crowhurst et al., 1997), related to east-west compressive stresses from the ongoing collision with the Finisterre Arc terrane (Hill and Raza, 1999). Contemporary seismicity suggests the PFB is still undergoing compressive deformation with focal mechanisms suggesting northeast-southwest directed convergence (Ekström et al., 2012). In fact, GPS plate velocities suggest that the PFB may be accommodating up to 15 mm of convergence between the New Guinea Highlands (Mobile Belt) and Australian plate (Stable Platform) annually (Wallace et al., 2004; Koulali et al., 2015; Stanaway

Fig. 1. **(a)** Tectonic components of New Guinea and the New Guinea Fold Belt. Tectonic elements modified from Hill and Hall (2003) and Baldwin et al. (2012). Trajectory of Tasman Line based on extent of Palaeozoic basement in outcrop and wells (see Fig. 1b). AUS, Australian plate; CAR, Caroline microplate; NBS, North Bismark plate; NNG; Northern New Guinea block; PAC, Pacific plate; PFB, Papuan Fold Belt; SBS, South Bismark plate; WDK, Woodlark microplate; WPFB, West Papuan Fold Belt. Yellow box indicates the location of Fig. 1b. **(b)** Structural elements of the PFB including arc-normal lineaments and locations of Late Palaeozoic-Early Mesozoic basement within the Strickland Gorge and wells across the foreland and PFB. Arc-normal lineaments based on Hill (1991) and Hill et al. (2000, 2002). EMR, Eastern Muller Ranges; KFTB, Kutubu Fold and Thrust Belt; NWFTB, North West Fold and Thrust Belt; SG, Strickland Granite; WFTB, Western Fold and Thrust Belt; WMR, Western Muller Ranges. Black dashed box indicates location of Fig. 1c. **(c)** Structural elements of the NWFTB, including the boundaries of the Greater Juha area which is the focus of this study. SRTM digital elevation model retrieved from USGS (2015). (For interpretation of the references to colour in this figure legend, the reader is referred to the web version of this article.)

and Noonan, 2015).

In the Late Miocene, crustal flexure associated with plate collision and Mobile Belt uplift resulted in the formation of foreland basins to the south and southwest of the Papuan Highlands (e.g., Davies, 1983). This prompted the deposition of variably thick Late Miocene to present, shallow marine to non-marine syn-tectonic sediments. The onset of Late Miocene uplift is recorded by the deposition of calcareous clastics and reworked limestone fragments in the Orubadi Formation (Fig. 2) (Home et al., 1990). In the Pliocene, the progression of uplift and erosion in the highlands, along with contemporary volcanism, contributed to the deposition of the thick non-marine Era and Strickland Formations in the southwest of the PFB (Fig. 2) (Davies, 1983; Home et al., 1990).

Prominent stratovolcanoes and associated intrusions throughout PNG are, in general, poorly understood. Potassium-argon (K-Ar) data suggests that volcanism in the Papuan Highlands had begun by at least the Middle Miocene (Page, 1976). However, the majority of the prominent stratovolcanoes and associated intrusions within the PFB and on the Stable Platform formed during the Plio-Pliestocene (Webb, 1973; Löffler et al., 1979).

2.2. Structural styles

The NGFB is characterised by variations in structural style along its length from the wide Kutubu Fold and Thrust Belt (KFTB) to the comparatively narrow, highly elevated West Papuan Fold Belt (WPFB) (Fig. 1a). Structural variations on the scale of the entire NGFB are most commonly attributed to the transition from hot, weak Late Palaeozoic lithosphere in the east, to cold, strong Proterozoic lithosphere in the west, apparently coincident with the Tasman Line (Hill and Hall, 2003).

Diverse structural styles within the PFB have previously been attributed to the relative role of thin- and thick-skinned tectonics (e.g., Hill et al., 2000, 2010). Structures observed at the surface within Darai Limestone are commonly detached within thick, incompetent underlying sediments. For instance, Hill et al. (2010) recognised multiple major detachment levels across the KFTB including within the Ieru Formation and Imburu/Barikewa Mudstones. Basement-involved faulting within the PFB has often been related to the inversion of Early Mesozoic extensional architecture such as grabens and half-grabens (e.g., Hill, 1991; Buchanan and Warburton, 1996). Well control to the north and south of the

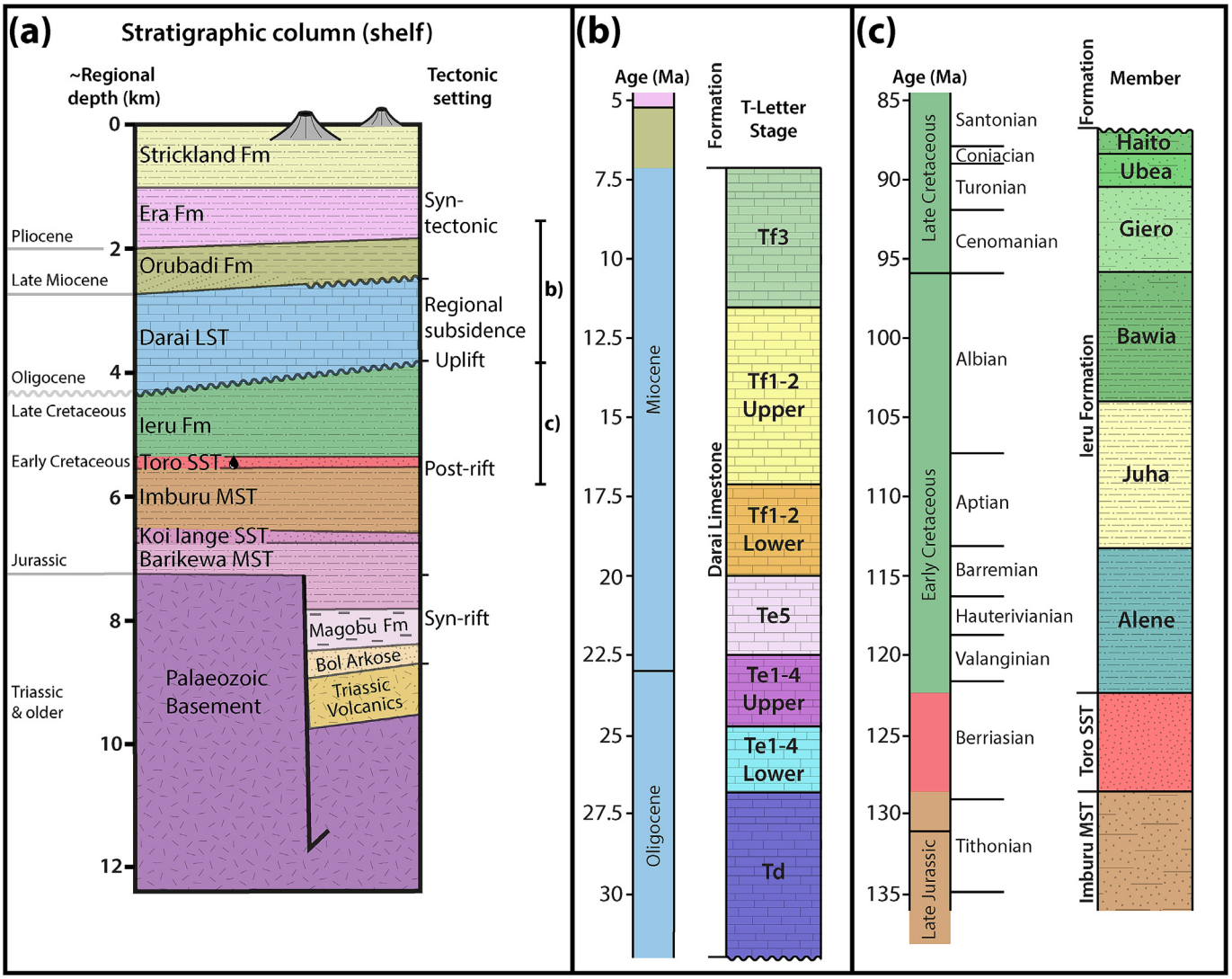

Fig. 2. Schematic stratigraphy of the Papuan Fold Belt (a) true stratigraphic thicknesses (TSTs) estimated from seismic and well data across the foreland of the Greater Juha area; (b) subdivision of the Darai Limestone into T-Letter stages (following Lunt and Allan, 2004) as used here; (c) subdivision of the Ieru Formation (following Bradley, 2014) as used here. Note the thickness of syn-tectonic sediments is based on foreland thicknesses and compaction modelling from the Juha Anticline (Hanani et al., 2016); thickness and extent across the EMR is unknown due to Plio-Pleistocene uplift and erosion.

40 km wide, 100 km long Darai Plateau to the southwest of the KFTB (Fig. 1b), make it the best documented inversion structure. An abrupt northwards increase in sedimentary thickness from 2.2 km to 4.8 km across the frontal Darai Fault led Hill et al. (2010) to suggest it was originally a major, long-lived basin-bounding fault. Similar, largely uninverted examples of basement extension structures have also been recognised in reflection seismic to the foreland of the KFTB (Schofield, 2000; McConachie et al., 2000) and across the foreland region directly to the southwest of the NWFTB (Kawagle and Meyers, 1996; Bennett et al., 2000).

Regional northeast-southwest (arc-normal) lineaments cross-cutting the PFB have long been recognised in both geological and geophysical datasets, commonly from distinct lateral changes in structural style and/or sublinear arrangements of volcanics. The most prominent example is the approximately northeast-southwest trending Bosavi Lineament (Fig. 1b) (e.g., Hill, 1989; Smith, 1990; Hill et al., 2008). The Bosavi Lineament marks the transition from the KFTB oil province to the NWFTB gas province (e.g., Hill et al., 2008) and is characterised by a zone of structural disruption and an abundance of Plio-Pleistocene volcanoes. The structure appears to offset the KFTB and NWFTB dextrally (Fig. 1b) (Osborne, 1990), consistent with 3D numerical models that suggest arc-normal oriented weaknesses would be prone to oblique dextral, up-to-the-southeast offset during northeast-southwest compression (Gow et al., 2002).

Over the last few decades other regional-scale northeast-southwest trending lineaments have been recognised in the NGFB, often related to the emplacement of New Guinea's mineralised intrusive bodies (e.g., Davies, 1991; Corbett, 1994; Hill et al., 1996b; White et al., 2014). Lineaments recognised in West Papua have been linked to a similar northeast-southwest fabric within Proterozoic and Palaeozoic basement in northern Australia (Hill et al., 1996a,b). Recent work by White et al. (2014) using a range of geophysical data showed that the lineaments were most prominent in lower resolution data that imaged deeper in the crust (e.g., gravity and tomography), but were much less prevalent and much more complex than previously mapped. Arc-normal lineaments are most commonly related to the compressional reactivation of regional-scale lateral ramps, with local zones of dilatation linked to the intrusion of magmatic fluids (e.g., Hill, 1991; Hill et al., 2002).

In addition to regional-scale lineaments, local-scale arc-normal structures have also been identified throughout the PFB. In contrast to past studies, and to avoid ambiguity, we have chosen to differentiate arc-normal lineaments observed in regional-scale datasets from arc-normal structures observed in local-scale datasets, noting that the relationship between regional arc-normal lineaments and

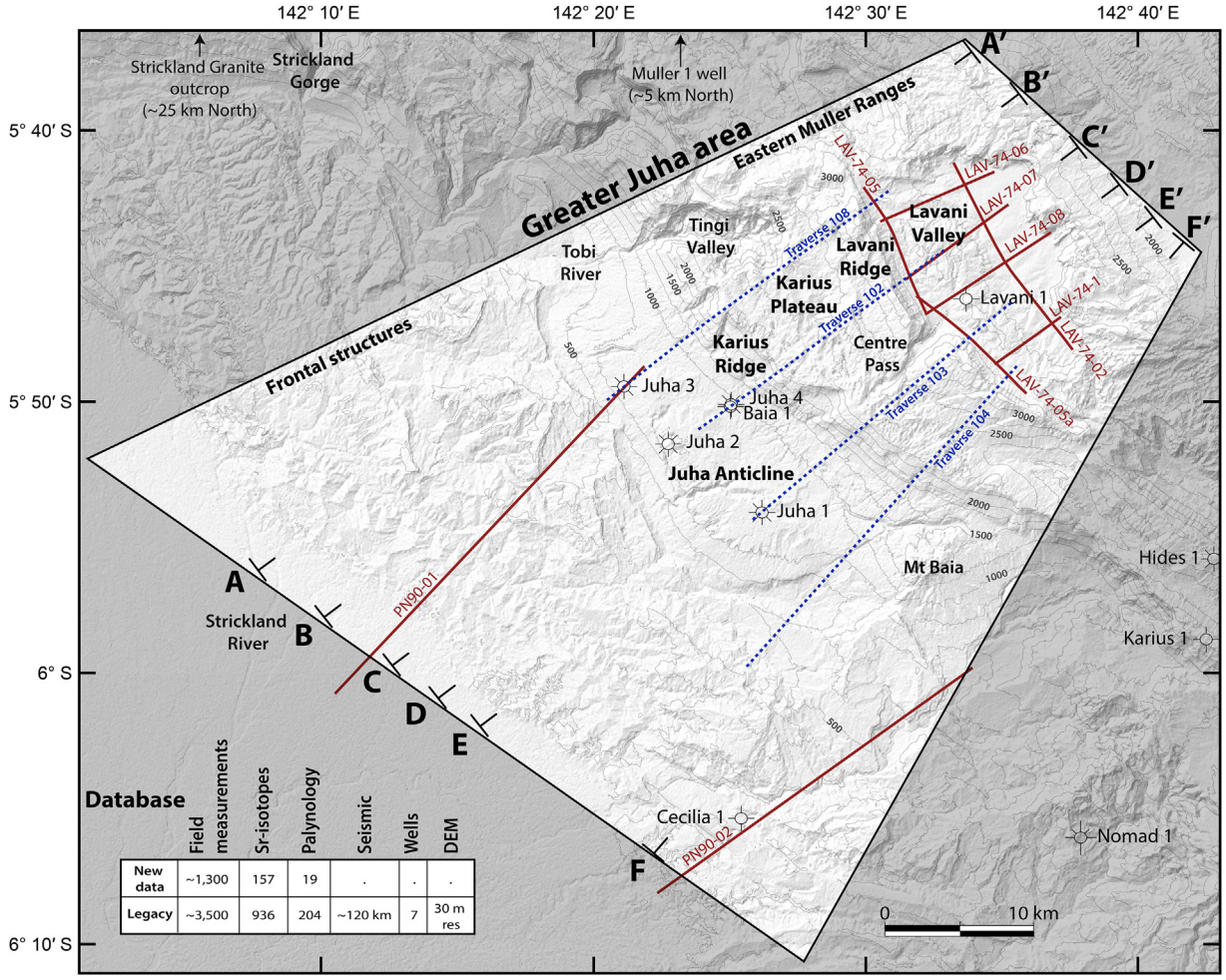

Fig. 3. Location of key localities and data sources within the Greater Juha area, including geological traverses (blue dash), available seismic lines (red), wells and cross-sections. Regional seismic lines PN-90-01 and PN-90-02, obtained in 1990 and reprocessed by Papuan Oil Search Ltd in 1996, have significantly improved our understanding of frontal structures. Lavani Valley seismic is of mostly poor quality and provides limited constraint. Geological traverses 102, 103, 104 and 108 have significantly increased the geological dataset across the Greater Juha area. SRTM digital elevation model retrieved from USGS (2015). (For interpretation of the references to colour in this figure legend, the reader is referred to the web version of this article.)

arc-normal structures is largely unknown. Geological and geophysical data suggest steeply-dipping arc-normal structures are abundant across the PFB, most commonly recognised in basement structure and as tear faults within the sedimentary sequence (e.g., Hill, 1989; Hill et al., 2008; Craig and Warvakai, 2009).

2.2.1. The Greater Juha area

The structurally complex Greater Juha area is located in the frontal trend of the NWFTB where the dominant structural trend is northwest-southeast, connecting the WNW-ESE trends of the neighbouring KFTB and Western Fold and Thrust Belt (WFTB) (Fig. 1b). The overall deformational style of the Greater Juha area appears transitional between the low-relief, dominantly thin-skinned style of the KFTB (e.g., Hill et al., 2010) and the higher-relief, dominantly thick-skinned style of the WFTB (e.g., Eisenberg, 1996). The Greater Juha area is dominated by the Eastern Muller Ranges (EMR), which combined with the Western Muller Ranges (WMR) defines a large ~25 km wide uplifted region extending westward > 150 km to near the West Papua border (Fig. 1b). The rest of the Greater Juha area, as defined here, lies to the southwest of the EMR and comprises the ~15 km wide and ~25 km long Juha Anticline and much smaller <5 km wavelength structures including the Wai Asi and Cecilia Anticlines (Fig. 1c). The Pliocene-Pleistocene syn-tectonic sediments are well preserved across this frontal region where they are clearly co-planar with the underlying Darai Limestone. The extent and thickness of syn-tectonic sediments across the EMR prior to uplift and erosion is largely unconstrained.

2.2.2. Frontal structures

Despite considerable resource exploration throughout the frontal structures of the Greater Juha area, published geological and geophysical data are limited (e.g., Davies and Norvick, 1974; Craig and Warvakai, 2009; Hanani et al., 2016). The Cecilia Anticline demonstrates the forelandward extent of Cenozoic compression-related structures within the NWFTB. It has been tested by a single well, Cecilia 1 (Fig. 3), which intersected the Cecilia Thrust and an associated Darai Limestone repeat, subsequently failing to reach the Early Cretaceous Toro Sandstone reservoir target (Texaco, 1971). In contrast, the nearby Juha Anticline has a long history of exploration following the discovery of a significant gas column in the Juha 1 well (Fig. 3) (Niugini Gulf Oil, 1983). Good geological and geophysical data coverage reveals the doubly plunging nature and lobate morphology of the wide Juha Anticline (Fig. 1c), but the subsurface geometry of the structure remains poorly constrained. Both thin-skinned (e.g., Hobson, 1986; Hill, 1989) and thick-skinned (e.g., Hanani et al., 2016) structural models have been proposed.

Regional seismic data have significantly improved our

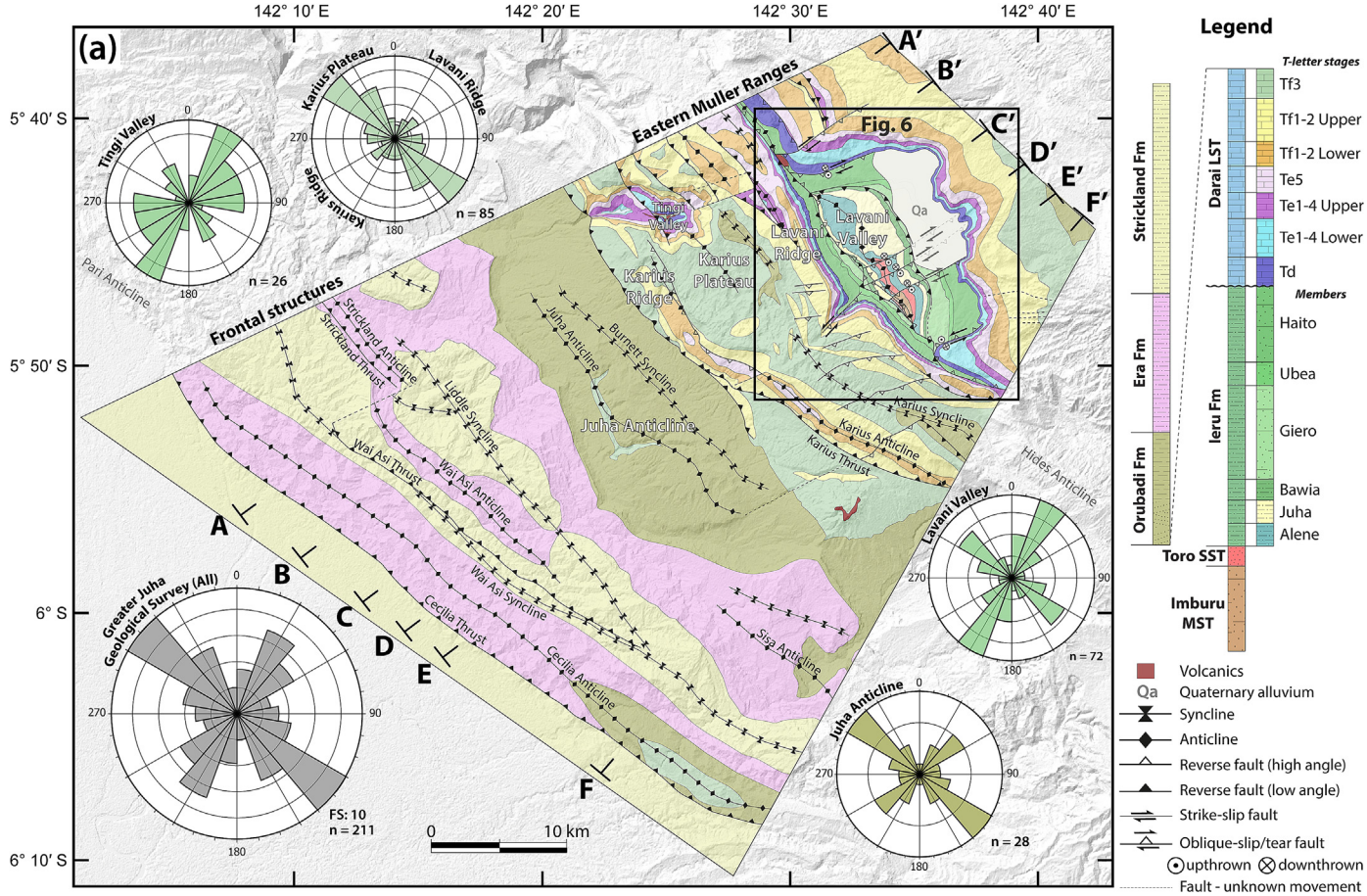

Fig. 4. (a) Geological map of the Greater Juha area including rose plots for fault and fracture strike across each subarea (see Fig. 3 for key localities and constraining data). The number of structural measurements (n) varies while the frequency scale (FS) is 5, except where otherwise stated. Representative strike and dip data, along with strontium isotope and palynological age constraints are included in Figs. S1 and S2 in the supplementary material. (b) Block diagram of quasi-3D model including the Greater Juha geological map and the six cross-sections constraining it. The Darai Limestone and Ieru Formation are sub-divided into T-letter stages and members, respectively (Fig. 3), in the cross-sections only where data permits. The vertical axis is in kilometres relative to mean sea level and is exaggerated by 1.5 times. (c) Segmented and total line length balance (LLB) shortening of the Darai Limestone horizon across the Greater Juha area. Shortening per segment is also included in (b). SRTM digital elevation model retrieved from USGS (2015).

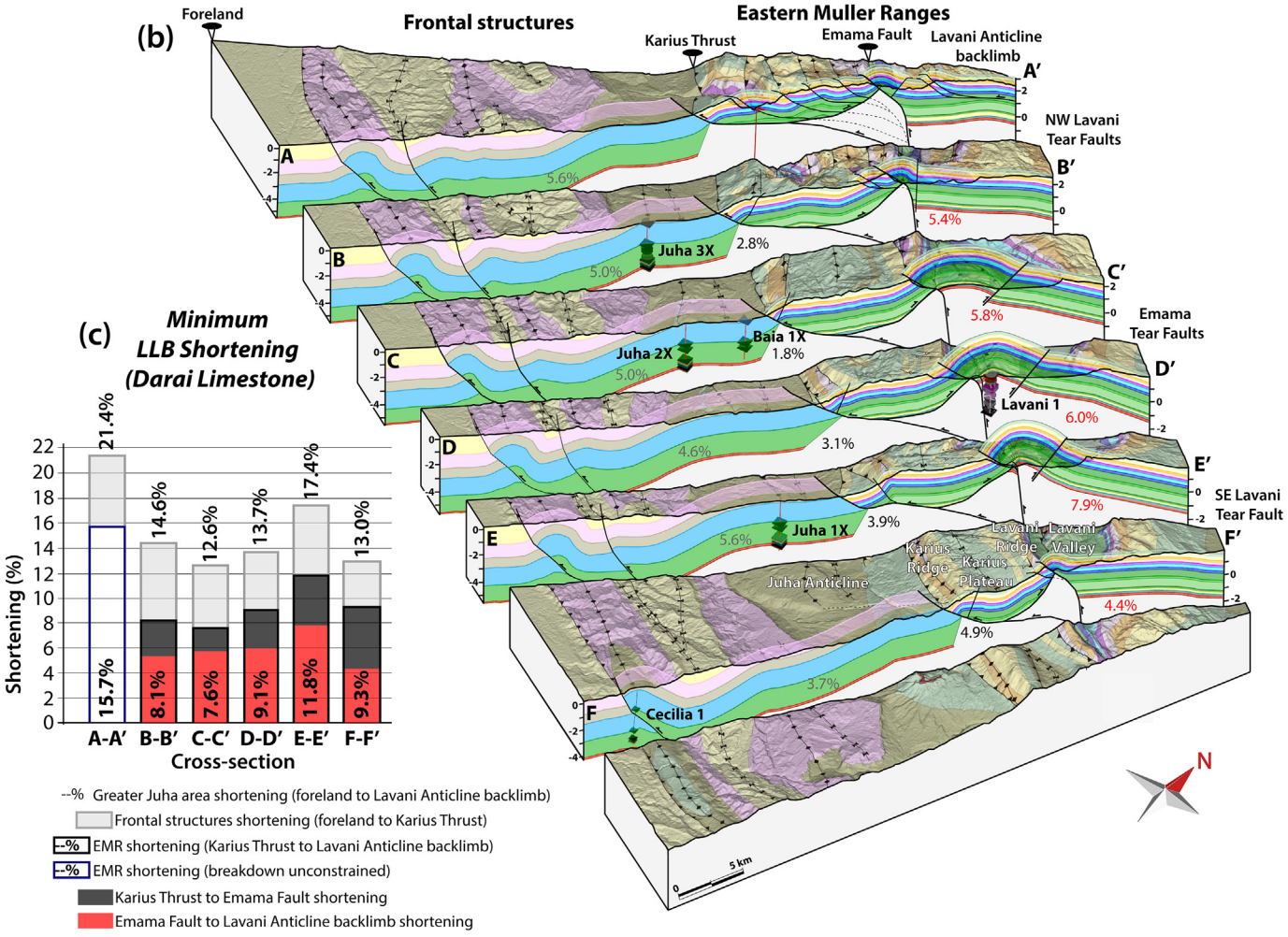

Fig. 4. (*continued*).

understanding of frontal structures across the Greater Juha area (Fig. 3). Initial seismic interpretations by Craig and Warvakai (2009) identified a common sub-Darai Limestone detachment for the Cecilia, Wai Asi and Strickland Anticlines (see Fig. 4a for structure locations), but made no attempt to interpret the deep structure. Subsequent geophysical interpretation and kinematic modelling of the frontal structure by Hanani et al. (2016) suggests an inverted graben-bounding basement fault beneath the wide Juha Anticline that shallows into a detachment horizon within the Jurassic sedimentary sequence, before eventually connecting to the Cecilia and Wai Asi Anticlines through triangle zones within the Ieru Formation.

2.2.3. Eastern Muller Ranges

In the Greater Juha area, the EMR are dominated by the Lavani Anticline and its eroded core, the Lavani Valley (Fig. 1c). The Lavani Valley is unique, characterised by Late Jurassic to Late Cretaceous sediments cropping out >2.5 km above mean sea level (AMSL), suggesting uplift of >7 km relative to regional depth in the foreland. Several seismic lines and gravity data were acquired during the Lavani Valley Seismic Survey in 1974, prior to drilling of the dry Lavani 1 well (Amoco, 1982). The generally poor-quality seismic and gravity data revealed: (1) a large down-to-the-east basement-involved fault beneath the northwest end of Lavani Valley (LAV-74-06; Fig. 3); (2) a corresponding eastward decrease in gravity and (3) a positive gravity anomaly directly to the southwest of Lavani Valley (Bidstone et al., 1974). The Lavani 1 well spudded within Toro Sandstone near the centre of the Lavani Valley (Fig. 3) and initial interpretations of the well included a major northeast-dipping reverse or thrust fault at ~500 m repeating the Toro section (Amoco, 1982). However, improved palynological dating and stratigraphic understanding instead revealed a Koi-Iange repeat overlying a ~1.8 km thick sequence of syn-rift sediments of the Magobu Formation (Denison, 1990). Although thrust repeats may have contributed to the thickening of the Magobu Formation within the Lavani 1 well, they are unlikely to be solely responsible for the observed thickness. The dry Muller 1 well (Mobil, 1991), located to the northwest of the Greater Juha area (Fig. 1b) on the northwest plunging nose of the Lavani Anticline, is the only other well in the EMR. It spudded in basal Darai Limestone and drilled a conformable sequence intersecting the Toro Sandstone reservoir at 1.8 km downhole depth (Mobil, 1991).

The evolution of the EMR is poorly understood, with previous workers proposing a range of models to explain uplift, including: (1) basement-involved thrusting and inversion (e.g., Jenkins, 1974; Davies, 1983); (2) thin-skinned deformation (Hobson, 1986); (3) blind thrusting/passive-backthrusting (Buchanan and Warburton, 1996); (4) a basement-cored triangle zone (Hill, 1989) and (5) igneous underplating (Buchanan and Warburton, 1996). Basement-involved thrusting is generally favoured due to the large positive gravity anomaly associated with the EMR (Bidstone et al., 1974) and the discovery of Triassic (222 ± 4 Ma from K-Ar; Page, 1976) granite

basement in the Strickland Gorge in the core of the Muller Ranges (Fig. 1c) (Jenkins and White, 1970; White and Marfleet, 1973). Interestingly, in contrast to the ~1.8 km of syn-rift sediment intersected in the Lavani 1 well, syn-rift sediments are absent in the Strickland Gorge with the Strickland Granite directly overlain by ~1.2 km of Jurassic post-rift sediments (Niugini Gulf Oil, 1983).

3. Methods

We present new data and models for the structure of the Greater Juha area based on new field observations and reinterpretations of the legacy dataset. Field access to the remote Greater Juha area was facilitated through a program of data acquisition carried out along >100 km of traverses (Fig. 3) by Papuan Oil Search and ExxonMobil from 2013 to 2015. Very high rainfall upwards of 5000 mm per annum is common across the frontal mountain range of the PFB and has created a heavily karstified landform. Furthermore, steep terrain is prone to slumping and landslides that complicate the surface geology. Outcrop is limited (e.g., Fig. 5) due to thick vegetation, so geological data collection is challenging and the quality of field data can be variable.

Fieldwork included the description of lithologies, macrofossil

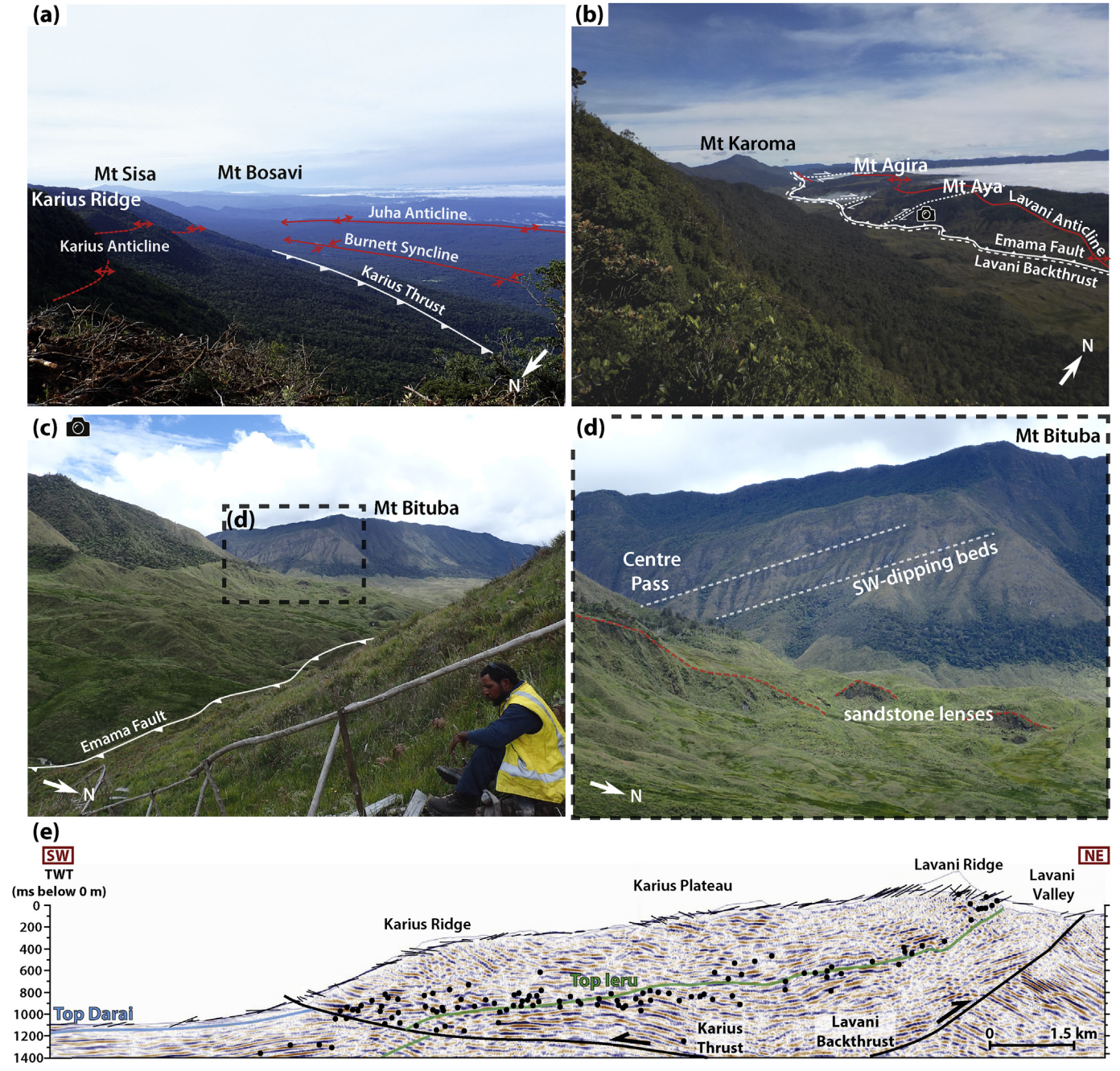

Fig. 5. (a) Foreland structures and the steep southwest-facing slope of Karius Ridge, looking southeast; (b) The major structural components and landform of the Lavani Valley from Lavani Ridge (Mt Uraka), looking northwest; (c) Centre Pass looking west from Mt Aya, with photo location marked in (b); (d) Centre Pass showing distinct southwest-dipping beds and northwest-southeast striking sandstone lenses within Ieru Formation at the base of Lavani Ridge, looking west; (e) Reflection seismic data across the EMR clearly show the shallowly northeast-dipping Karius Thrust and southwest-dipping Lavani Backthrust. Lines at surface are representative dip data and dots represent predicted Top-Ieru depth estimates based on strontium isotope ratios.

assemblages and sedimentary structures (way-up) along with the measurement of ~1300 bedding, fault and fracture orientations (Fig. 3). In addition, 157 Darai Limestone samples were collected for petrographic, biostratigraphic and $^{87}Sr/^{86}Sr$ analysis. Strontium isotope ratios were related to larger benthic foraminiferal T-Letter stages widely used in the Indo-Pacific (e.g., Lunt and Allan, 2004) and calibrated to the geological timescale by strontium isotope stratigraphy through the Papuan Basin in ongoing CSIRO research (Fig. 2b) (e.g., Allan et al., 2000). An additional 19 Mesozoic clastic samples were dated palynologically. Data obtained during this study were added to legacy data to form a contemporary database across the Greater Juha area comprising ~4800 outcrops with both lithological descriptions and structural measurements (Fig. 3). Of these ~1300 outcrop samples were successfully dated using strontium isotope or palynological analyses (Fig. 3). Legacy datasets are available in reports to the Papua New Guinea Government.

We also make extensive use of NASA Shuttle Radar Topography Mission (SRTM) data, sampled at 1 arc-second, or ~30 m resolution (USGS, 2015). Midland Valley's Move software suite was used for cross-section and map construction. Cross-sections were constructed perpendicular to strike and spaced in order to best represent lateral structural variations and to optimally utilise the available data. Seismic data within the PFB are generally of poor to moderate quality, and thus the constraint on structure at depth is limited. In particular, data constraints drop off significantly below the top of the Ieru Formation and no attempt has been made to interpret structure at depths below the Ieru, except where well and seismic data exists such as across the frontal structures and within Lavani Valley (Fig. 3). Seismic lines recently acquired across the EMR (e.g. along Traverse 102, 103, 104, 108; Fig. 3) were not available at the time of this study, except for the shallow portion of Line 102.

The true stratigraphic thickness (TST) of Darai Limestone T-letter stages was estimated from traverse data and downhole strontium isotope ratio measurements in the Juha 1 well. TSTs were then combined with structural measurements to predict depth to the base of the Darai Limestone, following Hornafius and Denison (1993). TSTs for the Mesozoic sequence were estimated from a combination of traverse, well and seismic data, extrapolated from better constrained areas where necessary. For instance, substantial deformation and lack of outcrop within the Lavani Valley means that good quality data are limited and therefore TSTs are less constrained. In this case, TSTs from wells across the neighbouring Hides, Juha and Muller structures (Figs. 1b and 3) provided a valuable guide.

The process of integrating the geological map and cross-sections produced a quasi-3D model of much higher quality than a simple 2D geological map. The cross-sections ensure the map is geologically plausible in the third-dimension and enable sub-surface data such as reflection seismic and well-derived TSTs to be fully integrated.

4. Geological and structural observations

The Greater Juha area can be subdivided into five structural domains: the Juha Anticline, the Karius Ridge, the Karius Plateau, the Lavani Ridge and the Lavani Valley (Fig. 3). The structure of each domain is illustrated on the geological map and associated cross-sections in Fig. 4. Strontium isotope, palynological and representative structural data used to constrain the geological map and cross-sections are presented in Fig. S1 and Fig. S2 in the supplementary material.

4.1. Observed fault and fracture trends

Outcrop within the Greater Juha area is commonly faulted and fractured. More than 200 fault and fracture measurements reveal the overall dominance of northwest-southeast striking structures (Fig. 4a), consistent with the trend of the PFB in this region (Fig. 1b). The majority of these arc-parallel faults and fractures are bedding sub-parallel and most plausibly relate to flexural slip and glide mechanisms. There is also a strong northeast-southwest striking structural trend which is pervasive across the Greater Juha area, particularly in the Lavani and Tingi valleys where the Ieru Formation dominates surface outcrop (Fig. 4a). This arc-normal trend is also evident in the Orubadi Formation across the Juha Anticline, but is less prominent in the Darai Limestone across the Karius Ridge, Karius Plateau and Lavani Ridge (Fig. 4a). The reduced prominence in Darai Limestone may relate to its greater competence compared with mudstones and siltstones of the Ieru Formation. An alternate explanation is that arc-normal structures are more concealed within Darai Limestone outcrop due to denser vegetation and intense karstification.

The arc-normal structural trend can also be inferred on the SRTM digital elevation model (DEM) and identified in geological mapping (Fig. 4a), where it is expressed as: (1) discrete faults, such as observed in abundance across the southeastern end of the Karius Plateau; (2) through-going zones characterised by the termination or disruption of structures, such as at the northwest and southeast ends of the Juha and Lavani anticlines and/or; (3) geomorphic features, such as Centre Pass (Fig. 3). The prevalence of this arc-normal structural trend across multiple scales suggests it has played an important role in the structural evolution of the area.

4.2. Juha Anticline

The Juha Anticline mainly exposes Orubadi Formation (Fig. 4) the basal unit of which is an often cross-bedded, medium- to coarse-grained calcarenite, which appears to control the surface expression of the anticline such that the bedding orientation approximates the slope (Fig. 4b). Field and seismic data suggest that the Orubadi Formation calcarenite lies conformably on the uppermost Darai Limestone across the entire Juha Anticline. Faulting and fracturing along two dominant structural trends (Fig. 4a) forms a tessellated landform consisting of cliff-faces up to several metres high and crevices up to several metres deep. Fault movement sense could be determined for several faults, with reverse, strike-slip and oblique-slip faults identified, leading us to the inference that this characteristic landform could relate to local transpressional and transtensional interactions between discrete blocks. The calcarenite comprises highly competent beds so is a good analogue for structures in the underlying, very competent Darai Limestone where heavy karstification may mask structural trends.

4.3. Karius Ridge

The Karius Ridge is entirely composed of Darai Limestone and exhibits ~1 km of topographic relief from its base on the northeast-limb of the Juha Anticline to its crest on the Karius Plateau (Fig. 3). The dominant bedding dip appears to be sub-parallel to the southwest-facing slope, although common boulders and slumping across steep terrain in this area (Fig. 5a) make it difficult to obtain high-confidence data.

The most prominent structures along the length of Karius Ridge are the Karius Thrust and associated Karius Anticline (Figs. 4 and 5a). Strontium isotope analyses show the Karius Thrust juxtaposes Tf3- to Te5-aged Darai Limestone in its hanging wall with younger Tf3-aged Darai Limestone and Orubadi Formation in its

footwall, with the oldest hanging wall rocks cropping out in the hinge of the Karius Anticline (Fig. 4). Darai Limestone along Karius Ridge is anomalously deformed compared to the surrounding areas, with an increased abundance of arc-parallel faults and fractures and a stronger developed bedding-parallel stylolitic fabric. Over 30 southwest-facing cliffs, each up to several metres high, are particularly prominent on the southwest side of the ridge crest, inferred to relate to steeply northeast-dipping reverse faults (Fig. 5a). A stepped series of 10–20 northeast-facing cliffs, each up to 5 m high, dominate for ~1 km northeast from the crest of Karius Ridge, inferred to relate to steeply southwest-dipping backthrusts. These structures are here interpreted to be conjugate backthrusts in the hanging wall of the southwest-vergent Karius Thrust and appear to have contributed to the uplift and subsequent erosion of the Karius Anticline towards the northwest (Fig. 4). While a distinct fault was not observed in outcrop at the base of the Karius Ridge, seismic data clearly show the truncation of bedding at the base of the thrust sheet (Fig. 5e). The Karius Anticline appears to be tighter towards the southeast (Fig. 4b), which is consistent with observations of overturned bedding in the Karius 1 well and outcrop immediately to the southeast of the Greater Juha area (Fig. 3) (Johnstone and Emmett, 2000).

Darai Limestone cropping out on the southwest-facing slope of the Karius Ridge is significantly older than on the Karius Plateau (Fig. 4). This is a consistent geomorphic characteristic of frontal structures in the PFB (e.g., KFTB: Hill et al., 2008; Mananda Anticline: Keenan and Hill, 2015) that is in part related to increased rainfall and weathering along southwest-facing slopes.

4.4. Karius Plateau

Elevation along the Karius Plateau ranges from ~2–2.5 km AMSL along the crest of the Karius Ridge to ~3.2–3.6 km AMSL at the crest of Lavani Ridge (Fig. 3). The plateau broadens from ~4 km wide in the southeast to ~11 km wide in the northwest (c.f. cross-sections F-F′ and B-B' in Fig. 4b). Outcrop across the plateau is dominated by shallowly-dipping Darai Limestone that has suffered moderate to intense karstification, with abundant rillenkarren and sinkholes up to hundreds of metres across. While karstification makes it difficult to identify discrete structures, the landform is clearly intersected by sub-linear trending zones of cliffs up to 10 m high. These zones are interpreted to represent intersecting arc-parallel and arc-normal oriented structures that can also be readily observed cross-cutting Karius Plateau at the scale of the SRTM DEM (e.g., Fig. 6a).

Strontium isotope data show that Tf3- and TF1-2 (Upper)-aged Darai Limestone crops out across most of the Karius Plateau except where the Orubadi Formation was observed on Traverse 108 and to the southeast of Traverse 104 (Fig. 4). Interestingly, the basal Orubadi Formation calcarenite conformably overlying the Darai Limestone across the Juha Anticline is absent across the Karius Plateau on Traverse 108, suggesting that the Orubadi Formation may unconformably overlie the Darai Limestone. This is consistent with observations of a similar unconformity around the Muller 1 well to the northwest of the Greater Juha Area (Fig. 3) (Hornafius, 1993), suggesting an unconformity may extend across large portions of the EMR. Alternatively these observations could be explained by the strongly diachronous nature of the Orubadi Formation in this region (e.g., Thornton et al., 1996).

The shallow structure of the Karius Plateau is dominated by the Karius Syncline in the southeast passing into a series of southwest-verging thrusts in the northwest. The syncline tightens significantly towards the southeast in a similar style to the Karius Anticline (Fig. 4b). To the northwest of cross-section D-D′, the Karius Syncline is replaced by an almost continuous southwest bedding dip in cross-section C-C′ and by gentle folding in cross-section B-B'. Further northwest on cross-section A-A', smaller wavelength folds and small to moderate offset thrusts are inferred and strontium isotope ages show older Darai outcrops. This change in structural style is interpreted to be accommodated along an arc-normal oriented zone of tear faulting that extends from the northeast of Tingi Valley to Lavani Ridge (Fig. 4a).

The Tobi River has eroded up to 1 km into the Karius Plateau to the northwest of the Greater Juha area, forming the steep-sided Tingi Valley (Fig. 3). In places, the Tobi River has eroded through the entire Darai Limestone sequence (Fig. 4). A northeast-dipping thrust has tentatively been interpreted to cross-cut the Tingi Valley (Fig. 4), based on strontium isotope ratios and field observations. Intermediate volcanics of the Tingi Valley Igneous Complex, including both diorites and andesites, are abundant throughout the Tingi Valley with scattered hornblende-phyric andesitic boulders present as far away as Traverse 108 on the Karius Plateau. Field observations suggest that the volcanics have spread out at the Darai Limestone/Ieru Formation contact, possibly facilitated by cave systems observed near the base of the Darai Limestone within Tingi Valley.

4.5. Lavani Ridge

The regionally prominent Lavani Ridge is bound to the northeast and southwest by steep slopes and is characterised by a variable crest elevation of ~3.2 km AMSL on Traverse 103 at Mt Uraka, to ~3.6 km AMSL on Traverse 108 at Mt Karoma (Fig. 6a). Structural measurements and strontium isotope data across Lavani Ridge reveals a persistent shallow southwest bedding dip, as do observations from the cross-cutting Centre Pass (Fig. 5c and d).

The southwest-facing slope of Lavani Ridge mostly comprises Tf3- and Tf1-2 (Upper)-aged Darai Limestone (Figs. 4 and 6b). Older areas of Tf1-2 (Lower)- and Te5-aged Darai Limestone on the crest and southwest side of Lavani Ridge around cross-sections A-A′, B-B′ and F-F' are interpreted to result from uplift in the hanging wall of southwest-verging thrust faults (Figs. 4 and 6b). This is consistent with field observations from these areas including an order of magnitude increase in the intensity of faulting and fracturing when compared to Karius Plateau, and an increased abundance of southwest-facing cliffs up to 10 m high.

The northeast-facing slope of Lavani Ridge (Fig. 5c) comprises a ~1 km, mostly conformable sequence from Tf1-2 (Upper)-aged Darai Limestone to Ieru Formation (Figs. 4 and 6b). Palynological data indicate that sandstones, siltstones and mudstones cropping out near the base of Lavani Ridge, in Lavani Valley, belong to the Haito and Ubea Members of the Ieru Formation (Fig. 6b). Comparatively erosion-resistant, southwest-dipping sandstone beds form northwest-southeast striking ridges (Fig. 5d) that can be recognised in the high-resolution SRTM DEM and which demonstrate structural continuity (e.g., Fig. 6a).

Centre Pass is a prominent valley cross-cutting Lavani Ridge (Fig. 6a). The Emama River (Fig. 6a) appears to have once drained to the southwest through Centre Pass, but subsequent drainage reorganisation to the northeast and southeast of Lavani Valley has left Centre Pass virtually dry. The Tingi Valley has a similar geomorphic expression (Fig. 3) suggesting it is a potential modern analogue for fluvial incision of Centre Pass into Lavani Ridge. Interestingly, the strike of Centre Pass is similar to the prominent arc-normal structural trend recognised throughout the Greater Juha area (Fig. 4a). Sinistral offset of Lavani Ridge across Centre Pass is here interpreted to be related to tear faulting (Fig. 4).

4.6. Lavani Valley

The ~10 km wide and ~15 km long Lavani Valley is located along

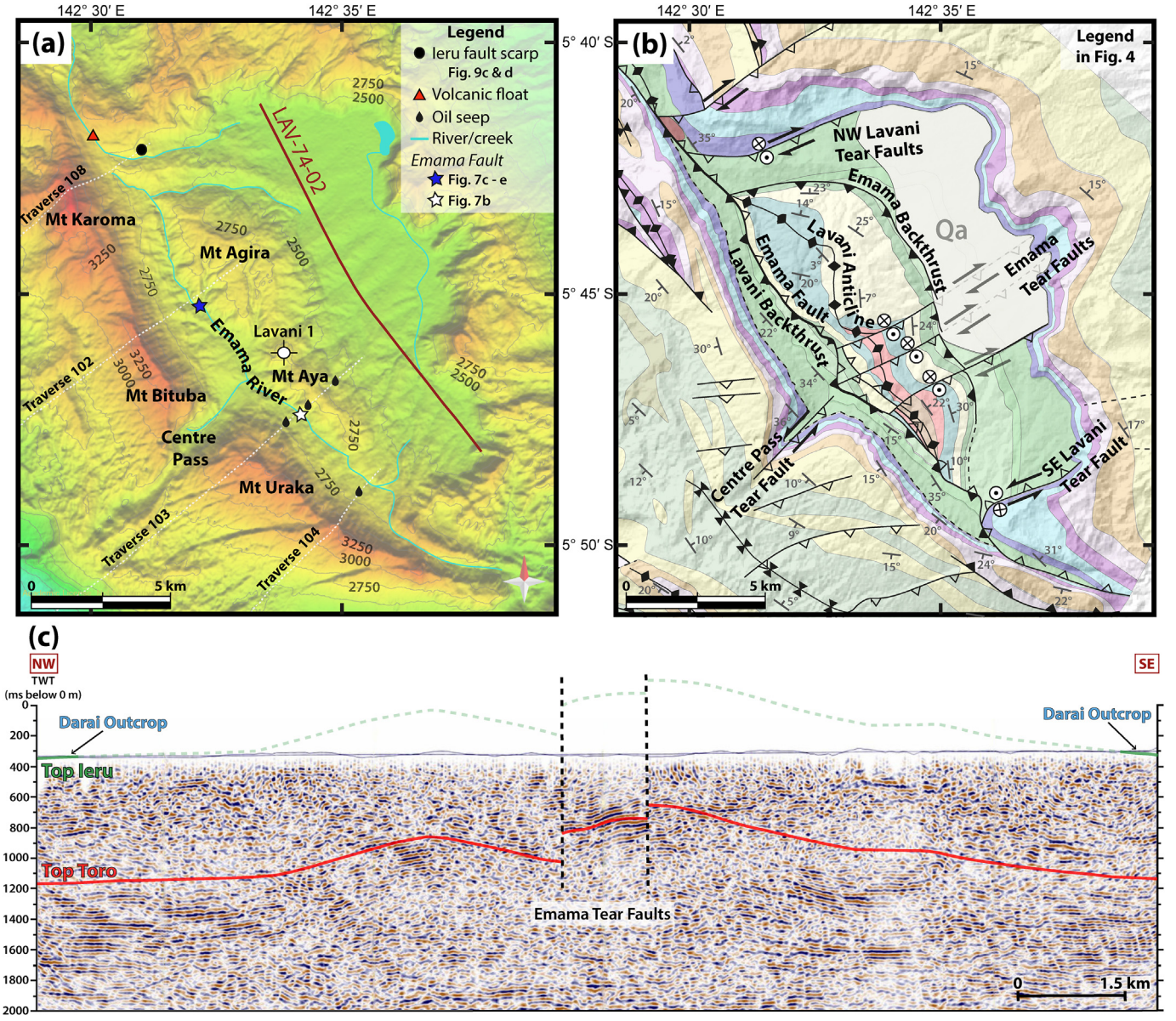

Fig. 6. (a) DEM of Lavani Valley and environs from SRTM dataset (USGS, 2015). Key geographic features and the location of geological traverses are indicated; (b) Detailed geological map of the Lavani Valley. Legend in Fig. 4. Note the dominant up-to-the-southeast offset on the NW Lavani Tear Faults, Emama Tear Faults and the series of faults cross-cutting the southwestern end of Karius Plateau. Variable topography combined with the vertical component of motion on the oblique-slip Emama Tear Faults masks the dextral sense of shear in map view. (c) LAV74-02 reflection seismic data along the length of Lavani Valley (location in (a) above) demonstrates up-to-the-southeast offset across the Emama Tear Faults, consistent with surface geological data (e.g., (b) above).

the hinge of the regionally prominent Lavani Anticline (Figs. 5b and 6). The surface geology is dominated by mudstones, siltstones and minor sandstones of the Ieru Formation, contributing significantly to its distinct, comparatively gentle sloping and open landform (Figs. 5b and 6a). The valley is almost completely surrounded by steep slopes of mostly conformable Darai Limestone that dip away to the southwest and northeast on either side (Fig. 4b). The geology of the Lavani Valley offers significant insight into the structure of the regionally-significant Lavani Anticline as a whole and indeed the entire EMR.

Dense grassland vegetation means that outcrop within the Lavani Valley is largely limited to the Emama River (Fig. 6a), and consequently observations are available mostly along strike, with few cross-cutting traverses. Our work provides new observations of the dip structure across this area. Importantly, observations suggest that while faulting and fracturing is pervasive throughout the Lavani Valley, deformation is clearly more severe within major fault zones such as around the regionally significant Emama Fault (Figs. 4b and 6b and c.f. Fig. 7a and b).

4.6.1. Emama Fault

The Emama River is a consistent feature at the base of the southwest side of Mt Agira and Mt Aya (Fig. 6a). Major fault zones were observed at two localities around 6 km apart within the Emama River (Fig. 6a), suggesting the river approximately follows the trace of a major fault.

Morphologically, the fault appears sub-vertical on Traverse 102, where it is expressed as a >10 m wide zone of steep, contorted bedding with localised fault gouge and brecciation (Fig. 7c–e). Around Traverse 103 the fault dips towards the northeast with fault

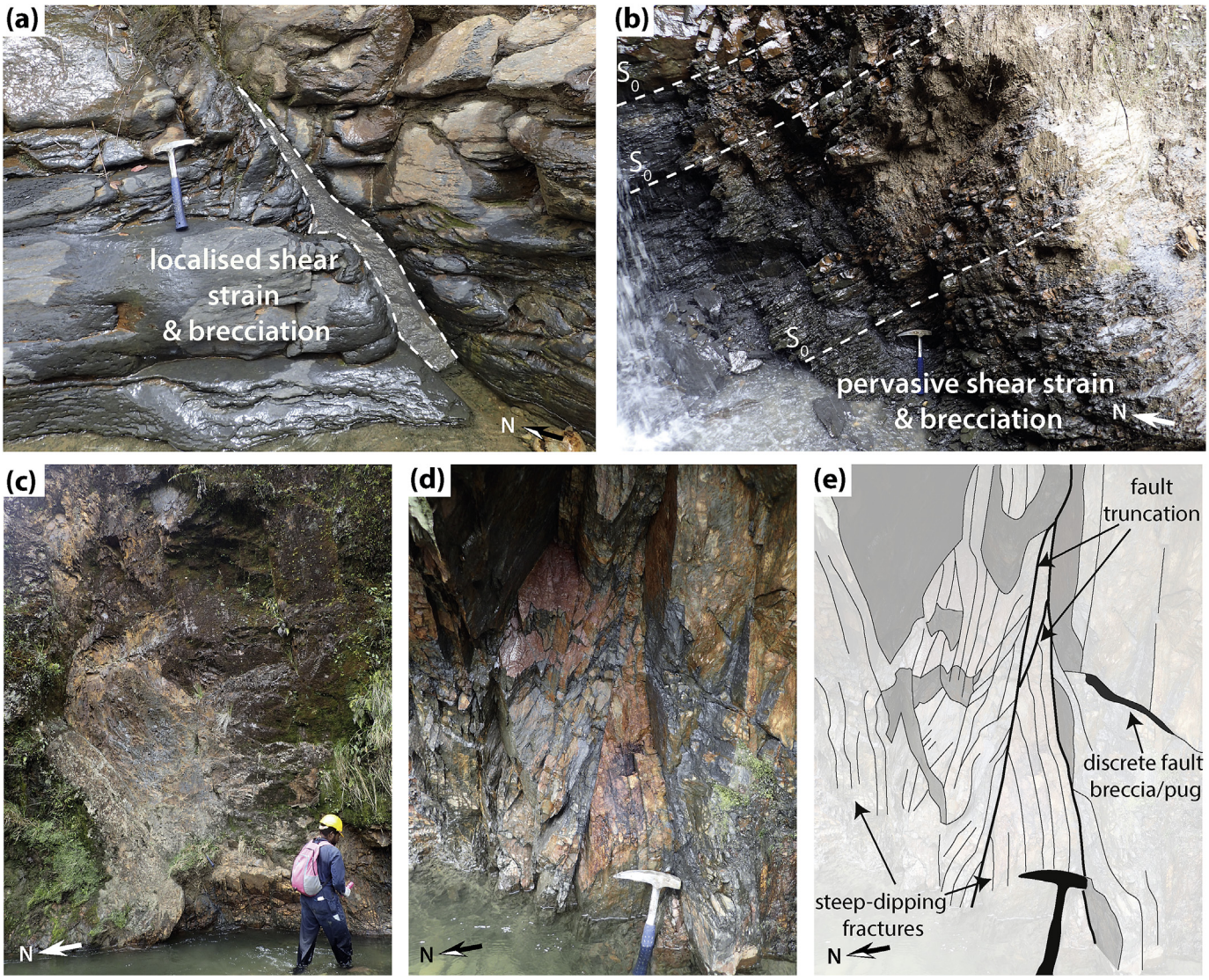

Fig. 7. Faulting within the Cretaceous Ieru Formation in Lavani Valley. (a) Abundant, widely distributed narrow/discrete (<1 m) faults and (b–e) wide fault zones (>10 m) with distributed shear strain. (b) Shows the Emama Fault on Traverse 103; (c), (d) and (e) show the Emama Fault along Traverse 102. Location of Emama Fault photos marked in Fig. 6a.

rounded and striated fine-grained sandstone fragments within highly sheared mudstones (Fig. 7b) suggesting that the amount of movement accommodated within this zone is significant. Further, there is no evidence of a major fault along-strike in re-interpretations of the Lavani 1 well, suggesting the fault must become very steep down-dip (Fig. 4b, cross-section D-D'). This fault is here referred to as the Emama Fault (Fig. 6b), a steeply northeast-dipping reverse fault that uplifts Mt Agira and Mt Aya in its hanging wall and which may be largely responsible for the formation of the Lavani Anticline.

In the uplifted northeast side of the Emama Fault, the geological complexity appears to increase from Mt Agira in the northwest to Mt Aya in the southeast (Fig. 6). The surface geology of Mt Agira comprises a ~5 km wavelength anticline, with the Alene and Juha members of the lowermost Ieru Formation cropping out at its peak at ~2.8 km AMSL (Fig. 8a). Its forelimb is characterised by predominantly southwest-dipping beds (Fig. 8b and c) consistent with the adjacent Lavani Ridge (Fig. 5d).

In contrast, Mt Aya has an apparent wavelength of ~2.5 km, is noticeably more asymmetric (Fig. 6a) and Toro Sandstone crops out at its crest at ~2.8 km AMSL (Fig. 8d). Traverse 103 demonstrates persistent shallow to moderate northeast dip along the southwest-facing slope of Mt Aya (Fig. 8e and f), suggesting the forelimb of the Lavani Anticline is mostly absent (Fig. 4b, cross-section E-E'). There is an accompanying increase in deformation intensity in this area, including widespread bedding sub-parallel shear strain, particularly evident in fine-grained lithologies (e.g., Fig. 7b). Traverse 103 also revealed a ~120 m thick sequence of fine- to coarse-grained sandstones located directly above intensely deformed Alene Member in the hanging wall of the Emama Fault. Earliest Cretaceous (Berriasian) palynological ages indicate that this sequence is the Toro Sandstone. Interestingly, previously unidentified sheared mudstone and siltstone directly overlying the sand-dominated sequence are of Late Jurassic (Tithonian) age, suggesting Imburu Mudstone directly overlies Toro Sandstone in this area. If correct, these are the oldest outcropping rocks in the Greater Juha area (Fig. 6b). Northeast-dipping Toro Sandstone crops out again at the crest of Mt Aya (Fig. 8d) as originally reported by Bidstone et al. (1974). Several low to moderate confidence way-up indicators (e.g., graded-bedding, cross-bedding) along the length of Traverse

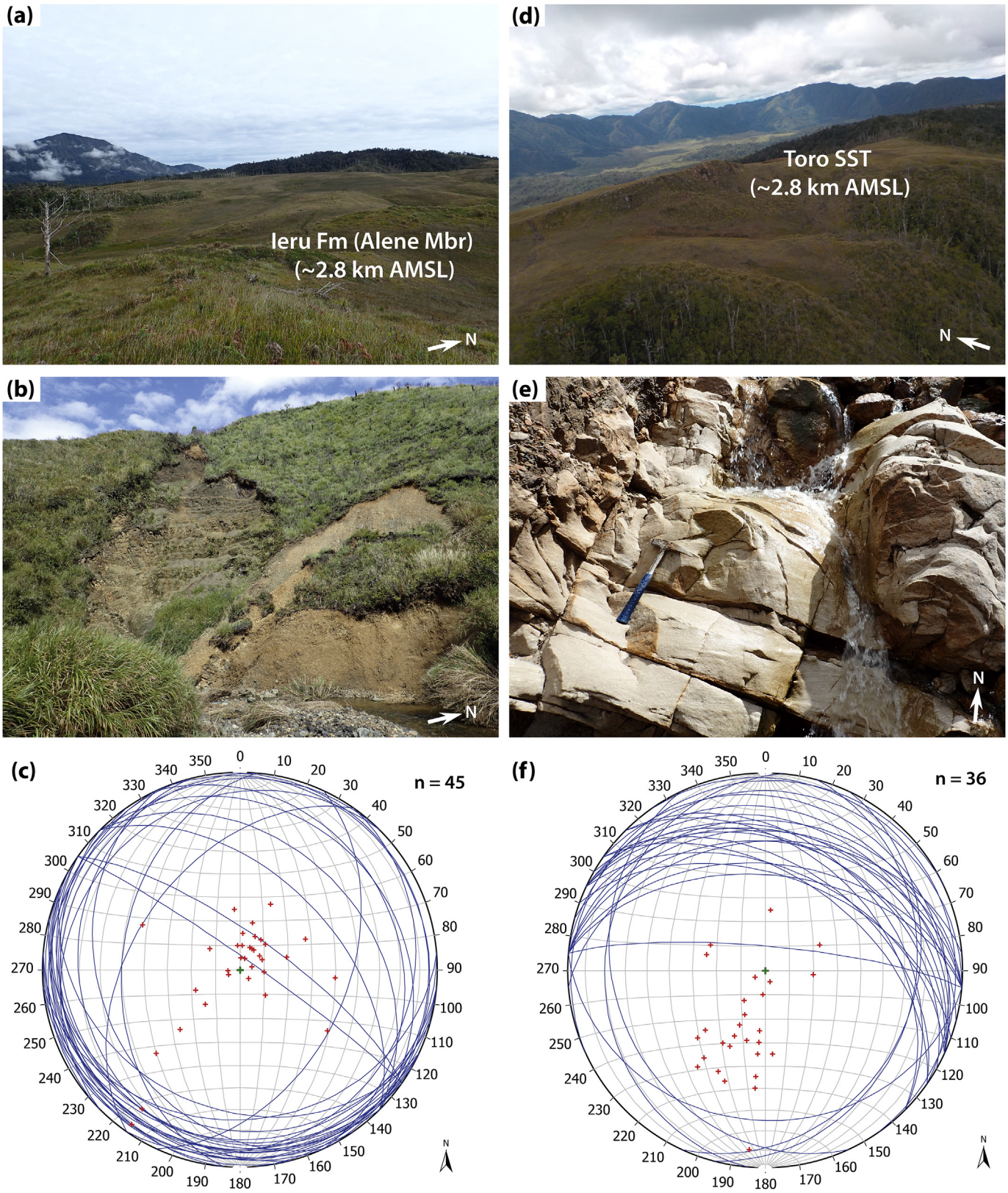

Fig. 8. Field photos and Schmidt stereonets (n = number of measurements) showing lateral geological variation within Lavani Valley. Mt Agira (Traverse 102) is associated with; (a) a relatively subdued landform; (b) Ieru Formation outcrop and (b & c) a southwest bedding dip. In contrast, Mt Aya (Traverse 103) is associated with (d) a steeper landform; (e) older outcrop, including Toro Sandstone and (e) & (f) a northeast bedding dip.

103 suggest that the sedimentary sequence is the right way up, however we are hesitant to completely rule out the possibility of an overturned limb.

Thus, the geometrically complex Emama Fault is a regionally significant structure that appears to be largely responsible for uplifting the Lavani Anticline in its hanging wall. Further, the intersection of thick syn-rift sediments nearly 2 km AMSL in the Lavani 1 well suggests the Emama Fault is connected to an inversion structure at depth; a decrease in Bouguer gravity from Lavani Ridge into Lavani Valley (Bidstone et al., 1974) suggests that, despite inversion, basement remains deeper in the hanging wall of the Emama Fault.

In summary, geological field data from within Lavani Valley reveal the structural complexity of the Emama Fault and Lavani Anticline. Outcropping rocks become older towards the southeast of Lavani Valley (Fig. 6b), suggesting increased displacement and hanging wall uplift along the Emama Fault towards the southeast. The southwest-facing slope of Mt Aya provides important insight into the subsurface structure of the Lavani Valley. Here, thrusted repeats of Ieru Formation, Toro Sandstone and Imburu Mudstone are interpreted as stacked horses with the bounding faults merging into a foreland-vergent roof thrust within the incompetent Ieru Formation (Fig. 4b, cross-section E-E'). This roof thrust and the overlying hangingwall rocks have since eroded away adjacent to Mt Aya. It is unclear whether this structural style extends along strike to beneath Ieru Formation cropping out over Mt Agira (Fig. 6b), but if so the roof thrust must lie just beneath the surface in the Alene Member, suggesting this is a prominent detachment layer. Alternatively, the structural style may change at a tear fault.

4.6.2. Emama Backthrust

Field data constraints across Mt Agira combined with the LAV74-02 seismic line to the northeast (Fig. 6a and c) define an abrupt transition from lower to upper Ieru Formation members around the northern flank of Mt Agira (Fig. 6b). In the absence of the steep bedding dips, the Emama Backthrust has been interpreted to explain this transition. Where it wraps around the northwestern flank of Mt Agira, the Emama Backthrust juxtaposes Bawia Member of the lowermost Ieru Formation with Haito member of the uppermost Ieru Formation (Fig. 6b). The significance of the Emama Backthrust decreases towards the southeast where seismic line LAV74-02 suggests older Ieru Formation crops out in its footwall (Fig. 6c). Moreover, it is plausible that uplift in the hanging wall of the Emama Backthrust has had a geomorphic control on the extent of Quaternary alluvium in the north of Lavani Valley (Fig. 6b).

4.6.3. Lavani Backthrust

Lavani Ridge appears to be located within the footwall of the Emama Fault, but is nevertheless associated with elevations >3.2 km AMSL along its length, making it the highest topographic feature in the Greater Juha area. Furthermore the steep northeast-facing slope appears to be unique regionally within the NWFTB, where the vast majority of steep slopes are southwest-facing (Fig. 1c). We interpret these characteristics to result from uplift along a significant backthrust within the Ieru Formation that originates from beneath Karius Ridge (Fig. 4b). This backthrust is imaged on seismic data where it truncates bedding beneath Lavani Ridge (Fig. 5e). Exactly where the backthrust intersects the surface within Lavani Valley is less clear, but strontium and palynological data from the northeast-facing slope of Lavani Ridge suggest a largely conformable sequence, such that the Lavani Backthrust may intersect the surface at approximately the same location as the Emama Fault (Figs. 4b, 5b and 6b). This makes it difficult to constrain the relative influence of the Emama Fault and Lavani Backthrust. Thickness variations within the lower Td Darai Limestone, particularly to the southeast of Lavani Valley, suggest the Lavani Backthrust could plausibly have a splay near the Darai Limestone/Ieru Formation contact (Fig. 6b).

4.6.4. Arc-normal structures

Throughout Lavani Valley, arc-normal faults and fractures are pervasive (e.g., Fig. 9a and b) and may even be more abundant than arc-parallel structures (Fig. 4a). Interestingly, arc-parallel structures, typically bedding (S_0) parallel, show evidence of both brittle and semi-ductile (e.g., Fig. 9b) deformation. In contrast, cross-cutting arc-normal structures appear to have formed exclusively from brittle processes (Fig. 9a and b) and often displace arc-parallel structures.

Additionally, a small southeast-facing fault scarp (Fig. 9c and d) was observed within the Ieru Formation near the end of Traverse 108 (Fig. 6a). Such an observation is abnormal within the usually very fast weathering mudstones and siltstones of the Ieru Formation, suggesting that arc-normal faulting may still be active, at least within the Lavani Valley. Slickenfibres and striations confirm a northeast-southwest striking fault plane with at least a component of strike-slip movement (Fig. 9c and d). Thus, the scarp is likely to relate to a restraining bend/transpressional zone along a strike-slip or tear fault. Given its proximity to the abrupt northwest termination of the Lavani Valley, it seems plausible that this scarp is related to a larger zone of significant northeast-southwest striking faults, here collectively defined as the NW Lavani Tear Faults (Fig. 6b).

Other prominent northeast-southwest striking structures can be identified at the scale of Lavani Valley. The most significant of these appear to be located at the southeast termination of Lavani Valley (SE Lavani Tear Fault) and in a zone through the centre of Lavani Valley (Emama Tear Faults) (Fig. 6b). The tear faults bounding either end of the Lavani Valley are recognised by the vertical juxtaposition of older than expected Ieru Formation members with the Darai Limestone (Fig. 6b). The Emama Tear Faults cutting through the centre of the valley are defined by lateral changes in landform, along with surface and subsurface geology (Fig. 6). Reflection seismic line LAV74-02 demonstrates a component of up-to-the-southeast offset across the Emama Tear Faults (Fig. 6c), consistent with surface geological observations (e.g., Fig. 6b). Interestingly, the horizontal component of displacement along the Emama Tear Faults appears to be dextral between Mt Agira and Mt Aya and sinistral through the Lavani Ridge (Fig. 6b). The Emama Fault and Lavani Backthrust are located between this apparent change in movement sense, suggesting they may be related.

4.6.5. Summary

New observations presented here significantly improve our understanding of the structure of Lavani Valley. First, the Emama Fault is a geometrically complex, regionally significant structure that is largely responsible for uplifting the Lavani Anticline. Thick syn-rift sediments in the hanging wall suggest the Emama Fault is connected to an inversion structure at depth; a decrease in Bouguer gravity from Lavani Ridge into Lavani Valley (Bidstone et al., 1974) suggests that, despite inversion, basement remains deeper in the hanging wall of the Emama Fault. The amplitude and wavelength of the Lavani Anticline decreases outwards from the northwest and southeast ends of Lavani Valley (Fig. 4b, cross-section A-A′ and F-F′); suggesting that the Emama Fault may be associated with less displacement in these areas (at least at depth). Interestingly, outcropping rocks become older from the northwest to southeast of Lavani Valley (Fig. 6b) implying increased displacement and hanging wall uplift along the Emama Fault towards the southeast (Fig. 4b, c.f. cross-sections B-B′ and E-E').

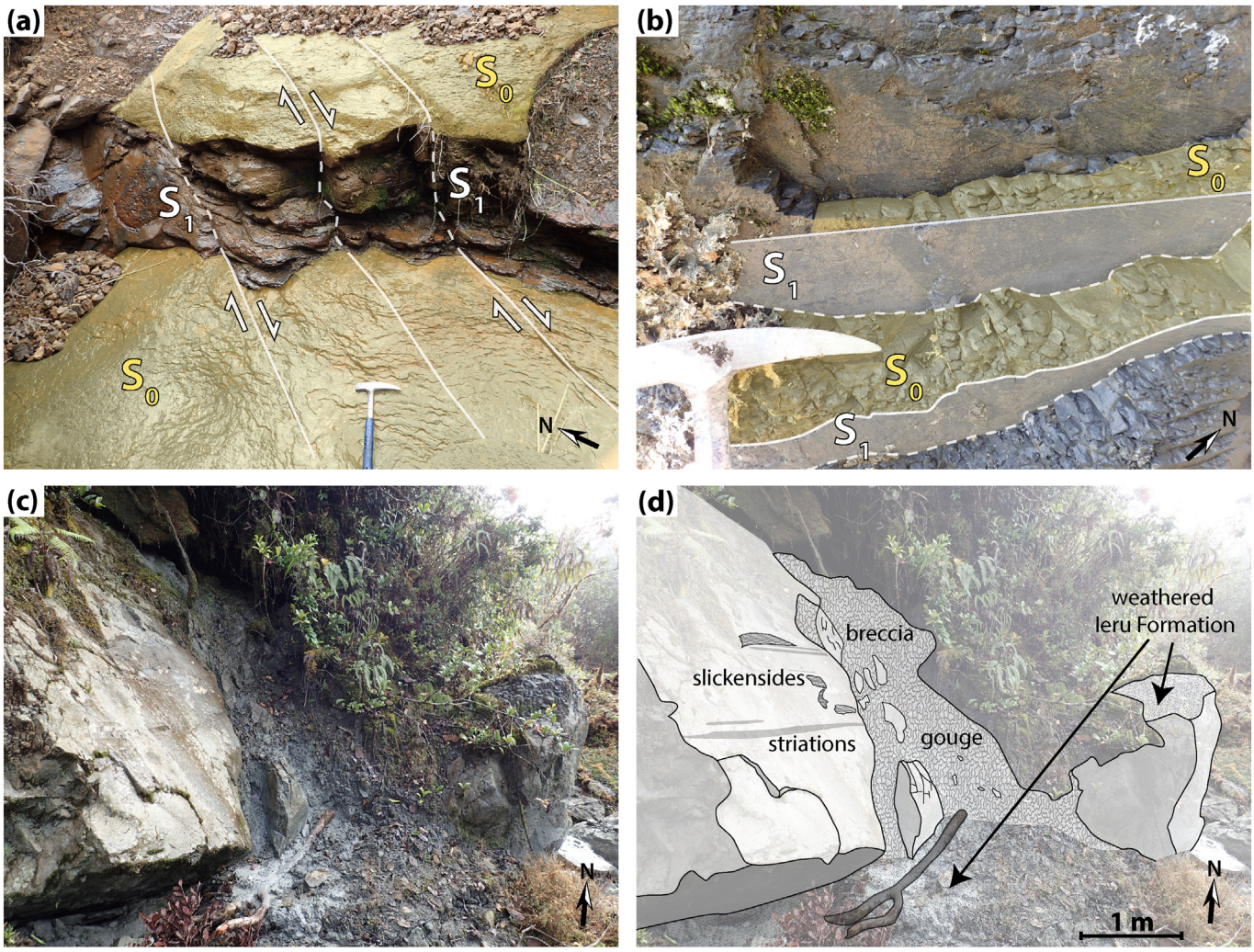

Fig. 9. Examples of outcrop scale arc-normal structures (S_1) in Lavani Valley including (a) northeast-southwest striking faults, predominantly associated with a component of dextral offset; (b) abundant northeast-southwest striking fractures across which offset is indeterminate or absent. Note the apparent change from wavy, semi-ductile, bedding parallel deformation (S_0) to the much more sharply defined brittle deformation (S_1). (c & d) a fault scarp within fast weathering Ieru Formation suggesting very recent to active strike-slip faulting (see Fig. 6a for location).

Forty kilometres along strike to the northwest, basement crops out at ~500 m AMSL in the Strickland Gorge yet it was not encountered in the Lavani 1 well that extends ~200 m below mean sea level, implying basement deepens towards the southeast. This is consistent with eastward decreasing Bouguer gravity and a large down-to-the-east basement fault recognised in seismic data within Lavani Valley (Bidstone et al., 1974).

Together these observations clearly show that areas with the deepest basement and thickest syn-rift sediments have undergone the most significant uplift during basin inversion. Thus, pre-compression margin architecture was complex and appears to have had a significant influence on evolution. Moreover, arc-normal structures appear to be closely associated with lateral changes in geology along the Lavani Valley and therefore may represent zones of tear faulting - some of which remain active.

4.7. Shortening analysis

Shortening calculations are a powerful method of quantitatively assessing lateral geological variation and can thus assist in identifying accommodating structures such as tear faults. Here, a line length balancing (LLB) technique was used to estimate shortening of the well-constrained Darai Limestone horizon in each of the cross-sections.

Minimum estimates for Darai Limestone shortening across the entire Greater Juha area vary from 12.6 to 21.4% (Fig. 4c), with the greatest shortening correlating with increased structural complexity along cross-section A-A' (Fig. 4a and b). Here, shortening analyses are broken down into subareas (Fig. 4c) to investigate potential relationships between lateral shortening variations and arc-normal structures observed across the Greater Juha area (e.g., Section 4.6.4). It is important to note that the complexity of the Darai Limestone in the Lavani Anticline in cross-section A-A′ highlights the potential for complex structure within the hinge of the Lavani Anticline where the Darai Limestone has been eroded in Lavani Valley. Here, we present the simplest structural interpretation for eroded portions of the crest of the Lavani Anticline (e.g., Fig. 4b, C-C′ to E-E') so that shortening estimates are likely to be minima.

Along the EMR (excluding cross-section A-A′), minimum shortening of the Darai Limestone from the Karius Thrust to the backlimb of the Lavani Anticline varies from 7.6 to 11.8% (Fig. 4c). Cross-section E-E′ was associated with the greatest shortening (11.8%), with shortening generally decreasing in sections to both

the northwest and southeast. Cross-section A-A' has anomalously high shortening (15.7%) but with additional surface geological constraints meaning that this represents a maximum rather than minimum shortening estimate. However, comparably high shortening may at least partially be attributed to an interpreted increase in structural complexity (Fig. 4a and b).

Shortening estimates from the Emama Fault to the backlimb of the Lavani Anticline show a similar trend to the Greater Juha area and EMR shortening estimates (Fig. 4c). Importantly, cross-section E-E′ has minimum shortening Darai Limestone interpreted above the eroded Lavani Anticline, yet has still undergone at least 700 m more shortening than cross-section F-F′, which has an almost complete Darai limestone section. Furthermore, E-E′ has ~450 m more shortening than cross-section C-C'. We suggest that lateral shortening variations of this magnitude may be at least partially accommodated along the SE Lavani Tear Fault and Emama Tear Faults respectively (Figs. 4b and 6b). Shortening variation is much less significant between cross-sections C-C′ and B-B' (<100 m) and thus does not offer convincing support for the presence of the NW Lavani Tear Faults, interpreted based on field observations and geological constraints (Fig. 4a).

Shortening of the Darai Limestone from the Karius Thrust to the Emama Fault appears much lower, varying from 1.8 to 4.9%. With the exception of cross-section A-A′, there is a general increased shortening trend from northwest to southeast, consistent with increased tightening of the Karius Syncline (Fig. 4a and b). Interestingly, the presence of the Centre Pass Tear Fault is supported by a difference in shortening between cross-sections C-C' (1.8%) and E-E' (3.9%) that equates to at least 300 m of lateral shortening variation accommodated along this structure.

5. Structural evolution of the Greater Juha area

There is significant evidence for extension and rifting along the New Guinea margin in the early-Mesozoic, including in the foreland directly adjacent to the Greater Juha area. Observations outlined here suggest this variable pre-existing rift architecture almost certainly underlies the Greater Juha area and has had significant influence on the evolution of structural styles during Cenozoic compression of the New Guinea margin.

There is substantial geological and geophysical evidence suggesting that the Juha and Lavani anticlines formed above partially inverted grabens. Firstly, these structures can be linked through substantial similarities in orientation and morphology (Fig. 1c), with their large wavelengths, asymmetric limbs and lobate morphologies characteristic of inversion structures (e.g., McClay, 1995; Bonini et al., 2012). Geophysical data across the Lavani Valley (Bidstone et al., 1974) and the thick Triassic synrift sequence intersected at ~1.9 km AMSL in the Lavani 1 well (>7 km above its foreland regional) presents a strong argument for the partial inversion of a graben beneath Lavani Valley. In fact, in order to sufficiently uplift the Lavani Anticline while still honouring geophysical observations of only partial inversion (i.e. basement hanging wall remains lower than basement footwall), the Lavani half-graben is likely originally to have been very deep, containing more than 7 km of syn-rift sediments (e.g., c.f. Fig. 10a and e).

Evidence from the Juha Anticline is less convincing but limited seismic and gravity data suggest it is also underlain by a deep graben (e.g., Hanani et al., 2016). Therefore the pre-compression architecture of the Greater Juha area may have included a set of listric northeast-dipping basement extensional faults and rotated basement hanging wall blocks responsible for the formation of the Juha and Lavani half-grabens (Fig. 10a).

Compression associated with continental collision along the New Guinea margin was originally accommodated within the Greater Juha area by the inversion of the normal-fault bounding the Lavani half-graben. The resulting steep Lavani inversion fault intersected the surface as the Emama Fault and the less significant Emama Backthrust, uplifting the Lavani Anticline (Fig. 10b). This occurred out-of-sequence early in the evolution of the NWFTB, as indicated by the relatively undeformed backlimb of the Lavani Anticline (Figs. 1 and 4a and b).

We suggest that during the evolution of the Lavani Anticline, the Lavani inversion fault shallowed into the incompetent Mesozoic sedimentary sequence beneath Lavani Ridge and, to a lesser extent, Karius Plateau. A single triangle zone—or more plausibly multiple triangle zones—formed within the Mesozoic sequence over this time, connected to a passive roof thrust, the Lavani Backthrust, within the Ieru Formation (Fig. 10c). This style of deformation relates to competence variations within the stratigraphic column, with the competent Darai Limestone much more resistant to shortening than the less competent underlying Mesozoic sequence. The forelandward propagating triangle zone(s) uplifted the Lavani Ridge, at least temporarily forming a frontal monocline (Fig. 10c) – a common characteristic of triangle zone-related deformation (e.g., Cooper, 1996 and examples within).

The Karius Thrust and associated Karius Anticline are here attributed to the most recent pulse of movement along the Lavani inversion fault (Fig. 10d). The now dry Centre Pass valley (see Section 4.5) provides considerable insight into the relative temporal evolution of this area of the EMR, with incision of the valley into the Lavani Ridge pre-dating uplift along Karius Ridge. Note the similarities between the structure of the Lavani Anticline in Fig. 10d compared to the present structure of the Juha Anticline on Fig. 10e (Hanani et al., 2016). This is consistent with the southwest propagation of the same structural style.

Despite their morphological similarities, the Juha Anticline has experienced significantly less uplift than the Lavani Anticline (Fig. 10e). One obvious difference between the two structures is the absence of an emergent frontal fault on the Juha Anticline (Fig. 4a and b). This characteristic suggests the Juha inversion fault shallows into the Mesozoic sedimentary sequence before connecting with forelandward structures (Fig. 10e), as suggested by Hanani et al. (2016). Important implications of this relationship are that displacement along the Juha inversion fault is restricted by the limited amount of displacement observed along structures towards the foreland (Fig. 4b).

5.1. 3D structural evolution of the eastern Muller Ranges

Observations from geological and geophysical data across Mt Aya in the Lavani Valley form a crucial foundation for our understanding of the 3D structural evolution of the EMR. In particular, the intersection of thick syn-rift sediments in the Lavani 1 well suggests the area was a regionally significant depocentre during Early Mesozoic rifting. But at the same time these sediments have been uplifted such that Jurassic strata crop out at the crest of Mt Aya indicating it has experienced the greatest uplift in the EMR and possibly in the entire PFB. Thus, there is a strong correlation between the magnitude of extension along the half-graben bounding Lavani normal fault and subsequent inversion along the Lavani inversion fault, a relationship also recently recognised within the Taranaki Basin in New Zealand (Reilly et al., 2016). The following model for the evolution of the EMR fits well with this type of inversion fault behaviour.

5.1.1. Early Mesozoic extension

Northeast-southwest to NNE-SSW extension of the Papua New Guinea margin in the Early Mesozoic (e.g., Home et al., 1990) was associated with the formation of the regionally extensive

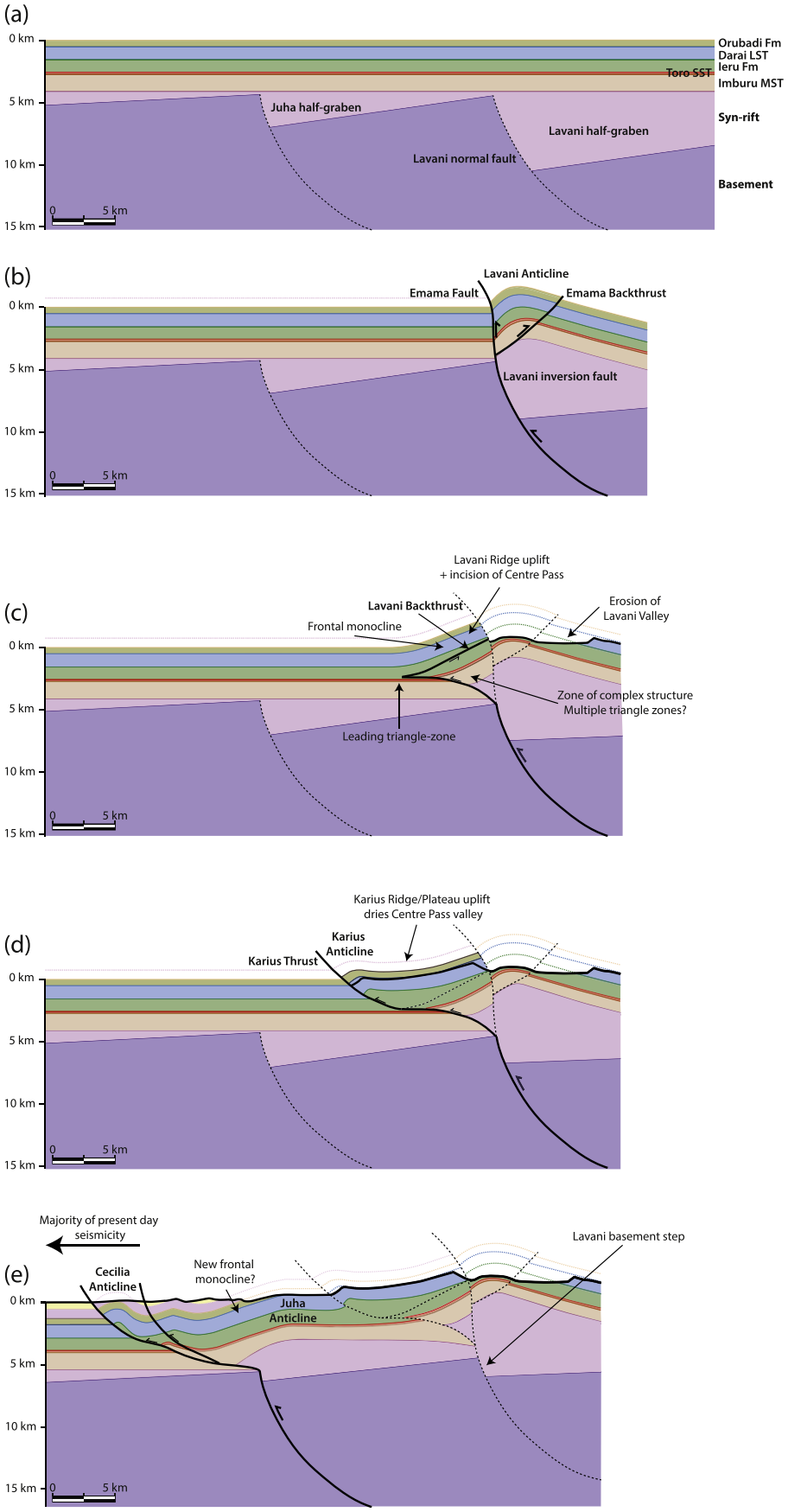

Fig. 10. Proposed schematic structural evolution of the Greater Juha area: (a) prior to compression; (b) during initial inversion and reverse displacement along the Lavani inversion fault, Emama Fault and Emama Backthrust; (c) during displacement along the Lavani Backthrust; (d) during displacement along the Karius Thrust and (e) during displacement along the Juha inversion.

northwest-southeast striking Lavani normal fault beneath the present day EMR (Fig. 11a). Over the course of the extensional evolution, a regional-scale, southeast-dipping relay ramp formed from at least as far northeast as the Muller 1 well (Fig. 1b) to the southeast-end of the present day Lavani Valley. This ramp may have formed to transfer extension between the Lavani normal fault beneath the EMR and another major basin-bounding normal fault to the north which continues into the WMR or Om Metamorphics (Figs. 1b and 11a). Syn-rift sediments accumulated on this regional relay ramp during its evolution, leading to thicker sediments towards the base of the ramp around the present day Lavani Valley.

Displacement along the Lavani normal fault was greatest towards its centre beneath the present day Lavani Valley, and decreased towards the southeast and northeast ends, thus approximating a commonly observed normal fault displacement-distance relationship (e.g., Muraoka and Kamata, 1983; Peacock and Sanderson, 1991; Gupta and Scholz, 2000; Frankowicz and McClay, 2010), but with an apparent level of asymmetry resulting from displacement decreasing more abruptly towards the southeast than the northwest (Fig. 11b). Here, this asymmetry is interpreted to have been accommodated along a number of cross-cutting, oblique-slip normal faults that breached the footwall block including the southeast-dipping relay ramp (Fig. 11b). Alternatively, the development of secondary oblique to cross-cutting structures could plausibly relate to an evolving extension direction on the New Guinea margin, in a style analogous to the nearby Bonaparte Basin in North West Australia (Frankowicz and McClay, 2010). A smaller relay ramp may have also formed at the southeast end of the present day Lavani Valley, but if so, was abruptly breached to accommodate a more rapid transition to higher displacement along the Lavani normal fault to the northwest (Fig. 11a and b). This scenario would have left a transfer fault that during subsequent extension may have connected the Lavani normal fault to another normal fault towards the east (Fig. 11a).

Relay ramps form as a means of transferring extension between overlapping normal faults and breaching is common (e.g., Hus et al., 2005; Fossen and Rotevatn, 2016). The example presented here differs in that multiple normal faults cross-cut the southeast-dipping relay ramp, representing a distributed zone of breaching rather than a single breach (Fig. 11a and b). Outcrop-scale evidence from better constrained extensional systems suggest that breached ramps are commonly complex, often involving multiple cross-cutting faults (Soliva and Benedicto, 2004). Pre-existing weaknesses are a likely influence on the evolution of multiple cross-cutting faults, as observed in Canyonlands National Park, Utah, where cross-cutting normal faults have formed along relay ramp-intersecting joint sets (Trudgill and Cartwright, 1994; Fossen and Rotevatn, 2016).

5.1.2. Cenozoic compression

Northeast-southwest compression associated with the formation of the PFB reached the Muller Ranges around the Late Miocene (Hill and Gleadow, 1989). The regional extent and large displacement of the Lavani normal fault made it particularly preconditioned for subsequent inversion (as per Eisenstadt and Withjack, 1995; Kelly et al., 1999; Panien et al., 2005; Reilly et al., 2016). However, despite significant inversion and hangingwall uplift along the Lavani inversion fault, it remains lower than the footwall beneath Lavani Ridge and Karius Plateau in the present day (Figs. 10e and 11d) (e.g., Bidstone et al., 1974).

Reverse displacement along the Lavani inversion fault was heterogeneously distributed with a strong correlation with its original extensional displacement (c.f. Fig. 11b and d). Similar to the rifting phase, inversion-related displacement differences were accommodated along the length of the relay ramp by inversion of oblique-slip cross-structures that subsequently dispersed into the sedimentary sequence forming the distributed regions of tear faulting observed in Lavani Valley (Fig. 11d). These zones are therefore characterised by the opposite movement sense to the original extension-related basement cross-structures (c.f. Fig. 11b and c). The greatest reverse displacement along the Lavani inversion fault and associated Emama Fault occurred around Mt Aya, where the sedimentary sequence was uplifted more than 7 km above regional. The great depth of basement beneath Mt Aya prior to compression (Fig. 11a and b) was crucially important in allowing such significant uplift without an associated present-day gravity high.

During the evolution of the EMR, the Lavani inversion fault shallowed to form triangle-zones beneath Lavani Ridge and Karius Plateau, with shortening of the Mesozoic sedimentary sequence accommodated along the Lavani Backthrust (Figs. 10c and 11d). Continued heterogeneous displacement along the Lavani inversion fault was then transferred to the surface largely along the Lavani Backthrust, causing increased northeast-directed thrusting of the Lavani Ridge into the southeast-end of Lavani Valley, driving sinistral offset at the Centre Pass Tear Fault (Fig. 11d). This model for the evolution of Centre Pass also accounts for opposing movement senses observed along the seemingly continuous Emama Tear Faults and Centre Pass Tear Fault; that is, each formed from a consistent shortening regime, but relate to structures with opposing vergence. During the final stages in the evolution of the EMR, the Karius Thrust uplifted Karius Ridge creating the Karius Anticline and Karius Syncline across Karius Plateau (Figs. 10d and 11d).

6. Discussion

6.1. Controls on structural style

The well-constrained Darai Limestone shows very low shortening of 12.6–21.4% across the Greater Juha area (see Section 4.7), which is unusual given the high magnitude of uplift across the EMR. In comparison, the much less elevated KFTB (Fig. 1b) is characterised by > 40% shortening (Hill, 1991). Triangle zone-related deformation is often invoked to explain large, internally complex mountain front structures characterised by only minor near-surface shortening (e.g., Suppe, 1980; Jones, 1996) and this model is consistent with structures observed within the leading-edge of the PFB including (from southeast to northwest) the Puri Anticline (Medd, 1996), Cecilia Anticline (Hanani et al., 2016) and P'nyang Anticline (Eisenberg, 1996). In the elevated EMR, the regionally-prominent Lavani Backthrust provides a mechanism to transfer shortening within the incompetent Early Mesozoic sequence through the competent Darai Limestone. Through time, as the Lavani Anticline was initially uplifted and eroded to form the Lavani Valley, this discontinuity within the Darai Limestone provided an easy pathway for shortening to reach the surface without having to be accommodated within thick competent Darai Limestone towards the foreland. Geological and geomorphic evidence suggests that the significance of the Lavani Backthrust decreases towards the northwest of the EMR, limiting the amount of shortening it can accommodate. In this area there is a recognisable change in structural style including increased structural complexity, more distributed and greater overall shortening within the Darai Limestone (e.g., cross-section, A-A′) meaning there are more structures likely to account for uplift of the EMR.

We suggest the inversion of pre-existing rift architecture is the primary influence on the evolution of the Greater Juha area. A number of prominent detachment-levels have been recognised within the Mesozoic sedimentary sequence in the KFTB (e.g., Hill

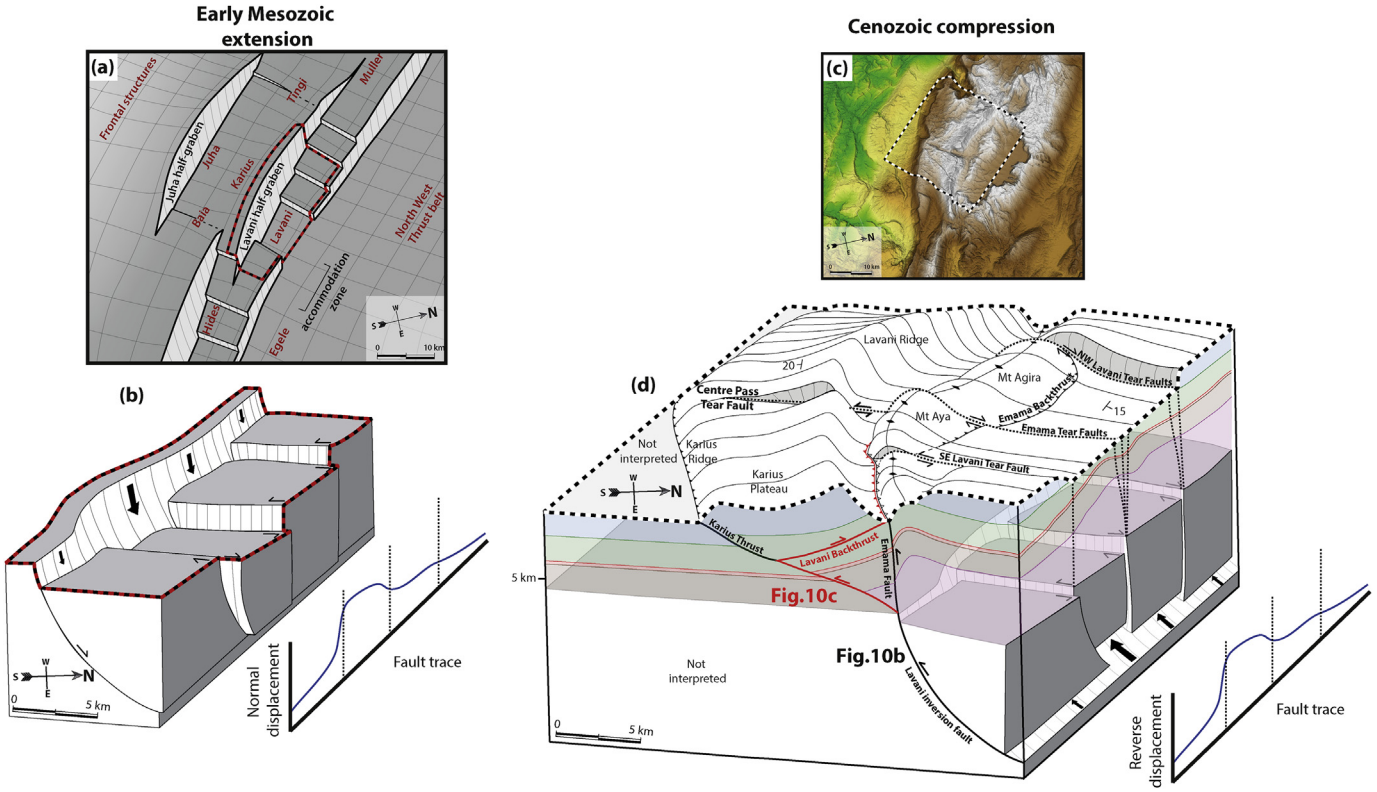

Fig. 11. Model of the 3D evolution of the Eastern Muller Ranges, (a) Schematic Early Mesozoic rift architecture beneath the Greater Juha area with red labels marking the location of present day structural features; (b) Schematic Early Mesozoic rift architecture beneath the Lavani Valley showing the Lavani normal fault, southeast-dipping relay ramp and cross-cutting normal structures. Location marked by dashed red box in (a); (c) SRTM DEM across the Eastern Muller Ranges (USGS, 2015); (d) Cenozoic inversion to form the eastern Muller Ranges, including basement-connected tear faults with opposing movement sense to original cross-cutting normal structures. Note: Mt Aya is simplified by showing its pre-erosion geometry – i.e. shown prior to the erosion of the forelimb of the Lavani Anticline and associated surface exposure of Toro Sandstone and Imburu Mudstone. Location marked by dashed box in (c). (For interpretation of the references to colour in this figure legend, the reader is referred to the web version of this article.)

et al., 2008, 2010), but their relationship with basement-inversion structures has often been unclear. In the Greater Juha area, thrust structures detach from similar horizons (e.g., Cecilia Anticline, Karius Thrust, both detached in the Ieru Formation) but with better-constrained connections to nearby inversion structures. For instance, the extensive and relatively undeformed backlimb of the Lavani Anticline suggests that thrust structures (including triangle zones) across the EMR (e.g., Karius Thrust, Lavani Backthrust) are proximally linked to the steep Lavani inversion fault, rather than distally to structures within the neighbouring North West Thrust Belt (Fig. 1c). Basement-connected triangle zones have been identified in other fold and thrust belts (e.g., Zapata and Allmendinger, 1996; Sterne, 2006), but in general appear less abundant than triangle zones with prominent sedimentary detachments (e.g., floor thrusts). The evolution of triangle zones within the Greater Juha area is likely to be controlled by competence contrasts within the stratigraphic column, in particular between: (1) competent crystalline basement, (2) largely incompetent Early Mesozoic sediments and (3) competent Darai Limestone. Perhaps the best documented analogue for this structure style is the Ellesmerian mountain front in North Greenland. There, balanced cross-sections reveal steeply-dipping, basement-connected inversion structures that connect to a major roof backthrust at the base of a thick carbonate shelf sequence, thus similarly forming triangle zones within the enclosed incompetent basinal sediments, and an elevated mountain front monocline (Soper and Higgins, 1990). Given access and logistical challenges in the PFB, identifying analogues from better understood fold and thrust belts worldwide is likely to be crucial to improve our understanding of sub-surface structure.

Also, robust geochronological data are required to constrain the temporal evolution of the Greater Juha area and to help develop kinematic and mechanical structural models. Furthermore, additional modelling is required to understand: (1) why the generally similar Lavani and Juha anticlines differ in having an emergent frontal fault (Emama Fault) and blind frontal fault (Juha inversion fault), respectively, and; (2) the geometric evolution of the Lavani inversion fault from the steep-dipping Emama Fault to shallowly-dipping detachments and thrust structures within the sedimentary sequence.

6.2. Arc-normal lineaments and structures

Arc-normal oriented structures are pervasive across a range of scales within the Greater Juha area of the PFB. We suggest this observed trend relates directly to zones of tear faulting that connect at depth to weakened pre-existing basement cross-structures that have inverted during compression to accommodate lateral displacement variations (Fig. 11d). The dominant movement sense along arc-normal structures is oblique dextral, up-to-the-southeast, consistent with structures also observed within the KFTB (Hill et al., 2008, 2010), the Hides Anticline (Johnstone and Emmett, 2000), between the Cecilia, Wai Asi and Strickland Anticlines (Craig and Warvakai, 2009), in the EMR (e.g., Legari Tear; Hornafius, 1993), WMR (Eisenberg, 1996) and in the WPFB (White et al., 2014). Regional-scale arc-normal lineaments are also commonly associated with dextral offset, including the Bosavi

Lineament (e.g., Osborne, 1990) and a lineament interpreted to run through the Strickland Gorge (Hill, 1989) (Fig. 1b).

Observations from geological data across the Greater Juha area highlight the secondary presence of arc-normal structures with oblique sinistral, up-to-the-northwest movement sense (e.g., Figs. 4a and 11d). We found no convincing evidence of regionally-continuous arc-normal lineaments intersecting the Greater Juha area regionally. This suggests that regional-scale lineaments observed across the PFB may consist of less continuous, smaller-scale arc-normal structures and thus may not necessarily relate to regional-scale rift architecture (i.e. transfer faults). For instance, arc-normal structures across Lavani Valley appear to be basement-connected, but discontinuous, as they do not appear to disturb the backlimb of the Lavani Anticline and Lavani Ridge. Even the apparently continuous Emama Tear Faults and Centre Pass Tear Fault appear to have differing movement senses (Fig. 6b). We suggest the Emama Tear Faults relate to foreland-vergent inversion along the underlying Lavani normal fault, while the Centre Pass Tear Fault relates to hinterland-vergent thrusting along the Lavani Backthrust, and thus the latter is not directly related to an underlying basement structure (Fig. 11d). This highlights the importance of understanding the relationship between arc-parallel structural style and arc-normal structures, something that is often overlooked during cross-section based studies.

The controls on, and relationships between, local-scale arc-normal structures and regional-scale arc-normal lineaments within the PFB are largely unclear, but are likely to be complex. Early Mesozoic rift architecture is clearly influencing lateral variations in structural style across the PFB (e.g., Hill, 1991; Hill et al., 2010) however arc-normal structures and lineaments that appear to accommodate this variation may ultimately relate to a complex basement fabric beneath the PFB with an overall northeast to southwest orientation (e.g., White et al., 2014).

The influence of basement fabrics on rift architecture (e.g., Smith and Mosley, 1993; Ring, 1994; Corti et al., 2007) and subsequent inversion (e.g., Piquer et al., 2016) is well-established elsewhere. Thus, it is plausible that Palaeozoic basement fabric controlled the structural framework of the Papuan Basin during rifting in the Early Mesozoic, forming regional-scale accommodation zones and related local-scale transfer structures that are now expressed as regional-scale arc-normal lineaments and local-scale arc-normal structures, respectively. Transfer structures, including complexly breached relay ramps, utilise northeast-southwest striking weaknesses associated with the basement fabric, as a mechanism for accommodating displacement along major northwest-southeast striking normal faults (e.g., Fig. 11a). These structures have subsequently been inverted to form arc-normal oriented zones of tear faulting that accommodate laterally variable displacement along inversion faults and connected thrust structures. Additional work should focus on developing a more robust understanding of the relationship between basement fabric, Early Mesozoic rift architecture and subsequent Cenozoic inversion, and the 3D spatio-temporal evolution of the PFB.

Acknowledgments

This work was funded by Papuan Oil Search Ltd and ExxonMobil through their PPL402 joint venture. Luke Mahoney acknowledges support of an Australian Postgraduate Award. Many thanks to Tony Allan and Tony Norman who were colleagues and mentors during the Greater Juha Geological Survey. Midland Valley Exploration kindly provided the Move software suite as a part of their Academic Software Initiative. We appreciate comments and suggestions from Hugh Davies and Mark Cooper.

Appendix A. Supplementary data

Supplementary data related to this article can be found at http://dx.doi.org/10.1016/j.jsg.2017.05.010.

References

Abers, G., McCaffrey, R., 1988. Active deformation in the New Guinea fold-and-thrust belt: seismological evidence for strike-slip faulting and basement-involved thrusting. J. Geophys. Res. Solid Earth 93, 13332–13354.
Allan, T.L., Trotter, J.A., Whitford, D.J., Korsch, M.J., 2000. Strontium isotope stratigraphy and the oligocene-miocene T-letter "stages" in Papua New Guinea. In: Buchanan, P., Grainge, A., Thornton, R. (Eds.), Petroleum Exploration, Development, and Production in Papua New Guinea: Proceedings of the Fourth PNG Petroleum Convention. Papua New Guinea Chamber of Mines and Petroleum, Port Moresby, pp. 155–168.
Amoco PNG Exploration Company, 1982. Lavani 1 Well Completion Report, p. 137.
Baldwin, S., Fitzgerald, P., Webb, L., 2012. Tectonics of the new Guinea region. Annu. Rev. Earth Planet. Sci. 40, 495–520.
Bennett, D.J., Brand, R.P., Mills, C.R., Morris, B.D., 2000. Exploration potential of the West Bosavi area, Papuan foreland basin, Papua New Guinea. In: Buchanan, P., Grainge, A., Thornton, R. (Eds.), Petroleum Exploration, Development, and Production in Papua New Guinea: Proceedings of the Fourth PNG Petroleum Convention. Papua New Guinea Chamber of Mines and Petroleum, Port Moresby, pp. 139–154.
Bidstone, B.J., St. John, V.P., Thomas, E.G., 1974. Report on the Lavani Valley Seismic and Gravity Survey, Geological Survey of Papua New Guinea Archive File F1/S/74–21 (unpubl.).
Bonini, Marco, Sani, Federico, Antonielli, Benedetta, 2012. Basin inversion and contractional reactivation of inherited normal faults: a review based on previous and new experimental models. Tectonophysics 522–523, 55–88.
Bradley, G., 2014. Western Papuan Basin to Western Aure: Generalised Cenozoic - Jurassic Chronostratigraphy (unpubl.), p. 1.
Buchanan, J.G., Buchanan, P.G. (Eds.), 1995. Basin inversion. Geological Society, London, Special Publications 88.
Buchanan, P., Warburton, J., 1996. The influence of pre-existing basin architecture in the development of the Papuan fold and thrust belt: implications for petroleum prospectivity. In: Buchanan, P. (Ed.), Petroleum Exploration, Development, and Production in Papua New Guinea: Proceedings of the Third PNG Petroleum Convention. Papua New Guinea Chamber of Mines and Petroleum, Port Moresby, pp. 89–109.
Chorowicz, Jean, 2005. The East African rift system. J. Afr. Earth Sci. 43 (1–3), 379–410.
Cooper, M., 1996. Passive-roof duplexes and pseudo-passive-roof duplexes at mountain fronts: a review. Bull. Can. Petrol. Geol. 44, 410–421.
Corbett, G., 1994. Regional structural control of selected Cu/Au occurrences in Papua New Guinea. In: Rogerson, R. (Ed.), Proceedings of the PNG Geology, Exploration and Mining Conference 1994. Australasian Institute of Mining and Metallurgy, pp. 57–70.
Corti, Giacomo, van Wijk, Jolante, Cloetingh, Sierd, Morley, Chris K., 2007. Tectonic inheritance and continental rift architecture: numerical and analogue models of the East African Rift system. Tectonics 26 (6), n/a-n/a.
Craig, M.S., Warvakai, K., 2009. Structure of an active foreland fold and thrust belt, Papua New Guinea. Aust. J. Earth Sci. 56 (5), 719–738.
Crowhurst, P., Hill, K., Foster, D., 1997. The structural and tectonic development of the Frieda River Mineral district, NW Papua New Guinea. In: Hancock, G. (Ed.), Proceedings of the PNG Geology, Exploration and Mining Conference 1997. Australasian Institute of Mining and Metallurgy, pp. 51–60.
Davies, H., 1983. Wabag 1:250 000 Geological Series Explanatory Notes Sheet SB/54-8. Geological Survey of Papua New Guinea, PNG Department of Minerals and Energy, Port Moresby.
Davies, H., 1991. Regional geologic setting of some mineral deposits of the New Guinea region. In: Rogerson, R. (Ed.), Proceedings of the Papua New Guinea Geology, Exploration and Mining Conference 1991. Australasian Institute of Mining and Metallurgy, pp. 49–57.
Davies, H., Norvick, M., 1974. Blucher Range 1:250 000 Geological Series Explanatory Notes Sheet SB/54-07. Geological Survey of Papua New Guinea, PNG Department of Minerals and Energy, Port Moresby.
Denison, C.N., 1990. Palynostratigraphic Revision of Amoco Lavani-1 Well, Papua New Guinea (unpubl.), p. 6.
Eisenberg, L.I., 1996. Strontium isotope analysis and structural interpretation of P'nyang Anticline, Papuan Fold belt, Western Highlands Province, Papua New Guinea. In: Buchanan, P. (Ed.), Petroleum Exploration, Development, and Production in Papua New Guinea: Proceedings of the Third PNG Petroleum Convention. Papua New Guinea Chamber of Mines and Petroleum, Port Moresby, pp. 231–244.
Eisenstadt, G., Withjack, M.O., 1995. Estimating Inversion: Results from Clay Models. Geological Society, London, Special Publications 88, pp. 119–136.
Ekström, G., Nettles, M., Dziewoński, A.M., 2012. The global CMT project 2004–2010: centroid-moment tensors for 13,017 earthquakes. Phys. Earth Planet. Inter. 200–201, 1–9.
Fossen, Haakon, Rotevatn, Atle, 2016. Fault linkage and relay structures in extensional settings—a review. Earth Sci. Rev. 154, 14–28.

Frankowicz, E., McClay, K.R., 2010. Extensional fault segmentation and linkages, Bonaparte Basin, outer North West Shelf, Australia. Bulletin 94 (7), 977–1010.
Gow, P.A., Upton, P., Zhao, C., Hill, K.C., 2002. Copper-gold mineralisation in New Guinea: numerical modelling of collision, fluid flow and intrusion-related hydrothermal systems. Aust. J. Earth Sci. 49 (4), 753–771.
Gupta, Anupma, Scholz, Christopher H., 2000. A model of normal fault interaction based on observations and theory. J. Struct. Geol. 22 (7), 865–879.
Hall, Robert, 1996. Reconstructing cenozoic SE Asia. Geol. Soc. Lond. Spec. Publ. 106 (1), 153–184.
Hall, R., 1997. Cainozoic tectonics of SE Asia and Australia. In: Howes, J., Noble, R. (Eds.), Proceedings of the International Conference on Petroleum Systems of SE Asia and Australia. Indonesian Petroleum Association, Jakarta, pp. 47–62.
Hall, Robert, 2002. Cenozoic geological and plate tectonic evolution of SE Asia and the SW Pacific: computer-based reconstructions, model and animations. J. Asian Earth Sci. 20 (4), 353–431.
Hall, Robert, 2012. Late Jurassic–cenozoic reconstructions of the Indonesian region and the Indian Ocean. Tectonophysics 570–571, 1–41.
Hanani, A., Lennox, P., Hill, K.C., 2016. The geology and structural style of the Juha gas field, Papua New Guinea. ASEG Ext. Abstr. 2016, 1–7.
Hill, Kevin C., 1989. The Muller anticline, Papua New Guinea; basement-cored, inverted extensional fault structures with opposite vergence. Tectonophysics 158 (1–4), 227–245.
Hill, K.C., 1991. Structure of the Papuan Fold belt, Papua New Guinea. Am. Assoc. Petrol. Geol. Bull. 75, 857–872.
Hill, K.C., Bradey, K., Iwanec, J., Wilson, N., Lucas, K., 2008. Structural exploration in the Papua New Guinea Fold Belt. In: Blevin, J.E., Bradshaw, B.E., Uruski, C. (Eds.), Eastern Australian Basins Symposium III, Petroleum Exploration Society of Australia, Special Publication 225238.
Hill, K.C., Gleadow, A.J.W., 1989. Uplift and thermal history of the Papuan Fold Belt, Papua New Guinea: apatite fission track analysis. Aust. J. Earth Sci. 36 (4), 515–539.
Hill, K.C., Hall, R., 2003. Mesozoic-Cenozoic evolution of Australia's New Guinea margin in a west Pacific context. Geol. Soc. Am. Special Pap. 372, 265–290.
Hill, K.C., Kendrick, R.D., Crowhurst, P.V., Gow, P.A., 2002. Copper-gold mineralisation in New Guinea: tectonics, lineaments, thermochronology and structure. Aust. J. Earth Sci. 49 (4), 737–752.
Hill, K.C., Lucas, K., Bradey, K., 2010. Structural styles in the Papuan Fold Belt, Papua New Guinea: constraints from analogue modelling. In: Goffey, G. (Ed.), Hydrocarbons in Contractional Belts. Geological Society, London, pp. 33–56. Special Publications 348.
Hill, K.C., Norvick, M., Keetley, J., Adams, A., 2000. Structural and stratigraphic shelf-edge hydrocarbon plays in the Papuan Fold Belt. In: Buchanan, P., Grainge, A., Thornton, R. (Eds.), Petroleum Exploration, Development, and Production in Papua New Guinea: Proceedings of the Fourth PNG Petroleum Convention. Papua New Guinea Chamber of Mines and Petroleum, Port Moresby, pp. 67–85.
Hill, G.S., Price, S.J., Foster, M.S., Stephenson, R.W., Ellis, D., Lyslo, J.A., 1996a. Seismic acquisition in the Papuan Fold belt – a new approach. In: Buchanan, P. (Ed.), Petroleum Exploration, Development, and Production in Papua New Guinea: Proceedings of the Third PNG Petroleum Convention. Papua New Guinea Chamber of Mines and Petroleum, Port Moresby, pp. 445–458.
Hill, Kevin C., Raza, Asaf, 1999. Arc-continent collision in Papua Guinea: constraints from fission track thermochronology. Tectonics 18 (6), 950–966.
Hill, K.C., Simpson, R., Kendrick, R., Crowhurst, P., O'Sullivan, P., Saefudin, I., 1996b. Hydrocarbons in New Guinea, controlled by basement fabric, Mesozoic extension and Tertiary Convergent margin tectonics. In: Buchanan, P. (Ed.), Petroleum Exploration, Development, and Production in Papua New Guinea: Proceedings of the Third PNG Petroleum Convention. Papua New Guinea Chamber of Mines and Petroleum, Port Moresby, pp. 63–76.
Hobson, D.M., 1986. A thin-skinned model for the Papuan thrust belt and some implications for hydrocarbon exploration. Aust. Petrol. Explor. Assoc. J. 26, 214–224.
Home, P., Dalton, D., Brannan, J., 1990. Geological evolution of the Western Papuan Basin. In: Carman, G., Carman, Z. (Eds.), Petroleum Exploration, Development, and Production in Papua New Guinea: Proceedings of the First PNG Petroleum Convention. Papua New Guinea Chamber of Mines and Petroleum, Port Moresby, pp. 107–118.
Hornafius, J.S., 1993. The 1990-1991 Muller Range Geological Survey – PPL 93. Mobil Exploration Niugini (unpubl.).
Hornafius, J.S., Denison, R.E., 1993. Structural interpretations based on strontium isotope dating of the Darai limestone, Papuan Fold belt, new Guinea. In: Carman, G., Carman, Z. (Eds.), Petroleum Exploration, Development, and Production in Papua New Guinea: Proceedings of the Second PNG Petroleum Convention. Papua New Guinea Chamber of Mines and Petroleum, Port Moresby, pp. 313–324.
Hus, R., Acocella, V., Funiciello, R., De Batist, M., 2005. Sandbox models of relay ramp structure and evolution. J. Struct. Geol. 27 (3), 459–473.
Jenkins, D., 1974. Detachment tectonics in western Papua New Guinea. Geol. Soc. Am. Bull. 85, 533–548.
Jenkins, D., White, M.F., 1970. Report on the Strickland River Survey, Permit 46, Papua New Guinea. BP Petroleum Development Australian Pty Ltd. Geological survey of Papua New Guinea archive file 4 BS (unpubl.).
Johnstone, D., Emmett, J., 2000. Petroleum geology of the Hides gas field, southern Highlands, Papua New Guinea. In: Buchanan, P., Grainge, A., Thornton, R. (Eds.), Petroleum Exploration, Development, and Production in Papua New Guinea: Proceedings of the Fourth PNG Petroleum Convention. Papua New Guinea Chamber of Mines and Petroleum, Port Moresby, pp. 319–335.
Jones, P.B., 1996. Triangle zone geometry, terminology and kinematics. Bull. Can. Petrol. Geol. 44, 139–152.
Kawagle, S.A., Meyers, J.B., 1996. Structural and sequence geometry of the Kiunga area, Papuan foreland basin, Papua New Guinea. In: Buchanan, P. (Ed.), Petroleum Exploration, Development, and Production in Papua New Guinea: Proceedings of the Third PNG Petroleum Convention. Papua New Guinea Chamber of Mines and Petroleum, Port Moresby, pp. 175–193.
Keenan, S.E., Hill, K.C., 2015. The Mananda Anticline, Papua New Guinea: a third oil discovery, appraisal programme and deep potential. In: AAPG/SEG International Conference and Exhibition 2015.
Kelly, P.G., Peacock, D.C.P., Sanderson, D.J., McGurk, A.C., 1999. Selective reverse-reactivation of normal faults, and deformation around reverse-reactivated faults in the Mesozoic of the Somerset coast. J. Struct. Geol. 21 (5), 493–509.
Koulali, A., Tregoning, P., McClusky, S., Stanaway, R., Wallace, L., Lister, G., 2015. New Insights into the present-day kinematics of the central and western Papua New Guinea from GPS. Geophys. J. Int. 202 (2), 993–1004.
Löffler, E., MacKenzie, D., Webb, A., 1979. Potassium-argon ages from some of the Papua New Guinea Highlands volcanoes, and their relevance to Pleistocene geomorphic history. J. Geol. Soc. Aust. 26, 387–397.
Longley, I.M., Buessenschuett, C., Clydsdale, L., Cubitt, C.J., Davis, R.C., Johnson, M.K., Marshall, N.M., Murray, A.P., Somerville, R., Spry, T.B., Thompson, N.B., 2002. The North West Shelf of Australia–a woodside perspective. Sediment. Basins West. Aust. 3, 27–88.
Lunt, P., Allan, T., 2004. Larger foraminifera in Indonesian biostratigraphy, calibrated to isotopic dating. In: GRDC Museum Workshop on Micropalaeontology. Bandung 1–109.
McClay, K.R., 1995. The geometries and kinematics of inverted fault systems: a review of analogue model studies. Geological Society, London, Special Publications 88, pp. 97–118.
McConachie, B., Lanzilli, E., Kendrick, D., Burge, C., 2000. Extensions of the Papuan Basin Foreland geology into Eastern Irian Jaya (West Papua) and the new Guinea Fold Belt in Papua New Guinea. In: Buchanan, P., Grainge, A., Thornton, R. (Eds.), Petroleum Exploration, Development, and Production in Papua New Guinea: Proceedings of the Fourth PNG Petroleum Convention. Papua New Guinea Chamber of Mines and Petroleum, Port Moresby, pp. 219–238.
Medd, D.M., 1996. Triangle zone deformation at the leading edge of the Papuan Fold Belt. In: Buchanan, P. (Ed.), Petroleum Exploration, Development, and Production in Papua New Guinea: Proceedings of the Third PNG Petroleum Convention. Papua New Guinea Chamber of Mines and Petroleum, Port Moresby, pp. 217–229.
Metcalfe, I., 2002. Permian tectonic framework and palaeogeography of SE Asia. J. Asian Earth Sci. 20 (6), 551–566.
Mobil Exploration Niugini, 1991. Muller 1X Well Completion Report, p. 58.
Morley, C.K., Nelson, R.A., Patton, T.L., Munn, S.G., 1990. Transfer zones in the East African rift system and their relevance to hydrocarbon exploration in rifts. Am. Assoc. Petrol. Geol. Bull. 74, 1234–1253.
Muraoka, Hirofumi, Kamata, Hiroki, 1983. Displacement distribution along minor fault traces. J. Struct. Geol. 5 (5), 483–495.
Niugini Gulf Oil Pty Ltd, 1983. Juha 1 Well Completion Report, p. 77.
Osborne, D.G., 1990. The hydrocarbon potential of the western Papuan Basin foreland—with reference to worldwide analogues. In: Carman, G., Carman, Z. (Eds.), Petroleum Exploration, Development, and Production in Papua New Guinea: Proceedings of the First PNG Petroleum Convention. Papua New Guinea Chamber of Mines and Petroleum, Port Moresby, pp. 197–213.
Page, R., 1976. Geochronology of igneous and metamorphic rocks in the New Guinea Highlands. Bureau Miner. Resour. Aust. Bull. 162, 117.
Panien, Marion, Schreurs, Guido, Pfiffner, Adrian, 2005. Sandbox experiments on basin inversion: testing the influence of basin orientation and basin fill. J. Struct. Geol. 27 (3), 433–445.
Peacock, D.C.P., Sanderson, D.J., 1991. Displacements, segment linkage and relay ramps in normal fault zones. J. Struct. Geol. 13 (6), 721–733.
Pigott, J.D., Trumbly, N.I., O'Neal, M.V., 1985. Northern New Guinea wrench fault system: a manifestation of Late Cenozoic interactions between Australian and Pacific plates. Tectonics 4, 613–620.
Pigram, C.J., Panggabean, H., 1984. Rifting of the northern margin of the Australian continent and the origin of some microcontinents in Eastern Indonesia. Tectonophysics 107 (3–4), 331–353.
Pigram, C.J., Symonds, P.A., 1991. A review of the timing of the major tectonic events in the New Guinea Orogen. J. Southeast Asian Earth Sci. 6 (3–4), 307–318.
Piquer, Jose, Berry, Ron F., Scott, Robert J., Cooke, David R., 2016. Arc-oblique fault systems: their role in the Cenozoic structural evolution and metallogenesis of the Andes of central Chile. J. Struct. Geol. 89, 101–117.
Reilly, C., Nicol, A., Walsh, J., 2016. Importance of Pre-existing Fault Size for the Evolution of an Inverted Fault System. Geological Society, London, Special Publications 439. SP439–2.
Ring, Uwe, 1994. The influence of preexisting structure on the evolution of the Cenozoic Malawi rift (East African rift system). Tectonics 13 (2), 313–326.
Saintot, Aline, Angelier, Jacques, 2002. Tectonic paleostress fields and structural evolution of the NW-Caucasus fold-and-thrust belt from Late Cretaceous to Quaternary. Tectonophysics 357 (1–4), 1–31.
Schofield, S., 2000. The Bosavi arch and the Komewu fault zone: their control on basin architecture and the prospectivity of the Papuan foreland. In: Buchanan, P., Grainge, A., Thornton, R. (Eds.), Petroleum Exploration,

Development, and Production in Papua New Guinea: Proceedings of the Fourth PNG Petroleum Convention. Papua New Guinea Chamber of Mines and Petroleum, Port Moresby, pp. 101–122.
Smith, R.I., 1990. Tertiary plate tectonic setting and evolution of Papua New Guinea. In: Carman, G., Carman, Z. (Eds.), Petroleum Exploration, Development, and Production in Papua New Guinea: Proceedings of the First PNG Petroleum Convention. Papua New Guinea Chamber of Mines and Petroleum, Port Moresby, pp. 229–244.
Smith, Martin, Mosley, Peter, 1993. Crustal heterogeneity and basement influence on the development of the Kenya Rift, East Africa. Tectonics 12 (2), 591–606.
Soliva, Roger, Benedicto, Antonio, 2004. A linkage criterion for segmented normal faults. J. Struct. Geol. 26 (12), 2251–2267.
Soper, N.J., Higgins, A.K., 1990. Models for the Ellesmerian mountain front in North Greenland: a basin margin inverted by basement uplift. J. Struct. Geol. 12 (1), 83–97.
Stanaway, R., Noonan, J., 2015. Geodetic measurement of deformation within the Papuan Fold and thrust belt. In: American Association of Petroleum Geologists International Conference and Exhibition, 13th-16th September 2015, Melbourne, Australia.
Sterne, E.J.N., 2006. Stacked,"evolved" triangle zones along the southeastern flank of the Colorado Front Range. Mt. Geol. 43, 65–92.
Storti, F., McClay, K., 1995. Influence of syntectonic sedimentation on thrust wedges in analogue models. Geology 23, 999–1002.
Suppe, J., 1980. Imbricated structure of western foothills belt, southcentral Taiwan. Petrol. Geol. Taiwan 17, 1–16.
Texaco Overseas Petroleum Company, 1971. Cecilia 1 Well Completion Report, p. 130.
Thornton, R., Emmett, J., Laslo, J., Gottschalk, R., 1996. Integrated structural and stratigraphic analysis in PPL 175, Papuan Fold belt, Papua New Guinea. In: Buchanan, P. (Ed.), Petroleum Exploration, Development, and Production in Papua New Guinea: Proceedings of the Third PNG Petroleum Convention. Papua New Guinea Chamber of Mines and Petroleum, Port Moresby, pp. 195–215.
Trudgill, B., Cartwright, J., 1994. Relay-ramp forms and normal-fault linkages, Canyonlands National Park, Utah. Geol. Soc. Am. Bull. 106, 1143–1157.
USGS, 2015. Shuttle Radar Topography Mission, 1-arc Second, Global Land Cover Facility, University of Maryland, College Park, Maryland. Accessed through USGS EarthExplorer.
Wallace, Laura M., Stevens, Colleen, Silver, Eli, McCaffrey, Rob, Loratung, Wesley, Hasiata, Suvenia, Stanaway, Richard, Curley, Robert, Rosa, Robert, Taugaloidi, Jones, 2004. GPS and seismological constraints on active tectonics and arc-continent collision in Papua New Guinea: implications for mechanics of microplate rotations in a plate boundary zone. J. Geophys. Res. 109 (B5).
Webb, A., 1973. Geochronology Report on Samples Submitted by BMR West Sepik Party. Australian Mineral Development Laboratories Report AN3049/73 (unpubl.).
White, M.F., Marfleet, M.J., 1973. Laigap Geological Survey, Permit 46, Papua New Guinea. BP Petroleum Development Australian Pty Ltd. Geological survey of Papua New Guinea archive file 13 BL (unpubl.).
White, L.T., Morse, M.P., Lister, G.S., 2014. Lithospheric-scale structures in New Guinea and their control on the location of gold and copper deposits. Solid Earth 5 (1), 163–179.
Zahirovic, S., Seton, M., Müller, R.D., 2014. The cretaceous and cenozoic tectonic evolution of southeast Asia. Solid Earth 5 (1), 227–273.
Zahirovic, S., Matthews, K.J., Flament, N., Müller, R.D., Hill, K.C., Seton, M., Gurnis, M., forthcoming, 2016. Tectonic evolution and deep mantle structure of eastern Tethyan domain since the latest Jurassic. Earth Sci. Rev. 162, 293–337.
Zapata, T.R., Allmendinger, R.W., 1996. Thrust-front zone of the Precordillera, Argentina: a thick-skinned triangle zone. Am. Assoc. Petrol. Geol. Bull. 80, 359–381.

Tectonophysics 752 (2019) 81–112

Contents lists available at ScienceDirect

Tectonophysics

journal homepage: www.elsevier.com/locate/tecto

Late Cretaceous to Oligocene burial and collision in western Papua New Guinea: Indications from low-temperature thermochronology and thermal modelling

Luke Mahoney[a,b,*], Sandra McLaren[a], Kevin Hill[a], Barry Kohn[a], Kerry Gallagher[c], Martin Norvick[a]

[a] School of Earth Sciences, University of Melbourne, Melbourne, Australia
[b] Papuan Oil Search Limited, Sydney, Australia
[c] Géosciences Rennes, Université de Rennes, Rennes, France

ARTICLE INFO

Keywords:
Papua New Guinea
Papuan Basin
Fold and Thrust Belt
Thermochronology
Tectonics
SE Asia

ABSTRACT

Recent field and analytical work have considerably improved our understanding of the structure of the Muller Range along the frontal trend of the Papuan Fold and Thrust Belt (PFTB) in western Papua New Guinea (PNG). However numerous questions remain unresolved concerning the geological evolution of the region. In particular, the Late Cretaceous to Oligocene history of the region is largely unknown due to the absence of a continuous stratigraphic record. Here, we use both new and existing low-temperature thermochronology data to investigate the geological history of the Muller Range. Thermal history models based on these data suggest two major Cenozoic cooling episodes. The youngest, and best constrained, is clearly recorded in the stratigraphic record and relates to Neogene collision at the northern margin of the Australian continent. An older episode of comparable or greater magnitude occurred in the Eocene to Oligocene and may relate to the removal of 1500–3000 m of Late Cretaceous to Eocene section across the Muller Range prior to the widespread deposition of the shelfal Darai Limestone. We suggest that extension along major faults beneath the Muller Range accommodated sedimentation from the Late Cretaceous to the Eocene, consistent with long-lived extensional structures observed in neighbouring regions. In contrast to the Muller Range area, an almost continuous Late Cretaceous to Eocene stratigraphic sequence is preserved in the hinterland < 50 km to the northeast. The selective removal of this sequence across the Muller Range suggests it was uplifted in the Eocene to Oligocene, possibly in part facilitated by the inversion of extensional faults in the Muller Range area. We suggest that this inversion was related to the Eocene to Oligocene collision of the expansive Sepik Terrane to the northwest of the PNG margin. The new data and interpretations presented here have significant implications for the evolution of the PFTB and for tectonic reconstructions of PNG.

1. Introduction

Tectonic reconstruction techniques have advanced significantly during the past decade to incorporate global kinematic and geodynamic controls, often validated using detailed seismic tomography (e.g. Zahirovic et al., 2014, 2016). This provides an excellent plate-scale framework for Papua New Guinea (PNG; Fig. 1), but investigating the detailed tectonic history remains particularly challenging due to complex Cenozoic tectonism, a lack of preserved oceanic crust and a general paucity of data from the isolated and inhospitable highlands.

The Papuan Basin, located on the leading edge of the northern Australian continental margin, has been subject to complex Cenozoic tectonism responsible for the formation of the Papuan Fold and Thrust Belt (PFTB). Current understanding of the geological history of the Papuan Basin is based on the Mesozoic to recent stratigraphic record, which chronicles early Mesozoic rifting, protracted passive-margin development and subsequent Cenozoic orogenesis (e.g. Home et al., 1990). A long standing question for the Papuan Basin is the origin of a prominent, regional Late Cretaceous to Oligocene unconformity that extends across most of the southern Papuan Basin (e.g. Jenkins, 1974; Brown et al., 1980; Home et al., 1990). Reconstructing what occurred on the margin over this time is vital for improving our understanding of the geological history and economic potential of the Papuan Basin.

Surrounding regions, such as the complexly deformed Mobile Belt to the north and Coral Sea to the southeast (Fig. 1a), offer some insight into the context of the southern Papuan Basin during the key period

* Corresponding author at: School of Earth Sciences, University of Melbourne, Melbourne, Australia.
E-mail address: luke.mahoney@oilsearch.com (L. Mahoney).

https://doi.org/10.1016/j.tecto.2018.12.017
Received 1 July 2018; Received in revised form 5 December 2018; Accepted 13 December 2018
Available online 22 December 2018
0040-1951/

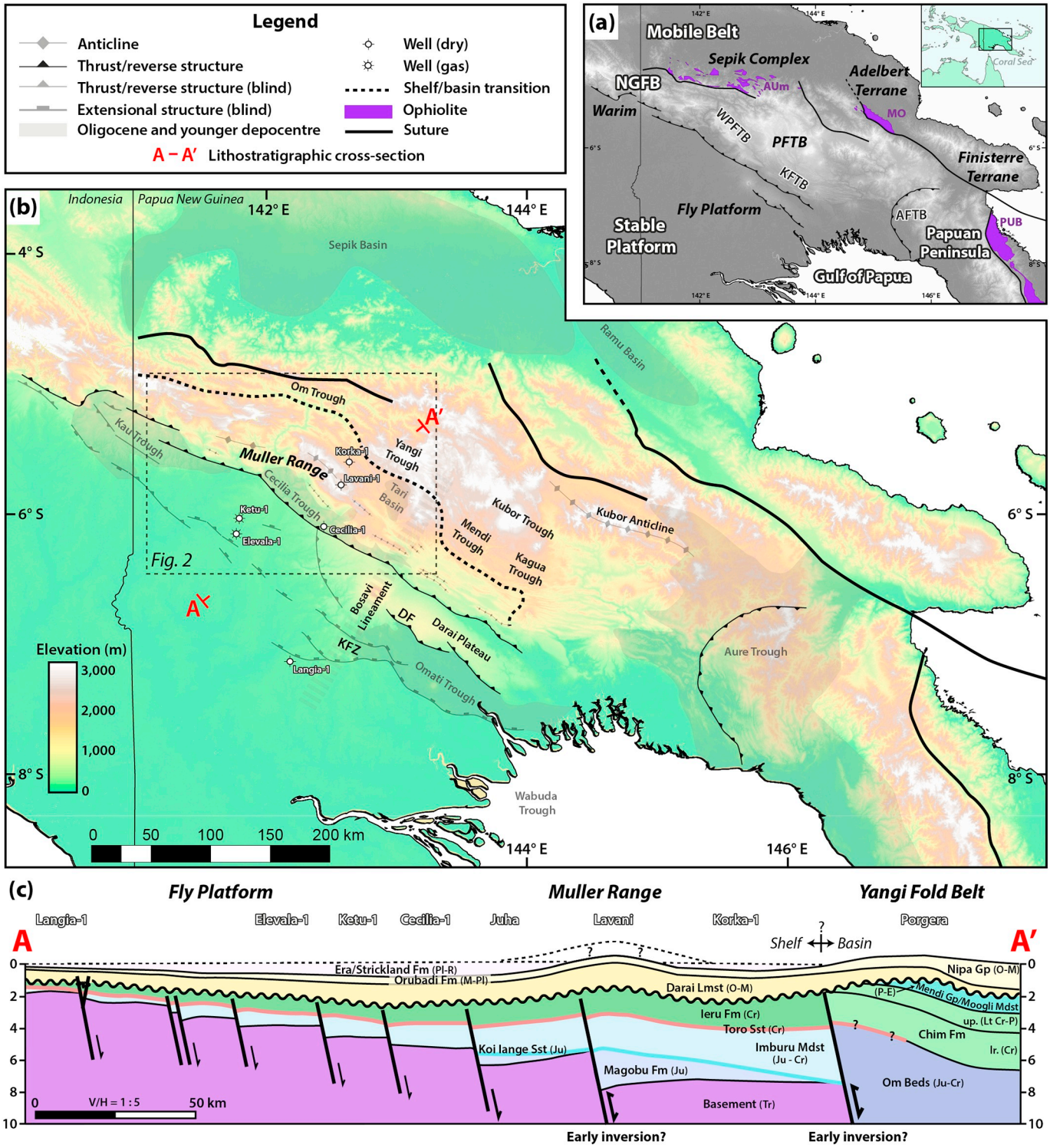

Fig. 1. (a) Tectonic-scale components of PNG. Frontal thrusts define the southerly extent of the PFTB while ophiolites delineate the suture zone between the PFTB and Mobile Belt. Tectonic features from Bain et al. (1973). AFTB, Aure Fold and Thrust Belt; KFTB, Kutubu Fold and Thrust Belt; NGFB, New Guinea Fold Belt; PFTB, Papuan Fold and Thrust Belt; WPFTB, western Papuan Fold and Thrust Belt; AUm, April Ultramafics; MO, Marum Ophiolite; PUB, Papuan Ultramafic Belt. (b) Major geological components of PNG. Geological features, including shelf/basin transition (as reflected in the stratigraphic record) from Bain et al. (1973). Only the largest anticlines that delineate the frontal trend of the PFTB are marked. Subsurface faults on the Stable Platform after McConachie and Lanzilli (2000). KFZ, Komewu Fault Zone; DF, Darai Fault. SRTM digital elevation model retrieved from USGS (2015). (c) Simplified early-thrust (Pliocene) lithostratigraphy of the Papuan Basin in western PNG, showing the relationship between long-lived extensional faults and basinward sedimentary thickening. Note the thick Late Cretaceous to Eocene sequence beneath the Yangi Fold Belt is absent across the frontal fold belt and Fly Platform. The extent to which thick Pliocene to recent molasse sedimentation covered the Muller Range and Yangi Fold Belt is unknown and depends on the interpreted timing of inversion. Refer to Fig. 2 for detailed stratigraphic legend. Modified from Bennett et al. (2000), Hill et al. (2000) and Mahoney et al. (2017).

from the Late Cretaceous to Oligocene. For example, to the southeast, Late Cretaceous to Eocene oceanic crust flooring the Coral Sea Basin suggests regional extensional tectonism (Weissel and Watts, 1979; Pigram and Symonds, 1991), which may have eventually led to rifting along the eastern and northern margins of PNG (Francis, 1990; Pigram and Symonds, 1991, 1993; Davies et al., 1997). Late Cretaceous to Palaeogene uplift and erosion in the southwest across the Fly Platform (Fig. 1a; e.g. Schofield, 2000), in part inferred from thermochronology and palaeotemperature data (e.g. Hill, 1989a; Hill et al., 1990; Cooper et al., 2012), has been linked by some authors to thermally-driven uplift associated with Coral Sea Rifting (e.g. Brown et al., 1980; Home et al., 1990). More recently, coupled plate tectonic and mantle convection modelling has shown that mid-Cretaceous to recent uplift of the eastern Australian margin may relate to continuous dynamic uplift (e.g. Muller et al., 2016). While the latter study did not consider the PNG margin, a northward extension of this model may provide a plausible alternate explanation for regional Late Cretaceous to Palaeogene uplift and erosion.

To the north of the Papuan Basin, the complexly deformed Mobile Belt (Fig. 1a) records Palaeogene collision on the northern PNG margin (e.g. Dow et al., 1972; Dow, 1977), however the number and timing of accretion events are widely debated (e.g. Pigram and Davies, 1987; Hill and Hall, 2003; Van Ufford and Cloos, 2005; Davies, 2012). While the details vary, many tectonic reconstructions include an initial Palaeogene collisional event, interpreted to relate to the docking of an expansive terrane at the northern PNG margin, referred to here as the Sepik Terrane (e.g. Pigram and Davies, 1987; Crowhurst et al., 1996; Davies et al., 1996; Hill and Hall, 2003; Hall, 2012; Schellart and Spakman, 2015). This event resulted in a highly deformed assemblage of continental and intra-oceanic arc fragments that are collectively referred to as the Sepik Complex (e.g. Rogerson et al., 1987; Davies, 1990). The Sepik Complex makes up most of the area known as the Mobile Belt, with the suture between the Mobile Belt and fold belt delineated by a disjointed ophiolite belt that extends along the length of the New Guinea Fold Belt (NGFB) and Papuan Peninsula (Fig. 1a). In the western Papuan Fold and Thrust Belt (WPFTB), the ophiolite belt is presently located < 100 km from the frontal fold belt (Fig. 1a), but the associated Palaeogene compressional event has gone largely unrecognised in the stratigraphy and structure of the fold belt.

Low-temperature thermochronology methods such as fission-track (e.g. Gleadow et al., 2002) and (U-Th)/He (e.g. Farley, 2002; Guenthner et al., 2013) can provide useful constraints on the thermal history of rocks across a range of geological processes (e.g. burial and exhumation) and have proven to be particularly suitable for investigating large gaps in the geological record (e.g. Japsen et al., 2012; Green and Duddy, 2016). In PNG, the absence of Late Cretaceous to Oligocene stratigraphy throughout much of the frontal PFTB and Fly Platform means that low-temperature thermochronology data from samples underlying the unconformity can be particularly valuable to identify and calibrate thermal events that can offer insight into the geological history of the margin. The isolated and inhospitable nature of the fold belt and Fly Platform means that previous thermochronological studies are limited, with the bulk of current apatite fission track (AFT) data based on studies by Hill and Gleadow (1989, 1990). Although hampered by poor apatite yields, Hill and Gleadow (1989, 1990) revealed that the Muller Range in the WPFTB experienced greater temperatures than the Fly Platform, subsequently relating increased temperatures to deeper Late Miocene to Pliocene burial by synorogenic sediments.

The recent Greater Juha and Pynang-Blucher geological surveys in the inhospitable Muller Range (e.g. Mahoney et al., 2017) provided a rare new opportunity to collect additional samples for thermochronological work. Indeed, the Muller Range provides one of few locations across the frontal PFTB where coarse-clastic rocks suitable for thermochronological analysis crop out. In addition, proximity to the April Ultramafics (Fig. 1a) makes the Muller Range an important area for investigating the evolution of the PNG margin. Here, we utilise the thermal modelling program QTQt (Gallagher, 2012) to model new AFT and (U-Th)/He data together with the existing AFT dataset to produce detailed thermal histories. In particular, the incorporation of modern annealing and diffusion models (e.g. Ketcham et al., 2007; Gautheron et al., 2009; Guenthner et al., 2013) permits further investigation of the enigmatic Late Cretaceous to Oligocene thermotectonic history of the PNG margin.

2. Geology

The island of New Guinea comprises a number of key tectonic components (after Hill and Hall, 2003): (1) the Stable Platform, (2) the Mobile Belt, and (3) the New Guinea Fold Belt (NGFB) (Fig. 1a). The Stable Platform is the northern edge of the relatively undeformed Australian continent while the Mobile Belt comprises island arcs and microcontinents accreted to the leading edge of the Australian plate during the Cenozoic (e.g., Hill and Raza, 1999). The NGFB separates the Stable Platform and Mobile Belt and formed predominantly within sediments of the Australian continental margin during the Late Miocene to Pliocene (Hill and Gleadow, 1989). In PNG, the Stable Platform and NGFB are referred to as the Fly Platform and PFTB, respectively (Fig. 1a).

The Fly Platform and PFTB are primarily underlain by Palaeozoic to early Mesozoic crystalline basement continuous with the Palaeozoic Tasman Orogen of eastern Australia (e.g. Hill and Hall, 2003; Crowhurst et al., 2004). In contrast, western New Guinea is largely underlain by Late Proterozoic basement (e.g. Parris, 1994). Limited outcrop and well intersections throughout the NGFB and Stable Platform suggest this transition occurs somewhere near the modern international border between PNG and Indonesia (e.g. Hill and Hall, 2003). The extent to which the formation of the Papuan Basin was controlled by crustal heterogeneity has been discussed in detail (e.g. Hill, 1991; Mahoney et al., 2017) but is largely unproven due to the general absence of basement outcrop and the poor quality of most geophysical imaging.

The stratigraphic and tectonic history of PNG is discussed briefly here, with a focus on those details relevant to our study of the Late Cretaceous to recent evolution of the margin. Detailed reviews of the stratigraphy of PNG and the Papuan Basin are provided by Dow (1977) and Home et al. (1990), respectively. Comprehensive tectonic history reconstructions can be found in Pigram and Symonds (1991), Hill and Raza (1999), Hill and Hall (2003), Van Ufford and Cloos (2005); Baldwin et al. (2012) and Zahirovic et al. (2014, 2016).

2.1. Early-mid Mesozoic

The non-marine to marine syn-rift sediment sequence overlying basement across much of the margin led to early ideas of early Mesozoic rifting (e.g. Pigram and Panggabean, 1984). Subsequently, abundant typically northwest-southeast and WNW-ESE oriented basement extension structures have been recognised in reflection seismic across the Stable Platform with hangingwall thickening suggesting that extension was long-lived from the early Mesozoic to Neogene (Fig. 1; Fischer and Warburton, 1996; Kawagle and Meyers, 1996; Bennett et al., 2000; Schofield, 2000; McConachie and Lanzilli, 2000; McConachie et al., 2000; Hill et al., 2010). Significant early Mesozoic extensional structures are also suspected beneath parts of the PFTB, including from west to east, beneath the westernmost PFTB (Mason, 1996), Muller Range (Mahoney et al., 2017), Juha Anticline (Hanani et al., 2016), Mananda Anticline (Keenan and Hill, 2015) and Kutubu Fold and Thrust Belt (KFTB) (e.g. Buchanan and Warburton, 1996; Hill et al., 2010, 2015). These authors suggest that the basement features exerted a primary control on the subsequent evolution of fold and thrust structures. The largest and best-known inverted extensional structure in the PFTB is in the eastern Muller Range, evidenced most convincingly by the thick

syn-rift sediment sequence (e.g. Magobu Formation; Fig. 1c) intersected in the Lavani-1 well (Amoco, 1982; Mahoney et al., 2017). Other significant extensional structures are commonly interpreted at significant shelf/basin facies transitions observed throughout the present day fold belt, for instance along the Om-Yangi-Mendi-Kagua trend (Fig. 1b, Hill et al., 2000).

The cessation of an initial phase of Middle Jurassic rifting is recorded throughout the Papuan Basin as a thick, widespread post-rift sequence mostly dominated by fine-grained clastic sediments including the Jurassic to Cretaceous-aged Imburu Mudstone and Cretaceous-aged Ieru Formation (Fig. 1c). A number of prograding sandstone sequences were deposited during the early post-rift phase, the most prominent of which are the Jurassic Koi Iange and Early Cretaceous Toro sandstones (Fig. 1c). These sands are thickest along the front of the present PFTB suggesting that this area was a near shelf-edge depocentre in the Late Jurassic to earliest Cretaceous (e.g. Home et al., 1990; Hill et al., 2000).

The middle Cretaceous (Cenomanian) marks the onset of an influx of coarse clastic sediments across the Northern Australian continental shelf (e.g. Giero, Ubea, Haito members of the upper Ieru Formation; Sari et al., 1996; Bradley, 2014) with a westward migration of the basin axis reflected in the stratigraphy (Jenkins, 1974; Schofield, 2000). The preserved sequence is characterised by significant spatial variations in thickness (e.g. Sari et al., 1996), potentially highlighting complex margin architecture at this time. This coarse-clastic influx and sedimentation rate increase is inferred to be related to the onset of rifting in the Coral Sea (e.g. Home et al., 1990), however it also correlates remarkably well with widespread uplift along the entire eastern Gondwanan margin (Muller et al., 2000, 2016).

2.2. Late Cretaceous to Early Oligocene

The Late Cretaceous to Oligocene histories of the frontal PFTB and Fly Platform regions are largely unknown due to the general absence of a preserved stratigraphic record from this time. Angular unconformities have been recognised in reflection seismic across the Fly Platform (e.g. McConachie et al., 2000; Schofield, 2000), frontal PFTB (Hanani, 2012 (unpub)) and in the Gulf of Papua (Botsford et al., 2012; Cooper et al., 2012), suggesting at least some uplift occurred over this time.

In contrast, more complete sequences of Late Cretaceous and Palaeogene sediments are preserved in other areas of the New Guinea margin, including from west to east, the West New Guinea Highlands (e.g. Van Ufford and Cloos, 2005), the Yangi and Mendi troughs (e.g. Hill et al., 2000), the Gulf of Papua (e.g. Botsford et al., 2012) and the Aure Trough (Home et al., 1990; Carman, 1993). The Yangi and Mendi troughs provide the best insight into the adjacent frontal PFTB and Fly Platform (Fig. 1). In these areas, Late Cretaceous mudstones of the Chim Formation are recorded with estimated thicknesses of 1500–3000 m (e.g. Davies and Norvick, 1974; Davies, 1983; Hill et al., 1990). The Palaeocene Moogli Mudstone and Eocene Mendi Group, the latter comprising mostly carbonates with variable clastic content, have a similar distribution with combined thicknesses of > 1000 m preserved throughout the Yangi and Mendi troughs (e.g. Davies, 1983; Brown and Robinson, 1982; Gunson et al., 1997, 2000). Mendi Group sediments have also been intersected in wells towards the Gulf of Papua including in the Omati and Wabuda troughs (Fig. 1b) and in the Morehead Graben to the far southwest of the Fly Platform (e.g. Tcherepanov et al., 2008; Cooper et al., 2012). Reflection seismic and well data show that Eocene strata in the Warim and Gulf of Papua regions (Fig. 1) lap out onto an apparently emergent Mesozoic high centred on the Fly Platform (e.g. McConachie et al., 2000), suggesting that there were limited Eocene strata deposited across the area.

While details regarding the nature and specific timing of Sepik Terrane collision remain controversial (e.g. Pigram and Davies, 1987; Davies et al., 1997; Van Ufford and Cloos, 2005), there is general agreement that it accreted to the PNG margin during the Palaeogene. An Eocene or Oligocene collision is most commonly suggested from geological evidence and from studies utilising kinematic plate tectonic models and/or seismic tomography (e.g. Schellart and Spakman, 2015; Zahirovic et al., 2016; Tobin et al., 2018). Geological evidence providing the most compelling evidence for an Eocene or Oligocene collision includes:

(1) Late Cretaceous to Eocene recrystallised limestones making up basement in the Sepik Basin (e.g. Fig. 1) are unconformably overlain by Late Oligocene to Middle Miocene conglomerates (Amogu Conglomerate) and limestones (Puwani Limestone) (Norvick and Hutchison, 1980; Hutchison and Norvick, 1978; Wilson et al., 1993).
(2) Map relationships around the Sepik Terrane suture zone suggest that deformed and metamorphosed Late Cretaceous to Eocene rocks (Salumei Formation) are overlain by significantly less deformed Late Oligocene fine micritic limestones (Kera Formation; Davies, 1983).
(3) Oligocene K-Ar and Rb-Sr ages of metamorphic minerals in the Ambunti Metamorphics just north of the April Ultramafics (Page, 1976).
(4) A major phase of Oligocene sinistral strike-slip faulting and fault reactivation limited to the northwest of the Bosavi Lineament on the Fly Platform (e.g. Kawagle and Meyers, 1996; McConachie and Lanzilli, 2000; McConachie et al., 2000).
(5) The short-lived deposition of coarse grained clastics across the Stable Platform in the Oligocene, including the Stanley Sandstone on the western Fly Platform and Sirga Formation in western New Guinea (e.g. McConachie and Lanzilli, 2000; McConachie et al., 2000).

Interestingly, there is very little evidence of Eocene to Oligocene collision in the fold belt, even directly adjacent to the suspected Sepik Terrane suture zone delineated by the April Ultramafics (Fig. 1a).

The unconformity observed across the frontal PFTB and Fly Platform becomes much more widespread in the Oligocene, coincident with one of the largest eustatic sea level falls in the Cenozoic (e.g. Haq et al., 1987; Haq, 2014). At this time, the unconformity extended into basinward areas (e.g. Hill et al., 2000) and across most of western and central New Guinea (as discussed in detail by Van Ufford and Cloos, 2005).

2.3. Mid Oligocene to Early Miocene

The Aure Trough (Fig. 1b) contains the oldest syn-orogenic sediments on the margin (~32 Ma; Edwards, 1950; Brown et al., 1975), interpreted to relate to the collision of the Papuan Peninsula (e.g. Davies et al., 1997). Many authors suggest an earlier or synchronous collision of the Sepik Terrane (Fig. 1a) along the northern margin (e.g. Pigram and Davies, 1987; Hall, 2012; Schellart and Sparkman, 2015; amongst others), however this collision is less clearly recorded in the stratigraphic record and remains controversial.

Nevertheless, subsequent mid Oligocene to Early Miocene subsidence of the PNG margin accommodated the deposition of up to 2000 m of the widespread Darai Limestone in shelfal areas and basinal equivalents of the Nipa Group to the north (Fig. 1c; e.g. Pigram and Symonds, 1991). Many structures across the Stable Platform from the Indonesian border to the Gulf of Papua (Fig. 1) were either reactivated or initiated in the mid-late Oligocene, with reverse and normal offset observed in reflection seismic data leading to interpretations of a largely sinistral strike-slip structural setting (e.g. Kawagle and Meyers, 1996; McConachie and Lanzilli, 2000; McConachie et al., 2000). Significant Darai Limestone growth observed across structures on the Fly Platform (e.g. Schofield, 2000; Hill et al., 2010) has led to suggestions that northwest-southeast oriented faulting acted as a regional hinge producing a mid-late Oligocene graben to the north (McConachie and Lanzilli, 2000).

2.4. Mid-late Miocene to recent

The New Guinea margin experienced a significant phase of arc-continent collision and mountain building from the mid-late Miocene to recent. Mid-late Miocene (~12 Ma) compressional deformation is interpreted from thermochronology data across the Mobile Belt (e.g. Hill and Raza, 1999), coincident with the initial influx of syn-orogenic flysch into the fold belt (e.g. Thornton et al., 1996). The PFTB may have been undergoing compressional deformation by 5–4 Ma (Hill and Gleadow, 1989), approximately synchronous with a transition to thick molasse syn-orogenic sedimentation in a number of foreland depocentres (Fig. 1). The nature and extent of syn-orogenic sediments is complex (e.g. Jones, 1991; Thornton et al., 1996) and particularly poorly known across uplifted and eroded areas of the PFTB, such as in the Muller Range (Fig. 1b and c).

The dominant orientation for compression-related structures throughout the PFTB reflects northeast-southwest compression, with an increasingly large sinistral strike-slip component recognised northwards in the Mobile Belt (e.g. Pigott et al., 1985; Crowhurst et al., 1997), related to east-west compressive stresses from the ongoing collision with the Finisterre Terrane (Fig. 1; Hill and Raza, 1999). On the Stable Platform, Plio-Pleistocene inversion is observed along structures to the east of the Bosavi Lineament, but not from the Bosavi Lineament to the Indonesian border (McConachie and Lanzilli, 2000).

Prominent stratovolcanoes and associated intrusions throughout PNG are, in general, poorly understood. Potassium argon (K-Ar) data suggests that volcanism in the Mobile Belt had begun by at least the Middle Miocene (Page, 1976). However, the majority of the prominent stratovolcanoes and associated intrusions within the PFTB and on the Fly Platform formed during the Plio-Pleistocene with an overall younging trend towards the south (Webb, 1973; Löffler et al., 1980). Significant stratovolcanoes between the KFTB and WPFTB, and associated flows up to 2000 m thick within the Tari Basin, appear to have amassed along the regionally significant northeast-trending Bosavi Lineament (Fig. 1b). To the west, the Muller Range and adjacent areas commonly contain Pliocene-Pleistocene intrusions (e.g. Davies and Norvick, 1974).

3. Sample acquisition and methodology

Approximately 20 sedimentary samples were collected for low-temperature thermochronology analyses from the Muller Range during the Greater Juha and Pynang-Blucher geological surveys (2014–2016) (e.g. Mahoney et al., 2017). Apatite and zircon mineral separation was performed using conventional rock crushing, sieving and heavy mineral concentration techniques (shaking table, magnetic, heavy liquid, and methylene iodide centrifuge). Papuan Basin sediments have notoriously low yields (e.g. Hill and Gleadow, 1989, 1990), yet sufficiently large samples are difficult to obtain from remote areas of the PFTB. A single basement sample, originally collected by Davies and Norvick (1974) in the Strickland Gorge, was also obtained from the Mineral Resources Authority in Port Moresby. This is the only known basement outcrop in the region. Apatite and/or zircon concentrates from four samples, originally used for AFT analysis (Hill and Gleadow, 1990), were also recovered from the University of Melbourne archives.

Although sampling along a vertical profile is optimal for thermochronological studies, such transects were not possible within the Greater Juha area due to a lack of outcrop, inhospitable terrain, intense karstification and thick vegetation. To enhance the resolution of our thermal models, we combine our new AFT, apatite (U-Th-Sm)/He and zircon (U-Th)/He data with existing AFT data published in Hill and Gleadow (1989, 1990). Thermal modelling approaches have advanced significantly since these data were obtained and much more information can now be extracted.

3.1. Low-temperature thermochronology

Here, we summarise the low-temperature thermochronology methods utilised in this study, including the apatite fission track (AFT) and (U-Th-Sm)/He techniques. Additional methodological details can be found in Appendix A. All analyses were performed at The University of Melbourne following the method of Gleadow et al. (2015).

AFT thermochronology relies on the production and retention of thermally sensitive linear damage traces, or fission tracks, from the spontaneous fission of ^{238}U (e.g. Gleadow et al., 2002). Over geological timescales fission tracks are generally considered to be stable at temperatures below ~50–60 °C, to undergo rapid complete annealing above ~110–120 °C and to progressively shorten at temperatures in-between, within what is known as the partial annealing zone (PAZ) (Gleadow and Duddy, 1981). The annealing characteristics of fission tracks are known to be a function of both time and temperature (e.g. Laslett et al., 1987; Ketcham et al., 2007) and thus combining track lengths and AFT age permits thermal history reconstruction of a sample within the PAZ (e.g. Gallagher, 1995; Ketcham, 2005). Where possible, apatite compositional variations such as chlorine content, or a compositional proxy such as Dpar, should be measured, as the annealing behaviour of fission tracks varies significantly depending on composition (e.g. Green et al., 1986; Barbarand et al., 2003). Reviews of the AFT technique are provided by Gleadow et al. (2002) and Donelick et al. (2005).

(U-Th-Sm)/He thermochronology relies on the production and thermally sensitive retention of ^{4}He during the radiogenic decay of ^{238}U, ^{235}U, ^{232}Th and ^{147}Sm (e.g. Farley, 2002). Comprehensive reviews of apatite and zircon (U-Th-Sm)/He methodologies can be found in Farley (2002), Farley and Stockli (2002) and Reiners et al. (2005).

^{4}He diffusivity is a function of time, temperature, crystal size and accumulated radiation damage (e.g. Farley, 2000; Reiners and Farley, 2001; Shuster et al., 2006). Over geological timescales, ^{4}He is partially retained at temperatures between ~40 °C and ~80 °C in apatite, and between ~130–210 °C in zircon, with the upper threshold of this partial retention zone (PRZ) representing the temperature above which ^{4}He is nearly instantaneously lost (e.g. Farley, 2002; Wolfe and Stockli, 2010). However, our understanding of the complex interplay of factors influencing helium retentivity is still developing, with grain size, grain breakage, parent isotope zonation, U and/or Th-rich inclusions and α-radiation damage likely to represent some of the primary influences on natural age dispersion (standard deviation of age/mean age), which can exceed 200% (e.g. Wildman et al., 2016). As a result, data interpretation and thermal history modelling of He data relies on close consideration of these influences, while the sample-averaged (U-Th-Sm)/He age is often difficult to interpret. Grain geometries are directly measured in our analyses, while models for the influence of α-radiation damage on the effective diffusivity of He are parameterised using the proxy effective uranium concentration ($eU = U + 0.235 * Th$ ppm). Additional information regarding the factors that cause age dispersion in apatite (U-Th-Sm)/He (AHe) datasets (also relevant to Zircon (U-Th)/He (ZHe) data) can be found in Fitzgerald et al. (2006), Wildman et al. (2016) and Danišík et al. (2017).

4. Results

Only nine of the sedimentary samples collected yielded sufficient apatite and/or zircon grains for analysis. Apatite and zircon were particularly sparse in sedimentary samples, with fine- to medium-grained argillaceous sandstones generally providing the best yields. The single basement sample from the Strickland Gorge and all four Lavani-1 well samples recovered from the University of Melbourne archives had sufficient apatite or zircon for analysis. The location and lithological description of samples that provided datable yields is provided in Table 1.

Three samples were newly analysed using the AFT technique, seven

Table 1
Sample descriptions (circle = existing data - see Appendix B, tick = new data/modelling).

Region	Longitude	Latitude	Sample type	Metres below base Darai	Elevation	Formation (member)	Lithology	Geological survey	Analysis			QTQt
Sample No.					Metres AMSL				AHe	AFT	ZrHe	
WMR												
R34832	141.920	-5.330	Surface	120	1,345	Ieru Fm (Haito Mbr)	Fine-grained argillaceous sst	Fly-Palmer (White *et al.* 1973)		○		✓
R34831	141.914	-5.353	Surface	718	1,000	Ieru Fm (Giero Mbr)	Fine-grained sst	Fly-Palmer (White *et al.* 1973)		○		✓
PY110-2171	141.726	-5.497	Surface	1,064	802	Ieru Fm	Fine- to medium-grained sst	P'nyang-Blucher 2016	✓	✓	✓	✓
Strick North												
R34809	142.147	-5.364	Surface	131	530	Ieru Fm	Sst (90% quartz)	Strickland River (Jenkins and White, 1970)		○		✓
R34810	142.146	-5.370	Surface	424	520	Ieru Fm	Fine-grained sst	Strickland River (Jenkins and White, 1970)		○		✓
R34811	142.138	-5.416	Surface	1,079	900	Toro SST	Fine-grained sst	Strickland River (Jenkins and White, 1970)		○		✓
R34808	142.095	-5.392	Surface	2,300	300	Basement	Quartz orthoclase biotite granite	Blucher Range (Davies and Norvick, 1974)	✓	○	✓	✓
Strick South												
R34835	141.985	-5.578	Surface	690	290	Ieru Fm (Giero Mbr)	Fine-grained argillaceous sst	Fly-Palmer (White *et al.* 1973)		○		✓
PY113-1863	141.946	-5.561	Surface	650	435	Ieru Fm	Fine-grained argillaceous sst	P'nyang-Blucher 2016	✓			
PY113-1893	141.966	-5.565	Surface	906	327	Ieru Fm	Fine-grained siltst	P'nyang-Blucher 2016	✓		✓	
PY113-1929.5	141.967	-5.560	Surface	1,028	324	Ieru Fm	Fine-grained sst	P'nyang-Blucher 2016	✓	✓	✓	✓
PY113-1977.5	141.970	-5.554	Surface	1,080	535	Ieru Fm	Fine-grained argillaceous sst	P'nyang-Blucher 2016	✓		✓	
PY113-1998.5	141.971	-5.552	Surface	1,308	624	Toro SST	Fine- to medium-grained sst	P'nyang-Blucher 2016			✓	
R34833	142.004	-5.548	Surface	1,830	800	Koi Iange	Fine-grained sst	Fly-Palmer (White *et al.* 1973)		○		✓
Lavani												
R34854	142.522	-5.767	Surface	120	2,880	Ieru Fm (Haito Mbr)	Fine-grained argillaceous sst	Lavani Anticline (Findlay and Leckie, 1973)		○		✓
GJLAV-1	142.566	-5.791	Surface	500	2,582	Ieru Fm (Giero Mbr)	Medium-grained argillaceous sst	Greater Juha (Mahoney *et al.* 2017)			✓	✓
GJLAV-4	142.570	-5.789	Surface	1,414	2,673	Toro SST	Medium-grained sst	Greater Juha (Mahoney *et al.* 2017)	✓		✓	✓
GJLAV-7	142.570	-5.789	Surface	1,423	2,682	Toro SST	Medium-grained sst	Greater Juha (Mahoney *et al.* 2017)			✓	✓
R34899	142.568	-5.775	Cuttings	2,377	1,728	Koi Iange/Magobu	Fine- to medium-grained sst	Lavani-1 well			✓	✓
R34900	142.568	-5.775	Cuttings	3,055	1,050	Koi Iange/Magobu	Fine- to medium-grained sst	Lavani-1 well			✓	✓
R34901	142.564	-5.769	Cuttings	3,686	431	Magobu	Fine-grained sst	Lavani-1 well		✓		✓
R34902	142.568	-5.775	Cuttings	4,386	-299	Magobu Fm	Medium- to coarse-grained sst	Lavani-1 well		○	✓	✓

Table 2
Muller Range apatite fission track (ICP-MS) data summary.

Region	Formation	No. of grains	N_S	ρ_s	^{238}U	Dpar	Dispersion	Chi-squared probability	Pooled age	[a]Central age	N_L	MTL	SD
Sample No.				x10^6cm^{-2}	(ppm)	(μm)	(%)	(%)	(Ma ± 1σ)	(Ma ± 1σ)		(μm ± SE)	(μm)
WMR													
PY110-2171	Ieru Fm	55	1000	0.359	9.47	1.85	27	< 1	76.0 ± 4.2	76.5 ± 4.1	108	11.4 ± 0.2	1.8
Strick South													
PY113-1929.5	Ieru Fm	31	472	0.373	8.03	1.78	23	< 1	85.8 ± 5.8	83.1 ± 5.7	99	11.0 ± 0.2	2.0
Lavani													
R34901	Magobu Fm	40	55	0.059	21.81	1.31	100	< 1	5.4 ± 6.7	10.7 ± 3.1	-	-	-

[a] Central ages calculated following Galbraith (2005).

samples using the apatite (U-Th-Sm)/He technique, and 12 samples using the zircon (U-Th)/He technique (Table 1). The new AFT, AHe and ZHe analytical data are listed in Tables 2–4 and summarised below.

4.1. Apatite fission track (AFT) results

Ieru Formation samples PY110-2171 and PY113-1929.5 are laterally ~25 km apart, share a similar structural context on the southern limb of the Muller Anticline and are sampled from similar stratigraphic levels approximately 1000 m below the base of the Darai Limestone (e.g. Fig. 2). Central AFT ages of 76.5 ± 4.1 Ma and 83.1 ± 5.7 Ma from PY110-2171 and PY113-1929.5 are within analytical error (Table 2). The confined mean track lengths (MTLs) are 11.4 ± 0.2 μm and 11.0 ± 0.2 μm, respectively. The standard deviation ranges from 1.8 μm to 2.0 μm and Dpars of ~1.78–1.85 μm are within analytical error. Both samples fail the chi-squared test for age homogeneity, thus necessitating further investigation prior to thermal modelling (discussed in Section 5.1).

Hill and Gleadow (1989, 1990) collected AFT data from six Ieru Formation samples throughout the Muller Range, with central ages ranging from 45.6 Ma to 79.8 Ma, MTLs ranging from 10.3 μm to 12.1 μm and standard deviations from 1.8 μm to 2.6 μm (Fig. 2, Appendix B). AFT ages for new and existing data from the Muller Range fall between 45.6 Ma and 83.1 Ma and are characterised by short to moderate MTLs (< 12.1 μm), low to moderate standard deviations (< 2.6 μm) and generally negatively skewed length distributions.

Reanalysis of Magobu Formation sample R34901 returned a central age of 10.7 ± 3.1 Ma, which is within analytical error of a central age of 9.9 ± 4.4 Ma calculated from Hill and Gleadow's (1990) original data following the updated formulae given in Galbraith (2005). The sparsity of track lengths in both analyses precludes the calculation of a statistically significant MTL and standard deviation. Hill and Gleadow (1990) collected AFT data from several sub-Ieru Formation stratigraphic samples, all returning mid-late Miocene to Pliocene central ages (3.8–12.4 Ma) with significant variations in mean track lengths ranging from 9.5–14.2 μm (Appendix B).

4.2. Apatite (U-Th-Sm)/He (AHe) results

AHe data for 45 grains across seven samples are detailed in Table 3. Single grain ages for sedimentary samples (n = 33) range from ~1 Ma to 68 Ma, with ~70% of ages < 10 Ma. Intrasample age dispersion is large. The Strickland basement sample R34808 yielded AHe ages (n = 11) with significantly less dispersion ranging from ~1 to 4 Ma, with only one pre-Pleistocene (> 2.5 Ma) age. eU concentrations range from 3 to 86 ppm for sedimentary samples and 12 to 49 ppm for the basement sample. Neither eU concentration nor grain size show a significant correlation with AHe age (Appendix C, Figs. C1 and C2).

4.3. Zircon (U-Th)/He (ZHe) results

ZHe data for 65 grains across 12 samples are detailed in Table 4. These analyses provide good coverage of the stratigraphic column: five samples from the Ieru Formation, three from the Toro Sandstone, three from the Koi Iange/Magobu formations and a single basement sample. Across all samples ~97% of single grain ages fall between 1 and 250 Ma. Negative ZHe vs eU correlations generally increase with stratigraphic age, from absent in the Ieru Formation samples to strong in the basement sample (Fig. 3 and Appendix C, Fig. C3), suggesting α-radiation damage is a major control on the age dispersion observed within the Koi Iange/Magobu formations and basement samples. Samples show variably weak to strong relationships between grain size and ZHe age (Appendix C, Fig. C4).

Ieru Formation sample PY113-1977.5 was an outlier returning mostly anomalously young single grain ages (n = 5), potentially related to a local influence such as volcanic activity, warm fluid circulation or another unknown factor leading to enhanced He loss. Consequently, this sample is excluded from further examination. Other single grain analyses on Ieru Formation samples PY110-2171, PY113-1893, PY113-1929.5 and GJLAV-1 (combined n = 20) from the mid-lower Ieru Formation yielded ages of 66–422 Ma, with 80% of ages between ~66–122 Ma and 20% of ages > 169 Ma (Fig. 3). eU contents vary significantly from 96 to 614 ppm, but show no clear correlation with age (Fig. 3).

Toro Sandstone samples GJLAV-4, GJLAV-7 and PY113-1998.5 (combined n = 14) yielded significantly older ZHe ages of 129–291 Ma, with > 50% of ages between 200 and 250 Ma (Fig. 3). eU contents vary significantly from 213 to 751 ppm, but again show no significant correlation with age (Fig. 3).

Koi Iange and Magobu formation samples R34899, R34900 and R34901 (combined n = 18) from the Lavani-1 well showed significant variation in single grain ages from 1 to 246 Ma and eU contents from 76 to 2959 ppm. There is a strong negative correlation between eU concentration and age (Fig. 3), with the oldest age (~246 Ma) showing the least accumulated radiation damage (eU = 76 ppm) and the youngest age (~1 Ma) showing the most (eU = 2959 ppm) with almost complete loss of helium retentivity.

Single grain ages from Strickland Gorge basement sample R34808 (n = 8) show high dispersion from 32 to 187 Ma. However, eU content is also highly variable, ranging from 268 to 929 ppm, with a very strong negative ZHe vs eU correlation (Fig. 3).

5. Thermal history reconstruction

The software QTQt (Gallagher, 2012) was used to perform both forward and inversion modelling to reconstruct thermal histories from new and existing low-temperature thermochronology data. Initially, the AFT dataset was explored using forward modelling, with a focus on investigating the importance of pre-depositional thermal histories of apatite grains within the Ieru Formation. The thermal history of the

Table 3
Muller Range apatite (U-Th-Sm)/He data summary

Region	Formation	Lab. No.	[4]He	Mass	[a]Mean FT	U	Th	Sm	Th/U ratio	[b][eU]	Uncorrected Age			Age			Grain length	Grain half-width	[c]Rs	[d]MWAR	[e]SD	[f]Grain morphology
Sample No.			(ncc)	(mg)		(ppm)	(ppm)	(ppm)		(ppm)	(Ma ± 1σ)			(Ma ± 1σ)			(μm)	(μm)	(μm)			
WMR																						
PY110-2171	Ieru Fm	13803	0.035	0.0225	0.83	1.9	10.5	96.3	5.54	4.4	2.8	±	0.2	**3.4**	±	**0.2**	307.7	93.8	107.9	-	-	2T
PY110-2171		13805	0.185	0.0091	0.77	0.9	9.5	68.8	11.09	3.1	52.3	±	3.1	*68.3	±	**4.2**	247.6	66.6	78.7	-	-	2T
PY110-2171		13960	0.165	0.0257	0.81	4.2	24.1	127.1	5.78	9.9	5.3	±	0.3	**6.5**	±	**0.4**	203.5	-	-	79.1	2.7	0T, 0T
PY110-2171		13961	0.065	0.0211	0.78	3.1	18.1	85.7	5.80	7.4	3.4	±	0.2	**4.3**	±	**0.3**	270.5	-	-	62.3	3.0	0T, 0T
PY110-2171		13962	0.070	0.0151	0.78	5.3	19.7	189.1	3.73	9.9	3.8	±	0.2	**4.8**	±	**0.3**	276.7	-	-	62.0	1.4	1T, 1T
PY110-2171		14058	0.044	0.0159	0.79	6.3	25.3	140.4	4.03	12.2	1.8	±	0.1	**2.3**	±	**0.1**	215.0	-	-	67.4	5.0	1T, 0T
PY110-2171		14059	0.045	0.0096	0.74	15.9	54.2	212.1	3.42	28.6	1.3	±	0.1	**1.8**	±	**0.1**	188.3	-	-	59.1	5.3	2T, 1T
PY110-2171		14281	0.062	0.0149	0.75	1.6	11.3	81.8	7.25	4.3	7.9	±	0.5	*10.5	±	**0.7**	313.5	-	-	57.0	1.5	1T, 1T
PY110-2171		14282	0.053	0.0161	0.78	5.8	28.4	145.2	4.87	12.5	2.1	±	0.1	**2.8**	±	**0.2**	217.7	-	-	70.1	1.6	1T, 2T
PY110-2171		14283	0.086	0.0138	0.77	4.3	18.7	165.2	4.40	8.7	5.7	±	0.3	**7.5**	±	**0.5**	225.2	-	-	65.0	9.3	1T, 2T
Strick North																						
R34808	Basement	11612	0.054	0.0071	0.74	13.5	30.3	57.3	2.23	20.6	3.0	±	0.2	**4.1**	±	**0.3**	376.4	49.9	66.1	-	-	1T
R34808		11613	0.032	0.0051	0.72	25.6	33.7	113.0	1.32	33.5	1.5	±	0.1	**2.1**	±	**0.1**	227.0	52.2	63.7	-	-	2T
R34808		11614	0.039	0.0048	0.69	25.3	60.7	93.9	2.39	39.6	1.7	±	0.1	**2.4**	±	**0.1**	276.7	45.9	59.0	-	-	2T
R34808		11615	0.044	0.0068	0.75	22.9	52.0	101.1	2.28	35.1	1.5	±	0.1	**2.0**	±	**0.1**	245.5	57.9	70.3	-	-	2T
R34808		11616	0.025	0.0035	0.72	33.2	69.1	122.6	2.08	49.4	1.2	±	0.1	**1.7**	±	**0.1**	201.5	49.9	60.0	-	-	1T
R34808		11686	0.046	0.0116	0.82	22.7	26.0	75.1	1.15	28.8	1.1	±	0.1	**1.4**	±	**0.1**	300.9	74.5	89.6	-	-	1T
R34808		11687	0.028	0.0078	0.79	20.2	24.8	72.8	1.23	26.0	1.1	±	0.1	**1.4**	±	**0.1**	154.0	70.9	72.8	-	-	0T
R34808		11688	0.031	0.0053	0.76	24.2	61.0	118.7	2.52	38.5	1.3	±	0.1	**1.6**	±	**0.1**	208.8	61.5	71.3	-	-	1T
R34808		11689	0.040	0.0201	0.84	11.9	36.6	100.2	3.08	20.5	0.8	±	0.0	**0.9**	±	**0.1**	347.6	91.8	109.0	-	-	1T
R34808		11690	0.026	0.0075	0.79	22.1	42.2	108.9	1.91	32.0	0.9	±	0.1	**1.1**	±	**0.1**	250.7	66.2	78.6	-	-	1T
R34808		11691	0.021	0.0108	0.79	7.7	18.4	81.6	2.38	12.0	1.3	±	0.1	**1.7**	±	**0.1**	289.1	60.9	75.5	-	-	0T
Strick South																						
PY 113-1863.0	Ieru Fm	13793	0.069	0.0033	0.68	5.8	19.5	170.8	3.35	10.4	15.9	±	1.0	**23.3**	±	**1.4**	169.1	48.8	56.8	-	-	2T
PY 113-1863.0		13795	0.104	0.0024	0.72	49.0	37.1	382.9	0.76	57.7	6.0	±	0.4	**8.4**	±	**0.5**	144.6	51.7	57.1	-	-	1T
PY 113-1863.0		13796	0.032	0.0018	0.67	42.4	72.6	378.5	1.71	59.5	2.4	±	0.1	**3.5**	±	**0.2**	137.4	45.5	51.2	-	-	1T
PY 113-1863.0		13958	0.113	0.0034	0.72	66.1	82.7	157.3	1.25	85.5	3.2	±	0.2	**4.5**	±	**0.3**	90.8	60.7	54.6	-	-	0T
PY 113-1863.0		13959	0.024	0.0057	0.75	6.9	6.8	27.4	0.99	8.5	4.1	±	0.3	**5.5**	±	**0.3**	204.5	52.6	62.7	-	-	0T
PY 113-1863.0		14060	0.155	0.0079	0.72	8.6	23.8	94.6	2.76	14.2	11.2	±	0.7	**15.6**	±	**1.0**	188.9	-	-	50.9	10.0	1T, 0T
PY 113-1893.0	Ieru Fm	13808	0.378	0.0161	0.83	20.6	20.3	112.3	0.98	25.4	7.6	±	0.5	**9.1**	±	**0.6**	203.0	88.8	92.7	-	-	0T
PY 113-1893.0		13963	0.043	0.0032	0.70	26.6	100.0	353.9	3.76	50.1	2.2	±	0.1	**3.1**	±	**0.2**	212.7	-	-	46.1	0.5	2T, 2T
PY 113-1893.0		13964	0.069	0.0076	0.73	3.6	19.7	238.1	5.49	8.2	8.7	±	0.5	**12.0**	±	**0.7**	152.7	-	-	52.7	13.6	1T, 0T
PY 113-1893.0		13965	0.242	0.0086	0.78	2.8	12.6	102.7	4.44	5.8	38.9	±	2.4	**49.6**	±	**3.1**	173.7	70.2	75.0	-	-	0T
PY 113-1893.0		14061	0.032	0.0120	0.76	2.8	17.2	108.6	6.22	6.8	3.1	±	0.2	**4.1**	±	**0.3**	165.2	-	-	60.2	5.8	0T, 1T
PY113-1929.5	Ieru Fm	13837	0.117	0.0058	0.73	2.3	10.4	84.7	4.62	4.7	34.2	±	2.0	**46.9**	±	**2.9**	263.7	46.9	59.7	-	-	0T
PY113-1929.5		13838	0.028	0.0042	0.71	2.2	10.3	121.2	4.63	4.6	11.4	±	0.7	**16.0**	±	**1.0**	147.1	58.7	62.9	-	-	2T
PY113-1929.5		13840	0.079	0.0048	0.73	4.8	18.9	228.3	3.98	9.2	14.1	±	0.8	**19.4**	±	**1.2**	162.8	59.8	65.6	-	-	2T
PY113-1929.5		13841	0.044	0.0021	0.61	4.3	16.2	138.3	3.74	8.1	20.5	±	1.2	**33.5**	±	**2.1**	175.9	38.1	47.0	-	-	2T
PY113-1929.5		13966	0.031	0.0156	0.78	1.5	6.6	80.3	4.35	3.1	5.3	±	0.3	**6.8**	±	**0.4**	199.2	-	-	62.6	2.0	0T, 0T
PY113-1929.5		14063	0.088	0.0098	0.76	7.3	25.9	335.4	3.56	13.4	5.3	±	0.3	**7.0**	±	**0.4**	200.9	-	-	59.7	10.3	1T, 1T
PY113-1929.5		14062	0.058	0.0152	0.76	2.4	10.0	126.5	4.18	4.8	6.3	±	0.4	**8.3**	±	**0.5**	236.5	-	-	60.1	1.8	0T, 2T
PY113-1929.5		14285	0.359	0.0124	0.78	36.0	3.7	135.1	0.10	36.9	6.4	±	0.4	**8.3**	±	**0.5**	195.8	-	-	56.2	1.5	0T, 0T
PY113-1929.5		14286	0.017	0.0080	0.73	1.6	6.8	115.5	4.20	3.2	5.2	±	0.3	**7.2**	±	**0.4**	153.3	-	-	56.9	2.2	0T, 1T
PY 113-1977.5	Ieru Fm	14456	0.094	0.0204	0.85	10.7	9.5	26.5	0.89	12.9	2.9	±	0.2	**3.5**	±	**0.2**	253.6	178.9	157.3	89.4	-	0T
Lavani																						
GJLAV-4	Toro SST	12243	0.026	0.0075	0.77	2.0	9.9	211.3	4.90	4.3	6.1	±	0.4	**7.9**	±	**0.5**	174.7	65.4	71.4	-	-	0T
GJLAV-4		12244	0.039	0.0045	0.74	6.5	36.6	230.5	5.65	15.1	4.6	±	0.3	**6.2**	±	**0.4**	208.1	56.6	66.7	-	-	1T
GJLAV-4		12246	0.032	0.0020	0.65	13.8	49.5	242.0	3.59	25.4	5.2	±	0.3	**8.0**	±	**0.5**	175.0	40.3	49.2	-	-	1T
Durango		13772	6.959	-	1.00	-	-	-	20.43	-	-	-	-	**31.0**	±	**1.9**	-	-	-	-	-	-
Durango		14108	3.665	-	1.00	-	-	-	21.89	-	-	-	-	**31.2**	±	**1.9**	-	-	-	-	-	-

(*continued on next page*)

Table 3 (*continued*)

Region	Formation	Lab. No.	^{4}He	Mass	[a]Mean FT	U	Th	Sm	Th/U ratio	[b][eU]	Uncorrected Age		Age			Grain length	Grain half-width	[c]Rs	[d]MWAR	[e]SD	[f]Grain morphology
Sample No.			(ncc)	(mg)		(ppm)	(ppm)	(ppm)		(ppm)	(Ma ± 1σ)		(Ma ± 1σ)			(μm)	(μm)	(μm)			
Durango		14466	6.379	-	1.00	-	-	-	22.86	-	-	-	-	**31.7**	± **2.0**	-	-	-	-	-	-

[a] F_T is the α-ejection correction after Farley (1996) calculated using mass-weighted radius.
[b] Effective uranium content [U ppm + 0.235$_*$Th ppm].
[c] Rs = (3$_*$(grain length)$_*$(grain half-width)/(2$_*$(grain length + grain half-width))
[d] MWAR is the mass-weighted average radius of apatite crystals analysed.
[e] Standard deviation of the MWAR is used as a guide for the 'tightness' of the range of single crystal radii picked within a sample.
[f] Grain morphology - 0T = no crystal terminations, 1T = one crystal termination and 2T = 2 crystal terminations.
[*] Analysis is problematic.

Muller Range was then further evaluated through inversion of AFT data and the joint-inversion of AFT, AHe and ZHe data in a series of vertical profiles.

5.1. Selection of samples for thermal modelling

Thermal history modelling of AFT data can reliably be carried out when measured single grain ages are statistically consistent with a single population (e.g. Carter and Gallagher, 2004). The standard approaches to assessing population homogeneity include the chi-squared (χ^2) and dispersion tests, with P(χ^2) values of < 0.05 or dispersion values of > 20% most commonly relating to multiple apatite populations and/or differential annealing kinetics between grains of differing composition within a single population (e.g. Galbraith and Laslett, 1993).

The bulk of AFT data available to this study was obtained from the Ieru Formation (Table 1), with all samples failing the chi-squared test and being associated with moderate to high dispersion (Table 2 and Appendix B). Conventionally, these data would be separated into independent populations for thermal history modelling, ideally based on some compositional criterion (i.e. Cl wt%, Dpar kinetic indicator). This provides a test of the potential influence of differing annealing kinetics on single grain age dispersion and a means for allowing for over-dispersion in the apatite age distribution. However a large proportion of AFT data from the Papuan Basin dataset are old and thus chemical composition data are limited. Dpar measurements were obtained from samples PY113-1929.5 and PY110-2171, but the Dpar-AFT age and Dpar-track length trends (Appendix D) did not imply any obvious statistically meaningful apatite populations. Given this, we believe that multiple sources of apatite are the best explanation for the observed heterogeneity in single grain ages.

A concern with inverting data as a single population from a sample with multiple apatite populations is that we will not account for multiple independent pre-depositional thermal histories. In particular, inherited tracks (i.e. those formed prior to deposition) may significantly influence the model-predicted palaeotemperatures, including the timing and magnitude of maximum temperatures (e.g. Carter and Gallagher, 2004). In the following section, we discuss our current understanding of Papuan Basin sediment provenance and use forward thermal modelling to explore the potential influence that multiple apatite populations (and inherited tracks) could have on thermal history reconstructions.

5.1.1. Sediment provenance

The pioneering regional PNG AFT studies of Hill and Gleadow (1989, 1990) revealed at least two sources of apatite in the Ieru Formation: (1) a large Albian to Cenomanian contemporaneous volcanic component (AFT age ≈ stratigraphic age) and a considerably smaller basement component (AFT age > stratigraphic age). This is consistent with ZHe ages from the Ieru Formation (Fig. 3) which indicate that ~80% of zircon grains relate to a contemporaneous source and ~20% relate to an older pre-depositional source (Fig. 3). In contrast, the pre-Ieru Formation strata, including the directly underlying Toro Sandstone, primarily comprise ZHe age (and age vs eU trends) that are suggestive of a source that underwent significant cooling in the Triassic (~250–200 Ma; Fig. 3).

This transition in sediment provenance is consistent with our understanding of the palaeogeographic evolution of the Papuan Basin (e.g. Home et al., 1990; Hill et al., 2000; Norvick, 2003) in particular that: (1) during the Triassic to earliest Cretaceous (top basement to Toro Sandstone) the shoreline was close to the southern edge of the present day fold belt and sands were likely sourced from exposed basement; and (2) in the Early Cretaceous, flooding of the margin moved the shoreline thousands of kilometres inland to mainland Australia, flooding basement sources of sand and thus reflecting a transition to primarily locally-sourced apatite and zircon from nearby contemporaneous

Table 4
Muller Range zircon (U-Th)/He data summary

Region	Formation	Lab. No.	^{4}He	Mass	[a]Mean FT	U	Th	Th/U ratio	[b][eU]	Uncorrected Age	Age	Grain length	Grain half-width	[c]Rs	[d]Grain morphology
Sample No.			(ncc)	(mg)		(ppm)	(ppm)		(ppm)	(Ma ± 1σ)	(Ma ± 1σ)	(μm)	(μm)	(μm)	
WMR															
PY110-2171	Ieru Fm	13798	21.420	0.0066	0.78	237.8	77.4	0.33	256.0	80.7 ± 5.0	103.4 ± 6.4	240.8	45.0	56.8	2T
PY110-2171		13799	10.342	0.0071	0.77	100.0	108.0	1.08	125.3	73.2 ± 4.5	95.0 ± 5.9	251.0	45.4	57.7	2T
PY110-2171		13800	5.367	0.0033	0.74	123.9	92.8	0.75	145.7	67.2 ± 4.2	90.8 ± 5.6	162.4	41.9	49.9	2T
PY110-2171		13801	23.992	0.0062	0.77	114.7	43.5	0.38	124.9	191.9 ± 11.9	249.2 ± 15.4	236.2	44.0	55.6	2T
PY110-2171		13802	13.269	0.0050	0.75	191.3	95.6	0.50	213.7	76.1 ± 4.7	101.4 ± 6.3	221.8	40.6	51.5	2T
Strick North															
R34808	Basement	11372	36.385	0.0066	0.78	365.7	221.4	0.61	417.7	83.3 ± 5.2	107.5 ± 6.7	240.0	22.6	30.9	2T
R34808		11373	27.998	0.0077	0.76	715.2	907.4	1.27	928.5	24.4 ± 1.5	32.1 ± 2.0	312.8	20.2	28.4	2T
R34808		11374	41.884	0.0068	0.76	524.7	628.0	1.20	672.3	56.6 ± 3.5	74.7 ± 4.6	283.5	20.2	28.3	2T
R34808		11375	46.980	0.0078	0.79	515.8	187.3	0.36	559.8	68.9 ± 4.3	87.4 ± 5.4	257.9	23.6	32.4	2T
R34808		11376	40.949	0.0067	0.77	236.4	157.6	0.67	273.4	140.5 ± 8.7	182.0 ± 11.3	248.1	22.1	30.4	2T
R34808		11575	26.463	0.0043	0.74	227.7	171.7	0.75	268.1	139.6 ± 8.6	187.4 ± 11.6	199.2	20.2	27.5	2T
R34808		11576	25.713	0.0039	0.75	298.2	199.8	0.67	345.1	115.8 ± 7.2	154.3 ± 9.6	169.7	22.5	29.8	2T
R34808		11577	29.564	0.0060	0.77	316.2	348.6	1.10	398.1	78.5 ± 4.9	101.3 ± 6.3	205.7	24.4	32.7	2T
Strick South															
PY 113-1893.0	Ieru Fm	13813	21.028	0.0092	0.77	140.1	51.6	0.37	152.2	94.4 ± 5.8	122.3 ± 7.6	363.9	80.4	98.8	2T
PY 113-1893.0		13814	9.220	0.0050	0.76	156.5	107.4	0.69	181.8	62.7 ± 3.9	82.6 ± 5.1	206.7	86.7	91.6	2T
PY 113-1893.0		13815	23.595	0.0036	0.72	94.9	116.4	1.23	122.3	304.0 ± 18.8	422.0 ± 26.2	201.9	72.2	79.8	2T
PY 113-1893.0		13816	21.105	0.0079	0.77	308.7	88.3	0.29	329.4	50.7 ± 3.1	65.9 ± 4.1	325.0	80.0	96.3	2T
PY 113-1893.0		13817	18.891	0.0046	0.75	303.6	200.5	0.66	350.8	71.9 ± 4.5	95.9 ± 5.9	207.2	81.6	87.8	2T
PY113-1929.5	Ieru Fm	13832	7.337	0.0073	0.79	81.9	60.3	0.74	96.1	67.4 ± 4.2	85.9 ± 5.3	234.7	48.8	60.6	2T
PY113-1929.5		13833	54.535	0.0081	0.80	483.1	556.6	1.15	613.9	71.3 ± 4.4	89.5 ± 5.5	222.3	55.4	66.6	2T
PY113-1929.5		13834	6.076	0.0045	0.76	116.8	83.0	0.71	136.3	61.8 ± 3.8	81.7 ± 5.1	185.3	44.6	53.9	2T
PY113-1929.5		13835	66.479	0.0064	0.77	307.6	154.4	0.50	343.9	187.8 ± 11.6	243.4 ± 15.1	243.7	43.6	55.5	2T
PY113-1929.5		13836	62.436	0.0104	0.80	389.0	113.3	0.29	415.6	94.8 ± 5.9	117.7 ± 7.3	292.6	50.5	64.6	2T
PY113-1977.5	Ieru Fm	13921	0.399	0.0050	0.76	103.6	80.7	0.78	122.6	4.0 ± 0.3	*5.4 ± 0.3	215.5	83.3	90.1	2T
PY113-1977.5		13922	1.505	0.0044	0.74	548.1	276.4	0.50	613.0	3.4 ± 0.2	*4.6 ± 0.3	216.6	76.4	84.8	2T
PY113-1977.5		13925	1.214	0.0030	0.73	694.5	131.9	0.19	725.5	3.3 ± 0.2	*4.6 ± 0.3	150.7	85.6	81.9	2T
PY113-1977.5		14454	1.827	0.0109	0.78	535.2	168.4	0.31	574.8	1.9 ± 0.1	*2.4 ± 0.1	398.0	83.2	103.2	2T
PY113-1977.5		14455	23.994	0.0053	0.74	405.4	183.1	0.45	448.4	61.7 ± 3.8	*83.1 ± 5.2	231.7	80.9	89.9	2T
PY 113-1998.5	Toro SST	13818	50.236	0.0042	0.74	372.4	130.5	0.35	403.1	177.7 ± 11.0	239.0 ± 14.8	208.9	76.8	84.2	2T
PY 113-1998.5		13819	41.868	0.0076	0.79	317.3	114.4	0.36	344.2	102.6 ± 6.3	129.4 ± 8.0	239.2	99.2	105.2	2T
PY 113-1998.5		13820	53.064	0.0038	0.75	469.7	166.1	0.35	508.7	166.6 ± 10.3	221.1 ± 13.7	166.5	89.9	87.6	2T
PY 113-1998.5		13821	92.713	0.0054	0.77	389.8	338.9	0.87	469.4	224.2 ± 13.9	291.3 ± 18.1	198.4	95.1	96.4	2T
PY 113-1998.5		13822	72.889	0.0069	0.79	535.4	68.4	0.13	551.5	122.6 ± 7.6	155.8 ± 9.7	238.7	93.0	100.4	2T
Lavani															
GJLAV-1	Ieru Fm	12271	44.649	0.0091	0.80	218.9	65.8	0.30	234.3	135.2 ± 8.4	169.5 ± 10.5	276.0	24.4	33.7	2T
GJLAV-1		12272	17.397	0.0037	0.74	401.5	174.4	0.43	442.4	64.3 ± 4.0	86.3 ± 5.4	177.6	20.6	27.7	2T
GJLAV-1		12273	17.301	0.0042	0.75	389.6	380.3	0.98	479.0	53.0 ± 3.3	71.0 ± 4.4	185.6	21.2	28.6	2T
GJLAV-1		12274	37.205	0.0060	0.77	423.1	237.9	0.56	479.0	81.5 ± 5.0	106.3 ± 6.6	235.3	21.5	29.6	2T
GJLAV-1		12275	9.703	0.0043	0.75	196.5	120.6	0.61	224.8	61.7 ± 3.8	82.4 ± 5.1	194.6	20.7	28.0	2T
GJLAV-4	Toro SST	12248	78.120	0.0082	0.79	286.7	108.4	0.38	312.2	193.9 ± 12.0	244.0 ± 15.1	253.5	24.7	33.8	2T
GJLAV-4		12249	42.142	0.0046	0.75	280.8	118.0	0.42	308.5	178.5 ± 11.1	238.8 ± 14.8	219.2	19.5	26.9	2T
GJLAV-4		12250	57.667	0.0081	0.78	229.1	72.6	0.32	246.1	181.9 ± 11.3	232.6 ± 14.4	289.1	22.0	30.7	2T
GJLAV-4		12251	37.711	0.0063	0.76	237.6	130.0	0.55	268.1	137.3 ± 8.5	180.7 ± 11.2	269.1	20.0	28.0	2T
GJLAV-4		12252	101.335	0.0087	0.79	387.4	118.4	0.31	415.2	179.6 ± 11.1	226.0 ± 14.0	272.0	24.1	33.1	2T
GJLAV-7	Toro SST	12266	74.998	0.0093	0.80	236.2	154.6	0.65	272.5	190.8 ± 11.8	238.0 ± 14.8	256.4	26.4	35.9	2T
GJLAV-7		12267	177.538	0.0137	0.83	718.5	137.1	0.19	750.7	116.4 ± 7.2	140.3 ± 8.7	292.2	29.9	40.7	2T
GJLAV-7		12269	63.134	0.0105	0.81	182.3	131.8	0.72	213.2	185.5 ± 11.5	228.1 ± 14.1	248.8	29.3	39.4	2T
GJLAV-7		12475	66.918	0.0060	0.76	351.0	143.5	0.41	384.7	176.7 ± 10.9	232.4 ± 14.4	259.4	20.1	27.9	2T

(*continued on next page*)

Table 4 (*continued*)

Region	Formation	Lab. No.	^{4}He	Mass	[a]Mean FT	U	Th	Th/U ratio	[b][eU]	Uncorrected Age	Age	Grain length	Grain half-width	[c]Rs	[d]Grain morphology
Sample No.			(ncc)	(mg)		(ppm)	(ppm)		(ppm)	(Ma ± 1σ)	(Ma ± 1σ)	(μm)	(μm)	(μm)	
R34899	Koi Iange/Magobu Fm	13853	21.195	0.0034	0.73	211.3	152.9	0.72	247.3	150.6 ± 9.3	204.5 ± 12.7	172.5	39.9	48.6	2T
R34899		13854	13.786	0.0027	0.71	164.7	114.5	0.70	191.6	151.3 ± 9.4	211.4 ± 13.1	166.9	35.9	44.3	2T
R34899		13855	24.169	0.0040	0.75	409.8	283.4	0.69	476.4	77.8 ± 4.8	104.1 ± 6.5	183.1	41.8	51.0	2T
R34899		14073	1.029	0.0027	0.74	2865.0	397.8	0.14	2958.5	0.8 ± 0.0	1.1 ± 0.1	130.8	49.7	54.0	2T
R34899		14074	22.149	0.0039	0.76	330.2	32.7	0.10	337.9	102.9 ± 6.4	135.7 ± 8.4	181.2	41.9	51.0	2T
R34899		14075	6.753	0.0027	0.70	448.7	163.6	0.36	487.2	29.8 ± 1.8	42.4 ± 2.6	164.0	35.9	44.2	2T
R34900	Koi Iange/Magobu Fm	13847	35.601	0.0065	0.78	192.0	167.6	0.87	231.4	148.8 ± 9.2	191.5 ± 11.9	224.6	47.4	58.7	2T
R34900		13848	38.540	0.0044	0.75	373.8	172.1	0.46	414.3	127.2 ± 7.9	169.6 ± 10.5	206.0	40.2	50.5	2T
R34900		13849	20.401	0.0077	0.80	109.7	23.3	0.21	115.2	148.1 ± 9.2	185.8 ± 11.5	235.5	50.6	62.5	2T
R34900		13850	25.188	0.0036	0.74	252.4	183.4	0.73	295.5	141.0 ± 8.7	189.3 ± 11.7	164.3	44.3	52.3	2T
R34900		13851	12.828	0.0014	0.66	374.8	289.2	0.77	442.7	110.7 ± 6.9	166.8 ± 10.3	109.9	36.5	41.1	2T
R34902	Magobu Fm	13842	15.685	0.0063	0.78	284.4	172.6	0.61	324.9	49.4 ± 3.1	62.9 ± 3.9	200.1	52.1	62.0	2T
R34902		13843	8.647	0.0039	0.75	419.5	333.9	0.80	498.0	27.3 ± 1.7	36.5 ± 2.3	168.6	45.2	53.4	2T
R34902		13845	11.585	0.0044	0.75	157.7	172.5	1.09	198.3	81.1 ± 5.0	107.6 ± 6.7	182.1	45.2	54.3	2T
R34902		13846	7.083	0.0033	0.74	224.4	168.5	0.75	264.0	49.6 ± 3.1	67.4 ± 4.2	158.0	42.7	50.4	2T
R34902		14070	9.739	0.0031	0.72	261.7	195.7	0.75	307.7	59.6 ± 3.7	83.1 ± 5.1	156.9	41.7	49.4	2T
R34902		14071	43.711	0.0082	0.82	420.9	19.7	0.05	425.5	83.9 ± 5.2	102.7 ± 6.4	215.7	57.7	68.2	2T
R34902		14072	9.642	0.0042	0.75	69.1	27.3	0.40	75.5	183.7 ± 11.4	245.8 ± 15.2	189.2	41.8	51.4	2T
Fish Canyon Tuff		13829	9.658	0.0077	0.79	317.2	165.2	0.52	356.0	22.8 ± 1.4	29.0 ± 1.8	249.7	95.8	103.8	2T
Fish Canyon Tuff		13830	9.499	0.0074	0.79	339.8	196.9	0.58	386.1	21.7 ± 1.3	27.4 ± 1.7	223.6	103.2	105.9	2T
Fish Canyon Tuff		14410	9.250	0.0074	0.78	324.4	173.0	0.53	365.0	22.1 ± 1.4	28.2 ± 1.7	248.3	93.9	102.2	2T
Fish Canyon Tuff		14412	5.908	0.0045	0.74	333.7	197.8	0.59	380.2	21.2 ± 1.3	28.6 ± 1.8	188.2	87.7	89.8	2T
Fish Canyon Tuff		14579	9.653	0.0064	0.78	391.1	185.9	0.48	434.8	22.0 ± 1.4	28.4 ± 1.8	233.2	90.9	98.1	2T

[a] F_T is the α-ejection correction after Farley (1996).
[b] Effective uranium concentration (U ppm + 0.235 Th ppm).
[c] Rs = (3*(grain length)*(grain half-width)/(2*(grain length + grain half-width))
[d] Grain morphology - 0T = no terminations, 1T = one termination, 2T = 2 terminations.
* Analysis is problematic.

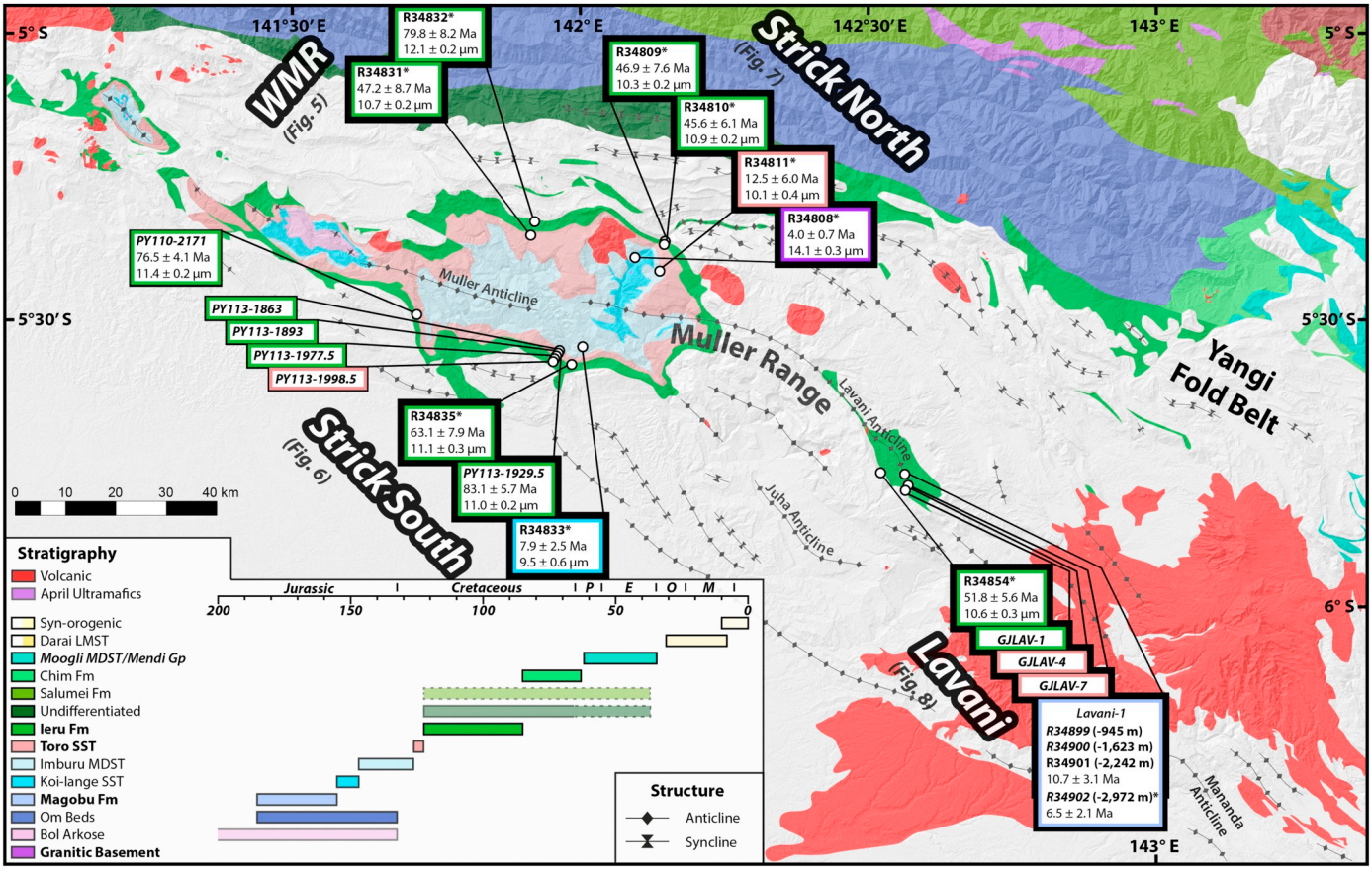

Fig. 2. Sample localities and AFT data from the Muller Range, Western Papuan Fold and Thrust Belt. Asterisked samples represent AFT ages and mean track lengths from Hill and Gleadow (1989, 1990). Samples are grouped in four vertical profiles for QTQt modelling: WMR: western Muller Range, Strick North: north Strickland Gorge, Strick South: south Strickland Gorge, Lavani: Lavani Valley. Geological information from Davies and Norvick, 1974; Davies, 1983; Brown and Robinson, 1982. SRTM digital elevation model retrieved from USGS (2015). Location marked on Fig. 1. (For interpretation of the references to colour in this figure legend, the reader is referred to the web version of this article.)

volcanics such as the Kondaku Tuff on the flanks of the Kubor Anticline (Fig. 1b; Bain et al., 1975). This understanding of sediment provenance is used to guide forward thermal modelling aimed at exploring the potential influences of the contemporaneous volcanic and basement apatite populations on thermal history modelling.

5.2. Forward thermal history modelling approach

Here, we use forward modelling of AFT data to assess the viability of a range of thermal history scenarios. The assessment of forward model results involves comparing predicted and observed data, or more specifically, the ability of a given thermal history to reproduce the observed AFT age, MTL and track length distribution (TLD). The forward models presented here were qualitatively assessed against observed AFT data from the three uppermost Ieru Formation samples, R34809, R34832 and R34854. All three samples were located < 131 m below the Darai Limestone base (Table 1), enabling us to robustly constrain the Oligocene to Late Miocene thermal history and thus focus on exploring plausible time-temperature paths in less well constrained areas (e.g. Fig. 4). The AFT ages for these samples range from 46.9 ± 7.6 Ma to 79.8 ± 8.2 Ma, with mean track lengths ranging from 10.3 ± 0.2 to 12.1 ± 0.2 µm (Appendix B). The samples share considerable similarity in TLD, including a major peak at ~10–12 µm and a negative skew due to a tail of short track lengths (Appendix F, Fig. F1).

To account for multiple sources of apatite within the Ieru Formation, each forward model comprised two independent pre-depositional time-temperature paths, including: (1) a slowly-cooled path from temperatures below the PAZ in the Early Triassic to surface temperatures in the Albian to Cenomanian and (2) a rapidly-cooled path from temperatures below the PAZ to surface temperatures in the Albian to Cenomanian (Fig. 4). Therefore, apatite grains that experienced the slow-cooling path spent considerably longer (> 50 Ma) in the PAZ prior to deposition (Fig. 4). Multiple pre-depositional history models were tested with three post-depositional thermal histories: (a) a Pliocene to recent thermal peak only, (b) a Late Cretaceous to Oligocene thermal peak only[1] and (c) both Late Cretaceous to Oligocene and Pliocene to recent thermal peaks (Fig. 4). Each of the post-depositional thermal histories (a–c) were tested with maximum temperatures of 60 °C, 80 °C, 90 °C, 100 °C and 110 °C (Fig. 4). Forward modelling utilised the annealing model of Ketcham et al. (2007) with apatite chlorine content fixed at 0.40 wt%, which equates to Dpar values between 1.5 and 2.5 µm based on Cl-Dpar comparisons in Donelick et al. (2005).

The predicted AFT age and MTL from each of the pre-depositional time-temperature paths was used to calculate weighted averages for each sample, with the weighting based on the assumed relative abundance of rapidly-cooled and slowly-cooled grains (e.g. 80:20 in Fig. 4). This enabled the resulting AFT age and MTL predictions to be directly compared to the observed data, with predicted data outside of the range ± the error of the observed AFT age (e.g. 39.3–88 Ma) and MTL (e.g. 10.1–12.3 µm) discarded. The final predicted track length

[1] All three post-depositional thermal histories include Oligocene to Late Miocene heating associated with the deposition of 1000–1500 m of Darai Limestone, but the maximum temperature associated with this burial remains at a palaeotemperature lower than the uppermost boundary of the PAZ.

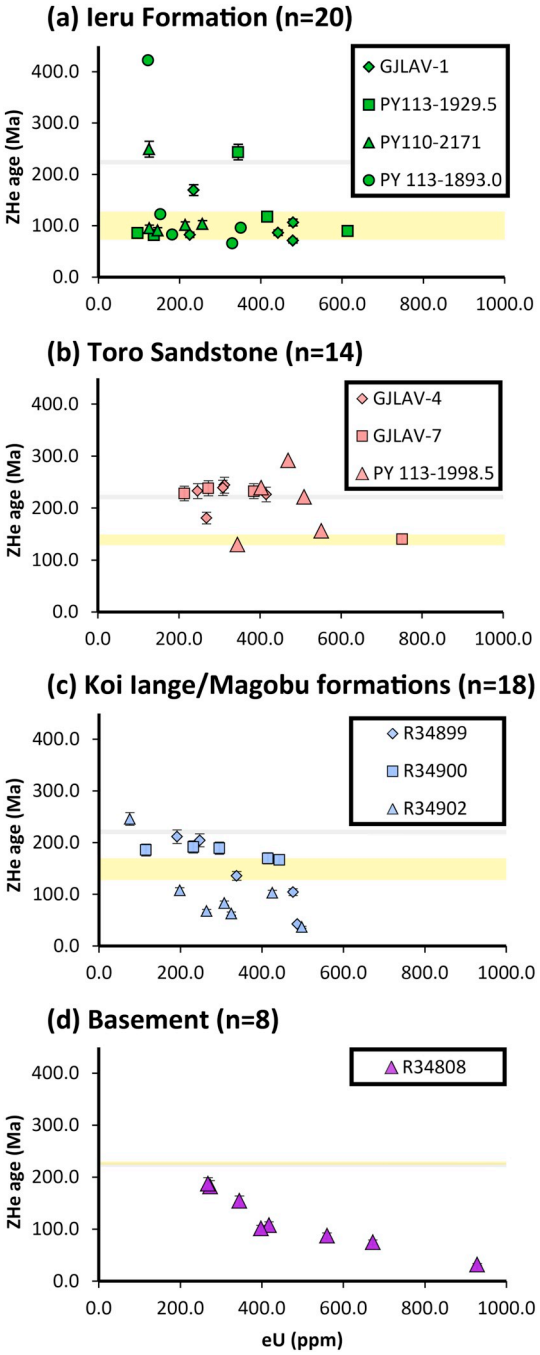

Fig. 3. ZHe age vs eU plot showing increase in negative correlation with stratigraphic age from Ieru Formation (a) to crystalline basement (d). Corrected ZHe ages plotted with 6.2% analytical uncertainty (1σ) bars. Yellow squares/bars represent the stratigraphic age of each formation. Grey line is the minimum known age of crystalline basement beneath the Papuan Basin (222 ± 4 Ma; Page, 1976). n = number of single grain ages in plot. (For interpretation of the references to colour in this figure legend, the reader is referred to the web version of this article.)

distribution histograms were subsequently constructed by combining the results for accepted models. These were compared directly to a composite TLD histogram comprising the three upper Ieru Formation samples (normalised to 100 tracks).

5.3. Forward thermal history modelling results

A total of 52 individual forward models were run to explore the potential influences of mixed apatite provenance on observed Ieru Formation AFT data. This included 26 forward models for the scenario considered most representative (e.g. Section 5.1.1) comprising 80% rapidly-cooled apatite and 20% slowly-cooled apatite (Fig. 4). The additional 26 forward models comprising 50% rapidly-cooled and 50% slowly-cooled apatite are included and discussed in Appendix E.

The 80:20 modelling included 26 independent time-temperature paths yielding 13 central AFT age, MTL and length distribution predictions. Of these, only four were consistent with the observed values from the three uppermost Ieru Formation samples. Despite significantly different post-depositional thermal histories, all four accepted models were characterised by maximum temperatures of 90 or 100 °C (Fig. 4). Model (a), comprising only a Pliocene to recent thermal peak produced the worse TLD fit, failing to reproduce the short track length component and asymmetric distribution recorded within the observed data (Fig. 4a). The best-fit TLD was produced by Model (b), comprising a Late Cretaceous to Oligocene thermal peak only and a maximum temperature of 90 °C (Fig. 4b).

Thus, forward modelling of multiple apatite populations (Fig. 4 and Appendix E) suggests that: (1) a Late Cretaceous to Oligocene thermal peak and maximum temperatures of around 90–100 °C are required to best reproduce the observed data and (2) thermal histories involving only a Pliocene to recent thermal peak do not satisfactorily reproduce the observed data. These forward modelling results provide a baseline for comparison to subsequent inversion modelling in which a single population is assumed, given we cannot separate the data without knowing the pre-depositional histories of different populations.

5.4. Inverse thermal history modelling approach

Thermal histories were subsequently inferred from the new and existing AHe, AFT and ZHe data using a Bayesian transdimensional Markov Chain Monte Carlo (MCMC) inversion approach implemented within the software QTQt (Gallagher, 2012). QTQt allows the user to select from a range of annealing (AFT) and diffusion (U-Th/He) models. For AFT data, we used the multi-kinetic annealing model of Ketcham et al. (2007), utilising the sample-average Dpar kinetic value for new data and an average of 0.40 Cl wt% for heritage data without composition/kinetic parameter measurements. ZHe and AHe data from euhedral (2 T) grains were jointly inverted taking into account radiation damage accumulation and annealing models of Guenthner et al. (2013) and Gautheron et al. (2009), respectively. Fragmented apatites with a single intact crystal termination (1 T) were modelled using the fragmentation model of Brown et al. (2013). AHe data from composite grain aliquots were not used in thermal modelling. Where available, published vitrinite reflectance (VR) data were also inverted, using the EasyRo% model of Sweeney and Burnham (1990).

QTQt utilises a Bayesian framework (Gallagher, 2012), with the prior incorporating a range of information, including a user-defined time-temperature domain and multiple thermal history constraints (e.g. present day temperature), discussed in more detail in Section 5.4.1 below. Using the MCMC approach, the user-defined modelling space is sampled by iteratively applying random perturbations to the thermal history or parameters. If the perturbation produces a thermal history with an improved posterior probability, it will tend to be accepted and that thermal history contributes to the final posterior probability distribution. A major advantage of the thermal modelling approach employed by QTQt is that the data determines the complexity of the thermal history, with the Bayesian approach favouring simpler solutions with adequate data fit over more complex ones, thus minimising the possibility of over interpreting thermal histories (Gallagher et al., 2009). Further, QTQt allows multiple samples to be modelled jointly as a vertical profile. An additional model parameter in vertical profile modelling is the temperature offset between the top and bottom samples, which can be fixed or allowed to vary through time. Gallagher et al. (2005) and Gallagher (2012) show that modelling multiple

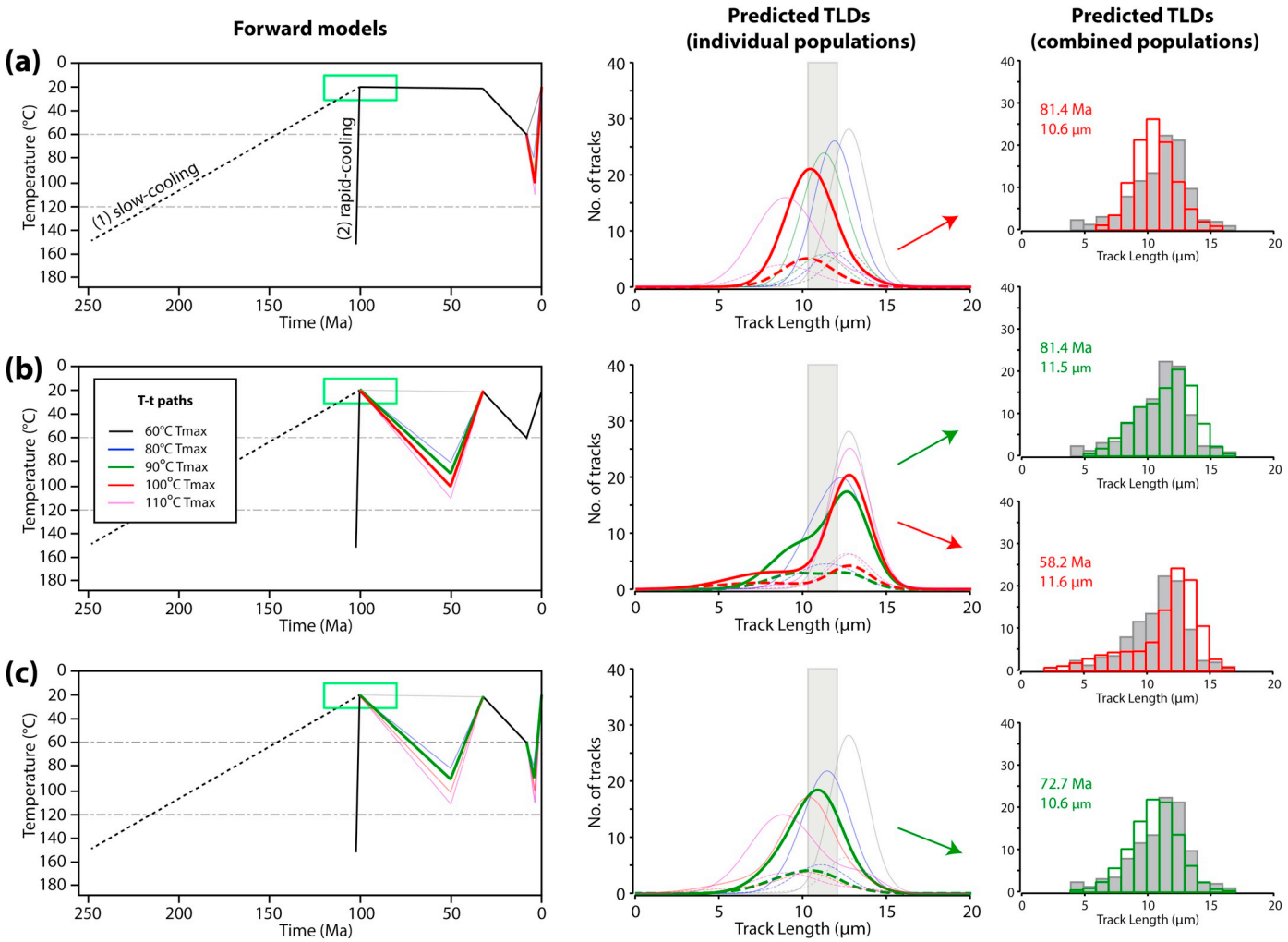

Fig. 4. Left: Forward models comprising two pre-depositional T–t paths (1–2), tested across a range of different post-depositional thermal histories (a–c). The green box represents a reasonable stratigraphic age range for the upper Ieru Formation samples. Middle: Predicted TLD curves for rapidly-cooled (solid line) and slow-cooled (dashed line) apatite populations, weighted based on a relative abundance of 4:1 (80:20%). Thicker red and green lines represent TLD curves from accepted models (i.e. models from which the weighted average of the predicted data fits within the observed data range). Light grey shade represents the MTL range from the observed data (e.g. 10.3 ± 0.2 to 12.1 ± 0.2 um). Right: TLD histograms (normalised to 100 tracks) comprising the combined rapidly-cooled and slow-cooled TLD curves for the four accepted models compared with a composite TLD histogram (dark grey) comprising observed data from three upper Ieru Formation samples. (For interpretation of the references to colour in this figure legend, the reader is referred to the web version of this article.)

samples in a vertical profile is generally preferable to modelling single samples as the latter can produce overly complex thermal histories as a result of overfitting or effectively fitting the noise in the data.

In all of the single sample and vertical profile thermal history models presented in Section 5.5, the MCMC sampler was initially allowed to explore the model space producing 50,000 t–T paths that were subsequently discarded (burn-in) prior to 250,000 t–T paths that were used to approximate the posterior distribution (post-burn-in). QTQt offers a range of individual outputs that should all be considered following any given model run. Basic descriptions of the individual outputs can be found in Section 5.5, with additional details provided in Gallagher (2012).

5.4.1. Additional model constraints

We define the basic prior for MCMC sampling in terms of a time range of the oldest age in the profile ± oldest age in the profile and a temperature range of 70° ± 70° for individual samples, and 100° ± 100 °C or 150° ± 150 °C for vertical profiles. The offset temperature parameter prior (e.g. the temperature difference between the top and bottom sample) was estimated based on a geothermal gradient of 27.5 °C/km and this offset temperature gradient was allowed to vary between 25 °C/km and 30 °C/km during the inversion. The model was allowed to explore pre-depositional thermal histories for all the samples. All models included some additional prior geological constraints (e.g. time-temperature regions through which all proposed thermal history models must pass) including at least: (1) the stratigraphic age and assumed depositional palaeotemperature of the sample and (2) the present day temperature of the sample. The stratigraphic age was determined from palaeontological age-dates on or near the sample, with an appropriate range (often 10–20 Ma) reflecting confidence in the age dating. The present day temperature for surface samples was 20° ± 10 °C or 10° ± 10 °C, depending on the elevation from which the samples were collected.

Initial modelling involved minimal constraints to explore the thermal history information retrievable from the data alone. Subsequent modelling involved at least two additional geological constraint domains, related to the well-constrained chronostratigraphy of the Oligocene to Late Miocene Darai Limestone. Sr-isotope and palaeontological dating enable estimates for the timing of initiation and cessation of Darai Limestone deposition (e.g. Eisenberg, 1996), while knowledge of Darai Limestone thickness from nearby geological traverses, reflection seismic and/or well data were used to estimate the

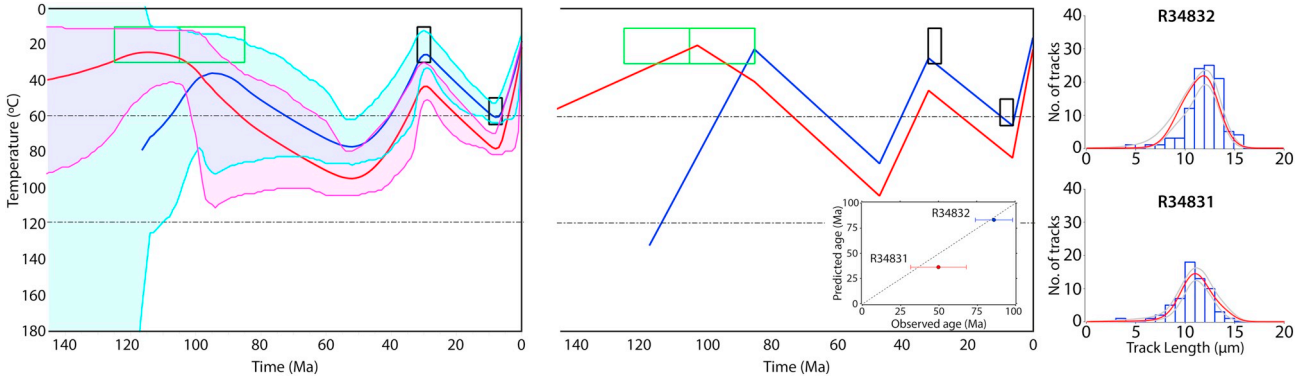

Fig. 5. Thermal history modelling results for a pseudo-vertical profile in the western Muller Range (WMR). The time-temperature domain on the left includes the expected model (weighted mean of the posterior distribution) with 95% confidence intervals for the uppermost (blue) and lowermost (pink) samples. The time-temperature domain in the centre includes the max posterior model (a relatively simple thermal history that fits the observed data adequately). Dot-and-dash lines represent the AFT PAZ. The green boxes represent the stratigraphic age/temperature constraint while the black boxes represent additional thermal history constraints discussed in Section 5.4.1. Observed (blue histograms) versus predicted (red curves) track length distributions and 95% confidence intervals (grey curves) are included on the right. The inset shows the observed AFT ages (and errors) plotted against the predicted ages. Track length distribution and age predictions were obtained from the max posterior model. (For interpretation of the references to colour in this figure legend, the reader is referred to the web version of this article.)

burial and potential temperature range of the sample based on geothermal gradients of 25 °C/km and 30 °C/km. Where time-temperature models deviated significantly from known Darai Limestone chronostratigraphic reference curves (Eisenberg, 1996), additional constraints were implemented between the initiation and cessation of deposition, thus redirecting the model to explore less-constrained components of the thermal history.

5.5. Inverse thermal history modelling results

Here we present thermal histories from four areas within the Muller Range (Fig. 2). We initially extracted thermal history information from individual Ieru Formation samples based on the inversion of AFT data alone (presented in Appendix F), followed by the joint-inversion of multiple samples along pseudo-vertical profiles combining AFT, He and VR data (where available). The pseudo-vertical profile modelling output includes the expected thermal history model (which is the weighted mean of the posterior distribution) presented with the 95% confidence intervals shown for the upper and lower samples (e.g. Fig. 5). The maximum posterior model (the best Bayesian model in that it tries to balance model simplicity with data fit) is also shown alongside the observed versus predicted data (e.g. Fig. 5). Unless otherwise stated, the temperatures reported are from the expected model and are from the uppermost sample for pseudo-vertical sections. However, the expected model is not a model sampled during the inversion. While it captures the general form of the thermal histories, it does not always represent the magnitudes of individual temperature changes that lead to better data fits. This is due to the smoothing over time and temperature when calculating the average of many thermal histories composed of linear heating and cooling segments. We observed that the expected model generally underestimates thermal maxima, by up to 20 °C versus the maximum posterior model that tends to fit the observed data better. Thus, the expected model should be considered alongside the maximum posterior model and the maximum temperatures reported below are considered to be conservative (low) estimates.

Post-deposition refers to the period following the deposition of the uppermost (i.e. youngest) stratigraphic sample, which is Ieru Formation in all cases below. Thermal peaks correspond to individual heating/cooling events; and multiple thermal peaks may characterise an individual samples thermal history. MaxT refers to the maximum post-depositional temperature and is therefore reached only once for a given thermal history.

5.5.1. Western Muller Range (WMR)

Ieru Formation samples R34831 and R34832 are located on the northern limb of the Muller Anticline with ~600 m of vertical stratigraphic separation (Fig. 2). Both samples were deposited in the mid-late Cretaceous (~125–85 Ma; e.g. White et al., 1973). Pseudo-vertical profile thermal history modelling (Fig. 5) indicates these samples experienced rapid cooling from a maximum temperature of ~100 °C in the Eocene (~55–50 Ma) to the initiation of Darai Limestone deposition (~30 Ma). The 95% credibility intervals suggest that Eocene to Oligocene cooling is well-recorded within the data, which implies comparably poorly resolved Late Cretaceous to Eocene heating in the order of ~40 °C (Fig. 5). The profile result suggests that a second thermal peak was reached at 8 Ma as the thermal history does not subsequently reach significantly higher temperatures. This timing is concurrent with the cessation of Darai Limestone deposition and is followed by the onset of rapid cooling to present day surface temperatures. Any post-Darai Limestone heating is poorly resolved, but is likely to be insignificant. Importantly, the modelled thermal history suggests that maxT was reached during the Eocene, with temperatures ~15–20 °C greater than at the Late Miocene (post-Darai) thermal peak.

5.5.2. South Strickland Gorge (Strick South)

A pseudo-vertical profile thermal history model was produced for the southern Strickland Gorge using data from three AFT and five ZHe single grain analyses, with sample separation deduced from the measured section of White et al. (1973). The profile includes Ieru Formation samples R34835 and PY113-1929.5, together with Koi Iange sample R34833 (Figs. 2 and 6). Palaeontological evidence suggests that the Ieru Formation samples were depositied in the Cretaceous (~130–80 Ma) and the Koi Iange sample was deposited in the latest Jurassic (~150–145 Ma; White et al., 1973). The uppermost (R34835) and lowermost (R34833) samples are characterised by 1140 m stratigraphic separation.

The resulting thermal history predictions are in reasonable agreement with the observed data (Fig. 6), with the thermal history model suggesting a significant phase of cooling from a thermal peak in the Campanian (~75 Ma) until Darai Limestone deposition (~30 Ma), necessitating rapid post-depositional heating of ~60 °C from the middle Cretaceous (~100 Ma) to the Campanian (~75 Ma). Post-Darai Limestone heating is negligible prior to cooling to present day surface temperatures. The thermal model suggests maxT was reached during the Campanian (~75 Ma) with temperatures ~15–20 °C greater than the Late Miocene (post-Darai) thermal peak.

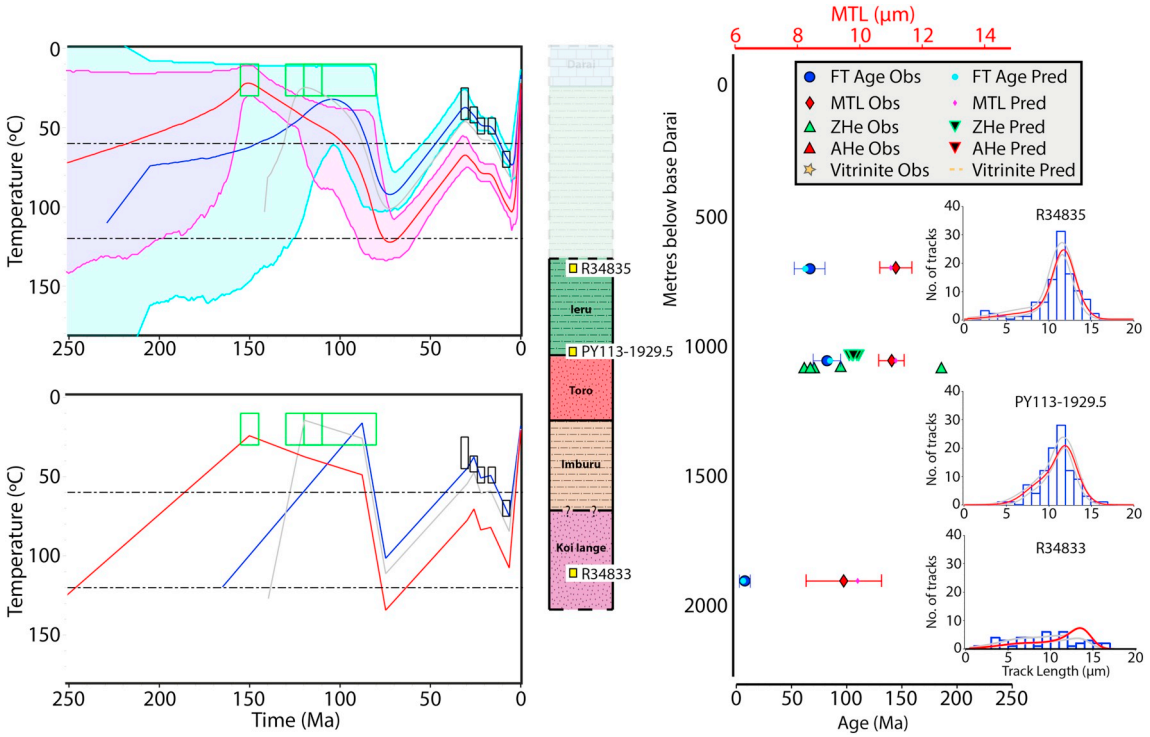

Fig. 6. Thermal history modelling results for a pseudo-vertical profile in the south Strickland Gorge (Strick South). The upper time-temperature domain (left) includes the expected model (weighted mean of the posterior distribution) with 95% confidence intervals for the uppermost (blue) and lowermost (pink) samples. The lower time-temperature domain (left) includes the max posterior model (a relatively simple thermal history that fits the observed data adequately). Dot-and-dash lines represent the AFT PAZ. The green boxes represent the stratigraphic age/temperature constraint while the black boxes represent additional thermal history constraints discussed in Section 5.4.1. The vertical profile (centre) is based on the measured sections of White et al. (1973). Observed versus predicted data (right) includes ages, mean track lengths (MTL), track length distributions, vitrinite reflectance (where available) and associated errors. Model predictions were obtained from the max posterior model. Legend for observed versus predicted data (top right) relevant to all subsequent thermal model figures. (For interpretation of the references to colour in this figure legend, the reader is referred to the web version of this article.)

5.5.3. North Strickland Gorge (Strick North)

A pseudo-vertical profile was produced for the northern Strickland Gorge based on the measured section of Jenkins and White (1970). Thermal modelling incorporated four AFT analyses from Ieru Formation samples R34809 and R34810, Toro Sandstone sample R34811 and basement sample R34808 (Figs. 2 and 7). These data were inverted alongside nine AHe and eight ZHe single grain ages from sample R34808, with an additional time-temperature constraint placed on this basement sample to reproduce its high-temperature K-Ar biotite emplacement age of 222 ± 4 Ma (Page, 1976). Limited palaeontological data in the vicinity of this profile necessitates wide stratigraphic age estimates of middle to late Cretaceous (~120–80 Ma) for the Ieru Formation samples and early Cretaceous (~132–122 Ma) for the Toro Sandstone sample. The uppermost (R34809) and lowermost (R34808) samples are characterised by ~2170 m stratigraphic separation (Fig. 7).

The resulting thermal history predictions provide an acceptable fit to the observed data (Fig. 7), except for the predicted ZHe single grain ages which fail to reproduce the dispersion in ages related to the very strong eU vs age trend observed within sample R34808 (cf. Figs. 3 and 7). This may be a limitation of the Guenthner et al. (2013) radiation damage-diffusion model, as suggested by Johnson et al. (2017) and Mackintosh et al. (2017).

The thermal history model (Fig. 7) suggests that these data record two periods of post-depositional cooling, consistent with the single sample models (R34809 and R34810; Appendix F). The earlier cooling to the initiation of Darai Limestone deposition (~30 Ma) began from a thermal maximum during the earliest Eocene (~55 Ma), necessitating prior heating of ~50 °C from the Late Cretaceous (~90 Ma). A second rapid cooling to present day surface temperatures initiated at ~7–6 Ma, necessitating ~20 °C of heating in the 1–2 Ma following the cessation of Darai Limestone deposition (~8 Ma). Thermal modelling suggests that considering the uncertainties, the earliest Eocene and Late Miocene thermal maxima were of approximately similar magnitude.

5.5.4. Lavani Valley (Lavani)

A pseudo-vertical profile was produced for Lavani Valley in the eastern Muller Range (Fig. 8) using constraints from field data (Mahoney et al., 2017) and the Lavani-1 well (Amoco, 1982; Denison, 1990). Thermochronology data was available for five samples, including Ieru Formation sample R34854, Toro Sandstone sample LAV#4 and Magobu and/or Koi Iange Formation samples R348900, R348901 and R348902.

Upper Ieru Formation sample R34854 has a particularly well-constrained stratigraphic context (120 m below Base Darai Limestone) and age (~88–84 Ma) from recent field work and associated palynological age determinations (Mahoney et al., 2017). Sample LAV#4, identified as Toro Sandstone based on lithology and stratigraphic context, was collected from a structurally very complex area and thus required a wide stratigraphic age constraint of ~145–125 Ma. Stratigraphic ages for samples R348900, R348901 and R348902 are also poorly constrained due to indeterminate palynology and a generally poor understanding of the stratigraphy at the base of the Lavani-1 well (e.g., Amoco, 1982; Denison, 1990). Here, these samples are interpreted to belong to the Magobu and/or Koi Iange formations, with stratigraphic constraints placed between ~165–135 Ma. Wider depositional constraints are favoured where the stratigraphy is poorly known, as they allow for the data to control the thermal history if there is appropriate information. The pseudo-vertical transect required the projection of surface samples R34854 and LAV#4 to the (now eroded) core of the Lavani Anticline above the Lavani-1 well. Prior to Late Miocene-

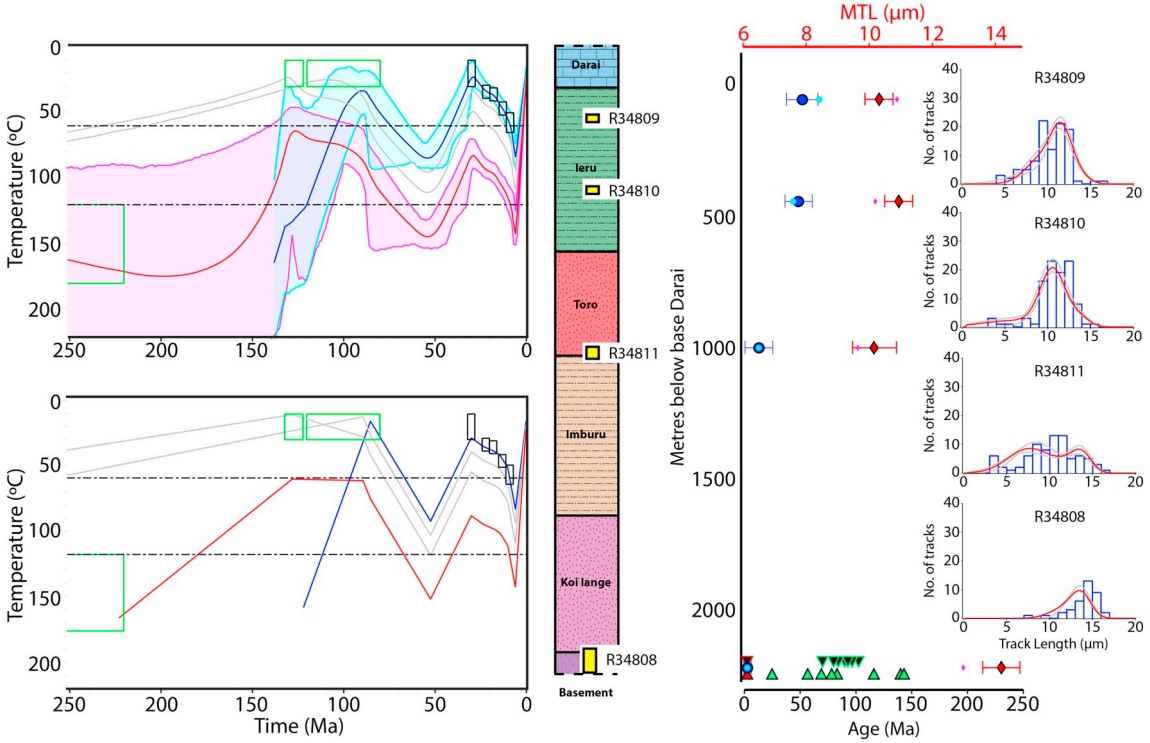

Fig. 7. Thermal history modelling results for a pseudo-vertical profile in the north Strickland Gorge (Strick North). Refer to Fig. 6 caption for model details and legend. The vertical profile (centre) is based on the measured sections of Jenkins and White (1970). (For interpretation of the references to colour in this figure legend, the reader is referred to the web version of this article.)

Pleistocene erosion, the uppermost (R34854) and lowermost (R348902) samples were separated by ~4250 m of stratigraphic section (Fig. 8).

Thermal modelling utilised AFT age and track length data from Ieru Formation sample R34854, along with AFT ages from Magobu Formation samples R34901 and R34902. These data were inverted together with two AHe and five ZHe single grain ages from lower Toro sample LAV#4, along with 12 ZHe single grain ages from Magobu Formation samples R34900 and R34902. Although not used here for

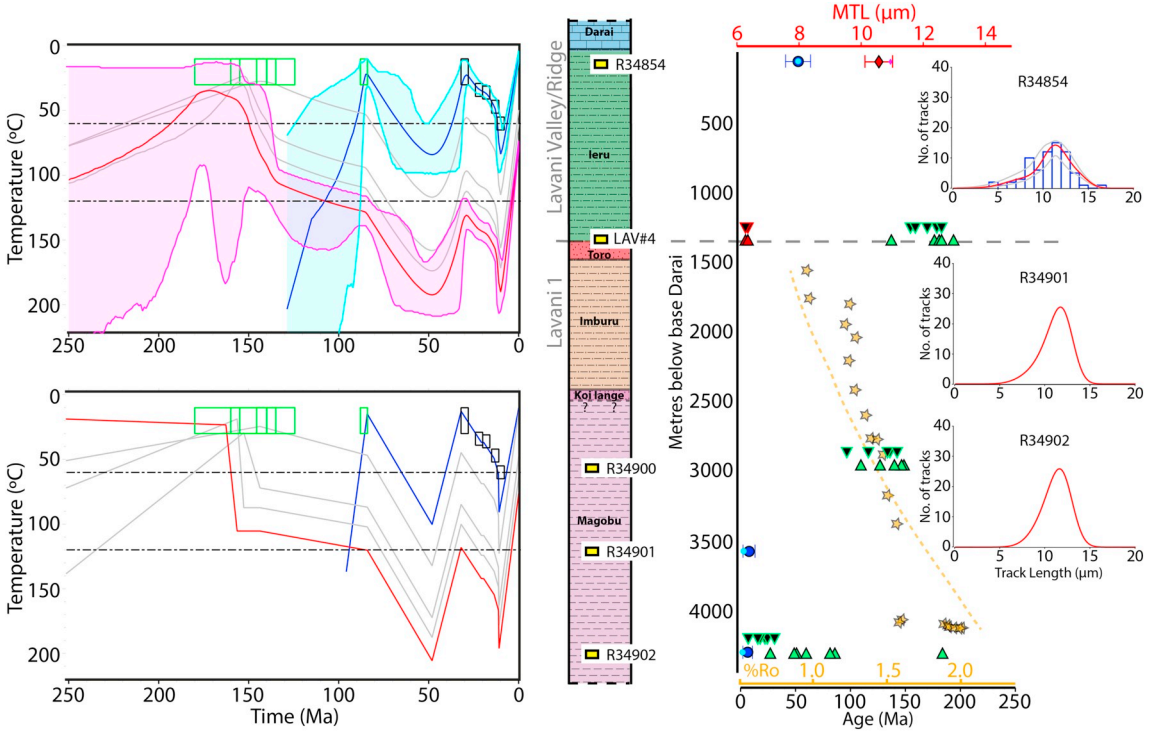

Fig. 8. Thermal history modelling results for a pseudo-vertical profile in the Lavani Valley (Lavani). Refer to Fig. 6 caption for model details and legend. Only predicted track length distributions are shown for samples R34901 and R34902, as no track lengths were measured.
The vertical profile (centre) is based on recent field work (Mahoney et al., 2017) and the Lavani-1 well (Amoco, 1982; Denison, 1990).

specific thermal history calibration, VR data from the Lavani-1 well (Amoco, 1982) provides additional validation of maxT predictions.

In general, the thermal model predictions reproduce the observed data well (Fig. 8). The predicted ZHe single grain ages again fail to reproduce the very strong age dispersion (eU vs age trend) observed within sample R34902 (cf. Figs. 3 and 8). The predicted VR reproduces the general observed trend reasonably well, although the observations are somewhat underpredicted and overpredicted at the top and bottom of the well respectively. This suggests that at the time of maxT the geothermal gradient was slightly lower than the ~25 °C/km gradient predicted by the model.

The resulting thermal history (Fig. 8) suggests these data record two periods of post-depositional cooling. The first period of cooling, from a thermal peak in the Early Eocene (~50–45 Ma) to the initiation of Darai Limestone deposition (~30 Ma), requires prior heating of ~60 °C from the Late Cretaceous (~85 Ma). The second period of cooling to present day temperatures commenced at ~5 Ma and requires post-Darai Limestone heating of ~15–20 °C. The magnitude of the Early Eocene and Late Miocene-Pliocene thermal maxima are very similar.

5.6. Summary: Muller Range T–t history

Both forward and inversion thermal history models for the Muller Range indicate two significant thermal peaks during the Late Cretaceous to Eocene and from the Late Miocene to recent (Figs. 4 and 9; Appendix F, Fig. F1). The consistency between forward and inversion models is reassuring, particularly given that only the former accounts for the possible influence of mixed apatite provenance through the inclusion of multiple independent pre-depositional thermal histories. Therefore, while AFT single grain ages are dispersed and not apparently related to the influence of any kinetic annealing factors, inherited tracks appear to have only a minor influence on the post-depositional thermal history.

The origin of Early Eocene to Oligocene cooling indicated by thermal history modelling is unknown, but if erosional, the event is represented stratigraphically as a regionally expansive Late Cretaceous to Early Oligocene unconformity (refer Section 2.2). In contrast, the Late Miocene to recent cooling is better known and likely related to the onset of uplift and erosion associated with the formation of the PFTB (e.g. Hill and Gleadow, 1989). Considering the uncertainties, thermal history models suggest that the Late Cretaceous to earliest Eocene (~75–55 Ma) and Late Miocene to Early Pliocene (~5–3 Ma) thermal maxima were of a similar magnitude (Fig. 9).

The seven Ieru Formation samples included in thermal modelling profiles experienced a maxT of ~75–100 °C, implying ~55–80 °C post-depositional heating and subsequent cooling prior to Darai Limestone deposition (Fig. 9). ZHe data from four Ieru Formation samples (Fig. 3) suggests that either: (1) maxT was not high enough for significant helium loss from variably radiation damaged grains, or (2) the radiation damage largely accumulated post-maxT. ZHe single grain ages are mostly similar to Ieru Formation stratigraphic ages (120–80 Ma), suggesting that the zircon grains underwent rapid cooling prior to deposition, consistent with indications of rapid pre-depositional cooling in the majority of thermal models (Fig. 9). Thus it seems highly likely that the majority of zircon grains in the Ieru Formation were sourced from contemporaneous volcanics, as suggested by Hill (1989a).

Modelling suggests that the two Toro Sandstone samples underwent ~90–100 °C of post-depositional heating to an Early Eocene maxT of ~110–120 °C (Fig. 9). As for the Ieru Formation samples, ZHe data from the Toro Sandstone suggests that either: (1) maxT was not high enough for significant helium loss from variably radiation damaged grains, or (2) the radiation damage largely accumulated post-maxT. The ZHe single grain ages cluster around the Triassic (~250–200 Ma; Fig. 3), consistent with the range of granitic basement ages reported from PNG (e.g. Page, 1976; Davies, 1990) and Eastern Australia (e.g. Murray, 2003; Glen, 2005). Thermal history modelling indicates protracted pre-depositional cooling (Fig. 9) suggesting that zircon grains in the Toro Sandstone may be sourced from slowly exhumed crystalline basement.

The five Koi Iange/Magobu Formation samples included in thermal modelling profiles attained a maxT of ~120–190 °C, requiring ~100–170 °C post-depositional heating (Fig. 9). ZHe single grain ages show a weak negative correlation with eU (Fig. 3), suggesting that the maximum temperatures experienced by the samples were sufficient to initiate preferential helium loss from the radiation damaged zircon grains. The grain with the lowest eU yielded a Triassic age (Fig. 3). Thermal modelling of Koi Iange/Magobu zircon suggests protracted cooling prior to deposition (Fig. 9), as also observed in the overlying Toro Sandstone zircon grains. Thus zircon grains within the Koi Iange/Magobu may have also been sourced from slowly exhumed crystalline basement.

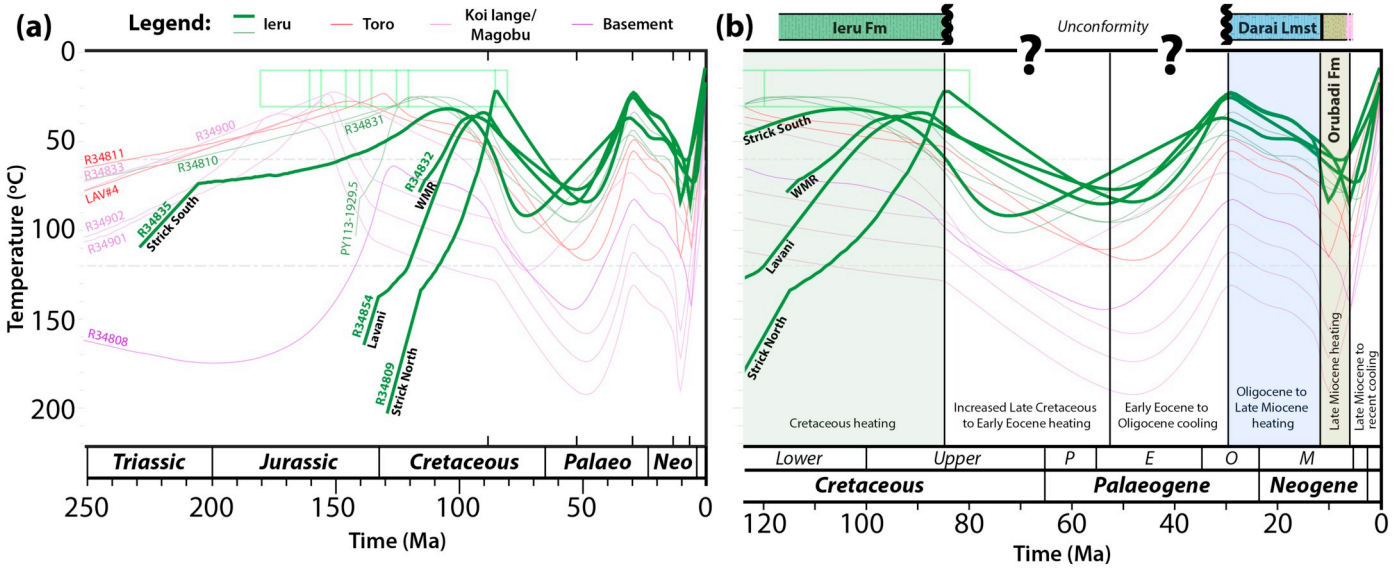

Fig. 9. Combined thermal histories of 14 samples from the Muller Range from (a) the Triassic to recent and (b) the mid-Cretaceous to recent. Time-temperature paths from pseudo-vertical profile expected models with the uppermost (Ieru Formation) sample for each profile included as a solid line. Grey dot-and-dash lines represent the AFT PAZ. The green boxes represent the stratigraphic age range for each sample. (For interpretation of the references to colour in this figure legend, the reader is referred to the web version of this article.)

The Strickland Gorge basement sample reached a maxT of ~145 °C, significantly lower than Koi Iange and Magobu samples from Lavani Valley and consistent with much less burial as also indicated from measured stratigraphic sections (cf. Figs. 7 and 8).

6. Discussion

In this section, we compare low-temperature thermochronology data from the Muller Range with the regional Papuan Basin dataset, before proposing potential mechanisms to explain the two major thermal peaks clearly recorded in data across the Muller Range. We subsequently discuss the wider implications of the Muller Range thermal history modelling for the evolution of the PFTB, the tectonic evolution of the PNG margin.

6.1. Regional thermal data

Our contemporary understanding of the thermal history of the Papuan Basin varies significantly both spatially and temporally. In contrast with observations from the Muller Range, thermochronology data from foreland areas provide significantly less evidence for a Late Cretaceous to Eocene thermal peak. Moreover, maxT is likely to have occurred in the Late Miocene to recent in parts of the Fly Platform including the Cecilia Graben, Morehead Graben and Omati Trough (e.g. Lund et al., 1998; Cooper et al., 2012). Hill and Gleadow (1990) found that fission track age distributions and lengths for upper Ieru Formation samples from wells throughout much of the Fly Platform and frontal structures of the KFTB (e.g. Iehi and Barikewa anticlines) were mostly similar, characterised predominantly by contemporaneous Albian to Cenomanian AFT ages and long track lengths (12.9–14.5 μm) (Fig. 10). These data are thus suggestive of minimal post-depositional annealing and maximum temperatures ≤60 °C. In contrast, upper Ieru Formation samples from the Muller Range are characterised by significantly younger Late Cretaceous to Early Eocene AFT ages and comparably much shorter track lengths (10.3–12.1 μm) (Fig. 10), with thermal history models necessitating a Late Cretaceous to Early Eocene thermal maximum in the order of ~75–100 °C (Fig. 9).

AFT from older, deeper samples in a number wells across the Fly Platform (e.g. Aramia-1, Komewu-1 and 2, Kanau-1 and Iamara-1) and frontal KFTB (e.g. Iehi-1) do however record some minor evidence for higher palaeotemperatures (Hill, 1989a). Detrital apatite in younger Eocene and Early Miocene samples from the Fly Platform have very long track lengths (e.g. Hill, 1989a) similar to those of the upper Ieru Formation, again suggesting that maxT is likely to have been ≤60 °C post-deposition. Thus Late Cretaceous to Eocene heating within the foreland region cannot be ruled out, but its magnitude must have been significantly less (~15–40 °C) than in the Muller Range (~55–80 °C).

In apparent contrast, Cooper et al. (2012) discuss a number of wells in the central foreland area (e.g. Koko-1, Langia-1 and Panakawa-1) where VR records an abrupt increase in maximum palaeotemperature below the Late Cretaceous to Eocene unconformity. Notably, this observed trend relies heavily on very limited VR data from above the Ieru Formation (e.g. in the Langia-1 well). The significant increase in maturity within the Ieru Formation is traditionally interpreted as being related to increased heat flow associated with Late Cretaceous to Palaeocene Coral Sea Rifting, with accompanying uplift and erosion of up to ~3300 m of overlying sediments (Cooper et al., 2012). Similarly, Hill et al. (2010) used combined AFT and VR data from the Kanau-1 well on the Darai Plateau (Fig. 10) to suggest Late Cretaceous to Palaeogene heating, uplift and erosion of > 2000 m of sediments above the Ieru Formation prior to Darai Limestone deposition. The deposition and subsequent removal of this thickness of sediment would demand a thermal perturbation comparable to or in excess of that proposed here for the Muller Range. However recent work on the Kanau-1 and Bosavi-1 wells, including analyses of porosity profiles, pressures, AFT and VR data, led Callot et al. (2017) to conclude that < 600 m of Late Cretaceous to Palaeogene sediments were eroded from the Darai Plateau prior to deposition of the Darai Limestone. Cooper et al. (2012) propose that elevated palaeotemperature data may relate to the selective advection of hot fluids from Early Miocene-Pliocene volcanism through sandier units within the basal stratigraphy. Interestingly, the inclusion of heat advection into their burial history modelling reduces the earlier Late Cretaceous to Eocene burial related heating to magnitudes more consistent with those predicted from AFT data across the foreland and much less than those recorded within the Muller Range.

Duddy et al. (1994) also recognised high maximum palaeotemperatures in the Ieru Formation and overlying syn-orogenic sequence in an unidentified well from the foreland region. They suggested that these observations related to post-Miocene advection of hot fluids from the thrust front, through confined aquifers near the Darai Limestone and syn-orogenic sequence contact, and potentially in the Toro Formation. It seems equally likely that hot fluids could have related to Plio-Pleistocene volcanism. Nevertheless, the inconsistencies between AFT and VR data, and spatially between wells, highlights that the spatio-temporal thermal history of the foreland region neighbouring the Muller Range is likely to be complex.

6.2. Late Cretaceous to Early Eocene heating

Thermal models clearly indicate a significant Eocene cooling event occurred across the Muller Range, thus requiring significant earlier heating. Late Cretaceous to Palaeocene Coral Sea Rifting is the most common explanation for: (1) pre-Darai Limestone heating recorded in thermochronology and palaeotemperature data (e.g. Hill and Gleadow, 1990) and, (2) uplift and erosion interpreted from the stratigraphic record (Brown et al., 1980; Home et al., 1990) and regional seismic reflection data (Schofield, 2000). However, as discussed above, the Papuan Basin dataset clearly records significant spatio-temporal variation and this needs to be taken into consideration in any regional explanation.

Any reasonable hypothesis for Late Cretaceous to Eocene heating (e.g. 55–80 °C) in the Muller Range must account for the absence of such a robust thermal perturbation across the foreland and frontal KFTB regions. We suggest that margin architecture and continental collision in northern PNG are central to understanding the thermal history of the margin. We do not wish to completely disregard the influence of regional explanations such as increased basal heat flow in the Late Cretaceous to Palaeocene associated with Coral Sea rifting (Home et al., 1990), or mantle upwelling (Muller et al., 2016), but rather to focus on accounting for the local variations recorded in the thermochronology dataset.

We suggest that long-lived crustal extension and associated burial may provide a geologically plausible explanation for Late Cretaceous to Eocene heating in the Muller Range. Indeed, major extensional structures are suspected beneath and adjacent to the Muller Range (e.g. Hill, 1989b; Buchanan and Warburton, 1996; Mahoney et al., 2017), but are poorly understood primarily due to poor sub-surface constraints typical of the old belt. On the Fly Platform, extensional structures have undergone significantly less or no shortening and are consequently better constrained by geological and geophysical data, providing valuable analogues for understanding the extensional architecture of the Papuan Basin. These faults show compelling evidence of being long-lived from early Mesozoic to Neogene (e.g. Fischer and Warburton, 1996; Kawagle and Meyers, 1996; Bennett et al., 2000; Schofield, 2000; McConachie and Lanzilli, 2000; McConachie et al., 2000; Hill et al., 2010). Furthermore, they noticeably control Cretaceous Ieru Formation depocentres across the Fly Platform (e.g. McConachie and Lanzilli, 2000; Schofield, 2000) and in the frontal KFTB (e.g. Sari et al., 1996). In fact, continued extension along major structures during the westward migration of the basin axis in the middle Cretaceous (Jenkins, 1974; Sari et al., 1996) may have been crucial to the preservation of significantly thicker sequences in hangingwall blocks versus often uplifted and

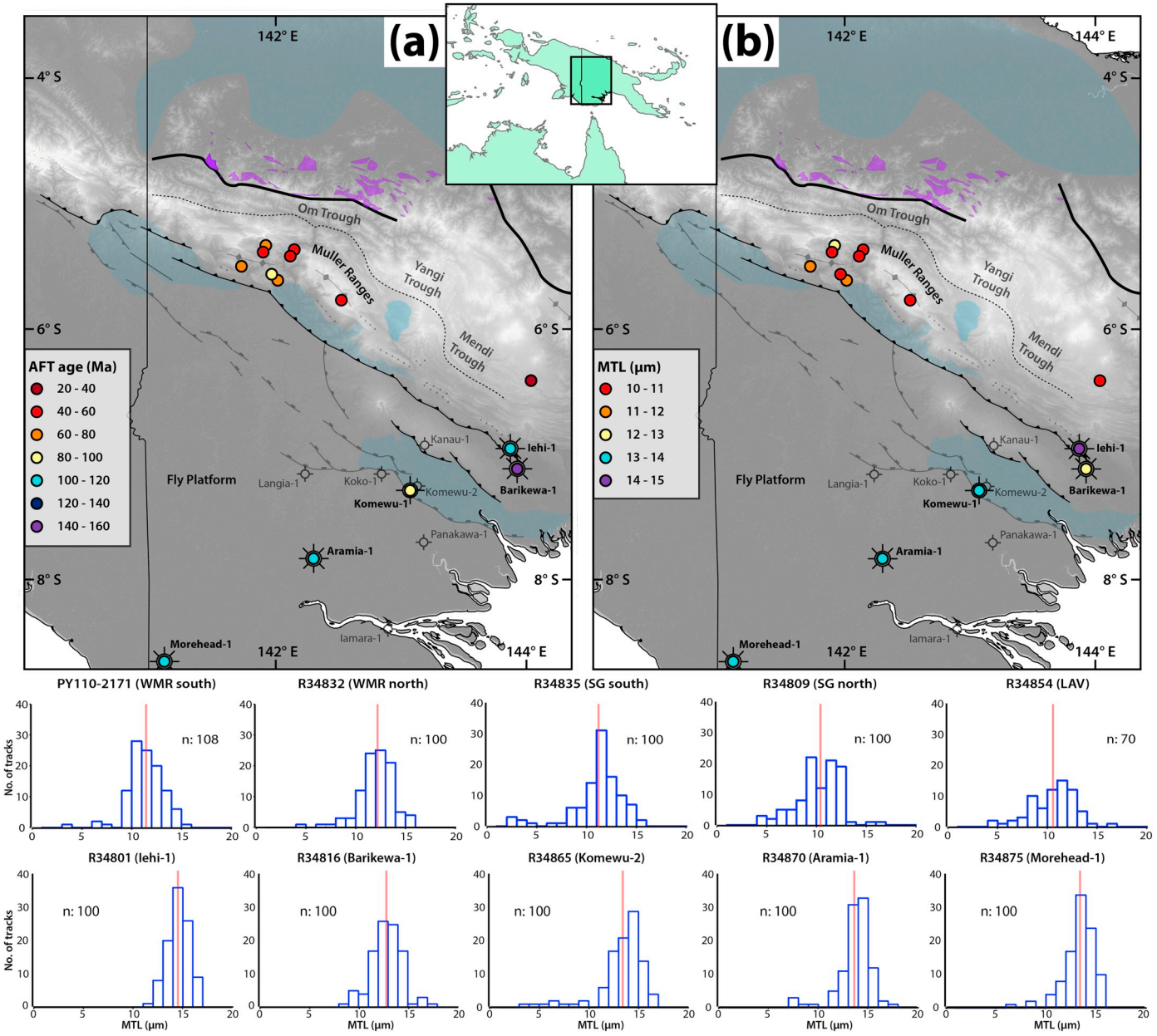

Fig. 10. (a) AFT age and (b) mean track length (MTL) for Ieru Formation samples across the Muller Range and Fly Platform. Refer to Fig. 1 for detailed legend. Track length distributions for five representative Ieru Formation samples from the Muller Range (upper bottom) and Fly Platform (lower bottom). Red line represents MTL and n is the number of track lengths measured in AFT analysis. (For interpretation of the references to colour in this figure legend, the reader is referred to the web version of this article.)

eroded footwall blocks (e.g. Schofield, 2000).

The youngest preserved Ieru Formation in the Muller Range is Late Turonian/Early Coniacian (~88 Ma, Mahoney et al., 2017), while the oldest overlying Darai Limestone is Late Oligocene (~32 Ma, Eisenberg, 1996), as a result much of the Late Cretaceous to Oligocene history is unknown. This prominent unconformity is commonly interpreted as representing the cessation of deposition across the area prior to commencement of Darai Limestone deposition in the Oligocene (e.g. Home et al., 1990; Hill et al., 2000; Norvick, 2003). But the results of the Muller Range thermal modelling presented here necessitate 55–80 °C of heating of the upper Ieru Formation over this time, which is unlikely to be explained without invoking burial. Further, any proposed mechanism should explain significantly less heating across the adjacent foreland. Volcanism may provide an alternate mechanism but can be discounted given the absence of Late Cretaceous to Eocene volcanics recorded in the region.

We suggest that major basin-bounding faults beneath the Muller Range were actively accommodating sediments throughout the Late Cretaceous to Eocene, providing a plausible mechanism for heating the underlying Ieru Formation sediments. In fact, given observations of significantly thicker hangingwall sequences across structures on the Fly Platform, it would be somewhat anomalous if basinward faults beneath the Muller Range did not also accommodate significantly thicker hangingwall sequences. In the Turonian (~90–88.5 Ma; upper Giero/lower Ubea) burial rates significantly increased towards the Muller Range in the northwest, with the uppermost Ieru Formation characterised by very significant spatial variations in thickness, highlighting complex margin architecture at this time, including an embayment in the present day Muller Range area (Sari et al., 1996). It therefore seems plausible that extension along major pre-existing faults beneath the present day Muller Range resulted in the formation of an active depocentre from the Late Cretaceous to Eocene.

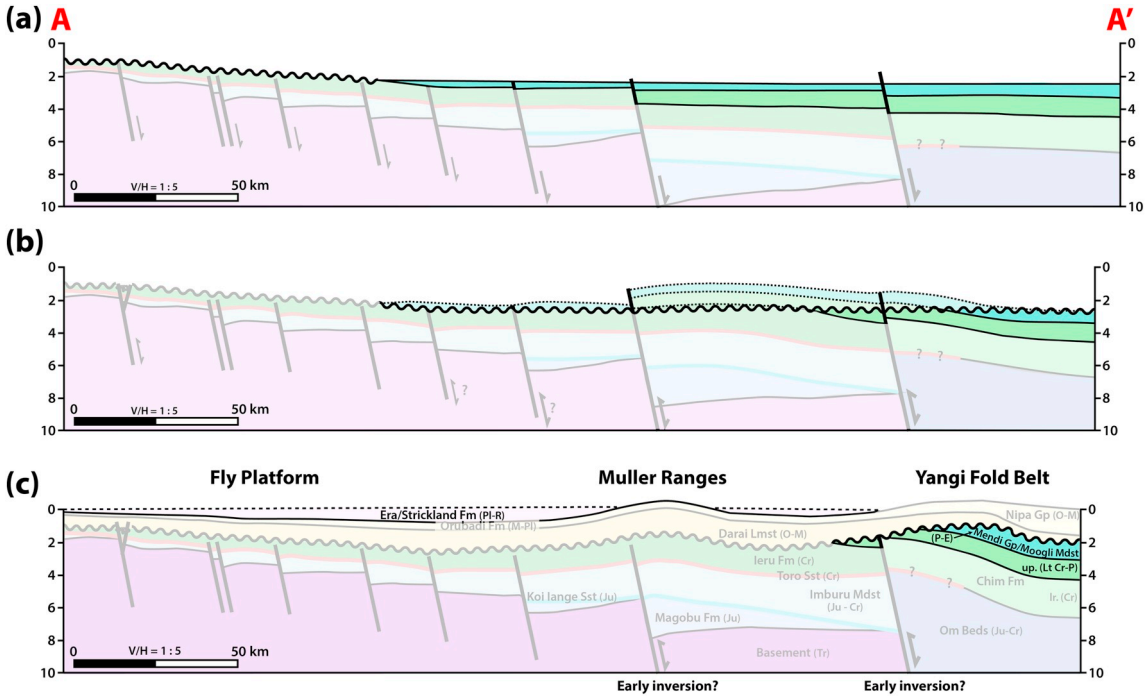

Fig. 11. Proposed schematic evolution of the eastern Muller Range based on low-temperature thermochronology data and thermal modelling: (a) Early Eocene distribution of Late Cretaceous to Eocene sediments (opaque colours); (b) Eocene to Oligocene uplift and erosion associated with collision of the Sepik Terrane (Fig. 1a) in western PNG; (c) Late Miocene to Pliocene uplift associated with the initiation of the PFTB. Note syn-orogenic sediments (e.g. Era/Strickland formations) were deposited to the northeast and southwest of the Muller Range from the Late Miocene to recent. (For interpretation of the references to colour in this figure legend, the reader is referred to the web version of this article.)

Therefore, as the Papuan Basin retreated towards the northwest during the Late Cretaceous, and while active extensional structures on the largely emergent Fly Platform were sheltering Ieru Formation from regional uplift, similar structures in more basinward areas (including the present day Muller Range) were potentially actively accommodating rapid sedimentation (Fig. 11a). Extension and associated subsidence may have accommodated sedimentation into the Palaeocene and Eocene, as recorded in the Yangi Fold Belt < 50 km to the northeast (Fig. 2) where an almost complete Late Cretaceous (Chim Formation) to Eocene (Mendi Group) sequence up to an estimated 4000 m thick is preserved (e.g. Davies, 1983; Gunson et al., 1997, 2000). High global eustatic sea level over this time (e.g. Haq et al., 1987; Haq, 2014) may have maximised the available accommodation space and thus continued extension may not have even been necessary. Assuming that Late Cretaceous to Eocene heating was primarily related to burial, sediment thickness beneath the Muller Range may have been up to 2200–3200 m at a palaeogeothermal gradient of 25 °C or up to 1800–2600 m at a paleogeothermal gradient of 30 °C. This magnitude of burial seems reasonable compared to the preserved sequence in the Yangi Fold Belt. However it is largely unclear whether this Late Cretaceous to Eocene sequence was regionally continuous (e.g. Fig. 11a) or restricted to local depocentres. Further low-temperature thermochronology data from the WPFTB could contribute to resolving this question.

6.3. Early Eocene to Oligocene cooling

Thermochronology data across the Muller Range also clearly record an Eocene to Oligocene cooling event of ~55–80 °C (e.g. Fig. 9). As discussed in Section 6.1, AFT data across the Fly Platform records significantly less heating and cooling despite proximity to rifting in the Coral Sea. A rift-related heating mechanism is therefore unlikely to explain the magnitude of the thermal peak observed in the distal Muller Range located > 100 km further to the NW. Thus, we suggest that Cenozoic collision and continental accretion at the northern PNG margin provides a possible mechanism to explain Eocene cooling in the Muller Range. We suggest the collision of the Sepik Terrane (Fig. 1a) provides an appropriate process for significant uplift and erosion, particularly given the Muller Range is underlain by significant extensional structures and located < 50 km south of the suture zone delineated by the April Ultramafics (Fig. 1).

The geology and extent of the Sepik Complex is particularly poorly known due to the overlying Sepik and Ramu basins, nevertheless it is generally considered to make up a large proportion of the Mobile Belt (e.g. Zahirovic et al., 2016). Further ambiguity exists due to the Late Miocene collision of the Finisterre and Adelbert terranes, which produced significant structural complexity and are the primary events recorded in isotopic data across the Mobile Belt (e.g. Crowhurst et al., 1996; Hill and Raza, 1999). Further plate realignment in the Pliocene led to intense sinistral strike-slip deformation that has also significantly disarticulated the northern PNG margin (Pigott et al., 1985; Crowhurst et al., 1997).

If the Sepik Terrane collided with northern PNG in the Palaeogene, it seems unlikely that the fold belt was undisturbed, particularly given its location directly adjacent to the suspected suture delineated by the April Ultramafics (Fig. 1a). As a comparison, the seismically active thrust front associated with the recent collision of the much smaller Finisterre and Adelbert terranes is > 250 km from the suspected suture (Marum Ophiolite) (Fig. 1a). Our new low-temperature thermochronology data and thermal models show a significant period of Eocene to Oligocene cooling across the Muller Range and provide, for the first time, potential evidence from the fold belt of the initiation of collision at the PNG margin.

We suggest that the Eocene to Oligocene collision of the Sepik Terrane in western PNG reactivated extensional structures across the western Papuan Fold and Thrust Belt and Fly Platform, including major faults around the present day Om Beds and Muller Range (Fig. 11b). This activity uplifted Late Cretaceous to Eocene strata that subsequently underwent extensive erosion prior to the initiation of Darai Limestone

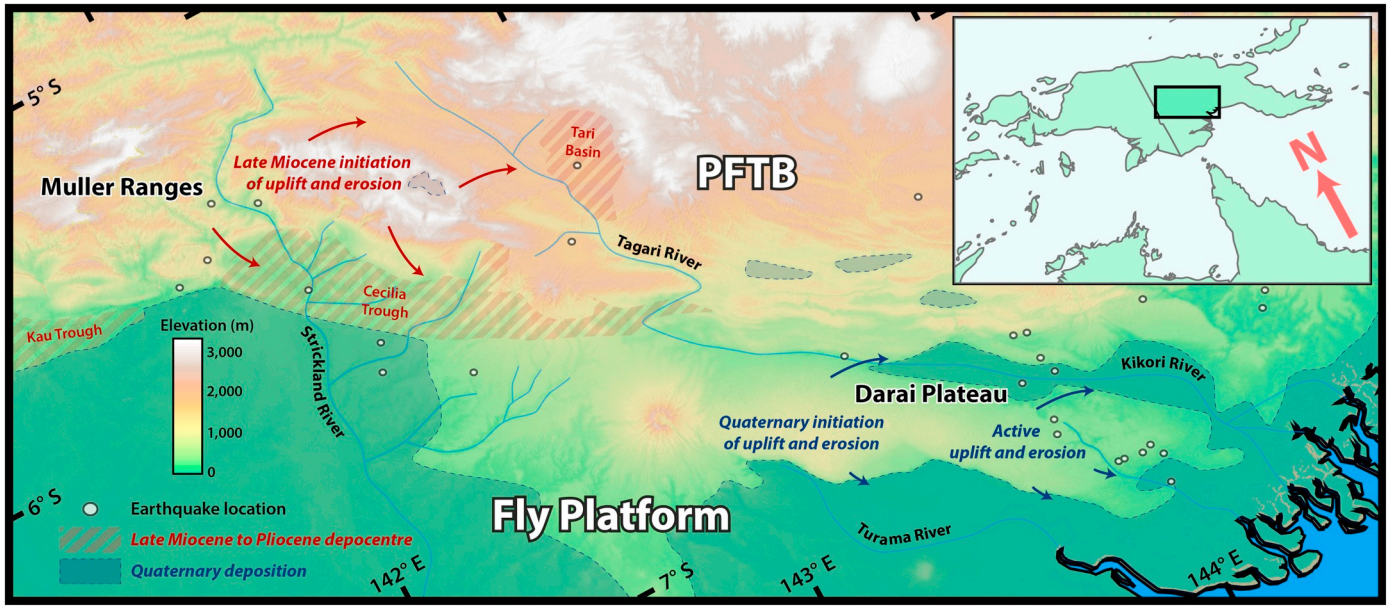

Fig. 12. Drainage system and syn-orogenic depocentre distribution across the Fly Platform and frontal PFTB. Arrows show the dominant direction of sediment transport away from uplifted areas.
Earthquake locations sourced from Ekström et al. (2012).

deposition in the Oligocene. The > 40 km wide Darai Plateau on the Fly Platform (Fig. 1b and 13) may provide a contemporary analogue for this style of large-wavelength inversion. The uplift and erosion was restricted to an area directly to the south and southwest of the colliding terrane, with Late Cretaceous to Eocene sediments preserved in the adjacent Yangi Fold Belt (e.g. Fig. 2). These sediments led Hill et al. (2000) and Norvick (2003) to suggest that the coastline was located in the Yangi area over this time. However, missing section indicated from this study suggests that the Late Cretaceous to Eocene coastline may have been located further south, at least to the south of major extensional structures within and adjacent to the Muller Range.

Given this model invokes Eocene to Oligocene uplift and erosion, we may expect to see an angular unconformity at the Ieru Formation/Darai Limestone contact throughout the Muller Range. However, only limited evidence exists for this angular unconformity in either geological or geophysical data. There are several reasons why this postulated angular unconformity is not prominently evident in the Muller Range, including: (1) Ieru Formation outcrop weathers quickly and is thus extremely limited; (2) 2D seismic reflection data is generally of insufficient quality to identify subtle dip variations; (3) the uppermost Ieru Formation is usually drilled with air-foam with no rock returns, and (4) the Ieru Formation is commonly highly deformed at the contact with the mechanically strong Darai Limestone, particularly near major inversion faults (e.g. Mahoney et al., 2017) making it impossible to discriminate between pre- and post-Darai Limestone structuring. Thus we do not think it is reasonable to reject this model based on a lack of local evidence to support an angular unconformity.

6.4. Late Miocene to recent

Thermal history models also provide significant insight into the Late Miocene to recent evolution of the Muller Range. High palaeotemperatures suggested from AFT and VR data from Lavani Valley and Strickland Gorge have previously been attributed to thick syn-orogenic sediment depocentres (e.g. Cecilia Trough, Tari Basin) extending across the Muller Range prior to Late Miocene to recent uplift and erosion (Amoco, 1982; Hill, 1989a). However, low-temperature thermochronology data consistently record only minor post-Darai Limestone heating (< 20 °C), suggesting: (1) < 1000 m of syn-orogenic burial prior to uplift of the Muller Range, and (2) the absence of a significant regional heating event associated with Late Miocene to Pliocene volcanics and intrusives identified throughout the Muller Range (e.g. Fig. 2). Thermal history models suggest that cooling, interpreted here to relate to uplift and erosion, began in the Late Miocene (~10–5 Ma) in the Strickland Gorge, consistent with the cooling of Strickland Basement (R34808) below the AFT closure temperature at ~4 Ma (Hill and Gleadow, 1990).

Therefore, the thick Late Miocene to recent syn-orogenic sediments characterising neighbouring depocentres are likely to have thinned significantly, or have been completely absent, across the Muller Range. Although facies changes (Mahoney et al., 2017) and angular unconformities (e.g. Hornafius, 1993) have been observed towards the centre of the Muller Range, evidence of onlap has yet to be recognised on either flank. The present day Darai Plateau may represent a useful analogue for the Muller Range at ~5 Ma. Active seismicity indicates the Darai Plateau is currently undergoing uplift and erosion, while Quaternary sediments are being deposited to the northeast and southwest by the Kikori and Turama river systems, respectively (Fig. 12). In the Late Miocene, the Muller Range was undergoing uplift and erosion perhaps representing the most easterly extent of thick-skinned deformation documented in the NGFB in Indonesia (Weiland and Cloos, 1996; Cloos et al., 2005). Over this time, sediments were being deposited to the northeast (Tari Basin) and southwest (Cecilia Trough) by the proto-Tagari and Strickland river systems, respectively (Fig. 12). This suggests that the Muller Range formed early in the evolution of the Western Papuan Fold and Thrust Belt and coeval to the formation of thick syn-orogenic depocentres to the northeast and southwest.

7. Conclusion

We have combined new and existing low-temperature thermochronology data with modern thermal history modelling techniques to provide insight into the thermotectonic history of the Muller Range in western PNG. Our models suggest two major episodes of cooling during the Cenozoic. The oldest cooling episode occurred during the Eocene to Oligocene and plausibly relates to the removal of 1500–3000 m of Late Cretaceous to Eocene section from the Muller Range area. The general absence of a thermal event at this time on the Fly Platform suggests that

uplift and erosion in the Muller Range resulted from a local influence such as the collision of the Sepik Terrane with the northwest PNG margin. The youngest cooling episode during the Late Miocene to recent resulted from the west-to-east propagation of uplift and erosion associated with the formation of the Papuan Fold and Thrust Belt. The Muller Range underwent initial uplift in the Late Miocene, early in the evolution of the Western Papuan Fold and Thrust Belt and coeval to the formation of thick syn-orogenic depocentres to the northeast and southwest. The new data and interpretations presented here provide new constraints on the evolution of the Papuan Fold and Thrust Belt and have significant implications for tectonic reconstructions of PNG.

Acknowledgements

This work was funded by Papuan Oil Search, ExxonMobil and Santos. Luke Mahoney acknowledges support of an Australian Government Research Training Program Scholarship. We gratefully acknowledge Ling Chung and Vhairi Mackintosh for their assistance with low-temperature thermochronology data acquisition and modelling. The University of Melbourne Thermochronology Lab receives infrastructure support under the AuScope program of the National Collaborative Research Infrastructure Strategy (NCRIS). Many thanks to Hugh Davies and Jeremy Iwanec for insightful discussion and assistance accessing heritage data. Mitch Furnass is acknowledged for the collection of samples during the P'nyang-Blucher geological survey. We appreciate comments and suggestions from the Editor (Rob Govers), Hugh Davies and Uri Shaanan.

Appendix A

A.1. Apatite fission track method

Apatite grains were mounted in epoxy resin (250 μm thick), ground and polished to an optical finish (1 μm) and etched in 5 N HNO_3 at 20 °C for 20 s to reveal the spontaneous fission tracks. Reflected light images of etched mounts were considerably improved through the application of a gold coating (5–7 nm thick) using a vacuum unit. Apatite grains favoured for analysis were characterised by (1) polished surfaces parallel to the crystallographic c-axis, (2) homogeneous track distributions, and (3) minimal dislocations and imperfections.

AFT analysis was carried out using an autonomous digital microscope operating under *Autoscan TrackWorks* control software (Gleadow et al., 2009). Spontaneous tracks were counted automatically on digital image sets using *FastTracks* image analysis software and manually corrected where necessary (Gleadow et al., 2009). *FastTracks* was also used to manually measure 3D confined track lengths and automatically determine their orientations in regards to the crystallographic c-axis direction; allowing anisotropic annealing and etching to be addressed in subsequent thermal modelling. Dpar (the long axis of a track etch pit parallel to the crystallographic c-axis) was used as a proxy for chemical composition (Donelick, 1993).

^{238}U concentrations were measured directly using laser-ablation ICP-MS (inductively coupled mass spectrometry) with uranium concentrations calibrated against NIST 612 standard glass with Mud Tank and Durango apatite as secondary reference standards. Fission Track ages were calculated from the spontaneous track densities and single grain ^{238}U concentrations following Hasebe et al. (2004) using an aggregate constant of 2.001×10^{-3}.

A.2. (U-Th-Sm)/He method

(U-Th-Sm)/He analysis followed the protocol of House et al. (2000) for laser He extraction from both apatite and zircon grains. Clear, non-fractured grains were generally favoured for analysis, but given low apatite yields were not always available. Grain geometries were microscopically imaged and measured for applying α-ejection correction (Farley, 1996), prior to being loaded into platinum capsules. Although single grain analyses were preferred, in some cases ^{4}He yields were too low and multiple grain capsules were required.

Apatite grains were outgassed using laser under vacuum at 900 °C for 5 min, while zircon grains were outgassed at 1200 °C for 20 min. ^{4}He content was determined using a Balzers quadrupole mass spectrometer with a hot blank run after each extraction to verify complete outgassing. Outgassed grains were then dissolved and analysed for parent isotopes using solution ICP-MS. Analytical uncertainties for The University of Melbourne helium facility are conservatively assessed to be ~6.2%, including the α-ejection correction, an estimated 5 μm uncertainty in grain dimensions, gas analysis (estimated as < 1%) and ICP-MS analytical uncertainties. This does not account for possible heterogeneity in parent isotope distributions.

Appendix B

Table B1
Existing Muller Range apatite fission track dataset obtained by Hill and Gleadow (1989; 1990) using the external detector method

Region	Formation	No. of grains	ρ_D (N_D)	ρ_s (N_s)	ρ_i (N_i)	Correlation Coefficient	[b]Dispersion	Chi-squared probability	Pooled age	[a]Central age	Uranium	N_L	MTL	SD
Sample No.			x10^{6}cm^{-2}	x10^{6}cm^{-2}	x10^{6}cm^{-2}		(%)	(%)	(Ma ± 1σ)	(Ma ± 1σ)	(ppm)		(μm ± SE)	(μm)
WMR														
R34832	Ieru Fm	20	1.240 (5282)	0.737 (777)	1.869 (1971)	0.929	21	< 1	85.6 ± 4.0	79.8 ± 8.2	19.6	100	12.1 ± 0.2	1.77
R34831	Ieru Fm	20	1.240 (5282)	0.169 (189)	1.165 (1300)	0.824	65	< 1	31.7 ± 2.5	47.2 ± 8.7	12.2	61	10.7 ± 0.2	1.85
Strick North														
R34809	Ieru Fm	20	1.197 (5140)	0.734 (330)	2.610 (1173)	0.938	45	< 1	58.7 ± 3.8	46.9 ± 7.6	28.6	100	10.3 ± 0.2	2.23

(*continued on next page*)

Table B1 (*continued*)

Region	Formation	No. of grains	ρ_D (N_D)	ρ_s (N_s)	ρ_i (N_i)	Correlation Coefficient	[b]Dispersion	Chi-squared probability	Pooled age	[a]Central age	Uranium	N_L	MTL	SD
Sample No.			x10^{6}cm^{-2}	x10^{6}cm^{-2}	x10^{6}cm^{-2}		(%)	(%)	(Ma ± 1σ)	(Ma ± 1σ)	(ppm)		(μm ± SE)	(μm)
R34810	Ieru Fm	21	1.197 (5140)	0.346 (299)	1.406 (1214)	0.792	43	< 1	51.4 ± 3.5	45.6 ± 6.1	15.4	100	10.9 ± 0.2	2.16
R34811	Toro SST	21	1.197 (5140)	0.054 (44)	1.188 (967)	-0.102	205	< 1	9.5 ± 1.5	12.5 ± 6.0	13	81	10.1 ± 0.4	3.15
R34808	Basement	31	1.197 (5140)	0.066 (44)	3.632 (2409)	0.229	50	8.5	3.8 ± 0.6	4.0 ± 0.7	39.7	37	14.1 ± 0.3	1.8
Strick South														
R34835	Ieru Fm	20	1.24 (5282)	0.594 (510)	1.990 (1708)	0.976	33	< 1	65.0 ± 3.5	63.1 ± 7.9	20.9	100	11.1 ± 0.3	2.58
R34833	Koi Iange	30	1.24 (5282)	0.031 (30)	1.249 (1228)	0.109	140	< 1	5.3 ± 1.0	7.9 ± 2.5	13.1	43	9.5 ± 0.6	3.96
Lavani														
R34854	Ieru Fm	20	1.237 (5142)	0.671 (467)	2.892 (2012)	0.963	34	< 1	50.0 ± 2.8	51.8 ± 5.6	30.7	70	10.6 ± 0.3	2.27
R34901	Magobu Fm	40	1.224 (4245)	0.145 (112)	2.495 (1931)	0.092	92	< 1	12.4 ± 1.2	9.9 ± 4.4	26.7	10	13.2 ± 1.0	-
R34902	Magobu Fm	30	1.224 (4245)	0.031 (19)	1.490 (910)	0.249	117	< 1	4.5 ± 1.0	6.5 ± 2.1	16	1	14.2	-

[a] Central ages calculated following Galbraith (2005)
[b] Dispersion calculated in RadialPlotter (Vermeesch, 2008)

Appendix C

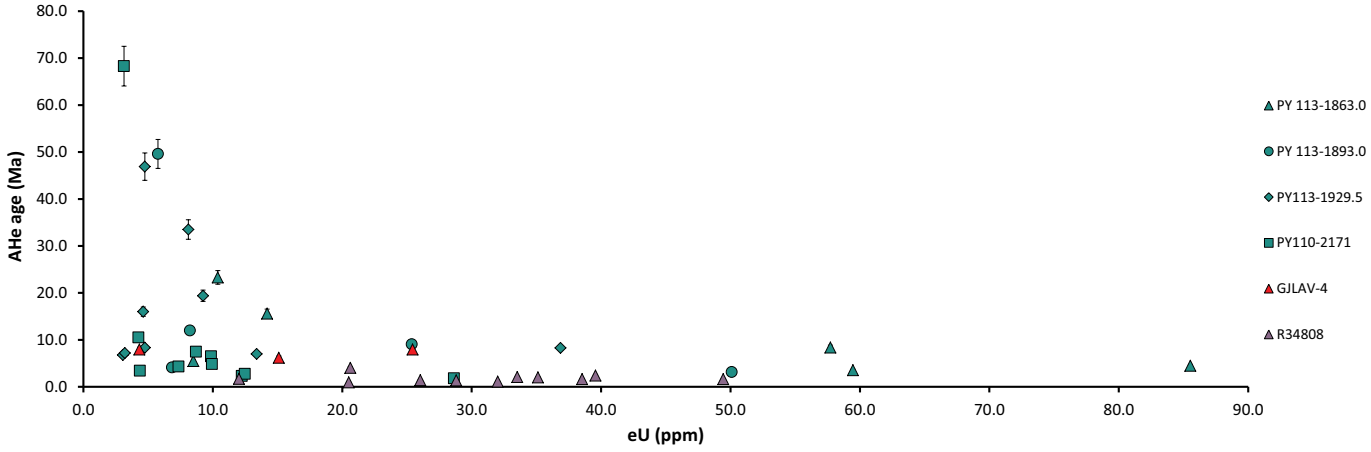

Fig. C1. AHe age vs effective uranium concentration (eU)

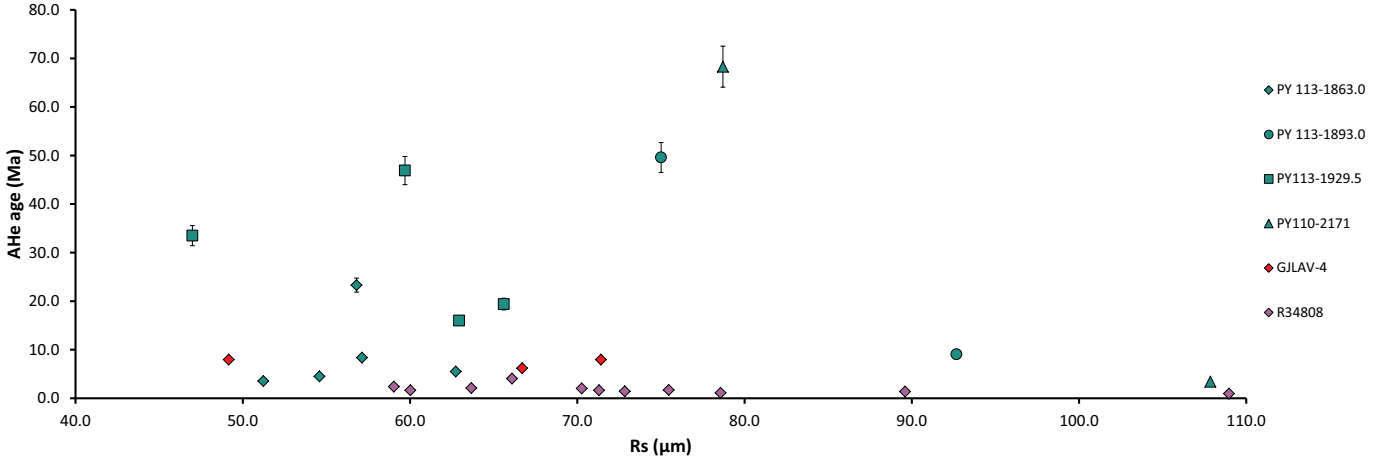

Fig. C2. AHe age vs equivalent spherical radius (Rs).

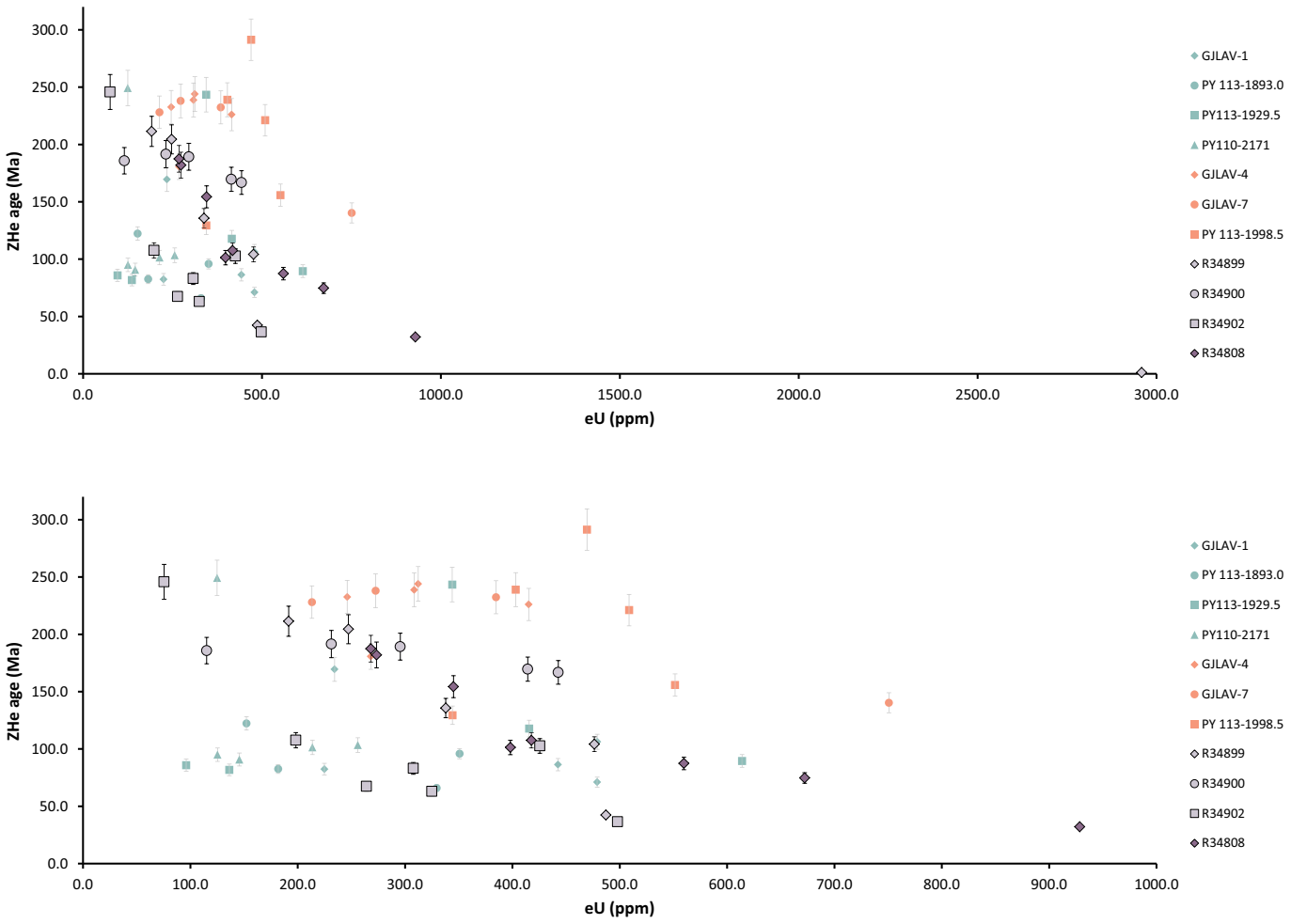

Fig. C3. ZHe age vs effective uranium concentration (eU). Bottom graph excludes the anomalously high eU grain in R34899.

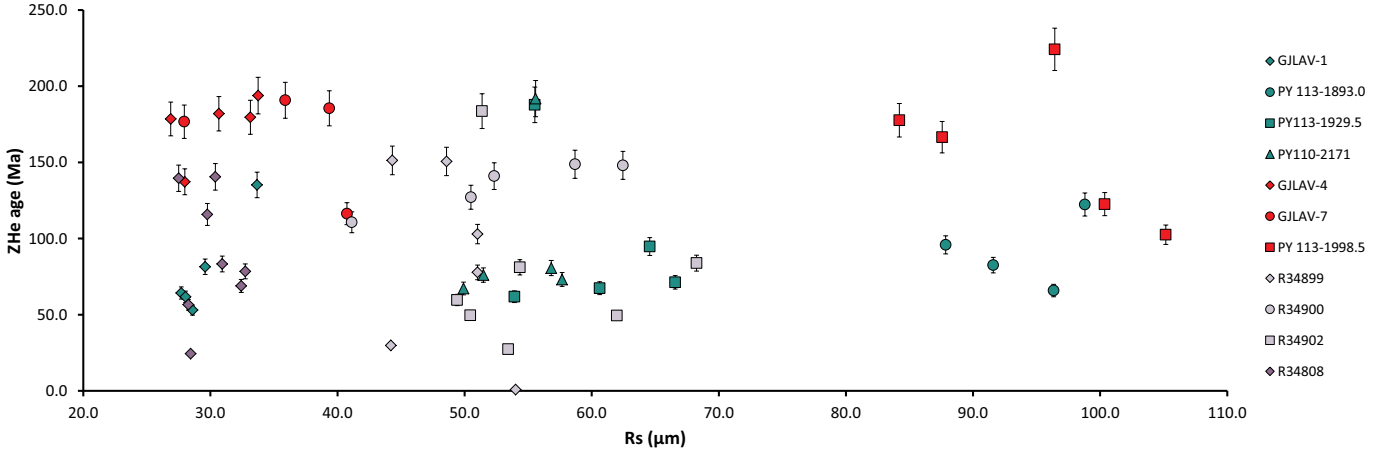

Fig. C4. Uncorrected ZHe age vs equivalent spherical radius (Rs).

Appendix D

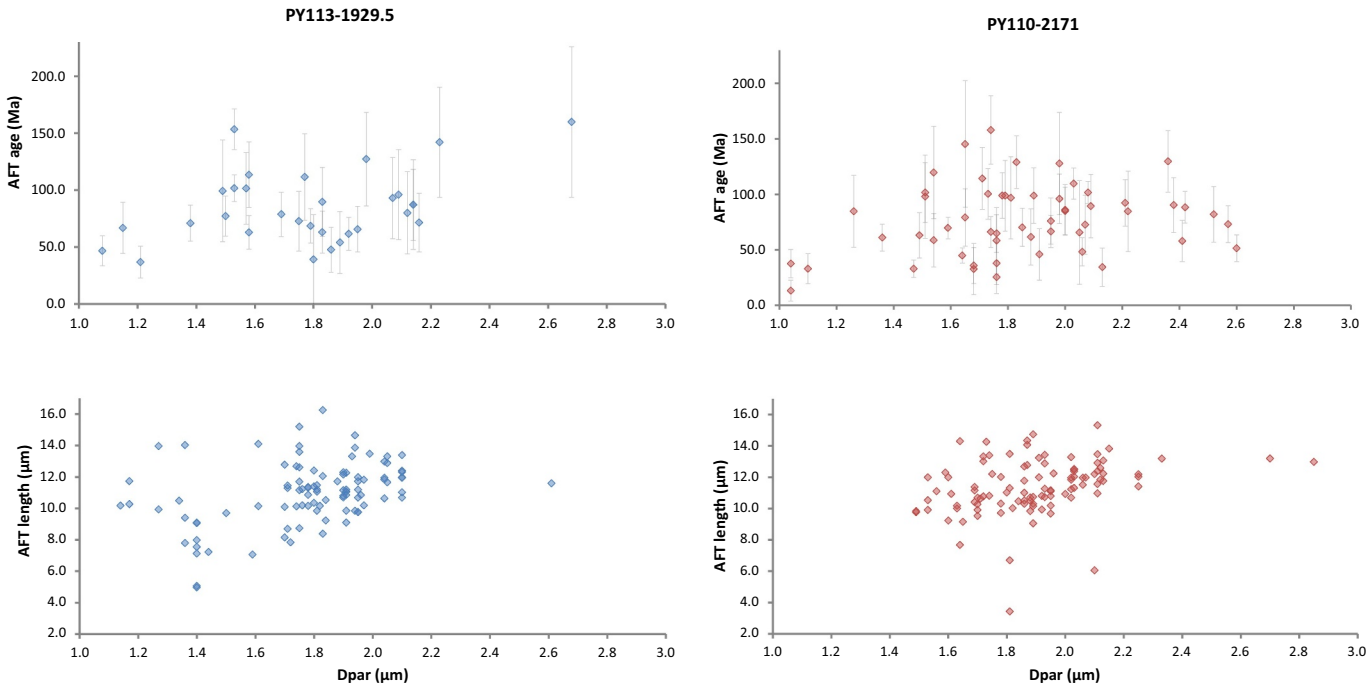

Fig. D1. AFT single grain age (top) and length (bottom) vs Dpar for samples PY113-1929.5 (left) and PY110-2171 (right).

D.1. Additional (50:50 split) forward models

Evidence is presented within Section 5.1.1 to support an 80:20 split of rapidly-cooled and slowly-cooled apatite within the Ieru Formation. To explore the influence that a greater proportion of slowly-cooled apatite may have on the resulting thermal history, we also carried out forward modelling with a 50:50 split, following the same approach described in Section 5.2.

The 50:50 modelling included 26 independent time-temperature paths yielding 13 central AFT age and MTL predictions. Of these, only two fell within error of the observed data range (see Section 5.2) from the three uppermost Ieru Formation samples; two less than with the 80:20 modelling (Section 5.3). The accepted models resulted from thermal histories that including a Late Cretaceous to Oligocene thermal peak, both with (Fig. A4c) and without (Fig. A4b) the Pliocene to recent thermal peak. No models involving only a Pliocene to recent thermal peak were accepted. Both accepted models reasonably reproduced the composite TLD (Fig. A4) and were characterised by maxT of 90 or 100 °C (Fig. A4). This magnitude of maxT is also consistent with all four accepted 80:20 models (Fig. 4).

Appendix E

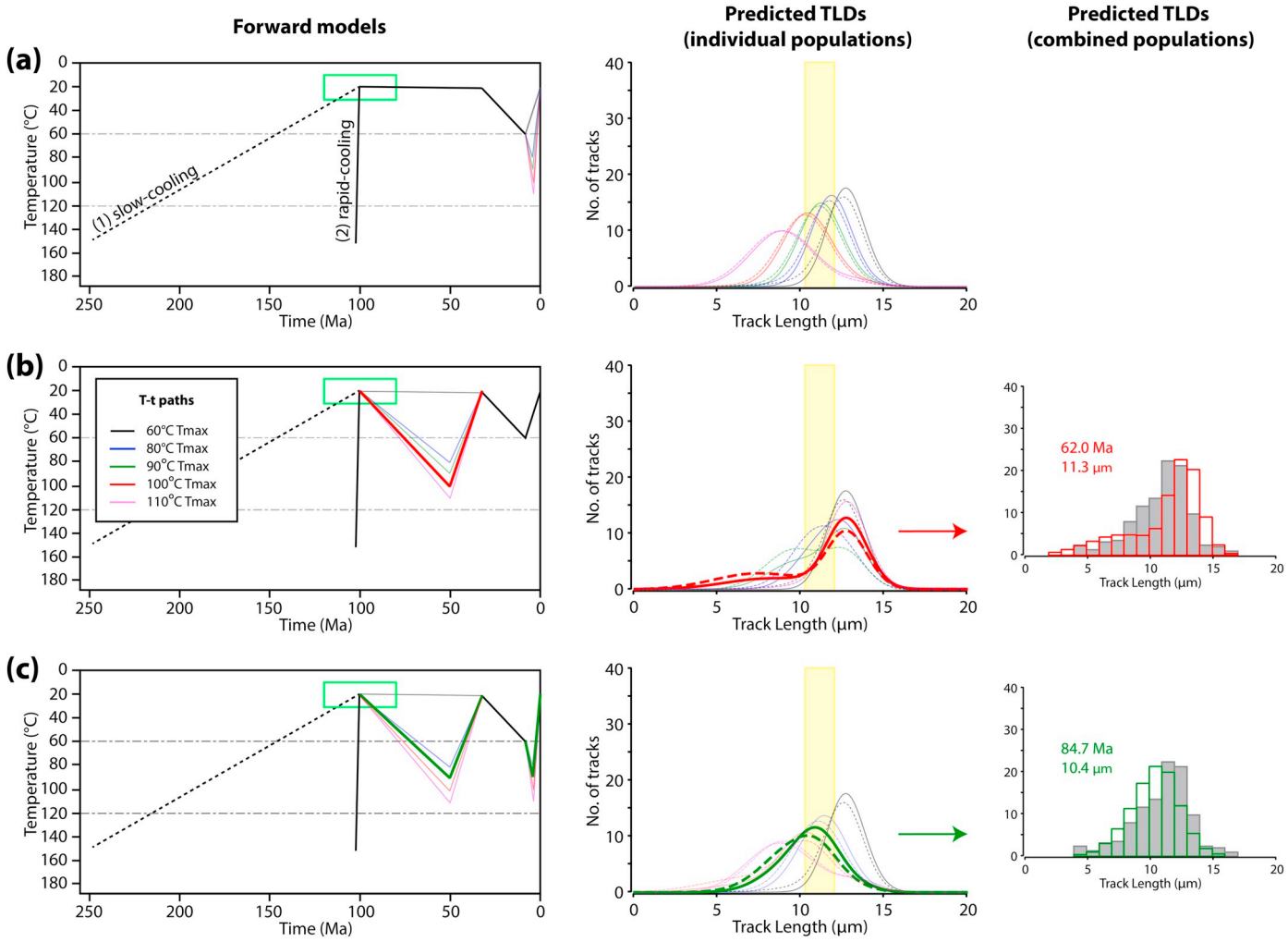

Fig. E1. Left: Forward models comprising two pre-depositional T–t paths (1–2), tested across a range of different post-depositional thermal histories (a–c). The green box represents a reasonable stratigraphic age range for the upper Ieru Formation samples. Middle: Predicted TLD curves for rapidly-cooled (solid line) and slow-cooled (dashed line) apatite populations, weighted based on a relative abundance of 1:1 (50:50%). Thicker red and green lines represent TLD curves from accepted models (i.e. models from which the weighted average of the predicted data fits within the observed data range). Light grey shade represents the MTL range from the observed data (e.g. 10.3 ± 0.2 to 12.1 ± 0.2 µm). Right: TLD histograms (normalised to 100 tracks) comprising the combined rapidly-cooled and slow-cooled TLD curves for the two accepted models compared with a composite TLD histogram (grey) comprising observed data from three upper Ieru Formation samples. Approach described in Section 5.2. (For interpretation of the references to colour in this figure legend, the reader is referred to the web version of this article.)

Appendix F

Thermal history modelling of AFT data from individual Ieru Formation samples.

In this appendix, we present and discuss the results of initial thermal history modelling of AFT data from individual Ieru Formation samples collected throughout the Muller Range. The results of single-sample thermal history models are grouped into four areas within the Muller Range, similar to multi-sample profile modelling. In the most part, the single sample thermal histories are remarkably consistent with pseudo-vertical profile models (cf. Appendix F and Section 5.5).

The individual Ieru Formation sample model output is represented as a colour map of the marginal posterior probability distribution of time-temperature histories (Fig. F1). The expected model (which is the weighted mean of the posterior distribution) and the maximum posterior model (the best Bayesian model in that it tries to balance model simplicity with data fit) are also shown. The observed AFT age and TLD histogram are presented alongside those predicted by the maximum posterior model, thus providing a visual assessment of model performance (e.g. Fig. F1). As with the pseudo-vertical profile modelling results (Section 5.5), thermal peaks correspond to individual heating/cooling events; and multiple thermal peaks may characterise an individual samples thermal history. MaxT refers to the maximum post-depositional temperature experienced and is thus only experienced once for a given thermal history.

F.1. Western Muller Range (WMR)

Despite being located on the north and south limbs of the Muller Anticline (Fig. 2) and separated by 900 m stratigraphically, Ieru Formation samples R34832 and PY110-2171 appear to have experienced remarkably similar post-depositional thermal histories (Fig. F1), including two

significant periods of cooling following deposition in the mid-late Cretaceous (~120–85 Ma). Initial cooling occurred from a maximum temperature of ~100–80 °C in the Aptian to Albian (~120–100 Ma) until the initiation of Darai Limestone deposition (~30 Ma). The cessation of Darai Limestone deposition at ~8 Ma gave way to a second post-depositional cooling to present day surface temperatures, with neither model showing evidence of significant post-Darai Limestone heating.

Ieru Formation sample R34831 is adjacent to and ~600 m stratigraphically below R34832 on the northern limb of the Muller Anticline (Fig. 2). Fewer track lengths were available for thermal modelling of R34831 (n = 61) versus R34832 (n = 100) and PY110-2171 (n = 108). The thermal history of R34831, also deposited in the mid-late Cretaceous (~125–85 Ma), is characterised by a comparably more rapid cooling from a maximum temperature of ~100 °C in the Eocene (~55–50 Ma) to the initiation of Darai Limestone deposition (~30 Ma). The data imply a secondary thermal peak of ~80 °C at ~5 Ma necessitating relatively insignificant post-Darai Limestone heating of ~10–20 °C prior to rapid cooling to present day surface temperatures.

Data from the WMR record a significant cooling event between the Late Cretaceous to Eocene, but cannot resolve the timing particularly well (Fig. F1). This low resolution then leads us to jointly-invert these data as a pseudo-vertical profile to see if the resolution improves (Section 5.5.1).

F.2. South Strickland Gorge (Strick South)

Samples R34835 and PY113-1929.5 were collected from the middle and lower Ieru Formation, respectively, at the southern end of the Strickland Gorge (Fig. 2), where they are vertically separated by ~330 m of stratigraphic section. Both samples were deposited in the Cretaceous (~130–80 Ma) and appear to have experienced similar post-depositional thermal histories (Fig. F1) including prolonged cooling from Late Cretaceous (~90–75 Ma) maximum temperatures of ~85–90 °C until the initiation of Darai Limestone deposition (~30 Ma). Following the cessation of Darai Limestone deposition at ~8 Ma, the data are consistent with a second phase of cooling from ~70–80 °C to present day surface temperatures, with neither model showing evidence of post-Darai Limestone heating.

F.3. North Strickland Gorge (Strick North)

Samples R34809 and R34810 were collected from the upper to middle Ieru Formation in the north Strickland Gorge ~25 km to the northwest of the southern Strickland Gorge profile (Fig. 2). Nearby palaeontological dating is limited, thus necessitating a wide stratigraphic age estimate of middle to late Cretaceous (~120–80 Ma). Individual thermal history models (Fig. F1) reveal a consistent post-depositional phase of cooling from maximum temperatures of ~80–95 °C in the earliest Palaeocene (~65 Ma) until the initiation of Darai Limestone deposition (~30 Ma). Following the cessation of Darai Limestone deposition (~8 Ma), sample R34810 appears to have immediately experienced a second cooling event to present day surface temperatures—albeit the data imply significant uncertainty. In contrast, sample R34809 records more rapid cooling to surface temperatures beginning at ~5–4 Ma, from greater temperatures (~80 °C), that are comparable to the Early Palaeocene thermal peak. Vertical profile modelling is clearly necessary to resolve the variation recorded within these data.

F.4. Lavani Valley (Lavani)

Sample R34854 was collected from the upper Ieru Formation within Lavani Valley in the eastern Muller Range (Fig. 2). Its stratigraphic context (120 m below Base Darai Limestone) and age (~88–84 Ma) are particularly well constrained by recent field work and geochronology (Mahoney et al., 2017). The thermal history model for sample R34854 (Fig. F1) was the only single sample model that required additional constraints to obtain a geologically reasonable thermal history—based on knowledge of Darai Limestone deposition between its initiation at ~30 Ma and cessation at ~10 Ma (e.g. Eisenberg, 1996). Despite considerable uncertainty (Fig. F1), the resulting thermal history suggests that the sample experienced two periods of cooling following Late Cretaceous deposition. An initial cooling started in the Early Eocene (~50 Ma) with a transition from ~80 °C to near-surface temperatures prior to the commencement of Darai Limestone deposition (~30 Ma). A second cooling event from ~75–80 °C at 6 Ma to present day surface temperatures implies post-Darai Limestone heating of ~10–15 °C.

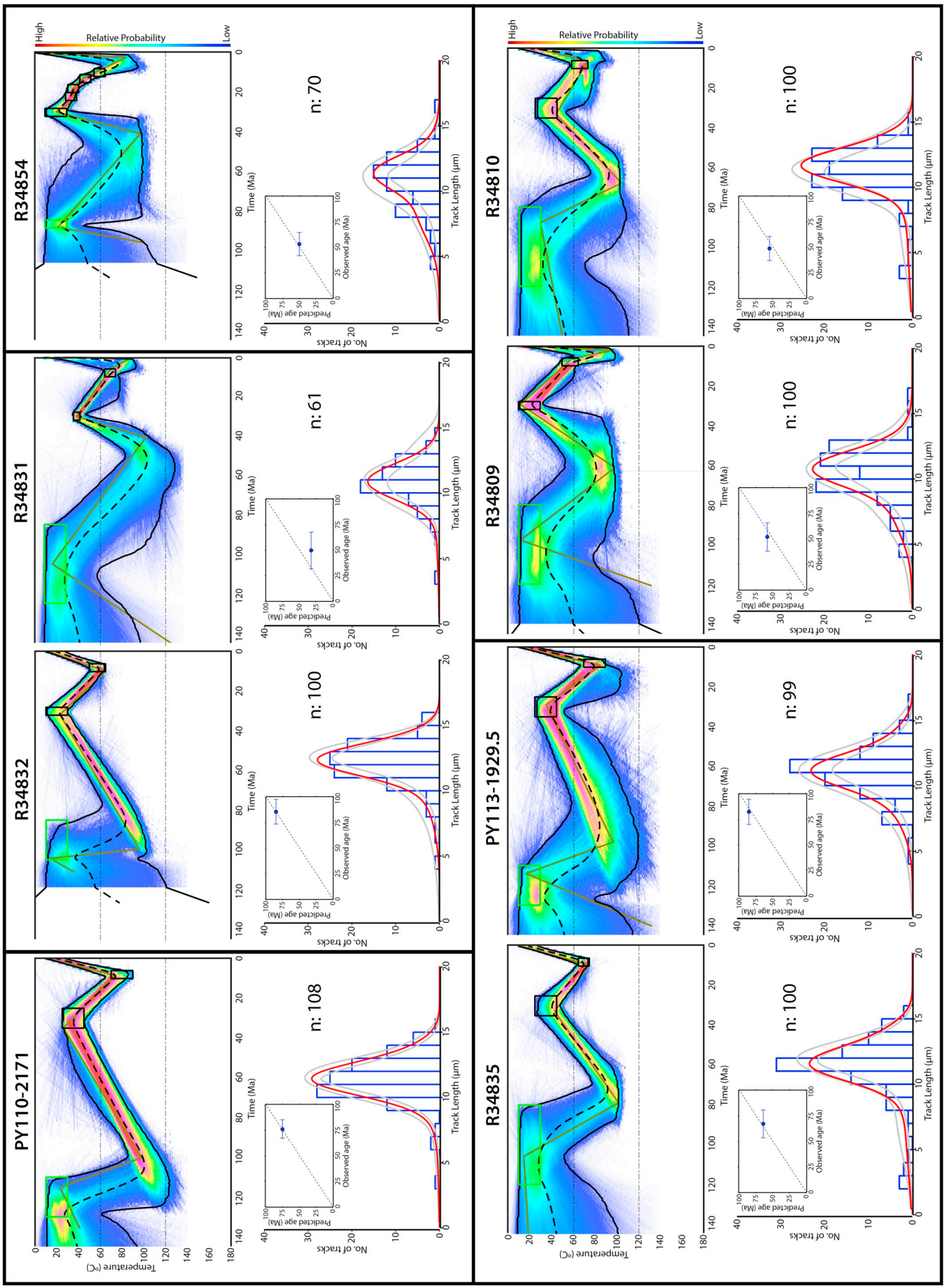
PY110-2171
R34832
R34831
R34854
R34835
PY113-1929.5
R34809
R34810
High
Relative Probability
Low
Temperature (°C)
Time (Ma)
Predicted age (Ma)
Observed age (Ma)
No. of tracks
Track Length (μm)
n: 108
n: 100
n: 61
n: 70
n: 100
n: 99
n: 100
n: 100

Fig. F1. Inverse thermal history modelling results for AFT data from eight Ieru Formation samples across the Muller Range highlighting two significant thermal peaks during: (1) the Cretaceous to Oligocene and (2) the Late Miocene to recent. The upper figure for each sample includes a colour map showing the marginal posterior probability distribution of time-temperature histories. The dashed line represents the expected model (weighted mean of the posterior distribution) and the solid brown line represents the max posterior model (the simplest, best fit time-temperature path). Dot-and-dash lines represent the AFT PAZ. The green box represents individual stratigraphic age/temperature constraints while the black boxes represent additional thermal history constraints discussed in Section 5.4.1. The lower figure for each sample shows the observed (blue histograms) versus predicted (red curves) track length distributions. The grey curves show the 95% confidence interval around the predicted track length distribution, n = the total number of measured track lengths. The insets show the observed AFT ages (and errors) plotted against the predicted ages. Track length distribution and age predictions were obtained from the max posterior model.

References

Amoco PNG Exploration Company, 1982. Lavani 1 Well Completion Report. (137 pp).

Bain, J.H.C., Davies, H.L., Hohnen, P.D., Ryburn, R.J., Smith, I.E., Grainger, R., Tingey, R.J., Moffat, M.R., 1973. Geological Map of Papua New Guinea 1:1,000,000 Scale. Bureau of Mineral Resources, Australia.

Bain, J.H.C., Mackenzie, D.E., Ryburn, R.J., 1975. Geology of the Kubor Anticline, Central Highlands of Papua New Guinea. Bureau of Mineral Resources, Geology and Geophysics Bulletin. 155 Australian Government Publishing Service (116 pp).

Baldwin, S.L., Fitzgerald, P.G., Webb, L.E., 2012. Tectonics of the New Guinea region. Annu. Rev. Earth Planet. Sci. 40, 495–520.

Barbarand, J., Carter, A., Wood, I., Hurford, T., 2003. Compositional and structural control of fission-track annealing in apatite. Chem. Geol. 198, 107–137.

Bennett, D.J., Brand, R.P., Mills, C.R., Morris, B.D., 2000. Exploration potential of the West Bosavi area, Papuan foreland basin, Papua New Guinea. In: Buchanan, P., Grainge, A., Thornton, R. (Eds.), Petroleum Exploration, Development, and Production in Papua New Guinea: Proceedings of the Fourth PNG Petroleum Convention. Papua New Guinea Chamber of Mines and Petroleum, Port Moresby, pp. 139–154.

Botsford, A., Endebrock, L., Harrington, A., 2012. Structural and Stratigraphic Evolution of the Gulf of Papua, Papua New Guinea: New Insights From a Modern 3D Seismic Survey. AAPG International Conference and Exhibition 2012, Search and Discovery Article #10456 (12 pp).

Bradley, G., 2014. Western Papuan Basin to Western Aure: Generalised Cenozoic - Jurassic Chronostratigraphy (unpubl.). (1 pp).

Brown, C.M., Robinson, G.P., 1982. Kutubu 1:250 000 Geological Series Explanatory Notes Sheet SB/54-12, Geological Survey of Papua New Guinea. PNG Department of Minerals and Energy, Port Moresby.

Brown, C.M., Pieters, P.E., Robinson, G.P., 1975. Stratigraphic and structural development of the Aure trough and adjacent shelf and slope areas. J. Aust. Petrol. Explor. Assoc. 15, 61–71.

Brown, C.M., Pigram, C.J., Swarko, S.K., 1980. Mesozoic stratigraphy and geological history of Papua New Guinea. Palaeogeogr. Palaeoclimatol. Palaeoecol. 29, 301–322.

Brown, R.W., Beucher, R., Roper, S., Persano, C., Stuart, F., Fitzgerald, P., 2013. Natural age dispersion arising from the analysis of broken crystals. Part I: Theoretical basis and implications for the apatite (U–Th)/He thermochronometer. Geochim. Cosmochim. Acta 122, 478–497.

Buchanan, P., Warburton, J., 1996. The influence of pre-existing basin architecture in the development of the Papuan fold and thrust belt: implications for petroleum prospectivity. In: Buchanan, P. (Ed.), Petroleum Exploration, Development, and Production in Papua New Guinea: Proceedings of the Third PNG Petroleum Convention. Papua New Guinea Chamber of Mines and Petroleum, Port Moresby, pp. 89–109.

Callot, J.P., Sassi, W., Roure, F., Hill, K., Wilson, N., Divies, R., 2017. Pressure and Basin Modeling in Foothill Belts: A study of the Kutubu area, Papua New Guinea Fold and Thrust Belt. In: AbuAli, M., Moretti, I., Nordgard Bolas, H. (Eds.), Petroleum Systems Analysis — Case Studies. vol. 114. AAPG Memoir, pp. 165–190.

Carman, G., 1993. Palaeogeography of the Coral Sea, Darai and Foreland Megasequences in the eastern Papuan Basin. In: Carman, G., Carman, Z. (Eds.), Petroleum Exploration, Development, and Production in Papua New Guinea: Proceedings of the Second PNG Petroleum Convention. Papua New Guinea Chamber of Mines and Petroleum, Port Moresby, pp. 291–309.

Carter, A., Gallagher, K., 2004. Characterizing the significance of provenance on the inference of thermal history models from apatite fission-track data—a synthetic data study. In: Bernet, M., Spiegel, C. (Eds.), Detrital Thermochronology — Provenance Analysis, Exhumation, and Landscape Evolution of Mountain Belts: Boulder. Colorado, Geological Society of America Special Paper, vol. 378. pp. 7–23.

Cloos, M., Sapiie, B., Quarles van Ufford, A., Weiland, R.J., Warren, P.Q., McMahon, T.P., 2005. Collisional Delamination in New Guinea: The Geotectonics of Subducting Slab Breakoff. Geological Society of America Special Paper 400 (51 pp).

Cooper, G., Kendrick, D., Waina, F., Hamilton, C., Nongkas, M., 2012. New Insights in to the Structural and Thermal Development of the Papuan Foreland: Implications for Hydrocarbon Charge and Prospectivity. Eastern Australasian Basins Symposium IV, Brisbane (14 pp).

Crowhurst, P.V., Hill, K.C., Foster, D.A., Bennett, A.P., 1996. Thermochronological and geochemical constraints on the tectonic evolution of northern Papua New Guinea. Geol. Soc. Lond., Spec. Publ. 106 (1), 525–537.

Crowhurst, P., Hill, K., Foster, D., 1997. In: Hancock, G. (Ed.), The Structural and Tectonic Development of the Frieda River Mineral District, NW Papua New Guinea. Proceedings of the PNG Geology, Exploration and Mining Conference 1997. Australasian Institute of Mining and Metallurgy, pp. 51–60.

Crowhurst, P., Maas, R., Hill, K.C., Foster, D.A., Fanning, C.M., 2004. Isotopic constraints on crustal architecture and Permo-Triassic tectonics in New Guinea: possible links with eastern Australia. Aust. J. Earth Sci. 51, 107–122.

Danišík, M., McInnes, B.I., Kirkland, C.L., McDonald, B.J., Evans, N.J., Becker, T., 2017. Seeing is believing: visualization of He distribution in zircon and implications for thermal history reconstruction on single crystals. Sci. Adv. 3 (2), e1601121.

Davies, H., 1983. Wabag 1:250 000 Geological Series Explanatory Notes Sheet SB/54-8, Geological Survey of Papua New Guinea. PNG Department of Minerals and Energy, Port Moresby.

Davies, H.L., 1990. Structure and evolution of the Border Region of New Guinea. In: Carman, G., Carman, Z. (Eds.), Petroleum Exploration, Development, and Production in Papua New Guinea: Proceedings of the First PNG Petroleum Convention. Papua New Guinea Chamber of Mines and Petroleum, Port Moresby, pp. 245–269.

Davies, H.L., 2012. The geology of New Guinea—the cordilleran margin of the Australian continent. Episodes 35 (1), 87–102.

Davies, H., Norvick, M., 1974. Blucher Range 1:250 000 Geological Series Explanatory Notes Sheet SB/54-07. Geological Survey of Papua New Guinea, PNG Department of Minerals and Energy, Port Moresby.

Davies, H.L., Winn, R.D., KenGemar, P., 1996. Evolution of the Papuan Basin: a view from the orogeny. In: Carman, G., Carman, Z. (Eds.), Petroleum Exploration, Development, and Production in Papua New Guinea: Proceedings of the Second PNG Petroleum Convention. Papua New Guinea Chamber of Mines and Petroleum, Port Moresby, pp. 53–62.

Davies, H.L., Perembo, R.C.B., Winn, R.D., Kengemar, P., 1997. Terranes of the New Guinea Orogen. In: Hancock, G. (Ed.), Proceedings of the PNG Geology, Exploration and Mining Conference. Madang, Australian Institute of Mining and Metallurgy, pp. 61–66.

Denison, C.N., 1990. Palynostratigraphic Revision of Amoco Lavani-1 Well, Papua New Guinea. (unpubl., 6 pp).

Donelick, R.A., 1993. Method of fission track analysis utilizing bulk chemical etching of apatite. U.S. Patent 5,267,274.

Donelick, R.A., O'Sullivan, P.B., Ketcham, R.A., 2005. Apatite fission-frack analysis. Rev. Mineral. Geochem. 58, 49–94.

Dow, D.B., 1977. A Geological Synthesis of Papua New Guinea. 201 Bureau of Mineral Resources Bulletin (58 pp).

Dow, D.B., Smit, J.A., Bain, J.H.C., Ryburn, R.J., 1972. Geology of the Sepik Region, New Guinea. 133 Bureau of Mineral Resources Bulletin (88 pp).

Duddy, I.R., Green, P.F., Bray, R.J., Hegarty, K.A., 1994. Recognition of the thermal effects of fluid flow in sedimentary basins. Geol. Soc. Lond., Spec. Publ. 78 (1), 325–345.

Edwards, A.B., 1950. The Petrology of the Miocene Sediments of Aure Trough. Papua: Proceedings of the Royal Society of Victoria 60. pp. 123–148.

Eisenberg, L.I., 1996. Strontium isotope analysis and structural interpretation of P'nyang Anticline, Papuan Fold Belt, Western Highlands Province, Papua New Guinea. In: Buchanan, P. (Ed.), Petroleum Exploration, Development, and Production in Papua New Guinea: Proceedings of the Third PNG Petroleum Convention. Papua New Guinea Chamber of Mines and Petroleum, Port Moresby, pp. 231–244.

Ekström, G., Nettles, M., Dziewonski, A., 2012. The global CMT project 2004-2010: centroid-moment tensors for 13,017 earthquakes. Phys. Earth Planet. Inter. 200, 1–9.

Farley, K.A., 1996. The effects of long alpha-stopping distances on (U-Th)/He ages. Geochim. Cosmochim. Acta 60, 4223–4229.

Farley, K.A., 2000. Helium diffusion from apatite: General behavior as illustrated by Durango fluorapatite. Solid Earth 105, 2903–2914.

Farley, K.A., 2002. (U-Th)/He dating: techniques, calibrations, and applications. Rev. Mineral. Geochem. 47, 819–844.

Farley, K.A., Stockli, D.F., 2002. (U-Th)/He Dating of Phosphates: Apatite, Monazite, and Xenotime. Rev. Mineral. Geochem. 48, 559–577.

Findlay, A.L., Leckie, G.G., 1973. Report on the Lavani Anticline Geological Survey, Permit 46, Papua New Guinea. BP Petroleum Development Australia Pty Ltd Report. Geological Survey of Papua New Guinea Data File 12 BS 26 (unpubl.).

Fischer, M.W., Warburton, 1996. The importance of pre-Tertiary basin architecture for hydrocarbon accumulation in the Papuan Fold and Thrust Belt: models, analogues and implications. In: Buchanan, P. (Ed.), Petroleum Exploration, Development, and Production in Papua New Guinea: Proceedings of the Third PNG Petroleum Convention. Papua New Guinea Chamber of Mines and Petroleum, Port Moresby, pp. 111–131.

Fitzgerald, P.G., Baldwin, S.L., Webb, L.E., O'Sullivan, P.B., 2006. Interpretation of (U–Th)/he single grain ages from slowly cooled crustal terranes: a case study from the Transantarctic Mountains of southern Victoria Land. Chem. Geol. 225, 91–120.

Francis, G., 1990. The North New Guinea Basin, and associated intra-basins. In: Carman, G., Carman, Z. (Eds.), Petroleum Exploration, Development, and Production in Papua New Guinea: Proceedings of the First PNG Petroleum Convention. Papua New Guinea Chamber of Mines and Petroleum, Port Moresby, pp. 445–460.

Galbraith, R.F., 2005. Statistics for Fission Track Analysis. Chapman and Hall/CRC Press (219 pp).

Galbraith, R.F., Laslett, G.M., 1993. Statistical models for mixed fission track ages. Nucl.

Tracks Radiat. Meas. 21 (4), 459–470.
Gallagher, K., 1995. Evolving temperature histories from apatite fission-track data. Earth Planet. Sci. Lett. 136 (3–4), 421–435.
Gallagher, K., 2012. Transdimensional inverse thermal history modeling for quantitative thermochronology. J. Geophys. Res. 117, 1–16.
Gallagher, K., Stephenson, J., Brown, R., Holmes, C., Fitzgerald, P., 2005. Low temperature thermochronology and modeling strategies for multiple samples 1: Vertical profiles. Earth Planet. Sci. Lett. 237 (1–2), 193–208.
Gallagher, K., Charvin, K., Nielsen, S., Sambridge, M., Stephenson, J., 2009. Markov chain Monte Carlo (MCMC) sampling methods to determine optimal models, model resolution and model choice for Earth Science problems. Mar. Pet. Geol. 26 (4), 525–535.
Gautheron, C., Tassan-Got, L., Barbarand, J., Pagel, M., 2009. Effect of alpha-damage annealing on apatite (U–Th)/He thermochronology. Chem. Geol. 266, 157–170.
Gleadow, A.J.W., Duddy, I.R., 1981. A natural long-term track annealing experiment for apatite. Nucl. Tracks 5, 169–174.
Gleadow, A.J., Belton, D., Kohn, B., Brown, R.W., 2002. Fission track dating of phosphate minerals and the thermochronology of apatite. Rev. Mineral. Geochem. 48 (1), 579–630.
Gleadow, A.J.W., Gleadow, S.J., Belton, D.X., Kohn, B.P., Krochmal, M.S., Brown, R.W., 2009. Coincidence mapping - a key strategy for the automatic counting of fission tracks in natural minerals. In: Lisker, F., Ventura, B., Glasmacher, U.A. (Eds.), Thermochronological Methods: From Palaeotemperature Constraints to Landscape Evolution Models. Geological Society, London, Special Publications, vol. 324. pp. 25–36.
Gleadow, A., Harrison, M., Kohn, B., Lugo-Zazueta, R., Phillips, D., 2015. Fish Canyon Tuff apatite: a new look at an old low-temperature thermochronology standard. Earth Planet. Sci. Lett. 424, 95–108.
Glen, R.A., 2005. The Tasmanides of eastern Australia. Geol. Soc. Lond. Spec. Publ. 246, 23–96.
Green, P.F., Duddy, I., 2016. Episodic Regional Burial and Subsequent Exhumation Exert a Major Influence on Hydrocarbon Prospectivity. AAPG/SEG International Conference and Exhibition 2015, Search and Discovery Article #30449 (26 pp).
Green, P.F., Duddy, I.R., Gleadow, A.J.W., Tingate, P.R., Laslett, G.M., 1986. Thermal annealing of fission tracks in apatite 1. A qualitative description. Chem. Geol. Isot. Geosci. 59, 237–253.
Guenthner, W.R., Reiners, P.W., Ketcham, R.A., Nasdala, L., Giester, G., 2013. Helium diffusion in natural zircon: radiation damage, anisotropy, and the interpretation of zircon (U-Th)/He thermochronology. Am. J. Sci. 313, 145–198.
Gunson, M., Haig, D.W., Kruman, B., Mason, R.A., Perembo, R.C.B., Stewart, R., 1997. Stratigraphic reconstruction of the Porgera region, Papua New Guinea. In: Hancock, G. (Ed.), Proceedings of the PNG Geology, Exploration and Mining Conference. Australian Institute of Mining and Metallurgy, Madang, pp. 99–108.
Gunson, M., Hall, G., Johnston, M., 2000. Foraminiferal coloration index as a guide to hydrothermal gradients around the Porgera Intrusive Complex, Papua New Guinea. Econ. Geol. 95, 271–282.
Hall, R., 2012. Late Jurassic–Cenozoic reconstructions of the Indonesian region and the Indian Ocean. Tectonophysics 570-571, 1–41.
Hanani, A., 2012. The Geology and Structural Style of the Juha Gas Field, Papua New Guinea. Honours Thesis (unpubl.). The University of New South Wales, Sydney (214 pp).
Hanani, A., Lennox, P., Hill, K.C., 2016. The Geology and Structural Style of the Juha Gas Field, Papua New Guinea. ASEG Extended Abstracts 2016. pp. 1–7.
Haq, B.U., 2014. Cretaceous eustasy revisited. Glob. Planet. Chang. 113, 44–58.
Haq, B.U., Hardenbol, J., Vail, P.R., 1987. Chronology of fluctuating sea levels since the Triassic. Science 235, 1156–1167.
Hasebe, N., Barbarand, J., Jarvis, K., Carter, A., Hurford, A.J., 2004. Apatite fission-track chronometry using laser ablation ICP-MS. Chem. Geol. 207 (3–4), 135–145.
Hill, K.C., 1989a. The Structure, Timing and Thermal History of the Papuan Fold Belt, Papua New Guinea. PhD Thesis (unpubl.). The University of Melbourne, Melbourne.
Hill, K.C., 1989b. The Muller Anticline, Papua New Guinea; basement cored, inverted extensional fault structures with opposite vergence. Tectonophysics 158, 227–245.
Hill, K.C., 1991. Structure of the Papuan Fold Belt, Papua New Guinea. Am. Assoc. Pet. Geol. Bull. 75, 857–872.
Hill, K.C., Gleadow, A., 1989. Uplift and thermal history of the Papuan Fold Belt, Papua New Guinea: Apatite Fission track analysis. Aust. J. Earth Sci. 36, 515–539.
Hill, K.C., Gleadow, A., 1990. Apatite fission track analysis of the Papuan Basin. In: Carman, G., Carman, Z. (Eds.), Petroleum Exploration, Development, and Production in Papua New Guinea: Proceedings of the First PNG Petroleum Convention. Papua New Guinea Chamber of Mines and Petroleum, Port Moresby, pp. 119–136.
Hill, K.C., Hall, R., 2003. Mesozoic-Cenozoic evolution of Australia's New Guinea margin in a West Pacific context. Geol. Soc. Am. Spec. Pap. 372, 265–290.
Hill, K.C., Raza, A., 1999. Arc-continent collision in Papua Guinea: Constraints from fission track thermochronology. Tectonics 18 (6), 950–966.
Hill, K.C., Medd, D., Darvall, P., 1990. Structure, stratigraphy, geochemistry and hydrocarbons in the Kagua-Kubor area, Papua New Guinea. In: Carman, G., Carman, Z. (Eds.), Petroleum Exploration, Development, and Production in Papua New Guinea: Proceedings of the First PNG Petroleum Convention. Papua New Guinea Chamber of Mines and Petroleum, Port Moresby, pp. 351–366.
Hill, K.C., Norvick, M., Keetley, J., Adams, A., 2000. Structural and stratigraphic shelf-edge hydrocarbon plays in the Papuan Fold Belt. In: Buchanan, P., Grainge, A., Thornton, R. (Eds.), Petroleum Exploration, Development, and Production in Papua New Guinea: Proceedings of the Fourth PNG Petroleum Convention. Papua New Guinea Chamber of Mines and Petroleum, Port Moresby, pp. 67–85.
Hill, K.C., Lucas, K., Bradey, K., 2010. Structural styles in the Papuan Fold Belt, Papua New Guinea: constraints from analogue modelling. In: Goffey, G. (Ed.), Hydrocarbons in Contractional Belts. vol. 348. Geological Society, London, Special Publications, pp. 33–56.
Hill, K.C., Wightman, R., Munro, L., 2015. Structural Style in the Eastern Papuan Fold Belt, From Wells, Seismic, Maps and Modelling. AAPG/SEG International Conference and Exhibition 2015 In.
Home, P., Dalton, D., Brannan, J., 1990. Geological evolution of the Western Papuan Basin. In: Carman, G., Carman, Z. (Eds.), Petroleum Exploration, Development, and Production in Papua New Guinea: Proceedings of the First PNG Petroleum Convention. Papua New Guinea Chamber of Mines and Petroleum, Port Moresby, pp. 107–118.
Hornafius, J.S., 1993. The 1990–1991 Muller Range Geological Survey – PPL 93. Mobil Exploration Niugini (unpubl.).
House, M.A., Farley, K.A., Stockli, D., 2000. Helium chronometry of apatite and titanite using Nd-YAG laser heating. Earth Planet. Sci. Lett. 183 (3–4), 365–368.
Hutchison, D.S., Norvick, M.S., 1978. Wewak 1:250,000 Geological Series Explanatory Notes Sheet SA/54-16, Geological Survey of Papua New Guinea. PNG Department of Minerals and Energy, Port Moresby.
Japsen, P., Chalmers, J.A., Green, P.F., Bonow, J.M., 2012. Elevated, passive continental margins: not rift shoulders, but expressions of episodic, post-rift burial and exhumation. Glob. Planet. Chang. 90, 73–86.
Jenkins, D., 1974. Detachment tectonics in western Papua New Guinea. Geol. Soc. Am. Bull. 85, 533–548.
Jenkins, D., White, M.F., 1970. Report on the Strickland River Survey, Permit 46, Papua. BP Petroleum Development Report. 89 Geological Survey of Papua New Guinea Data File 4 BS (unpubl.).
Johnson, J.E., Flowers, R.M., Baird, G.B., Mahan, K.H., 2017. “Inverted” zircon and apatite (U–Th)/He dates from the Front Range, Colorado: High-damage zircon as a low-temperature (< 50 °C) thermochronometer. Earth Planet. Sci. Lett. 466, 80–90.
Jones, R.W., 1991. Cenozoic stratigraphy of the Papuan Basin, Papua New Guinea (unpubl.). GSPNG Open File No. F/R/91-215.
Kawagle, S.A., Meyers, J.B., 1996. Structural and sequence geometry of the Kiunga Area, Papuan Foreland Basin, Papua New Guinea. In: Buchanan, P. (Ed.), Petroleum Exploration, Development, and Production in Papua New Guinea: Proceedings of the Third PNG Petroleum Convention. Papua New Guinea Chamber of Mines and Petroleum, Port Moresby, pp. 175–193.
Keenan, S.E., Hill, K.C., 2015. The Mananda Anticline, Papua New Guinea: A Third Oil Discovery, Appraisal Programme and Deep Potential. AAPG/SEG International Conference and Exhibition 2015.
Ketcham, R.A., 2005. Forward and inverse modeling of low-temperature thermochronology data. Rev. Mineral. Geochem. 58, 275–314.
Ketcham, R.A., Carter, A., Donelick, R.A., Barbarand, J., Hurford, A.J., 2007. Improved modeling of fission-track annealing in apatite. Am. Mineral. 92, 799–810.
Laslett, G.M., Green, P.F., Duddy, I.R., Gleadow, A.J.W., 1987. Thermal annealing of fission tracks in apatite 2. A quantitative analysis. Chem. Geol. Isot. Geosci. 65, 1–13.
Löffler, E., MacKenzie, D., Webb, A., 1980. Potassium-argon ages from some of the Papua New Guinea Highlands volcanoes, and their relevance to Pleistocene geomorphic history. J. Geol. Soc. Aust. 26, 387–397.
Lund, D., Waples, D., Robinson, P., 1998. The Thermal History and Hydrocarbon Maturation, Generation and Migration in the Foreland Region of the Papuan Basin. Report for the PPL179, PPL188 and PPL193 Joint Ventures (unpubl.). Oil Search Ltd.
Mackintosh, V., Kohn, B., Gleadow, A., Tian, Y., 2017. Phanerozoic morphotectonic evolution of the Zimbabwe Craton: Unexpected outcomes from a multiple low-temperature thermochronology study. Tectonics 36 (10), 2044–2067.
Mahoney, L., Hill, K., McLaren, S., Hanani, A., 2017. Complex fold and thrust belt structural styles: examples from the Greater Juha area of the Papuan Fold and Thrust Belt, Papua New Guinea. J. Struct. Geol. 100, 98–119.
Mason, R.A., 1996. Structure of the Western Papuan Fold Belt. In: Buchanan, P. (Ed.), Petroleum Exploration, Development, and Production in Papua New Guinea: Proceedings of the Third PNG Petroleum Convention. Papua New Guinea Chamber of Mines and Petroleum, Port Moresby, pp. 161–173.
McConachie, B., Lanzilli, E., 2000. Stanley gas condensate field discovery and the oil potential of the Western Papuan Basin. In: Buchanan, P., Grainge, A., Thornton, R. (Eds.), Petroleum Exploration, Development, and Production in Papua New Guinea: Proceedings of the Fourth PNG Petroleum Convention. Papua New Guinea Chamber of Mines and Petroleum, Port Moresby, pp. 427–442.
McConachie, B., Lanzilli, E., Kendrick, D., Burge, C., 2000. Extensions of the Papuan Basin foreland geology into Eastern Irian Jaya (West Papua) and the New Guinea Fold Belt in Papua New Guinea. In: Buchanan, P., Grainge, A., Thornton, R. (Eds.), Petroleum Exploration, Development, and Production in Papua New Guinea: Proceedings of the Fourth PNG Petroleum Convention. Papua New Guinea Chamber of Mines and Petroleum, Port Moresby, pp. 219–237.
Muller, R.D., Gaina, C., Tikku, A., Mihut, D., Cande, S.C., Stock, J.M., 2000. Mesozoic/Cenozoic tectonic events around Australia. In: Richards, M.A., Gordon, R.G. van der Hilst, R.D. (Eds.), The History and Dynamics of Global Plate Motions. American Geophysical Union Geophysical Monograph, vol. 121. pp. 161–188.
Muller, R.D., Flament, N., Matthews, K.J., Williams, S.E., 2016. Formation of Australian continental margin highlands driven by plate-mantle interaction. Earth Planet. Sci. Lett. 441, 60–70.
Murray, C.G., 2003. Granites of the northern New England Orogen. In: The Ishihara Symposium: Granites and Associated Metallogenesis, Geoscience Australia, pp. 101–108.
Norvick, M.S., 2003. New Palaeogeographic Maps of the Northern Margins of the Australian Plate: Updated Report (unpubl.). Report for Geoscience Australia, September 2003.
Norvick, M.S., Hutchison, D.S., 1980. Aitape-Vanimo 1:250,000 Geological Series Explanatory Notes Sheet SA/54-15, Geological Survey of Papua New Guinea. PNG

Department of Minerals and Energy, Port Moresby.
Page, R., 1976. Geochronology of Igneous and Metamorphic Rocks in the New Guinea Highlands. 162 Bureau of Mineral Resources Australia Bulletin (117 pp).
Parris, K.R., 1994. Basement Structures and Implications for Control of Igneous Activity, Central Ranges, Irian Jaya, Indonesia. PT Freeport Indonesia Report (unpubl.).
Pigott, J.D., Trumbly, N.I., O'Neal, M.V., 1985. Northern New Guinea wrench fault system: a manifestation of Late Cenozoic interactions between Australian and Pacific plates. Tectonics 4, 613–620.
Pigram, C., Davies, H.L., 1987. Terranes and accretion history of the New Guinea Orogen. Bur. Mineral Resour. J. Aust. Geol. Geophys. 10, 193–212.
Pigram, C., Panggabean, H., 1984. Rifting of the northern margin of the Australian continent and the origin of some microcontinents in eastern Indonesia. Tectonophysics 107, 331–353.
Pigram, C., Symonds, P.A., 1991. A review of the timing of the major tectonic events in the New Guinea Orogen. J. SE Asian Earth Sci. 6, 307–318.
Pigram, C., Symonds, P.A., 1993. Eastern Papuan Basin—a new model for the tectonic development and implications for petroleum prospectivity. In: Carman, G., Carman, Z. (Eds.), Petroleum Exploration, Development, and Production in Papua New Guinea: Proceedings of the Second PNG Petroleum Convention. Papua New Guinea Chamber of Mines and Petroleum, Port Moresby, pp. 213–231.
Reiners, P.W., Farley, K.A., 2001. Influence of crystal size on apatite (U-Th)/He thermochronology: an example from the Bighorn Mountains, Wyoming. Earth Planet. Sci. Lett. 188, 413–420.
Reiners, P.W., Ehlers, T.A., Zeitler, P.K., 2005. Past, present and future of thermochronology. In: Reiners, P.W., Ehlers, T.A. (Eds.), Low-temperature Thermochronology: Techniques, Interpretations, and Applications, pp. 1–18.
Rogerson, R.J., Hilyard, D., Finlayson, E.J., Holland, D.S., Nion, S.T.S., Sumaiang, R.S., Duguman, J., Loxton, C.D.C., 1987. The Geology and Mineral Reserves of the Sepik Headwaters Region, Papua New Guinea. 12 Geological Survey of Papua New Guinea Memoir (130 pp).
Sari, J., Failing, R., Wulff, K., 1996. The Giero Sandstone: a potentially new play in the Papuan Basin. In: Buchanan, P. (Ed.), Petroleum Exploration, Development, and Production in Papua New Guinea: Proceedings of the Third PNG Petroleum Convention. Papua New Guinea Chamber of Mines and Petroleum, Port Moresby, pp. 301–312.
Schellart, W.P., Spakman, W., 2015. Australian plate motion and topography linked to fossil New Guinea slab below Lake Eyre. Earth Planet. Sci. Lett. 421, 107–116.
Schofield, S., 2000. The Bosavi Arch and Komewu Fault Zone: their control on basin architecture and the prospectivity of the Papuan Foreland. In: Buchanan, P., Grainge, A., Thornton, R. (Eds.), Petroleum Exploration, Development, and Production in Papua New Guinea: Proceedings of the Fourth PNG Petroleum Convention. Papua New Guinea Chamber of Mines and Petroleum, Port Moresby, pp. 101–122.
Shuster, D.L., Flowers, R.M., Farley, K.A., 2006. The influence of natural radiation damage on helium diffusion kinetics in apatite. Earth Planet. Sci. Lett. 249, 148–161.
Sweeney, J.J., Burnham, A.K., 1990. Evaluation of a simple model of vitrinite reflectance based on chemical kinetics. AAPG Bull. 74, 1559–1570.
Tcherepanov, E.N., Droxler, A.W., Lapointe, P., Dickens, G.R., Bentley, S.J., Beaufort, L., Peterson, L.C., Daniell, J., Opdyke, B.N., 2008. Neogene evolution of the mixed carbonate-siliciclastic system in the Gulf of Papua, Papua New Guinea. J. Geophys. Res. Earth Surf. 113 (15 pp).
Thornton, R., Emmett, J., Laslo, J., Gottschalk, R., 1996. Integrated structural and stratigraphic analysis in PPL 175, Papuan Fold Belt, Papua New Guinea. In: Buchanan, P. (Ed.), Petroleum Exploration, Development, and Production in Papua New Guinea: Proceedings of the Third PNG Petroleum Convention. Papua New Guinea Chamber of Mines and Petroleum, Port Moresby, pp. 195–215.
Tobin, J., Zahirovic, S., Hassan, R., Rey, P., 2018. Tectonic and Geodynamic Evolution of the Northern Australian Margin and New Guinea. ASEG Extended Abstracts 2018 (7 pp).
USGS, 2015. Shuttle Radar Topography Mission, 1-Arc Second, Global Land Cover Facility. University of Maryland, College Park, Maryland (Accessed through USGS EarthExplorer).
Van Ufford, A.Q., Cloos, M., 2005. Cenozoic tectonics of New Guinea. Am. Assoc. Pet. Geol. Bull. 89 (1), 119–140.
Vermeesch, P., 2008. Three new ways to calculate average (U–Th)/He ages. Chem. Geol. 249 (3–4), 339–347.
Webb, A., 1973. Geochronology Report on Samples Submitted by BMR West Sepik Party. Australian Mineral Development Laboratories Report AN3049/73 (unpubl.).
Weiland, R.J., Cloos, M., 1996. Pliocene-Pleistocene asymmetric unroofing of the Irian fold belt, Irian Jaya, Indonesia: Apatite fission-track thermochronology. Geol. Soc. Am. Bull. 108 (11), 1438–1449.
Weissel, J.K., Watts, A.B., 1979. Tectonic evolution of the Coral Sea Basin. J. Geophys. Res. 84, 4572–4582.
White, M.F., Boxall, A.M., Findlay, A.L., Sweetman, I.A.D., Visser, B., 1973. Report on the Fly-Palmer Geological Survey. BP Petroleum Development Report (unpubl.). Geological Survey of Papua New Guinea data file 4 BQ.
Wildman, M., Brown, R., Beucher, R., Persano, C., Stuart, F., Gallagher, K., Schwanethal, J., Carter, A., 2016. The chronology and tectonic style of landscape evolution along the elevated Atlantic continental margin of South Africa resolved by joint apatite fission track and (U-Th-Sm)/He thermochronology. Tectonics 35, 511–545.
Wilson, C., Barrett, R., Howe, R., Leu, L.K., 1993. Occurrence and character of outcropping limestones in the Sepik Basin: Implications for hydrocarbon exploration. In: Buchanan, P. (Ed.), Petroleum Exploration, Development, and Production in Papua New Guinea: Proceedings of the Third PNG Petroleum Convention. Papua New Guinea Chamber of Mines and Petroleum, Port Moresby, pp. 111–124.
Wolfe, M.R., Stockli, D.F., 2010. Zircon (U-Th)/He thermochronometry in the KTB drill hole, Germany, and its implications for bulk He diffusion kinetics in zircon. Earth Planet. Sci. Lett. 295, 69–82.
Zahirovic, S., Seton, M., Müller, R.D., 2014. The Cretaceous and Cenozoic tectonic evolution of Southeast Asia. Solid Earth 5, 227–273.
Zahirovic, S., Matthews, K.J., Flament, N., Müller, R.D., Hill, K.C., Seton, M., Gurnis, M., 2016. Tectonic evolution and deep mantle structure of the eastern Tethys since the latest Jurassic. Earth-Sci. Rev. 162, 293–337.

AGU ADVANCING EARTH AND SPACE SCIENCE

Tectonics

RESEARCH ARTICLE
10.1029/2020TC006667

Key Points:

- Complex spatiotemporal distribution of ground deformation revealed during the 2018 Papua New Guinea Highlands earthquake sequence
- The M_w 7.5 mainshock was related to tectonic inversion on a hidden extensional fault system beneath the Papuan Fold and Thrust Belt (PFTB)
- The northern Australian passive margin architecture has a primary control on structural styles within the PFTB

Supporting Information:

Supporting Information may be found in the online version of this article.

Correspondence to:

L. Mahoney,
luke.g.mahoney@gmail.com

Citation:

Mahoney, L., Stanaway, R., McLaren, S., Hill, K., & Bergman, E. (2021). The 2018 M_w 7.5 Highlands earthquake in Papua New Guinea: Implications for structural style in an active fold and thrust belt. *Tectonics*, *40*, e2020TC006667. https://doi.org/10.1029/2020TC006667

Received 3 JAN 2021
Accepted 22 MAR 2021

The 2018 M_w 7.5 Highlands Earthquake in Papua New Guinea: Implications for Structural Style in an Active Fold and Thrust Belt

Luke Mahoney[1,2], Richard Stanaway[3], Sandra McLaren[1], Kevin Hill[1,4], and Eric Bergman[5]

[1]School of Earth Sciences, University of Melbourne, Melbourne, VIC, Australia, [2]Papuan Oil Search Ltd, Sydney, NSW, Australia, [3]Quickclose Pty Ltd, Melbourne, VIC, Australia, [4]Hill Geostructure Pty Ltd, Melbourne, VIC, Australia, [5]Global Seismological Services, Golden, CO, USA

Abstract The Papuan Fold and Thrust Belt (PFTB) in Papua New Guinea is actively forming within a complex tectonic setting at the boundary of the obliquely converging Australian and Pacific plates. The tectonic setting and inaccessibility of the PFTB make it one of the least well-understood fold and thrust belts on Earth. On February 25, 2018, a M_w 7.5 earthquake occurred within the PFTB, triggering an aftershock sequence which included five events $\geq M_w$ 6. In this study, we combine seismological, GPS and remote sensing observations to investigate the spatiotemporal distribution of crustal deformation during these events. All earthquakes $\geq M_w$ 6 were related to reverse offset on northeast-dipping fault planes and five out of the six, including the mainshock, were associated with midcrustal focal depths (~15–30 km). During the sequence, the PFTB underwent up to 1.2 m of uplift and ground deformation occurred over 7,500 km^2. Combining these observations with our geological knowledge of this convergent margin highlights the primary control of the northern Australian passive margin on PFTB structural style. We propose that the earthquake sequence was related to tectonic inversion on a hidden extensional fault system beneath the PFTB and lateral variations along this fault zone had significant influence on the complex distribution of ground deformation. It follows that this fault system has had an important control on the evolution of variable structural styles within the PFTB. This study highlights the complexity that can characterize the evolution and structural style of fold and thrust belts.

1. Introduction

The process by which continental crust accommodates shortening at convergent tectonic margins is a topic of broad interest as these processes control the distribution of natural hazards and resources (e.g., Cooper, 2007; Groves et al., 1998; Stern et al., 2016). Fold and thrust belts form in response to crustal shortening at such margins and often contain myriad deformational styles—also termed structural styles—which commonly differ between deformed belts or even within individual belts. Many tectonic and geological factors are recognized to influence fold and thrust belt structural styles, most of which relate in some way to (1) the tectonic setting; (2) the crustal composition and architecture of the deforming margin; and/or (3) the dynamic interaction between fold and thrust belt evolution and surface processes. Comprehensive reviews of the factors influencing fold and thrust belt evolution and structural style are provided in Lacombe and Bellahsen (2016), Nemcok et al. (2005), and Poblet and Lisle (2011).

One of the most discussed characteristics of fold and thrust belt structural style relates to the degree to which crystalline basement rocks are involved in contractional deformation. Where only the sedimentary cover is involved, it is known as thin-skinned deformation; where basement rocks are involved, it is known as thick-skinned deformation. However, it is often difficult to identify the relative influences of thin- and thick-skinned processes from the many other factors that influence fold and thrust belt evolution, and due to the time frame over which they act. Furthermore, fold and thrust belt interpretation is inherently biased toward overemphasizing thin-skinned deformation, as thick-skinned processes are often more difficult to identify, both geologically and geophysically, due to the depth at which they commonly occur.

In actively deforming fold and thrust belts, such as the Papuan Fold and Thrust Belt (PFTB) in Papua New Guinea (PNG), the nature and distribution of contemporaneous seismicity and the associated crustal deformation provide valuable insight into evolutionary processes and geological structure at both the surface and

in the subsurface. On February 25, 2018, UTC (February 26, 2018, PNG local time), a M_w 7.5 earthquake occurred within a remote area of the PFTB (also known as the PNG Highlands). It was the largest seismic event ever recorded in the region with modern seismic instruments. The ensuing aftershock sequence, as recorded on global seismic monitoring networks, was spread across >7,500 km^2 of the PFTB. The earthquake shaking and associated extensive slope failure in steep mountainous terrain collectively devastated the local inhabitants and resulted in a widespread humanitarian crisis (e.g., WHO, 2018).

In this study, we use seismological, GPS and remote sensing observations to investigate the nature and spatiotemporal distribution of crustal deformation during the 2018 PNG Highlands earthquake sequence. We combine the new insights with our geological knowledge of this convergent margin to define the factors impacting the structural style and evolution of the PFTB.

2. Tectonic and Geological Background

Papua new guinea (PNG) is the Eastern half of the island of New Guinea, with the Western half being part of Indonesia. The island has undergone a complex tectonic and geological history, particularly throughout the Cenozoic, associated with its location between the obliquely converging Australian and Pacific Plates (Figure 1, inset map). Detailed reviews of the tectonic history of PNG can be found in Hill and Hall (2003), Pigram and Symonds (1991), and Van Ufford and Cloos (2005). The present day setting of PNG is one of the most tectonically complex regions in the world, comprising an assortment of tectonic features including rotating microplates, subduction zones, orogenic belts, rifts, and transform boundaries (e.g., Baldwin et al., 2012; Koulali et al., 2015). These microplate interactions combine to accommodate ~110 mm yr^{-1} of convergence between the Pacific and Australian Plates (DeMets et al., 1994; Tregoning et al., 1998).

Onshore PNG can be split into three major tectonic components following Hill and Hall (2003). In the South, the Stable Platform (SP; Figure 1, inset map) represents the northern Australian continental margin which has been shaped by Mesozoic and Cenozoic extension but remains largely unaffected by Cenozoic deformation along the northern margin. The SP preserves the passive margin architecture that formed the Papuan Basin which continues to the North into what is now the PFTB. Along the northern margin of PNG, the intensely deformed Mobile Belt (MB; Figure 1, inset map) comprises an assortment of island arcs and continental terranes that have been accreted to the leading edge of the northern Australian continental margin during collisional events throughout the Cenozoic. The PFTB separates the SP and MB and comprises laterally discontinuous folded and thrusted structures that collectively form a ~550 km long NW to SE trending belt across PNG (Figure 1). The PFTB formed in response to shortening within the Australian continental passive margin including within the Papuan Basin sediments during convergent movements throughout the Cenozoic, most significantly from the Late Miocene to present (Hill & Raza, 1999; Mahoney et al., 2019; Van Ufford & Cloos, 2005).

Active deformation is presently occurring within onshore PNG, evidenced by widespread seismicity (e.g., Figure 1, inset map). Earthquake locations show that deformation is concentrated around major convergent (Ramu-Markham) and strike-slip (Bewani-Torricelli) fault zones to the North and, to a lesser extent, within the PFTB (e.g., Figure 1) which may accommodate up to 20% of Australian and Pacific plate convergence (e.g., Abers & McCaffrey, 1988, 1994; Wallace et al., 2004). Recent modeling of GPS velocities suggests that the PFTB is rotating in a clockwise manner relative to the Australian Plate, with the rate of convergence varying from 6.8 mm yr^{-1} in the West to 12 mm yr^{-1} in the East (Koulali et al., 2015). Although it is largely unclear how the associated lateral variations in crustal shortening are accommodated within the northern Australian passive margin and PFTB, abundant arc-normal oriented structures and lineaments are observed throughout the PFTB (e.g., Hill et al., 1996; 2008; Mahoney et al., 2017; White et al., 2014) and may provide a suitable mechanism.

The geological complexity, isolation, and challenging terrain of the PFTB make it one of the least well-understood fold belts in the world. Data acquisition is expensive and geological studies are largely limited to resource exploration activities aimed at exploiting a range of richly endowed natural resources. The PFTB contains an abundance of Late Miocene to Pliocene intrusions, some of which host world-class copper-gold deposits (e.g., Porgera, Ok Tedi mines) and a prolific petroleum system including some large hydrocarbon accumulations (e.g., Hides Gas Field, Kutubu Oil Field). Crustal structure is perceived as the primary

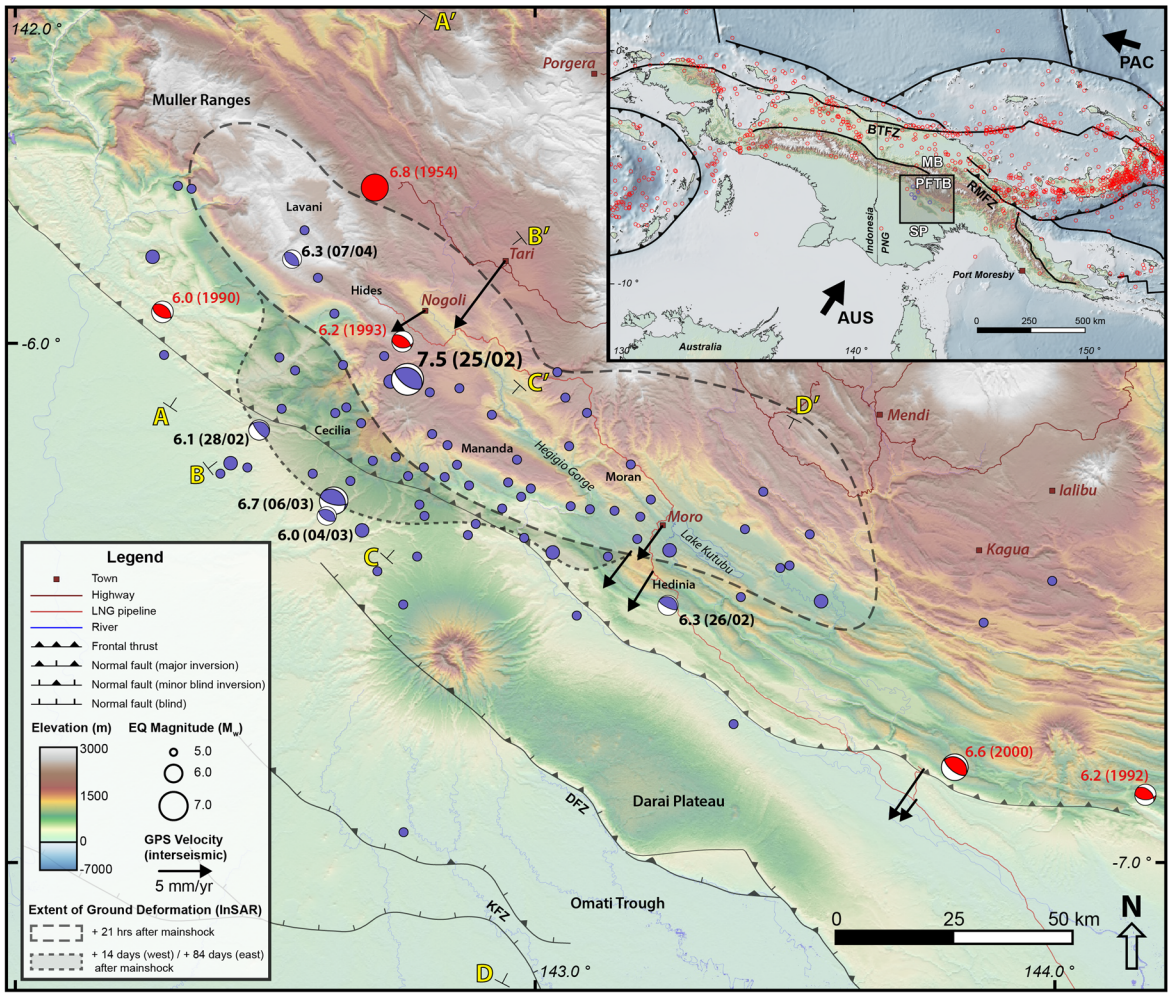
142.0 °
-6.0 °
-7.0 °
143.0 °
144.0 °
A
A′
B
B′
C
C′
D
D′
Porgera
Muller Ranges
6.8 (1954)
Lavani
6.3 (07/04)
Tari
Hides
Nogoli
6.0 (1990)
6.2 (1993)
7.5 (25/02)
6.1 (28/02)
Cecilia
Mananda
Heggigio Gorge
Moran
6.7 (06/03)
6.0 (04/03)
Moro
Lake Kutubu
Hedinia
6.3 (26/02)
Mendi
Ialibu
Kagua
6.6 (2000)
6.2 (1992)
Darai Plateau
DFZ
KFZ
Omati Trough
0 25 50 km
N
PAC
BTFZ
MB
PFTB
RMFZ
SP
Indonesia
PNG
Port Moresby
AUS
Australia
0 250 500 km
Legend
Town
Highway
LNG pipeline
River
Frontal thrust
Normal fault (major inversion)
Normal fault (minor blind inversion)
Normal fault (blind)
Elevation (m)
3000
1500
0
-7000
EQ Magnitude (Mw)
5.0
6.0
7.0
GPS Velocity (interseismic)
5 mm/yr
Extent of Ground Deformation (InSAR)
+ 21 hrs after mainshock
+ 14 days (west) / + 84 days (east) after mainshock

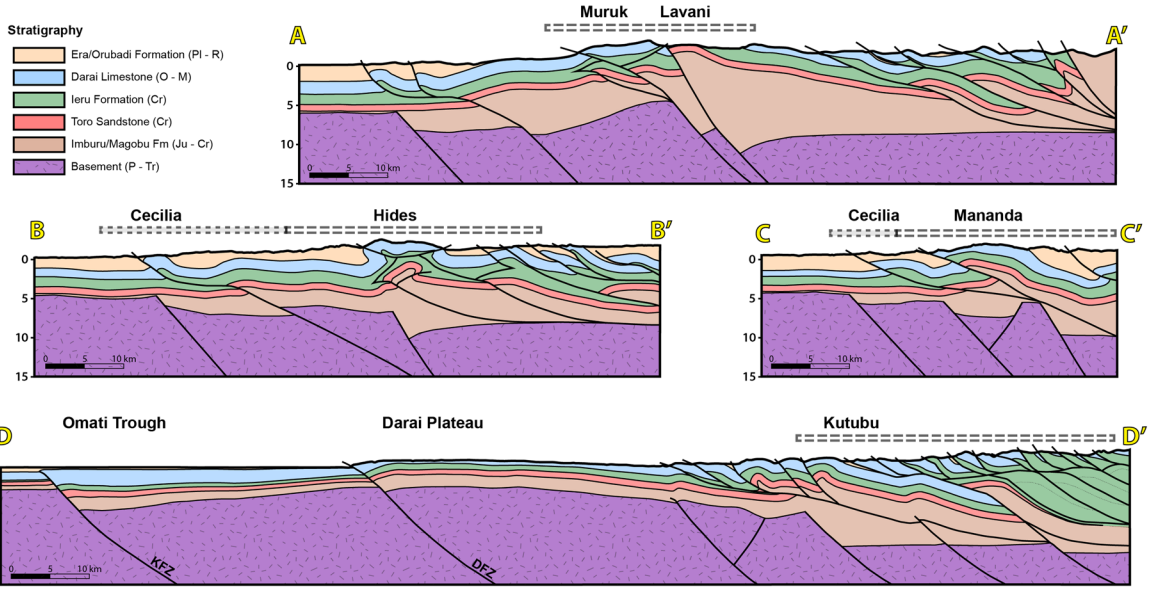
Stratigraphy
Era/Orubadi Formation (Pl - R)
Darai Limestone (O - M)
Ieru Formation (Cr)
Toro Sandstone (Cr)
Imburu/Magobu Fm (Ju - Cr)
Basement (P - Tr)
Muruk
Lavani
A
A′
B
Cecilia
Hides
B′
C
Cecilia
Mananda
C′
D
Omati Trough
Darai Plateau
Kutubu
D′
0
5
10
15
0 5 10 km
KFZ
DFZ

control on both mineral and hydrocarbon systems and thus most studies have focused on understanding the structure and evolution of the margin and PFTB (e.g., Buchanan & Warburton, 1996; Darnault & Hill, 2020; Findlay, 1974; Giddings et al., 2020; Hanani et al., 2016; Hill, 1991; Hill et al., 2000, 2002, 2008, 2010; Hill & Mahoney, 2018; Hobson, 1986; Jenkins, 1974; Keetley et al., 2001; Mahoney et al., 2017; Mason, 1996; Medd, 1996; Thornton et al., 1996).

While it is beyond the scope of this study to provide a comprehensive review of PFTB structural styles, we include an overview of the key structural elements. Various structural styles have been proposed for the PFTB, with an overall progression evident from models primarily comprising thin-skinned deformation (e.g., Findlay, 1974; Hobson, 1986; Jenkins, 1974) to models with variable combinations of both thin- and thick-skinned deformation (e.g., Darnault & Hill, 2020; Giddings et al., 2020; Mahoney et al., 2017). This transition has been driven by multiple factors including: (1) the recognition of pre-existing basement heterogeneities, including both uninverted and inverted Mesozoic extensional structures (e.g., Figure 1) within the northern Australian passive margin in seismic reflection data, mostly across the SP where seismic imaging is of the highest quality (e.g., Bennett et al., 2000; Kawagle & Meyers, 1996; McConachie et al., 2000; Schofield, 2000); (2) the identification of uplifted syn-rift sediments and basement in outcrop and in wells drilled within the PFTB (e.g., Amoco, 1982; Bain et al., 1975; Davies & Norvick, 1974; Eisenberg, 1996); and (3) the increasing recognition, on a global scale, of the important control of passive margin architecture on fold and thrust belt geometry and evolution (e.g., Bonini et al., 2012; Buchanan & Buchanan, 1995; Hinsch et al., 2019).

Almost all contemporary structural cross-sections across the PFTB incorporate thick-skinned deformation, most commonly in the form of inverted normal faults. The associated shortening links through the overlying Papuan Basin sediments as a spatially variable assortment of thin-skinned deformational styles, often including multiple detachment levels, thrusts, backthrusts, and associated fault-related folding (e.g., Figure 1, cross-sections). Indeed, many workers propose spatial variations within the passive margin architecture as the primary influence on significant lateral changes in structural style observed throughout the PFTB (Buchanan & Warburton, 1996; Hill, 1991; Hill et al., 2000; Mahoney et al., 2017). However, as seismic imaging across the fold belt is generally of poor quality (e.g., Hill et al., 2008; 2010), the nature and extent of the extensional architecture deep beneath the PFTB is poorly understood and the degree to which it is involved has been difficult to demonstrate.

3. 2018 PNG Highlands Earthquake Sequence

The 2018 M_w 7.5 PNG Highlands earthquake occurred on February 25, 2018, at 17:45 UTC (03:45 on February 26, PNG local time), with an epicenter located ~96 km West of Mendi (Figure 1) and hypocentral depth in the range variable 15–30 km, depending on the agency determining the location. The moment tensor solution provided by the US Geological Survey (USGS) indicates that the mainshock was associated with reverse movement along an approximately NW to SE striking fault, with a dip of ~30° toward the NE; consistent with the convergent tectonic setting and the structural orientation of the PFTB at the epicentral location (Figure 1). The USGS finite-fault model comprises a single fault plane, but they note that the complex source time function and variable rake are suggestive of a multifault rupture (USGS, 2018). Other published finite-fault inversion studies utilizing seismic data and coseismic observations from spaceborne synthetic

Figure 1. Tectonic, geological, and structural setting of the 2018 PNG Highlands earthquake sequence. Main map: Earthquake locations, extent of earthquake-related ground deformation, and major geological elements of the PFTB. *Blue* circles are seismic events >M_w 5 related to the 2018 PNG Highlands earthquake sequence (UTC occurrence day/month in brackets; events plotted up to May 2019) and *red* circles are historical events >M_w 6 (year in brackets). GPS velocities (Stanaway et al., 2020; Stanaway & Noonan, 2015) plotted with respect to the Australian Plate using ITRF2014 plate motion model (Altamimi et al., 2017). Subsurface faults on the SP after Schofield (2000). Inset map: Tectonic setting of New Guinea including PNG Highlands earthquake-related (*blue*) and historical (*red*) seismic events >M_w 6. *Black* lines represent tectonic boundaries modified from Hill and Hall (2003) and Baldwin et al. (2012). All earthquake data were accessed via the USGS Earthquake Portal (USGS, 2020). SRTM digital elevation model retrieved from USGS (2015). Cross-sections: structural cross-sections along the length of the PFTB illustrating our contemporary understanding of structural styles. Note the along strike structural variability and the complex interactions between thick- and thin-skinned deformation. Cross-sections are constrained by surface (i.e., field geological) and subsurface (i.e., well, seismic reflection) data and have been calibrated with the Bouguer gravity data set shown in Figure 7. AUS, Australian Plate; BTFZ, Bewani-Torricelli Fault Zone; DFZ, Darai Fault Zone; KFZ, Komewu Fault Zone; MB, Mobile Belt; PAC, Pacific Plate; PFTB, Papuan Fold and Thrust Belt; PNG, Papua New Guinea; RMFZ, Ramu-Markham Fault Zone; SP, Stable Platform.

aperture radar (SAR) data have yielded highly variable predictions of the number and orientation of faults activated during the event. After testing both single- and multiple-fault models, Wang et al. (2020) conclude that a four-fault model best fits the data, whereas Zhang et al. (2020) argue for a single-fault model. Chong and Huang (2020) present a model containing three faults (including a detachment). The preferred fault plane orientation in all the aforementioned finite-fault studies strikes NW to SE and dips toward the NE, however the fault dips vary significantly from 6° to 55° (33°, USGS, 2018; 6°–26°, Chong & Huang, 2020; 32°–55°, Wang et al., 2020; 30°, Zhang et al., 2020).

The 2018 PNG Highlands earthquake was the largest ever recorded in the region with modern seismic instruments, with a return period estimated at ~150 years (McCue et al., 2018). The mainshock was followed by an aftershock sequence which included five events ≥M_w 6, spread across ~100 km of the frontal portion of the PFTB (Figure 1). By comparison, the USGS earthquake catalog containing events from 1904 to present includes only five historical (e.g., prior to 2018) earthquakes ≥M_w 6 in the frontal area of the PFTB (Figure 1). The largest aftershock (M_w 6.7) in the earthquake sequence was the third largest event ever recorded—the second largest event was a M_w 6.8 earthquake in 1954, with an epicentral location ~40 km to the NNW of the 2018 PNG Highlands earthquake (Figure 1). The final aftershock ≥M_w 6 and equal third largest earthquake in the sequence was a M_w 6.3 event which occurred 41 days following the main rupture. Five out of the six earthquakes ≥M_w 6, including the mainshock, were associated with focal depths within the upper- to mid-crust (~15–30 km). Preferred moment tensor solutions for all five aftershocks ≥M_w 6 are consistent with the mainshock, indicative of reverse movement along NE-dipping faults with only minor variations in orientation and degree of obliquity (Figure 1).

Shaking associated with the earthquake sequence caused widespread slope failure in the steep topography of the PFTB, particularly within gorges and the unstable flanks of the large Pliocene to Pleistocene stratovolcanoes in the area (e.g., Figure 2a). Landslides were particularly catastrophic along the southern wall of the Hegigio Gorge (Figure 1), where giant slabs of the Miocene Darai Limestone broke free from the steep backlimb of the Mananda Anticline, sliding along bedding-parallel failure planes into the gorge below (Figure 2b). Although surface ruptures were not directly observed following the earthquake sequence, this is most likely because of the remote and densely vegetated nature of the area. Indeed, published analyses of remotely sensed data suggest that significant surface rupturing did likely occur (e.g., Chong & Huang, 2020; Wang et al., 2020). At Lake Kutubu (Figure 1), uplift in the NW manifested as an increase in the lake bank height relative to the water level (~1 m; e.g., Figure 2c), while subsidence in the South led to flooding. The "severe to violent" earthquake shaking (USGS, 2018; based on scale from Worden et al., 2012) and associated extensive land slips and rock falls devastated local communities with at least 125 fatalities and widespread building and infrastructure damage (WHO, 2018). Operations at the nearby Porgera and Ok Tedi mines were suspended temporarily and oil and gas operations and associated facilities were closed for months.

3.1. Earthquake Locations

The earthquake locations shown in Figure 1 were resolved by the USGS National Earthquake Information Centre (NEIC) based on recordings from the global seismographic network (GSN) and the global 1-D travel time model AK135 (Kennett et al., 1995). The GSN includes a single station within PNG, located in the nation's capital of Port Moresby >600 km from the 2018 PNG Highlands earthquake mainshock location. This is the only GSN station within 1,500 km of the event. The next closest seismographs are scattered throughout northern Australia, SE Asia, and the Pacific Islands (e.g., Gee & Leith, 2011). Because of the remoteness of the PNG Highlands earthquake sequence relative to the GSN, significant earthquake location uncertainties exist which could be in the order of 10–30 km, depending on the magnitude of velocity variations within the surrounding regions (USGS, 2018). Local seismograph recordings are central to identifying velocity variations and thus, where present, provide a valuable means of refining earthquake locations. Although the Port Moresby Geophysical Observatory operates a limited local seismograph network across PNG (e.g., Ghasemi et al., 2018), its condition is unknown and no data were available to this study.

In lieu of arrival time data from local seismic stations, we attempted to reduce the locational uncertainty of the earthquake cluster using the multiple event earthquake relocation software mloc, which incorporates the hypocentroidal decomposition method of Jordan and Sverdrup (1981). A detailed description of

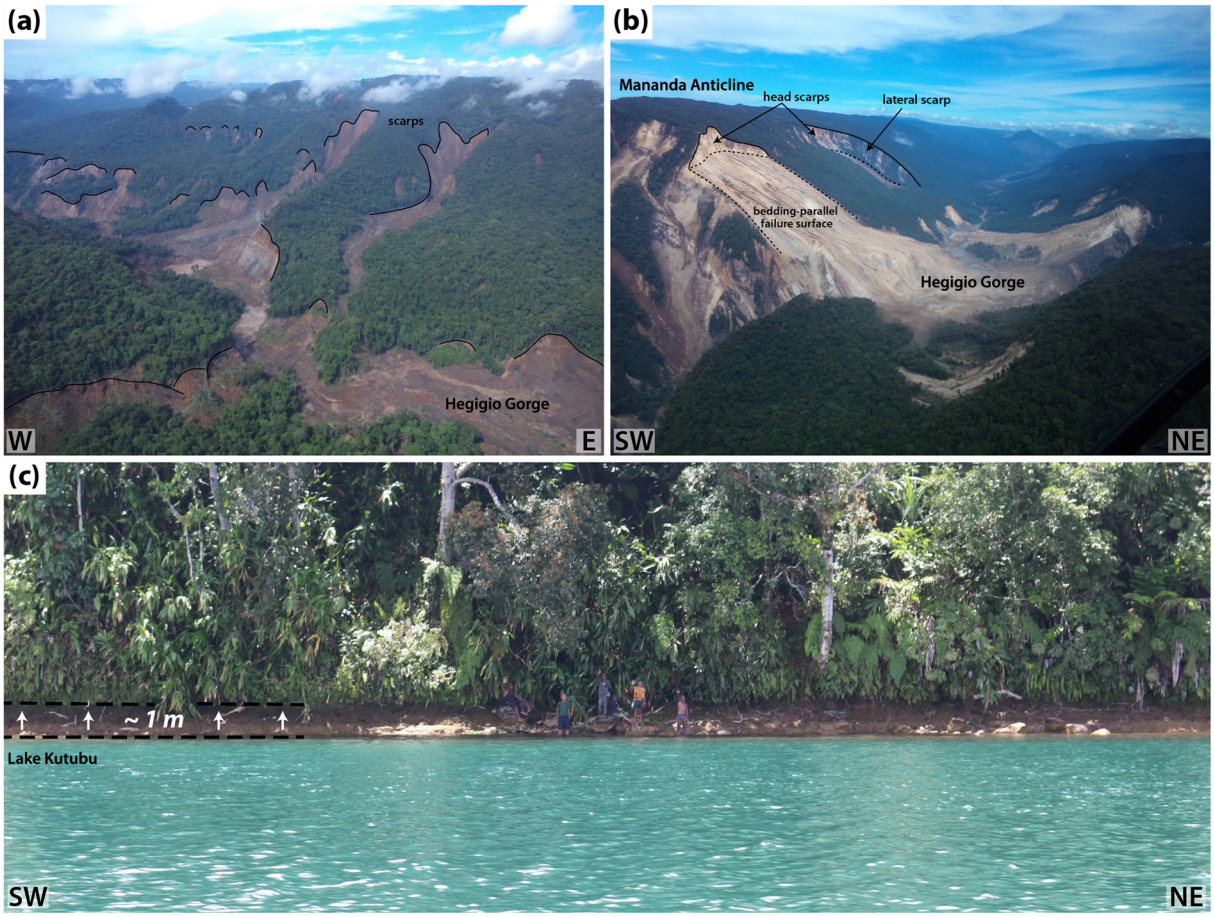

Figure 2. Photos showing the aftermath of the 2018 PNG Highlands earthquake sequence: (a) northern wall of the Hegigio Gorge showing landslides within unconsolidated reddy-brown volcanic rocks in the flanks of the Mt Kerewa stratovolcano; (b) southern wall of the Hegigio Gorge showing bedding-parallel sliding of large slabs of Darai Limestone from the backlimb of the Mananda Anticline; (c) NW bank of Lake Kutubu showing an increase in the lake bank height relative to the water level. Photo credits: (a, b) Papuan Oil Search, (c) Nick Hannaford. Photo locations are shown in Figure 6.

mloc can be found on the program website (https://seismo.com/mloc/). To minimize the biasing effect of unknown velocity structure, the available NEIC data set was restricted to teleseismic P arrivals—the most stable and accurate branch of the global travel time model—between 30° and 90° and ~24,000 readings were used to estimate the absolute locations of the earthquake cluster. The relative locations of events within the cluster (e.g., cluster vectors) were recalculated using a larger data set including all available arrival time data.

The relocated earthquakes are plotted in Figures 3 and 4. The M_w 7.5 mainshock shifted ~10 km toward the East, but the most prominent overall trend was for events to shift between 5–15 km toward the NE. We believe the relocated events are a significant improvement on the USGS locations because: (1) numerous events that were previously located forelandward of the frontal thrust shifted to within the PFTB and (2) the relocated events provide an improved fit with the distribution of ground deformation observed during the earthquake sequence (e.g., Figure 4). Although the relocated events are improved, we suspect based on the data and analyses presented within this study that many are still located 5–10 km forelandward (i.e., toward the SW) of their true locations. This is, however, difficult to demonstrate in the absence of local velocity calibration and earthquake locations remain poorly constrained.

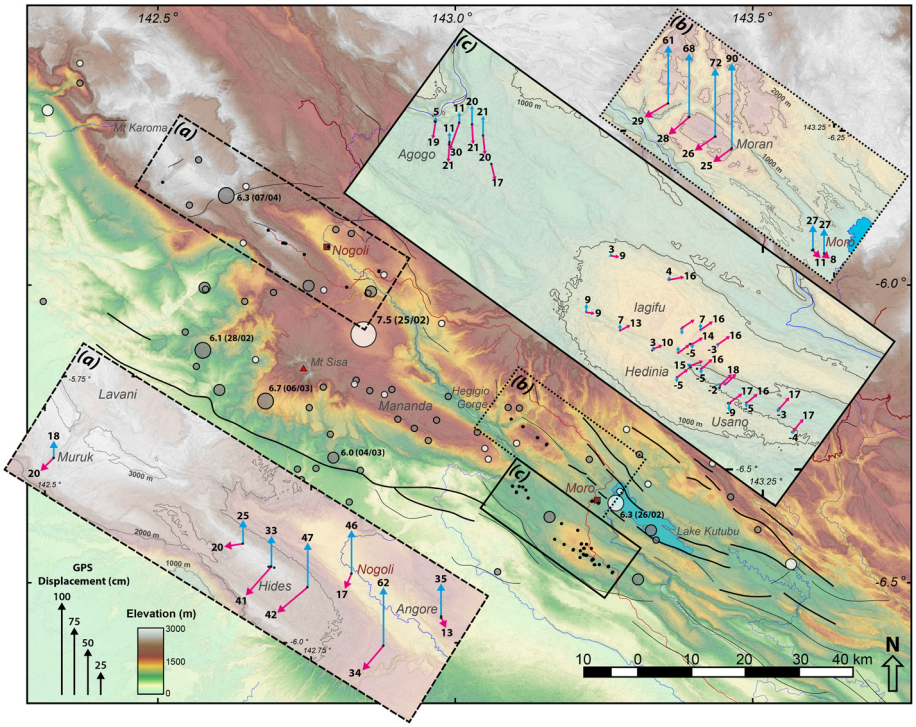

Figure 3. GPS surface displacements, relocated earthquakes >M_w 5 and surface rupturing interpreted from InSAR (e.g., Figures 4 and 5). Legend shown in Figure 4. Vectors show coseismic displacements observed by static GPS and are in terms of ITRF2014. Events >M_w 6 are labeled with magnitude and UTC occurrence time (day/month). *Magenta* arrows show horizontal displacement and *blue* arrows show vertical displacement. For display purposes—(a and b) insets are spatially exaggerated × 1.75; (c) inset is spatially exaggerated × 3.5. GPS displacement arrows are displayed at a consistent scale in all insets.

3.2. Crustal Deformation

In this section, we combine GPS measurements with remote sensing observations to analyze the spatiotemporal distribution of crustal deformation associated with the 2018 PNG Highlands earthquake and aftershock sequence. To support oil and gas exploration and development within the remote frontal PFTB, a geodetic network has been established and maintained since 2005 across much of the area affected by the PNG Highlands earthquake sequence. GPS measurements for many of the stations in the PFTB network have <20 mm accuracy (95% CI) and so provide a high fidelity means of monitoring both interseismic and coseismic displacement and for ground truthing remotely sensed geodetic observations such as interferometric synthetic aperture radar (InSAR). InSAR is a powerful technique for measuring widespread ground deformation (e.g., Gabriel et al., 1989; Rosen et al., 2000) and thus is an effective tool for understanding the spatial and temporal distribution of displacement related to earthquake sequences. Following the PNG Highlands earthquake, the Geospatial Information Authority of Japan (GSI) published a series of InSAR displacement maps produced from Advanced Land Observing Satellite 2 (ALOS-2) data (GSI, 2018). In this section, we use GPS- and InSAR-derived displacements to analyze the magnitude and distribution of coseismic deformation associated with the PNG Highlands earthquake sequence.

Approximately 700 GPS stations within the PFTB have been surveyed since 2005; however, the remoteness of most of the sites means that only a small proportion have been reobserved regularly. For these sites, each set of observed positions can be stacked to form a time series of station movement within the ITRF2014, allowing for the estimation of interseismic site velocities (e.g., velocities largely due to secular plate motion). The ITRF2014 trajectories have been transformed to an Australian Plate frame using ITRF2014 plate motion model of the Australian Plate (Altamimi et al., 2017). Observations made after the 2018 PNG Highlands earthquake can therefore be isolated from the time series analysis in order to estimate coseismic displacement arising from the event.

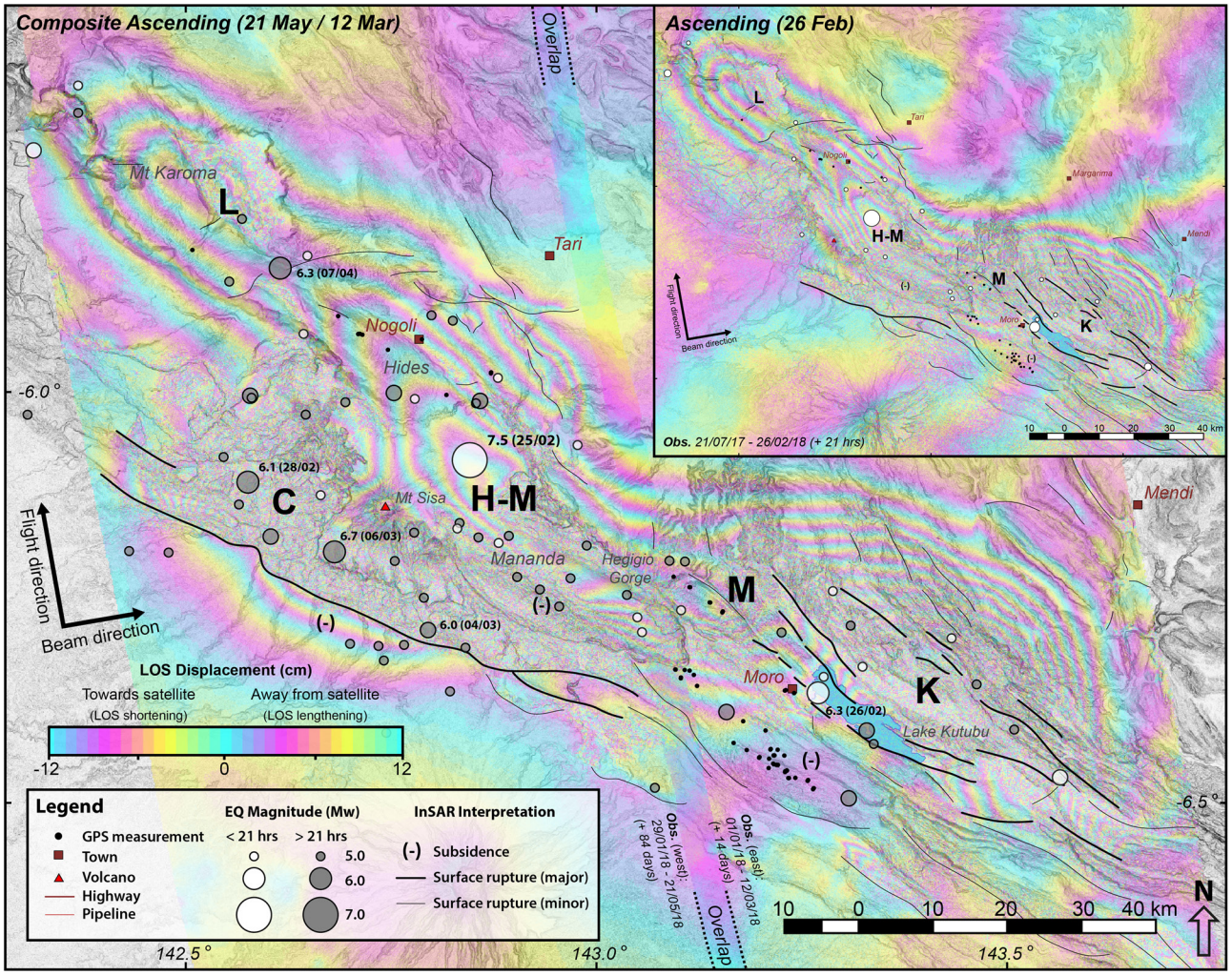

Figure 4. Ascending interferograms (GSI, 2018) collectively showing the evolution of LOS displacement, relocated earthquakes >M_w5 and interpretation of coseismic surface rupturing related to the 2018 PNG Highlands earthquake sequence. Earthquake data are split at the time of the second ascending observation in the inset (14:46, February 26, 2018 (UTC) or + 21 h after the mainshock): *white* circles represent earthquakes before the satellite pass and *gray* circles represent earthquakes after the satellite pass. Events >M_w 6 are labeled with magnitude and occurrence time (day/month). Main: Interpreted composite ascending interferogram showing surface deformation associated with the mainshock and aftershock sequence, up to the second observation dates of March 12, 2018 (+14 days after mainshock) in the East and May 21, 2018 (+84 days after mainshock) in the West. Inset: Interpreted ascending interferogram showing the distribution of earthquakes and extent of surface deformation up to February 26, 2018 (+21 h after mainshock). H-M, Hides-Mananda zone; K, Kutubu zone; L, Lavani zone; M, Moran zone; C, Cecilia zone. InSAR analysis was carried out by the Geospatial Information Authority of Japan (GSI) using ALOS-2 data of the Japan Aerospace Exploration Agency (JAXA). The interferograms are published on the GSI website (GSI, 2018).

Following the 2018 PNG Highlands earthquake, a GPS resurvey of 71 sites was conducted between March 15 and October 5, 2018, across ~200 km of the strike-length of the frontal PFTB. Every effort was made to avoid survey stations that had been disturbed during the earthquake sequence by localized ground instability. Observations were taken at variable time following the mainshock and consequently include some postseismic deformation and additional coseismic deformation from the aftershock sequence. In some cases, there is also a significant time lag between previous observations (pre-earthquake) and the occurrence of the event, so it is noted that additional movements (e.g., unrelated to the PNG Highlands earthquake sequence) during this time could be incorrectly attributed to the PNG Highlands earthquake sequence.

GPS measurements reveal the spatial distribution of ground deformation during the earthquake sequence in remarkable detail (Figure 3). Significant variations in vertical and horizontal displacement were detected, suggestive of a complex pattern of deformation, potentially associated with movement along multiple faults. The most dominant surface displacement was up and to the SW, recorded at Muruk, Hides, Nogoli,

and Moran (Figure 3). From NW to SE across these areas, an overall trend toward increased vertical and decreased horizontal displacement was detected. Angore, Agogo, and Moro were also uplifted, but with dominantly South to SE horizontal movement (Figure 3). Areas of subsidence and East to NE horizontal displacements were observed at Hedinia, Iagifu, and Usano, to the South of the uplifted zone (Figure 3).

A composite ascending interferogram is shown with GPS measurement locations in Figure 4 and shows the lateral extent of ground deformation within the PFTB, extending ~170 km in a NW-SE direction and ~50 km in a NE-SW direction. The InSAR-derived displacement appears broadly consistent with GPS control points (c.f. Figures 3 and 4) but would not be expected to be in perfect agreement due to the InSAR being a one-dimensional measurement along the line of sight (LOS) of the satellite. One of the advantages of the InSAR technique is that it provides a widespread and mostly continuous map of ground deformation. The distribution of earthquakes relative to LOS displacement (i.e., earthquakes mostly located to the South-SW) suggests that ground deformation was related to hanging wall uplift (e.g., fault-related folding) along NE-dipping fault planes—which is consistent with moment tensor and finite-fault model solutions (USGS, 2018; Wang et al., 2020; Zhang et al., 2020). We interpret at least five distinct zones of ground deformation based on GPS measurements and the ascending and descending interferograms published on the GSI website (GSI, 2018), along with an abundance of small-scale features that may represent surface ruptures such as fissures or scarps.

3.2.1. Hides-Mananda Zone

The elongate, oval-shaped Hides-Mananda ground deformation zone is spatially the most significant, with a NE to SW extent of ~25–30 km and strike length of ~80 km from the NW end of the Hides Anticline to the SE end of the Mananda Anticline (Figure 4). GPS measurements along the length of the Hides Anticline indicate increasing uplift from 25 cm in the NW to 62 cm in the SE (Figure 3a). LOS shortening (displacement toward the satellite) on the composite ascending interferogram (Figure 4) reaches a maximum of ~70 cm immediately to the North of the Mananda Anticline in the Hegigio Gorge—the focus of landslide activity during the earthquake sequence (e.g., Figures 2a and 2b). Ground movement decreased rapidly toward the SE of the Hegigio Gorge, with GPS measurements at Agogo recording up to 21 cm of uplift and up to 30 cm of approximately South-directed movement (Figure 3c).

The M_w 7.5 mainshock occurred within the NW of the Hides-Mananda zone and, as the only earthquake $>M_w$ 6 within the zone, it was probably the source of most of the observed ground deformation. There is no field or remotely sensed evidence for surface rupturing around the Hides Anticline, suggesting that most of the displacement was related to fault slip at depth—an observation that is supported by finite-fault slip inversions (e.g., S1 and S2 in Wang et al., 2020; Asperity A in Zhang et al., 2020). However, to the SW of the Mananda Anticline, within the frontal-most structures of the fold belt, an area of strong interferometric decorrelation on the interferograms relates to an abundance of near-surface movements which are probably mostly landslides, but could also be surface rupturing associated with the Hides-Mananda uplift zone (e.g., Figure 4). Indeed, Chong and Huang (2020) detect surface rupturing on the Mananda Fault along with several major landslides throughout the area using SAR subpixel offsets. An oval-shaped area of LOS lengthening (displacement away from the satellite) is evident on the descending interferogram (Figure 5) centered on the Mananda Anticline, immediately to the North of the suspected surface rupture zone. It is, however, unclear whether this occurrence is related to local slope failure or ground subsidence related to the overthrusting of the Hides-Mananda zone to the North.

3.2.2. Kutubu Zone

The Kutubu zone is located to the East of the Hides-Mananda zone and signifies a hinterland-directed shift in the overall ground deformation trend relative to the fold belt (Figure 4). LOS shortening in the Kutubu zone strikes NW to SE and is parabolic in shape: convex to the NE and sublinear to the SW. The zone has similar spatial dimensions to the Hides-Mananda zone—a SW to NE extent of ~30 km and strike length of ~70 km—which gives the two zones an en echelon appearance (Figure 4). GPS observations within the Kutubu zone were limited to its southern margin at Moro where 27 cm of uplift and 8–11 cm of SE displacement was recorded (Figure 3b). Immediately to the South of the Kutubu zone, GPS measurements from the Hedinia, Iagifu, and Usano anticlines indicated a decrease in the magnitude of vertical displacement and change to NE horizontal movement, which ranged from 9 cm in the NW to 17 cm in the SE (Figure 3c).

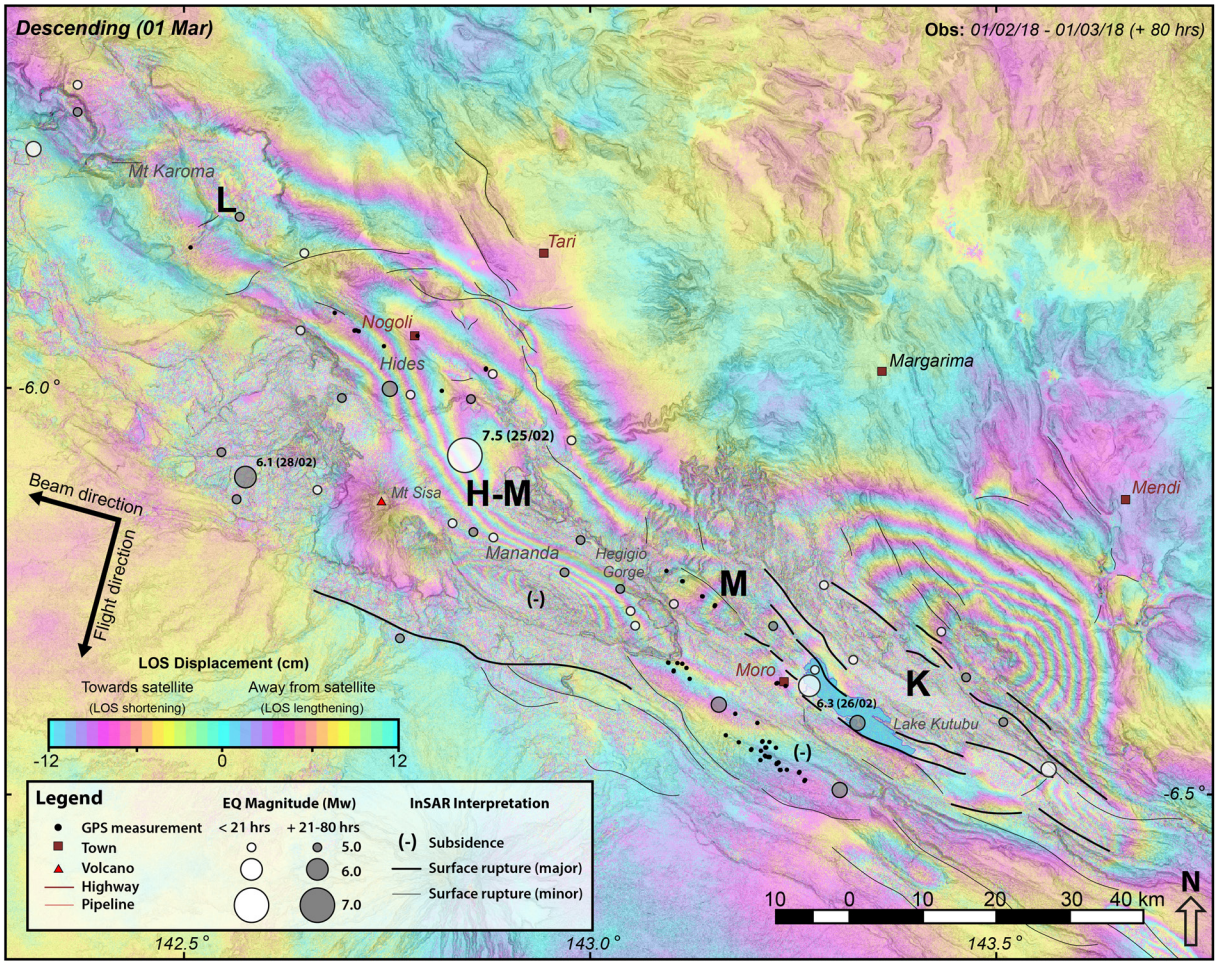

Figure 5. Interpreted descending interferogram (GSI, 2018) with second observation at 02:05, March 1, 2018 (UTC), + 80 h after mainshock. Relocated earthquakes >M_w 5 occurring prior to the time of second observation plotted (e.g., events occurring within 80 h of the 2018 PNG Highlands mainshock), along with an interpretation of possible surface rupturing. Note the oval-shaped area of LOS lengthening centered on the Mananda Anticline and the circular area of LOS shortening centered on the Moran Anticline—features that are less evident on the ascending interferograms (e.g., Figure 4). Descending LOS displacements differ from ascending LOS displacements due to differences in satellite sensor viewing geometry (e.g., western ground motion may contribute to cancelling out uplift in the descending geometry).

Vertical ground movements at Hedinia and Iagifu were variable with a general NW to SE trend from uplift (up to 9 cm) to subsidence (up to 5 cm). Further to the SE, Usano also underwent subsidence of between 2 and 9 cm (Figure 3c). Subsidence and NE movement throughout this area of the frontal fold belt most likely resulted from footwall subsidence in response to the overthrusting of the Kutubu zone to the North.

Based on the interferograms, the Kutubu zone underwent the greatest magnitude of ground displacement during the earthquake and aftershock sequence, reaching >120 cm of LOS shortening to the NE of Lake Kutubu (Figure 4). The largest aftershock in the area was a M_w 6.3 event with an epicentral location to the SW of the zone. Most of the seismicity and associated ground deformation in the Kutubu zone occurred within 21 h of the mainshock (Figure 4, cf. inset and main). A prominent zone of interferometric decorrelation in the area of greatest LOS shortening to the North and NE of Lake Kutubu suggests significant near-surface deformation may have occurred, attributable in part to landslides, but also potentially indicative of surface rupturing—as predicted within this area based on SAR analyses and finite-fault modeling (e.g., Mubi Fault in Chong & Huang, 2020; USGS, 2018; S4 in Wang et al., 2020).

3.2.3. Lavani Zone

The Lavani zone is centered on the Lavani Valley to the NW of the Hides Anticline in the eastern Muller Range. The ascending interferograms suggest that ground deformation within this zone extended ~30 km SW to NE and ~40 km from NW to SE (Figure 4). The only GPS locality within the Lavani zone was at Muruk, which underwent 18 cm of uplift and 20 cm of SW displacement (Figure 3a). On the ascending interferograms, the greatest magnitude of LOS shortening in the Lavani zone was ~40 cm around Mt Karoma (Figure 4)—which is the highest mountain in this region of the fold belt reaching ~3,600 m above mean sea level. The Lavani zone appears semicontinuous to the Hides-Mananda zone, with a slightly en echelon appearance. The two zones are differentiated based on: (1) a "saddle" evident within interferometric displacement between the NW end of the Hides Anticline and SE end of Lavani Valley, and (2) significant rake angle differences in finite-fault models (e.g., USGS, 2018; S2 and S3 in Wang et al., 2020). The largest seismic event within the zone was a M_w 6.3 aftershock which occurred at a midcrustal depth (~18 km) over 40 days after the mainshock. However, a comparison of ascending interferograms from prior to, and following this aftershock (Figure 4, cf. inset and main) suggests that the event was not associated with significant ground deformation and that most of the ground deformation in the Lavani zone occurred within 21 h of the mainshock. There is a scarcity of evidence for near-surface deformation within the Lavani zone, except for some minor approximately West to East striking discontinuities within the interferograms (e.g., Figures 4 and 5).

3.2.4. Moran Zone

The Moran zone is most identifiable within the descending interferogram (Figure 5), located between the more extensive Hides-Mananda and Kutubu zones. The zone is characterized by a circular area of LOS shortening with a diameter of ~20 km, centered on the Moran Anticline. Despite being located over 30 km from the mainshock epicenter, the Moran zone was associated with the greatest magnitude of ground deformation of all the areas surveyed by GPS. Uplift reached 90 cm near the crest of the Moran Anticline (Figure 3b). Measurements along the length of the anticline revealed a trend of increasing uplift to the SE, from 61 to 90 cm, with an accompanying decrease in horizontal SW movement from 29 to 25 cm (Figure 3b).

The Moran zone is recognizable on both the ascending and descending interferograms (Figures 4 and 5) but is located within an area of significant interferometric decorrelation. This makes it difficult to determine the precise magnitude of LOS shortening, which appears to be ~60–90 cm (Figures 4 and 5), an amount that is broadly consistent with GPS measurements. Uplift in the Moran zone occurred within 21 h of the mainshock, coeval with uplift in the neighboring Hides-Mananda and Kutubu zones (Figure 4, inset). The complex pattern of ground deformation evident on the interferograms plausibly relates to increased structural complexity within the area. The abundance and severity of interferometric decorrelation in this zone result from widespread slope failure—also recognized in SAR subpixel offsets (Chong & Huang, 2020)—within the unconsolidated volcanic and volcanoclastic rocks surrounding the Moran Anticline, which is located between the towering Mt Kerewa stratovolcano to the North and the steep-sided Hegigio Gorge to the South (e.g., Figures 2a, 2b and 6).

3.2.5. Cecilia Zone

The Cecilia zone is located to the West and SW of the Hides-Mananda zone and represents the most forelandward extent of ground deformation resulting from the 2018 PNG Highlands earthquake sequence (Figure 4, main). No GPS measurements were acquired within this zone due to its remoteness and the absence of infrastructure such as buildings and roads. The Cecilia zone is characterized by a greater severity of interferometric decorrelation than the other zones—a result of the steep terrain and geology of the area, which is dominated by unconsolidated synorogenic sediments and volcanic and volcanoclastic rocks surrounding the Mt Sisa stratovolcano (Figure 6). The decorrelation challenges any detailed interpretation of ground deformation.

But it is clear from the interferograms that, unlike the other zones, most of the ground deformation within this area occurred >21 h after the mainshock (Figure 4, cf. main and inset). Deformation most likely resulted from a series of aftershocks that occurred within the Cecilia zone following the mainshock, including: a M_w 6.1 event ~2.5 days later; a M_w 6 event ~7 days later; and a M_w 6.7 event ~9 days later (e.g., Figure 6). The SW edge of interferometric decorrelation forms a sublinear trend that parallels the strike of the frontal thrust of the PFTB, a structure that has historically been associated with some of the largest seismic events

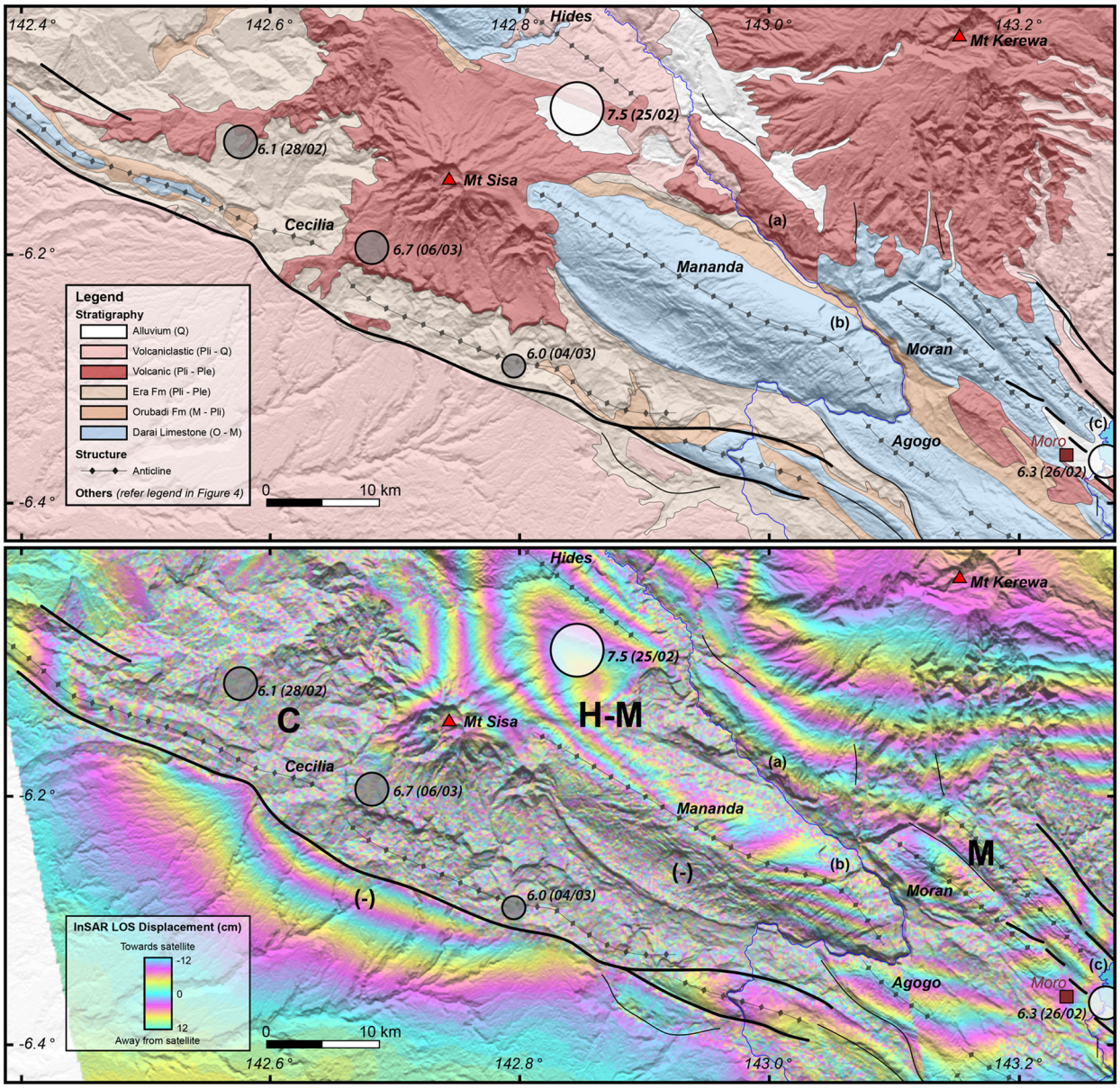

Figure 6. Geological map (top) and interpreted composite ascending interferogram (bottom) for part of the area affected by the 2018 PNG Highlands earthquake. Maps are plotted at the same scale and include both relocated earthquakes >M_w 6 and interpreted coseismic surface rupturing. Note: (1) the folded southern flank of Mt Sisa—a Plio-Pleistocene stratovolcano—suggestive of recent activity on the frontal thrust and associated Cecilia Anticline and (2) the sublinear trend along the frontal thrust within the interferogram, interpreted here as a major surface rupture. Geological map modified from Brown and Robinson (1982). Labels (a–c) represent the locations of photos within Figure 2. Composite ascending interferogram retrieved from GSI (2018), observation dates are detailed within Figure 4 (Main). SRTM digital elevation model retrieved from USGS (2015).

in the PFTB (Figure 1). In the Cecilia zone, the frontal thrust and associated hanging wall anticline—the Cecilia Anticline—clearly deform the southern flank of Mt Sisa, a Pliocene to Pleistocene stratovolcano, signifying neotectonic activity on the thrust (e.g., Figure 6). We interpret the sublinear trend in the interferogram at leading edge of the Cecilia Anticline as a potential surface rupture (Figures 4 and 6). The ascending interferogram indicates a parabolic convex to the SW zone of LOS lengthening up to ~36 cm directly to the SW of the Cecilia Thrust (Figures 4 and 6), potentially indicative of footwall subsidence, possibly in response to overthrusting of the Cecilia Anticline. Chong and Huang (2020) and Wang et al. (2020) do not recognize ground deformation, surface rupturing, and/or faulting within this area, but it is noted that their

second SAR observations of this area (February 28, 2018 and March 01, 2018, respectively) pre-date the occurrence of the M_w 6 and M_w 6.7 aftershocks.

4. Discussion

4.1. Implications of Seismicity and Ground Deformation for PFTB Structural Style

The distribution of seismicity and ground deformation associated with the 2018 PNG Highlands earthquake sequence has provided significant new insight into the controls on structural style within the PFTB. The broad spatial distribution of seismicity and ground deformation, along with the midcrustal hypocentral depths of many of the largest seismic events, implies a deep crustal influence on the earthquake sequence. Indeed, there is a clear disparity between the dimensions of fold and thrust structures within the PFTB (typically tens to hundreds of square kilometers) and the spatial extent of ground deformation associated with the PNG Highlands earthquake sequence (>7,500 km^2; e.g., Figures 1 and 7). In contrast, there are remarkable spatial and morphological similarities between the ground deformation and the Darai Plateau located ~50 km to the South on the SP (Figures 1 and 7). The Darai Plateau is bound to the SW by an inverted listric extensional fault, the Darai Fault, across which to the NE the thickness of Papuan Basin sediments more than doubles (Figure 1, D-D′, Darai Fault Zone [DFZ]; Hill et al., 2010). Approximately 50 km South of the Darai Plateau, the Omati Trough has a similar spatial extent and is bound to the SW by the Komewu Fault—a similar listric extensional fault that had undergone only very minor inversion (Figure 1, D-D′, Komewu Fault Zone [KFZ]). The Komewu Fault also accommodates significant sediment thickening toward the NE into the Omati Trough (Figure 1, D-D′; Schofield, 2000). As such, the Komewu and Darai faults formed as a pair of major NE-dipping listric extensional faults on the northern Australian passive margin that have likely had a principal control on the formation of the Papuan Basin. The comparable scale and form of ground deformation observed during the PNG Highlands earthquake sequence, along with its location along the same approximately North-South trend defined by the Omati Trough and Darai Plateau (e.g., Figure 1), is compelling evidence that the earthquake sequence initiated along an analogous listric normal fault located deep beneath the PFTB (e.g., Figure 7e). While several authors have hypothesized that major extensional structures exist beneath the PFTB (e.g., Buchanan & Warburton, 1996; Hill, 1991; Hill et al., 2008), their existence has not been convincingly demonstrated due to the poor quality of seismic imaging and a lack of deep well penetrations. We believe that our analysis of the PNG Highlands earthquake sequence and associated ground deformation provides important new support for the presence of a major actively inverting extensional structure beneath the PFTB.

Airborne and land-based gravity data sets are used to delineate density distributions within the earth and one of their common applications has been to investigate the basement architecture beneath fold and thrust belts (e.g., Ali et al., 2009; Ayarza et al., 2005; Snyder & Barazangi, 1986; Vera et al., 2010). A merged data set comprising the highest resolution Bouguer corrected gravity data available across this area of PNG is shown in Figure 7c. The Bouguer gravity anomaly decreases into the Omati Trough and increases over the inverted Darai Plateau, as expected for deeper and shallower high-density basement respectively (e.g., Figure 1, D-D′). Excluding these areas, there is an overall regionally decreasing trend in the Bouguer gravity anomaly toward the NE, which is consistent with sedimentary thickening and deepening basement into the Papuan Basin. Interestingly, there is an abrupt decrease in the Bouguer gravity anomaly of >50 mGal evident near the leading edge of the fold belt in the East which wraps around toward the hinterland in the West (Figure 7c). The abrupt nature of this decrease suggests a step-like decrease in density toward the NE, as would be expected across a significant (>3 km offset) normal fault. This provides further evidence for the presence of a major extensional structure beneath the PFTB, across which the Papuan Basin sediment fill is likely to thicken significantly toward the NE. Additionally, the lateral distribution of this step-like decrease in Bouguer gravity anomaly correlates well with the distribution of seismicity and ground deformation associated with the PNG Highlands earthquake sequence (e.g., Figure 7). We interpret this relationship as additional evidence that the 2018 PNG Highlands earthquake was related to inversion on a significant but previously unidentified listric extensional fault beneath the PFTB.

Prior to discussing the nature of this concealed structure in more detail, it is important to note that while we refer to the Komewu and Darai faults as single faults above for simplicity, they are more likely complex

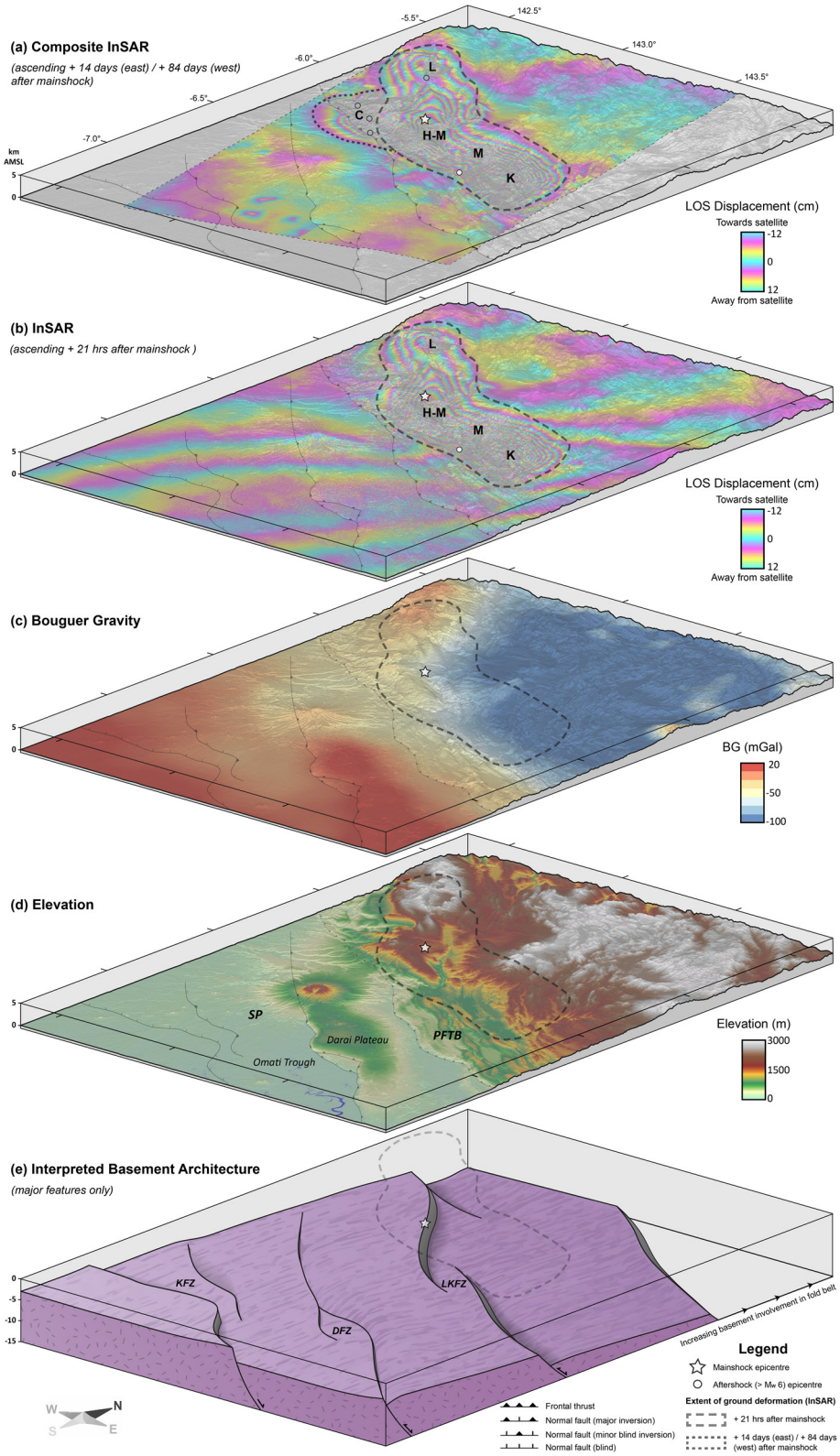
(a) Composite InSAR
(ascending + 14 days (east) / + 84 days (west) after mainshock)
-5.5°
142.5°
-6.0°
143.0°
-6.5°
143.5°
-7.0°
km AMSL
5
0
L
C
H-M
M
K
LOS Displacement (cm)
Towards satellite
-12
0
12
Away from satellite
(b) InSAR
(ascending + 21 hrs after mainshock)
L
H-M
M
K
LOS Displacement (cm)
Towards satellite
-12
0
12
Away from satellite
(c) Bouguer Gravity
BG (mGal)
20
-50
-100
(d) Elevation
SP
Darai Plateau
PFTB
Omati Trough
Elevation (m)
3000
1500
0
(e) Interpreted Basement Architecture
(major features only)
0
-5
-10
-15
KFZ
DFZ
LKFZ
Increasing basement involvement in fold belt
W
N
S
E
Legend
Mainshock epicentre
Aftershock (> Mw 6) epicentre
Extent of ground deformation (InSAR)
+ 21 hrs after mainshock
+ 14 days (east) / + 84 days (west) after mainshock
Frontal thrust
Normal fault (major inversion)
Normal fault (minor blind inversion)
Normal fault (blind)

extensional "zones" comprising multiple listric normal faults that interact as single extensional structures at a regional scale. Such structures are detected across the SP in seismic images (e.g., Kawagle & Meyers, 1996; McConachie et al., 2000; Schofield, 2000). The detailed architecture of the KFZ is particularly well resolved by a dense network of 2D seismic lines of good quality (enabled by flat topography), which facilitates imaging of multiple overlapping listric normal faults connected by soft- and hard-linked transfer zones (e.g., Schofield, 2000). No seismic data exists across the DFZ, but transfer zones are clearly evident within the leading edge of the Darai Plateau (e.g., Figures 1 and 7d). The transfers within the inverted fault system are likely to reflect underlying complexities within the extensional fault zone that are analogous to those imaged within less-inverted structures in the adjacent KFZ (e.g., Figure 7e). This kind of extensional architecture has been suspected beneath parts of the fold belt (e.g., Hill et al., 2010; Mahoney et al., 2017), but has been difficult to demonstrate.

It follows that the major extensional structure beneath the PFTB that has been reactivated during the 2018 PNG Highlands earthquake sequence comprises a similarly complex zone of listric normal faults, which we refer to collectively as the Lavani-Kutubu Fault Zone. Indeed, the compressional reactivation (i.e., inversion) of multiple normal faults during the earthquake sequence provides a possible explanation for the distinct zones of ground deformation (e.g., Section 3.2) and is consistent with the preferred finite-fault model of Wang et al. (2020) which includes four faults that extend to midcrustal depths. For example, the observed en echelon appearance of the Hides-Mananda and Kutubu ground deformation zones (e.g., Figures 4 and 7) may reflect the reactivation of two (or more) listric normal faults separated by basement transfer zones (e.g., Figure 7e). While it is not uncommon for multiple faults to fail during large earthquake sequences within convergent settings (e.g., Jiang et al., 2018; Kao & Chen, 2000; Xu et al., 2009; among many others), there are very few documented examples of multiple pre-existing extensional structures actively inverting during a single seismic event (e.g., Camanni et al., 2013; 2016; Hirata et al., 2005; Kato et al., 2006; 2008).

An unexplained element of the ground deformation during the 2018 PNG Highlands earthquake sequence remains the complex distribution of interpreted surface rupturing (e.g., Figures 4 and 5). In contrast to the broad overall wavelength of ground deformation, the distribution of surface rupturing appears to conform well with the topographic expression of fold and thrust structures—many of which exhibit evidence for neotectonics (e.g., Figure 6). There appear to be lateral variations in how crustal shortening associated with the deep seismic event has been accommodated throughout the sedimentary section. For instance, across the Kutubu and Cecilia ground deformation zones, surface rupturing appears to have been concentrated to the SW (e.g., Figure 4), as would be expected for reverse offset on a foreland vergent fault system. Toward the NW, surface rupturing is interpreted to the NE of the Hides-Mananda ground deformation zone, particularly around the Hides Anticline, potentially reflecting an increased prevalence of hinterland vergent faults within the sedimentary section. Interestingly, these observations are generally consistent with our understanding of structural style along the length of the PFTB, which transitions from abundant, smaller-wavelength and low-relief foreland vergent structures in the SE to larger-wavelength, high-relief structures comprising abundant backthrusting and triangle-zone faulting in the NW (Figure 1, cf. A-A′/B-B′ and C-C′/D-D′).

However, in apparent disagreement with the interpreted surface rupturing to the North of Hides, GPS measurements indicate that the Hides Anticline was shifted up to 42 cm toward the SW during the 2018 PNG Highlands earthquake sequence (Figure 3a), highlighting the primary influence on ground deformation to be inversion on the underlying NE-dipping Lavani-Kutubu Fault Zone. The surface rupturing in this area may relate to shallower, smaller-scale structures, such as antithetic faults, that have formed as a means of

Figure 7. Schematic perspective view of the Papuan Fold and Thrust Belt and Stable Platform, showing geological and geophysical observations pertinent to the 2018 PNG Highlands earthquake sequence. (a) Composite ascending interferogram (GSI, 2018) with second observation dates of March 12, 2018 (+14 days after mainshock) in the East and May 21, 2018 (+84 days after mainshock) in the West (Figure 4, main). (b) Ascending interferogram (GSI, 2018) with second observation date of February 26, 2018 (+21 h after mainshock) (Figure 4, inset). Ground deformation zones (refer Section 3.2): L, Lavani; H-M, Hides-Mananda; M, Moran; K, Kutubu; C, Cecilia. (c) Regional Bouguer corrected gravity data set comprising high-resolution airborne data merged with open-file land-based data. Airborne gravity data provided by Sander Geophysics, Ottawa, Canada. (d) 30 m SRTM digital elevation model (USGS, 2015). Note the spatial and morphological similarities between the topographic expression of the Darai Plateau and extent of ground deformation during the earthquake sequence. SP, Stable Platform; PFTB, Papuan Fold and Thrust Belt. (e) Schematic block model showing the basement architecture of the northern Australian passive margin. Major fault zones include the Komewu Fault Zone (KFZ), the Darai Fault Zone (DFZ), and the Lavani-Kutubu Fault Zone (LKFZ). Earthquake epicenter colors are consistent with Figure 4.

accommodating deep crustal shortening through the complex mechanical stratigraphy of the Papuan Basin. The complex distribution of ground deformation and surface rupturing during the PNG Highlands earthquake sequence aptly demonstrates the enormous complexity and laterally variable interaction between inverting passive margin architecture and shallow fold and thrust structures. As such, it is unsurprising that structural style is a topic of ongoing debate in the PFTB, and indeed, in fold and thrust belts worldwide.

4.2. Influence of Crustal Structure on Earthquake-Related Stress Release

Another interesting aspect of the 2018 PNG Highlands earthquake sequence relates to the spatial and temporal release of stress during the seismic event and the implications this has for understanding the influences on the evolution of the PFTB. In the ~21 h following the M_w 7.5 mainshock, the aftershock sequence and associated ground deformation formed a NW to SE trend that tracked the deep extensional fault system that we have interpreted beneath the PFTB (e.g., the Lavani-Kutubu Fault Zone; Figure 7, cf. b and e). Seismicity over this period likely represented the propagation of slip into regions that experienced relatively small slip during the mainshock. Interestingly, within the initial 21 h of the earthquake sequence, the general abundance and magnitude of aftershocks and the lateral extent of ground deformation away from the epicentral location were greater to the SE than NW (e.g., Figure 4, inset). We believe this relates to lateral variations in the underlying margin architecture. Indeed, the lower Bouguer gravity anomaly in the East versus the West (Figure 7c) implies that high-density crystalline basement is likely deeper—indicating that the Papuan Basin sediments are thicker and therefore the underlying crust may be more attenuated and weaker than it is in the NW. As a result, it more readily underwent shortening and uplift to accumulate strain, and large seismic events were limited to approximately the first 21 h or so of the earthquake sequence in these areas. In the NW, the sequence impinged on less attenuated and thus stronger crust, which was much more resistant to strain. Following the mainshock, stress accumulated on the basement footwall high in this area, to eventually be released more slowly as a series of large aftershocks to the South and West of the mainshock (e.g., within the Cecilia and Lavani zones), including four >M_w 6 aftershocks between ~2.5 and 41 days after the mainshock. The midcrustal focal depths and moment tensors of these events are similar to the mainshock (Figure 1), leading to our hypothesis that they were either related to: (1) inversion on subsidiary listric extensional faults located inboard (to the SW) of the main extensional fault trend activated during the mainshock (e.g., Figure 1, A-A'), and/or (2) reverse movement on a deep-rooted shortcut thrust within the footwall block of the main extensional fault trend (e.g., Figure 1, B-B'). Interestingly, the hypothesized transition from stronger crust in the West to weaker crust in the East also provides a fitting explanation for the clockwise rotation of the PFTB recognized from modeling of GPS velocities (e.g., Koulali et al., 2015).

Where complex patterns of stress release have been observed within contractional settings, crustal heterogeneities such as changes in composition or structure are most often invoked as the primary controlling factors (e.g., Kato et al., 2006; Mercier et al., 2011). The most significant change in crustal composition on the northern Australian passive margin is the Tasman Line—a transition from stronger Proterozoic lithosphere in the West to weaker Late Palaeozoic crust in the East (e.g., Hill & Hall, 2003). Wang et al. (2020) propose this transition was the principle control on strain partitioning observed during the 2018 PNG Highlands earthquake. But observations from outcrop and well intersections throughout the SP and PFTB in PNG suggest that Palaeozoic and younger basement rocks extend to at least near the PNG-Indonesia border (e.g., Figure 1b in Mahoney et al., 2017), thus the crustal transition begins over 100 km from the western most extent of ground deformation associated with the PNG Highlands earthquake. This leads us to believe that crustal structure, rather than composition, was the primary control on the pattern of stress release and strain partitioning during the PNG Highlands earthquake and we can therefore infer that basement structure has also had a principal role in the evolution of variable structural styles observed throughout the PFTB. Although crustal composition may not have been the primary control on PNG Highland earthquake-related deformation, it likely had an important indirect influence having impacted the form and distribution of basement structure (e.g., the Komewu, Darai, and Lavani-Kutubu fault zones) during the evolution of the margin—an association that is well documented in extensional settings worldwide (e.g., Brune et al., 2017; Kharazizadeh et al., 2017; Smith & Mosley, 1993).

5. Conclusion

Our study of the 2018 M_w 7.5 PNG Highlands earthquake and aftershock sequence has yielded significant insight into the structure and evolution of the PFTB. We have identified and delineated an actively inverting, basin-bounding extensional fault system beneath the PFTB, indicating that the architecture of the northern Australian passive margin has a primary control on structural style. The observed distribution of seismicity and ground deformation is indicative of a thick-skinned system that is both spatially and temporally linked to complex thin-skinned structural styles observed within the thick and mechanically variable sediments of the Papuan Basin. Given the estimated return period for a seismic event of this magnitude is ~150 years (McCue et al., 2018), it is possible that the PFTB has experienced over 30,000 comparably sized events—each associated with similarly complex crustal and ground deformation—during its evolution from the Late Miocene to present. This highlights the true complexity that characterizes the evolution and resulting structural styles of the PFTB. An improved understanding of the PFTB requires that we: (1) accept and embrace the spatiotemporal complexity that has been so well demonstrated during the 2018 PNG Highlands earthquake sequence, (2) acknowledge the limitations of, and challenge the capability of, traditional and generic fold and thrust belt models to account for such complexity, and (3) seek more bespoke solutions—ideally tools and techniques that can incorporate pre-existing anisotropies within the deforming margin, the mechanical stratigraphy of the cover sequence, and the evolving stress conditions under which the fold and thrust belt formed.

Data Availability Statement

Data is available through the USGS National Earthquake Information Centre Earthquake Portal (USGS, 2020) and the Geospatial Information Authority of Japan website (GSI, 2018).

Acknowledgments
This work was funded by Papuan Oil Search and their Joint Venture Partners ExxonMobil and Santos. Luke Mahoney acknowledges support of an Australian Government Research Training Program Scholarship. This study benefited greatly from open-file data and publications by government agencies, particularly the USGS National Earthquake Information Centre and the Geospatial Information Authority of Japan. Special thanks to Gavin Hayes (USGS) and Yu Morishita (formerly GSI) for their guidance and support. The Oil Search Exploration Team is acknowledged for their contribution, particularly Nigel Wilson, Pedro Restrepo-Pace, John Noonan, and Keith Bradey. The authors would also like to thank Marco van der Kooij and Mark Quigley for stimulating initial discussions following the 2018 PNG Highlands earthquake. We appreciate valuable comments and suggestions from two anonymous reviewers.

References

Abers, G., & McCaffrey, R. (1988). Active deformation in the New Guinea fold-and-thrust belt: Seismological evidence for strike-slip faulting and basement-involved thrusting. *Journal of Geophysical Research*, *93*(B11), 13332–13354. https://doi.org/10.1029/jb093ib11p13332

Abers, G. A., & McCaffrey, R. (1994). Active arc-continent collision: Earthquakes, gravity anomalies, and fault kinematics in the Huon-Finisterre collision zone, Papua New Guinea. *Tectonics*, *13*(2), 227–245. https://doi.org/10.1029/93tc02940

Ali, M. Y., Sirat, M., & Small, J. (2009). Integrated gravity and seismic investigation over the Jabal Hafit structure: Implications for basement configuration of the frontal fold-and-thrust belt of the northern Oman Mountains. *Journal of Petroleum Geology*, *32*(1), 21–37. https://doi.org/10.1111/j.1747-5457.2009.00433.x

Altamimi, Z., Métivier, L., Rebischung, P., Rouby, H., & Collilieux, X. (2017). ITRF2014 plate motion model. *Geophysical Journal International*, *209*(3), 1906–1912. https://doi.org/10.1093/gji/ggx136

Amoco. (1982). Lavani 1 well completion report (p. 137).

Ayarza, P., Alvarez-Lobato, F., Teixell, A., Arboleya, M. L., Teson, E., Julivert, M., & Charroud, M. (2005). Crustal structure under the central High Atlas Mountains (Morocco) from geological and gravity data. *Tectonophysics*, *400*(1–4), 67–84. https://doi.org/10.1016/j.tecto.2005.02.009

Bain, J. H. C., Mackenzie, D. E., & Ryburn, R. J. (1975). Geology of the Kubor Anticline, Central Highlands of Papua New Guinea. In Bureau of Mineral Resources, Geology and Geophysics Bulletin (Vol. 155, p. 116). Australian Government Publishing Service.

Baldwin, S. L., Fitzgerald, P. G., & Webb, L. E. (2012). Tectonics of the New Guinea region. *Annual Review of Earth and Planetary Sciences*, *40*, 495–520. https://doi.org/10.1146/annurev-earth-040809-152540

Bennett, D. J., Brand, R. P., Mills, C. R., & Morris, B. D. (2000). Exploration potential of the West Bosavi area, Papuan foreland basin, Papua New Guinea. In P. Buchanan, A. Grainge, & R. Thornton (Eds.), *Petroleum exploration, development, and production in Papua New Guinea: Proceedings of the fourth PNG petroleum convention* (pp. 139–154). Port Moresby: Papua New Guinea Chamber of Mines and Petroleum.

Bonini, M., Sani, F., & Antonielli, B. (2012). Basin inversion and contractional reactivation of inherited normal faults: A review based on previous and new experimental models. *Tectonophysics*, *522-523*, 55–88. https://doi.org/10.1016/j.tecto.2011.11.014

Brown, C. M., & Robinson, G. P. (1982). Kutubu 1:250 000 geological series explanatory notes sheet SB/54-12, geological survey of Papua New Guinea. Port Moresby: PNG Department of Minerals and Energy.

Brune, S., Heine, C., Clift, P. D., & Pérez-Gussinyé, M. (2017). Rifted margin architecture and crustal rheology: Reviewing Iberia-Newfoundland, central South Atlantic, and South China Sea. *Marine and Petroleum Geology*, *79*, 257–281. https://doi.org/10.1016/j.marpetgeo.2016.10.018

Buchanan, J. G., & Buchanan, P. G. (Eds.). (1995). Basin inversion (Vol. *88*, p. 596). Geological Society, London, Special Publications.

Buchanan, P., & Warburton, J. (1996). The influence of pre-existing basin architecture in the development of the Papuan fold and thrust belt: Implications for petroleum prospectivity. In Buchanan P. (Ed.), *Petroleum exploration, development, and production in Papua New Guinea: Proceedings of the third PNG petroleum convention* (pp. 89–109). Port Moresby: Papua New Guinea Chamber of Mines and Petroleum.

Camanni, G., Alvarez-Marron, J., Brown, D., Ayala, C., Wu, Y. M., & Hsieh, H. H. (2016). The deep structure of south-central Taiwan illuminated by seismic tomography and earthquake hypocenter data. *Tectonophysics*, *679*, 235–245. https://doi.org/10.1016/j.tecto.2015.09.016

Camanni, G., Brown, D., Alvarez-Marron, J., Wu, Y.-M., & Chen, H. A. (2013). The Shuilikeng fault in the central Taiwan mountain belt. *Journal of the Geological Society*, *171*(1), 117–130. https://doi.org/10.1144/jgs2013-014

Chong, J. H., & Huang, M. H. (2020). Refining the 2018 Mw 7.5 Papua New Guinea earthquake fault-slip model using subpixel offset. *Bulletin of the Seismological Society of America*, *111*, 1032–1042.
Cooper, M. (2007). Structural style and hydrocarbon prospectivity in fold and thrust belts: A global review, *Special Publication-Geological Society of London*, *272*, 447–472.
Darnault, R., & Hill, K. C. (2020). Four-dimensional analog and geometrical modeling of the Hides anticline, Papua New Guinea: Structure of a giant gas field. *Bulletin*, *104*(4), 961–985. https://doi.org/10.1306/08161918261
Davies, H., & Norvick, M. (1974). Blucher range 1:250 000 geological series explanatory notes sheet SB/54-07. Geological survey of Papua New Guinea. Port Moresby: PNG Department of Minerals and Energy.
DeMets, C., Gordon, R. G., Argus, D. F., & Stein, S. (1994). Effect of recent revisions to the geomagnetic reversal time scale on estimates of current plate motions. *Geophysical Research Letters*, *21*(20), 2191–2194. https://doi.org/10.1029/94gl02118
Eisenberg, L. I. (1996). Strontium isotope analysis and structural interpretation of P'nyang Anticline, Papuan Fold belt, Western Highlands Province, Papua New Guinea. In Buchanan P. (Ed.), *Petroleum exploration, development, and production in Papua New Guinea: Proceedings of the third PNG petroleum convention* (pp. 231–244). Port Moresby: Papua New Guinea Chamber of Mines and Petroleum.
Findlay, A. L. (1974). The structure of foothills south of the Kubor Range, Papua New Guinea. *The APPEA Journal*, *14*(1), 14–20. https://doi.org/10.1071/aj73002
Gabriel, A. K., Goldstein, R. M., & Zebker, H. A. (1989). Mapping small elevation changes over large areas: Differential radar interferometry. *Journal of Geophysical Research*, *94*(B7), 9183–9191. https://doi.org/10.1029/jb094ib07p09183
Gee, L. S., & Leith, W. S. (2011). The global seismographic network: U.S. *Geological Survey Fact Sheet*, *2011–3021*, 2.
Ghasemi, H., Itikarai, I., Hazelwood, M., Mckee, C., & Allen, T. (2018). A low-cost seismic network for Papua New Guinea. In Paper presented at Australian Earthquake Engineering Society 2018 Conference Extended Abstract (p. 10). Perth, Australia.
Giddings, J. A., Aden, L. J., Darby, B. J., Leech, D. L., Lyons, D. Y., Djakic, A. L., et al. (2020). The Muruk gas field: Insights into structural style in the western foldbelt of Papua New Guinea. In Paper presented at AAPG/EAGE 1st Petroleum Geoscience Conference and Exhibition, PNG's Oil and Gas Industry Maturing through Exploration, Development and Production (p. 4). Port Moresby.
Groves, D. I., Goldfarb, R. J., Gebre-Mariam, M., Hagemann, S. G., & Robert, F. (1998). Orogenic gold deposits: A proposed classification in the context of their crustal distribution and relationship to other gold deposit types. *Oregeology Reviews*, *13*(1–5), 7–27. https://doi.org/10.1016/s0169-1368(97)00012-7
GSI. (2018). The 2018 Papua New Guinea Earthquake: Crustal deformation detected by ALOS-2 data. Geospatial Information Authority of Japan. Retrieved from https://www.gsi.go.jp/cais/topic180301-index-e.html
Hanani, A., Lennox, P., & Hill, K. (2016). The geology and structural style of the Juha gas field, Papua New Guinea. *ASEG Extended Abstracts*, *2016*, 1–7. https://doi.org/10.1071/aseg2016ab272
Hill, K. C. (1991). Structure of the Papuan Fold belt, Papua New Guinea. *American Association of Petroleum Geology Bulletin*, *75*, 857–872.
Hill, K. C., Bradey, K., Iwanec, J., Wilson, N., & Lucas, K. (2008). Structural exploration in the Papua New Guinea Fold Belt. In J. E. Blevin, B. E. Bradshaw, & C. Uruski (Eds.), *Eastern Australian Basins Symposium III* (pp. 225–238). Petroleum Exploration Society of Australia, Special Publication.
Hill, K. C., & Hall, R. (2003). Mesozoic-Cenozoic evolution of Australia's New Guinea margin in a west Pacific context (pp. 265–290). Geological Society of America. Special Papers.
Hill, K. C., Kendrick, R. D., Crowhurst, P. V., & Gow, P. A. (2002). Copper-gold mineralisation in New Guinea: Tectonics, lineaments, thermochronology and structure. *Australian Journal of Earth Sciences*, *49*(4), 737–752. https://doi.org/10.1046/j.1440-0952.2002.00944.x
Hill, K. C., Lucas, K., & Bradey, K. (2010). Structural styles in the Papuan Fold Belt, Papua New Guinea: Constraints from analogue modelling. In G. Goffey (Ed.), Hydrocarbons in contractional belts (Vol. 348, pp. 33–56). Geological Society, London, Special Publications.
Hill, K., & Mahoney, L. (2018). Compressional evolution of the PNG margin from an orogenic transect from Juha to the Sepik. *ASEG Extended Abstracts*, *2018*(1), 1–3. https://doi.org/10.1071/aseg2018abt5_3a
Hill, K. C., Norvick, M., Keetley, J., & Adams, A. (2000). Structural and stratigraphic shelf-edge hydrocarbon plays in the Papuan Fold Belt. In P. Buchanan, A. Grainge, & R. Thornton (Eds.), *Petroleum exploration, development, and production in Papua New Guinea: Proceedings of the fourth PNG petroleum convention* (pp. 67–85). Port Moresby: Papua New Guinea Chamber of Mines and Petroleum.
Hill, K. C., & Raza, A. (1999). Arc-continent collision in Papua Guinea: Constraints from fission track thermochronology. *Tectonics*, *18*(6), 950–966. https://doi.org/10.1029/1999tc900043
Hill, K. C., Simpson, R., Kendrick, R., Crowhurst, P., O'Sullivan, P., & Saefudin, I. (1996). Hydrocarbons in New Guinea, controlled by basement fabric, Mesozoic extension and tertiary convergent margin tectonics. In Buchanan P. (Ed.), *Petroleum exploration, development, and production in Papua New Guinea: Proceedings of the third PNG petroleum convention* (pp. 63–76). Port Moresby: Papua New Guinea Chamber of Mines and Petroleum.
Hinsch, R., Asmar, C., Nasim, M., Abbas, M. A., & Sultan, S. (2019). Linked thick- to thin-skinned inversion in the central Kirthar Fold Belt of Pakistan. *Solid Earth*, *10*(2), 425–446. https://doi.org/10.5194/se-10-425-2019
Hirata, N., Sato, H., Sakai, S. i., Kato, A., & Kurashimo, E. (2005). Fault system of the 2004 Mid Niigata Prefecture Earthquake and its aftershocks. *Landslides*, *2*(2), 153–157. https://doi.org/10.1007/s10346-005-0050-8
Hobson, D. M. (1986). A thin skinned model for the Papuan thrust belt and some implications for hydrocarbon exploration. *The APPEA Journal*, *26*(1), 214–225. https://doi.org/10.1071/aj85021
Jenkins, D. A. L. (1974). Detachment tectonics in western Papua New Guinea. *Geological Society of America Bulletin*, *85*(4), 533–548. https://doi.org/10.1130/0016-7606(1974)85<533:dtiwpn>2.0.co;2
Jiang, Z., Huang, D., Yuan, L., Hassan, A., Zhang, L., & Yang, Z. (2018). Coseismic and postseismic deformation associated with the 2016 Mw 7.8 Kaikoura earthquake, New Zealand: Fault movement investigation and seismic hazard analysis. *Earth, Planets and Space*, *70*(1), 62. https://doi.org/10.1186/s40623-018-0827-3
Jordan, T. H., & Sverdrup, K. A. (1981). Teleseismic location techniques and their application to earthquake clusters in the south-central Pacific. *Bulletin of the Seismological Society of America*, *71*(4), 1105–1130.
Kao, H., & Chen, W. P. (2000). The Chi-Chi earthquake sequence: Active, out-of-sequence thrust faulting in Taiwan. *Science*, *288*(5475), 2346–2349. https://doi.org/10.1126/science.288.5475.2346
Kato, A., Sakai, S. I., Hirata, N., Kurashimo, E., Iidaka, T., Iwasaki, T., & Kanazawa, T. (2006). Imaging the seismic structure and stress field in the source region of the 2004 mid-Niigata prefecture earthquake: Structural zones of weakness and seismogenic stress concentration by ductile flow. *Journal of Geophysical Research*, *111*(B8), 18. https://doi.org/10.1029/2005jb004016
Kato, A., Sakai, S., Sakai, S., Kurashimo, E., Igarashi, T., Iidaka, T., et al. (2008). Imaging heterogeneous velocity structures and complex aftershock distributions in the source region of the 2007 Niigataken Chuetsu-oki Earthquake by a dense seismic observation. *Earth, Planet and Space*, *60*(11), 1111–1116. https://doi.org/10.1186/bf03353145

Kawagle, S. A., & Meyers, J. B. (1996). Structural and sequence geometry of the Kiunga area, Papuan foreland basin, Papua New Guinea. In Buchanan P. (Ed.), *Petroleum exploration, development, and production in Papua New Guinea: Proceedings of the third PNG petroleum convention* (pp. 175–193). Port Moresby: Papua New Guinea Chamber of Mines and Petroleum.

Keetley, J. T., Hill, K. C., & Nguyen, C. (2001). Mesoscopic fold and thrust structures at Cape Liptrap, Victoria, Australia—A PNG analogue? PESA eastern Australasian Basins Symposium (pp. 179–186). Petroleum Exploration Society of Australia Special Publication.

Kennett, B. L. N., Engdahl, E. R., & Buland, R. (1995). Constraints on seismic velocities in the Earth from travel times. *Geophysical Journal International*, *122*(1), 108–124. https://doi.org/10.1111/j.1365-246x.1995.tb03540.x

Kharazizadeh, N., Schellart, W. P., Duarte, J. C., & Hall, M. (2017). Influence of lithosphere and basement properties on the stretching factor and development of extensional faults across the Otway Basin, southeast Australia. *Marine and Petroleum Geology*, *88*, 1059–1077. https://doi.org/10.1016/j.marpetgeo.2017.08.034

Koulali, A., Tregoning, P., McClusky, S., Stanaway, R., Wallace, L., & Lister, G. (2015). New insights into the present-day kinematics of the central and western Papua New Guinea from GPS. *Geophysical Journal International*, *202*(2), 993–1004. https://doi.org/10.1093/gji/ggv200

Lacombe, O., & Bellahsen, N. (2016). Thick-skinned tectonics and basement-involved fold–thrust belts: Insights from selected Cenozoic orogens. *Geological Magazine*, *153*(5–6), 763–810. https://doi.org/10.1017/s0016756816000078

Mahoney, L., Hill, K., McLaren, S., & Hanani, A. (2017). Complex fold and thrust belt structural styles: Examples from the Greater Juha area of the Papuan Fold and Thrust Belt, Papua New Guinea. *Journal of Structural Geology*, *100*, 98–119. https://doi.org/10.1016/j.jsg.2017.05.010

Mahoney, L., Mclaren, S., Hill, K., Kohn, B., Gallagher, K., & Norvick, M. (2019). Late Cretaceous to Oligocene burial and collision in western Papua New Guinea: Indications from low-temperature thermochronology and thermal modelling. *Tectonophysics*, *752*, 81–112. https://doi.org/10.1016/j.tecto.2018.12.017

Mason, R. A. (1996). Structure of the Western Papuan Fold Belt. In P. Buchanan (Ed.), *Petroleum exploration, development, and production in Papua New Guinea: Proceedings of the third PNG petroleum convention* (pp. 161–173). Papua New Guinea Chamber of Mines and Petroleum.

McConachie, B., Lanzilli, E., Kendrick, D., & Burge, C. (2000). Extensions of the Papuan Basin Foreland geology into Eastern Irian Jaya (West Papua) and the new Guinea Fold Belt in Papua New Guinea. In Buchanan P., Grainge A., & Thornton R. (Eds.), *Petroleum exploration, development, and production in Papua New Guinea: Proceedings of the fourth PNG petroleum convention* (pp. 219–238). Papua New Guinea Chamber of Mines and Petroleum.

McCue, K., Gibson, G., & Love, D. (2018). The mainshock of 25 February 2018 and aftershocks in the Central Highlands of Papua New Guinea. In Australian Earthquake Engineering Society 2018 Conference Extended Abstract, Perth, Australia (p. 23).

Medd, D. M. (1996). Triangle zone deformation at the leading edge of the Papuan fold belt. In Buchanan P. (Ed.), *Petroleum exploration, development, and production in Papua New Guinea: Proceedings of the third PNG petroleum convention* (pp. 217–229). Port Moresby: Papua New Guinea Chamber of Mines and Petroleum.

Mercier de Lépinay, B., Deschamps, A., Klingelhoefer, F., Mazabraud, Y., Delouis, B., Clouard, V., et al. (2011). The 2010 Haiti earthquake: A complex fault pattern constrained by seismologic and tectonic observations. *Geophysical Research Letters*, *38*(22), 7. https://doi.org/10.1029/2011gl049799

Nemcok, M., Schamel, R., & Gayer, R. (2005). Thrustbelts: Structural architecture, thermal regimes and petroleum systems (p. 541). Cambridge University Press.

Pigram, C. J., & Symonds, P. A. (1991). A review of the timing of the major tectonic events in the New Guinea Orogen. *Journal of Southeast Asian Earth Sciences*, *6*(3–4), 307–318. https://doi.org/10.1016/0743-9547(91)90076-a

Poblet, J., & Lisle, R. J. (2011). Kinematic evolution and structural styles of fold-and-thrust belts. *Geological Society, London, Special Publications*, *349*(1), 1–24. https://doi.org/10.1144/sp349.1

Rosen, P. A., Hensley, S., Joughin, I. R., Li, F. K., Madsen, S. N., Rodriguez, E., & Goldstein, R. M. (2000). Synthetic aperture radar interferometry. *Proceedings of the IEEE*, *88*(3), 333–382. https://doi.org/10.1109/5.838084

Schofield, S. (2000). The Bosavi Arch and Komewu Fault Zone: Their control on basin architecture and the prospectivity of the Papuan Foreland. In Buchanan P., Grainge A., & Thornton R. (Eds.), *Petroleum exploration, development, and production in Papua New Guinea: Proceedings of the fourth PNG petroleum convention* (pp. 101–122). Port Moresby: Papua New Guinea Chamber of Mines and Petroleum.

Smith, M., & Mosley, P. (1993). Crustal heterogeneity and basement influence on the development of the Kenya Rift, East Africa. *Tectonics*, *12*(2), 591–606. https://doi.org/10.1029/92tc01710

Snyder, D. B., & Barazangi, M. (1986). Deep crustal structure and flexure of the Arabian plate beneath the Zagros collisional mountain belt as inferred from gravity observations. *Tectonics*, *5*(3), 361–373. https://doi.org/10.1029/tc005i003p00361

Stanaway, R., Mahoney, L., Noonan, J., & McLaren, S. (2020). Neotectonics of the Papuan Fold and Thrust Belt—Insights from space geodetic analysis. In *Paper presented at 2020 AAPG/EAGE 1st Petroleum Geoscience Conference and Exhibition, PNG's Oil and Gas Industry Maturing through Exploration, Development and Production* (p. 8). Port Moresby.

Stanaway, R., & Noonan, J. W. (2015). Geodetic measurement of deformation within the Papuan Fold and thrust belt. 2015 International Conference and exhibition (p. 114). Melbourne, Australia: Society of Exploration Geophysicists and American Association of Petroleum Geologists.

Stern, R. J., Scholl, D. W., & Fryer, G. (2016). An introduction to convergent margins and their natural hazards. In *Plate boundaries and natural hazards* (pp. 77–98).

Thornton, R. C. N., Emmett, J. K., Lyslo, J. A., & Gottschalk, R. R. (1996). Integrated structural and stratigraphic analysis in PPL 175, Papuan Fold Belt, Papua New Guinea. In Buchanan P. (Ed.), *Petroleum exploration, development, and production in Papua New Guinea: Proceedings of the third PNG petroleum convention* (pp. 195–215). Port Moresby: Papua New Guinea Chamber of Mines and Petroleum.

Tregoning, P., Lambeck, K., Stolz, A., Morgan, P., McClusky, S. C., van der Beek, P., et al. (1998). Estimation of current plate motions in Papua New Guinea from global positioning system observations. *Journal of Geophysical Research*, *103*(B6), 12181–12203. https://doi.org/10.1029/97jb03676

USGS. (2015). Shuttle radar topography mission, 1-arc second, global land cover facility. University of Maryland. Retrieved from https://earthexplorer.usgs.gov/

USGS. (2018). United States geological survey events page: M 7.5—83km SW of Porgera. Earthquake Hazards Program. Retrieved from https://earthquake.usgs.gov/earthquakes/eventpage/us2000d7q6

USGS. (2020). United States geological survey earthquake portal. Earthquake Hazards Program. Retrieved from https://www.usgs.gov/natural-hazards/earthquake-hazards/earthquakes

van Ufford, A. Q., & Cloos, M. (2005). Cenozoic tectonics of New Guinea. *Bulletin*, *89*(1), 119–140. https://doi.org/10.1306/08300403073

Vera, E. A. R., Folguera, A., Valcarce, G. Z., Giménez, M., Ruiz, F., Martínez, P., et al. (2010). Neogene to Quaternary extensional reactivation of a fold and thrust belt: The Agrio belt in the Southern Central Andes and its relation to the Loncopué trough (38–39 S). *Tectonophysics*, *492*(1–4), 279–294.

Wallace, L. M., Stevens, C., Silver, E., McCaffrey, R., Loratung, W., Hasiata, S., et al. (2004). GPS and seismological constraints on active tectonics and arc-continent collision in Papua New Guinea: Implications for mechanics of microplate rotations in a plate boundary zone. *Journal of Geophysical Research*, *109*, B05404. https://doi.org/10.1029/2003jb002481

Wang, S., Xu, C., Li, Z., Wen, Y., & Song, C. (2020). The 2018 Mw 7.5 Papua New Guinea Earthquake: A possible complex multiple faults failure event with deep-seated reverse faulting. *Earth and Space Science*, *7*(3), e2019EA000966. https://doi.org/10.1029/2019ea000966

White, L. T., Morse, M. P., & Lister, G. S. (2014). Lithospheric-scale structures in New Guinea and their control on the location of gold and copper deposits. *Solid Earth*, *5*(1), 163–179. https://doi.org/10.5194/se-5-163-2014

WHO. (2018). Papua New Guinea earthquake. World Health Organisation. Retrieved from https://www.who.int/westernpacific/emergencies/papua-new-guinea-earthquake

Worden, C. B., Gerstenberger, M. C., Rhoades, D. A., & Wald, D. J. (2012). Probabilistic relationships between ground-motion parameters and modified Mercalli intensity in California. *Bulletin of the Seismological Society of America*, *102*(1), 204–221. https://doi.org/10.1785/0120110156

Xu, X., Wen, X., Yu, G., Chen, G., Klinger, Y., Hubbard, J., & Shaw, J. (2009). Coseismic reverse- and oblique-slip surface faulting generated by the 2008 Mw 7.9 Wenchuan earthquake, China. *Geology*, *37*(6), 515–518. https://doi.org/10.1130/g25462a.1

Zhang, X., Feng, W., Du, H., Li, L., Wang, S., Yi, L., & Wang, Y. (2020). The 2018 Mw 7.5 Papua New Guinea earthquake: A dissipative and cascading rupture process. *Geophysical Research Letters*, *47*(17), 10. https://doi.org/10.1029/2020gl089271